MODAL MODELS OF CONVECTION.

by

NICHOLAS H. BRUMMELL

May 1988

A thesis submitted for the degree of
Doctor of Philosophy
of the
University of London
and the
Diploma of Imperial College

Applied Mathematics Section
Department of Mathematics
Imperial College of Science and Technology
London
SW7 2BZ

ABSTRACT.

Convection in a viscous, incompressible fluid under the Boussinesq approximation is studied using modal approximations, where a complete set of basis functions satisfying the periodic, horizontal boundary conditions is truncated at some finite number of modes to reduce the partial differential equations of the problem to a system of ordinary differential equations for the vertically dependent variables. Stress-free and constant temperature vertical boundary conditions close the system, and the resulting two-point boundary value problem is solved to fourth order accuracy on the mesh by a Newton-Raphson-Kantorovich method.

A two-dimensional, steady solution of fully non-linear, penetrative convection is calculated under a quadratic equation of state like that of the ice-water problem. For low amplitudes of convection it was found that for Prandtl numbers only two orders of magnitude below that of water, the system exhibited supercritical behaviour in comparison to the normal subcritical behaviour, with lower heat transport, different cell geometry and a strong influence of the vorticity. The vorticity at lower Prandtl number couples the main convecting cell with the overlying counter-cells, which are no longer passively conductive. This Prandtl number dependence, unseen in 2-D Rayleigh-Benard convection, leads to the breakdown of an earlier model of the system and so adjustments to this model are made.

The 2-D influence of vorticity suggest that a 3-D model is needed to include the full vorticity vector. A modal calculation in 3-D requires some subset of the horizontal modes, so harmonics of two of the usual horizontal planforms, the hexagon and the square, are investigated algebraically via the non-linear terms of the Navier-Stokes equations. At third order and above, the Christopherson hexagonal planform is found to generate an inherent vertical vorticity component, whereas squares never do. The planforms and their vertical vorticity components are presented up to order five. The relationship to the Helmholtz equation is also investigated.

Using the complete set of horizontal basis functions up to fourth order, 3-D Rayleigh-Benard convection is investigated modally, for both hexagonal and square convection. Inclusion of the vertical vorticity for hexagons does not produce strong horizontal motions at low amplitudes, but does affect the mean quantities of the flow such as the heat transport and the temperature profile. Low order truncations are shown to be inaccurate even for such mean quantities. Both squares and hexagons show a strong but different Prandtl number dependence, and the cellular nature of the flows, particularly the squares, becomes clouded at low σ.

ACKNOWLEDGEMENTS.

I would like to express my appreciation to my supervisor Dr. Dan Moore who first introduced me to this subject and who then subsequently spent a great deal of his time and energy helping me. I am greatly indebted to him for his ever cheerful and patient guidance, and it is his enthusiasm that has always stimulated my interest.

I would also like to express my appreciation to the staff, secretaries and students of the Mathematics Department of Imperial College as a whole, who have constantly supplied knowledge and moral support at the times when they were needed. In particular, I would like to thank Professor J.T.Stuart for his advice and guidance during Dan's absence, and would also like to express my appreciation of the efforts of Geoff and Gary Reason to get the computer systems running as smoothly as possible in the Mathematics Department. Thanks are also due to my partners-in-crime Susan, Mike, Gillian, Seamus, Panaghis, Ric, Bob and all the others for buying the drinks, answering the phone, sharing the misery, telling the jokes and for putting up with various outbursts and outrages in the terminal rooms.

A special mention must go to all the people concerned with the computational side of my work. I would like to thank Neil Readwin for being the person who stimulated my interest in computer systems rather than just number-crunching, and who increased my knowledge, and therefore my ability to work, considerably. This led to an association with College Computer Centre via part-time work at Program Advisory and brought me many fruitful contacts. I would like to thank especially Mike Nock for being my understanding, ever-helpful boss, Thomas Sippel-Dau for allowing excursions into his vast knowledge and Nick James for being particularly understanding of my VAX needs and for laughing at my e-mail.

Thanks are also due to Dr. Steve Piacsek for allowing me the pleasure of working with him in Italy for three months, and to the organisers of the Woods Hole Geophysical Fluid Dynamics Summer Study Program for allowing me to attend in 1986, particularly to Professor Ed Spiegel and Dr. Bill Young for enlightening discussions concerning Chapter 4.

A special thank-you goes to a good friend, Steve Herbert, without whom the copies of this thesis would not have been so colourful.

Due credit must also go to Alison and my parents for understanding.

Finally, I should like to thank the Science and Engineering Research Council for supplying the funds for this project.

For my parents.

TABLE OF CONTENTS.

Abstract....2
Acknowledgements....3
Table of contents....5

Chapter 1. Introduction.

1.1. The real world....8
1.2. The scientific world....9
1.3. The scope of the present work....10
1.4. Previous work....12
1.5. Aims of the current work and model chosen....16

Chapter 2. Formulation of the modal model.

2.1. The equations of convection....19
2.2. Vorticity-streamfunction form....20
2.3. The dimensionless numbers....21
2.4. The boundary conditions....23
2.5. The modal model.
    2.5.1. The basis....25
    2.5.2. Numerical methods....27

Chapter 3. Non-linear, low Prandtl number penetrative convection.

3.1. Abstract....30
3.2. Introduction....30
3.3. The formulation of the model.
    3.3.1. The equation of state....33
    3.3.2. The 2-D streamfunction....33
    3.3.3. The boundary conditions....36
    3.3.4. The modal equations....38
    3.3.5. The computational methods.
        3.3.5.1. Grids and number of modes....42
        3.3.5.2. Eigenvalues....43
        3.3.5.3. The solution process....45
        3.3.5.4. A linear initial guess....45
        3.3.5.5. Recovery of a finite amplitude approximation from a linear solution....46
        3.3.5.6. Scaling through parameter space....49
        3.3.5.7. The parameter space searched....50

3.4. Results and discussion.
3.4.1. The effect of modal truncations.....50
3.4.2. The Prandtl number dependence.
3.4.2.1. High Rayleigh numbers, low heat transport.....54
3.4.2.2. The Moore and Weiss model.....60
3.4.3. Low Prandtl number flow.
3.4.3.1. Flow characteristics - ψ, ω and T.....66
3.4.3.2. Critical Prandtl numbers.
3.4.3.2.1. The expansion.....77
3.4.3.2.2. Calculation of R_2 and the solvability condition.....81
3.4.3.2.3. Computational methods.....85
3.4.3.2.4. The results.
a) Cross-checking with previous solutions....87
b) Critical values of the Prandtl number.....90
3.4.4. Variation with cell geometry.....99
3.4.5. Extension of the Moore and Weiss model.....104
3.5. Summary and conclusions.....105

Chapter 4. Planform modes for 3-D convection.
4.1. Abstract.....107
4.2. Introduction.....107
4.3. Method of approach.....110
4.4. Discussion.
4.4.1. The individual harmonics of the hexagon.....112
4.4.2. Superposition of hexagonal harmonics.....128
4.4.3. Square planform harmonics.....136
4.4.4. Solutions of the Helmholtz equation.....139
4.5. Conclusions.....151

Chapter 5. Three-dimensional Rayleigh-Benard convection.
5.1. Abstract.....153
5.2. Introduction.....153
5.3. Formulation of the model.
5.3.1. The equation of state.....159
5.3.2. The 3-D streamfunctions.....159
5.3.3. The modal equations.....160
5.3.4. The boundary conditions.....165

5.3.5. The computational methods.
5.3.5.1. Grids and number of modes.....168
5.3.5.2. Eigenvalues and parameters.....169
5.3.5.3. The solution process.....170
5.3.5.4. FIRST system initial guess.....171
5.3.5.5. Recovery of higher order solutions from lower order solutions.....173
5.3.5.6. Scaling through parameter space.....174
5.3.5.7. The parameter space searched.....175
5.4. Results and discussion.
5.4.1. The effects of the various modal truncations.
5.4.1.1. Hexagonal horizontal periodicity.....176
5.4.1.2. Square horizontal periodicity.....222
5.4.2. The Prandtl number dependence.
5.4.2.1. Hexagonal horizontal periodicity.....244
5.4.2.2. Square horizontal periodicity.....271
5.4.3. The Nusselt number dependence.....285
5.4.4. The wavenumber dependence.....294
5.4.5. A comparison of the hexagonal and square horizontal periodicities.....301
5.5. Conclusions.....306

Chapter 6. Summary and conclusions.....311

Appendix 1. Formulation of adjoint problems.....316

Appendix 2. Other work undertaken during thesis period.....321

References.....322

Microfiche.

CHAPTER 1

INTRODUCTION.

1.1. The real world.

Convection is arguably the most abundant fluid flow in the Universe, and occurs in many forms and over widely disparate scales, from the everyday world to the faraway outer reaches of the stars. Rooms are heated by convection from a source, water is boiled by turbulent convection and convection occurs in an evaporating puddle. The Earth's atmosphere is warmed by convection from ground-absorbed radiation, and the world's weather is then governed by convection, both on a large scale in convection current circulation, and on a local scale in the form of thermals and down-draughts. Also in the atmosphere, meterologists find convection theories applicable to the dynamics of cumulus clouds (Simpson, Simpson, Andrews and Eaton (1965)). In the oceans, mixing of various water masses involves convection in both the large scale circulation (e.g Phillips (1966)) and in small scale doubly-diffusive effects such as salt-fingering (see Double Diffusion chapter in Turner (1973)). Tectonic processes in the Earth's crust, including Continental Drift, are convection driven, and even deeper in the Earth, it is also likely that the dynamo action of convective flows in the liquid core of our planet give rise to its geomagnetic field. At the other extreme, observations (Danielson (1966)) and numerical calculations (Schwarzchild (1958)) show that almost every star possesses a convecting layer, be it interior for hot stars, or exterior, as for cool stars such as our sun. Many of the motions observed in the outer stable regions of the Sun are widely believed to be manifestations of motions in the lower solar convection zone (for a review, see Leighton (1963)). Convection is also of fundamental importance in some less natural situations, inside nuclear reactors, chemical reaction chambers and solar heating panels, for example.

If we are to be able to understand any of these phenomena, then we must first understand the basic processes of convection to some extent. In order to predict the weather, to understand the circulation of the oceans and their distributions of salinity and temperature, to calculate the size and ages of stars, and to estimate the movements of the Earth's mantle, we must first understand convection and be able to use it as a tool in the complicated models of these common physical situations.

Convection is also of outstanding importance in the ever growing field of the study of turbulence. Convection provides an easily accessible experimental

transition to turbulence, and many surprising and remarkable results have been forthcoming. The transition to convection is one of the simplest hydrodynamic stability problems, and the cellular nature of convective patterns in the various regimes allows a dimension of beauty and aesthetic appeal into the study, often not available in other courses of research, providing instant motivation for such work.

However, convection is still a complex process, and the physical situations that are the aim of all studies involving convection are extremely difficult to attain. A real problem is three-dimensional and time-dependent. The fluid must be compressible and allow for all the small scale complex processes which drive such flows, such as ionisation, molecular diffusion, opacity, conductivity, viscosity and surface tension. These processes are affected by the type of fluid and the environment, such as the temperature, and allowances should be made for this. Next, most realistic situations are bounded in some way, and so edge effects must be taken into account. Then, large scale external influences, such as rotation, electromagnetic fields and gravity must be brought to bear on the system, in order to allow for the planetary motion and its effects. A solution of such a problem must also be able to account for phenomena on many different scales, for example, in the ocean, where small double diffusive effects, measured in meters, large eddies, measured in kilometers, and the Coriolis effects of the Earth's rotation, which affects the general hemispherical circulation must all be included. Similar scales may be involved in the time-dependence, where, for example, in modelling the Sun, a full model should be capable of displaying steady features such as granulation and super-granulation, medium time-scale flares, right up to the 22 year sunspot cycle.

1.2. The scientific world.

Obviously, analytical techniques will not solve this general problem in the near future, if at all. Numerical calculations still struggle to model a complete picture despite the increasing computer power available today. The most feasible method of approach is to simplify the problem and to hope that reasonable approximations will lend some physical or quantitative insight into the overall situation. A technique may be developed to explore a simple model as extensively as possible, whereafter, having gained experience of the technique and its limitations, along with some knowledge of the simplified model, conditions may be relaxed to give a more physical situation and a more sophisticated model. In this way, scientific knowledge is built up from a wide and therefore sound base. New phenomena will

hopefully be found as new techniques are experimented with, and more complete sophisticated models are attacked, but the basis of such a body of research is the rigid core of understanding, underlying all other knowledge, and it is this which must be made secure.

1.3. The scope of the present work.

It is with these aims in mind, that this thesis sets out to advance some of the more fundamental knowledge of convection systems, paying due respect to the fact that the basics are fairly far-removed from reality.

In this case, the general features of convection are of primary interest. For example, the effect of the geometry of the problem or the shape and type of the boundaries on the flow, are considered far less important than more fundamental ideas such as the form of the instability and the relation between the degree of the instability and the resultant convective transport of heat. Hence, a much simplified model is considered.

For astrophysical applications, a compressible model is required, but this is considered as one extra degree of difficulty which may be incorporated into a model if possible at a later stage. The models used herein consider fluids which are incompressible in nature. The fluid is assumed to be homogeneous and confined to an infinite horizontal layer held between two parallel boundaries. An assumption is made on the nature of the physical constants in the equations describing the heat transfer and the velocity fields, which states that the relative temperature changes are going to be small, and thus temperature differences and density changes are only important in so far as they affect the main convective driving terms, and do not affect the conductivity or viscosity of the fluid. This approximation is due to Oberbeck (1879) and Boussinesq (1903) independently, and is therefore known as the the Oberbeck-Boussinesq approximation, or just simply as the Boussinesq approximation. Rigorous descriptions can be found in Chandrasekhar (1962) or Spiegel and Veronis (1960), but see also the book of Drazin and Reid (1981).

Convection occurs in a viscous fluid when temperature differences between sections of the fluid become such that the density changes induced can produce buoyancy forces sufficient to overcome the frictional forces of viscous dissipation and diffusion. At this point, heat transfer changes from complete conduction to include convection. The simplest dynamical model of a convection process is Rayleigh-Benard convection, where the infinite horizontal layer of viscous fluid is

heated from below. Here, under the Boussinesq approximation, the equation of state describes the density as a linear function of the temperature difference between the upper and lower boundary, and, since this is adverse, denser fluid lies above less dense, providing a potential gravitational instability, which may be released if the temperature difference becomes great enough. This process has been the starting point for all convection studies and many results are well established since the process has been studied by a variety of authors using many different techniques. However, there are aspects of even this fundamental convection problem which are not fully understood, and there are possibly some that have not been encountered at all.

An obvious step towards a more physical model is to allow a convecting region to be bounded by stable regions. This has many applications, such as in the Sun, where the convection zone is buried below outer stable zones, in meterology where convection induced at ground level by re-radiation from the earth is topped by stable atmospheric zones, or in oceanography, where convecting layers near the weather-influenced surface may sit on stably stratified lower layers. This is an obvious step mathematically as well, because it can be modelled by a relaxation of the equation of state from a simple linear profile to a quadratic dependence of the density on temperature, providing that the temperature differences are not too great. Then, depending on the nature of the quadratic dependence and the applied temperature gradients, some of the fluid layer is stably stratified and some unstably, and so a gravitational instability may manifest itself in the unstable layer, if conditions are right. Motions may then overshoot the (imaginary) boundary between the two regions, exhibiting 'penetrative' convection, and important questions arise as to the effect of the overlying region on the heat transport, the degree of penetration and the scales of motion.

This is a much less explored area in convection, but fortunately has a physically tractable natural example, since water has the required anomalous quadratic density dependence. Water has a density maximum near 3.98°C, and thus if a layer of water has its bottom boundary at a temperature lower than 3.98°C and its upper boundary at a temperature greater than 3.98°C, then the layer below the maximum density is unstably stratified, whereas the layer above is stable. Thus, if the temperature gradient across the whole layer is increased past a critical value, convection will occur in the lower layer and may then penetrate into the upper. This situation may be easily modelled by having a layer of water overlying ice, in what is known as the 'ice-water' experiment.

The new work presented here concentrates on simple models of both the more complicated ice-water system in a two-dimensional calculation, and the easier Rayleigh-Benard situation in a more complex three-dimensional calculation. The

aim of the original project was to study penetrative convection from an astrophysical viewpoint, but as always, a standardisation and testing for the three−dimensional problem was necessary on the more simple Rayleigh−Benard problem. It was found that this had not been comprehensively covered in certain areas by previous models, and so this calculation had to be completed before the required penetrative simulation could begin. Unfortunately, the limitations of three years doctoral study did not allow time for a fully three−dimensional penetrative calculation, because the equivalent Rayleigh−Benard calulation proved more productive than expected.

1.4. Previous work.

It is not the intention of the author to give a comprehensive literature survey here, as that alone would provide a sizeable monograph, but rather to give a guide to the more important texts, relevant to the thesis herein, and to offer some pointers to review and other motivating articles which may be abundant sources of further information. Work closely related to the present will be referenced within the text.

The subject started with the early experiments of Thomson (1882) and Benard (1900,1901), who reported very regular cellular patterns occuring in thin layers of various fluids, including melted spermaceti and paraffin, heated from below. The aesthetic quality of the hexagonal cells that appeared effectively stimulated the whole interest in the subject, although convection had been recognized earlier by Count Rumford (1797). Benard established that a critical temperature gradient across the layer was necessary for convection to set in, and that when it does, convection manifests itself in a cellular pattern. Ironically, the experiments performed were later shown to be actually driven by surface tension effects rather thermal, so that Benard's experiments are in fact not Rayleigh−Benard convection. Lord Rayleigh (1916) formulated the linear stability problem and found the critical value of the non−dimensional number, thereafter known as the Rayleigh number, for the onset of convection, considering a two−dimensional cellular pattern, known as rolls, and also square and cylindrical planforms, between free boundaries (i.e. modelled as if the fluid were bounded by another fluid, not a rigid wall). Hence, this type of convection, where a layer of fluid is heated from below became known as Rayleigh−Benard convection. Jeffreys (1926,1928) advanced the linear theory to different cell geometries and different boundary conditions, and Pellew and Southwell (1940), continuing into other geometries, showed by

separation methods that the full problem reduced to a planform problem as the solution of a Helmholtz equation for the horizontal functions, and a vertical problem. For more details on the linear stability problems of convection, study the books of Chandresekhar (1961), Salzman (1962) and Gershuni and Zhukovitskii (1976).

Non-linear analysis of the Rayleigh-Benard problem was begun by Gorkov (1957) and Malkus and Veronis (1958) who independently introduced perturbation methods to the problem. Malkus and Veronis expanded the equations as sequences of the linear eigenfunctions of the problem, valid for any planform, but only near marginal stability, thus rendering finite amplitude solutions available from the linear solutions. To be able to infer stability results, they introduced the arbitrary condition that the most stable solution had the maximum root-mean-square temperature gradient, and consequently found that squares were the preferred planform near the critical Rayleigh number, that for Rayleigh numbers less than ten times the critical, the Rayleigh number was linearly proportional to the measure of the heat transport, the Nusselt number, and that the horizontal wave number increased with increasing Rayleigh number.

Schluter, Lortz and Busse (1965) continued the stability analysis and showed that three-dimensional cells can be unstable to infinitesimal disturbances for rigid or free boundary conditions, and that there existed a parameter range where only two-dimensional rolls are stable, albeit for a restricted range of wavenumbers (Busse (1967)). The question of preferred planform and the stability of particular modes of convection is an endless topic for research, which has been attacked by Busse and various co-workers. For a review of these findings, see Palm (1975) or Busse (1978). If the temperature-independence constraint on viscosity is relaxed, then vertically asymmetrical layers are immediately allowed, and hexagons become the preferred mode (Graham (1933), Palm (1960), Segel and Stuart (1962)). One striking point is that hexagons in gases are observed to have descending centres, whereas in liquids the centres would rise (g- and l-hexagons respectively). This was neatly demonstrated to be due to the change of viscosity with temperature, which has an opposite dependence in liquids and gases, by Tippelskirch (1956). Tippelkirch experimented with liquid sulphur, whose variation of viscosity with temperature flips sign at 153°C. The direction of the vertical velocity in the central region of his experiments also changed at this point, thus proving the theory.

The importance of one non-linear effect is thus shown, and another which was treated fairly rigorously is that of the surface tension effects on a free surface of the convecting layer. It was found by Pearson (1958) and subsequently others (e.g. Koschmeider (1967)) that the original photographs of Benard showed surface

tension driven cells rather than convection driven cells since the layer he experimented with was far too thin to support convection. However, the non−linear selection mechanism for this type of cells is the same as for convective cells, and so the relevance of the experiments and the importance of hexagonal cells is not lost.

Early observational data came from the meteorological side, with cells shown in clouds by Phillips and Walker (1932) and Brunt (1952). Schmidt, working with Milverton (1935) carried out experiments to confirm the critical Rayleigh number calculations, and, with Saunders (1938) gathered heat transport data. Many authors worked on the relationship between the Rayleigh number and the Nusselt number, including Schmidt and Saunders (1938), Malkus (1954a), Globe and Dropkin (1959), Fitzjarrald (1975) and Threlfall (1975). A review of heat transport results is given in Rossby (1969). The transitions between modes was also a popular experimental area, with the transition between hexagons and rolls exhibited by Silveston (1958) and Somerscales and Dougherty (1970), and further transitions shown by the detailed work of Krishnamurti (1968,1970a,b,1973), and Busse and Whitehead (1974).

Highly non−linear effects in Rayleigh−Benard convection have also received much attention with the increase in desire for models of turbulence. Experiments were performed by Willis and Deardorff (1965,1967), but the majority of advances came from the numerical efforts. Deardorff (1964) and Fromm (1965) modelled steady, two−dimensional effects for free or rigid boundaries using finite difference techniques. Veronis (1966) used a Galerkin method for non−linear rolls on a fairly wide parameter range, with the Rayleigh number up to thirty times critical, for free boundaries, and similar work was done for rigid boundaries by Busse (1967b). The parameter range was extended to much higher Rayleigh numbers by Schneck and Veronis (1967), Plows (1971), Moore and Weiss (1973) and Clever and Busse (1974) with the emphasis on calculating the correct empirical relationship between the Rayleigh number and the Nusselt number. Even on todays computers, computation of a fully three−dimensional flow is barely viable, and so calculations are limited to specific examples or simplified three−dimensional models. Lipps (1976) worked in detail on time−dependent convection in air at moderate Rayleigh numbers specifically, and Jones, Moore and Weiss (1976) calculated axisymmetrical flows. A popular method of attacking the non−linear problem has been to adopt a mean−field or a mixing−length approach. The mixing−length theory is astrophysically based and reviews can be found in Kraichnan (1962) and Gough (1977). The mean−field approach simplifies the governing equations considerably by neglecting all non−linear interactions apart from those which interact with mean flow properties. In this way, the highly turbulent non−linear effects arising from

purely non−linear interactions are ignored in favour of the more important interactions between non−linear and mean quantities. This approach has been taken by Herring (1963,1964), Howard (1965), Roberts (1966) and Stewartson (1966), but the theory is only valid for high Prandtl numbers, and tends to overestimate the heat flux. This method is the most severe truncation of a modal method, and less devastating truncations, which have proved to be a reasonable basis for calculation for they allow the Prandtl number to become a real parameter again, have been explored by Roberts (1966) and various permutations of the authors Gough, Toomre and Spiegel (Gough, Spiegel and Toomre (1975), Toomre, Gough and Spiegel (1977), Toomre, Gough and Spiegel (1982)), who calculated simple modal equation solutions. This thesis extends this line of work in a similar but more expansive format for the three−dimensional calculations of Rayleigh−Benard convection.

The body of literature on penetrative convection is minimal in comparison with the work on Rayleigh−Benard convection. The 'ice−water' experiment was proposed by Malkus (1960) and has been carried out by many authors since then including Furumoto and Rooth (1961), Townsend (1964), Myrup et al. (1970) and Adrian (1975). The theoretical discussion was started by Veronis (1963), who investigated the linear problem by a perturbation method in the same way as Malkus and Veronis (1958) had done for ordinary convection. Veronis found a criterion for the onset of convection similar to that found by Lord Rayleigh (1916) for Rayleigh−Benard convection, but also showed that the system was unstable to finite amplitude disturbances at Rayleigh numbers below the critical value for linear instability. This finite amplitude instability was explained in terms of the driving force of penetrative convection, the distortion of the mean temperature profile, and the resultant effective Rayleigh number which is thus caused, which may be higher than the normal Rayleigh number, thus allowing convection to set in at lower levels. Similar stability criteria were calculated by Sparrow, Goldstein and Jonsson (1963) for other boundary conditions. The non−linear problem was first treated by Musman (1968) who numerically found the lowest Rayleigh number for which convection could occur, calculated the heat transport in terms of the Nusselt number and clarified Veronis's explanation of the finite amplitude instability. His work was based on the mean−field equations and thus overestimated the heat flux, as was subsequently shown by Moore and Weiss (1973b). Moore and Weiss formulated a simple model of penetrative convection by taking a basic driving cell, found on the basis of effective Rayleigh and Nusselt numbers, and using this coupled with flux matching conditions to calculate heat transport results for many penetrative geometries. They also numerically explored the onset of non−linear convection, obtaining good agreements with their model, and then extended the

work to include time−dependence and the more unusual fixed−flux boundary conditions. The model, however, was calculated only for moderate Prandtl number, and this thesis extends this work to low Prandtl number regimes, showing that the flow behaviour is distinctly different.

Other experiments have been carried out by Deardorff, Willis and Lilly (1969) and Whitehead and Chen (1970), where stably bounded convecting layers have been observed to grow with time to steady states. The astrophysical world has also produced some literature on solar penetration, where the calculations usually work with compressible fluids, and, for these, the reader is pointed to works by combinations of the authors Hurlburt, Latour, Massaguer, Toomre, Weiss and Zahn (e.g. Massaguer, Latour, Toomre and Zahn (1984), Hurlburt, Toomre, Massaguer (1984, 1986), Hurlburt and Toomre (1987), Massaguer and Zahn (1980)) and for a review, to Moore (1981).

1.5. Aims of the project and the model chosen.

The project undertaken was to carry out a numerical investigation of penetrative convection with an astrophysical slant. The full non−linear equations were to be solved in some manner, without recourse to drastic simplifications such as those of the mean−field approximation. The main parameter of interest was to be the Prandtl number and the effect of lowering the Prandtl number away from the previously explored moderate and high regimes, as encountered in the 'ice−water' experiments, towards a more astrophysical region, was to be studied.

For such a task, a computational model was required which offered simplicity and a small budget at the expense of greater analytical and physical understanding. To solve the fully non−linear partial differential equations of convection in finite difference form would require on the order 10^4 points for two−dimensions and on the order of 10^6 points for three dimensions, and so models would require a sizeable time and memory allocation for even a single run, let alone enough runs to cover a complete parameter space. Hence, the modal method of solution, first formulated from an idea by Lorenz (1963), and later used extensively by many authors such as Baker and Spiegel (1975) and Gough, Spiegel and Toomre (1975, 1977, 1982), was chosen. This method involves the specification of the solution to the horizontal problem, assuming that the full equations are solvable in separable form, as an expansion in Fourier−type modes. The correct solution to this, the planform problem, would involve an infinite set of modes, but for computational viability, this set of modes must be truncated at some finite value. This truncation

is in itself a matter for contemplation, and truncations must be made with regard to the type of solution required. Having specified some truncated solution of the horizontal problem, then the computational effort can be concentrated on accurately solving the ordinary differential equations which are produced for the vertically dependent variables as a two point boundary value problem. Hence, we have to solve a much simpler numerical problem, although extra work is necessary to achieve a sensible model in the first place. Modal models offer a method very similar to the perturbation type method as used by many, including Malkus and Veronis (1958) and Veronis (1966) in that an expansion is truncated at some order, but are more accurate since no linearisation of the equations takes place. These methods are also universally applicable unlike mixing-length theories which can only be applied in the absence of external influences such as rotation, penetration and variable density. A modal representation is also more sophisticated than a mean-field approach, since it will allow full non-linearity and thus will not suppress important effects such as a Prandtl number dependence.

Free boundaries were used throughout to relate to the astrophysical situations where fluid layers would more than likely be bounded by other fluid layers, rather than the experimental laboratory set up involving rigid boundaries. Rigid boundaries would provide a greater influence of the Prandtl number from the viscous boundary layers that appear, but the greater simplicity of the free boundaries makes them the chosen conditions here.

Less astrophysically, the fluid was assumed to be incompressible and Boussinesq and was not investigated at high Rayleigh numbers. The reason for the latter was that sufficient new material was found in the simple states at marginal and moderate Rayleigh numbers to conduct a reasonable discussion of the relevance of previous models.

All calculations are assumed steady state, time dependence being a further complication which could be explored at a later date.

Thus, the work in this thesis is constructed as follows. After this introduction, a general description of the equations of convection is given, along with a more precise definition of the modal type model. The third chapter then uses these models to explore fully non-linear, two-dimensional, steady penetrative convection. The results of this calculation lead to the need for a three-dimensional calculation, and so Chapter Four examines the requirements of the modal procedure for three dimensions. This proves to be more extensive than previously found, involving vertical vorticity in a previously unseen, natural way, and the chapter goes on to discuss the physical implications of these findings and relates them to more general situations. Chapter Five then uses the modal analysis of Chapter Four for two common planforms, the hexagon and the square, to explore fully non-linear

Rayleigh–Benard convection for low Prandtl numbers, moderate Rayleigh numbers and a range of wavenumbers. The impact of the new modal expansions is discussed. Chapter Six draws the conclusions from the whole work, and offers guidance as to the possibilities of extensions of this work and their physical implications.

CHAPTER 2

FORMULATION OF THE MODAL MODEL.

2.1. THE EQUATIONS OF CONVECTION.

The governing equations for convection in a viscous, incompressible fluid are a conservation of momentum equation, in the form of the usual Navier–Stokes equations, including a buoyancy driving term:

$$\frac{\partial \mathbf{u}}{\partial t} + (\mathbf{u}.\nabla)\mathbf{u} = - \frac{\nabla p}{\rho_0} + \frac{\rho \mathbf{g}}{\rho_0} + \nu \nabla^2 \mathbf{u} \quad , \qquad [2.1]$$

the continuity equation,

$$\nabla . \mathbf{u} = 0 \quad , \qquad [2.2]$$

and a diffusion equation for heat,

$$\frac{\partial T}{\partial t} + (\mathbf{u}.\nabla)T = \kappa \nabla^2 T \quad , \qquad [2.3]$$

where $\mathbf{u}$ is the vector velocity field, p is the pressure field, $\mathbf{g}$ is the gravitational field, t is the time, T is the scalar temperature, ρ is the density, ρ_0 is the maximum density, ν is the dynamic viscosity and κ is the thermometric conductivity. Typically, $\mathbf{g}$ is taken to be $\mathbf{g} = - g \mathbf{k}$, where $\mathbf{k}$ is the unit vector in the vertical direction.

These equations are formulated under the Boussinesq approximation (Oberbeck (1879), Boussinesq (1903)). This approximation assumes that the temperature differences across the infinite, horizontal layer of fluid in question are small, and therefore the density varies little, despite the fact that it is buoyancy that is driving the motion. The density variations are then neglected everywhere in the problem except in this driving buoyancy term, where the order of magnitude of the term is significantly larger due to the gravitational multiplicative factor.

The equation of state of the viscous fluid may be written as

$$\rho = \rho_0 (1 - \alpha F(T)) \quad , \qquad [2.4]$$

where α is the constant coefficient of expansion, and is small (on the order of 10^{-3} for a gas, and 10^{-4} for an experimental liquid). The variations of the thermodynamic constants, ν and κ, are of the same order or even smaller

(Chandresakhar (1961)), and therefore can be neglected. For a formal justification of the above approximations, see Spiegel and Veronis (1960) or Mihaljan (1962).

The nature of the temperature dependence is specified by F(T) in the equation of state, and is now what distinguishes the two different types of convection studied in this thesis. The Rayleigh−Benard case is governed by the linear form

$$\rho = \rho_0 (1 - \alpha_r (T-T_0)) \quad , \qquad [2.5]$$

whereas the penetrative form is quadratic

$$\rho = \rho_0 (1 - \alpha_p (T-T_0)^2) \quad , \qquad [2.6]$$

where T_0 is the temperature of the maximum density.

2.2. VORTICITY−STREAMFUNCTION FORM.

Calculations on these equations may be made with the equations in the above form, but it is often thought preferrable to work in a non−primitive variable formulation involving streamfunction and vorticity vectors, since this may enable solution of a system involving less variables, and with a different physical interpretation available.

Since the velocity field is divergence−free or solenoidal in the absence of sources and sinks, the velocity may be expresses as a curl, thus

$$\mathbf{u} = \mathrm{curl}(\psi) = \nabla \times \psi \quad , \qquad [2.7]$$

where ψ is the vector potential

The vorticity field is then defined by

$$\omega = \mathrm{curl}(\mathbf{u}) = \nabla \times \mathbf{u} \quad . \qquad [2.8]$$

Now, taking the curl of equation [2.1], using gravity as stated earlier and using equation [2.4] eliminates the explicit dependence on the pressure field, and produces a vorticity equation

$$\frac{\partial \omega}{\partial t} + (\mathbf{u}.\nabla) \omega - (\omega.\nabla) \mathbf{u} = \alpha g \, \mathrm{curl}(F(T) \, \mathbf{k}) + \nu \nabla^2 \omega \quad , \qquad [2.9]$$

where the other two non−linear terms $\mathbf{u}(\nabla.\omega)$ and $\omega(\nabla.\mathbf{u})$ from the curl of the $(\mathbf{u}.\nabla)\mathbf{u}$ drop out since $\nabla.\nabla\times$ (i.e div curl) is always identically zero and by [2.2], respectively. The first of the remaining non−linear terms represents the convection of vorticity by velocity, and the second corresponds to the tilting and stretching of vortex lines.

The equations [2.3] and [2.9], together with equations [2.7] and [2.8] combined, forms a viable system of equations for the three unknowns, ψ, ω and T. This system is then non−dimensionalised by choosing natural scales for length, temperature and time. Choose a distance, d (usually the distance between the upper and lower boundaries of the fluid or the distance across the unstable layer), as a typical length scale, and a temperature, ΔT (usually the temperature difference across d), as a typical temperature scale. Also choose the thermal diffusion time, d^2/κ, as a typical time increment, so that

$$\mathbf{x} = (x, y, z) = d\mathbf{x}' = (dx', dy', dz') \quad , \qquad [2.10]$$

$$T = T_0 + \Delta T.T' \quad , \qquad [2.11]$$

$$t = \frac{d^2}{\kappa} t' \quad . \qquad [2.12]$$

Then, the dimensionless system of equations becomes, on dropping all the primes on the dimensionless variables,

$$\frac{\partial \omega}{\partial t} + (\mathbf{u}.\nabla)\omega - (\omega.\nabla)\mathbf{u} = \frac{g\alpha d^3 (\Delta T)^i}{\kappa^2} \mathrm{curl}(F(T)\mathbf{k}) + \frac{\nu}{\kappa} \nabla^2\omega \quad , \qquad [2.13a]$$

or

$$\frac{1}{\sigma} \left[\frac{\partial \omega}{\partial t} + (\mathbf{u}.\nabla)\omega - (\omega.\nabla)\mathbf{u} \right] = \frac{g\alpha d^3 (\Delta T)^i}{\kappa\nu} \mathrm{curl}(F(T)\mathbf{k}) + \nabla^2\omega \quad , \qquad [2.13b]$$

$$\frac{\partial T}{\partial t} + (\mathbf{u}.\nabla)T = \nabla^2 T \quad , \qquad [2.14]$$

$$\omega = \nabla \times \mathbf{u} \quad , \qquad [2.15]$$

$$\mathbf{u} = \nabla \times \psi \quad , \qquad [2.16]$$

where i = 1 for Rayleigh−Benard convection, and i = 2 for penetrative convection, and F(T) is now simply F(T) = T for Rayleigh−Benard convection, or

$F(T) = T^2$ for penetrative convection.

2.3. THE DIMENSIONLESS NUMBERS.

Two dimensionless numbers are apparent from the above equations. The first is the ratio of the dynamic viscosity to the thermometric conductivity, and is therefore simply a characteristic of the fluid. This ratio is known as the Prandtl number,

$$\sigma = \frac{\nu}{\kappa} \quad , \qquad [2.17]$$

and may be interpreted as the ratio of the diffusion of momentum to the diffusion of heat.

The second is an extension of Lord Rayleigh's (1916) dimensionless number, the Rayleigh number,

$$Ra = \frac{g\alpha d^3 (\Delta T)^i}{\kappa \nu} \quad , \qquad [2.18]$$

where $i = 1$ for Rayleigh–Benard convection, and $i = 2$ for penetrative convection.

The Rayleigh number is the product of a potential energy term, derived from the unstable temperature gradient,

$$\frac{g\alpha (\Delta T)^i}{d} \quad ,$$

and two internal dissipative terms,

$$\frac{d^2}{\nu} \text{ and } \frac{d^2}{\kappa} \quad .$$

Hence, the Rayleigh number is a measure of the strength of the instability, balanced against the frictional forces of the problem, and so an increasing Rayleigh number means an increase in the rate of release of potential energy or the removal of dissipative forces, both of which will tend to destabilise a system.

Define also a measure of the efficacy of convection, the Nusselt number as the ratio of the heat flux that is carried after convection has begun, to that which would be carried by conduction alone. Thus,

$$Nu = \frac{G}{\kappa} \frac{d}{(\Delta T)} \quad , \qquad [2.19]$$

where G is the horizontally–averaged thermometric flux. Note that the Nusselt number would be unity if there was no convection i.e. heat transport was by conduction alone.

Including these constants into the complete set of equations, and assuming that a steady state solution is required, produces the system

$$(\mathbf{u}.\nabla)\omega - (\omega.\nabla)\mathbf{u} = Ra\, \sigma\, curl\, (f(T)\mathbf{k}) + \sigma \nabla^2 \omega \quad , \qquad [2.20]$$

$$(\mathbf{u}.\nabla)T = \nabla^2 T \quad , \qquad [2.21]$$

$$\omega = \nabla \times \mathbf{u} \quad , \qquad [2.22]$$

$$\mathbf{u} = \nabla \times \psi \quad . \qquad [2.23]$$

It was decided to search for steady solutions only, since these states, or a tendency towards these states, are often found in many cases in experiments (e.g Krishnamurti (1970)) and in numerical simulations (Veronis (1966), Gough, Toomre and Spiegel (1975)), and the problem of following a time evolution of the convection would extend the scope of this thesis considerably.

2.4. THE BOUNDARY CONDITIONS.

The fluid is assumed to be confined between two horizontal, infinite planes, situated at vertical positions z_l for the lower plane, and z_u for the upper plane, and hence there can be no flow through these planes. This specifies that the vertical velocity at z_l and z_u must be zero i.e. if

$$\mathbf{u} = (u, v, w),$$

then

$$w = 0 \text{ at } z = z_l, z_u \quad . \qquad [2.24]$$

There are two possible types of boundary at z_l and z_u. These horizontal boundaries may be actual physical boundaries, such as the rigid walls of a tank experiment where the fluid is held underneath a lid. Such conditions are known as rigid boundary conditions and they specify, since the fluid is viscous, that the

tangential velocities as well as the vertical velocity must also be zero along the boundaries, so that in general,

$$u = 0 \text{ at } z = z_l, z_u \quad . \qquad [2.25]$$

This condition demands the formation of viscous boundary layers within the flow, which may affect the flow pattern and heat transport drastically, and so this boundary condition is disregarded in favour of the more astrophysical free boundary condition. Here the fluid in question is not bounded by physical boundaries as in the experimental situation, but is bounded by another fluid, as would be the case in the atmospheres of stars, where convection takes place in a layer of fluid buried in the many layers of the stars outer zones. Equation [2.24] still holds, but now the other condition is not one of 'no slip' but one of 'no stress', because a free surface requires that the perturbations of stress are zero. A formal perturbation explanation can be found in Drazin and Reid (1981), but the outcome of this assumption is that a free surface acts as a rigid surface (hence [2.24] holds once again) with tangential slip but no tangential stress. The boundary condition is thus a more physical constraint, pertaining to astrophysical conditions, where fluids are bounded by other fluids, but is not completely equivalent to these conditions, since interfacial disturbances and gravity waves which may exist on real fluid−fluid boundaries have been suppressed. The tangential components of the stress, s_{xz} and s_{yz}, are

$$s_{xz} = \frac{\partial w}{\partial x} + \frac{\partial u}{\partial z} \quad ,$$

$$s_{yz} = \frac{\partial w}{\partial y} + \frac{\partial v}{\partial z} \quad ,$$

and so, since $w = 0$ at $z = z_l, z_u$, the no−stress condition reduces to

$$\frac{\partial u}{\partial z} = \frac{\partial v}{\partial z} = 0 \text{ at } z = z_l, z_u \quad . \qquad [2.26]$$

Notice that, if the vorticity is written as $\omega = (\omega_1, \omega_2, \omega_3)$ then the definition of vorticity coupled with [2.26] implies that

$$\omega_1(z_l) = \omega_1(z_u) = 0 \quad , \qquad [2.26a]$$

$$\omega_2(z_l) = \omega_2(z_u) = 0 \quad , \qquad [2.26b]$$

$$\frac{\partial \omega_3(z_l)}{\partial z} = \frac{\partial \omega_3(z_u)}{\partial z} = 0 \quad , \qquad [2.26c]$$

and, by differentiating the continuity equation with respect to z, that

$$\frac{\partial^2 w(0)}{\partial z^2} = \frac{\partial^2 w(1)}{\partial z^2} = 0 \quad . \qquad [2.26d]$$

Boundary conditions on the temperature field are specified by assuming that the horizontal limiting planes are held at constant temperatures, so that

$$T = T_l \text{ at } z = z_l \quad , \qquad [2.27a]$$

$$T = T_u \text{ at } z = z_u \quad . \qquad [2.27b]$$

A possibly more physical boundary condition would be to specify that the heat flux across the boundaries is constant, but the above was chosen for numerical simplicity, with a view to incorporating the more complex boundary conditions at a later stage.

The problem is now fully determined.

2.5. THE MODAL MODEL.

2.5.1. The basis.

The cellular nature of convection has been known from the onset of the subject with the experiments of Benard, and so it is reasonable to assume that instead of studying an infinite extent of the fluid layer, a single, isolated cell may be examined in the belief that this unit will repeat itself across the complete region. This amounts to saying that the horizontal structure of the problem is periodic.

Examination of the linear problem shows that it may be assumed to be separable, so that any scalar variable or vector component may be written in the form

$$A = A'(z)\, f(x,y)\, e^{st} \quad , \qquad [2.28]$$

where A is a general scalar variable, A' is the vertical dependence of A and is unknown, and f is the horizontal dependence, which will be the same for all variables. Substitution of [2.28] in the governing equations shows f(x,y) to be determined by the Helmholtz or membrane equation,

$$\nabla_h^2 f = - \alpha^2 f \quad , \qquad [2.29]$$

where ∇_h is the horizontal Laplacian,

$$\nabla_h = \frac{\partial^2}{\partial x^2} + \frac{\partial^2}{\partial y^2} \quad ,$$

and where α can be interpreted as a real horizontal wavenumber.

Hence it is possible to use the periodic assumption to intuitively specify the horizontally dependent function, f, derived from the linear problem, and then, assuming that these horizontal scales will still hold true, the solution of the full problem may be reduced to a simplified problem involving only the vertical and time dependences. To specify f, it can be expanded as a Fourier−type series of orthogonal functions, f_n, which satisfy the horizontal, periodic boundary conditions, and then this may be truncated at some appropriate stage to allow a limited rather than infinite set of equations to close the problem. This method is known variably as a Galerkin technique or a modal method, and will be referred to as the latter here. The general variable of [2.28] would then look like

$$A = e^{st} \sum_{n=0}^{N<\infty} A_n'(z) \; f_n(x,y) \quad . \qquad [2.30]$$

The e^{st} may be ignored, since for initial simplicity, steady state solutions will be sought. Substitution of such forms for the variables ψ, ω and T into the governing equations and boundary conditions, multiplication by the appropriate f_n's and horizontal averaging (i.e. effectively picking out those parts of the full equations which purport to each f_n separately) reduces the full partial differential equations to a system of ordinary differential equations for the vertically dependent variables ($A_n(z)$ in the general description) and a corresponding set of boundary conditions. Hence, now, the computational effort can be concentrated on solving this system as accurately as possible.

It is implicitly assumed, since the above method is exact if an infinite number of horizontal modes are taken, that if N is suitably large enough, then the solution to this process is a reasonable approximation to the true solution i.e that as N is increased then the solution obtained at each N is better in some sense than the previous so that the solution is converging onto the true solution with increasing N. The 'cascade' type procedure described below allows simple checking of this fact.

2.5.2. Numerical methods.

The problem has now been reduced by the above procedure to a system of possibly high order ordinary differential equations plus boundary conditions. This system may be reduced to a larger system of first order ordinary differential equations by the inclusion of the higher order derivatives as intermediate variables. Hence, the final outcome is a one-dimensional system of first-order, ordinary differential equations between two boundaries, and these may be solved by any normal two-point boundary value methods. For the purpose of this thesis, an existing solver code of a Newton-Raphson-Kantorovich method, known as NRK (Readwin (1986)), was used. The code replaces the differential equations by finite difference approximations, which are single step i.e. based on a mesh point and its neighbour. The finite difference equations, a generalisation of Simpson's Rule, for the problem

$$\frac{dy}{dx} = f(x,y)$$

are

$$y_{i+1}-y_i = \frac{h}{6}\left\{ f(x_i,y_i) + f\left[\frac{(x_{i+1}+x_i)}{2}, z_{i+1/2}\right] + f(x_{i+1},y_{i+1}) \right\},$$

where

$$z_{i+1/2} = \frac{y_{i+1/2}}{2} + \frac{y_i}{2} - \frac{h_i}{8}\left(f(x_{i+1},y_{i+1}) - f(x_i,y_i) \right),$$

$$h_i = x_{i+1} - x_i \quad .$$

The set of algebraic equations produced are iterated by a Newton-Raphson method until the required convergence criteria are reached. This scheme is fourth order accurate on the mesh spacing, and further details may be found in Cash and Moore (1980). The convergence criterion used for all the calculations contained in this thesis is that

$$\text{Error} = \sum_{i=1}^{ID} \text{abs}\left[\frac{\max\ (\delta Y^i)}{\text{range}\ (Y^i)} \right] < 10^{-10},$$

where Y^i, $i = 1,..,ID$, are the variables of the ordinary differential equations and δY^i is the change in value of the variable Y^i over the iteration. Thus,

convergence is considered to be achieved when all the (suitably scaled) maximum components of the variables are below a certain limit, which was, in general, set to the order of 10^{-10}.

The major problem of this method is that some initial guess of the solution on the whole mesh has to be provided for the scheme to calculate the corrections and iterate, and this is not necessarily a simple matter when the solution field may involve up to 74 variables. This is overcome by adopting a 'cascade' approach to the modal solution. Firstly, a very severe truncation of the modal equations is used. This may be a single mode model (N = 1 in [2.30]) of the non−linear equations − a mean−field type solution − or it may be a simple model of the linear problem. This problem is formulated and a solution calculated from knowledge of the form of the vertical eigenvectors of this simple problem. Then, a less severe truncation of the equations is modelled, and, for an initial guess of the solution of this more complicated problem, a suitably scaled and extended version of the first problem is used (the scalings and extensions are described later). Then an even less severe truncation is implemented and the second−type solution is modified to act as the initial input for this problem. Thus the process continues until the required truncation is attained. If a relatively 'inactive', i.e. nearly conductive, solution is used initially, then convergence may be achieved without enormous strain. This process has the advantage that a complete guess at the whole complicated, full truncation is never needed, and that the lower orders often offer comparisons with previous work. It also offers a simple guide to the efficiency and usability of the modal solutions, for one truncation can be compared to the next, and the differences in the flows and heat fluxes etc. may be calculated and used in a decision as to whether a higher order truncation is necessary for an accurate solution of the problem, i.e the convergence towards a true solution with increasing N can be examined. In general, in this thesis, a modal truncation was deemed a suitable approximation if the calculated Rayleigh number in the higher amplitude, more non−linear regions did not differ from the next available truncation by more than 5%, or if the next truncation did not fit into the available computer resources, whichever came first. These conditions are less stringent than some, for example, Bolton and Busse (1984), who required a 1% agreement between one truncation and the next.

Once one solution has been found for a particular truncation, the parameter space can then be thoroughly searched by incrementing the parameter of interest and using a suitable scaling of the previous solution (same truncation, different parameters) as an initial guess for the new solution field. Obviously, the accuracy of the scaling and the variability or robustness of the solution are of paramount importance in the choice of increment in parameter space, the simple

scaling procedure being less likely to cope with the more active high amplitude, non−linear regimes, where the solution will be changing rapidly, than near to the linear, critical solution. The particular initial guesses, scalings, and truncations utilised for the different problems are described in the relevant chapters.

The NRK solver is already fourth order accurate but also allows for sixth order and eighth order deferred correction of the solution by the method of Cash (1983). It also allows the problem to be solved for 'eigenvalues' (where the word eigenvalues when related to the NRK package means eigenvalues in the Gough and Moore sense i.e. 'overall system parameters') simultaneously with the full solution, provided that appropriate extra boundary conditions may be applied. This utility is used in all the present work so that a slightly unusual method of solution may be employed. In most explorations of convection, the level of instability is set i.e. the Rayleigh number is given a fixed value, and then the heat flux is computed as the Nusselt number. Here, the Nusselt number is fixed and included as an extra boundary condition to the system by specifying that the gradient of the mean temperature at the lower boundary must equal this Nusselt number, and this enables the corresponding Rayleigh number to be sought as an eigenvalue of the equations. Which approach is more physical is arguable, but both are reasonable and the method used allows results in previously unstable portions of the Nusselt−Rayleigh number parameter space to be found (see Chapter 3).

The vertical grid used was always equally spaced since free boundaries had been chosen to eliminate the growth of viscous boundary layers, and the range of Nusselt numbers considered was sufficiently limited to prevent the formation of any sub−grid size boundary layers. The grids were always sufficient according to Aziz and Hellums (1966) and the cautious estimates of Moore and Weiss (1973a), since the Nusselt number never strayed above the value Nu = 3.0 and the Rayleigh number was kept moderate. Indeed, the grids were much more refined in the three−dimensional model of Rayleigh−Benard convection in Chapter 4.

CHAPTER 3.

NON-LINEAR, LOW PRANDTL NUMBER, PENETRATIVE CONVECTION.

3.1. ABSTRACT.

Fully non-linear penetrative convection in a viscous, incompressible fluid between free boundaries in two dimensions was investigated using a modal representation of the horizontal dependencies, whilst solving the vertical problem accurately by numerical techniques. The effect of the Prandtl number was followed for Rayleigh numbers close to the critical and for low Nusselt numbers and it was found that for Prandtl numbers only two orders of magnitude lower than the original ice-water experiment, the system exhibited supercritical behaviour in comparison to the normal subcritical behaviour for higher Prandtl numbers, with lower heat transport, different cell geometry and a much stronger influence of the vorticity. The vorticity at lower Prandtl number couples the main convecting cell with the overlying counter-cells, which are no longer passive. This Prandtl number dependence is not seen in ordinary 2-D Rayleigh-Benard convection and leads to the breakdown of an earlier model of penetrative convection.

3.2. INTRODUCTION.

Convection in a layer of viscous fluid occurs in the presence of an unstable density gradient. In general, conventional fluids have a positive coefficient of thermal expansion so that warmer fluid is less dense than cooler, and so, if a layer of such fluid is heated from below or cooled from above, then less dense fluid lies under colder, more dense fluid. Then the consequent gravitational instability requires buoyancy forces to act in an attempt to rectify this state, and a circulation develops if the temperature instability is strong enough to overcome viscous diffusion and dissipation. This process, where a layer of fluid is heated from below, is the most commonly studied form of convection, and is known as Rayleigh-Benard convection after the early experiments of Benard (1900), and the first theory by Lord Rayleigh (1916).

A slightly less common situation may be investigated, where this layer of convecting fluid is not constrained by some physical upper boundary, but lies below

another layer of fluid which is initially stable in nature. Now the convective motions caused by the instability are no longer confined solely to its own layer, but may overshoot or penetrate into the originally stable layer in what is known as penetrative convection. The degree of mixing, the extent of penetration and the effects on the stable layer are of considerable interest in many physical situations. For example, in astrophysics, motions are observable in the outer stable regions of the sun which are assumed to be related to motions in the solar convection zone below (for summary, see Leighton (1963)). In meteorology, the dynamics of cumulus clouds show similar penetrative effects (Simpson, Simpson, Andrews and Eaton (1965)) and general atmospheric convection, where ground warmed air rises aloft into stably stratified regions, may also be considered as penetrative. In the ocean, convection under the thermocline may also be of this type (Phillips (1966)).

There exists an easily accessible model of penetrative convection in the 'ice−water experiment'. This was proposed by Malkus (1960) and has been carried out since by Furumoto and Rooth (1961), Townsend (1964), Myrup et al. (1970) and Adrian (1975), and exhibits penetration as a consequence of the peculiar quadratic equation of state of water. If a layer of water overlies ice, then its lower boundary will be fixed at $0^{o}C$. If the upper boundary is maintained at a temperature greater than $3.98^{o}C$ then there exists a maximum of the density in the fluid layer near $3.98^{o}C$. Thus, there is a gravitationally stable layer (between approximately $4^{o}C$ and the upper temperature) overlying an unstable layer (between $0^{o}C$ and approximately $4^{o}C$). Now any convective motions in the lower layer may penetrate into the upper layer.

The theoretical discussion of this problem was started by Veronis (1963) who investigated the linear problem by perturbation expansion techniques and found a criterion for the onset of convection similar to that found originally by Lord Rayleigh for Rayleigh−Benard convection (Rayleigh (1916)). Veronis also showed that the system was unstable to finite amplitude disturbances at Rayleigh numbers below the critical predicted by linear theory. The non−linear problem was later treated by Musman (1968) who numerically found the lowest Rayleigh number for which steady convection could occur, calculated the heat transport as a function of Rayleigh number and also clarified Veronis's explanation of the instability, by using a numerical model involving the mean−field approximations (Herring (1963), Spiegel (1967,1971)) where the non−linear terms generally associated with turbulence are omitted.

Moore and Weiss (1973b) (hereafter known as MW) continued by formulating a simple model which allowed the distortion of the mean temperature profile (the driving force behind the finite amplitude instability, according to Veronis (1963)

and Musman (1968)) and which balanced the convective and conductive fluxes. Very good agreement with their own numerical results was achieved. The Rayleigh number for the onset of non−linear penetrative convection was calculated more accurately, and heat transport results showed Musman's mean−field results to be over−estimates. They also extended the work from the usual fixed temperature boundary conditions to the fixed flux case, and investigated time dependence.

Matthews (1988) investigated a different model of penetrative convection where the unstable layer is bounded above and below by two stable regions and the convection is driven by a cubic mean temperature profile, using amplitude equation techniques. The model is different from the Veronis or ice−water model (apart from the physical setup) in that Matthews uses a non−linear temperature profile with a linear equation of state unlike the model here which uses a linear temperature profile and a non−linear equation of state. The ice−water models fix the temperature difference across the unstable regions but allow its depth to vary, whereas Matthews allows the temperature to vary, so that the 'S' profile is eroded. Using this model, it is found that convection leaves the conductive state via a supercritical bifurcation for all Prandtl numbers, whereas the ice−water model here may be sub− or super−critical depending upon σ.

In this chapter, penetrative convection in a two−dimensional layer of viscous, incompressible fluid is investigated numerically. The effect of lowering the Prandtl number away from the previously researched ice−water experimental level is followed, so that the fluids under examination range through the everyday fluids (water, with $\sigma = 6.8$, air, with $\sigma = 0.71$) towards the more astrophysical regime, where σ is of the order 10^{-6}. It is found that the characteristics of this low Prandtl number convection are distinctly different from the ice−water experiment, unlike the higher Prandtl numbers, and that this leads to a breakdown of the previous simple model (Moore and Weiss (1973b)). The Prandtl number dependence of the flow, unseen in normal 2−D Rayleigh−Benard convection, is exhibited here, and adjustments to the Moore and Weiss model are shown to be necessary to allow for the flow differences.

3.3. FORMULATION OF THE MODEL.

3.3.1. The equation of state.

The equation of state for water in its pure state is given by Gill (1982) as

$$\rho = 999.842594 + (6.793652 \times 10^{-2})T - (9.095290 \times 10^{-2})T^2 + (1.001685 \times 10^{-2})T^3 - (1.120083 \times 10^{-6})T^4 + (6.536332 \times 10^{-9})T^5$$

where T is the temperature $(^{\circ}C)$ and ρ is the density. This may be rewritten as

$$\rho = 999.975 + (3.725 \times 10^{-9})T_1 - (8.001 \times 10^{-3})T_1^2 + (8.337 \times 10^{-5})T_1^3 - \ldots$$

where $T_1 = T - T_0$, and $T_0 = 3.98168^{\circ}C$, the temperature of maximum density. Thus, the equation of state may be written approximately in the form [2.6] since the linear and third order coefficients are much smaller than the quadratic coefficient. This formula is accurate to within 4% in the range $0-8^{\circ}C$ at standard pressure, and is only out by 20% by $24^{\circ}C$. The governing equations are then those given by equations [2.20] – [2.23] of Chapter 2 with $F(T) = T^2$.

3.3.2. The two–dimensional streamfunction.

The flow is assumed to be two–dimensional with no dependence in the y direction, so that

$$\mathbf{u} = (u(x,z), 0, w(x,z)) \quad , \qquad [3.1]$$

and then a streamfunction may be defined by

$$\mathbf{u} = \nabla \times (\psi(x,z)\mathbf{j}) = \left[-\frac{\partial \psi}{\partial z}, 0, \frac{\partial \psi}{\partial x} \right], \qquad [3.2]$$

where j is the unit vector into the two–dimensional plane. This

two−dimensionality forces the vorticity to be written as

$$\omega = \nabla \times \mathbf{u} = (0, \omega(x,z), 0) \quad . \qquad [3.3]$$

Then, equation [2.20] with $F(T) = T^2$ reduces from a vector equation for the three components of the velocity to a single y−component equation for the scalar vorticity,

$$\frac{1}{\sigma} (\mathbf{u}.\nabla)\omega = Ra. \left[-2 T \frac{\partial T}{\partial x} \right] + \nabla^2 \omega \quad . \qquad [3.4]$$

Equation [2.21] remains the same, but equations [2.22] and [2.23] combined now become a Poisson equation,

$$\omega = -\nabla^2 \psi \quad . \qquad [3.5]$$

Notice that the buoyancy term here is altered from that of Rayleigh−Benard convection and that it is this term that defines the penetrative nature of the problem.

Normally, as would be the case for Rayleigh−Benard convection, the length scale, d, and the temperature scale, ΔT, are chosen to be the height and temperature differences across the whole layer. The situation here, however, is different since there are two physically different regions at the onset of conduction − the upper stable region and the lower unstable region. In this case, it is more appropriate to define a Rayleigh number over the unstable region only, so that large, overlying stable layers do not overshadow the region of interest. For this, the length scale, d, is chosen as the depth of the unstable layer, and the temperature scale, ΔT, is chosen as the temperature across the unstable region. Then, a penetrative Rayleigh number may be defined as

$$R = \frac{2g\alpha_p d^3 (\Delta T)^2}{\kappa \nu} \quad . \qquad [3.6]$$

Notice that if the ratio of the unstable depth to the total depth is $1:\lambda$ then the constant $R = 2Ra_{rb}/\lambda^4$, where Ra_{rb} is the conventional Rayleigh number defined by equation [2.18] for Rayleigh−Benard convection, since both d and ΔT are reduced by a factor of λ. Also then, $R = 2Ra_{pc}/\lambda^5$ where Ra_{pc} is the true penetrative version of [2.18], and R is also a factor of π^4 different from Veronis's (1963) parameter R. Note that when the term 'the Rayleigh number' is referred to in this chapter, it is taken to mean the parameter R here. This definition is

deemed more sensible by some authors (MW, Whitehead and Chen (1970)), although others stick to the original definition whilst keeping total layer depths small (Sparrow, Goldstein and Jonsson (1963), Krishnamurti (1967)), but it is used here since it decouples the upper boundary from the problem as the layer depth increases. This is shown to be true by table 3.1, where the linear critical Rayleigh numbers (by this definition) and their corresponding wavenumbers are shown to become independent of the total depth, λ, as it increases above $\lambda = 5$.

Noting the vector identity

$$\nabla.\alpha\mathbf{u} = \alpha\,(\nabla.\mathbf{u}) + \nabla\,\alpha.\mathbf{u}$$

and using equation [2.2], then the equations can be further reduced to

$$\frac{1}{\sigma}\,\nabla\omega.\mathbf{u} = -RT\,\frac{\partial T}{\partial x} + \nabla^2\omega \quad , \qquad [3.7]$$

$$\nabla T.\mathbf{u} = \nabla^2 T \quad , \qquad [3.8]$$

$$\nabla^2\psi = -\omega \quad , \qquad [3.9]$$

or

$$\frac{1}{\sigma}\,J(\omega,\psi) = -RT\,\frac{\partial T}{\partial x} + \nabla^2\omega \quad , \qquad [3.10]$$

$$J(T,\psi) = \nabla^2 T \quad , \qquad [3.11]$$

$$\omega = -\nabla^2\psi \quad , \qquad [3.12]$$

Layer depth, λ	Linear critical Rayleigh number R_c	Linear critical wavenumber squared α_c^2
1.5	497.8032	2.2893
2.0	531.0460	2.2918
3.0	550.3758	2.5267
4.0	551.3240	2.5374
5.0	552.0854	2.5384
6.0	553.4094	2.5399

TABLE 3.1. Values for the linear critical Rayleigh number and the corresponding wavenumber for various layer depths, λ, showing the decoupling of the upper boundary for greater depths.

where

$$J(A,B) = \frac{\partial A}{\partial z}\frac{\partial B}{\partial x} - \frac{\partial A}{\partial x}\frac{\partial B}{\partial z} \quad . \qquad [3.13]$$

Thus the problem has been reduced to one of finding three scalar fields, ψ, ω and T from the above set of equations.

3.3.3. The boundary conditions.

The isolated, two-dimensional cellular unit considered for this numerical calulation, known as a roll, is defined by the limits $0 \leqslant x \leqslant L$ and $-1 \leqslant z \leqslant \lambda-1$, and the boundary conditions imposed are those identified in Chapter 2.

The temperature on the top and bottom horizontal boundaries is assumed to be fixed, such that

$$T(x,\lambda-1) = \lambda-1, \; T(x,-1) = -1 \quad . \qquad [3.14]$$

for all x, where λ is the depth of the layer. The scaling of the temperature dependence to a unit of the temperature difference across the unstable layer, means that, at the onset of convection, where the temperature profile is linear, the depth of the unstable region is also scaled to be unity, with the temperature of maximum density taking the value zero at the depth $z = 0$. Then λ becomes the measure of depth in units of the unstable height, and the temperature and depth scale together.

The horizontal boundaries are also assumed to be free so that the stress vanishes there as explained in Chapter 2. Equation [2.26] is reduced to

$$\frac{\partial u}{dz} = 0 \quad , \quad \text{at } z = -1, \lambda-1 \quad , \qquad [3.15]$$

since $v = 0$ everywhere, and thus, with $w = 0$ on the boundary and

$$(0, \omega, 0) = \nabla \times (u, 0, w) = \left[0, \frac{\partial u}{\partial z} - \frac{\partial w}{\partial x}, 0 \right] \quad , \qquad [3.16]$$

then

$$\omega (x,\lambda-1) = \omega (x,-1) = 0 \quad . \qquad [3.17]$$

Free boundaries are chosen because the results are similar to the rigid boundaries cases, whilst being easier to solve, and they are more appropriate for geophysical and astrophysical applications (Bolton and Busse (1984), Busse and Bolton (1984)).

The vertical velocity is zero on the boundary and so, by equation [3.2],

$$\psi(x,-1) = C_1 \ , \quad \psi(x,\lambda-1) = C_2 \ ,$$

where C_1 and C_2 are constants. The governing equations, equations [3.10] – [3.12] are invariant to a Galilean transformation i.e. the superposition of a constant horizontal velocity on the whole flow. The simplest problem has no flow superposed, or at least appears so in the frame of reference. To ensure this to be true, impose the condition that there should be no net flow through any vertical plane contained in the fluid, then this effectively eliminates any overall horizontally drifting solutions. Mathematically, this condition becomes

$$\int_{z=-1}^{z=\lambda-1} u(x,z)\, dz = 0 \ .$$

So, using [3.2],

$$-\int_{z=-1}^{z=\lambda-1} \frac{\partial \psi}{\partial z}\, dz = \Big[\psi \Big]_{z=\lambda-1}^{z=-1} = 0 \ ,$$

and thus,

$$\psi(x,\lambda-1) = \psi(x,-1) = C, \qquad [3.18]$$

where C is an arbitrary constant, along the boundaries. The constant C is chosen to be zero.

The cellular aspect of convection known since the earliest days of Thompson (1882) and Benard (1900,1901) allows us to study a single, isolated cellular module of the convection with vertical boundaries that allow no flow of heat or mass through the cellular walls (Chandrasekhar (1961), Stuart (1964)). This creates periodic boundary conditions on the side–walls of the cell

$$\frac{\partial T(0,z)}{\partial x} = \frac{\partial T(L,z)}{\partial x} = 0 = \frac{\partial w(0,z)}{\partial x} = \frac{\partial w(L,z)}{\partial x} , \qquad [3.19]$$

where the cell stretches horizontally from $x = 0$ to $x = L$ and contains a single roll (so L is half the full wavelength). These 'no−flux' conditions provide a limited periodic boundary condition since they do not allow a travelling wave solution. Inclusion of the other trigonometrical terms in the solution (sines where there are cosines and vice versa) and extension of x to 2L would allow this solution (see Bretherton and Spiegel (1983), Knobloch, Deane, Toomre and Moore (1986)).

3.3.4. The modal equations.

Now, following the general principles of a modal model, inspection of the horizontal boundary conditions allows us to make assumptions about the trigonometrical form of the horizontal dependencies. The following modal expansions satisfy the horizontal boundary conditions:

$$\psi(x,z) = \sum_{n=1}^{\infty} \frac{\psi_n(z)}{(\pi/L)} \sin\left[\frac{n\pi x}{L}\right] , \qquad [3.20]$$

$$\omega(x,z) = \sum_{n=1}^{\infty} \frac{\omega_n(z)}{(\pi/L)} \sin\left[\frac{n\pi x}{L}\right] , \qquad [3.21]$$

$$T(x,z) = \sum_{n=0}^{\infty} T_n(z) \cos\left[\frac{n\pi x}{L}\right] , \qquad [3.21]$$

where $\pi/L = \alpha$ becomes the horizontal wave number. Notice that the specification of the temperature field allows for a mean profile, dependent only on the vertical co−ordinate, and that a scaling factor of α is introduced to some scalar fields for convenience, since this brings out the natural parameter α^2 rather than a variety of powers of α later on in the equations. This is allowable, since the z−dependent scalar fields include a constant scaling factor.

These expansions may then be approximated by truncating at some finite N instead of infinity and then substituted into the governing equations. Comparison of trigonometric terms of wave numbers less than or equal to $N\pi/L$ (the naturally forming higher wave numbers being higher modes coupling into the equations which are to be disregarded) then produces a viable system of ordinary differential

equations for N modes of each of the scalar fields. The linear equations will be derived here as an example of this tedious process. For higher N, where there are many modes and complicated trigonometrical identities must be used, computer algebra (CAMAL on a VAX 8600, see Barton and Ffitch (1980)) is used to expand the terms and sort the equations. The choice of the basis functions as simple trigonometric functions rather than other functions e.g. Bessel functions, mercifully avoids the complications of the projection of the non−linear interactions of modes back onto a representation by those modes as would be encountered in other Galerkin−type procedures, since the trigonometric functions and their derivatives possess such an easy orthogonality.

Thus, for N = 1, the process proceeds as follows. The expanded scalar variables become

$$\psi(x,z) = \frac{\psi_1(z)}{\alpha} \sin\alpha x \quad , \qquad [3.22]$$

$$\omega(x,z) = \frac{\omega_1(z)}{\alpha} \sin\alpha x \quad , \qquad [3.23]$$

$$T(x,z) = T_0(z) + T_1(z)\cos\alpha x \quad . \qquad [3.24]$$

Substituting these into the governing equations, [3.10] − [3.12], and using the abbreviations that $s_i = \sin(i\alpha x)$, $c_i = \cos(i\alpha x)$, gives,

$$\frac{1}{\sigma}\left[\frac{\partial}{\partial z}\left[\frac{\omega_1 s_1}{\alpha}\right].\frac{\partial}{\partial x}\left[\frac{\psi_1 s_1}{\alpha}\right] - \frac{\partial}{\partial x}\left[\frac{\omega_1 s_1}{\alpha}\right].\frac{\partial}{\partial z}\left[\frac{\psi_1 s_1}{\alpha}\right] \right] = -R\left[T_0 + T_1 c_1\right]\frac{\partial}{\partial x}\left[\frac{\psi_1 s_1}{\alpha}\right] + \left[\frac{\partial^2}{\partial x^2} + \frac{\partial^2}{\partial z^2}\right]\left[\frac{\omega_1 s_1}{\alpha}\right] \quad , \qquad [3.25]$$

$$\left[\frac{\partial}{\partial z}\left[T_0 + T_1 c_1\right].\frac{\partial}{\partial x}\left[\frac{\psi_1 s_1}{\alpha}\right] - \frac{\partial}{\partial x}\left[T_0 + T_1 c_1\right].\frac{\partial}{\partial z}\left[\frac{\psi_1 s_1}{\alpha}\right] \right] = \left[\frac{\partial^2}{\partial x^2} + \frac{\partial^2}{\partial z^2}\right]\left[T_0 + T_1 c_1\right] \quad , \qquad [3.26]$$

$$\left[\frac{\omega_1 s_1}{\alpha}\right] = -\left[\frac{\partial^2}{\partial x^2} + \frac{\partial^2}{\partial z^2}\right]\left[\frac{\psi_1 s_1}{\alpha}\right] \quad . \qquad [3.27]$$

Hence, on differentiation and combination of the trigonometric terms, these become, writing $D = d/dz$,

$$\frac{1}{\sigma}\left[\frac{1}{2} D\omega_1\psi_1 s_2 - \frac{1}{2} \omega_1 D\psi_1 s_2 \right] = RT_0T_1\alpha^2 s_1 + \frac{1}{2} \alpha^2 RT_1^2 s_2 - \alpha^2\omega_1 s_1 + D^2\omega_1 s_1 \quad , \qquad [3.28]$$

$$DT_0\psi_1 c_1 + \frac{1}{2} DT_1\psi_1(c_2-1) + \frac{1}{2} T_1 D\psi_1(1-s_2) = -\alpha^2 T_1 c_1 + D^2T_0 + D^2T_1 c_1 \quad , \qquad [3.29]$$

$$\omega_1 s_1 = \alpha^2\psi_1 s_1 - D^2\psi_1 s_1 \quad . \qquad [3.30]$$

So, comparing like trigonometric terms, this gives, first of all,

$$D^2T_0 = \frac{1}{2} (-DT_1\psi_1 + T_1 D\psi_1) \quad . \qquad [3.31]$$

If the linear equations are to be solved, then the terms on the right hand sides of [3.28] and [3.29] arising from the non−linear $(\mathbf{u}.\nabla)\mathbf{u}$ and $(\mathbf{u}.\nabla)T$ terms of the original equations, may be dropped. In this case,

$$D^2T_0 = 0 \quad ,$$

so

$$T_0 = Az + B \quad ,$$

where A and B are constant coefficients. These can be used to satisfy the fixed temperature boundary conditions [3.14], by taking $A = 1$ and $B = 0$, so that

$$T_0 = z \quad . \qquad [3.32]$$

The non−linear terms in T_0 may be ignored to create a simple, linear model approximation as shown here in [3.32], but in general, in the higher order modal expansions, they are not, and so T_0 is not normally explicitly known before solution of the full system. Thus, an equation like [3.31] is normally included in the system of equations to be solved, along with the two fixed temperature boundary conditions. This allows non−linear feedback into the mean−field for higher order solutions, but this is deemed to be unnecessary for the simple starting model. The example here, although of first order ($N = 1$) has been included

with all the non−linear terms present to show the general operation of the modal procedure.

The other equations from comparing trigonometrical terms are in this case unaffected by whether the equations are linearised or not, and are given by

$$(D^2 - \alpha^2)\omega_1 = - \alpha^2 R T_0 T_1 \quad , \qquad [3.33]$$

$$(D^2 - \alpha^2)T_1 = \psi_1 \quad , \qquad [3.34]$$

$$(D^2 - \alpha^2)\psi_1 = -\omega_1 \quad . \qquad [3.35]$$

This procedure has thus produced the linear equations.

Notice that for higher modal approximations here all non−linear interactions will be taken into account, unlike the mean−field approximations (Herring 1963) of Musman (1968) who omits those terms generally associated with turbulence i.e. the interactions between fluctuating quantities, retaining only non−linear interactions between mean and fluctuating quantities.

The boundary conditions for these and the higher order modal truncations will be as follows. The fixed temperature boundary conditions, [3.14], become

$$T_0(-1) = -1 \ , \quad T_0(\lambda-1) = \lambda-1, \qquad [3.36a]$$

$$T_i(-1) = T_i(\lambda-1) = 0, \quad i \neq 0 \quad , \qquad [3.36b]$$

where the first two have already been explicitly solved if the linear equations with equation [3.32] instead of [3.31] are used.

The no−stress, free boundary condition, [3.16], becomes

$$\omega_i(-1) = \omega_i(\lambda-1) = 0, \text{ for all } i \quad , \qquad [3.37]$$

and the 'no vertical velocity' boundary condition, [3.18], becomes,

$$\psi_i(-1) = \psi_i(\lambda-1) = 0, \text{ for all } i. \qquad [3.38]$$

Equation [3.31] or [3.32] together with equations [3.33] to [3.38] form a closed solvable system, provided that the parameters σ, R are supplied. The linear set of equations are those defined by equations [3.32] − [3.38] but taking equation [3.31] together with the set [3.33] − [3.38] gives a better impression of the general higher order modal procedure.

The equations for the higher order modes are included only in Fortran form, together with their boundary conditions, as listings of the main programs on microfiche.

3.3.5. The computational methods.

3.3.5.1. Grids and numbers of modes.

The ordinary differential equations like those equations [3.31] – [3.35] together with their boundary conditions [3.36] – [3.38] were solved by the existing implementation of the Newton–Raphson–Kantorovich (NRK) method of iteration on finite differences (Readwin (1986)) as described in Chapter 2. Each solution is found to fourth order accuracy on the grid spacing, and may be increased to sixth and eighth order by deferred correction. It was found unnecessary for the following exploration to go beyond fourth order except for purposes of checking the more suspect or unusual results. The differences were calculated on a fixed mesh of usually sixteen intervals but finer meshes were used for verification purposes. This mesh is adequate according to Aziz and Hellums (1966), since the Rayleigh number is always kept close to critical, and is deemed suitable for $Nu < 3$ and for $R/R_c < 4$ by the cautious estimations of Moore and Weiss (1973a), where R_c is the critical Rayleigh number for the onset of penetrative convection. The coarsest feasible grids were always used because doubling of the grid size effectively doubles the computational cost of a run. Higher λ in general requires a greater number of mesh intervals (usually 32 were used for $\lambda = 6$ only) although the flow pattern results were altered little by this change.

For most of the production work the expansions of the horizontal modes were truncated at $N = 4$ but results were checked with higher numbers of modes (up to 8). For the range of Nusselt numbers considered, in general $Nu < 2$, two modes are sufficient for reasonably accurate results around a Prandtl number of order 10, where the ice–water experiment would lie since the Prandtl number of water at 4°C is 11.2 (Batchelor (1967)), but as the Prandtl number is lowered, the need for more modes in the calculation becomes imperative to allow for the more vigorous flows and to resolve the small scales of vorticity that develop even at these modest amplitude levels. Many previous models of convection have used fewer modes and these prove to be adequate at moderate or high Prandtl numbers, modelling the heat transport and some temperature profiles reasonably well (Marcus (1981), Toomre, Gough and Spiegel (1977)). However, these models fail at low Prandtl numbers. For example, Gough, Spiegel and Toomre (1975) could not, using single mode equations, get the expected Prandtl number dependence of low Prandtl number, rigid boundary Rayleigh–Benard convection predicted by Schluter, Lortz and Busse (1965).

3.3.5.2. Eigenvalues.

There are one or two features of the NRK solver which were further exploited. As mentioned in Chapter 2, the package allows for the solution of the problem along with the evaluation of a number of 'eigenvalues' (problem−wide undetermined parameters) simultaneously, provided that enough boundary conditions are specified. Two eigenvalues were extracted during the solution process of this calculation. First of all, the Rayleigh number was included as an eigenvalue by using the Nusselt number as an extra boundary condition,

$$DT_0(-1) = Nu \quad . \qquad [3.39]$$

This is contrary to normal practice, where the Rayleigh number is set and the Nusselt number calculated, but allows unstable (Musman (1968), MW) regions of the Nusselt−Rayleigh number space to be investigated (see later).

The parameter α^2 was also sought as a constrained eigenvalue. Normal practice either treats the horizontal wave number, α, as fixed at some suitable value e.g. the critical value for the onset of convection (Lipps and Somerville (1971)), or uses α as another parameter, along with Nu, Ra and σ, and thus requires a search of the whole Nusselt−Rayleigh−Prandtl number space for varying wave numbers (e.g. Lopez and Murphy (1984)). The first method is not very satisfactory, since the dependence of the solution on the wave number is eliminated entirely, whereas the second method is costly on the computer budget. Since the main aim of this calculation was to test the effect of the Prandtl number on penetrative convection, a compromise was sought. The basis of this compromise is to seek that solution which minimizes the Rayleigh number with respect to α^2. By this procedure, α is allowed to select a possibly physical value automatically, and this value is neither fixed, nor has to be searched for at the expense of vast amounts of computer time. This α−selection process seems possibly physical in some respect, since it implies that the particular α selected is that which reduces the level of instability (Ra) as much as possible for a given heat flux through the system (Nu). This type of argument has been used by many as a criterion in the stability argument for deciding which is the most stable mode out of the many which the problem admits. For example, Malkus and Veronis (1958) choose the most stable mode to be that which minimizes the root−mean−square temperature flux, which is a sort of reverse argument to the one used here. This is also effectively the process for finding the linear critical Rayleigh number for the onset of convection, and so to use this criterion once more seems a natural

progression.

Implementation of this requires an extension to the original equations, and therefore some increase in computer expenditure, however. The system of equations must be differentiated with respect to α^2, then $dR/d\alpha^2$ must be set to zero, and this extended system, together with extended boundary conditions, solved. The best way to illustrate this, is to continue working the example of the previous section through the procedure. Differentiate equations [3.31] and [3.33] – [3.35] with respect to α^2 to get an additional set of equations,

$$D^2T_0^\alpha = \frac{1}{2}\left(-DT_1^\alpha\psi_1 - DT_1\psi_1^\alpha + T_1^\alpha D\psi_1 + T_1 D\psi_1^\alpha \right) , \qquad [3.40]$$

$$\left(D^2 - \alpha^2 \right)\omega_1^\alpha - \omega_1 = - RT_0T_1 - \alpha^2R^\alpha T_0T_1 - \alpha^2RT_0^\alpha - \alpha^2RT_0T_1^\alpha , \qquad [3.41]$$

$$\left(D^2 - \alpha^2 \right)T_1^\alpha - T_1 = \psi_1^\alpha , \qquad [3.42]$$

$$\left(D^2 - \alpha^2 \right)\psi_1^\alpha - \psi_1 = -\omega_1^\alpha , \qquad [3.43]$$

where a superscript of α implies that the variable is differentiated with respect to α^2.

Setting $R^\alpha = 0$ requires that the minimum Rayleigh number with respect to α^2 is sought, and this eliminates one term from equation [3.40]. Hence, with this term removed, the equations [3.40] – [3.43] provide four more equations for the four new unknowns, T_0^α, T_1^α, ψ_1^α and ω_1^α.

The boundary conditions [3.36] – [3.38] are extended similarly to

$$T_0^\alpha(-1) = 0 , \quad T_0^\alpha(\lambda-1) = 0 , \qquad [3.44a]$$

$$T_i^\alpha(-1) = T_i^\alpha(\lambda-1) = 0, \text{ for all } i \neq 0 , \qquad [3.44b]$$

$$\omega_i^\alpha(-1) = \omega_i^\alpha(\lambda-1) = 0, \text{ for all } i , \qquad [3.45]$$

$$\psi_i^\alpha(-1) = \psi_i^\alpha(\lambda-1) = 0, \text{ for all } i , \qquad [3.46]$$

along with the equivalent of [3.39]

$$DT_0^\alpha(-1) = 0 , \qquad [3.47]$$

so that, in all, the system of equations has doubled in size but now allows the solution to naturally select a wave number, and to provide the Rayleigh number as an eigenvalue. Notice that this new set of equations and boundary conditions is very similar to the original equations in structure, and is therefore simple to code.

3.3.5.3. Solution process.

The solution was sought from an initial seed of the linear problem, described above in the example procedure ([3.32] − [3.38]), at a Nusselt number of value unity. This solution is independent of the Prandtl number. Solutions are then built up in cascade manner so that, with the specification of a particular Nusselt number and a Prandtl number, the linear solution is used as a basis for the initial approximation to the two mode solution. The two mode is used in a similar manner for the four, etc. Solving the linear solution for Nu = 1 means that effectively the Rayleigh number for the onset of convection is sought for each case. The linear, two and four mode solution sets incorporated the α^2 derivative technique, but higher N (N = 6 and N = 8) solutions were limited to solving the original set of equations for a particular wave number due to lack of computer memory and time. In general, there are 6N + 2 equations in the normal system, since there are three scalars per mode plus a mean temperature field with each of the differential equations for these scalars being second order, but this doubles up to 12N + 4 for the extended α^2 system. Hence, the linear system would involve 14 coupled, non−linear ordinary differential equations, but the mean tempreature field was explicitly solved ([3.32]) *a priori* thus dropping the system to 12 equations. The second order system reverts to the general formula, being 28 equations, the fourth order system, 52, and then the α^2 extension is dropped, leaving the sixth order system to contain 38 equations, and the eighth order system, 50.

3.3.5.4. Linear initial guesses.

The major problem of all boundary value solvers is that of obtaining an initial guess to the whole solution field for the method to iterate upon. This problem is mainly circumvented by this cascade solution procedure since, now, a complete guess must only be supplied for the simple linear problem, and the other initial guesses are only a matter of scaling up a previous solution.

The initial guess for the linear problem is not too difficult. The linear eigenfunctions for Rayleigh−Benard convection are simple sines and cosines, but for this penetrative problem are not. However, the linear eigenfunctions may, of course, be expressed as infinite sums of sines and cosines, and, for small λ such that counter−cells are not formed, a single $\sin(\pi z'/\lambda)$, where $z' = z + 1$, is a

good initial approximation to the eigenfunction. The initial solution field is started from the knowledge that $DT_1(-1) = 1$, so, for a particular layer depth, λ,

$$T_1(z) = \frac{1}{\pi} \sin\left[\frac{\pi z'}{\lambda} \right] , \qquad [3.48]$$

is a reasonable fit, and then, assuming ω and ψ are directly proportional to T, equations [3.33] – [3.35] suggest

$$\omega_1(z) = \frac{R\, \alpha^2\, T_1(z)}{\pi^2 + \alpha^2} , \qquad [3.49]$$

$$\psi_1(z) = - T_1(z) \, (\pi^2 + \alpha^2) , \qquad [3.50]$$

where R and α^2 are initial guesses to the true values at this point.

The initial approximations for the z–derivatives are simply the z–derivatives of the above, and for the α^2–derivatives, the approximations are taken as the same as for the original variable, but scaled down by 10^{-5}, a value obtained by trial and error and used simply because it works. Obviously, once one solution is obtained via any style of initial guess, then the process can continue on to other solutions using this solution, or some scaled form of it, as the best available initial guess. Insight into better initial guesses can be obtained in hindsight.

3.3.5.5. Recovery of finite amplitude initial approximations from linear solutions.

To obtain an approximation to the second order solutions from the linear solutions, a 'shape' assumption (Stuart (1958), Christopherides and Davis (1970)) is made. This means that it is assumed that the first non–linear mode is actually very similar in structure to the linear mode provided that the Nusselt number is close to unity. Since the procedure followed for these calculations is to start at low Nusselt numbers to build up a high order modal model, then to search parameter space with this high order model by using further scaling techniques described later, this assumption is valid.

Assume that the fluctuating part of the mean temperature field makes the mean profile take the form

$$T_0(z) = z' + A \sin(2\beta z') , \qquad [3.51]$$

where $z' = z + 1$, and $\beta = \pi/\lambda$.

Then

$$DT_0(z) = 1 + 2\beta A \cos(2\beta z') \quad ,$$

and since, approximately,

$$DT_0(z'=0) = Nu \quad ,$$

then

$$A = \frac{Nu - 1}{2\beta} \quad . \qquad [3.52]$$

Now, this with [3.31] gives

$$D^2T_0 = \frac{1}{2} (\psi_1 DT_1 + D\psi_1 T_1) = - 2\beta (Nu-1) \sin(2\beta z') \quad ,$$

and hence, assuming that the first modes of the higher expansion are directly proportional to the linear functions i.e.

$$S2_1 = Q\ S1 \quad , \qquad [3.53]$$

where S1 is a general linear scalar and $S2_i$ a general second order truncation scalar of expansion order i (i.e. the vertical dependences associated with terms in sin(iαx) ans cos(iαx)), then, substitution of [3.53] in the above expression for D^2T_0 gives

$$Q^2 = \frac{4\beta^2(Nu-1)}{(\beta^2 + \alpha^2)} \quad . \qquad [3.54]$$

Thus, the first modes of the higher order expansion have been approximated.

The second order equations are

$$(D^2 - 4\alpha^2)T_2 = 2\psi_2 DT_0 + \frac{1}{2} (\psi_1 DT_1 - D\psi_1 T_1) \quad , \qquad [3.55]$$

$$(D^2 - 4\alpha^2)\omega_2 = -2R\alpha^2 T_2 T_0 - \frac{\alpha^2}{2} T_1^{\,2} + \frac{\alpha^2}{2\sigma} (\psi_1 D\omega_1 - D\psi_1 \omega_1) \quad , [3.56]$$

$$(D^2 - 4\alpha^2)\psi_2 = -\omega_2 \quad . \qquad [3.57]$$

Using the N = 2 first mode approximations derived earlier ($S2_1$ from [3.53] and [3.54]), the terms highlighted in bold above are zero. Then, assume that the N = 2 modes of second expansion order, $S2_2$, have the following form,

$$S2_2(z) = S2_2' \sin(\beta z') \quad .$$

Assuming the linear $T_0 = z$, equations [3.55] − [3.57] give

$$\omega_2' = (\beta^2 + 4\alpha^2) \psi_2' \quad , \qquad [3.58]$$

$$\psi_2' = - \frac{(\beta^2 + 4\alpha^2)}{2} T_2' \quad , \qquad [3.59]$$

$$- (\beta^2 + 4\alpha^2) \omega_2' \sin(\beta z') = -2\alpha^2 \beta T_2' z' \sin(\beta z') - \frac{Q^2}{2\beta^2} R\alpha^2 \sin^2(\beta z') \quad . \qquad [3.60]$$

Vertically averaging the latter i.e. taking

$$\frac{1}{\lambda} \int_{z'=0}^{z'=\lambda} dz'$$

gives

$$- (\beta^2 + 4\alpha^2) \omega_2' = - \frac{\alpha^2 R T_2' \pi}{\beta} - \frac{\alpha^2 R Q^2 \pi}{8 \beta^2} \quad ,$$

and so eventually,

$$\omega_2' = \frac{\alpha^2 R Q^2 \pi (\beta^2 + 4\alpha^2)^2}{8\beta \left[\beta (\beta^2 + 4\alpha^2)^2 + 2\alpha^2 R \pi \right]} \quad , \qquad [3.61]$$

$$T_2' = - \frac{2\alpha^2}{(\beta^2 + 4\alpha^2)} \cdot \omega_2' \quad , \qquad [3.62]$$

$$\psi_2' = \frac{\omega_2'}{(\beta^2 + 4\alpha^2)} \quad . \qquad [3.63]$$

Again, derivative approximations can be made by taking the z−derivative of the approximation or by scaling down by a factor of 10^{-5} for the α^2−derivative.

Thus, [3.58] and [3.61] − [3.63] form a complete approximation for the second

modes of the second order approximation, and together with [3.53] and [3.54], the approximations for the first modes, constitutes a complete initial guess of the second order expansion variables.

3.3.5.6. Scaling through parameter space.

Once one solution has been established for a high N modal expansion at low Nusselt number, then the parameter space may be searched by incrementing through it, using a suitable scaling of the previous solution as the initial guess for the next. Such a suitable scaling system is inherent in Malkus and Veronis (1958) and is as follows.

When changing Nusselt number from Nu_o to Nu_n, the mean temperature profile remains the same but the derivative changes as the ratio of the two Nusselt numbers, i.e.

$$DT_{0n} = \frac{Nu_n}{Nu_o} DT_{00} \quad ,$$

where an 'o' subscript describes an old variable, and an 'n' subscript describes a new one. Then, the i^{th} variables scale as a ratio of the Nusselt numbers to the power of i/2 i.e

$$S_{1n} = \left[\frac{Nu_n - 1}{Nu_o - 1} \right]^{1/2} S_{1o} \quad , \qquad [3.64]$$

$$S_{2n} = \left[\frac{Nu_n - 1}{Nu_o - 1} \right] S_{2o} \quad , \qquad [3.65]$$

and so on.

When changing from Prandtl number, σ_o to σ_n, the temperature variables do not scale at all, and all other variables scale as the ratio of the Prandtl numbers, i.e.

$$S_{in} = \left[\frac{\sigma_n}{\sigma_o} \right] S_{io} \quad . \qquad [3.66]$$

Hence, provided small enough increments in the parameters are taken, these incremental scalings will suffice as initial guesses for the iterative solver.

Obviously, the size of increment necessary for this procedure to attain convergence is dependent on how drastically the solution is varying at that point. Low Prandtl numbers or high Rayleigh numbers tend to indicate a more vigorous regime of flow, and so much smaller parameter steps are needed to enter into these regions, and hence the amount of computer time spent also increases.

3.3.5.7. The parameter space searched.

Using the above methods of initial approximation and scaling, the whole of a limited range of parameter space was searched with relative ease. The relaxation ability of the NRK method was not used, but set to the maximum relaxation possible at all times, and in general, all solutions converged within 8 iterations of the procedure, and some in a lot less (at the higher σ, lower Nu end of the ranges).

The production solutions were calculated with modal truncation at N = 4. Only a small number of higher order solutions were calculated to check unusual results. Nusselt numbers between the linear, conductive solution of Nu = 1, and a maximum of Nu = 3 were calculated, for Prandtl numbers of σ = 0.1, σ = 1.0 and σ = 10.0, and for various layer depths, ranging from λ = 1.5 to λ = 6.0. All the computations for this Chapter were carried out on CDC Cyber machines, either a Cyber 720 for the lower order solutions, or a Cyber 855 for the more memory intensive higher order solutions.

3.4. RESULTS AND DISCUSSION.

3.4.1. THE EFFECT OF MODAL TRUNCATIONS.

The figures in Table 3.2 show the effect of various modal models on the results for a particular value of the Nusselt number, for a particular layer depth and for varying Prandtl numbers. Low order modal results can reasonably predict heat transport results (Toomre et al. 1977) if calculated under the right conditions. Authors such as the various combinations of Toomre, Gough and Spiegel (1975, 1977, 1982) have calculated astrophysical models on modal calculations using at most three modes and mainly with just a single mode, for wide ranges of

parameters, with the Prandtl number as low as $\sigma = 10^{-6}$. In the calculations presented here, the simple low order calculations for two modes in the horizontal fare quite well at Prandtl numbers above 0.5. For $\sigma = 11.2$, being that of water at 4°C, two modes predict the Rayleigh number to within 1% of that described by higher 6 and 8 mode calculations, and for larger σ the results are similar. However, at $\sigma = 0.5$, the two mode calculation is already overestimating the Rayleigh number by approximately 13%. By $\sigma = 0.2$, it is 70% out, by $\sigma = 0.1$ it is 150% out, and by the lowest calculated Prandtl number for two modes, $\sigma = 0.05$, it is 260% out of alignment with the next highest modal calculation performed (4 modes). Note that these Prandtl numbers are not even reaching the low order of magnitude required for truly astrophysical convection.

However, the four mode calculation exhibits a much better agreement with higher mode calculations. For Prandtl numbers down to $\sigma = 1.0$, the four mode solution Rayleigh number only differs from that of the sixth order solution by 0.07%. At $\sigma = 0.1$, this has worsened to 6% in comparison with a six mode solution, and 6.8% with an 8 mode solution, but this is deemed acceptable. Indeed, the four mode solution differs only by 13% at the minimum Prandtl number calculated, $\sigma = 0.04$, in comparison with a six mode solution. Similar results hold for the α^2 calculations, and are, if anything more accurate.

Thus, Table 3.2 emphasises that the two mode results are reasonable for Prandtl numbers around the order of the ice−water experiment, but, as the Prandtl number is lowered, they become much more unreliable and are intolerably inaccurate below $\sigma = 0.75$. However, the next modal set including an extra two modes, enables modal solutions to be obtained with reasonable accuracy down to Prandtl numbers on the order of $\sigma = 0.1$.

This result is not unexpected when considered in the light of the types of structure found in previous convective experiments. Consider the vorticity equation, [3.7], as a driving $RT\partial T/\partial x$ term with a diffusive $\nabla^2\omega$ destructive term in balance with the storage−like nature of the left hand Jacobian term. For large σ the storage capacity is much reduced and all that is created is destroyed, whereas for small σ nearly all vorticity is 'stored'. From Moore and Weiss (1973a), for Rayleigh−Benard convection with $5 \leqslant \sigma \leqslant 100$, which may be considered as high σ, the non−linear storage terms are either inconsequential, with total creation and destruction of vorticity in thermal plumes at the highest σ, or allow a style of solution known as the 'sugar loaf' solution, where the vorticity is constant on the streamlines but not across them (so that the vorticity amplitude forms a circularly symmetric, smooth 'dome' or 'sugar loaf'). However, for lower σ, the storage terms dominate and the flow becomes the inertial 'flywheel' type (MW, Proctor (1977), Clever and Busse (1980)) where the vorticity is constant across the cell

σ	Rayleigh number			α^2		
	2 mode	4 mode	best (6 modes or $^+\!\!\rightarrow$8)	2 mode	4 mode	best (6 modes or $^+\!\!\rightarrow$8)
a) λ = 3, Nusselt number = 2.0						
∞	678.41			1.7995		
10^4	678.43			1.7996		
10^3	678.64			1.8006		
100.	680.73			1.8106		
50.	683.09			1.8218		
20.	690.31			1.8558		
11.2	700.53	716.87	717.37	1.9034	2.1262	2.133
3.0	770.46		788.81	2.2007		2.410
1.0	1050.09	1045.13	1045.83	3.1475	3.2729	3.285
0.5	1736.27	1529.94	1527.33	5.2336	4.7378	4.737
0.4	2191.29	1791.78		6.4901	5.4582	
0.3	3097.14	2243.21	2225.82	8.6988	6.5991	6.53
0.2	5440.06	3199.55		13.3259	8.7105	
0.1	16687.43	6618.85	6202.1$^+$	28.0204	14.5357	13.6$^+$
0.08		8676.25	8027.4		17.3543	16.15
0.06		12636.52	11444.11		22.0078	20.25
0.05	58692.	16286.86		59.12	25.7209	
0.04		22577.80	19994.9		31.3163	28.9
b) λ = 6, Nusselt number = 2.0						
10.		624.31			0.8032	
6.		653.09			0.8287	
3.		746.28			0.9913	
2.		866.54			1.2435	
1.		1260.63			2.1077	
0.8		1447.99			2.4979	
0.6		1745.85			3.0922	
0.4		2318.60			4.1691	
0.3		2891.38			5.1744	
0.2		4085.39			7.0657	
0.1		8192.20			12.0967	
0.08		10562.43			14.3847	
0.06		15007.30			18.0514	
0.05		19008.51			20.9230	
0.04		25696.01			25.1545	
0.03		38329.42			31.9217	

TABLE 3.2. Values of the Rayleigh number for two distinct layer depths and a fairly non−linear regime (Nu = 2), for various Prandtl numbers, σ, showing the effect of modal truncations on the results, and the obvious Prandtl number dependence.

except for sharp boundary layers at the edges, thus differing from the high σ solutions since the vorticity is constant across the streamlines as well as along them. In the penetrative case studied here, the motion is similar for high σ, the vorticity being constant on the streamlines in the 'sugar−loaf' manner. Low order harmonic models seem to be able to cope with these simple structures, but, as can be seen from Table 3.2, they collapse for the low σ penetrative case, implying that the structure of the flow is now more complicated than the simple flywheel, and thus requires more modes in the harmonic solution for the necessary resolution of that structure.

For the work which follows, the accuracy gained from the four mode solutions will suffice, providing Prandtl numbers no lower than 0.1 are taken, although this condition is not as stringent as Bolton and Busse's (1984) who demanded a 1% agreement between one truncation and the next for an accurate answer.

Comparison of the figures of MW with the results of the four mode calculations here are encouraging. The Nusselt−Rayleigh number dependence exhibited in MW figures 9 and 11 agree almost exactly for values of λ = 1.5, 3 and 6, and for all Rayleigh numbers less than $50R_c$, at least. The values for the onset of sub−critical convection agree exactly, as do the values of the Nusselt number where the Rayleigh number once again passes through the critical value. It must be stated however, that these figures are for a Prandtl number of the ice−water experiment (σ = 11.2) where the solutions are expected to be accurate, but it is a useful check that the modal code gives answers compatible with the full finite difference code of MW. It must also be noted that some of the streamline contours and isotherms are not in complete agreement with those presented here, but the numerical experiments of MW were carried out at one fixed aspect ratio, whereas, as explained earlier, the present calculations were allowed to seek a cell geometry hopefully selected by a physical system. This discrepancy allows the geometry of the two different styles of calculation to differ by up to 30%, and so physical differences may be expected.

3.4.2. THE PRANDTL NUMBER DEPENDENCE.

3.4.2.1. High Rayleigh numbers, low heat transport.

The four−mode figures for the Rayleigh number shown in Table 3.2 exhibit a strong dependence on the Prandtl number. Above $\sigma = 10$, as for 2−D Rayleigh−Benard (Moore and Weiss (1973a)), the flow is effectively Prandtl number independent, with the Rayleigh number decreasing only very slightly, about 4%, for Prandtl numbers between $\sigma = 10$ and $\sigma = \infty$. However, the value of the Rayleigh number almost doubles between $\sigma = 10$ and $\sigma = 0.5$ and almost quadruples again between $\sigma = 0.5$ and $\sigma = 0.1$, showing a strong dependence of the flow on the Prandtl number for $\sigma \leqslant 10$. This is surprising considering the statements by Schluter, Lortz and Busse (1965), Moore and Weiss (1973a) and Gough, Spiegel and Toomre (1975) that no Prandtl number dependence was expected for stress free rolls in Rayleigh−Benard convection. Moore and Weiss (1973a) states that the flow is totally independent of the Prandtl number for $\sigma \leqslant 1$ and $\sigma \geqslant 6.8$, and between these two values the Rayleigh number only declines very slightly, rendering the flow virtually Prandtl number independent. The situation is very different for penetrative convection.

Consider the physical impact of the Rayleigh number again as explained in section 2.3. An increase in R implies a decrease in dissipation, or an increase in the rate of release of potential energy, both of which lead to destabilisation. Thus at low Prandtl numbers the system is destabilised and the convection can be seen to be considerably less efficient, working harder (i.e. larger R) to realise the same heat flux (i.e. same Nu). The effect exists for all layer depths (Table 3.2 shows another example) and for other values of the Nusselt number too, and the dependence is heightened at higher Nusselt numbers where the system is already working harder carrying the heat flux.

Figures 3.1 show logarithmic plots of Rayleigh number and α^2 for a variety of Prandtl numbers. The values are taken from the four mode column of Table 3.2 for both layer depths and a Nusselt number of 2.0. The strong σ dependence of both parameters can be seen for low Prandtl numbers, below a value of around unity, where the curve rises steeply towards higher values of R or α^2. Above $\sigma = 1$, the curves tail off towards the horizontal, showing that the σ dependence is lost for higher Prandtl numbers, in agreement with Rayleigh−Benard convection. Rough measurement of gradient from these curves seem to indicate that the Rayleigh number scales with the Prandtl number ($R \approx \sigma$) and that α^2 scales as

Figure 3.1a) Rayleigh no. versus Prandtl no.

Nu = 2.00, λ = 3, 6

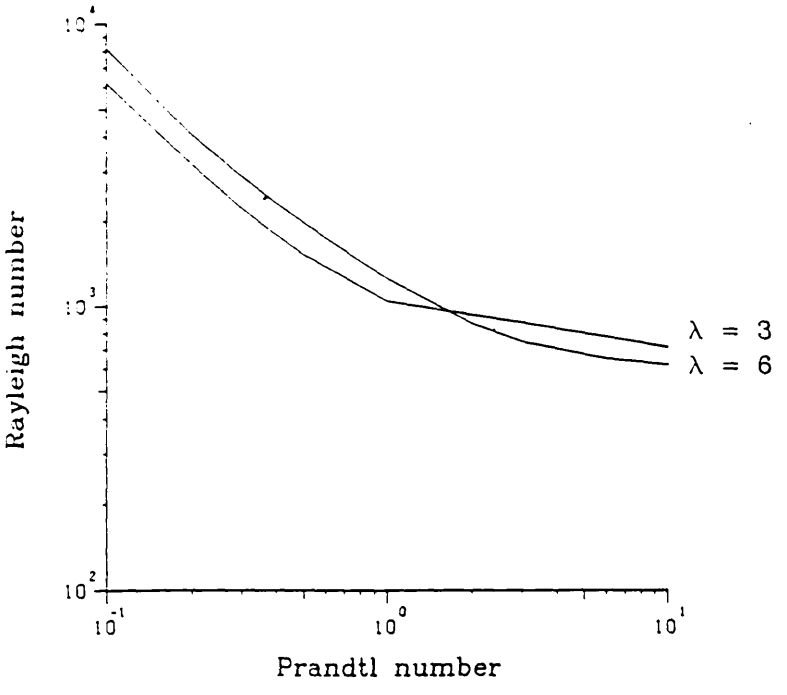


Figure 3.1b) Wave no., α^2, versus Prandtl no.

Nu = 2.00, λ = 3, 6

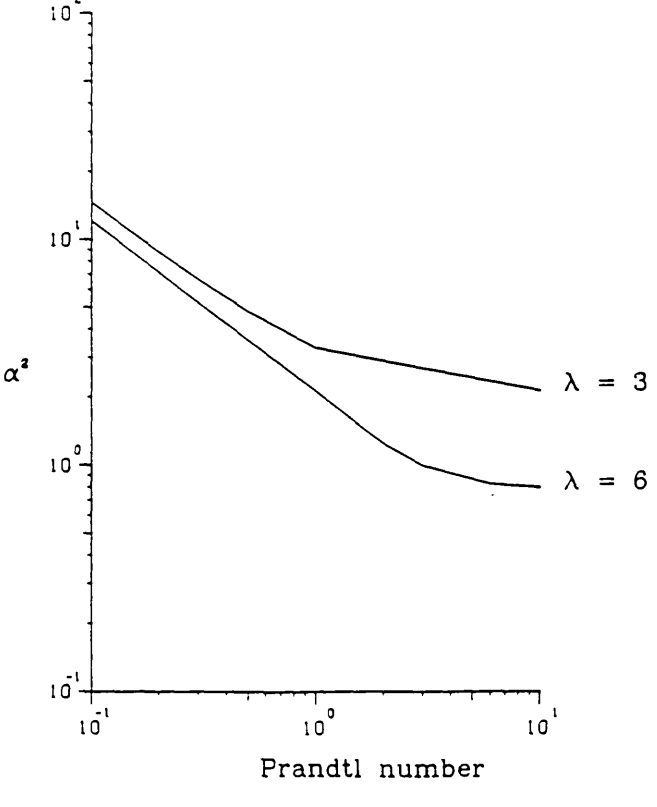


Figure 3.2a)
Rayleigh number against Nusselt number
$\lambda = 1.5$

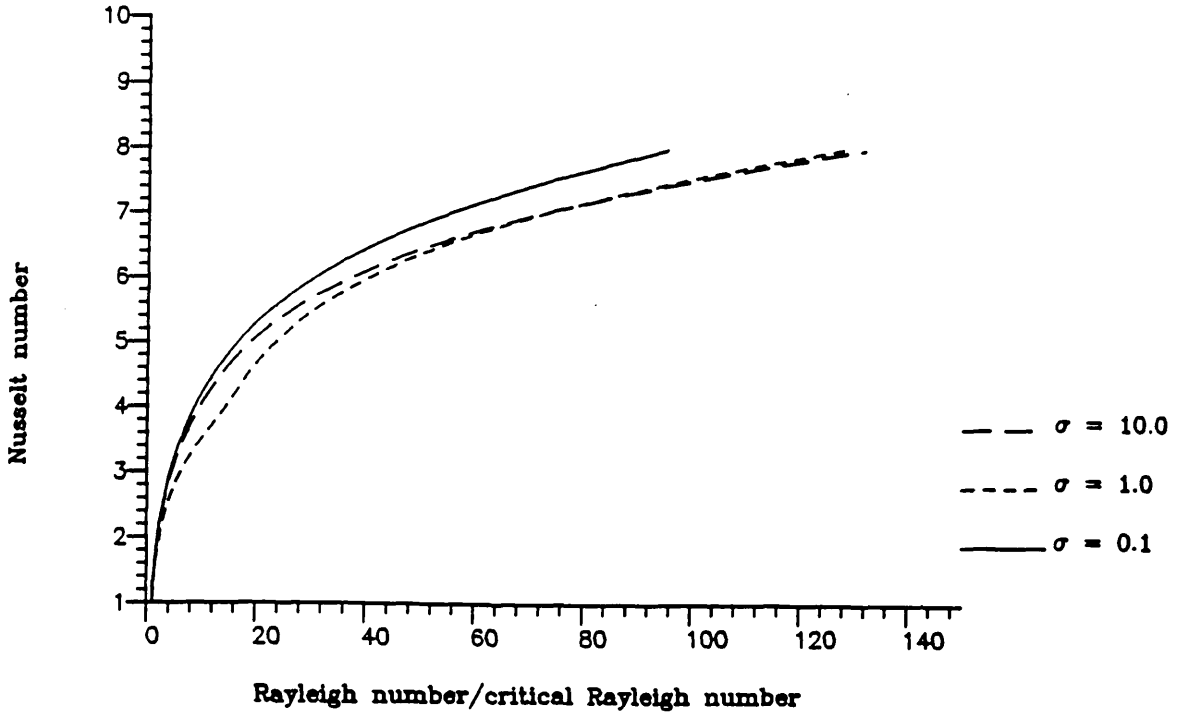


Figure 3.2b)
Rayleigh number against Nusselt number
$\lambda = 3.0$

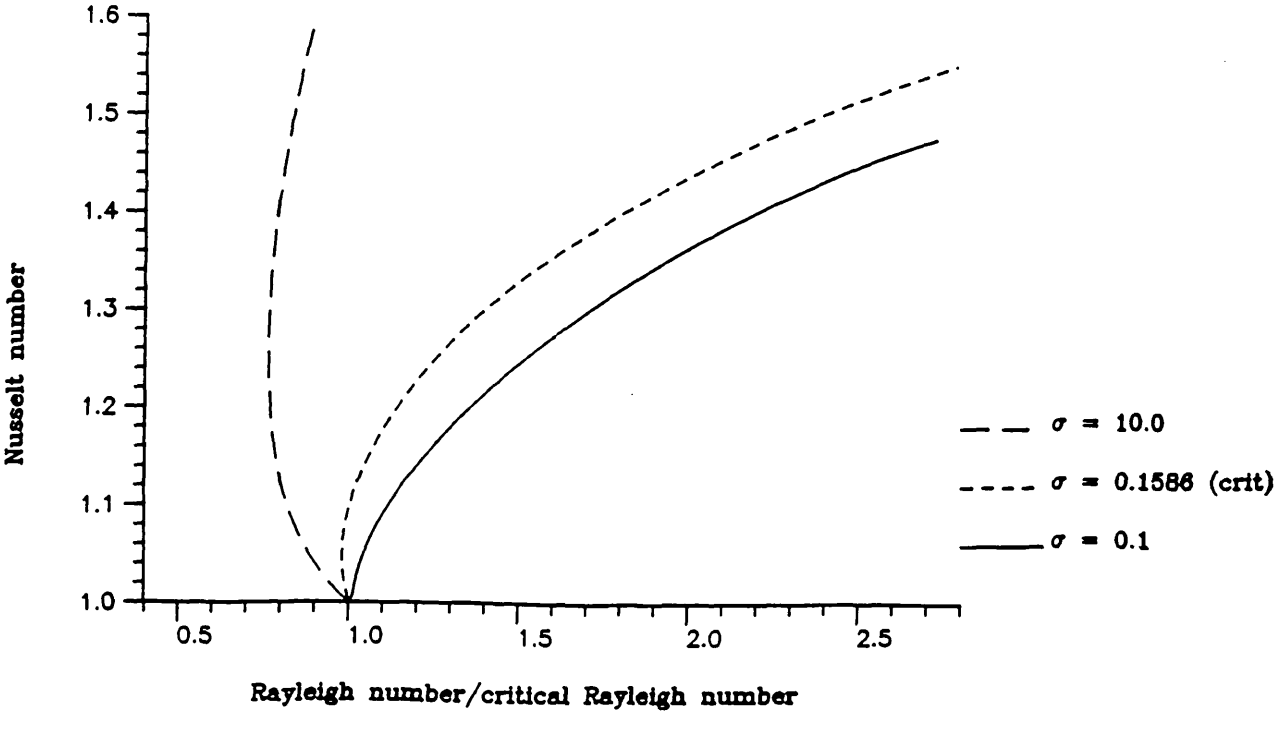


Figure 3.2c)
Rayleigh number against Nusselt number
λ = 4.0

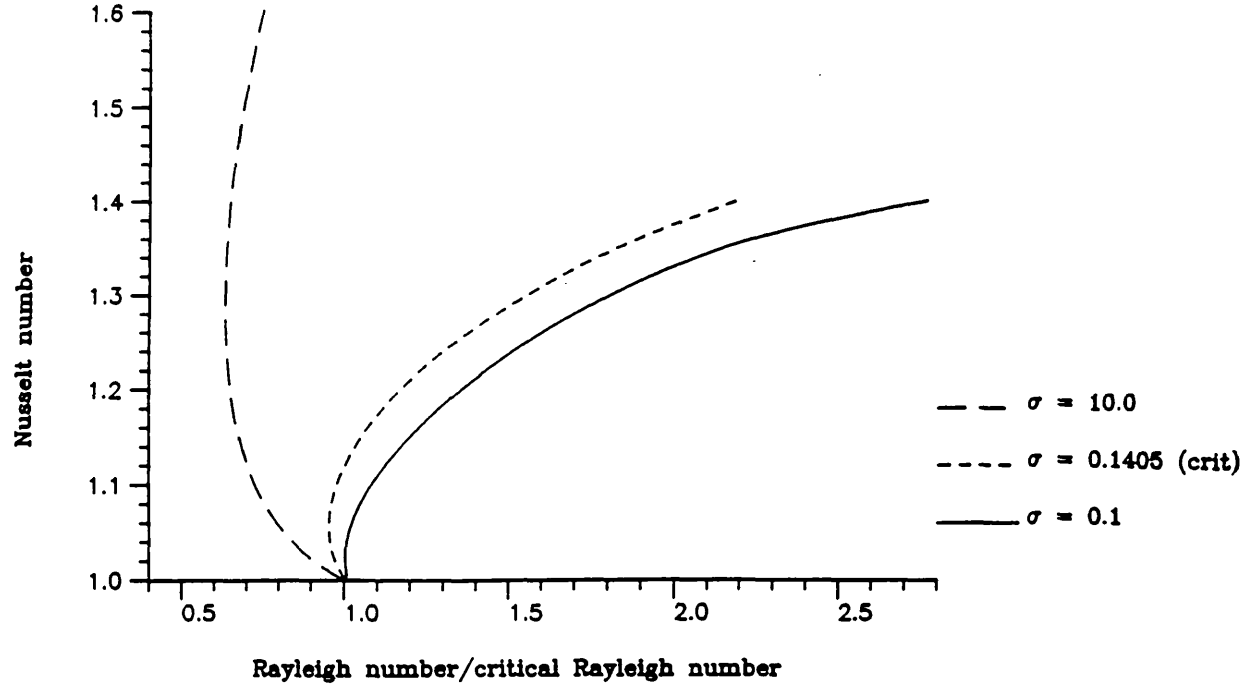
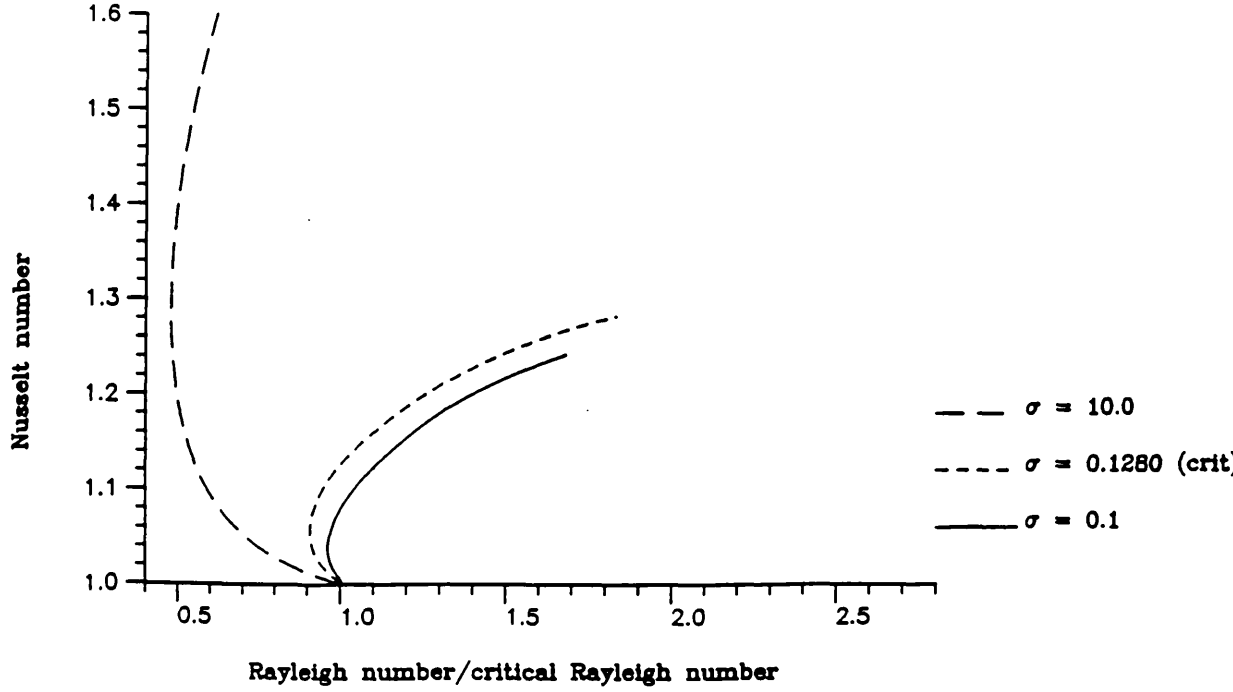


Figure 3.2d)
Rayleigh number against Nusselt number
λ = 6.0



$\sigma^{3/4}$ for $\sigma \leqslant 1$. The Rayleigh number scaling is more true near $\sigma = 0.1$, and shows slight lessening of the gradient of the curve approaching $\sigma = 1.0$, whereas the gradient is fairly consistent for the whole of the range $0.1 \leqslant \sigma \leqslant 1.0$ for the α^2 curve.

The figures 3.2a) – 3.2d) of Nusselt number against Rayleigh number show clearly that for varying layer depths, given a Nusselt number, the Rayleigh number for the lower Prandtl number is far higher than that of the ice–water experiment, and so the low σ system is much less efficient than the ice–water experiment. An alternative viewpoint to this is to consider that the Rayleigh number, R/R_c, is fixed and examine the corresponding Nusselt numbers. For 2–D Rayleigh–Benard convection, all Prandtl numbers would have the same heat transport for a given Rayleigh number, but as can be seen here, in the supercritical regime (i.e. $R/R_c \geqslant 1$), the lower Prandtl numbers have a significantly lower heat transport than the higher σ, and again the conclusion that the lower σ cases are struggling to transport heat as efficiently as the higher σ for the given amount of instability, may be drawn. This is somewhat strange intuitively as one would expect the less viscous fluid to invite easier, more freely flowing convective motions and thus greater heat transport, but imagining the situation as one with greater κ instead,

R/R_c	$\sigma = 0.1$		$\sigma = 1.0$		σ=6.8	σ=10.0
	RB	P	RB	P	RB	P
6	3.61	3.46	3.58	2.97	3.55	3.34
10	4.39	4.18	4.38	3.51	4.24	4.04
15	5.11	4.82	5.06	4.07	4.85	4.63
20	5.67	5.23	5.62	4.60	5.33	5.05
50	7.92*	6.78	7.81*	6.30	7.45	6.36
100	10.18*	8.08	10.09*	6.50	9.61	7.46

TABLE 3.3. Comparison of two–dimensional Rayleigh–Benard (RB) Nusselt numbers and penetrative (P) Nusselt numbers as functions of R and σ. RB results from Moore and Weiss (1973a) and Veronis (1966) for $\lambda = 1$ (shown by *) or $\lambda = \surd 2$. Penetrative results for $\lambda = 1.5$.

then it is possible to envisage that more heat may be lost laterally between the overturning plumes, thus reducing vertical heat transport. The reverse result may be true only for subcritical motions, where lower σ values may have a higher heat transport than the higher σ solutions if convection could exist on the lower part of the subcritical curve. This portion of the curve, however, is an unstable regime (Musman (1968), MW) i.e. on increasing the Rayleigh number from a low value ($R \ll 1$) convection may first occur via a finite amplitude instability at the non−linear critical Rayleigh number (the 'nose' of the curve) below the linear critical Rayleigh number and then continue rising on the upper branch of the curve increasing the heat transport with increasing R rather than choosing the lower branch where the heat transport decreases. An alternative possibility, for which there exists some experimental evidence (Azouni (1983)) is that the system may not be unstable to finite amplitude instabilities and then may operate in a hysteresis type manner, whereby convection would not occur until the linear critical Rayleigh number was reached and then the solution would jump straight to high Nusselt number solution shown on the Rayleigh number versus Nusselt number curves above $R = R_c$. If the Rayleigh number was then lowered, subcritical convection could occur until the minimum value of R was reached, at the 'nose' of the R−Nu curves, whence the solution would return straight to the conductive $Nu = 1$ solution . Either way, this section of the subcritical curve could never be physically traversed. Convection on the upper portion of the subcritical curve is of the same style as the supercritical solutions, and thus it appears that the heat transport is always lower for a lower Prandtl number in penetrative convection. The main distinguishing feature between high and low Prandtl number in penetrative convection, therefore, is shown in figures 3.2 and 3.6, and seems to be that the two regions have totally different bifurcations away from the critical, linear Rayleigh number for the onset of convection. In the high Prandtl number case, as is always seen in penetrative convection, the bifurcation is subcritical, whereas for low Prandtl number convection, the bifurcation is supercritical. These numerical results suggest that at low Prandtl number, the system is not prone to the finite amplitude instability of Veronis (1963) and thus convection sets in first at the value predicted by linear theory rather than that shown to exist for other Prandtl numbers in non−linear theory. The nature of these bifurcations is discussed in detail in section 3.4.3.2

Table 3.3 and Figure 3.2a) show the Nusselt number characteristics for the layer depth, $\lambda = 1.5$. Veronis (1966) used $\lambda = \sqrt{2}$ for his calculations, whilst Moore and Weiss (1973a) calculated comparisons to Veronis's results with $\lambda = 1$. These results are contrasted with those produced here for penetrative convection at $\lambda = 1.5$ in Table 3.3. The slight dip in the value of the Nusselt number for the

Rayleigh−Benard Prandtl number dependent region (Prandtl numbers between Nu = 0.1 and Nu = 10.0) as observed by Moore and Weiss is now much more pronounced. The overall Nusselt numbers are also lower by factors varying between 4% and 35%, depending on the Rayleigh number, showing that heat transport for penetrative convection is considerably lower than that for the corresponding Rayleigh−Benard convection. However, as can be seen by comparing figures 3.2a) − 3.2c), $\lambda = 1.5$ is in fact an unusual case, in that the Nusselt−Rayleigh number curve for $\sigma = 1.0$ lies below the $\sigma = 0.1$ curve, unlike any of the other layer depths. If this were the case, then the dip in the penetrative results for the Rayleigh−Benard Prandtl number dependent region would be replaced by a steady increase of the Nusselt numbers. The difference of this $\lambda = 1.5$ set of solutions can probably be explained with respect to the greater influence of the upper boundary. MW states that after $\lambda = 1.91$ the structure of the convection changes from that containing only one main convecting cell to one containing a main convecting cell topped by a less active, conducting counter−cell. When one or more counter−cells form, the upper boundary becomes more decoupled from the convecting cell and so has less influence on the dynamics of the problem. Thus, $\lambda = 1.5$ still feels the effect of the upper boundary quite strongly in comparison to the other layer depths studied, and therefore is not necessarily a good penetrative comparison to the Rayleigh−Benard results. This segregation of the whole cell into an active region with a counter−cell overlying is the basis for MW's simple model of penetration.

3.4.2.2. The Moore and Weiss model.

Penetrative convection is identified by the overshooting of the unstable driving in the lower region into the originally stable overlying region. The effect of this is to smear out a large proportion of the body of the fluid so that it has it has a temperature just below that of the maximum density (Furumoto and Rooth (1961), Veronis (1963), MW). However, this extension of the lower unstable region may not penetrate all the way to the upper boundary of the fluid layer, and for layer depths greater than $\lambda = 1.91$ (MW) the fluid layer divides itself into two or more counter−rotating cells. The lower, or main, cell contains the driving unstable region and a region of overshoot, and has a roughly isothermal mean temperature just below the temperature of maximum density. Above this, for $\lambda > 1.91$, there may be one or more counter−cells, each of which rotates in the opposite sense to the cell below, and is much weaker than that cell (Musman

(1968) and figure 3.7).

The model in MW simplifies this structure, by splitting the cell into the two regions, for $\lambda > 1.91$, using an imaginary, horizontal, slippery plate at a fixed temperature. It was assumed that the heat flux above the plate is carried by conduction alone, whereas below the plate it is carried purely by convection, and so the plate was positioned in the cell such that the fluxes above and below were balanced, assuming that no internal heating or cooling was required to keep the plate at that fixed temperature (Malkus (1960)). This effectively divides the cell into an active convecting region, with an overlying passive, conducting region.

It is useful to introduce the concept of 'effective' constants in parallel with the basic constant parameters of the problem already mentioned. The division of the region of interest in this problem into an active and a passive region leads to new definitions of an effective Rayleigh number and an effective Nusselt number as follows,

$$R_{eff} = \frac{2g\alpha\,(\Delta T)^2 d'^3}{\kappa\nu} , \qquad [3.67]$$

$$Nu_{eff} = \frac{F}{\kappa} \cdot \frac{d'}{\Delta T'} , \qquad [3.68]$$

where the length scale, d', is now defined over the lower, active region instead of the original unstable region (for the penetrative Rayleigh number, R, used here) or the full layer depth (for the 'true' penetrative Rayleigh number, Ra), and $\Delta T'$ is the temperature across the active layer. Note that

$$R_{eff} = R\,d'^3 = 2Ra_{rb}\frac{d'^3}{\lambda^3} = 2Ra_{pc}\frac{d'^3}{\lambda^5} \qquad [3.69]$$

$$Nu_{eff} = Nu \cdot \frac{d'}{\Delta T'} . \qquad [3.70]$$

Notice also that this definition then offers an explanation for the onset of non-linear convection at a Rayleigh number below that of the critical because the effective Rayleigh number may be above critical, whilst the Rayleigh number is not (Musman (1968), Moore and Weiss (1973a)).

The principle of the Moore and Weiss model was to create a basic building block from the major, lower, active convecting cell from which it should be possible to construct any total depth of fluid simply by adding passive fluid on top. Then the assumption that the fluxes must balance in the two layers provides a means of scaling up from the effective Rayleigh and Nusselt numbers of the basic lower cell to the Rayleigh number and the Nusselt number of the full layer.

Figure 3.3a)
Rayleigh number against Nusselt number
MW model and numerical results, $\lambda = 3$, $\sigma = 10.0$

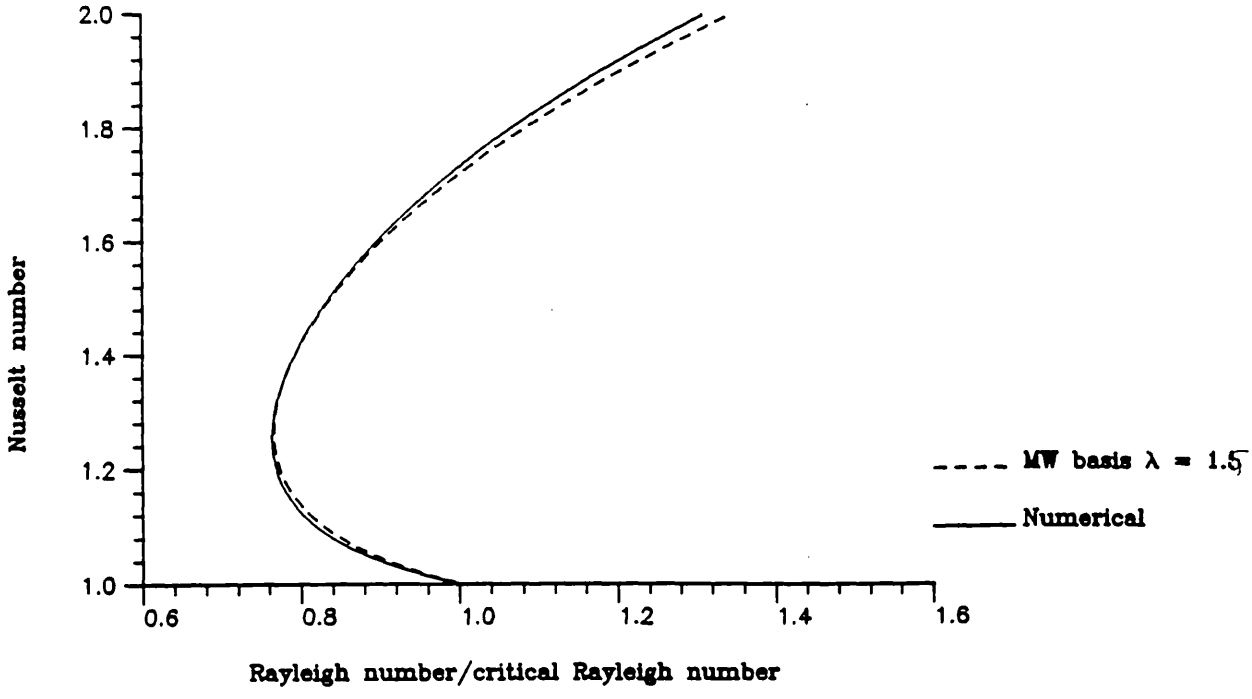


Figure 3.3b)
Rayleigh number against Nusselt number
MW model and numerical results, $\lambda = 6$, $\sigma = 10.0$

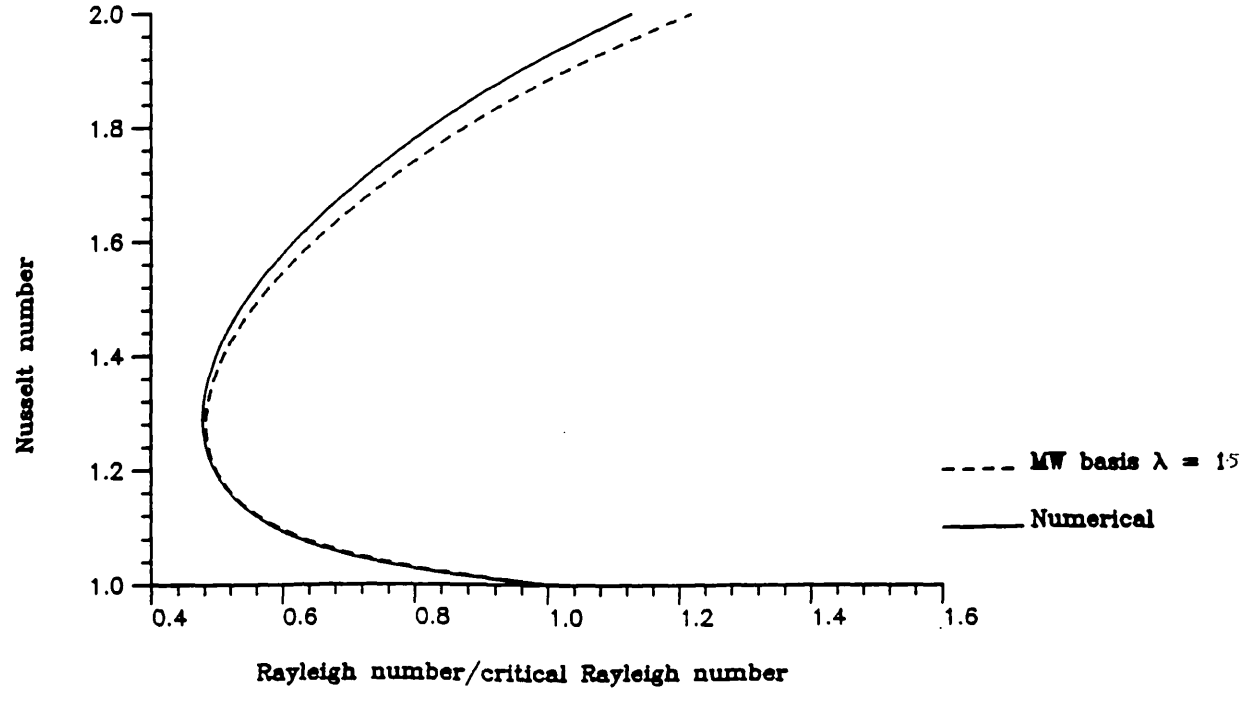


Figure 3.3c)
Rayleigh number against Nusselt number
MW model and numerical results, $\lambda = 3$, $\sigma = 0.1$

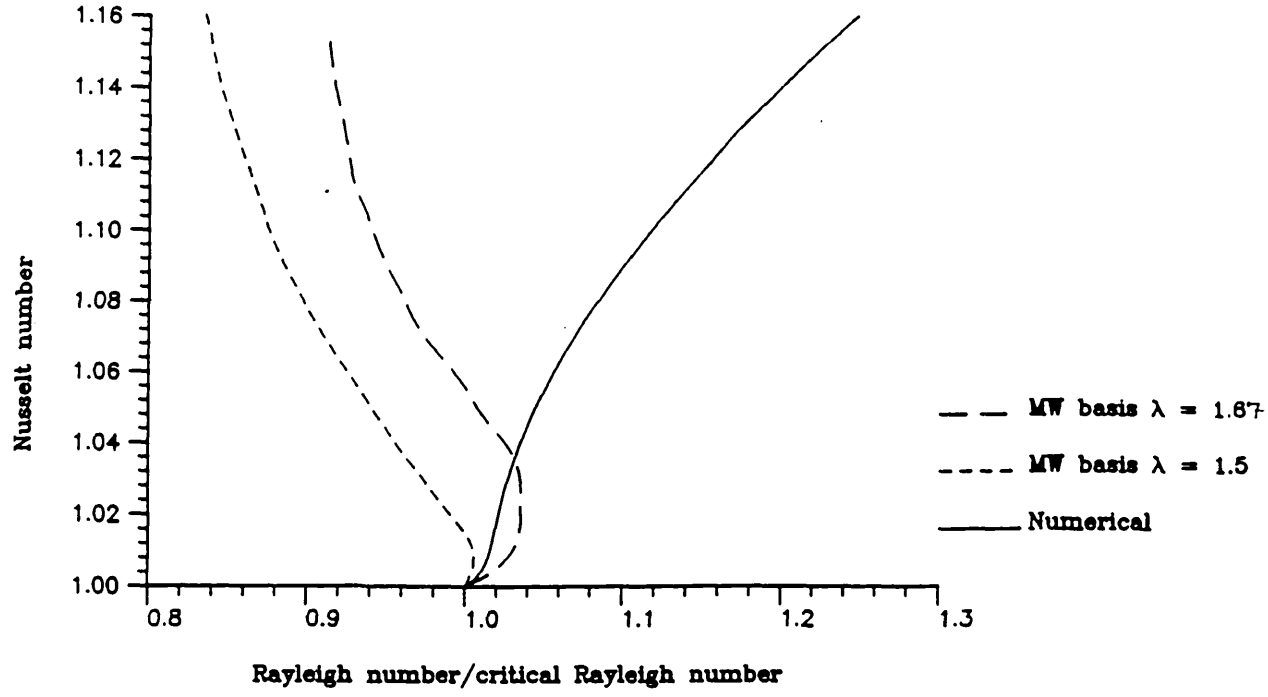
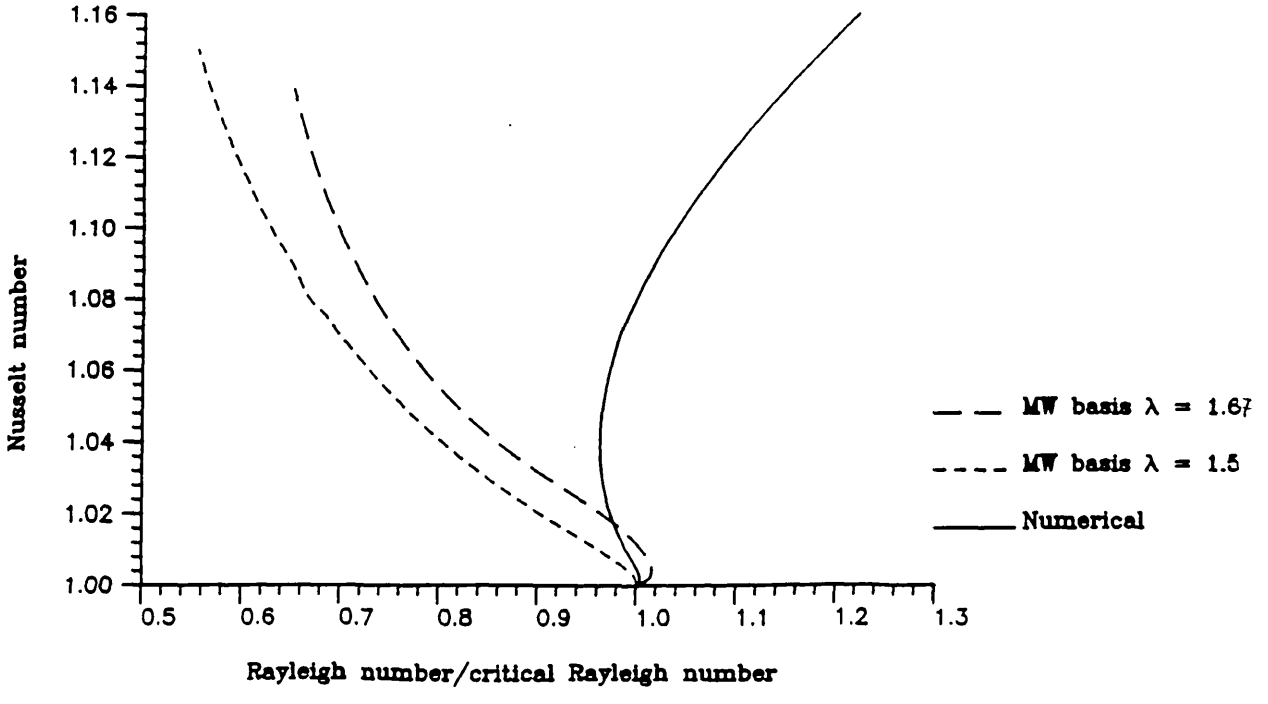


Figure 3.3d)
Rayleigh number against Nusselt number
MW model and numerical results, $\lambda = 6$, $\sigma = 0.1$

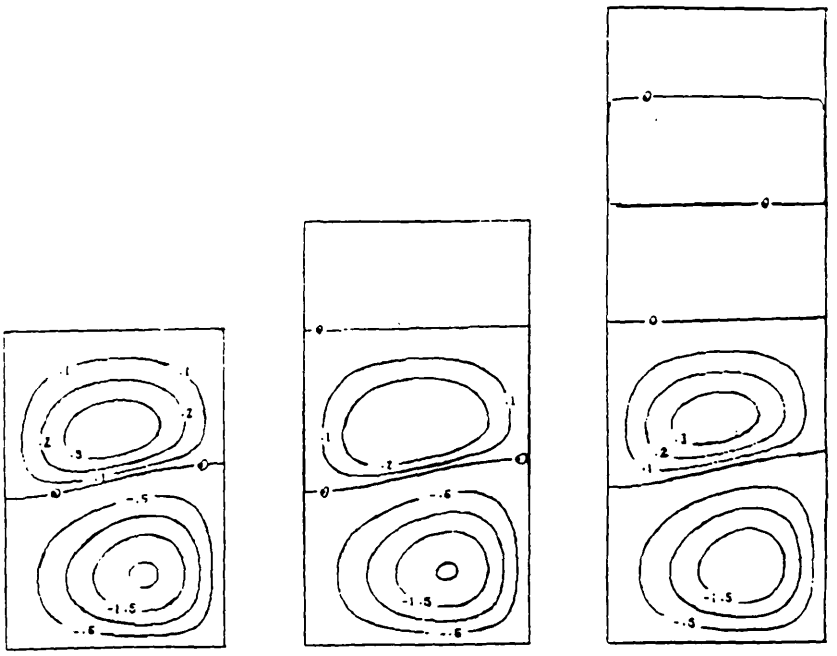


This idea was implemented by taking the case where the cell just fits the whole layer and using that value of the temperature at the top boundary as the fixed value of the temperature on the slippery plate of the model, and then using a graphical procedure, scaling the values for this cell up to predict the parametric constants of interest for other layer depths. These techniques were used successfully to predict the heat transport values for varying layer depths, but only for a moderate Prandtl number around that of the ice−water experiment. These results are confirmed in Figures 3.3a) and 3.3b) where the procedure is used to scale up the solution obtained numerically at $\lambda = 1.5$ to solutions at $\lambda = 3$ and $\lambda = 6$ and then compared with results obtained by direct numerical simulation for a Prandtl number of $\sigma = 10.0$. These results show that the predicted results coincide with the numerical ones almost exactly. However, when the procedure was repeated for lower Prandtl numbers, as shown in Figures 3.3c) and 3.3d), the predicted results were not at all in agreement with numerically calculated versions. Figures 3.3c) and 3.3d) compare the heat transport as a function of the Rayleigh number as predicted by the model and the numerically calculated result, for a layer depths $\lambda = 3$ and 6, and for a Prandtl number, $\sigma = 0.1$, and the discrepancy is large. In fact, figures 3.3c) and 3.3d) show that the numerically determined curve for the heat transport against the Rayleigh number in fact leaves the bifurcation point at the onset of convection and continues to increase monotonically, whereas the model−predicted curve is not monotonic, but curves back on itself. It seems as if the model version tries to retain a subcritical type bifurcation structure, despite the fact that the required result is actually supercritical. It can be seen that this occurs for both layer depths shown, $\lambda = 3$ and $\lambda = 6$, despite the fact that the greater layer depth has a less obvious supercritical style bifurcation. All this occurs even at these very low instability levels (low R) and low non−linearity levels (low Nu) and thus seems to indicate that the model fails due to some fundamental differences in the flow at the different Prandtl numbers.

The model was also recalibrated with a value of the temperature of the top of the main convecting cell as 1.67, a more realistic value than the 1.5 for the low Prandtl number flow where the top of the main cell is slightly warmer as gauged by the numerical calculations, but the results for heat transport, also shown in figures 3.3c) and 3.3d), still display vastly different behaviour when compared to the numerically calculated results.

Examine this failure further by consulting figures 3.2a) and 3.6a) which compares the numerically calculated results for Nusselt number against Rayleigh number for Prandtl numbers of $\sigma = 10$ (in the vicinity of the ice−water experiment) and $\sigma = 0.1$, both for a layer depth of $\lambda = 3$ (other λ are shown later as figures

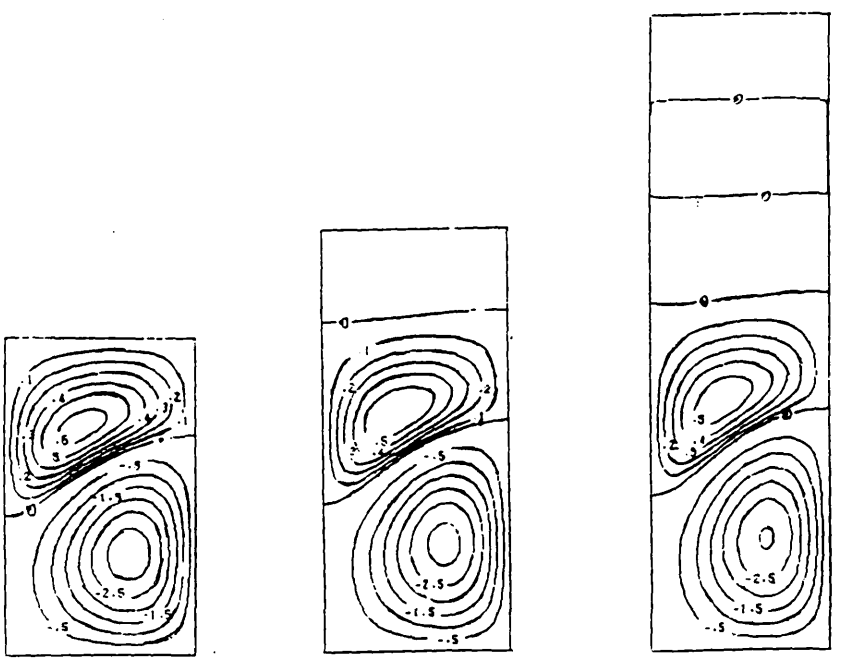
Figure 3.4



$\lambda = 3.0$
$\sigma = 10.0$
Nu = 1.08
$Nu_{eff} = 1.16$

$\lambda = 4.0$
$\sigma = 10.0$
Nu = 1.06
$Nu_{eff} = 1.16$

$\lambda = 6.0$
$\sigma = 10.0$
Nu = 1.04
$Nu_{eff} = 1.16$



$\lambda = 3.0$
$\sigma = 0.1$
Nu = 1.20
$Nu_{eff} = 1.4$

$\lambda = 4.0$
$\sigma = 0.1$
Nu = 1.15
$Nu_{eff} = 1.4$

$\lambda = 6.0$
$\sigma = 0.1$
Nu = 1.10
$Nu_{eff} = 1.4$

3.2c), 3.2d), 3.6c), 3.6d)). Notice again that the lower Prandtl number has a different bifurcation away from the critical value than the higher, with a supercritical curve being presented rather than the normal subcritical curve. This enlightens the failure of the model, which has its basis in the latter, a subcritical curve and so lacks the flexibilty to be able to follow the true supercritical behaviour (figure 3.3).

On the other hand, the principle behind the MW model seems sound i.e. an active region defined by the empirical constants, the effective Rayleigh and Nusselt numbers, may be used to predict results for varying layer depths. This can be verified by looking at numerical results, all of which have the same N_{eff} but are of differing total depth. These turn out to have very similar flow structures (figure 3.4) except that the larger layer depths have counter−cells sitting on top of the main convecting region. That is, the flows are similar in that the main convecting cells are of the same depth and have the same shaped interface, with similar temperature variation over the main cell, and, if the depths are sufficient, some of the counter−cells may overlay reasonably accurately too. Thus the failure of the previously successful model must lie in the fact that the behaviour of the fluid at low Prandtl number is sufficiently different from the behaviour at values of the parameter around the ice−water experiment, and that some aspect of the Moore and Weiss model is too simple, misses this difference and so fails to predict results accurately for this new regime.

The next section outlines the major differences between the flows at low and high Prandtl number, points out where the model will break down and attempts to offer modifications to the model to render it usable for the present area of interest.

3.4.3. LOW PRANDTL NUMBER FLOW.

3.4.3.1. Flow characteristics − ψ, ω and T.

In an attempt to reconcile the differences in the style of bifurcation between the low and high Prandtl number versions of the heat transport graphs, and the similar differences in the comparison of the model and numerical results, it is necessary to take a closer look at the physical flow characteristics.

As described in MW, for $\lambda > 1.91$ the convecting region does not fill the whole layer of fluid, but is topped by one or more weakly conductive,

Figure 3.5a)
Main cell–counter cell interface position
Effective Nusselt number = 1.16, σ = 10.0

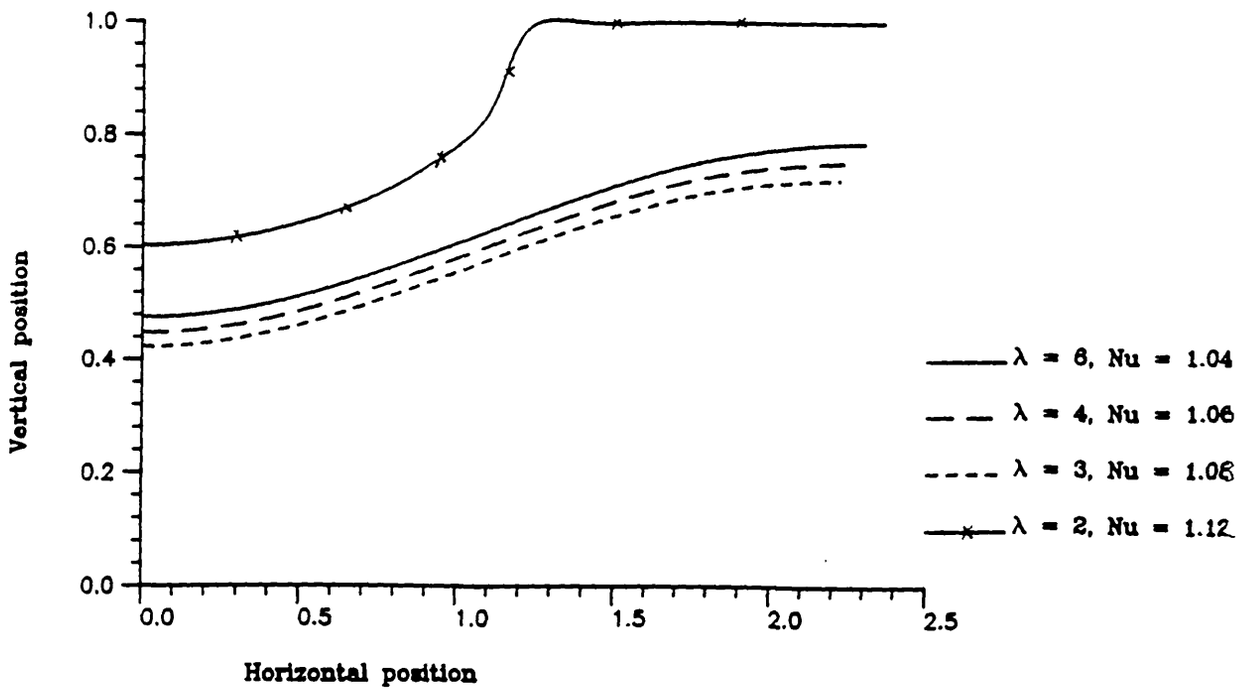


Figure 3.5b)
Main cell–counter cell interface temperature
Effective Nusselt number = 1.16, σ = 10.0

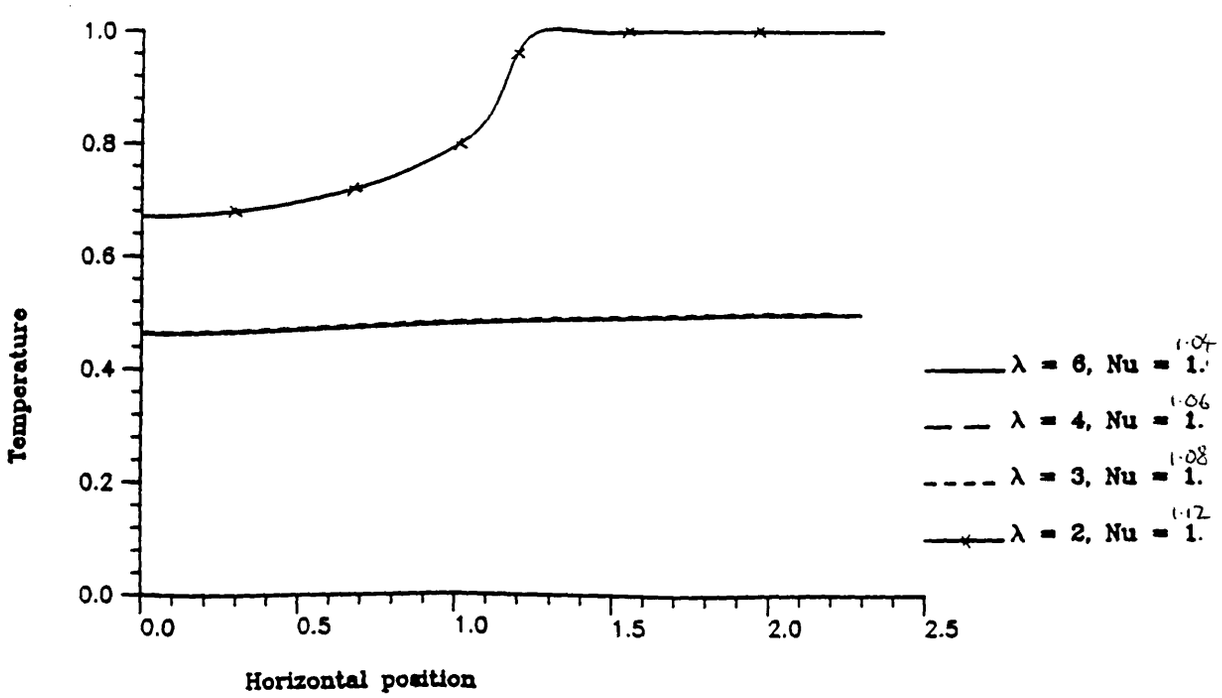


Figure 3.5c)
Main cell–counter cell interface position
Effective Nusselt number = 1.40, σ = 0.1

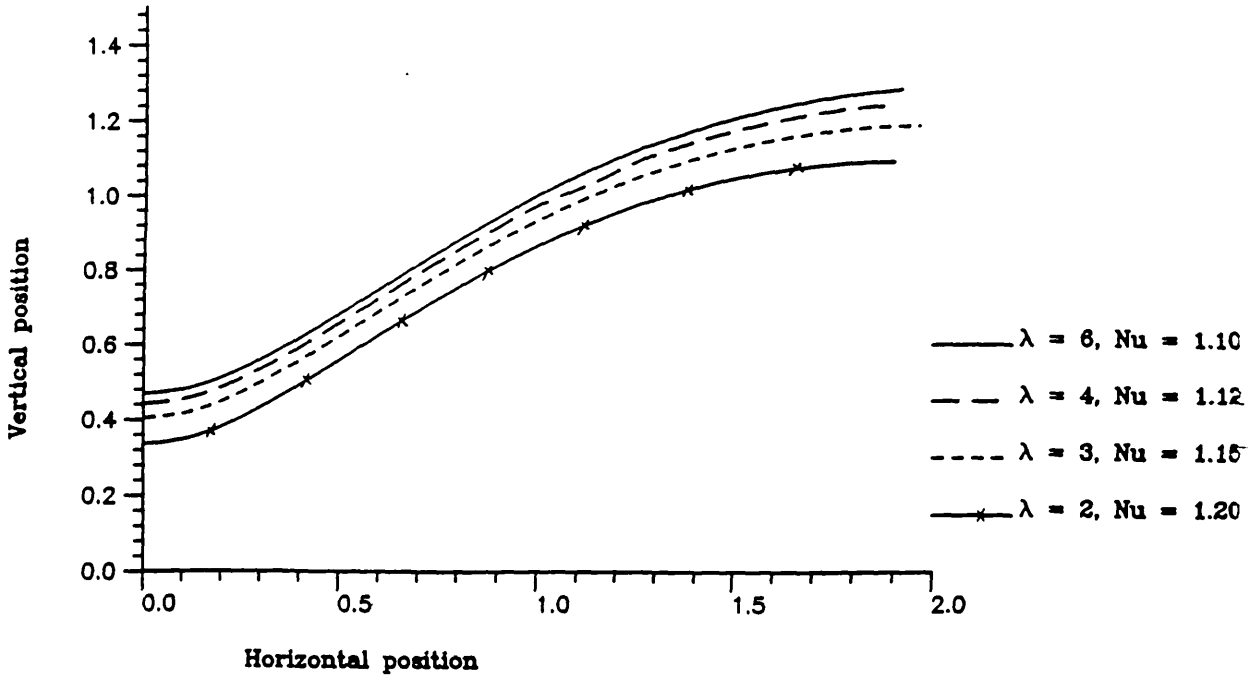


Figure 3.5d)
Main cell–counter cell interface temperature
Effective Nusselt number = 1.40, σ = 0.1

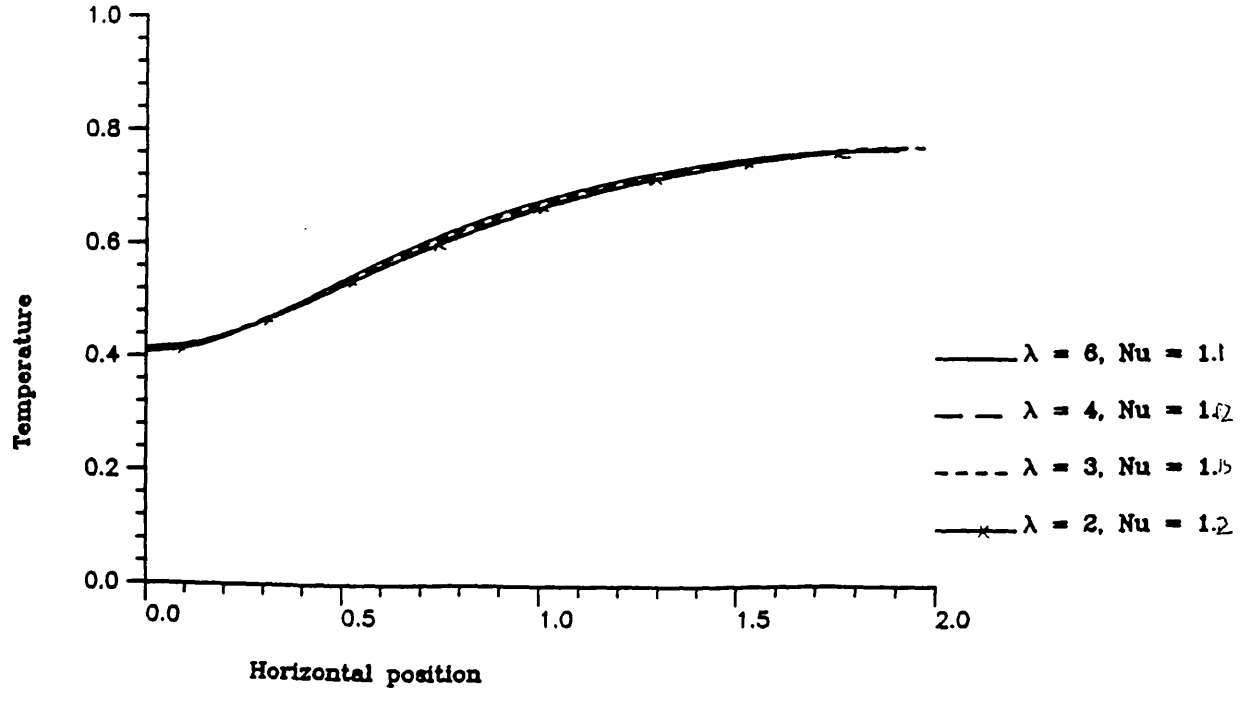


Figure 3.6a)
Rayleigh number against Nusselt number
$\lambda = 3.0$

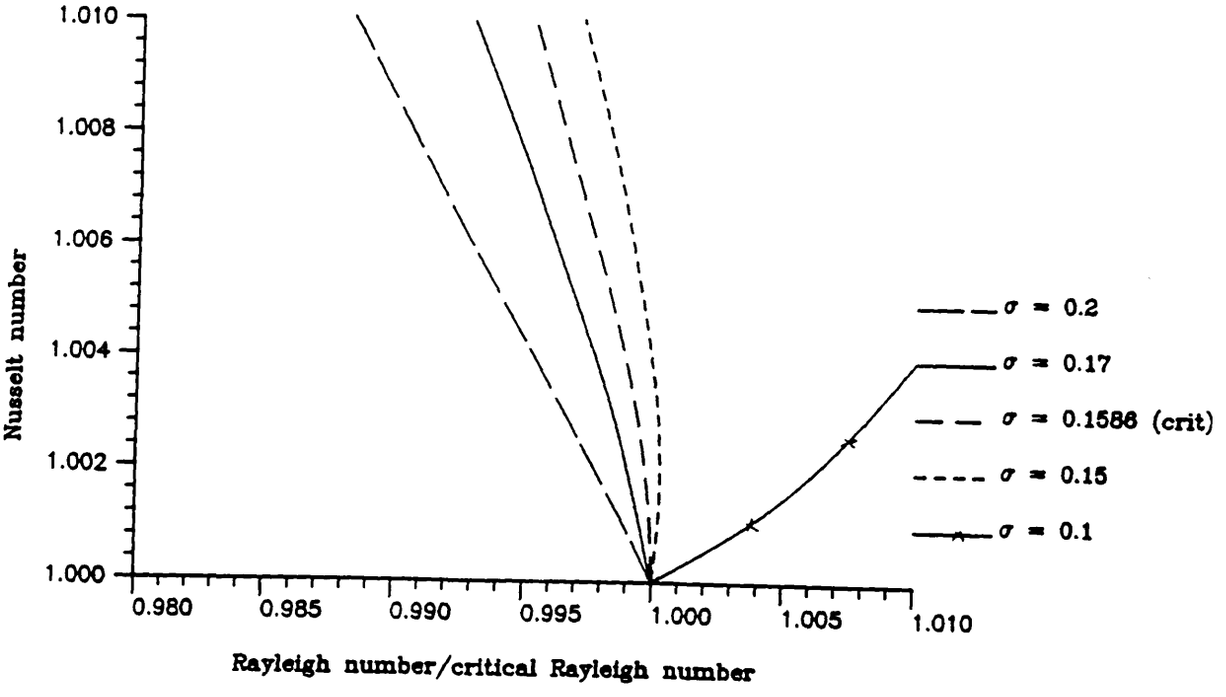


Figure 3.6b)
Rayleigh number against Nusselt number
$\lambda = 4.0$

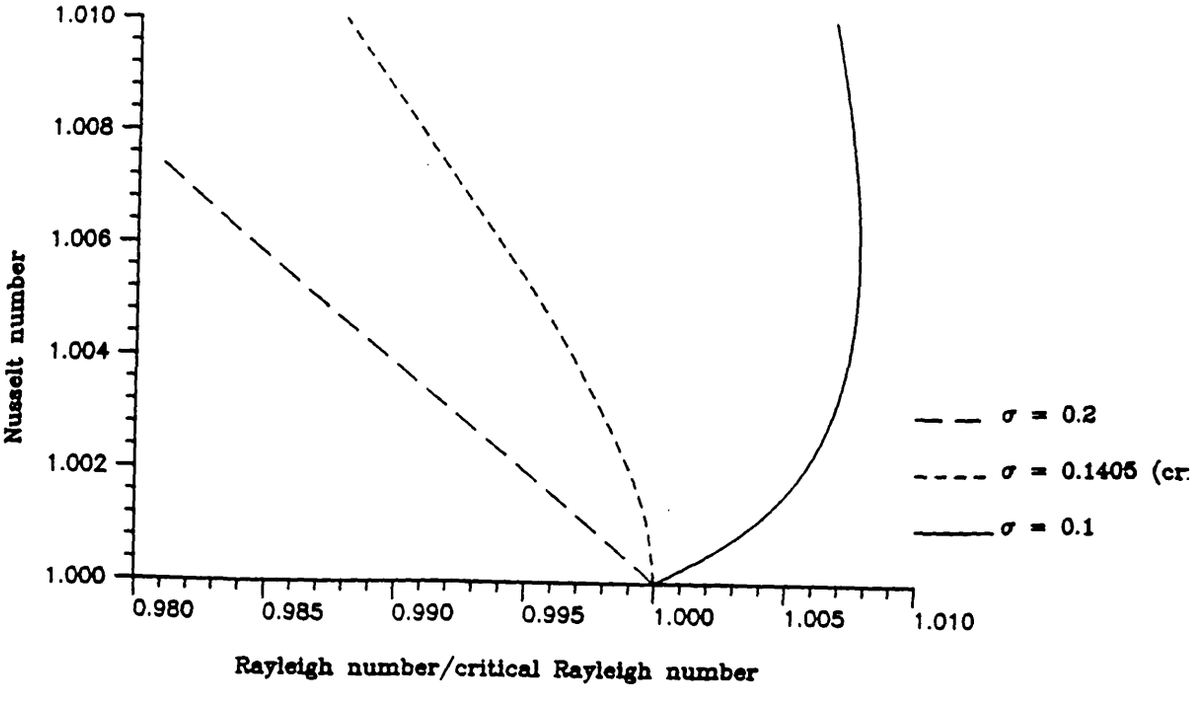
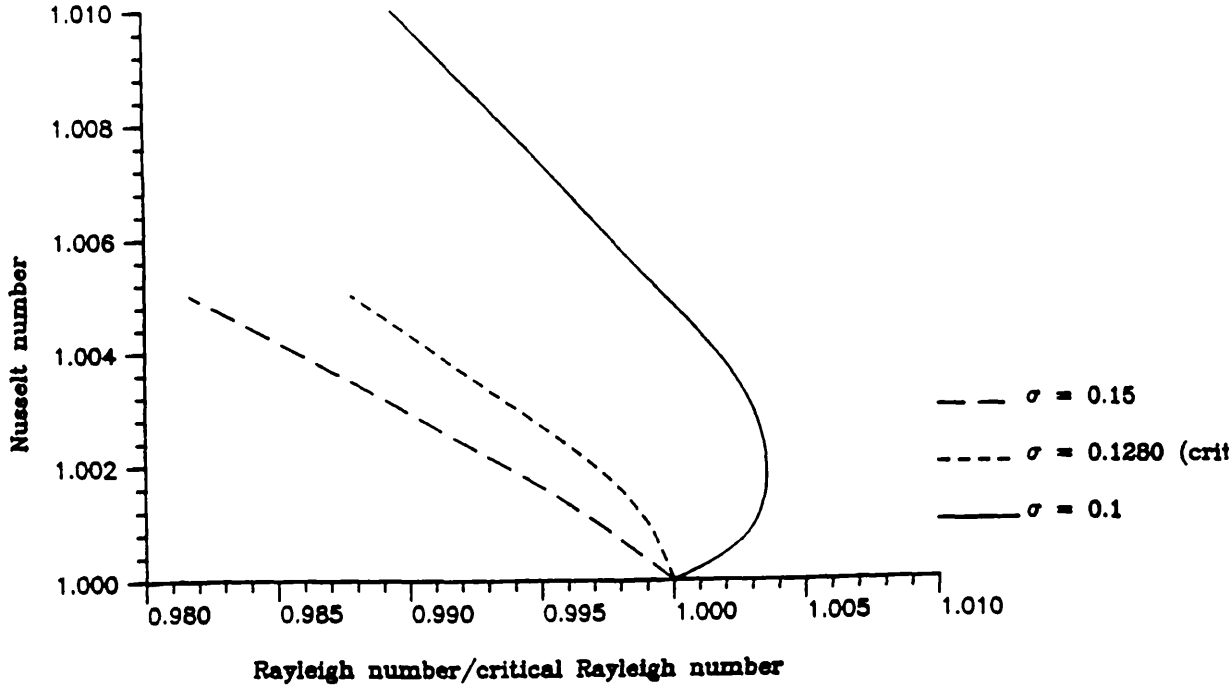


Figure 3.6c)
Rayleigh number against Nusselt number
$\lambda = 6.0$



counter−rotating cells. Penetration has been occurring for all $\lambda > 1$ but has been influenced by the upper boundary until $\lambda > 1.91$, whereafter the convective main cell is allowed to seek its own level. Thus $\lambda \geqslant 2$ is studied so that the upper boundary is not a restrictive effect and is decoupled from the problem.

Figures 3.5(a) − 3.5(d) show information pertaining to the free streamline across the divide between the main convecting cell and the first counter−cell. The position and temperature along that streamline are given for a high and a low Prandtl number for varying layer depths λ, with the Nusselt number adjusted for each so that the effective Nusselt number is the same in each case. The first two (figures 3.5(a), 3.5(b)) show results for a Prandtl number around that of the ice−water experiment i.e. $\sigma = 10$. Notice that even $\lambda = 2$ is still an exception to the pattern, being near enough to the critical λ where the first counter−cell occurs to have retained some influence of the upper boundary, but, in general, the temperature of the interface between the main and first counter−cells is consistently around 0.48 in the scaled units, corresponding to $\lambda \approx 1.5$. Notice also that the main cell has a flat−ish top with the interface varying little from a position on the $z = 0.5$ mark. All this information complies with the MW model which was based on the divide between main and counter−cell being a flat, imaginary plate at a fixed temperature, corresponding to $\lambda = 1.5$.

Examine the results in the figures for the lower Prandtl number, $\sigma = 0.1$ (figures 3.5(c), 3.5(d)). Now the spread of temperature along the interface is no longer only 0.03 between 0.46 and 0.49 but has increased ten−fold to a range

Fig. 3.7a)

λ = 3.0
σ = 10.000
Nu = 1.0600
Ra = 476.2352
α^2 = 2.0465

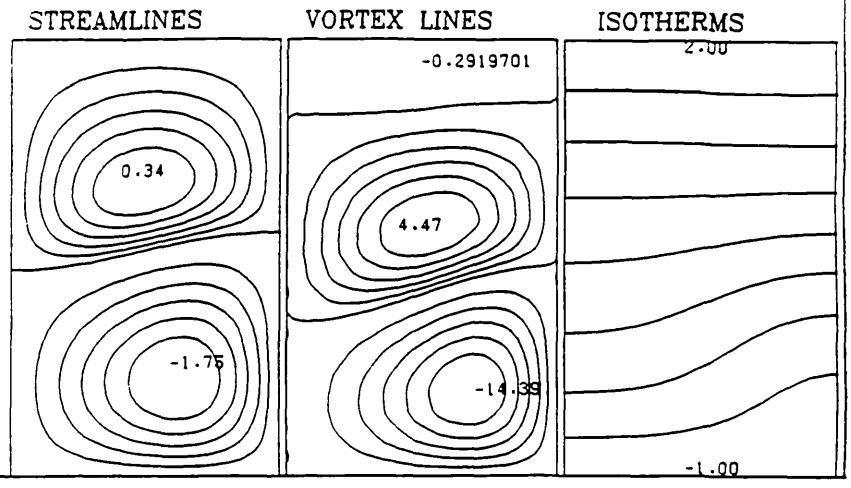


Fig. 3.7b)

λ = 3.0
σ = 10.000
Nu = 1.2000
Ra = 423.0665
α^2 = 2.0545

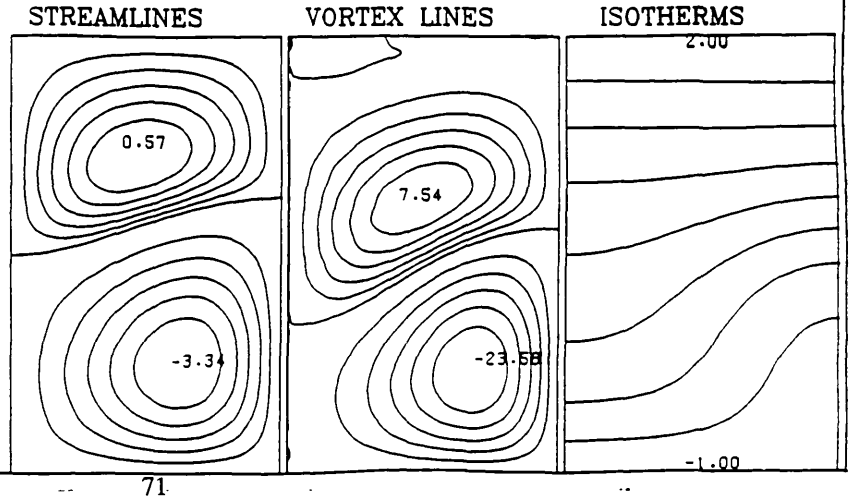
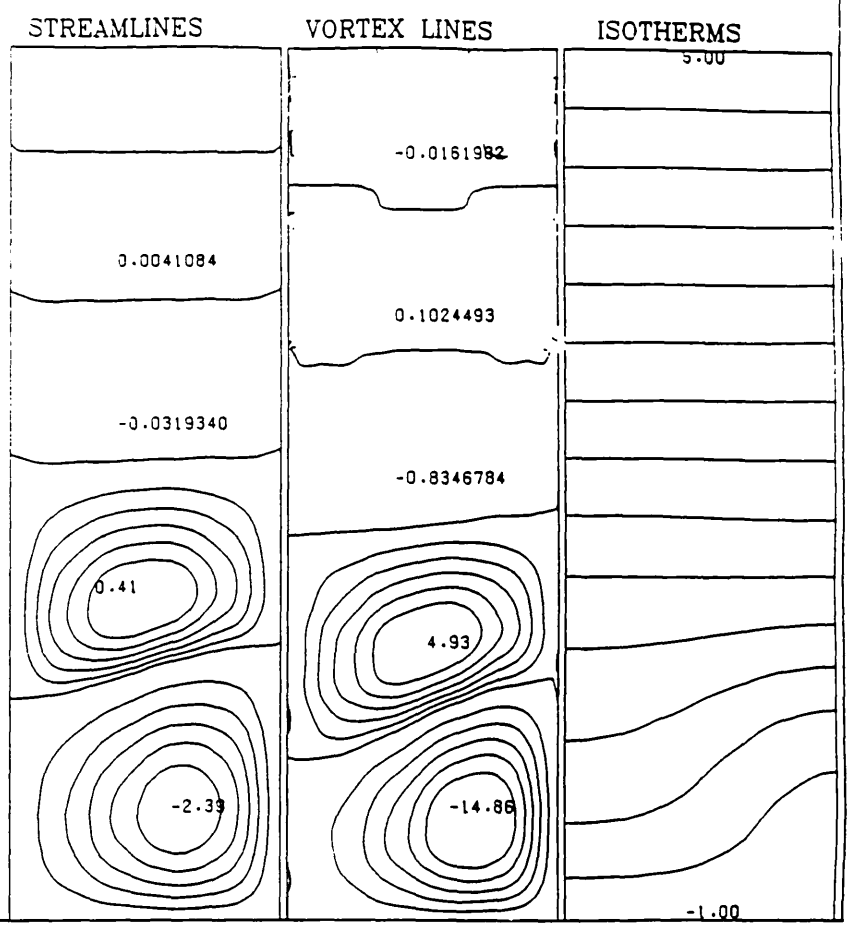
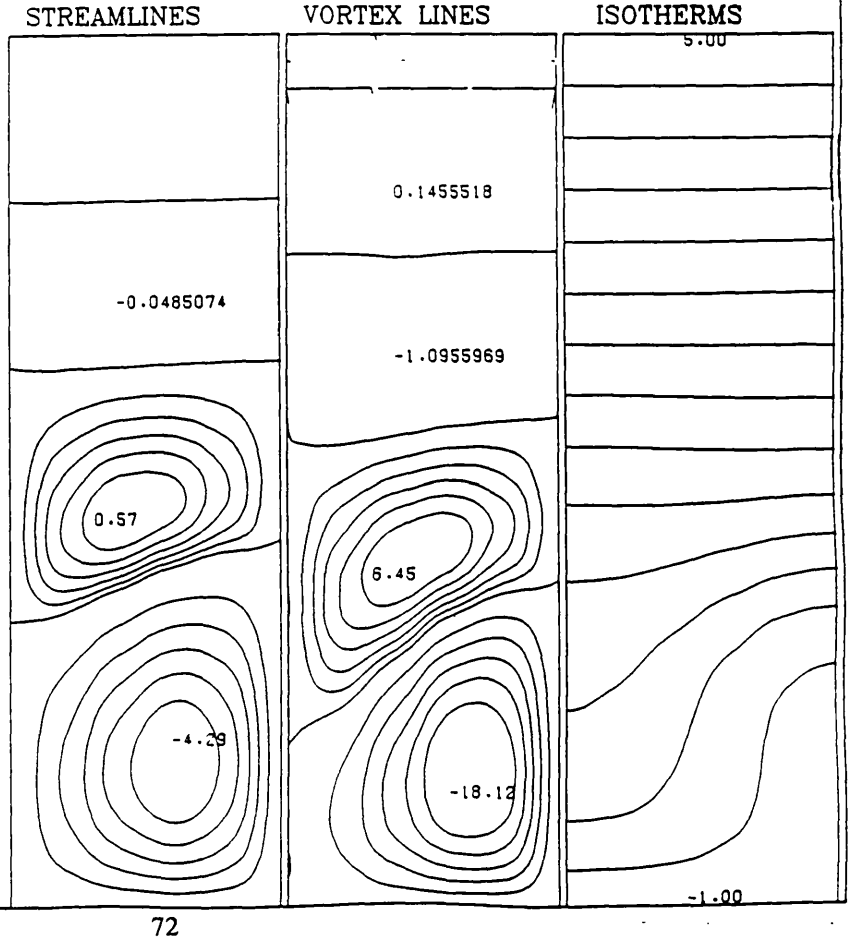


Fig. 3.7c)



λ = 6.0
σ = 10.000
Nu = 1.0600
Ra = 375.2980
α^2 = 1.7972

Fig. 3.7d)



λ = 6.0
σ = 10.000
Nu = 1.2000
Ra = 274.3458
α^2 = 1.5901

Fig. 3.7e)

λ = 3.0
σ = 0.100
Nu = 1.0600
Ra = 581.1150
α^2 = 2.9886

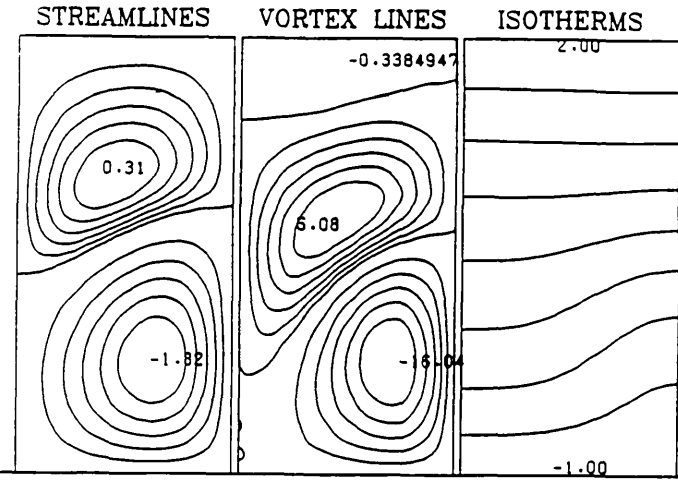


Fig. 3.7f)

λ = 3.0
σ = 0.100
Nu = 1.2000
Ra = 747.0580
α^2 = 2.7248

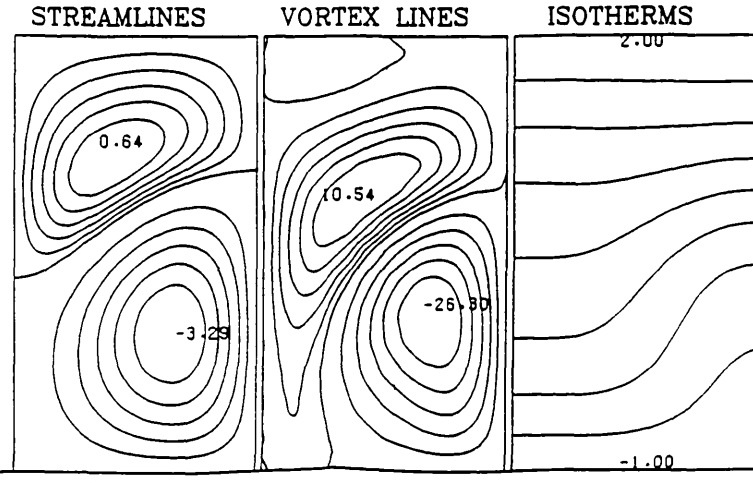
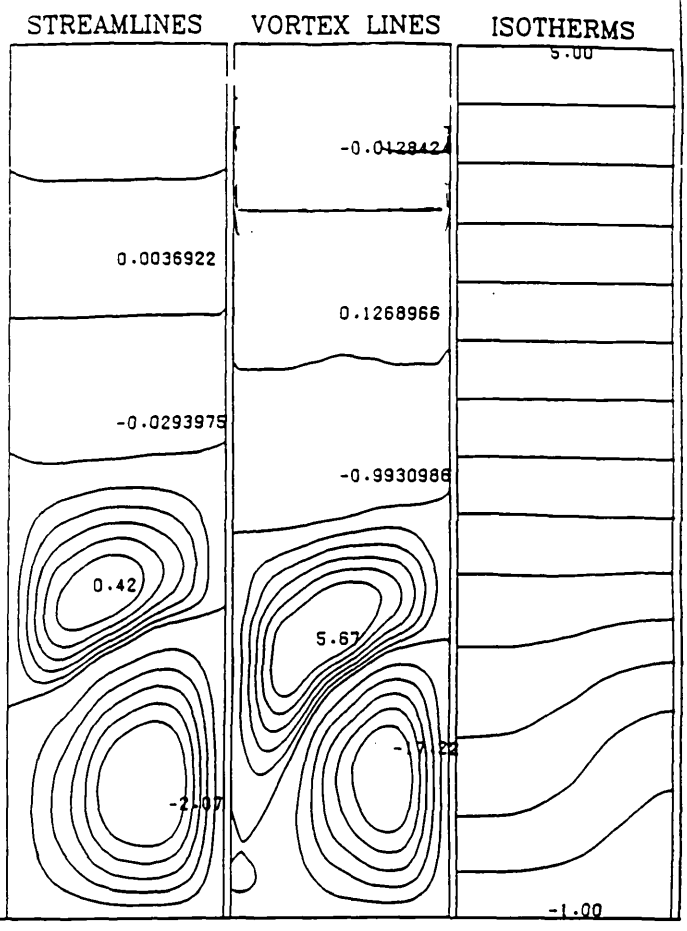
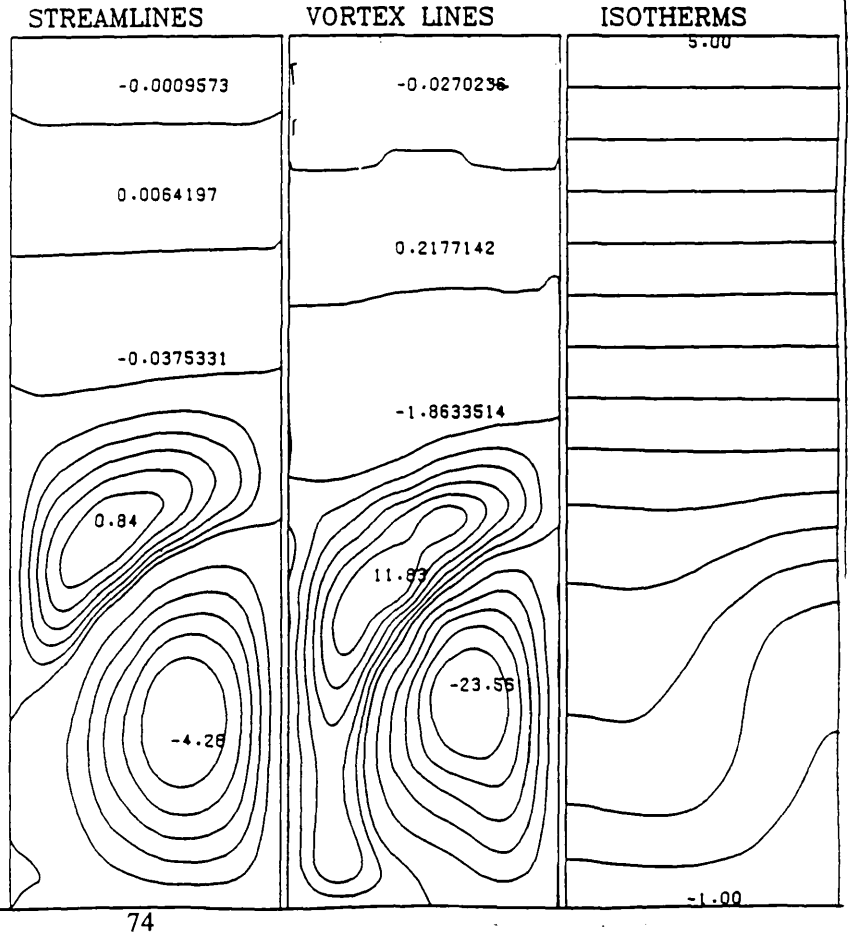


Fig. 3.7g)



λ = 6.0
σ = 0.100
Nu = 1.0600
Ra = 539.2421
α^2 = 2.6469

Fig. 3.7h)



λ = 6.0
σ = 0.100
Nu = 1.2000
Ra = 777.2415
α^2 = 1.8096

of 0.35 between 0.40 and 0.75 approximately. The interface is now no longer as flat, with a range of position between z = 0.3 and z = 1.3 as compared to the consistent z = 0.5 to z = 0.8 of the higher Prandtl number. So at the lower Prandtl number the cell boundary interface between the main cell and the first counter−cell is no longer flat nor isothermal as for the higher Prandtl number.

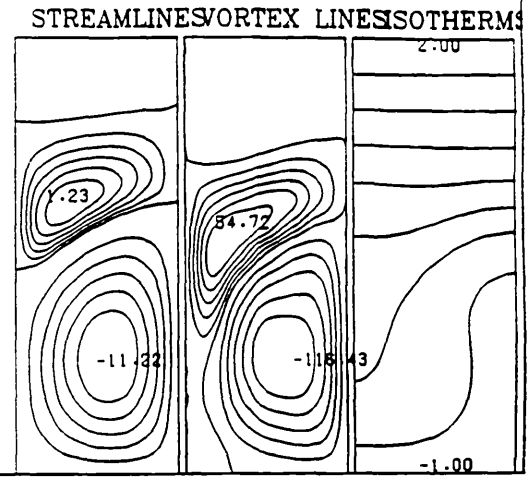
Figures 3.7a) − 3.7h) show the contours of constant streamfunction, constant vorticity and constant temperature for flows of two layer depths, $\lambda = 3$ and $\lambda = 6$, at two Nusselt numbers and two Prandtl numbers. Examining the contours of streamlines confirms that the interface between the main cell and its first counter−cell is reasonably flat and isothermal for the Prandtl number of $\sigma = 10$ as is expected in the MW model for both layer depths and both non−linearity levels, but that this is not true of the lower Prandtl number. For $\sigma = 0.1$, the boundary is tilted and cuts across the isotherms, the degree of the tilt increasing with the Nusselt number. In a purely conductive solution, the isotherms would be horizontal, so the distortion of the temperature profile is a good indication of the non−linear, penetrative effects. The isotherms shown here are not unusual, in that they show the descending plume of warmer fluid on the left, and the rising cool liquid on the right as is usually associated with convective mixing, but the lower Prandtl number isotherms are generally much more distorted than the higher σ (distortion increasing with a higher Nusselt number in both cases), showing the increasing penetration and efficiency due to the greater significance of the non−linear effects at lower Prandtl number.

The contours of constant vorticity give the greatest insight into the major differences between the high and low Prandtl number flow. The contours for $\sigma = 10$ divide themselves up into main cell and counter−cell in a fashion very similar to the streamlines, so that the vortex lines follow the streamlines reasonably closely. The low Prandtl number case shows a very different style of vorticity, the vortex lines now not being aligned with the streamlines in the sugar−loaf type solution. For low σ, the interface between the main vorticity cell and its first counter−cell dips sharply down on the warmer side of the cell, even plunging to the lower boundary for higher Nusselt numbers. Fluid elements are now transporting and exchanging vorticity as they circulate around the streamlines in the flow, rather than keeping a constant vorticity on any streamline.

The cause of the non−linear effects of penetration is the distortion of the mean temperature profile (Veronis (1963), Musman (1968)). The following procedure was adopted to investigate the possibility that the stretching of the unstable region in the distortion of the mean temperature profile was the cause of these low Prandtl number effects. The driving, penetrative term in the vorticity equation is the $RT\partial T/\partial x$ buoyancy term. This was replaced in the equations by the term

Fig. 3.8)

λ = 3.0
σ = 0.100
Nu = 1.5000
Ra = 4868.3306
α^2 = 5.4739



$Rz\partial T/\partial x$ so that the unstable region is effectively now confined to lie below the z = 0 mark, by the fact that the T=0 isotherm is now tied to the z = 0 line, whereas penetration would normally move the position of this isotherm upwards. This is a safe method as long as the Nusselt number is kept low. If not, the problem becomes insoluble, since penetrative convection works by balancing the conductive and convective heat fluxes (Malkus (1960)) in the main cell and counter−cells respectively. Confining the lower unstable region to a smaller area would mean that the large heat fluxes would have to be carried by conduction alone across the overly large stable region, which would lead to a strange and unphysically strong thermal gradient in the upper layer, characterized by a collection of closely spaced horizontal isotherms. Figure 3.8 shows a comparison of the results with the different driving term, and it may be seen that the effects described earlier for the low Prandtl number cases still persist despite this restriction, and thus it seems that the distortion of the unstable region does not account for these effects.

It may be concluded from these results that in outward appearance, low Prandtl number convection is not apparently much different from high, in that the

isotherms and streamlines do not show any more than the expected, slight increase in the vigour of penetration, but there is a less obvious change in the flow field inherent in the vorticity structure. The actual cell shape is only slightly distorted for $\sigma = 0.1$, but the 'flywheel' construction has been lost, and vorticity is now transported as the fluid elements follow the circular trajectory ensuring that vorticity is no longer constant on the streamlines. This new style of vorticity pattern indicates a greater degree of coupling between the main cell and the first counter−cell as vorticity is transported across the interface by the dipping first counter−cell in the vorticity structure. The interface between the main cell and the first counter−cell is also now definitely non−isothermal, and thus provides a mechanism for creating a temperature driven convection within the counter−cell as opposed to the expected totally conductive and passive nature of the overlying fluid. However, other interfaces between counter−cells may now be isothermal if the layer depth is deep enough to support them.

The failure of the MW model becomes apparent because the model uses a fixed temperature, flat, slippery, horizontal plate to divide the main cell from the counter−cells. At low Prandtl number, it can be seen that the interface is no longer flat, or horizontal, or isothermal, or of constant vorticity and thus the greater degree of coupling between the main and counter−cells exhibited in the low Prandtl number solution implies that more fluid than the main convecting cell is needed to provide a basic building unit for the model. However, the isothermal nature of other interfaces, if they are supported, lends credence to the principle of the MW model once again, and extensions to the model are discussed in section 3.4.4.

3.4.3.2. Critical Prandtl numbers.

3.4.3.2.1. The expansion.

Figures 3.2 and 3.6 showing the different bifurcations for low and high σ solutions of the penetrative problem demand an investigation into the flows in the parameter regions associated with the bifurcations. The change from subcritical to supercritical is of paramount interest because this may yield information about the limitations of such models of convection as the MW model, where it appears that a model which is based on one style of flow may fail for the other style. That Prandtl number where the bifurcation is neither subcritical or supercritical will be

referred to as the critical Prandtl number for this transition, and an investigation of these critical values was carried out as follows.

Expansion of the physical system as a singular perturbation expansion about a small parameter, ϵ, representing the amplitude of convection, in the style of Malkus and Veronis (1958) and later Veronis (1963) was used as a useful construction for finding critical values of the Prandtl number. This process is also a different approach from the original modal expansion and so comparison of the two sets of results also serves as a useful cross−check of the validity of the programming.

The physical quantities are expanded as follows,

$$\psi = \epsilon \sum_{i=1}^{\infty} \psi_1^i(z) \sin(i\alpha x) + \epsilon^2 \sum_{i=1}^{\infty} \psi_2^i(z) \sin(i\alpha x) + \ldots \qquad [3.71]$$

$$\omega = \epsilon \sum_{i=1}^{\infty} \omega_1^i(z) \sin(i\alpha x) + \epsilon^2 \sum_{i=1}^{\infty} \omega_2^i(z) \sin(i\alpha x) + \ldots \qquad [3.72]$$

$$T = T_0(z) + \epsilon \sum_{i=1}^{\infty} T_1^i(z) \cos(i\alpha x) + \epsilon^2 \sum_{i=1}^{\infty} T_2^i(z) \cos(i\alpha x) + \ldots \qquad [3.73]$$

$$R = R_0 + \epsilon R_1 + \epsilon^2 R_2 + \ldots \qquad [3.74]$$

Substitution of these expansions into the governing equations [3.10] − [3.12] creates an equation set involving an infinity of trigonometric functions, all prefixed by some power of the expansion coefficient, ϵ. Now collect the terms in powers of this coefficient and examine the equations produced at each order.

At $O(\epsilon)$, the linear equations are

$$0 = \alpha R_0 T_0 \sum_i i T_1^i \sin(i\alpha x) + \sum_i D^2 \omega_1^i \sin(i\alpha x) - \alpha^2 \sum_i i^2 \omega_1^i \sin(i\alpha x) \quad , \qquad [3.75]$$

$$\left[\alpha \sum_i i \psi_1^i \cos(i\alpha x)\right] . DT_0 = D^2 T_0 - \alpha^2 \sum_i i^2 T_1^i \cos(i\alpha x) + \sum_i D^2 T_1^i \cos(i\alpha x) \quad , \qquad [3.76]$$

$$- \alpha^2 \sum_i i^2 \psi_1^i \sin(i\alpha x) + \sum_i D^2 \psi_1^i \sin(i\alpha x) = - \sum_i \omega_1^i \sin(i\alpha x) \quad , \qquad [3.77]$$

which become, on comparison of trigonometric terms,

$$D^2\omega_1^i - i^2\alpha^2\omega_1^i = -i\alpha R_0 T_0 T_1^i \quad , \qquad [3.78]$$

$$D^2T_0 = -D^2T_1^i \quad , \qquad [3.79]$$

$$D^2T_1^i - i^2\alpha^2T_1^i = i\alpha\psi_1^i . DT_0 \quad , \qquad [3.80]$$

$$D^2\psi_1^i - i^2\alpha^2\psi_1^i = -\omega_1^i \quad , \qquad [3.81]$$

for all $i = 1,2,...$

However, this infinity of solutions for the i's is degenerate in the sense that they only represent solutions in multiples of the lowest order wavelength which is given by $i = 1$, i.e., the $i = 1$ solution represents one cell-width of a function $\sin\alpha x$, whereas $i = 3$, for example, represents a cell width three times wider, but filled by a $\sin 3\alpha x$ function, and so the overall physical solution is exactly the same. Thus, the superscript index may be dropped, and only one linear solution rather than an infinity may be considered.

This degeneracy is not necessarily true of higher order solutions, however, and so expansion of the higher order ϵ equations and comparison of trigonometric terms reveals, after a lot of tedious algebra, the reduced set of non-degenerate, non-null functions

$$\psi = \epsilon\psi_1^1 \sin\alpha x + \epsilon^2\psi_2^2 \sin 2\alpha x + \epsilon^3(\psi_3^1 \sin\alpha x + \psi_3^3 \sin 3\alpha x) + \ldots \qquad [3.82]$$

$$\omega = \epsilon\omega_1^1 \sin\alpha x + \epsilon^2\omega_2^2 \sin 2\alpha x + \epsilon^3(\omega_3^1 \sin\alpha x + \omega_3^3 \sin 3\alpha x) + \ldots \qquad [3.83]$$

$$T = T_0 + \epsilon T_1^1 \cos\alpha x + \epsilon^2(T_2^0 + T_2^2 \cos 2\alpha x) + \epsilon^3(T_3^1 \cos\alpha x + T_3^3 \cos 3\alpha x) + \ldots \qquad [3.84]$$

$$R = R_0 + \epsilon R_1 + \epsilon^2 R_2 + \ldots \qquad [3.85]$$

where any sub- or super-scripted variable is a function of z.

Once again, as in the derivation of the normal set of equations, it is possible to introduce α as a scalar multiplier for vorticity and streamfunction terms, in order to bring out the natural parameter α^2 in the equations. This is done here to enable sensible comparisons between this section of work and the previous sections, but on introduction of the α scaling factor and substitution, the primes on the new variables are dropped immediately. Hence, the corresponding equations for the scaled variables are,

Order ϵ:

$$D^2\omega_1^1 - \alpha^2\omega_1^1 = -\alpha^2 R_0 T_0 T_1^1 \,, \qquad [3.86]$$

$$D^2T_1^1 - \alpha^2 T_1^1 = DT_0\,\psi_1^1 \,, \qquad [3.87]$$

$$D^2\psi_1^1 - \alpha^2\psi_1^1 = -\omega_1^1 \,, \qquad [3.88]$$

Order ϵ^2:

$$D^2\omega_2^2 - 4\alpha^2\omega_2^2 = \frac{1}{2\sigma}\left[\,\psi_1^1 D\omega_1^1 - D\psi_1^1\omega_1^1\,\right] - 2\alpha^2 R_0 T_0 T_2^2 - \frac{\alpha^2 R_0 (T_1^1)^2}{2} \,, \qquad [3.89]$$

$$R_1 = 0 \,, \qquad [3.90]$$

$$D^2T_2^2 - 4\alpha^2 T_2^2 = \frac{1}{2\sigma}\left[\,\psi_1^1 DT_1^1 - D\psi_1^1\omega_1^1\,\right] + 2\psi_2^2 DT_0 \,, \qquad [3.91]$$

$$D^2T_2^0 = \frac{1}{2}\left[\,\psi_1^1 DT_1^1 + D\psi_1^1 T_1^1\,\right] \,, \qquad [3.92]$$

$$D^2\psi_2^2 - 4\alpha^2\psi_2^2 = -\omega_2^2 \,, \qquad [3.93]$$

Order ϵ^3:

$$D^2\omega_3^1 - 4\alpha^2\omega_3^1 = \frac{1}{\sigma}\left[\,\frac{\psi_1^1 D\omega_2^2}{2} + D\psi_1^1\omega_2^2 - \psi_2^2 D\omega_1^1 - \frac{D\psi_2^2\omega_1^1}{2}\,\right] - \alpha^2 R_0 T_0 T_3^1 - \alpha^2 R_0 T_1^1 T_2^0 - \frac{\alpha^2}{2} R_0 T_1^1 T_2^2 - \alpha^2 R_2 T_0 T_1^1 \,, \qquad [3.94]$$

$$D^2\omega_3^3 - 9\alpha^2\omega_3^3 = \frac{1}{\sigma}\left[\,\frac{\psi_1^1 D\omega_2^2}{2} - D\psi_1^1\omega_2^2 + \psi_2^2 D\omega_1^1 - \frac{D\psi_2^2\omega_1^1}{2}\,\right] - 3\alpha^2 R_0 T_0 T_3^3 - \frac{3}{2}\alpha^2 R_0 T_1^1 T_2^2 \,, \qquad [3.95]$$

$$D^2T_3^1 - \alpha^2 T_3^1 = \left[\,\frac{DT_2^2\psi_1^1}{2} + DT_1^1\psi_2^2 + T_1^1 D\psi_2^2 + \frac{T_2^2 D\psi_1^1}{2}\,\right] + DT_0\psi_3^1 + DT_2^0\psi_1^1 \,, \qquad [3.96]$$

$$D^2T_3^3 - 9\alpha^2 T_3^3 = \left[\,DT_1^1\psi_2^2 + DT_2^2 - \frac{T_1^1 D\psi_2^2}{2} - \frac{T_2^2 D\psi_1^1}{2}\,\right] + 3DT_0\psi_3^3 \,, \qquad [3.97]$$

$$D^2\psi_3^1 - \alpha^2\psi_3^1 = -\omega_3^1 \,, \qquad [3.98]$$

$$D^2\psi_3^1 - 9\alpha^2\psi_3^3 = -\omega_3^3 \,. \qquad [3.99]$$

Notice that the term in the Rayleigh number at order ϵ drops out as a by-product of the ϵ^2 equation in ω, since it turns up in the term involving the interaction of the first linear temperature mode and the mean temperature profile, thus having a $\sin\alpha x$ dependence, whereas all other terms in the equation are dependent on $\sin 2\alpha x$. Hence $R_1 \equiv 0$ due to the orthogonality of $\sin\alpha x$ and $\sin 2\alpha x$ (see Veronis (1963), or for a more rigorous argument, see the Rayleigh-Benard version of Schluter, Lortz and Busse (1965). The solvability condition explained later also proves this more rigorously.). The parameter of interest is now R_2 since its sign determines whether the Rayleigh number is sub- or super-critical.

3.4.3.2.2. Calculation of R_2 and the solvability condition.

It is now required to evaluate R_2 and the critical Prandtl number i.e. that Prandtl number such that $R_2 = 0$.

Equations [3.86] - [3.99] show that, at each order of ϵ, there are a number of sets of ordinary differential equations produced. In general, at order ϵ^i, the set of equations may be described by

$$\Lambda^n[\ \Phi_i^n\ ] = R_i^n \qquad [3.100]$$

where $\Phi_i^n = (\ \omega_i^n,\ T_i^n,\ \psi_i^n\ )^T$, Λ^n is a vector differential operator and R_i^n is a vector of remainders. Note that not all orders of ϵ take all values of the superscript n, since at each order, many of the trigonometric dependences have been eliminated by the earlier comparison of the trigonometric terms, and the reduction of the equations to the non-null variables. At first order, only $n = 1$ solutions exist, at second, only $n = 2$, but at third, both $n = 1$ and $n = 3$ remain. The vector differential operator, Λ^n, is in general explicitly given by

$$\Lambda^n = (\ D^2 - n^2\alpha^2\ ) + \begin{bmatrix} 0 & n\alpha^2 R_0 DT_0 & 0 \\ 0 & 0 & -1 \\ 1 & 0 & 0 \end{bmatrix}\ , \qquad [3.101]$$

and the rest of the terms in equations [3.86] - [3.99] are remainder vectors dependent solely on physical quantities of lower order in ϵ.

The linear order ϵ equations give rise to a homogeneous problem,

$$\Lambda^1[\Phi_1^1] = 0\ ,\quad \text{i.e.}\quad R_1^1 = 0\ , \qquad [3.102]$$

which is immediately soluble using the usual boundary conditions. However, each subsequent order produces an inhomogeneous vector equation where R_n^i is not zero, and this introduces the next component in the expansion of R as an extra unknown. For example, the linear equations are in terms of the subscript 1 (linear) variables and the critical Rayleigh number, R_0. The second order equations (ϵ^2) have left hand sides of subscript 2 variables and R_1, and a right hand side of lower order subscript 1 variables. The order ϵ^3 equations are in terms of the subscript 3 variables and R_2, with a right hand side involving previously calculated lower order variables. Now, R_0 is known from linear theory, and it turns out that $R_1 = 0$ so that both $O(\epsilon)$ and $O(\epsilon^2)$ may be solved. However, the $O(\epsilon^3)$ equations contain the unknown R_2 term, so a new condition is needed to solve the equations at next order. The condition to do this is known as the 'solvability condition' (Ince (1926), Malkus and Veronis (1958), Veronis (1963)), and this eventually enables us to solve for R_2 as the ratio of two integrals as follows.

The solvability condition, as given by Ince (1926) states that, if a series of differential equations exist, such that

$$\Lambda(u_1) = 0 \quad ,$$

$$\Lambda(u_2) = r_2 \quad ,$$

$$\Lambda(u_3) = r_3 \quad , \quad \ldots$$

where Λ is a scalar differential operator, acting on scalars $u_i(x)$, then

$$\int_{\text{range}[x]} u_1^* r_i \, dx = 0 \quad , \quad i = 2,3,..$$

where u_1^* is a solution of the adjoint linear problem. A formal proof that this is also valid if Λ is a vector operator, Λ, operating on vectors $\mathbf{u_i}$, is given in Stakgold (1979), but a hopefully clearer explanation is offered here in Appendix 3. R_2 occurs in the remainder, R_3^1, of equation [3.94], which has the same vector differential operator Λ^1 as the linear system, and so the solvability condition can be applied to equation [3.94] to produce a condition including R_2 if the adjoint linear problem is solved first. That is, there exists

$$\Lambda^1[\Phi_1^1] = 0 \quad , \qquad [3.103]$$

and

$$\Lambda^1[\Phi_3^1] = R_3^1 \quad , \qquad [3.104]$$

therefore a solvability condition,

$$\int_{-1}^{\lambda-1} \Phi_1^{1*} . R_3^1 \, dz = 0 \quad , \qquad [3.105]$$

also exists.

To apply this, the adjoint linear system and its solution must be found. The linear system may be written as

$$D\Phi_{e_1}^1 = \underline{A} \, \Phi_{e_1}^1 \quad , \qquad [3.106]$$

where $\Phi_{e_1}^1 = (\omega_1^1 , D\omega_1^1 , T_1^1 , DT_1^1 , \psi_1^1 , D\psi_1^1)^T$ is the extended vector for the system of first order differential equations arising from the original linear system, and

$$\underline{A} = \begin{bmatrix} 0 & 1 & 0 & 0 & 0 & 0 \\ \alpha^2 & 0 & -DT_0\alpha^2R_0 & 0 & 0 & 0 \\ 0 & 0 & 0 & 1 & 0 & 0 \\ 0 & 0 & \alpha^2 & 0 & 1 & 0 \\ 0 & 0 & 0 & 0 & 0 & 1 \\ -1 & 0 & 0 & 0 & \alpha^2 & 0 \end{bmatrix} . \qquad [3.107]$$

This system is equivalent to $\Lambda \, \Phi = 0$, where $\Lambda = D - \underline{A}$, and thus the adjoint system $\Lambda_a \, \Phi_a = 0$, required is given by $\Lambda_a = D + \underline{A}^*$, where $\underline{A}^*$ is the conjugate transpose of $\underline{A}$ (Coddington and Levinson (1955), page 70).

Thus, $D \, \Phi_a = - \underline{A}^* \, \Phi_a$, where $\Phi_a = (\Phi_{a1} , \Phi_{a2} , \Phi_{a3} , \Phi_{a4} , \Phi_{a5} , \Phi_{a6})^T$, and

$$-\underline{A}^* = \begin{bmatrix} 0 & -\alpha^2 & 0 & 0 & 0 & 1 \\ -1 & 0 & 0 & 0 & 0 & 0 \\ 0 & DT_0\alpha^2R_0 & 0 & -\alpha^2 & 0 & 0 \\ 0 & 0 & -1 & 0 & 0 & 0 \\ 0 & 0 & 0 & -1 & 0 & -\alpha^2 \\ 0 & 0 & 0 & 0 & -1 & 0 \end{bmatrix} , \qquad [3.108]$$

and re-writing this as a second order system, the equations revealed are

$$(D^2 - \alpha^2) \Phi_{a2} = - \Phi_{a6} \quad , \qquad [3.109]$$

$$(D^2 - \alpha^2) \Phi_{a4} = - \alpha^2 DT_0 R_0 \Phi_{a2} \quad , \qquad [3.110]$$

$$(D^2 - \alpha^2) \Phi_{a6} = \Phi_{a4} \quad . \qquad [3.111]$$

Comparing this to the original system of linear equations, it may be seen that the solution to these is the same as the solution of that linear system if Φ_{a2} is identified as T_1^1 , Φ_{a4} is identified as ω_1^1 , and Φ_{a6} is identified as ψ_1^1 . The only problem with this association is the identification of the necessary boundary conditions for the adjoint problem from the original, linear problem. However, it turns out that in this case, the boundary conditions are exactly the same for both problems, i.e. the boundary conditions on the adjoint variables are the same as the boundary conditions on the associated linear problem variables. Thus, the solution of the linear problem can be used directly as a solution to the adjoint problem, simply by the appropriate permutation of the variables. A clarification of the appropriateness of the solvability condition for systems, and an explanation of how to find the necessary adjoint boundary conditions from the original system are included in Appendix 1.

Hence, the solvability condition may now be applied with the appropriate linear variables as the adjoint variables, i.e. the solvability condition becomes,

$$\int_{-1}^{\lambda-1} \begin{bmatrix} T_1^1 \\ \omega_1^1 \\ \psi_1^1 \end{bmatrix} . R_3^1 \, dz = 0 \quad , \qquad [3.112]$$

and so,

$$\int_{-1}^{\lambda-1} \left\{ T_1^1 \left[- \alpha^2 R_2 DT_0 - \alpha^2 R_0 T_1^1 T_2^0 - \frac{\alpha^2}{2} R_0 T_1^1 T + \frac{1}{2\sigma}(\psi_1^1 D\omega_2^2 - D\psi_2^2 \omega_1^1) + \frac{1}{\sigma}(D\psi_1^1 \omega_2^2 - \psi_2^2 D\omega_1^1) \right] + \omega_1^1 \left[DT_2^0 \psi_1^1 + 2(DT_1^1 \psi_2^2 + T_2^2 \psi_1^1) + (DT_2^2 \psi_1^1 + T_1^1 D\psi_2^2) \right] + \psi_1^1 \left[0 \right] \right\} dz = 0 \quad , \qquad [3.113]$$

and, thus R_2 can be expressed as the ratio of two integrals,

$$R_2 = \frac{\int_{-1}^{\lambda-1} \left\{ \begin{array}{l} -\alpha^2 R_0 T_2^0 (T_1^1)^2 - \frac{\alpha^2}{2} R_0 (T_1^1)^2 T_2^2 + \frac{T_1^1}{2\sigma}(\psi_1^1 D\omega_2^2 - D\psi_2^2 \omega_1^1) \\ + \frac{T_1^1}{\sigma}(D\psi_1^1 \omega_2^2 - \psi_2^2 D\omega_1^1) \\ + \omega_1^1 DT_2^0 \psi_1^1 + \omega_1^1 (DT_1^1 \psi_2^2 + T_2^2 D\psi_1^1) + \frac{\omega_1^1}{2}(DT_1^2 \psi_2^2 + T_1^1 D\psi_2^2) \end{array} \right\} dz}{\int_{-1}^{\lambda-1} \left\{ \alpha^2 DT_0 (T_1^1)^2 \right\} dz} \quad . \quad [3.114]$$

Hence, given a solution to the linear problem with a solution to the order ϵ^2 system as well, R_2 can be found by the above ratio of integrals.

3.4.3.2.3. Computational methods.

Evaluation of such an integral can be included into the solution of a system of ordinary differential equations as follows. To evaluate

$$\int_{-1}^{\lambda-1} f(z')\, dz' \ ,$$

set

$$Y(z) = \int_{-1}^{z} f(z')\, dz' \ ,$$

then $DY = f(z)$ is an equation which can be included amongst the set to be solved by the NRK package, with its corresponding boundary condition $Y(-1) = 0$. The solution to the evaluation required, is the value $Y(\lambda-1)$ returned from the solver.

Hence a program was written to work in two modes. Firstly, both λ and σ could be supplied, and then the program would solve for R_2, or secondly, λ only could be specified and the program would search for the critical value of σ as an

	Equations	No. of eqns	Boundary conditions	No.of b.c's
A	Linear equations $O(\epsilon^2)$	6	$\omega_1^1 = \psi_1^1 = T_1^1 = 0$ at $z = -1$ and $z = \lambda - 1$	6
B	Linear equations $d/d\alpha^2$	6	$\omega_{1\alpha}^1 = \psi_{1\alpha}^1 = T_{1\alpha}^1 = 0$ at $z = -1$ and $z = \lambda - 1$	6
C	Eigenvalues R_0, α^2		$D\omega_1^1 = 1 = D\omega_1^1$ at $z = -1$	2
D	Second order $O(\epsilon^2)$	8	$\omega_2^2 = \psi_2^2 = T_2^0 = T_2^2 = 0$ at $z = -1$ and $z = \lambda - 1$	8
E	Eigenvalue σ			
F	Numerator of R_2	1	$\int_{-1}^{\lambda-1} F = 0$	2
G	Denominator of R_2	1	$\int_{-1}^{-1} F = \int_{-1}^{-1} G = 0$	2

DIAGRAM 3.1. Schematic of the program to calculate R_2 and the critical values of the Prandtl number.

To calculate R_2 given λ and σ :
- Equations — A, B, D, F, G
- Eigenvalues — C
- Boundary conditions — A, B, C, D, F

(24 equations, 13 left boundary conditions, 11 right)

To calculate critical σ given λ :
- Equations — A, B, D, F
- Eigenvalues — C, E
- Boundary conditions — A, B, C, D, F

(24 equations, 12 left boundary conditions, 12 right)

eigenvalue such that $R_2 = 0$. Diagram 3.1 shows a schematic of the program operation. The numerator and denominator of the quadrature for R_2 are incorporated as two separate integrals. The linear and second order (ϵ^2) systems of equations must be solved exactly i.e. the first and second order parts of a fourth order solution cannot be used. However, the equations for the linear and two mode 'normal' solution are exactly the same as the linear and second order equations required here, so they may be extracted from previous programs and added into the program here. Actual computations proceed as for the exact solutions i.e. initial guesses will be as the previous guesses for the linear and relevent two mode solutions, boundary conditions are as before, and the grids are used in the same manner as before. As previously mentioned, the variable ω and ψ are scaled by α to obtain α^2 as a parameter, and the linear system is solved with R_0 and α^2 required as parameters by including the equations differentiated with respect to α^2 as before. The extra boundary conditions incorporated to allow these eigenvalues to be sought are that $D\omega_1^1(-1) = 1$ and $D\omega_{a\,1}^1(-1) = 1$, which are simply normalisation factors. Notice that if a solution to the third order in ϵ (ϵ^3) equations was to be calculated (now possible since R_2 can be found by the solvability condition) then a homogeneous element of the solution in the ω_3^1 equations must be eliminated by incorporating another boundary condition such as $D\omega_3^1 = 0$.

If R_2 is to be evaluated, then both the numerator and denominator integrals are evaluated as previously mentioned, and the result found, otherwise, to find the critical σ where $R_2 = 0$, the boundary conditions are changed so that instead of having the numerator and denominator functions take a value of zero at $z = -1$ as the two necessary conditions, the denominator is ignored and the numerator function is required to vanish at $z = -1$ and $z = \lambda - 1$ also, thus ensuring that the numerator and therefore R_2 is identically zero.

3.4.3.2.4. The results.

a). Cross checking with previous solutions.

Notice now that the Nusselt number no longer enters into the problem, but is determined by the value of the amplitude factor ϵ, since

$$T(x,z) = z + \epsilon T_1^1(z)\cos(\alpha x) + \epsilon^2(T_2^0(z) + T_2^2(z)\cos(2\alpha x)) + \ldots$$

If DT_0 is assumed linear, then the Nusselt number is

$$Nu = \frac{\overline{\partial T(z=-1)}}{\partial z} = 1 + \epsilon^2 DT_2^0(z=-1) + \ldots \quad , \qquad [3.115]$$

where an overbar stands for a horizontal average, and so approximately,

$$\epsilon^2 = \frac{Nu - 1}{DT_2^0(z=-1)} \quad . \qquad [3.116]$$

An approximate calculation of the full Rayleigh number is thus allowed from equation [3.85] by selecting a Nusselt number, calculating ϵ^2 and so R. This may then be compared with the Rayleigh number produced by the exact solution at that Nusselt number for an estimate of the accuracy of the ϵ expansion procedure.

An alternative estimate of ϵ may be obtained as a result of the scaling boundary conditions that were applied. The approximate solution procedure introduced a scaling boundary condition of $D\omega_{1a}(-1) = 1$, where the subscript 'e' is introduced to denote the exact solution, and subscript 'a' will denote the approximation/solution. However, the approximation equivalent to the full, exact-solution mode, $D\omega_{1e}\sin(\alpha x)$, is the approximate $\epsilon D\omega_{1a}\sin(\alpha x)$, and so $D\omega_{1e} = \epsilon D\omega_{1a}$ and ϵ may be estimated as

$$\epsilon = D\omega_{1e}(z=-1) \quad . \qquad [3.117]$$

Both these methods were used to estimate ϵ and thus R from the expansion results, and the values were compared with the exact solutions and a characterisation of the error was calculated by

$$Error = \frac{| R_e - R_a |}{R_e} \times 100\ \% \quad . \qquad [3.118]$$

These results are shown in Table 3.4 for various λ, Nu and σ. As expected, the expansion results are only valid for low Nusselt number, the Nu = 1.001 results showing a maximum error for the parameters shown of 0.3%, whereas for Nu = 1.2 the expansion values are hopelessly inaccurate, with errors on the order of 100%. The parameter ϵ is a measure of the amplitude of convection and the expansion results are thus only valid for low Nusselt numbers.

The error is in general worse for the higher layer depths, λ, but this is not necessarily a function of the expansion, but may be more the fact that the method is more likely to be inaccurate for the deeper λ since a fixed grid is used. For

	R_e	R_{a1}	Error R_{a1}	R_{a2}	Error R_{a2}
Nu = 1.001					
σ = 0.1					
λ = 3	552.4124	552.7861	0.068	552.6961	0.051
4	553.3014	553.9137	0.111	553.7751	0.086
6	555.1655	556.3993	0.222	556.1738	0.182
σ = 10					
λ = 3	548.6586	548.8457	0.034	548.6750	0.003
4	548.4951	548.4727	0.004	550.1152	0.295
6	548.3066	548.2739	0.006	548.4527	0.027
σ = ∞					
λ = 3	548.6544	548.6417	0.002	548.6710	0.003
4	548.4894	548.4674	0.004	548.5346	0.008
6	548.2980	548.2661	0.006	548.4452	0.027
Nu = 1.01					
σ = 0.1					
λ = 3	558.5687	574.4792	2.84	566.9133	1.49
4	554.2679	577.2209	4.14	566.5626	2.22
6	545.3094	583.3085	6.97	566.7074	3.92
σ = 10					
λ = 3	534.0157	533.0750	0.18	535.6715	0.31
4	524.7262	522.8110	0.36	528.8295	0.78
6	506.8002	502.0542	0.94	518.4238	2.29
σ = ∞					
λ = 3	533.9564	533.0343	0.17	535.6370	0.31
4	524.6418	522.7579	0.36	528.7876	0.79
6	506.6565	501.9765	0.92	518.3707	2.31
Nu = 1.20					
σ = 0.1					
λ = 3	747.0580	1032.3758	38.2		
4	745.4714	1069.2627	43.4		
6	777.2415	1054.7948	35.7		
σ = 10					
λ = 3	423.0665	203.3396	51.7		
4	357.8362	-18.9704	94.6		
6	274.3458	-1085.7414	495.0		

TABLE 3.4. A comparison of results for the Rayleigh number produced by the exact solutions (R_e) and the expansion solutions (R_a). The first method (R_{a1}) uses ϵ calculated from the Nusselt number, and the second (R_{a2}) uses ϵ calculated from the derivative of the first vorticity mode, $D\omega_1$, at the lower boundary.

instance, at Nusselt number Nu = 1.0005 and Prandtl number σ = 0.1, the result for layer depth λ = 3 improved from an error of 1.04% to an error of 1.03% only in a doubling of the mesh, whereas the corresponding result for λ = 6 improved from an error of 6.48% to 5.60%, showing that a refining of the grid would certainly help the deeper layers. However, the standard results were all calculated with usual 16 intervals in the vertical grid.

Veronis (1963) quotes a value for R_2 from his calculations for σ = 6.8 and λ = 2, but this result could not be recovered from the R_2 results available here. Many attempts at recovering Veronis's solution were tried, with varying interpretations of the scalings and normalisations that he uses, and with numerous methods (actual straight calculation of R_2, comparison of the implied Nusselt numbers, size of vertical solutions fields etc.), all to no avail. However, the qualitative aspect of the results remain consistent with Veronis's work, and the two solution types calculated in this Chapter, the full solution and the small amplitude expansion, prove consistent at low Nusselt number, so faith is held in the results quoted.

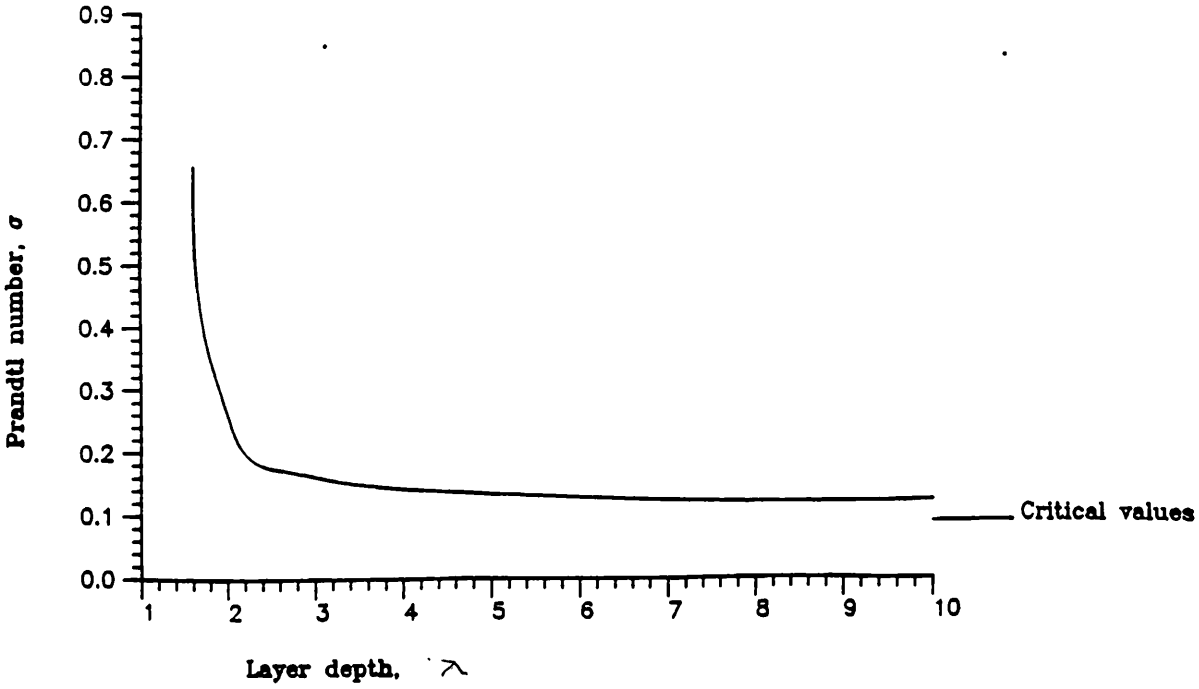
b). The critical values of the Prandtl number.

Figure 3.9 shows the boundary between the sub− and super−critical regions for any λ, calculated from the expansion program. Layer depths greater than λ = 5 were calculated with a grid of 32 intervals reather than 16 for greater accuracy. The graph shows that the division between subcritical (right or above the divide) and supercritical (left or below the divide) remains at a constant value of the layer depth, around λ = 1.6, for all σ > 0.5. This shows that supercritical bifurcation will only occur for low values of the layer depth for higher Prandtl number convection. These low λ have not been previously studied, for example, Veronis (1963) concentrated his theoretical efforts on λ = 2, and MW study penetration mainly for λ > 1.91. Thus the subcritical bifurcation is the only one observed and documented. Figure 3.2a) confirms that such a low value of λ (= 1.5) is supercritical for all σ. The value of σ = 0.5 is a rough estimate of the onset of the Prandtl number dependence of the flow, since at higher Prandtl numbers the flows vary little in style, whereas the lower Prandtl number solutions differ greatly from each other.

Between Prandtl numbers σ = 0.5 and σ = 0.15, the curve goes through a transitional period, during which the layer depth varies gently between λ = 1.6 and λ = 2.2, before changing to a horizontal curve where the critical value of σ

Figure 3.9

Prandtl number, σ, against layer depth, λ



does not vary with λ.

In this second constant regime, the division between subcritical and supercritical bifurcation tends towards a constant value of the Prandtl number around $\sigma = 0.11$ for all layer depths $\lambda > 2.2$, and so for $\sigma < 0.15$, convection can be seen to be supercritical for possibly all values of the layer depth. This value of σ compares very favourably with the result found by Matthews (1988) by an amplitude equation method in a different model of penetrative convection. Thus, for Prandtl numbers in the $\sigma-$independent region the flows are subcritical for nearly all layer depths, whereas in the strongly $\sigma-$dependent region there is a sharp transition between subcritical and supercritical flow at $\sigma = 0.12$ for all values of the layer depth.

The transitional period between these two clear cut regimes occurs for $\lambda = 1.6 - 2.2$ and it is tempting to speculate, bearing in mind the accuracy of the experiments, that this value is actually the $\lambda = 1.91$ of MW, suggesting that, until σ is low enough, a counter-cell is necessary to maintain subcritical convection. Again, counter-cells appear to be more important to the flow than previously realised. The temperature of the top of the main convecting cell is usually around 1.6 - 1.7 and this may herald the start of this transitional region (since depth and temperature scale together). The figure of $\lambda = 1.91$ given in MW for the appearance of the first counter-cell is slightly higher since very small cells cannot be supported.

Graphs of Nusselt number against Rayleigh number are included as figures 3.2a) − 3.2d) for λ = 1.5, 3, 4 and 6 showing the style of the variation of heat transport for the division of the σ−space into sub− and super−critical regions. At higher λ, the solutions become more sub− or super−critical as appropriate. Close−ups of the critical region near the conducting solution, Nu = 1 and R = R_0, follow as figures 3.6a) − 3.6c) to show the sensitive style of the critical Prandtl number graphs because the full nature is not obvious on the larger figures. Critical values of the Prandtl number were calulated from the expansion results, but all solutions exhibited were drawn from the full, exact, four mode calculations.

The curve for the critical Prandtl number appears to be a much less obvious divide between the two regions than expected. Whilst being a reasonably monotonic, vertical departure from the critical point for λ = 3, for higher layer depths, the bifurcation is critical in the sense that it starts out perpendicular to the Rayleigh number axis but it curves back towards the sub−critical nature of the higher Prandtl number curve, rather than being a smooth monotonic increasing function away from the critical values. This is more pronounced at higher layer depths, where even the super−critical low Prandtl number curves, show first of all a super−critical bifurcation, followed by a reversal so that after initially having Rayleigh numbers increasing with increasing Nusselt number, the Rayleigh number then decreases again, before reversing once again and continuing monotonically. This effect is very noticeable in the λ = 6 graph, where the reversal leads to a sub−critical style graph even for low σ despite the super−critical bifurcation. Hence, it seems that for deeper layer depths, subcritical convection is possible even though the style of the bifurcation is supercritical due to the low Prandtl number. The possible hysteresis of convection development is now different. As the Rayleigh number is increased through the critical value for the onset of linear convection, for high λ and low σ, the heat transport and the amplitude of convection grow from nothing steadily until a second critical level of instability is reached whereupon the amplitude jumps discontinously to an efficient stable regime of higher Nusselt numbers, much as the high Prandtl number convection does at the linear critical value. If the Rayleigh number is subsequently reduced, then the low σ, high λ convection is similar to the high σ (any λ) as far as heat transport goes, since both simply reduce in efficiency with reducing R through R_0 until the critical value for the onset of non−linear convection is reached, whereupon the solution becomes the conducting solution once again. Lower values of λ , for example, λ = 3 or 4, at low σ have this 'S' type Nu−R curve, but never actually achieve subcritical convection.

Thus, it seems as if the distinction between the types of flow is not as clear as would be desired. This is borne out by the sequence of contours shown in figures

Fig. 3.10a)

λ = 3.0
σ = 2.000
Nu = 1.2000
Ra = 434.4952
α^2 = 2.1888

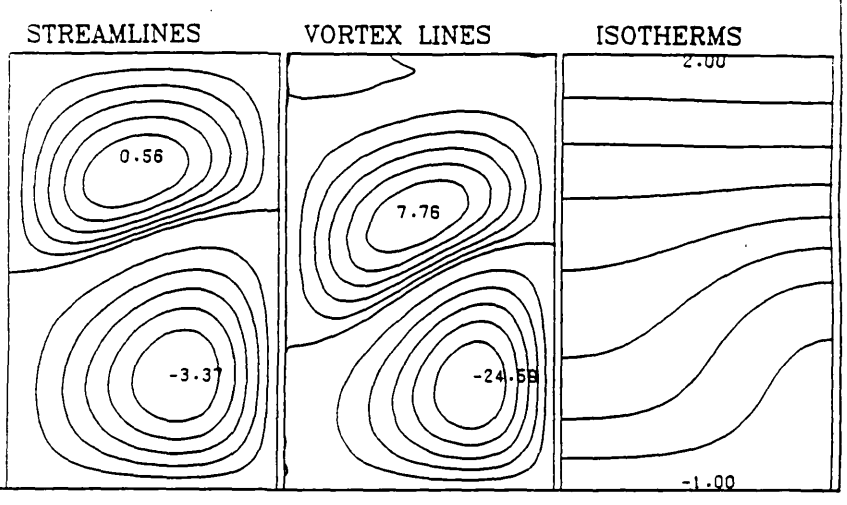


Fig. 3.10b)

λ = 3.0
σ = 0.200
Nu = 1.2000
Ra = 583.0309
α^2 = 2.9754

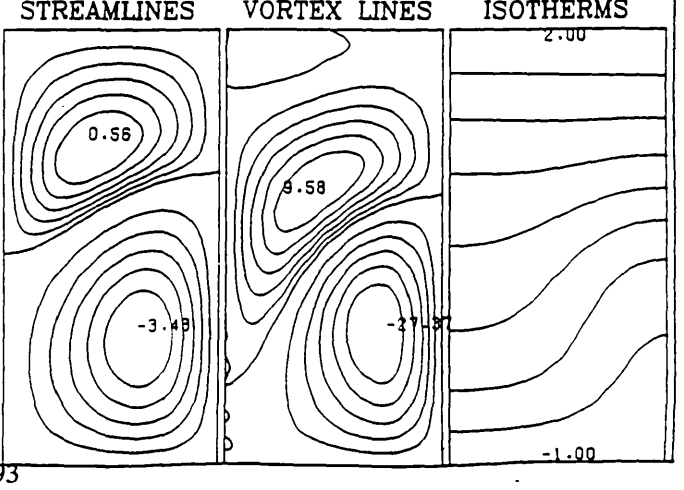


Fig. 3.10c)

λ = 3.0
σ = 0.170
Nu = 1.2000
Ra = 613.9500
α^2 = 2.9974

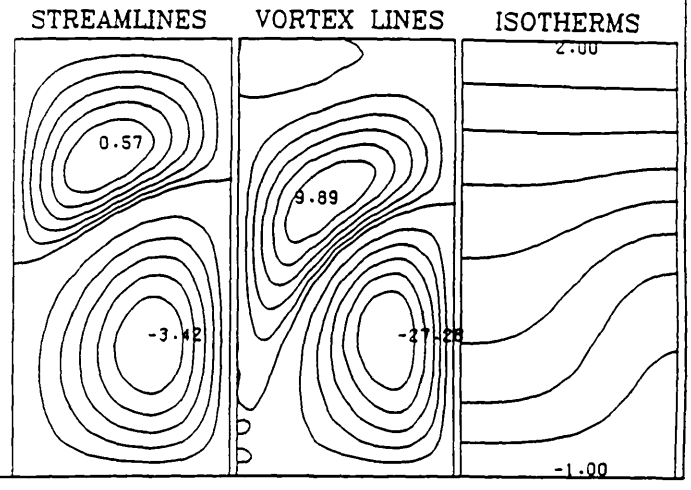


Fig. 3.10d)

λ = 3.0
σ = 0.159
Nu = 1.2000
Ra = 628.6414
α^2 = 2.9943

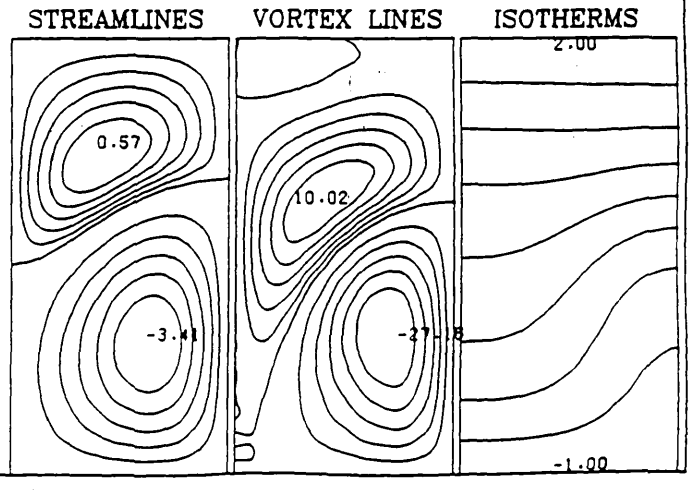


Fig. 3.10e)

λ = 3.0
σ = 0.150
Nu = 1.2000
Ra = 641.2140
α^2 = 2.9849

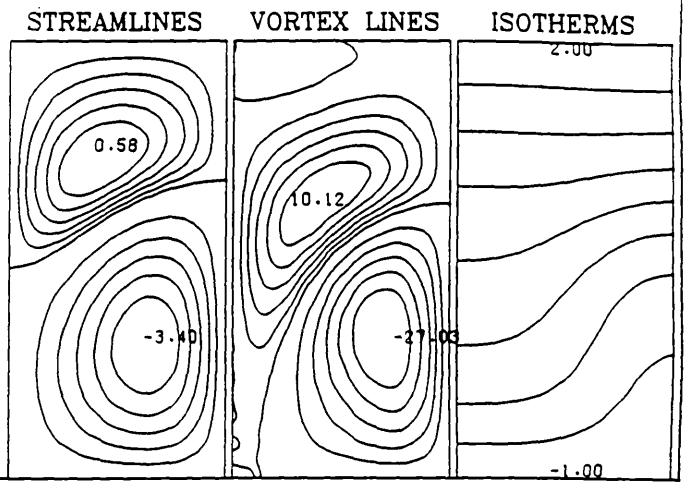


Fig. 3.11a)

λ = 4.0
σ = 0.200
Nu = 1.2000
Ra = 552.2982
α^2 = 2.8132

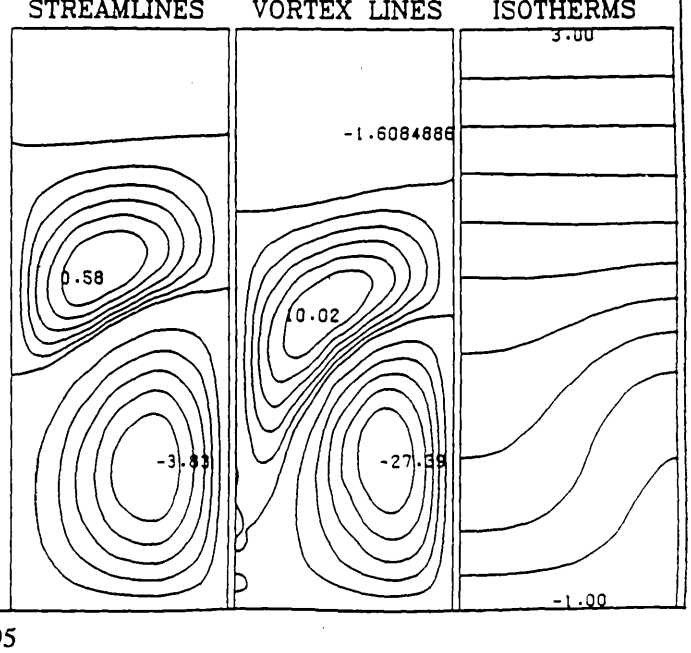
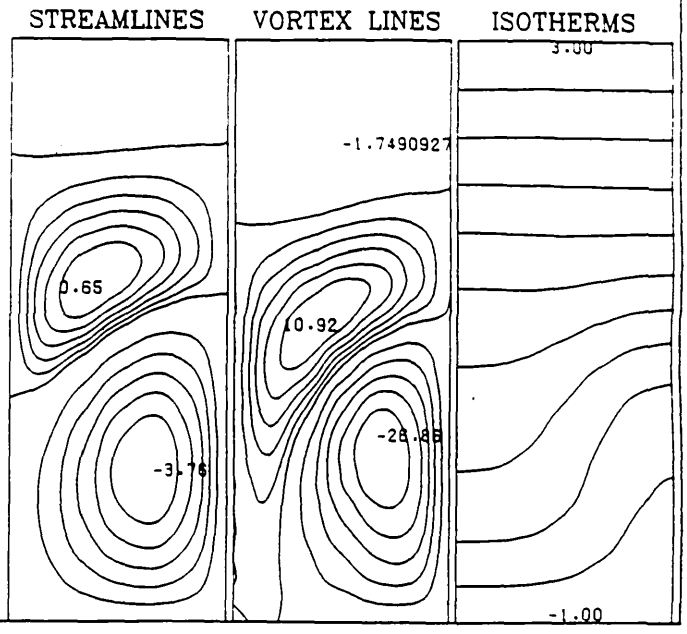
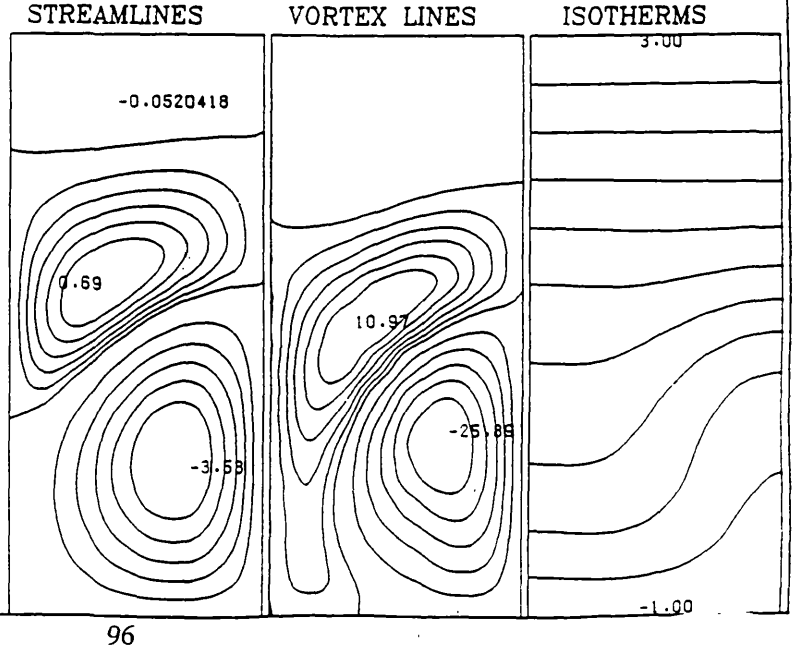


Fig. 3.11b)



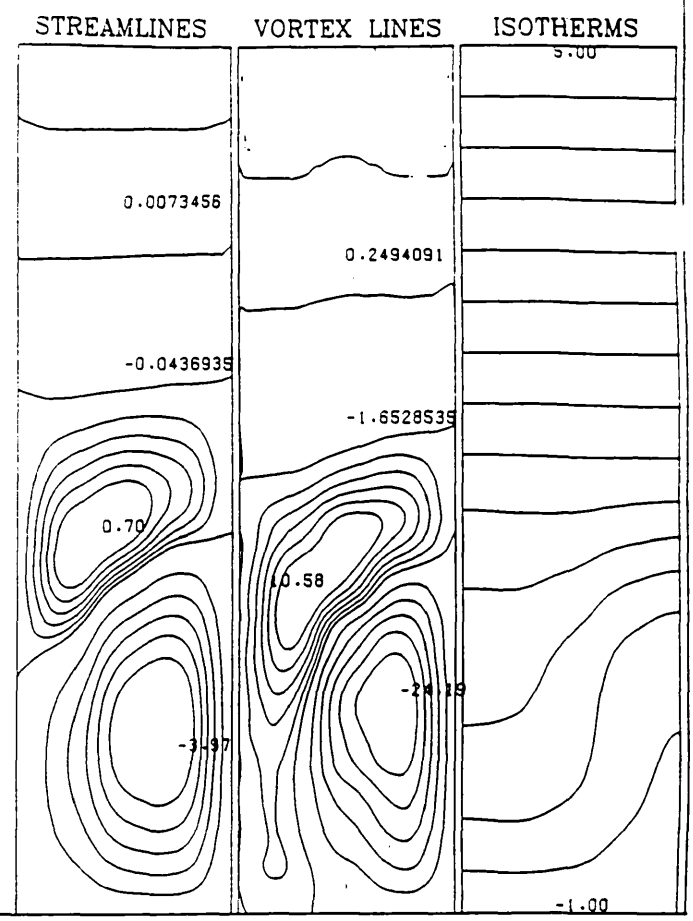
λ = 4.0
σ = 0.141
Nu = 1.2000
Ra = 643.7204
α^2 = 2.6744

Fig. 3.11c)



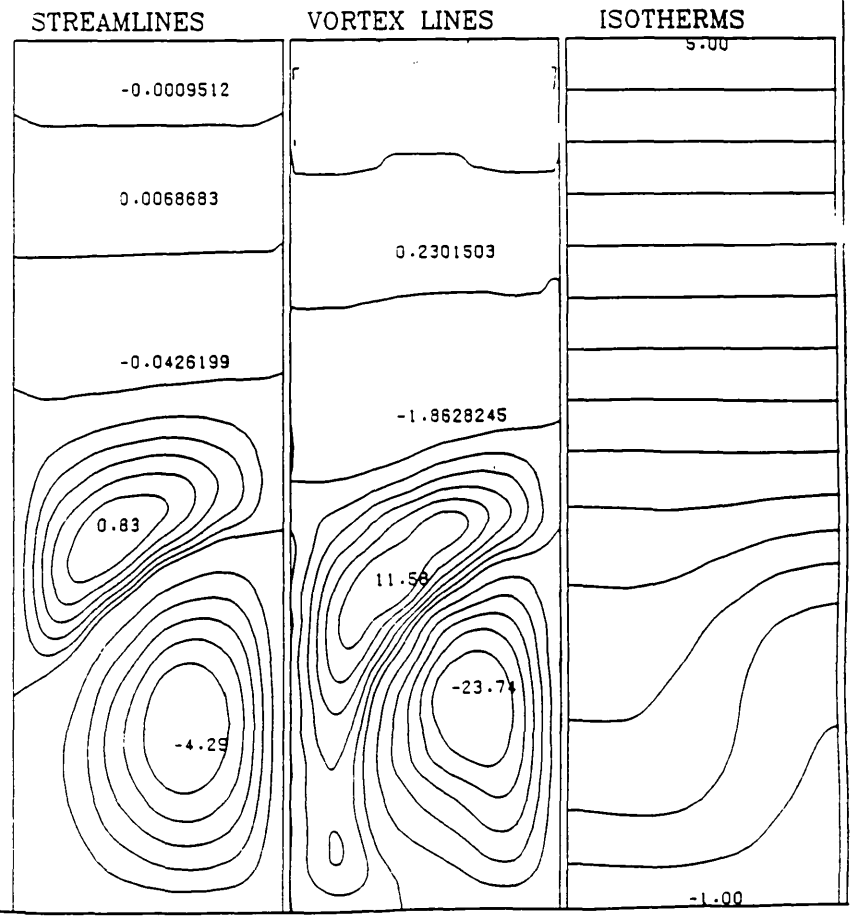
λ = 4.0
σ = 0.100
Nu = 1.2000
Ra = 745.4714
α^2 = 2.3490

Fig. 3.12a)



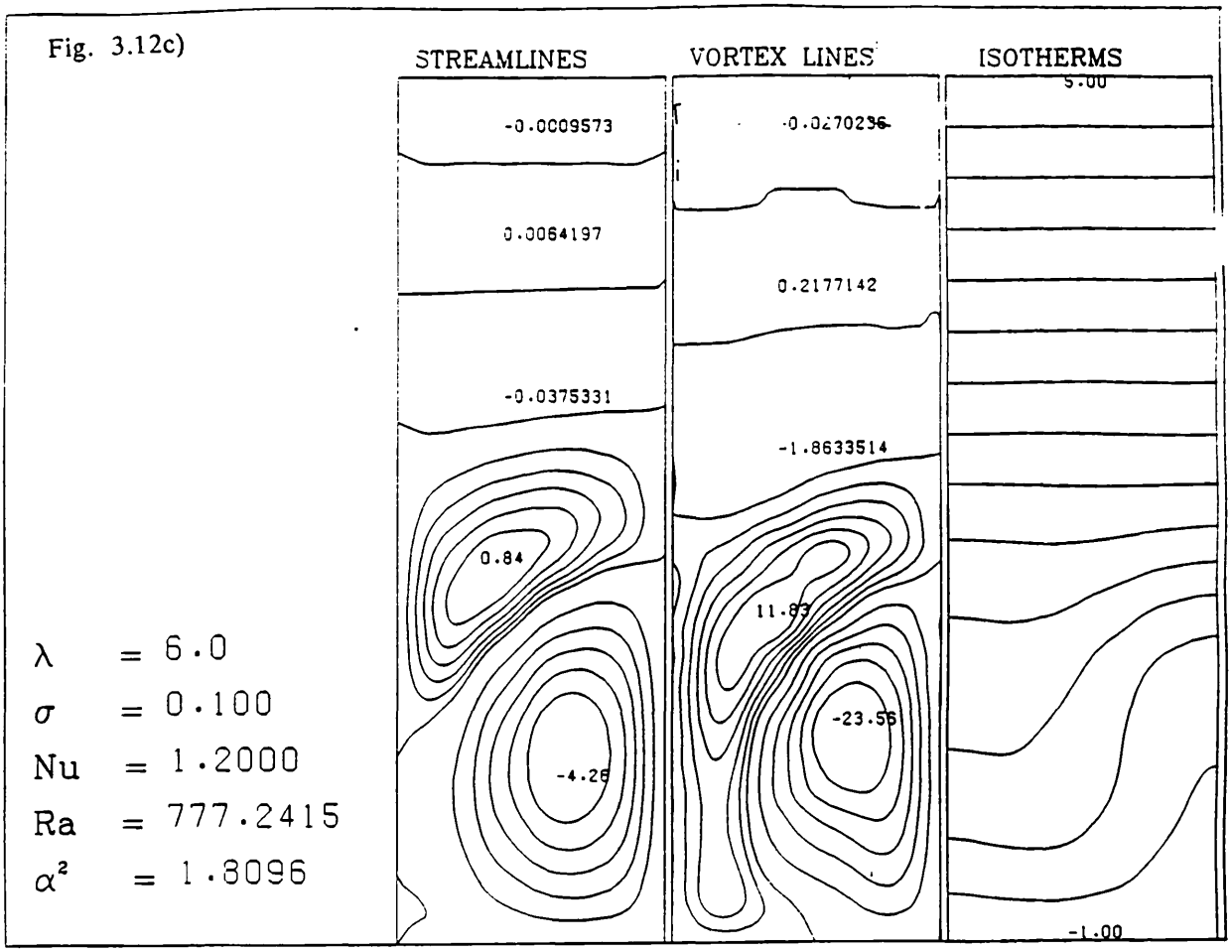
λ = 6.0
σ = 0.150
Nu = 1.2000
Ra = 647.3252
α^2 = 2.0425

Fig. 3.12b)



λ = 6.0
σ = 0.128
Nu = 1.2000
Ra = 698.3280
α^2 = 1.8919

Fig. 3.12c)



3.10, 3.11 and 3.12 for the flow characteristics around the critical Prandtl number for various layer depths. A theory which described the critical Prandtl number as that Prandtl number where the vorticity counter−cell first dipped so deep into the main vorticity cell as to touch the lower boundary, holds for $\lambda = 3$, but is quoshed by the figures pertaining to $\lambda = 4$ and 6. Figure 3.10 shows an incremental sequence of σ values for $\lambda = 3$ and Nu = 2.0. At $\sigma = 2.0$ (figure 3.10a)), a small, corner, third counter−cell may be seen in the vorticity, and the interface of the first vorticity counter−cell with the main convecting cell is already well tipped, overlapping the streamfunction main cell by about half its depth. As the Prandtl number decreases to $\sigma = 0.2$, the vorticity counter−cell dips more towards the lower boundary, and as σ is reduced still further to $\sigma = 0.17$, a value just above the critical Prandtl number, the counter−cell begins to reach for the lower left hand corner, detaching itself from the wall. At the critical Prandtl number, the vorticity counter−cell reaches the lower boundary, and if σ is decreased still further, the vorticity counter−cell attaches itself to the bottom. This behaviour is repeated in figures 3.11 and 3.12, but unfortunately the point

where the counter−cell dips so far as to reach the lower boundary does not occur distinctly at the critical Prandtl number, as in the previous case, but rather the counter−cell is well attached to the lower boundary by the time that the critical value of σ is reached. It may be noted however, that the numerical inaccuracies introduced by the truncation of modes and the particular mesh used are likely to be largest at these deeper layer depths, but it seems as if the distinction between the nature of subcritical and supercritical flows is not as clear−cut as would be liked.

3.4.4. VARIATION WITH THE CELL GEOMETRY.

The geometry of the convection is determined by the layer depth, λ, which is imposed here as a parameter of the problem, and the width of the roll, π/α, which is determined by the calculated α^2.

As shown earlier and in figure 3.2a), for $\lambda \leqslant 1.6$ the flow is supercritical regardless of the Prandtl number, σ, and hence this flow regime is subtly different from the other λ, where sub− or super−criticality depends on whether $\sigma \geqslant 0.12$ or $\sigma \leqslant 0.12$ respectively. As can be seen in all the figures pertaining to this section (figures 3.13, 3.14), the results for $\lambda = 1.5$ are distinct from those for the other λ, and cannot be fitted into the trends easily. Recall also that MW state that the formation of the first counter−cell occurs for $\lambda > 1.91$, and note that the temperature of the top of this counter−cell as shown in these calculations is around the value of 1.6. Hence this lower λ flow is physically different from the higher λ ($\lambda = 3$, 4 and 6) flows since it involves no counter−cells. It seems as though counter−cells would like to form at a value of λ around $\lambda = 1.6 - 1.7$ for the changeover from supercritical to subcritical at moderate or high Prandtl numbers, but that the 'cost' of supporting a small counter−cell suppresses this instinct until there is room enough for a larger overlying cell at around $\lambda = 1.91$.

Figures 3.13 show the variation of the Rayleigh versus Nusselt number curves with λ for two Prandtl numbers, $\sigma = 0.1$ and $\sigma = 10.0$. The figure for the higher σ (figure 3.13a)) shows that as more fluid is added to the system the curves exhibit greater subcriticality, the critical Rayleigh number for the onset of non−linear convection decreasing dramatically with increasing λ. This can be understood in terms of the effective Rayleigh number, R_{eff}, defined in equation [3.69]. As λ increases, d' increases (for a fixed Nusselt number), and thus the effective Rayleigh number increases. If the onset of non−linear convection is

Figure 3.13a)
Rayleigh number against Nusselt number
Variation with λ for σ = 10.0

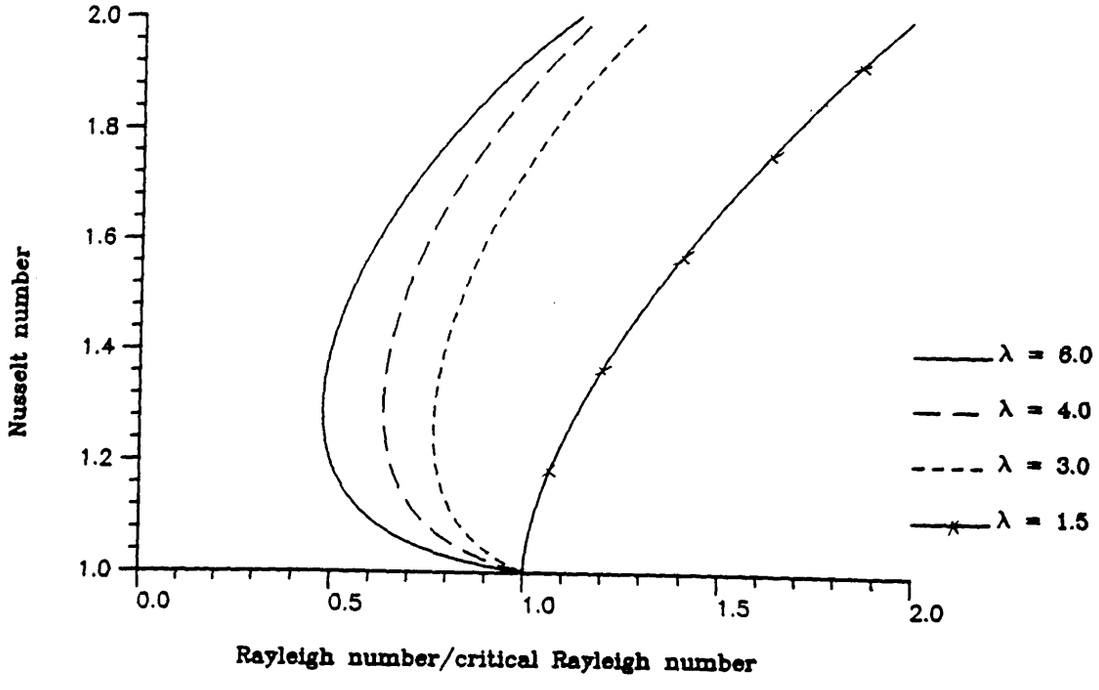


Figure 3.13b)
Rayleigh number against Nusselt number
Vvariation with λ for σ = 0.1

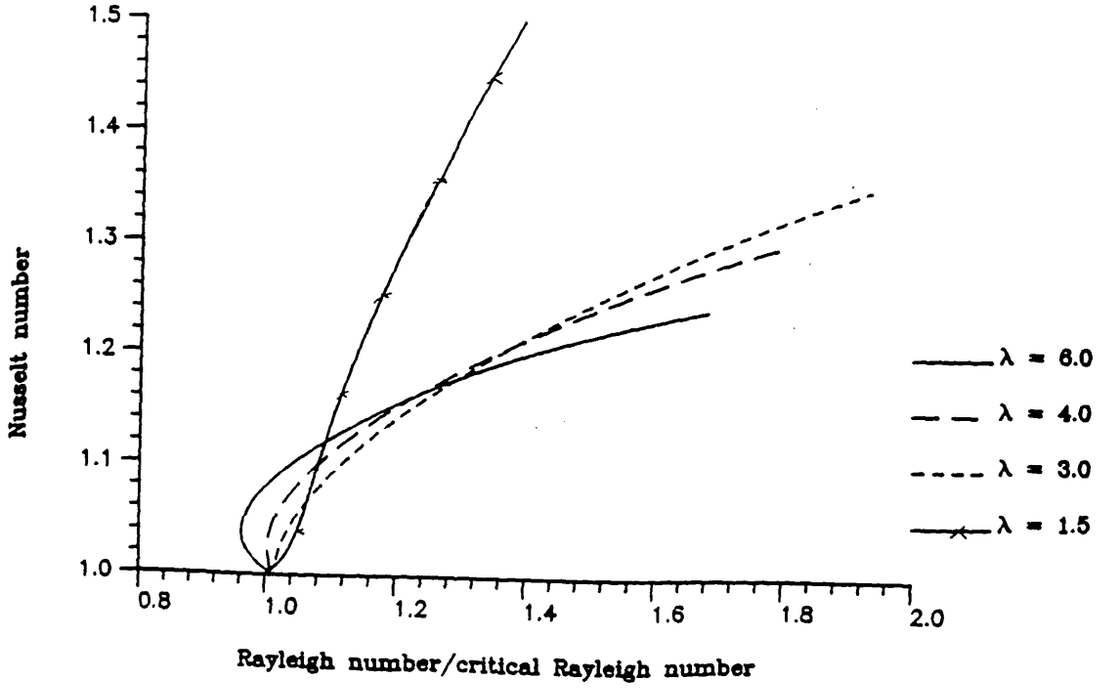


Figure 3.14a)
Cell width, π/a, against Nusselt number
Variation with λ for σ = 10.0

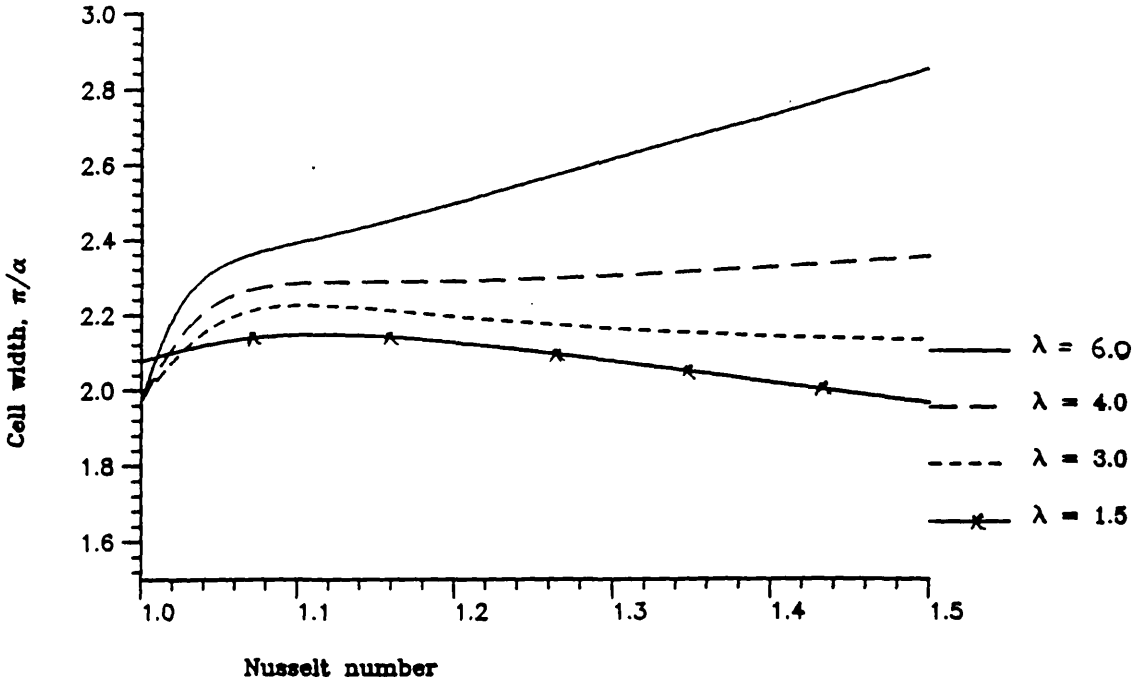
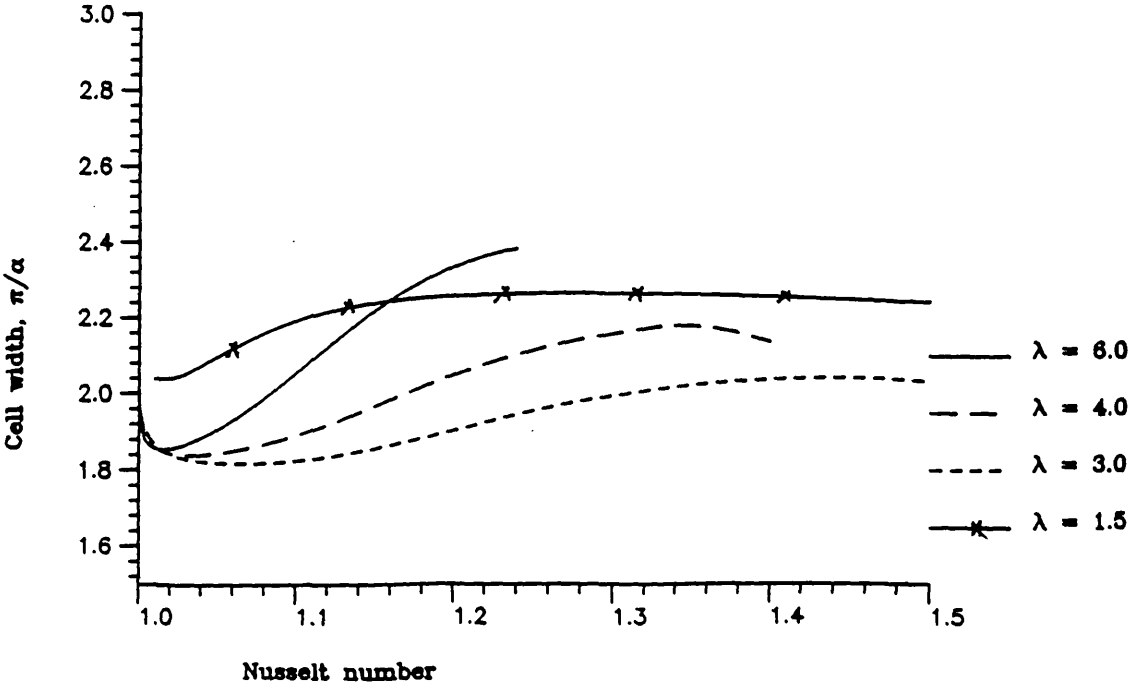


Figure 3.14b)
Cell width, π/a, against Nusselt number
Variation with λ for σ = 0.1



regarded as the effective Rayleigh number reaching a critical value, then this value will be attained for a lower true R with increasing λ. The low Prandtl number, σ = 0.1, curves show much the same behaviour, despite their original supercritical bifurcation, but at much lower amplitudes. The R_c line is not crossed again for the σ = 10.0 cases until at least Nu = 1.8, whereas for σ = 0.1, R_c has been recrossed by all the λ curves by Nu = 1.08.

At higher Rayleigh numbers, these two sets of curves show distinctly different behaviours. At high Prandtl number, as described in MW all the curves tend towards the predicted $R^{1/3}$ asymptote where the flow becomes independent of depth and this tendency can be seen in figure 3.13a) for σ = 10.0. However, at lower σ, as shown in figure 3.13b), the curves cross over at a Rayleigh number of about $1.3R_0$ and then the order of efficiency of convection is reversed i.e. previously, for $R < 1.3R_0$, the higher λ, the more efficient the convection, but now for $R > 1.3R_c$, the higher λ are less efficient. These curves also show no sign of any obvious asymptote for high R at this stage. The more complicted nature of low σ curves could be due to the system physically requiring transitions to other, possibly 3−dimensional, modes of convection, as is the case for the rigid boundary results shown in MW's figure 14. Figures 3.14 show the variation of the horizontal cell dimension with the Nusselt number, but note that the curves shown are not for constant R/R_c. For σ = 10.0, the cell width increases rapidly from the critical value for all values of λ under subcritical convection (i.e. not for λ = 1.5), whereas for σ = 0.1, the opposite occurs, and once convection has started, the cell width decreases rapidly. For all σ, the deeper layers prefer a wider cell, with the disparity being greater for the lower σ. This appears logical since tall, thin cells would not allow for the complicated structures exhibited at low σ, and in general would feel greater viscous effects than are necessary as the sublayers come closer together. The quick increase of cell size in the high σ case then eases off at Nusselt numbers around Nu = 1.5 and the cell widths then tail off, to either slowly decrease for the lower λ or slowly increase for the higher λ. At lower σ, the rapid decrease in cell in cell size finishes earlier by Nu = 1.2 or so and then all λ proceed towards a maximum value, either gently, in the lower λ cases, or fairly steeply in the higher λ case. In general, it appears that the lower σ convection can support thinner cells since the viscous effects are not as strong.

Figure 3.15a)
Rayleigh number against Nusselt number
Effective values for σ = 10.0

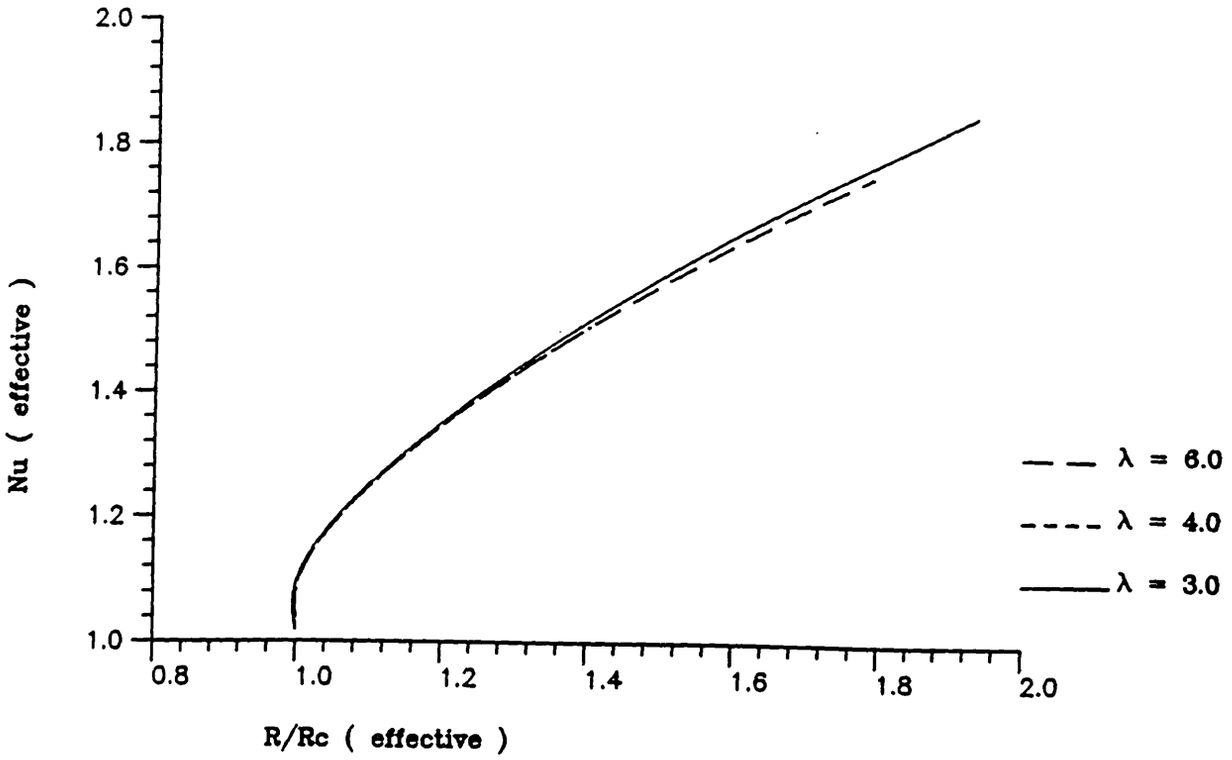
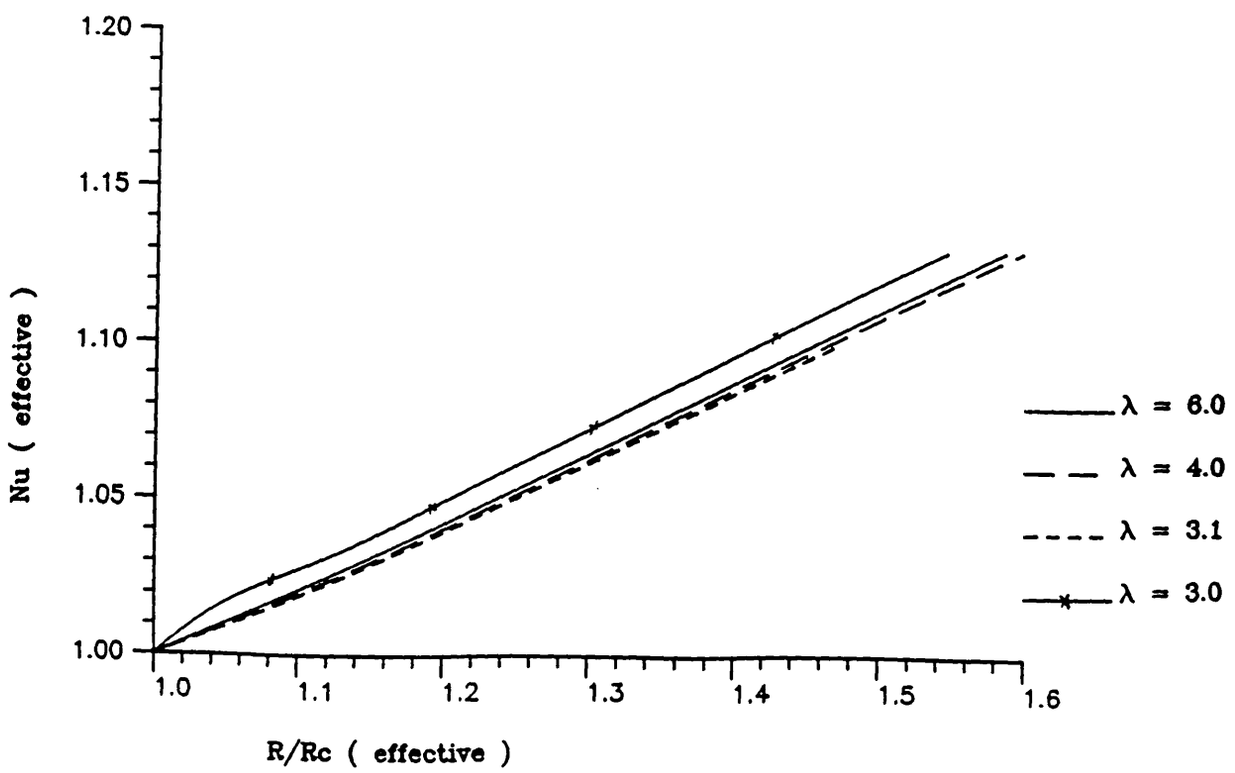


Figure 3.15b)
Rayleigh number against Nusselt number
Effective values for σ = 0.1



3.4.5. EXTENSION OF THE MOORE AND WEISS MODEL.

As discussed earlier, the MW model seems to be soundly based on the division of the flow into an active and a passive region. However, for Prandtl numbers lower than that of the ice−water experiment it is necessary to include more fluid than the main convecting cell in the basic unit, since the different vorticity structure couples the overlying counter−cells more deeply into the convecting flow.

The basis of the model is that flows in different layer depths should have a body of fluid which is active, and that the effective Nusselt and Rayleigh numbers for this region should remain constant for all λ. This is shown to be true for $\sigma = 10$ and layer depths of $\lambda = 3$, 4 and 6 using the active region as $\lambda = 1.5$ in MW and also in figure 3.15a), where the effective Nusselt and Rayleigh numbers for higher layer depths are shown to be equivalent to that of $\lambda = 1.5$ for $\sigma = 10.0$. However, if similar $N_{eff}-R_{eff}$ graphs are drawn for $\sigma = 0.1$ (figure 5.15b)), it may be seen that the $\lambda = 1.5$ graph does not coincide with any of the other curves for higher λ. In fact, curves only start to become reasonably similar for $\lambda > 3$, with the $\lambda = 4$ and $\lambda = 6$ curves almost coinciding, showing that the computational domain necessary for predicting higher layer depth flows at $\sigma = 0.1$ is definitely above $\lambda = 3$ and below $\lambda = 4$. The effective Nusselt numbers and Rayleigh numbers calculated here are for an irregular domain, since the cells are no longer horizontally topped, and so the constants are calculated on values at the horizontal mid−point of the interface of the non−symmetrical cell.

Values for an active unit slightly above $\lambda = 3$ emulate the higher λ curves reasonably accurately, and indeed a value around $\lambda = 3.1$ offers a reasonable fit to the $\lambda = 4$ and $\lambda = 6$ results (see figure 3.15b)). Note that this value marks approximately the top of the first counter−cell. Notice that this is, once again, a flat, isothermal surface, despite the distortion of its lower interface with the main convecting cell. This new interface now satisfies the prerequisites of the MW model. Thus, it may be conjectured that an adequate active region for Prandtl numbers around $\sigma = 0.1$ and possibly lower, is the main cell plus one overlying counter−cell. However, this theory has not been tested for lower Prandtl numbers. If the coupling continued to increase with decreasing Prandtl number, then to satisfy the conditions of the Moore and Weiss model, and thus to be able to build deep layer depths from smaller λ, it would be necessary to take sufficient depth so that the lower, active basic unit reaches the first horizontal and isothermal cellular division. If the top of a counter−cell is distorted then vorticity will still be advected across this boundary, coupling into the next cell, and so any model must include this in the active region.

3.5. SUMMARY AND CONCLUSIONS

A fully non−linear two−dimensional investigation of penetrative convection was carried out using a modal representation of the horizontal structure and numerical techniques to ascertain the vertical dependences. A strong σ dependence was found for low values of σ below the usual value of that for water, for free boundary convection. This dependence of the flow on Prandtl number led to the breakdown of the simple analytical model built by Moore and Weiss (1973b) that predicted the values of interest for other layer depths from a single active unit of fluid, and which worked well for a higher Prandtl number. It was found that the relationship between the measure of heat transport, the Nusselt number, and the measure of instability, the Rayleigh number, showed sub−critical bifurcation for high Prandtl numbers, but a super−critical bifurcation for low σ. Comparison of the physical quantities associated with the two cases showed that whilst outward appearances of the flows remained similar, in that the streamlines and isotherms exhibited similar behaviours at both low and high Prandtl numbers, albeit slightly more vigorous at the lower, the vorticity structure of the sub− and super−critical flows showed a different behaviour. The flywheel type of flow, where the vorticity is constant on and across the streamlines and the non−linear advection terms are annihilated eliminating the Prandtl number dependence from the steady problem, as found in free boundary, low Prandtl number Rayleigh−Benard flow (Moore and Weiss (1973a), Proctor (1977), Jones, Moore and Weiss (1976)), is not found in penetrative convection. Thus, the penetrative problem is more akin to the rigid boundary Rayleigh−Benard problem where this lack of Prandtl number dependence at low σ is not displayed (Schluter, Lortz and Busse (1965), Gough, Spiegel and Toomre (1975)). For penetrative convection at low σ, the inertial solution breaks down as the vortex lines separate from the near−circular streamlines and the first counter−cell of vorticity dips across the interface between the main convecting cell and its first counter−cell. This implies that transport of vorticity between the first two cells takes place and that a greater degree of coupling between the cells exists for low σ. The first counter−cell is convectively driven, if only weakly, in comparison to the mainly conducting passive overlying units of the higher σ. The coupling increases with decreasing Prandtl number and increasing amplitudes of convection, until near the critical value of the Prandtl number for the switch from sub− to super−critical convection, the vorticity interface dips to encounter the lower boundary. However, the division between sub− and super−critical flows is not clearly defined, and even flows with a supercritical bifurcation can support subcritical convection. These effects were found not to be a result of the

distortion of the mean temperature profile.

The simple model of MW fails because it was confined to the Prandtl number independent region and so fails to compensate for the physical shape and coupling differences that are found in the lower Prandtl number flows ($\sigma < 0.5$). However, if a larger basic active unit is chosen such that the assumptions of an isothermal and horizontal top to the unit are satisfied, then the theory behind the model is sound and predictions can be made on the strength of it.

In conclusion, there exists a strong Prandtl number dependence for Prandtl numbers below $\sigma = 0.5$ in two−dimensional, non−linear penetrative convection between free boundaries that is not present in the corresponding Rayleigh−Benard case. Further investigation of penetrative convection in three dimensions may reveal the greater significance of the vertical vorticity and illuminate the difference between penetrative and Rayleigh−Benard convection.

CHAPTER 4.

PLANFORM MODES FOR THREE-DIMENSIONAL CONVECTION.

4.1. ABSTRACT.

The higher harmonics of the hexagonal and square horizontal planform functions usually used for three dimensional calculations in natural convection are investigated purely algebraically, with no dynamics, via the non-linear advection terms of the Navier-Stokes equations. The possible physical implications of the inclusion of these higher harmonics in any expansion used to solve the equations of convection are investigated. It is found that at third order and above, the harmonics of the Christopherson hexagonal planform may generate an inherent vertical vorticity structure. Such structures are not available to square convection. The planform harmonics of the hexagon with the possible vertical vorticity structures that they may generate, are presented and discussed up to order five. The relationship to a more general solution of the Helmholtz equation is investigated.

4.2. INTRODUCTION.

Spatially periodic patterns have been observed in natural and experimental convection throughout the course of the investigation of this subject (e.g. Benard (1900,1901), Krishnamurti (1970, 1973)). In a layer of viscous fluid, at the point where the conduction state loses stability, $R = R_c$ and the linear stability problem admits infinitely many solutions to the problem (Chandrasekhar (1961)). At the onset of instability, although the solution will be characterised by a particular wave number, the pattern in which the convection manifests itself is totally unspecified, since any given wave vector can be resolved into two orthogonal components in infinitely many ways. These solutions described by a single, critical wave vector are known as rolls, and thus a general solution of the linear stability problem is any linear combination of rolls. The infinity of solutions may be recognised by their different horizontal structure. Arguments requiring complete symmetry within the horizontal plane of convection (Chandrasekhar (1961)) and physical observations have led to discussion of convection with horizontal planforms which look like rolls, squares, rectangles and hexagons (Malkus and Veronis (1958),

Stuart (1964)). The non−linear terms of the basic convection equations are responsible for choosing one of these planforms of the linearised problem but this stability problem is discussed elsewhere (Busse (1978), Golubitsky et al. (1983)).

Chapter 3 has shown that vorticity can play an important role in convection. Two−dimensional solutions do not contain a full vorticity vector and thus three−dimensional solutions are often necessary to incorporate the full non−linear effects. Obviously, a three−dimensional numerical model is likely to be more costly on computer resources than the simpler two−dimensional models and thus, the method of solution must be chosen carefully. Two common approaches to the problem of modelling convection in three−dimensions are as follows. The system of equations may be solved by a computational finite difference scheme (Roberts and Weiss (1966), Lipps and Somerville (1971), Lipps (1976)) which solves the complete problem but is expensive to run on an adequately sized grid. Secondly, a modal approach may be employed once more, where the problem is separated, by use of the planform functions, so that the horizontal dependences are specified and the problem need only be solved for the vertical variables. The second method of modal expansion, formulated from an idea by Lorenz (1963) and used by many since (e.g. Baker and Spiegel (1975), Jones, Moore and Weiss (1976)), is popular because it cuts down on the computational budget by making use of the cellular structure of the problem.

To use the modal method, a planform function of the horizontal variables must be chosen and substituted into the equations to yield the dependencies of the vertical variables. The horizontal boundary conditions as usual do not necessarily admit only one solution to the horizontal problem, but often a class of solutions, a subset of which must be chosen to make the computation viable, as was seen in Chapter 3, where the periodicity of the horizontal boundary condition allowed trigonometric solutions for the horizontal dependences which describe the roll structure so often observed. However, the boundary conditions allowed infinitely many trigonometrical functions to be the solution of the horizontal problem, so the most general solution was a sum over all of them, as a Fourier series. In that case, the planform was one−dimensional since the problem was only two−dimensional, but the principle of the modal calculation carries through to three dimensions. The modal expansion used must be truncated at some point to enable finite computation, and so the severity of the truncation of these series and their validity to real convection becomes a new problem in itself which must also be considered (Marcus (1981), Gough, Spiegel and Toomre (1975), Toomre, Spiegel and Gough (1977,1982)).

Platzman (1965) and Roberts (1966) both comment on possible harmonics of the hexagonal planform, and Gough, Spiegel and Toomre (1975,1977,1982) showed that

it was possible to investigate convection using single− and multi−mode equations and that credible results could be obtained for some of the more major physically interesting variables, for example, the heat transport. Their work effectively truncates an expansion of the two−dimensional horizontal planforms extremely severely, so that their calculations included at most three modes, and often only one. However, this chapter now investigates what the full modal expansions of the common two−dimensional planforms of convection are, and examines the amount of information that is available in the previously excluded higher modes of the expansion. It is shown that inclusion of the higher order terms requires the inclusion of the often omitted vertical vorticity, and thus that, in the solution of some of the more physical convection problems, use of a more full harmonic expansion could give a possible insight into some of the observed, complicated, non−linear results.

Much of the natural convection that occurs is observed as a hexagonal style pattern (Benard (1900,1901), Krishnamurti (1970,1973)). Benard's original experiments, which effectively started the study of thermal convection, showed beautifully regular, hexagonal convection cells, although the surface−tension driving mechanism was confused for straight−forward thermal convection until the process was clarified later (Pearson (1958), Koschmeider (1967)). Also, the hexagonal planform is found to be the preferred planform structure at the onset of convection for the problem with a weakly temperature−dependent viscosity (Graham (1933), Palm (1960), Segel and Stuart (1962)). Hence, much modelling effort has gone into theories with hexagonal planforms. Baker and Spiegel (1975), Murphy and Lopez (1983,1984), Massaguer and Mercader (1988) and others have modelled classical Rayleigh−Benard convection using the planform known as the Christopherson hexagon (Christopherson (1940)). This is the standard hexagonal planform, and the authors then go on to investigate various aspects of physical convection with this as a base.

Other planforms are also stable in particular problems. For example, squares are stable near the onset of convection, and possibly sub−critically, for convection with a strongly temperature−dependent viscosity (Jenkins (1987)), and hence, these must be taken into account when examining the planform problem. This chapter, however, will concentrate on the richer hexagonal problem, but the square planform problem is also presented in less detail, as is the more general, related problem of arbitrary solutions of the Helmholtz equation.

(*) The functions χ and ψ are termed streamfunctions in this thesis. They should be more correctly termed scalar potentials. Where the term 'streamline' is used, it should be taken to mean 'contours of constant χ or ψ'.

4.3. THE METHOD OF APPROACH.

To study the flow, it is again convenient to move away from the primitive variables in favour of a streamfunction−vorticity formation of the problem. The general method for this is to introduce a single streamfunction, as in equation [2.7], but it is possible here to introduce two streamfunctions, χ and ψ, to describe the general solenoidal (i.e. divergence free) velocity field (Busse (1972), Joseph (1978)) as

$$\mathbf{u} = \mathrm{curl}\ \mathrm{curl}(\chi\mathbf{k}) + \mathrm{curl}(\psi\mathbf{k}) = \nabla \times (\nabla \times (\chi\mathbf{k})) + \nabla \times (\psi\mathbf{k}) \quad , \qquad [4.1]$$

where $\mathbf{k}$ is the unit vector in the vertical direction. Obviously, this can be expressed as a single curl and so is indeed a general streamfunction in terms of a combination of χ and ψ. Other general descriptions of a divergence free velocity field are available, but are mathematically equivalent, and lack the convenience of the above description which separates the generation of vertical vorticity to be solely dependent on the streamfunction ψ, rather than a complicated mixture of the two functions, χ and ψ, as follows.

The description of [4.1] in expanded component form is

$$\mathbf{u} = \left[\frac{\partial^2\chi}{\partial x \partial z} + \frac{\partial \psi}{\partial y} , \frac{\partial^2 \chi}{\partial y \partial z} - \frac{\partial \chi}{\partial x} , - \nabla_h{}^2 \chi \right] \quad , \qquad [4.2]$$

where $\nabla_h{}^2$ is the horizontal Laplacian, and so the vorticity,

$$\omega = \nabla \times \mathbf{u} \ ,$$

when calculated is

$$\omega = \left[- \nabla^2 \left[\frac{\partial \chi}{\partial y} \right] + \frac{\partial^2 \psi}{\partial x \partial z} , \nabla^2 \left[\frac{\partial \chi}{\partial x} \right] + \frac{\partial^2 \psi}{\partial y \partial z} , - \nabla_h{}^2 \psi \right] \quad , \qquad [4.3]$$

with ∇^2 being the full Laplacian, and so it can be seen that there is no contribution to the vertical component of vorticity from χ. This makes this formulation particularly attractive to studies where non−linear and thus vorticity effects are of primary importance, as will be the case in Chapter 5, for which this is the preliminary study.

For many studies, for example those by the authors Gough, Toomre and Spiegel,

, the vertical vorticity is neglected from the problem, so that $\omega_z \equiv 0$ and $\psi \equiv 0$, as is the case at the onset of convection (Chandrasekhar (1961)). That assumption is made here to start with, although, as shall be seen later, this is found to be invalid in the higher order solutions.

Examining equation [2.1] shows that the non−linear terms are all embodied in the $(\mathbf{u}.\nabla)\mathbf{u}$ and so to examine the effect of non−linearity on the modal planforms it is sufficent to examine the effect of these terms on the planform χ functions. Thus the following scheme was adopted to investigate the harmonics of the natural planforms that may arise through the inclusion of all the non−linear effects of the convection equations.

Firstly, the standard hexagonal planform is taken i.e. the Christopherson hexagon as written in the form

$$\chi_h(x,y,z) = f_h(z) \left(2\cos(rx)\cos(y) + \cos(2y) \right) , \qquad [4.4]$$

where $f_h(z)$ is the unknown functional dependence of χ, depending on the boundary conditions, and $r = \sqrt{3}$. Substitution of this into [4.2] allows the structure of the velocity field $\mathbf{u}$ to be calculated and hence the algebraic form of $(\mathbf{u}.\nabla)\mathbf{u}$ can also be calculated. The curl of this expression is also taken to give [4.3] and thus to access the vorticity that such a streamfunction may describe. It has been assumed initially that $\psi = 0$, so that there is no vertical component of vorticity, but horizontal vorticity does exist. This calculation and all the subsequent were carried out using an algebraic manipulation language called CAMAL (Barton and Fitch (1972)) on a VAX 8600. The output produces a complicated sum of trigonometrical terms with numerical and functional coefficients from which groups of terms are identified by the following rules. Any term in the resulting equation is made up of a trigonometric dependence on the horizontal variables, coupled with a coefficient built from an integer coefficient and a functional dependence on the vertical spatial variable, z. Trigonometrical dependences which have identical coefficients, both integer and z−functional, are grouped together into clusters. Any cluster of collected horizontal trigonometric dependences that appears, will appear regularly, albeit with differing z−functional and integer coefficients. These trigonometrical terms define another periodically repeating pattern, which contains all the symmetry of the original χ, and are the harmonics of the original planform function. All the harmonics generated can be described as a simple sum of three cosine−cosine products (see equation [4.7] later) but the simple non−vorticity harmonics have two of these products the same (see table 4.1, to be described later). All the terms created by the non−linear advection interactions can be accounted for in this manner and so the approach is complete. These individual

harmonics can then be included in the expression for χ in any combination, to search for, and evaluate, higher order harmonics. The figures in this chapter relate to individual harmonics found by the above process unless otherwise stated.

Hence, by this process, it is possible to build up the horizontally dependent functions which are the naturally occuring harmonics of the basic Christopherson hexagon which completely account for the terms generated by the non−linear advection terms of the Navier−Stokes equation. No comment is made on the stability of the possible planform functions presented here; it is simply stated that these are the functions that arise naturally out of the manipulation of the initial state via the equations.

A similar investigation can also be carried out for a general square planform, where now the original planform function is taken as

$$\chi_s(x,y,z) = f_s(z)\cos(x)\cos(y) \quad , \qquad [4.5]$$

but this proves to provide a far less rich field than the hexagonal planforms.

4.4. DISCUSSION.

4.4.1. The individual harmonics of the hexagon.

Using this method the harmonics whose trigonometrical forms are given in table 4.1 were found. The table shows characteristics of individual harmonics as defined by the previously outlined process. The planform function defines the structure of the harmonic and is the actual cluster of trigonometrical terms produced by the search process. The vorticity function, if it exists, is the possible source term for vertical vorticity allowed by this planform structure i.e. the vorticity function is the trigonometrical form of a possible ψ function (see the original streamfunction definition of the velocity field, equation [4.1]) which must be included to balance the non−linear terms produced if the particular planform function to which it corresponds is incorporated in the expansion. The order given in the table corresponds to the power of ϵ at which the harmonic overtone structure appears in an expansion in powers of an amplitude factor, ϵ, of the interactions in the non−linear driving term. Thus, assuming the basic Christopherson hexagon to be of order ϵ, the two second overtones produced as a result of this base interacting with itself, become 2^{nd} order, the results of a second overtone/Christopherson

TABLE 4.1. Nomenclature and characteristic properties of individual hexagonal harmonics generated in the non-linear term. The parameter r = √3 and α is an arbitrary horizontal wavenumber which may be imposed on the whole pattern.

Name (+nicknames)	Planform function	Vorticity function	Order	Formative interactions
H1 (Christopherson)	$2\cos(r\alpha x)\cos\alpha y$ $+\cos(2\alpha y)$	-	1	-
H2 (aligned,half)	$2\cos(2r\alpha x)\cos(2\alpha y)$ $+\cos(4\alpha y)$	-	2	H1/H1
RH√3 (Rotated,reduced)	$2\cos(r\alpha x)\cos(3\alpha y)$ $+\cos(2r\alpha x)$	-	2	H1/H1
H3 (aligned,third)	$2\cos(3r\alpha x)\cos(3\alpha y)$ $+\cos(6\alpha y)$	-	3	H1/H2
VH 28 (VH1/Complex1)	$\cos(1r\alpha x)\cos(5\alpha y)$ $+\cos(2r\alpha x)\cos(4\alpha y)$ $+\cos(3r\alpha x)\cos(1\alpha y)$	$\sin(1r\alpha x)\sin(5\alpha y)$ $-\sin(2r\alpha x)\sin(4\alpha y)$ $+\sin(3r\alpha x)\sin(1\alpha y)$	3	H1/H2 H1/RH√3
H4 (aligned,fourth)	$2\cos(4r\alpha x)\cos(4\alpha y)$ $+\cos(8\alpha y)$	- -	4 4	H2/H2 H1/H3
RH2√3 (Rot.,twice red.)	$2\cos(2r\alpha x)\cos(6\alpha y)$ $+\cos(4r\alpha x)$	-	4	H2/H2 RH√3/RH√3
VH 52 (VH2/Complex2)	$\cos(1r\alpha x)\cos(7\alpha y)$ $+\cos(3r\alpha x)\cos(5\alpha y)$ $+\cos(4r\alpha x)\cos(2\alpha y)$	$\sin(1r\alpha x)\sin(7\alpha y)$ $-\sin(3r\alpha x)\sin(5\alpha y)$ $+\sin(4r\alpha x)\sin(2\alpha y)$	4	H1/H3 H2/RH√3
H5 (aligned,fifth)	$2\cos(5r\alpha x)\cos(5\alpha y)$ $+\cos(10\alpha y)$	-	5	H1/H4
VH 84 (VH4/Complex4/ Rot.,red. VH1)	$\cos(1r\alpha x)\cos(9\alpha y)$ $+\cos(4r\alpha x)\cos(6\alpha y)$ $+\cos(5r\alpha x)\cos(3\alpha y)$	$\sin(1r\alpha x)\sin(9\alpha y)$ $-\sin(4r\alpha x)\sin(6\alpha y)$ $+\sin(5r\alpha x)\sin(3\alpha y)$	5	H1/H4 H3/RH√3 RH√3/RH23
VH 76 (VH8/Complex8)	$\cos(2r\alpha x)\cos(8\alpha y)$ $+\cos(3r\alpha x)\cos(7\alpha y)$ $+\cos(5r\alpha x)\cos(1\alpha y)$	$\sin(2r\alpha x)\sin(8\alpha y)$ $-\sin(3r\alpha x)\sin(7\alpha y)$ $+\sin(5r\alpha x)\sin(1\alpha y)$	5	H1/VH52 RH3/VH28 H1/RH2√3
Additional unusual modes (order 6-8):				
VH 124 (VH7/Complex7)	$\cos(1r\alpha x)\cos(11\alpha y)$ $+\cos(5r\alpha x)\cos(7\alpha y)$ $+\cos(6r\alpha x)\cos(4\alpha y)$	$\sin(1r\alpha x)\sin(11\alpha y)$ $-\sin(5r\alpha x)\sin(7\alpha y)$ $+\sin(6r\alpha x)\sin(4\alpha y)$		VH28/VH52
VH 148 (VH6/Complex6)	$\cos(3r\alpha x)\cos(11\alpha y)$ $+\cos(4r\alpha x)\cos(10\alpha y)$ $+\cos(7r\alpha x)\cos(1\alpha y)$	$\sin(3r\alpha x)\sin(11\alpha y)$ $-\sin(4r\alpha x)\sin(10\alpha y)$ $+\sin(7r\alpha x)\sin(1\alpha y)$		VH28/VH52
VH 156 (VH5/ Rot.,red. VH2)	$\cos(2r\alpha x)\cos(12\alpha y)$ $+\cos(5r\alpha x)\cos(9\alpha y)$ $+\cos(7r\alpha x)\cos(3\alpha y)$	$\sin(2r\alpha x)\sin(12\alpha y)$ $+\sin(5r\alpha x)\sin(9\alpha y)$ $+\sin(7r\alpha x)\sin(3\alpha y)$		VH52/VH52

hexagon interaction become 3rd order (if they have not appeared at lower order) etc.

Harmonics are named with the following naming conventions. The original Christopherson hexagon and those harmonics which are mere reproductions of this, in the same alignment but scaled down, are denoted by an H prefix, followed by the linear scaling factor by which they are reduced. Those overtones which are as above but are not aligned with the original hexagon, but are rotated through 30^{o}, are prefixed by RH and are followed by a similar linear scaling factor. A prefix of VH represents a harmonic which cannot be interpreted as either of the above forms i.e. a straightforward aligned or rotated overtone, but have a more complicated planform structure and possibly offer a vertical vorticity generating source term. The number following the prefix in this case is uniquely defined by the two-dimensional wave number K^2, where K^2 satisfies

$$\nabla_h^2 f(x,y) = -K^2 f(x,y) \quad , \qquad [4.6]$$

for the planform function f(x,y), i.e. $K^2 = 3k_i^2 + l_i^2$, $i = 1, 2, 3$ where the planform function is

$$f(x,y) = \sum_{i=1}^{3} \cos(k_i r x)\cos(l_i y) \quad , \qquad [4.7]$$

and $r = \sqrt{3}$, as usual. The harmonics could all be identified uniquely by their wave number, K, so H1 could be called H4, and VH28 could then be simply H28, but a prefix is used to give some indication of the planform's structural shape. Notice that the difference between the straight-forward modes (H1, H2, RH$\sqrt{3}$ etc.) and the other harmonic modes, is that the linear reductions and rotations of the standard hexagon and the Christopherson hexagon itself have $k_1 = k_2$ and $l_1 = l_2$.

Substitution of the Christopherson hexagon into the non-linear terms produces three identifiable harmonics. The first is itself, i.e. an exact replica of the Christopherson hexagon, the second is a half size replica of itself, and the third is a replica of itself, scaled down by $\sqrt{3}$ linearly and with the pattern rotated around by 30^{o}. All the patterns still being hexagonal, of course, tile the infinite plane of convection, and all retain the symmetries of the original pattern i.e. two reflectional symmetries and a symmetry by a rotation of 60^{o}.

The next order of harmonics is obtained by the interaction of these second

Figure 4.1a)
Cell walls – mode H1

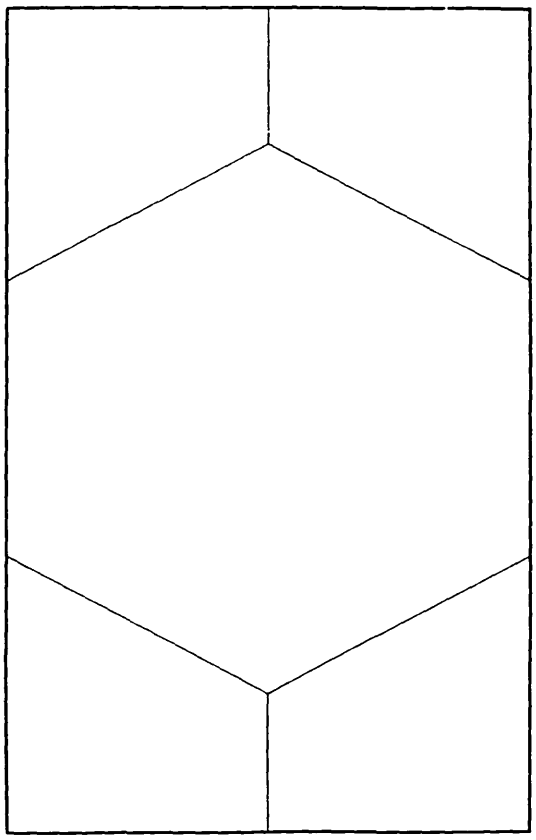


Figure 4.1b)
Cell walls – mode RH√3

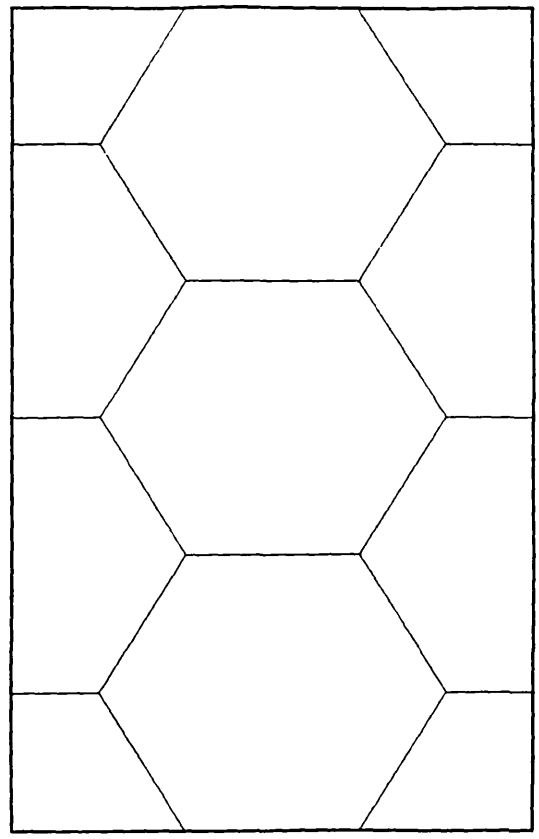


Figure 4.1c)
Cell walls – mode VH28

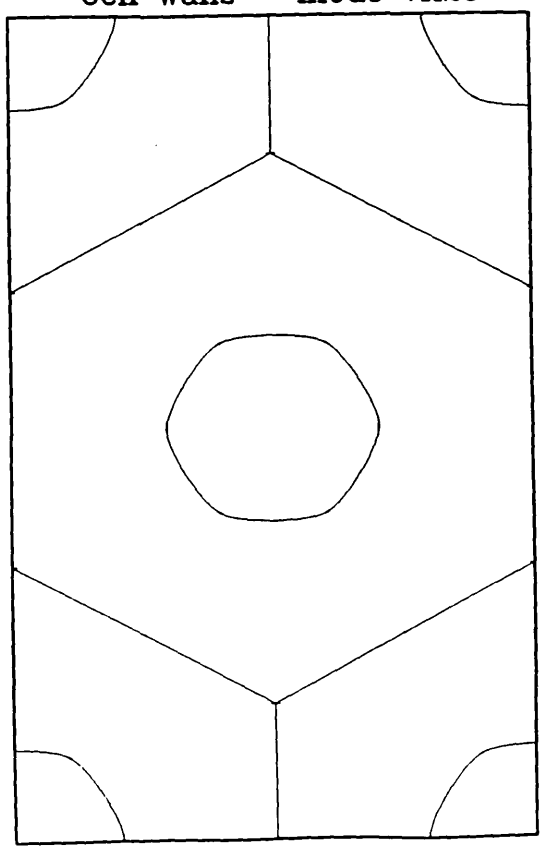


Figure 4.1d)
Cell walls – mode VH52

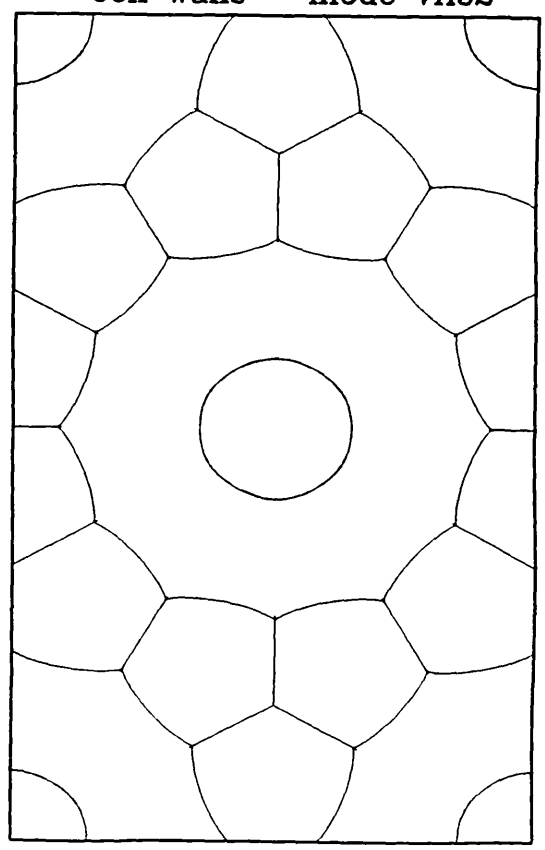


Figure 4.1e)
Cell walls – mode VH76

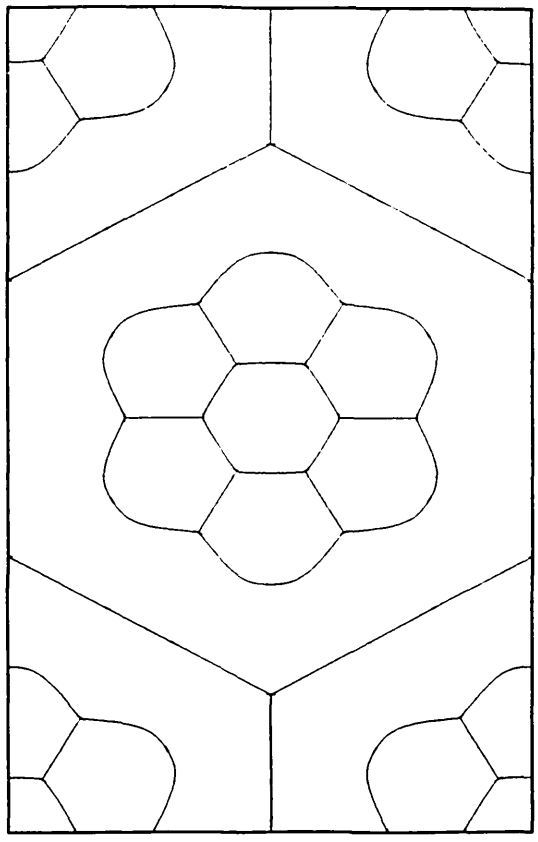


Figure 4.1f)
Cell walls – mode VH124

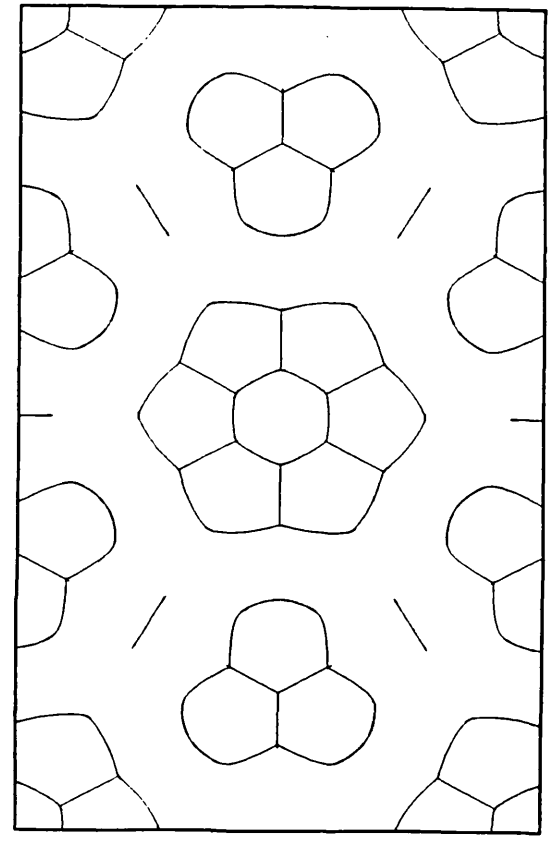
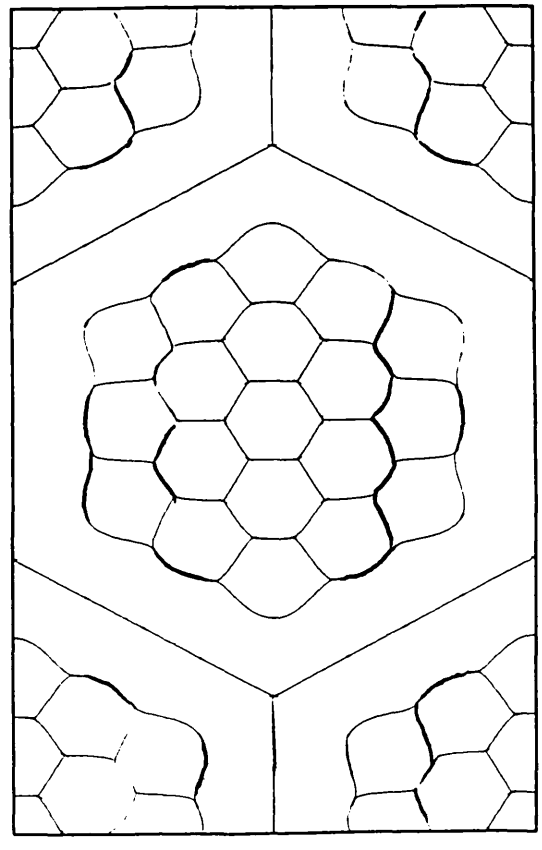


Figure 4.1g)
Cell walls – mode VH148



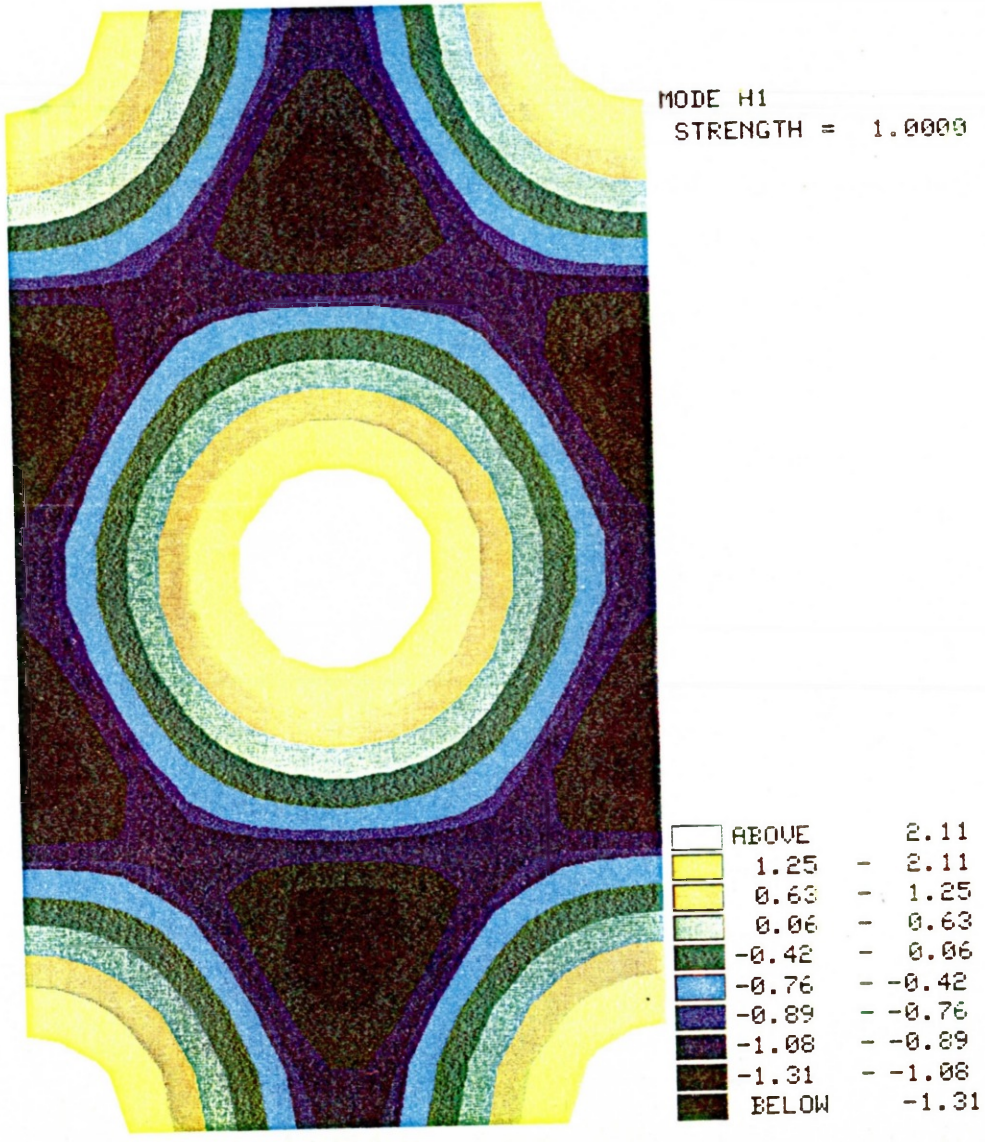
order harmonics with the original Christopherson hexagon in the non−linear terms. The fourth order is found by the interaction between these second order modes or by interaction between the third order modes and the fundamental, and so on. Table 4.1 also shows the order of the modes found, and examples of interactions that produced the modes.

Figures 4.1a) − 4.1g) show line drawings of the horizontal cellular structure of the harmonics found. These drawings were produced using the definition of a cell wall according to Stuart (1964) i.e. that a cell wall is any curve on which the vertical velocity is all of one sign and where there is no normal flow of fluid across the curve in the fluid. Figures 4.2a) − 4.2g) show the contours of χ for the planforms shown, (table 4.1) in both normal line form, and as shaded contours, which may be more appropriate for physical interpretations, and figures 4.3a)−4.3e) show the lines of constant vorticity, (table 4.1) where applicable. Note that the contours of χ are effectively the contours of a vertical velocity field to within a constant multiplying factor, since the vertical component of velocity in this streamfunction formulation depends solely on χ.

It may be seen that at third order, a novel mode appears (see figures 4.1c), 4.2c), 4.3a)). For the first time, the pattern has strayed away from simple variants of the standard hexagon and has produced a mode which is a Christopherson hexagon with the inclusion of a smaller shape within. This smaller shape no longer has straight cell walls joining the extrema of the vertical velocity, but curved walls have appeared in a smoothed−out hexagonal cell shape. The appearance of these curved cell walls in the mode coincide with the appearance of a non−zero vertical component of the $\nabla \times (\mathbf{u}.\nabla)\mathbf{u}$. This means that there is a source for a vertical component of vorticity, and that this is inherent in the model and is not an artificially introduced perturbation. This vertical vorticity is going to be present in the system at finite Prandtl number as soon as it starts convecting with a finite amplitude hexagonal planform. How strong or stable the effect will be, however, is not examined here. Notice that this vertical vorticity mode is not the planform mode used by authors such as Murphy and Lopez (1984) or Massaguer and Mercader (1988) when they introduce vertical vorticity. The practice used by these authors is to include vertical vorticity as a Christopherson hexagon mode, the same as their single mode of velocity. The harmonic mode found here may be a more physical way of expressing the vertical vorticity.

The vertical vorticity itself appears as a spoked pattern of triangular cells (figure 4.3a)), each triangular cell being one twelfth of the full hexagon and lying next to an identical, reflected triangular cell with the opposite vorticity, the two together making up the 60° section of the hexagon. The function that defines the vorticity has the same wavenumbers as the planform pattern that produced it

Figure 4.2a)
Streamlines – mode H1



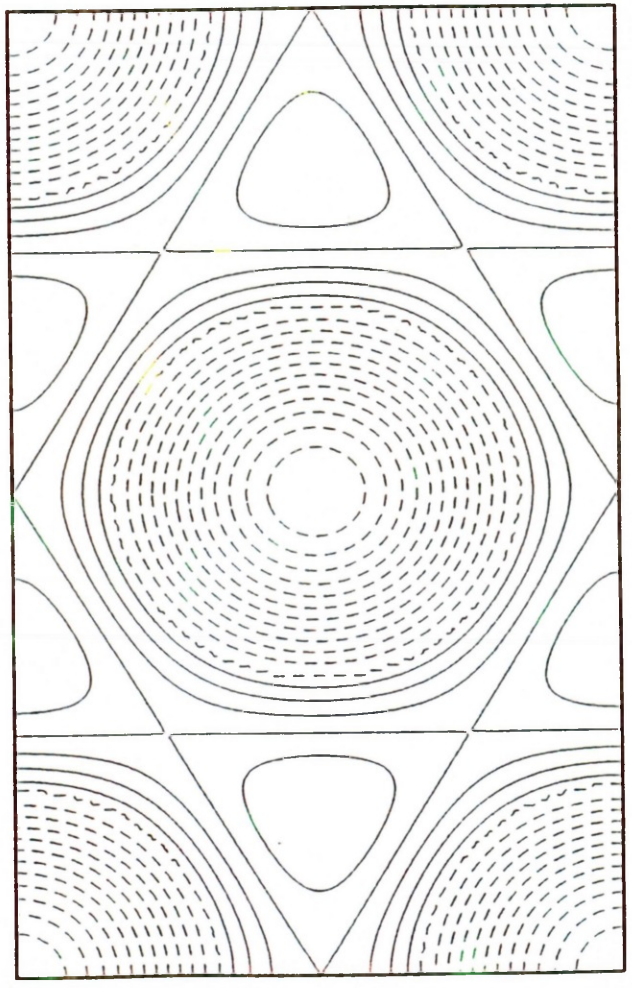
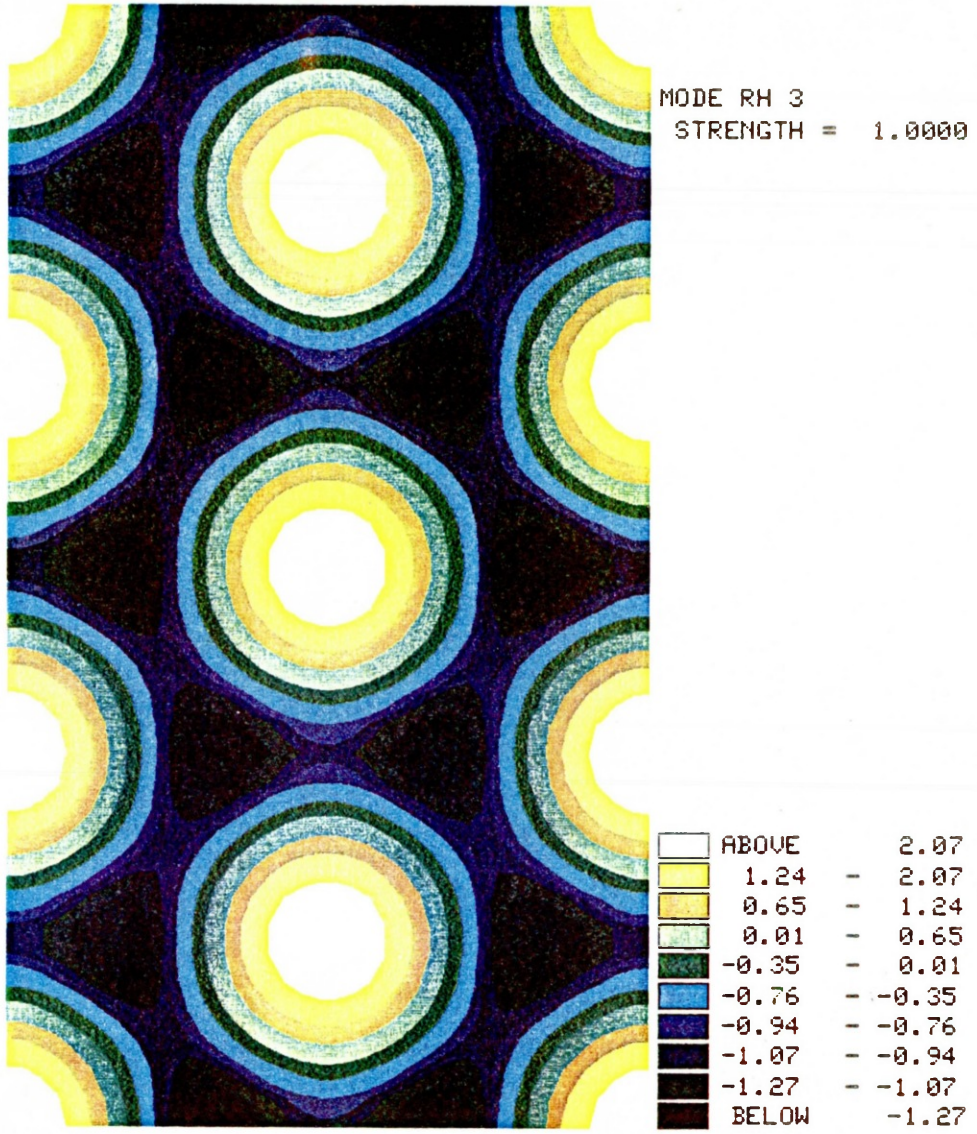


Figure 4.2b)
Streamlines – mode RH√3



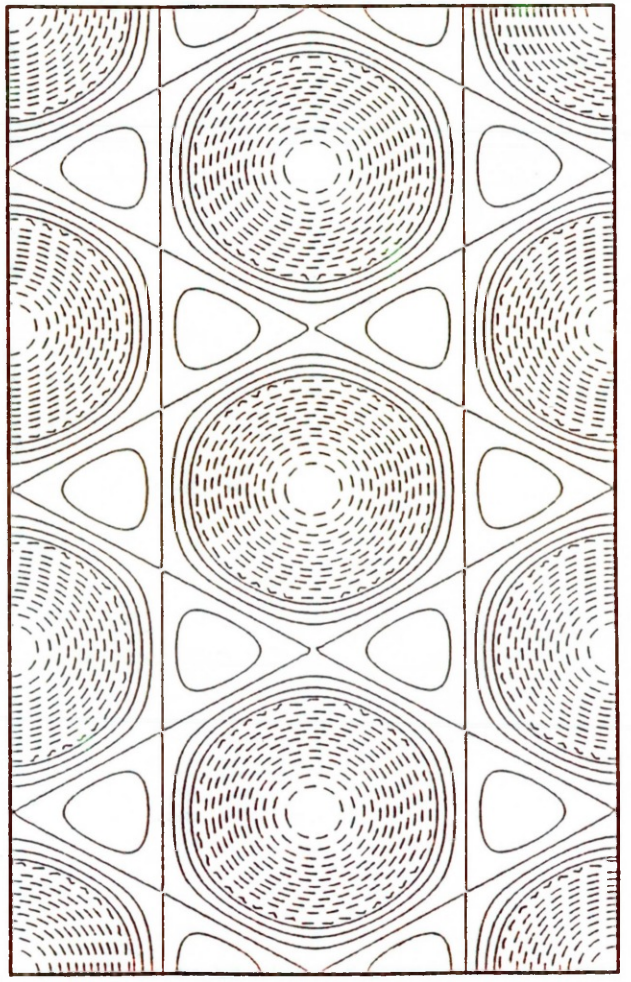
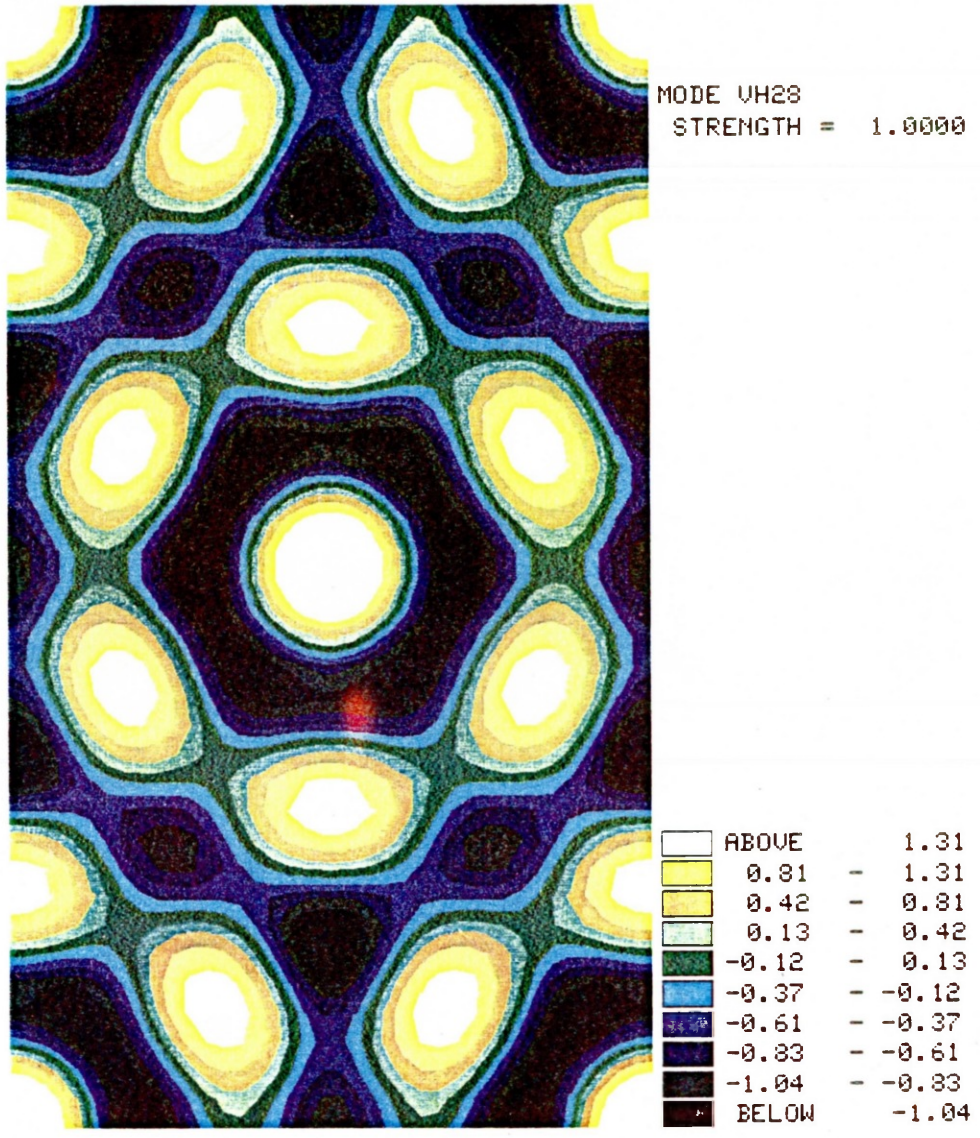


Figure 4.2c)
Streamlines – mode VH28



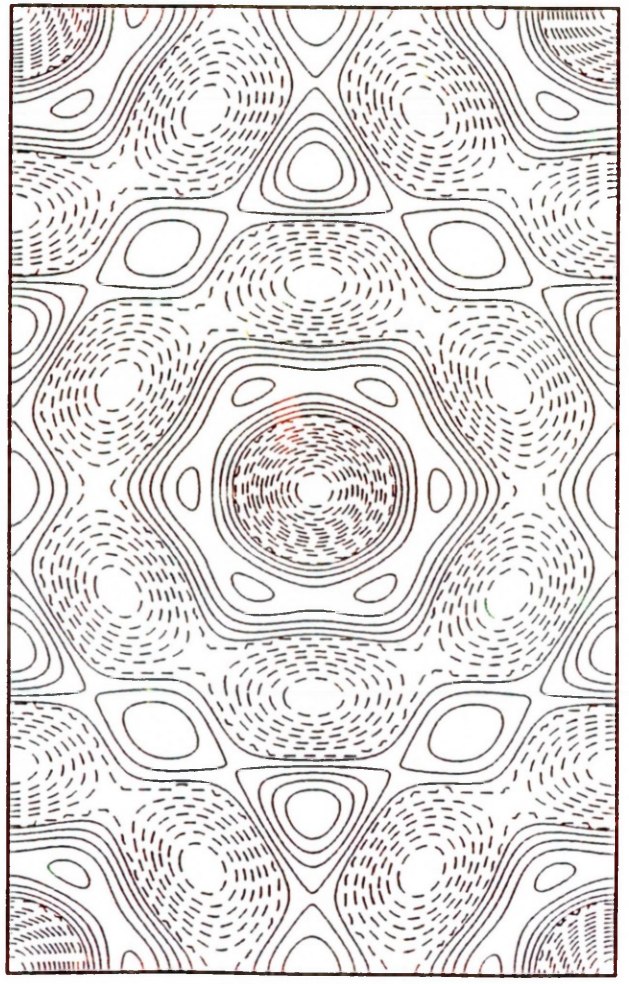
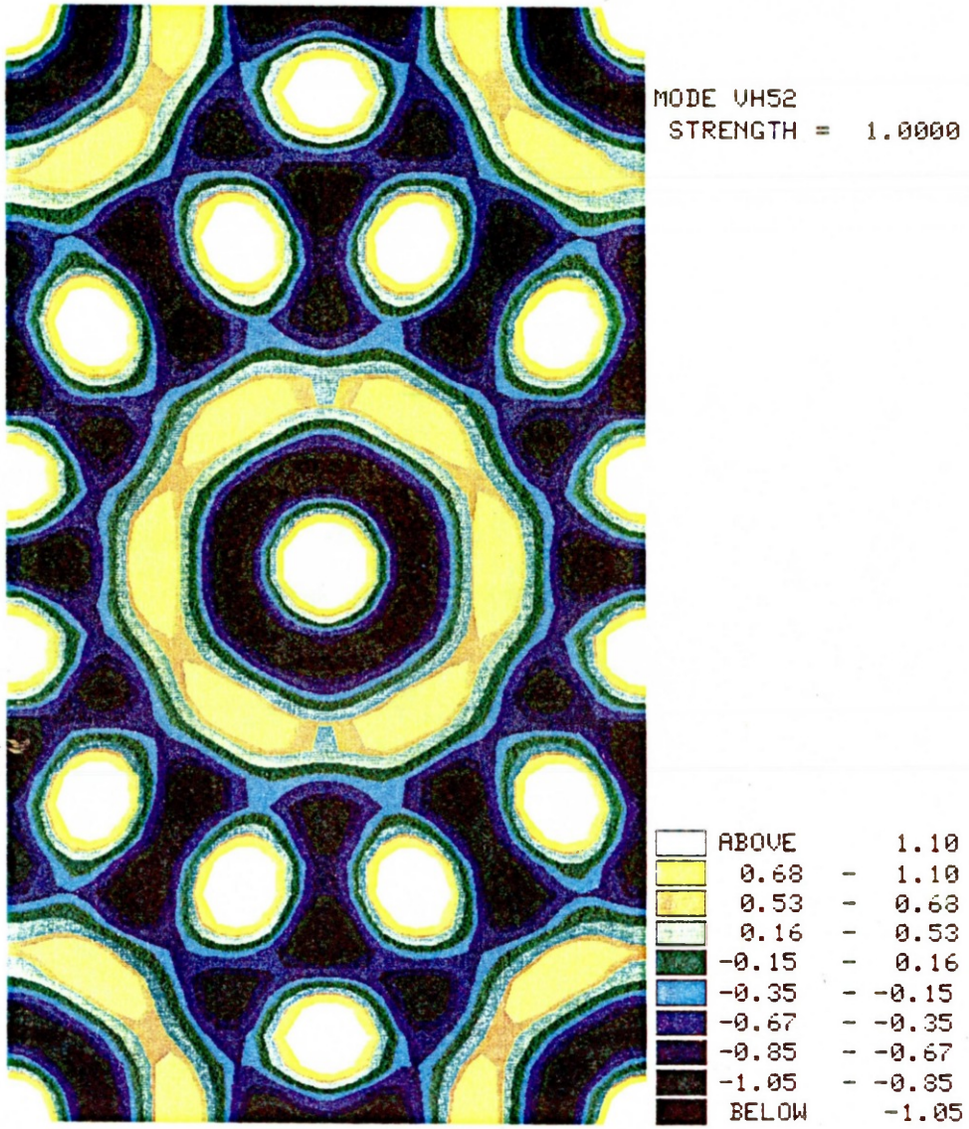


Figure 4.2d)
Streamlines – mode VH52



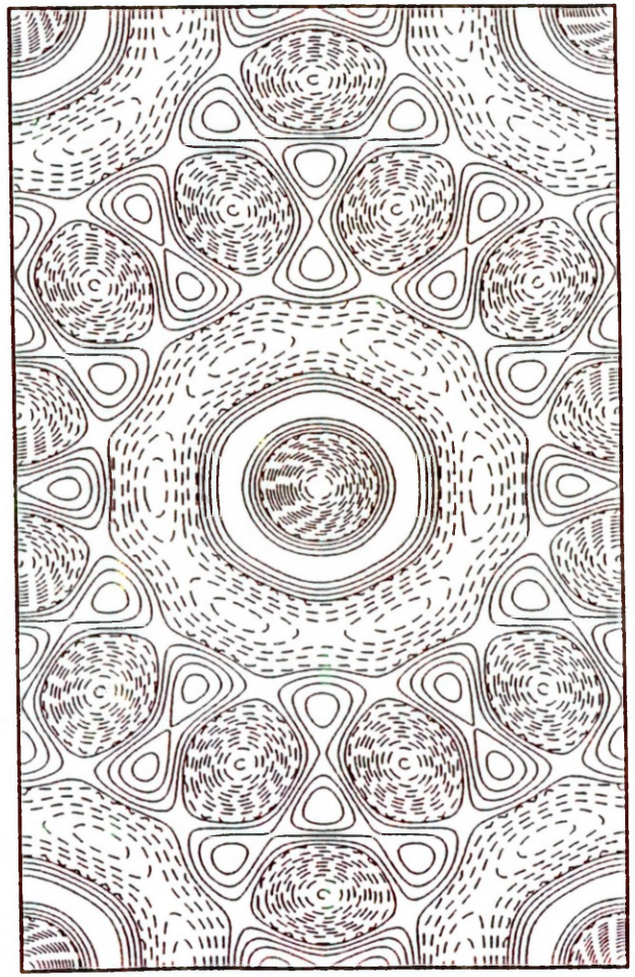
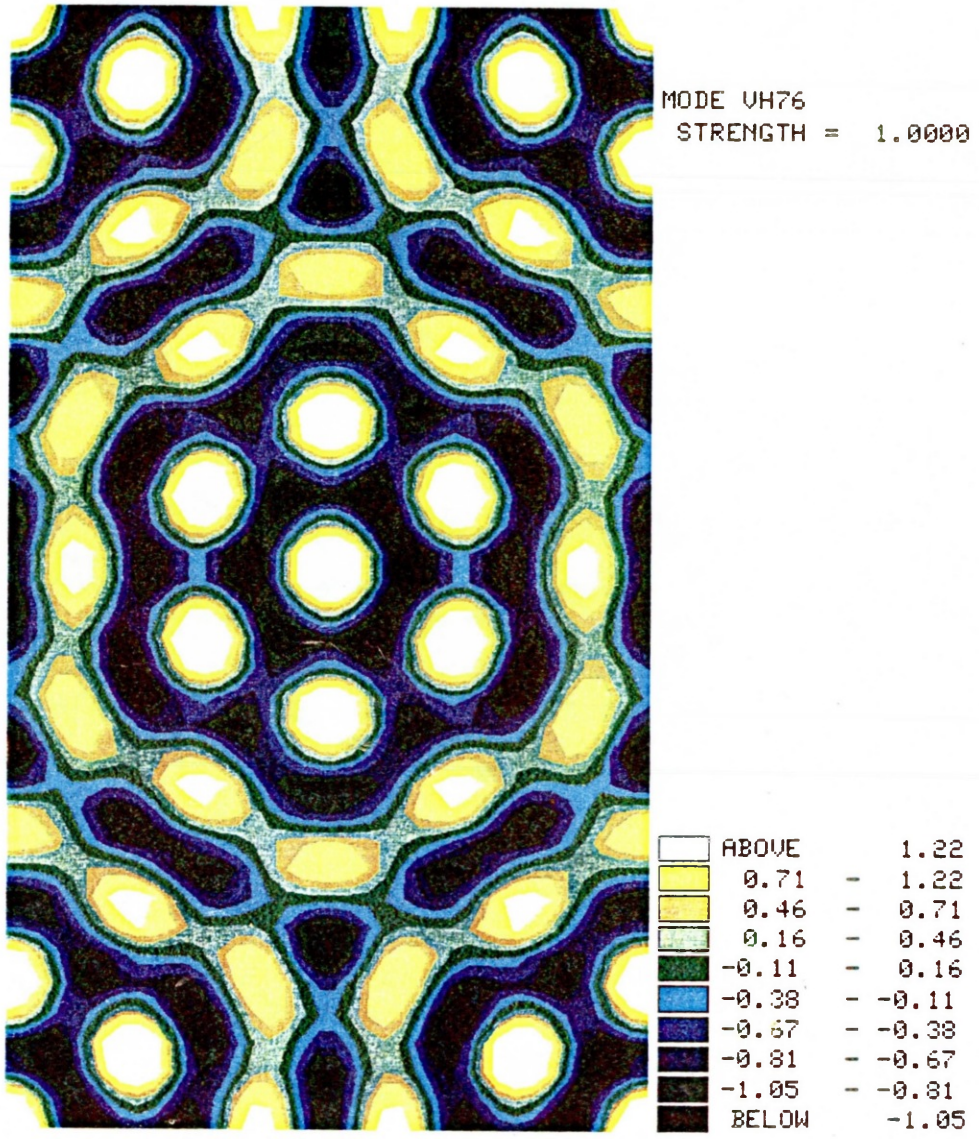


Figure 4.2e)
Streamlines – mode VH76



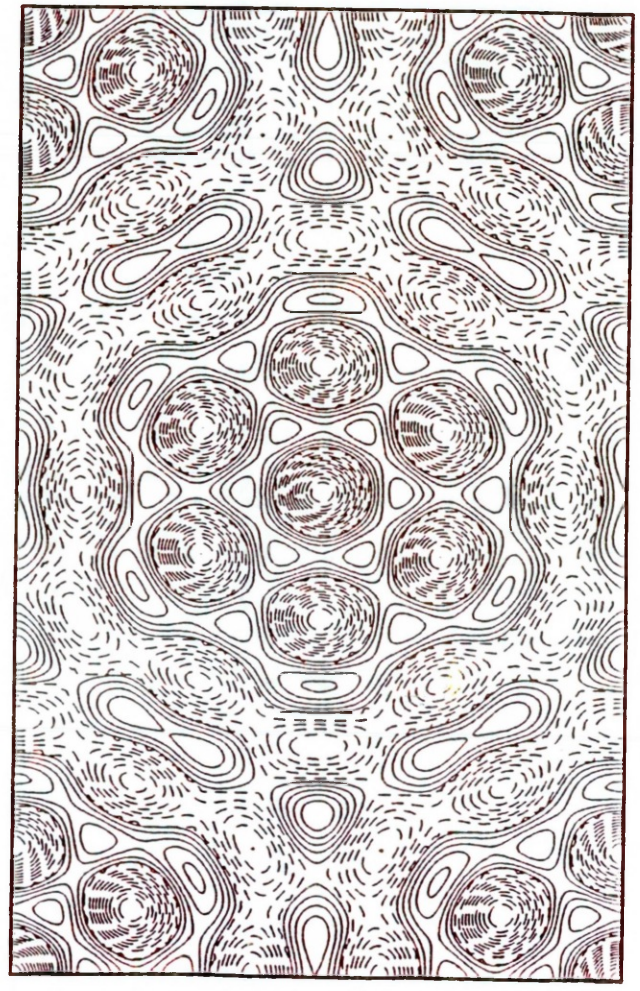
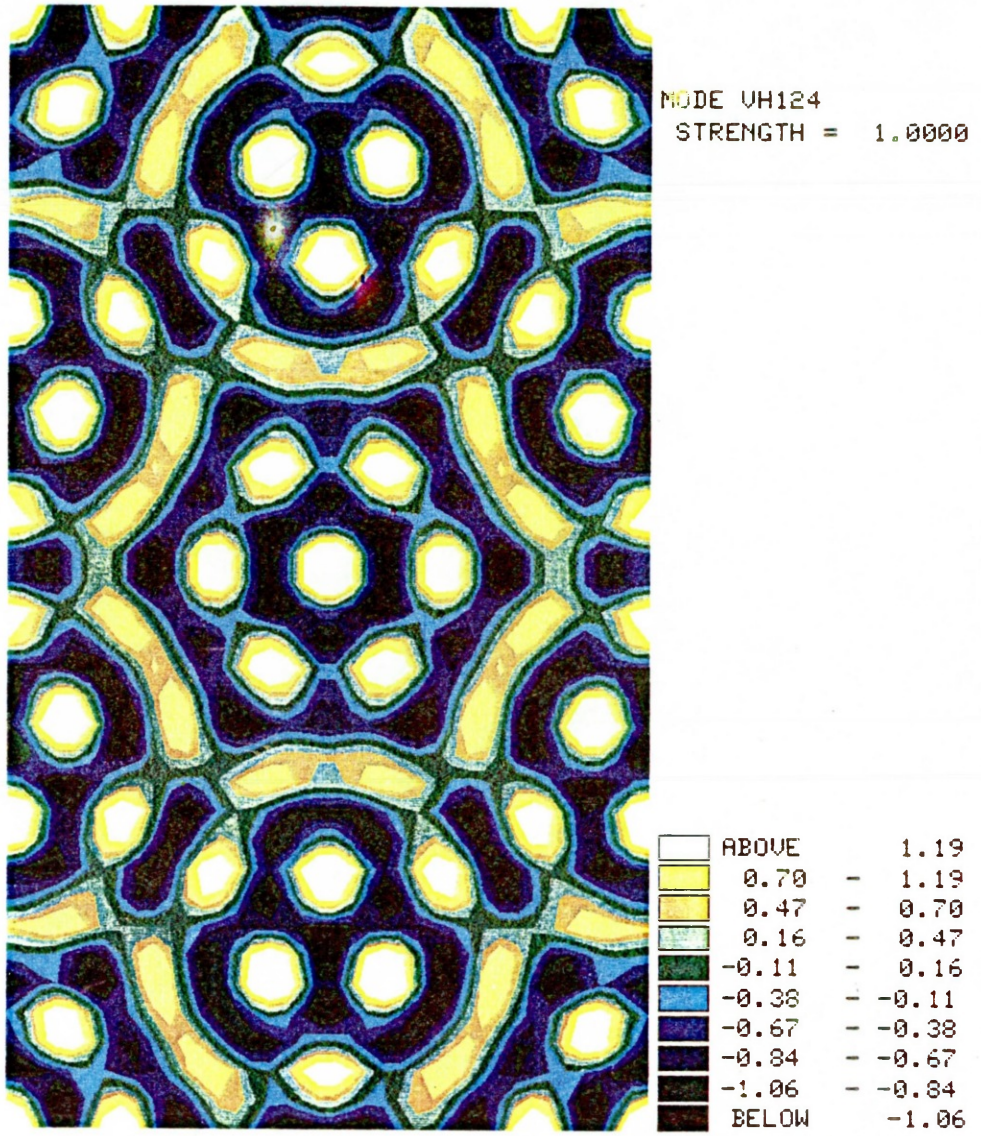


Figure 4.2f)
Streamlines – mode VH124



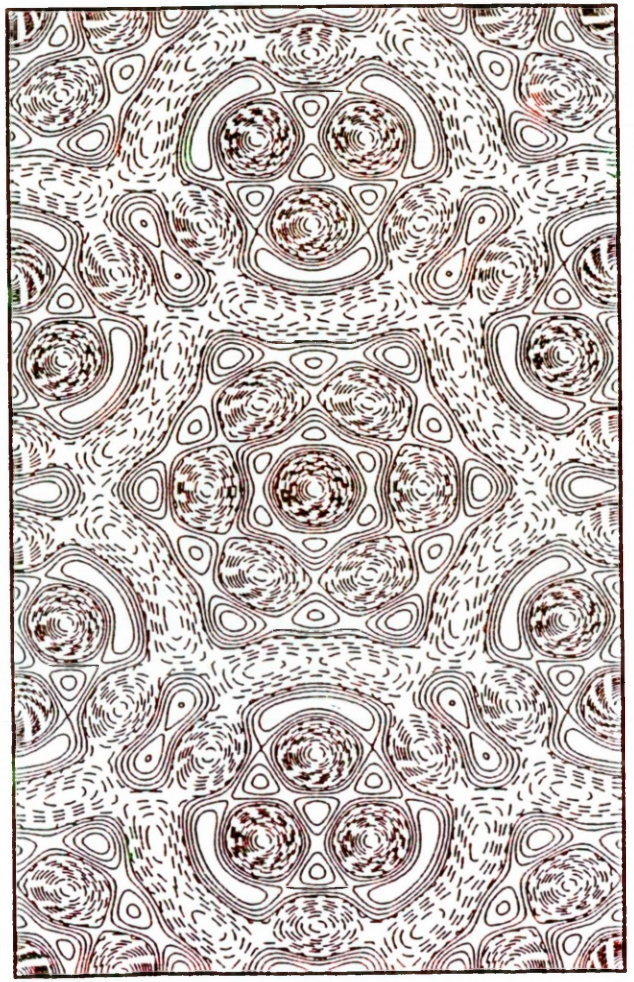
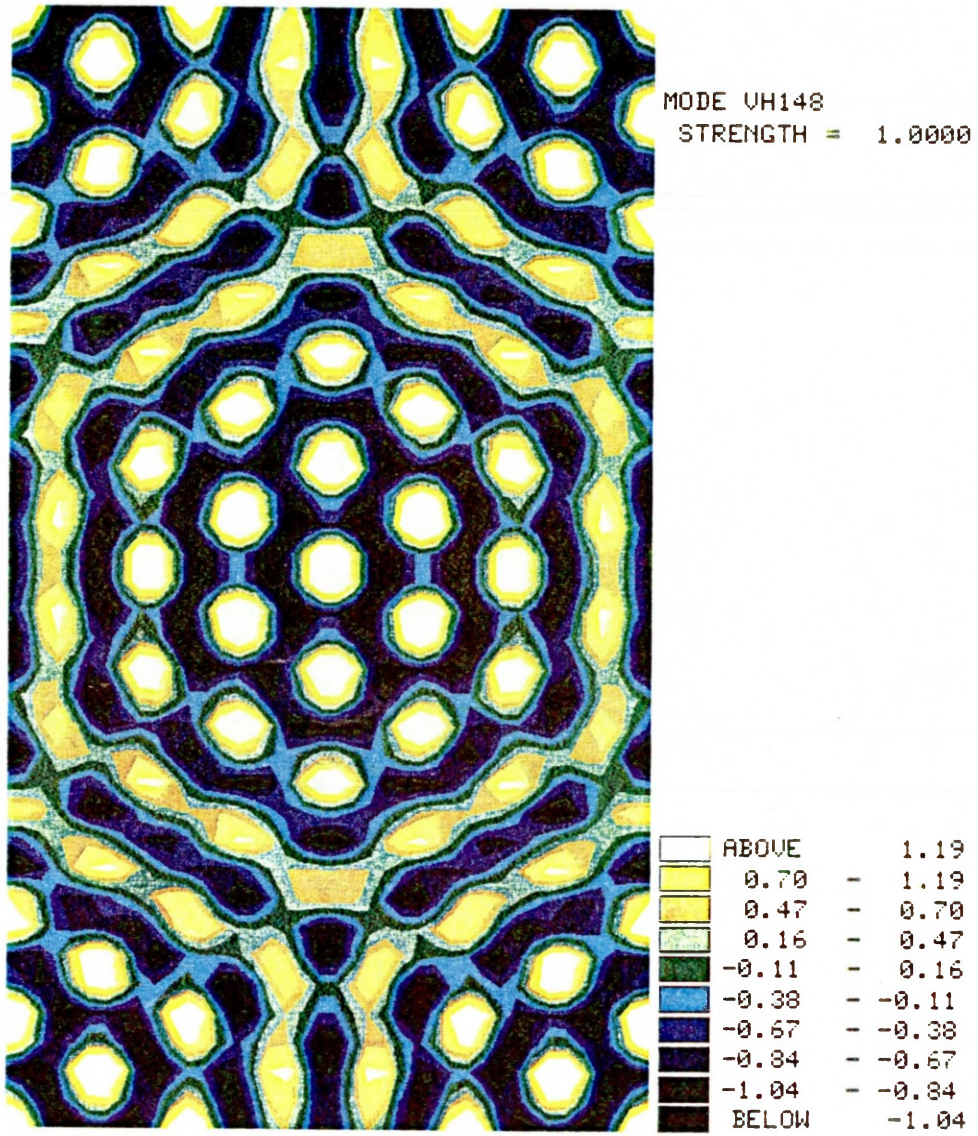
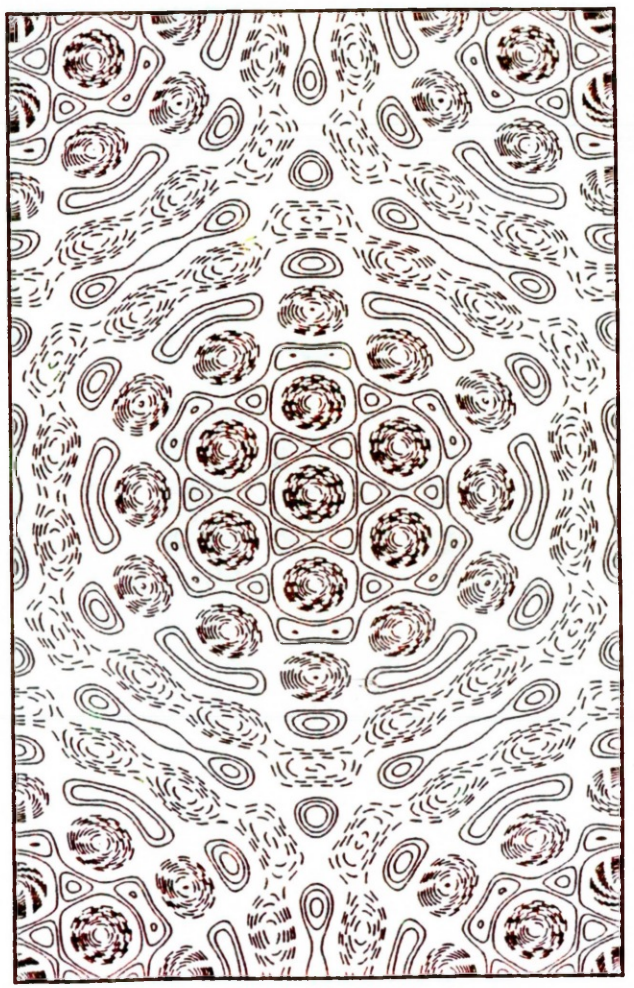


Figure 4.2g)
Streamlines – mode VH148





but the trigonometric functions are changed from cosines to sines and the signs now alternate rather than agreeing as they do in the planform function (see Table 4.1). The vorticity pattern has the same symmetries as the planform functions but also includes a splitting up into two vortex cells for each section of the planform, thus conserving the vorticity.

At fourth order, another curved and vorticity generating harmonic appears (figures 4.1d), 4.2d), 4.3b)). This harmonic has an even more obvious curved nature than the first, with the loss of the main Christopherson characteristic altogether. There now appears a main twelve sided cell containing a now near−circular inner cell, with the main figure surrounded by smaller cells (figure 4.1d)). These smaller cells also have curved walls and are, remarkably, pentagonal, so that it is observed that the non−linear interactions alone have led from a purely six sided tiling of the plane, to one which could include five sided figures in the patterns.

The vortex pattern (figure 4.3b)) shows how the new cellular pattern in fact disguises the still underlying Christopherson hexagonal structure in the pattern. The vortex lines once again show a similar spoked arrangement of cells with the opposite vorticity, but this time an extra concentric 'layer' of vortex cells has been added inside the boundary of the original Christopherson hexagon, and the strange curved twelve wall boundary of the planform function itself reflects the interface between the outer two of these layers. Once again, as will be seen always, the symmetries of the figures have been preserved in all of the planform, stream and vortex lines.

If higher order modes are examined, stranger shapes appear. At order 5, a replica of the third order vorticity mode, mode VH28, appears with cells linearly reduced by a scaling factor of $\sqrt{3}$ and rotated by 30^{o}, along with a harmonic once again based around the basic hexagonal structure, but this time including an inner 'cluster' of cells. This inner cluster has one central and almost straight walled hexagonal cell in the middle, surrounded by some extremely curved but similar sized cells (figure 4.1e)). Looking once again at the vorticity pattern (figure 4.3c)), another vortex cell has been added to each triangular segment, not as another ring as in the transition from the first vertical vorticity mode to the second, but this time as the splitting of the outer ring into another two cells per segment.

At even higher orders, two new modes appear which are even more bizarre. One mode is similar to the fifth order new mode, but has reduced the size of the inner cluster of curved cells and added another layer of cells onto this cluster (figure 4.1g)). The cells in this pattern show a remarkable similarity to the 'modified rectangular cells' of Stuart (1964). The associated vortex pattern

Figure 4.3a)
Vorticity – mode VH28

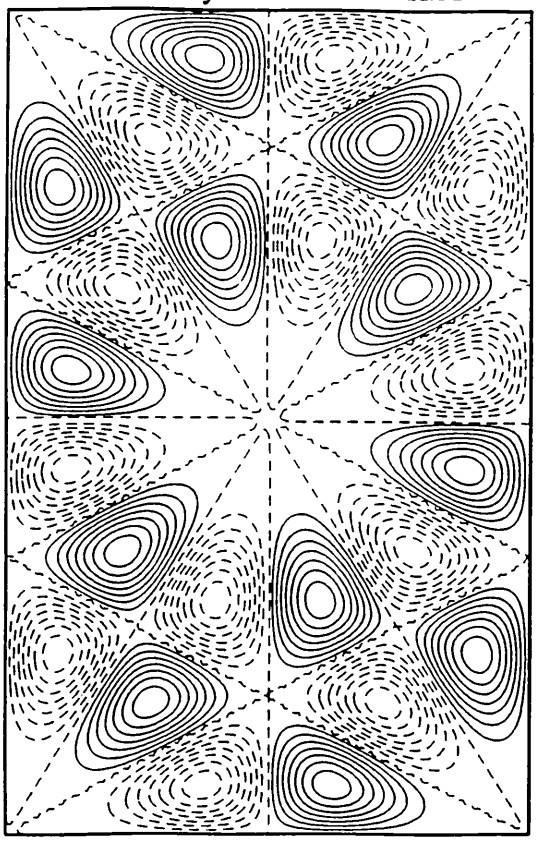


Figure 4.3b)
Vorticity – mode VH52

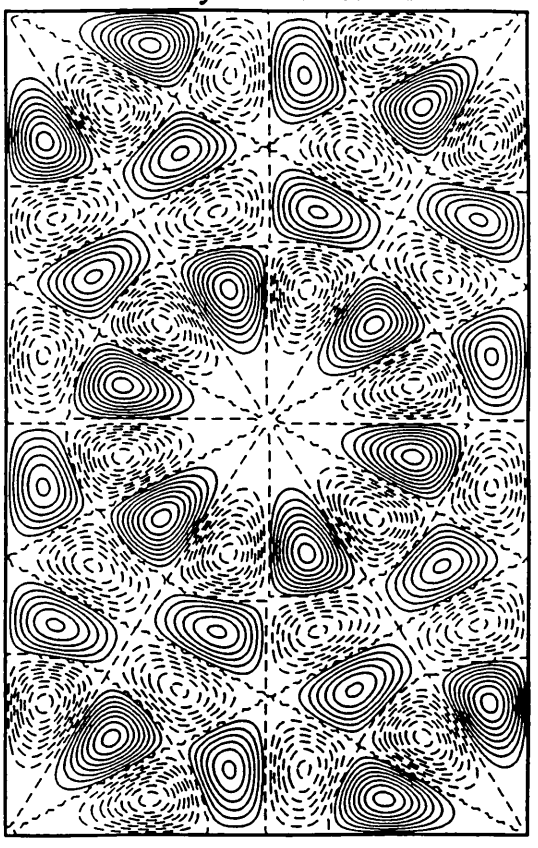


Figure 4.3c)
Vorticity – mode VH76

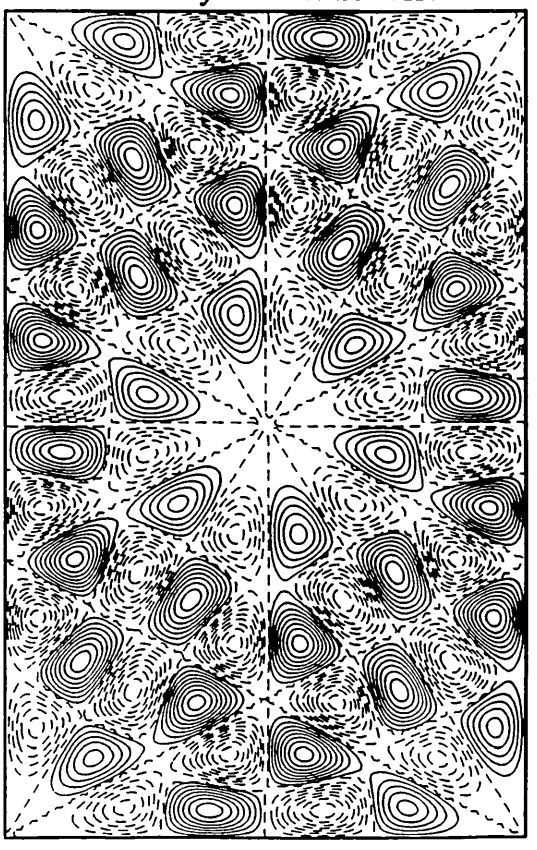


Figure 4.3d)
Vorticity – mode VH124

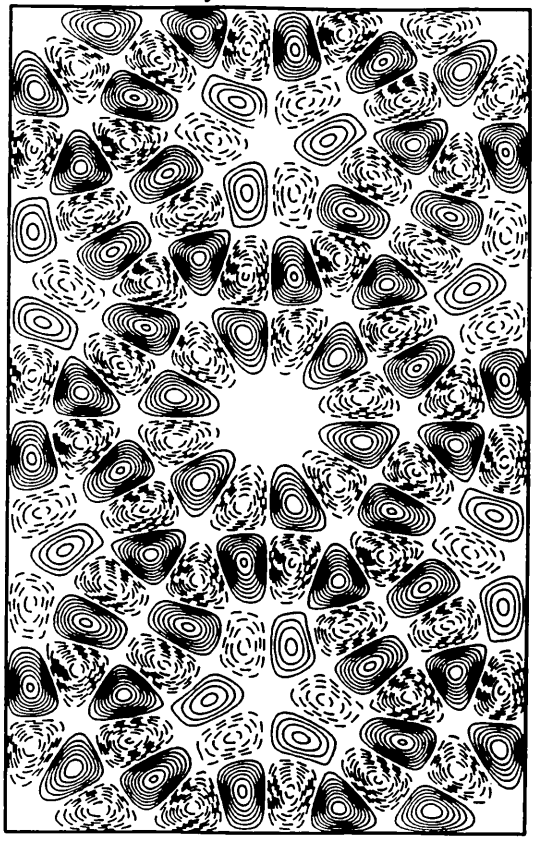
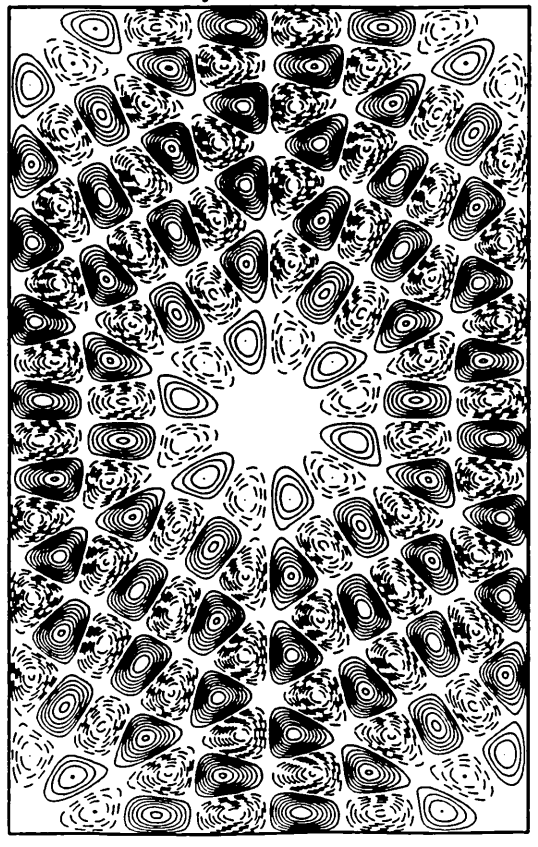


Figure 4.3e)
Vorticity – mode VH148



(figure 4.3e)) now has the outer ring of cells split such that there are three cells per triangular section with the middle ring now split into two cells per section, making a total of six vortex cells for every triangular section.

Another mode also appears before or at order eight and defies rationalisation. This mode, VH148 (figure 4.1f)), apparently has cell walls, as defined by Stuart (1964), that are not joined onto other walls to form a closed cellular structure, but which appear to 'float' in a body of fluid. This is intuitively unnerving. The present definition of a cell wall (Stuart (1964)) does not require cell walls to be joined in a manner so as to create a closed pattern, although it is implicitly understood that a cell wall is the wall of a cell, which, by definition is a closed, isolatable unit. The calculations here seem to have revealed a different kind of wall, a 'dividing' wall, rather than a cell wall, in this mode. The wall has all the properties of a cell wall, but allows a continuous flow to encompass both of its sides i.e. an unbroken streamline may be drawn which completely encircles the wall, and yet no complete streamline is encircled by the wall itself. However, the original aim of this study was to consider modes up to, and including, order 5, and so the last few modes have not been studied in as much detail, but the figures for these modes (figures 4.1f), 4.1g), 4.2f), 4.2g), 4.3d), 4.3e)) are also included for interest.

4.4.2). Superposition of hexagonal harmonics.

The preceding work has examined only individual harmonics in isolation from each other. Physical problems seldom have a solution as a single harmonic, but are a combination of some or all of the harmonics that the conditions of the problem allows. The initial basis on which this work was founded, the convectional planform problem, allows all the previously discussed harmonics to exist as solutions to the problem, and to possibly co−exist with each other in some manner. It is likely that in physical situations, although one planform may dominate, the other planforms may contribute to the overall picture, especially in the highly complex and non−linear situations of the real world.

An example of a convection problem in astrophysics is the solar granulation, which is the observed pattern of dark and light areas in photographs of the sun. These are conjectured to be the result of an underlying convective region in the sun's atmosphere and indeed hexagonal patterns are claimed in its content. However, other structures are talked of in the examination of the available photographs (Kuiper (1953), Bray, Loughead and Durrant (1984), Schwarzschild

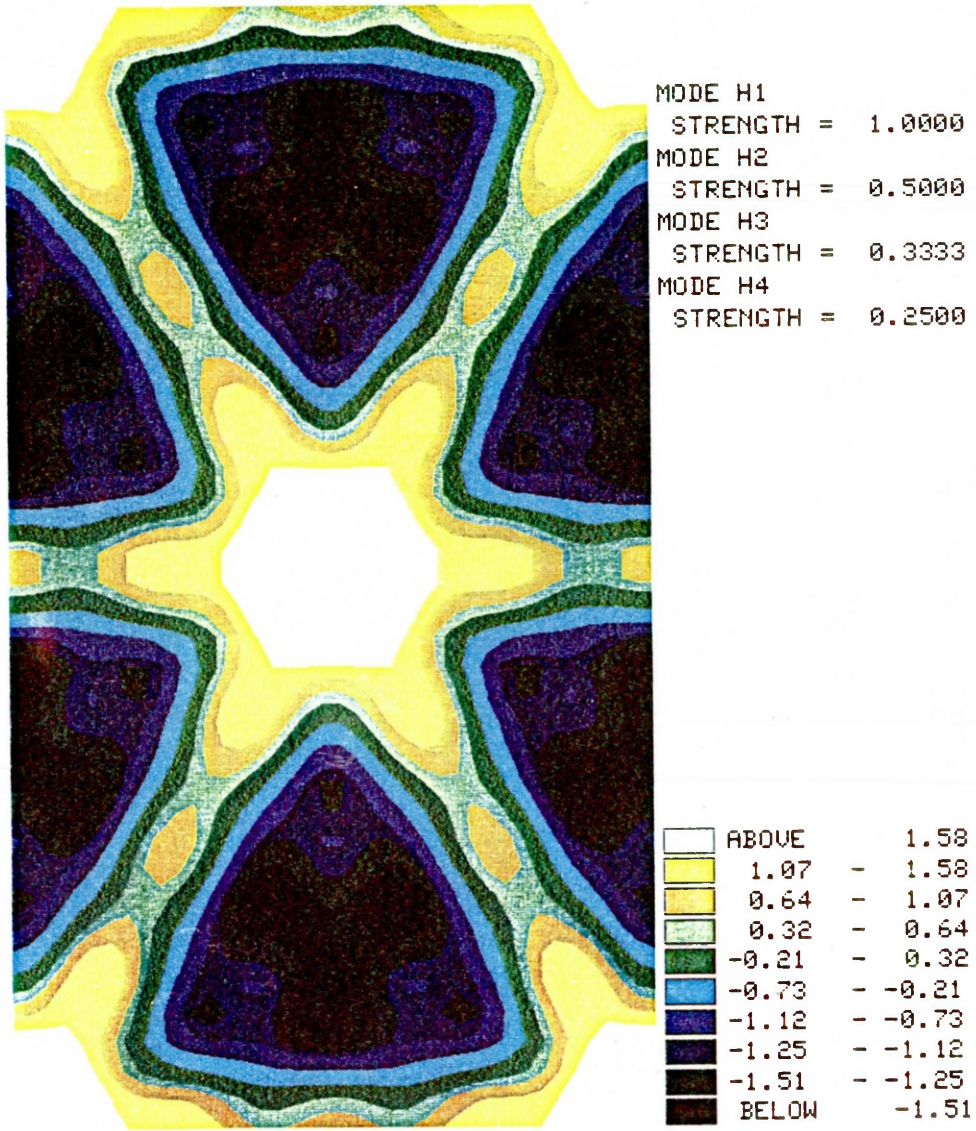
(1961)) such as 'doughnut cells', 'clusters of cells', 'spoke patterns' and other odd shaped cells. These sort of structural phenomena seem more feasible as convective features with the inclusion of the higher order planforms exhibited here. Consider further that what is actually observed can be a superposition of these planforms with varying strengths, and that there may be packet−like collections of similar but not identical wavenumbers present, and then a whole range of unusual topographies are available simply through the combination of a few of the relatively low order harmonics. For example, the inclusion of higher planform structures which incorporate many smaller pentagonal cells (e.g. VH52) offers a possible insight through simple theory into the fact that the mean number of sides of cellular patterns seen on the sun is often quoted as 5.7 by astrophysicists, rather than 6 as would be expected for a purely hexagonal pattern.

Superpositions of the simple harmonics studied here are exhibited in figures 4.4a) − 4.4f). Planform functions were calculated as for figures 4.2, but were added together with an optional scaling 'strength' factor for each planform superposed. This allows an interpretation of the way physical convection would superpose the horizontal harmonics of the series in some naturally selected way, with a bias in amplitude towards some preferred modes. Values used for the strengths here are arbitrarily chosen with some experience of three dimensional physical solutions (see Chapter 5).

General inferences may be drawn from the figures 4.4. Figure 4.4a) shows that superposition of aligned modes e.g. H1, H2, H3 and H4, tends to produce a spoked convective planform pattern, as exhibited by Toomre et al (1982). Superposition of the vorticity generating modes tends to emphasise the hexagonal cell wall of the original Christopherson planform, spreading the downward−moving fluid of the wall into a more obvious, sharply−defined channel. The VH28 planform leaves this as a smooth wall (figure 4.4b)), whereas VH52 tends to undulate it, leaving the wall divided into a number of cellular bumps (figure 4.4c)). This effect is also created by superposition of the first rotated overtone, RH3, (figure 4.4d)) which is not surprising, because the VH52 planform contains an infra−structure of a similar nature. Superposition of a large number of modes (figures 4.4e), 4.4f)) seems to lead to more isolated, deep cell centres, precisely hexagonal in shape, which are surrounded by wide channels of upward−moving fluid.

Thus, it may be seen that a large variety of planforms structures are available through simple superposition of these low order modes. More unusual modes may be created by adding the modes together with more equal strengths, or by superposing the more exotic higher order modes, but those superpositions exhibited here are at least reasonably physical.

FIG. 4.4a) . SUPERPOSITION PLANFORMS



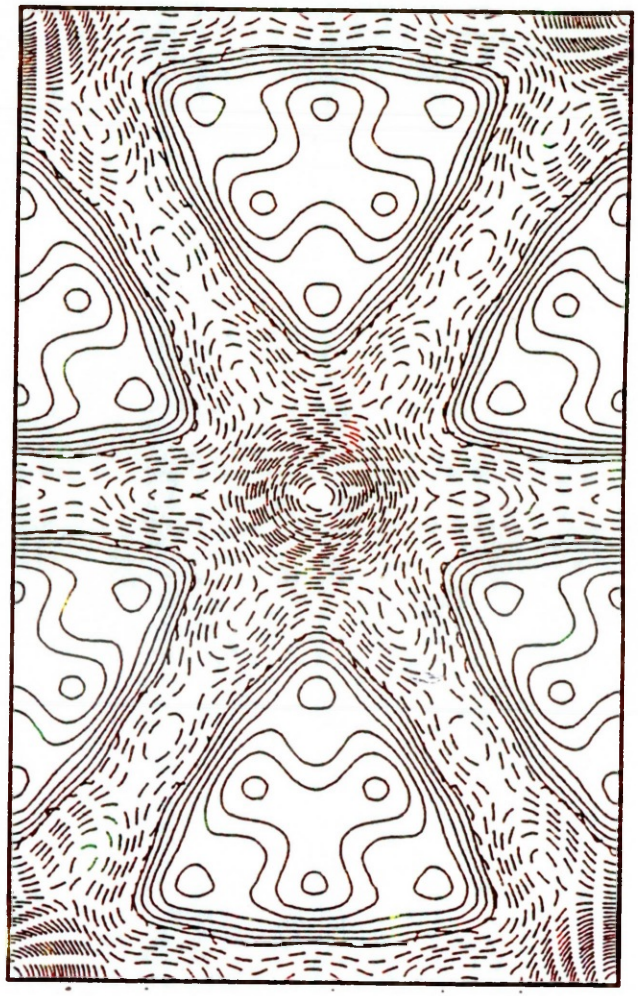
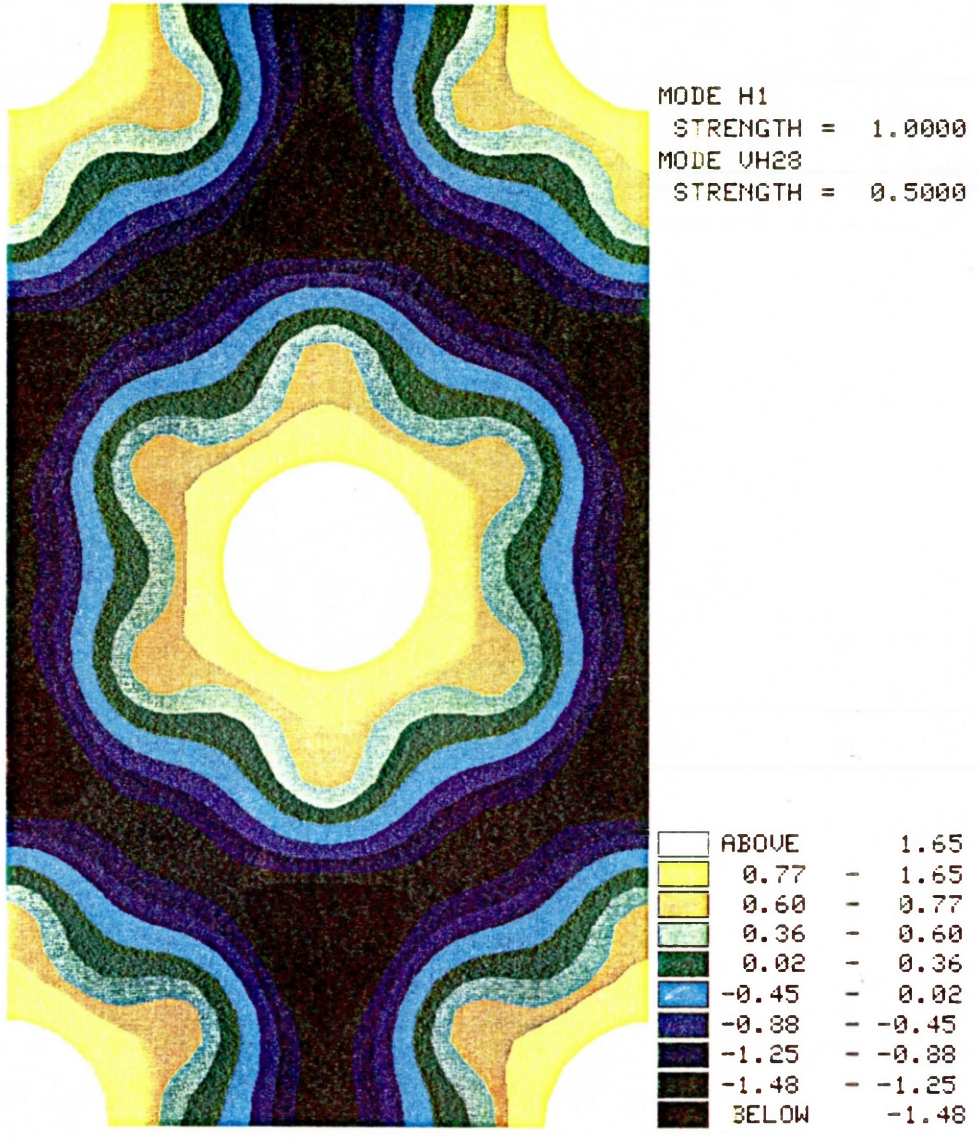


FIG. 4.4b) . SUPERPOSITION PLANFORMS



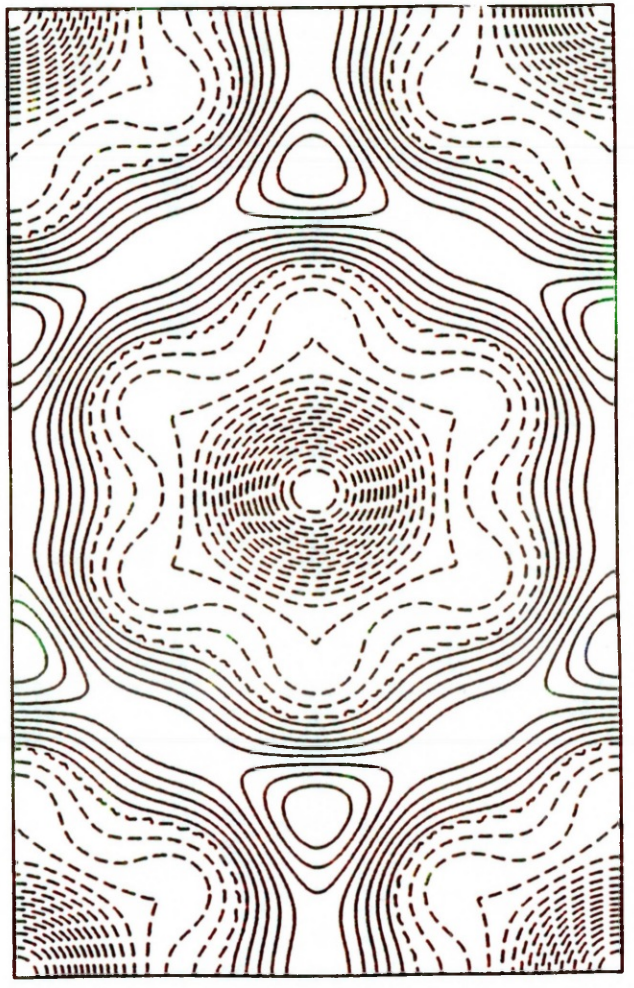
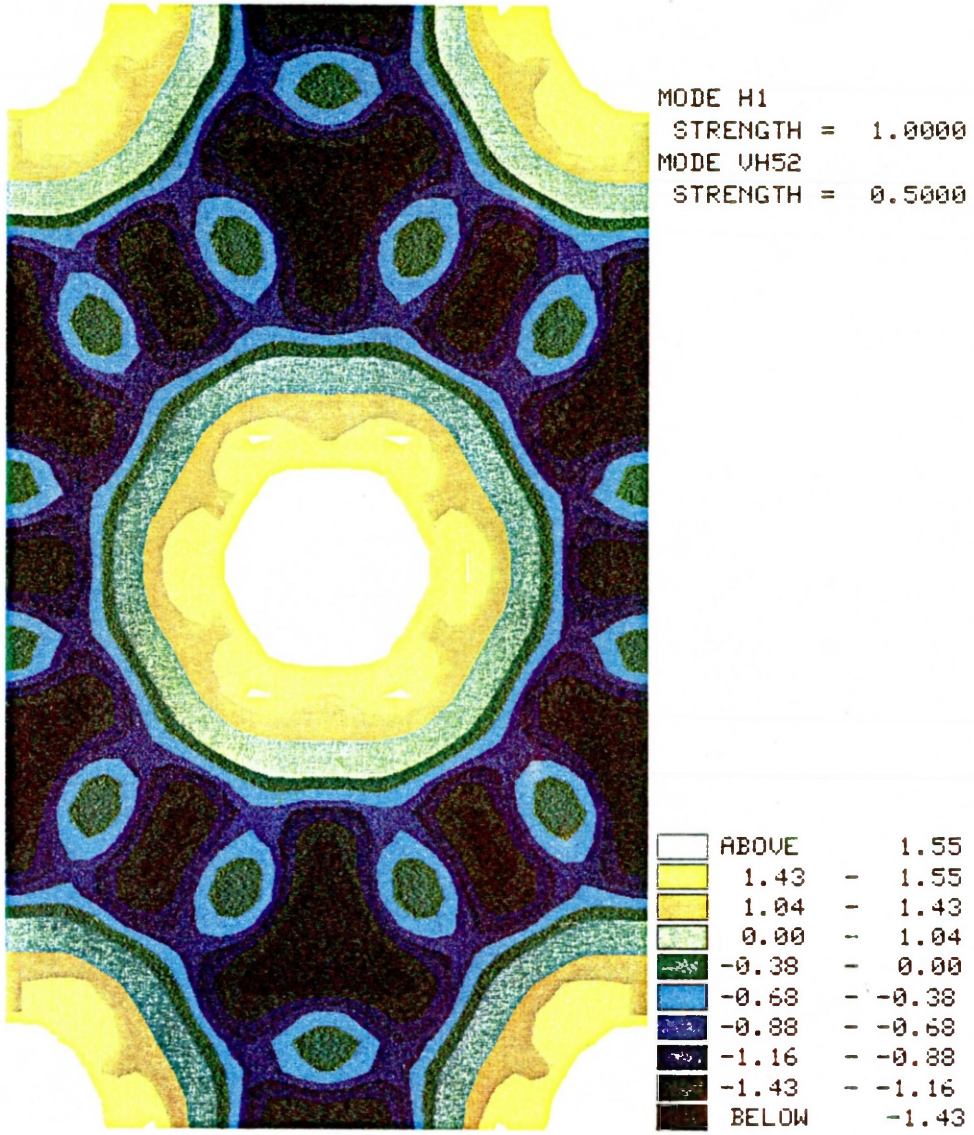


FIG. 4.4c) . SUPERPOSITION PLANFORMS



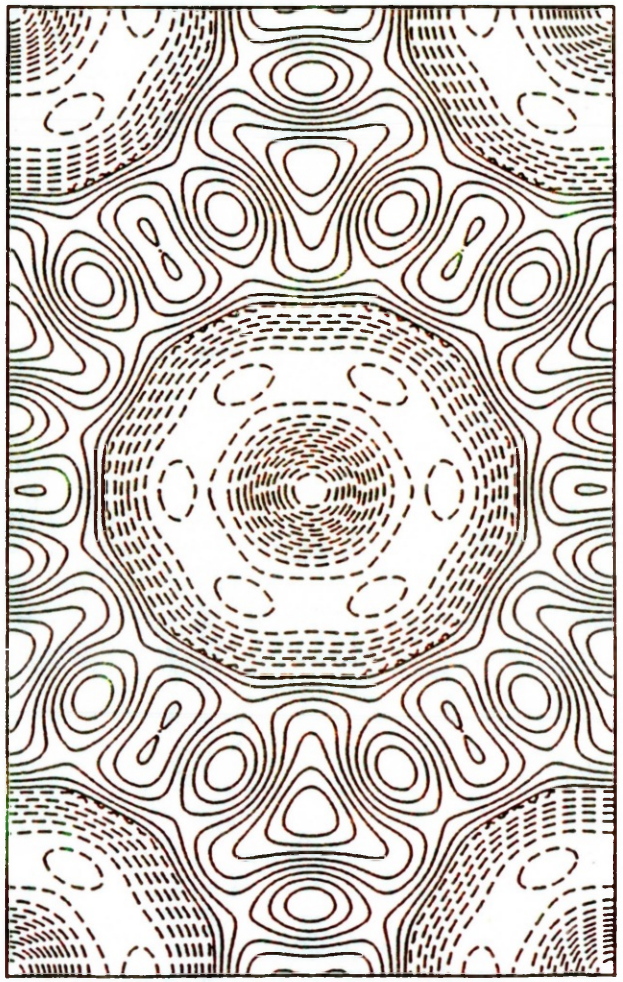
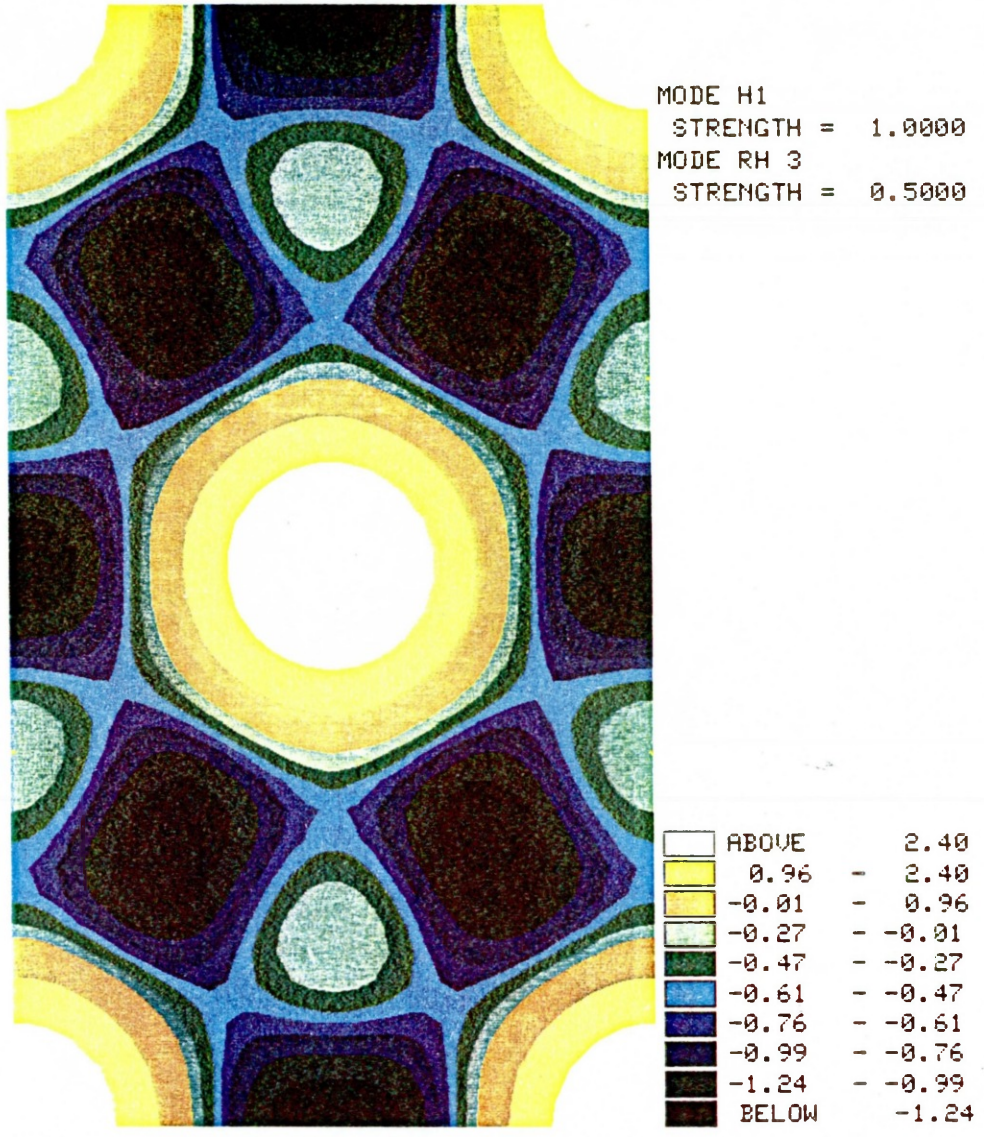


FIG. 4.4d) . SUPERPOSITION PLANFORMS



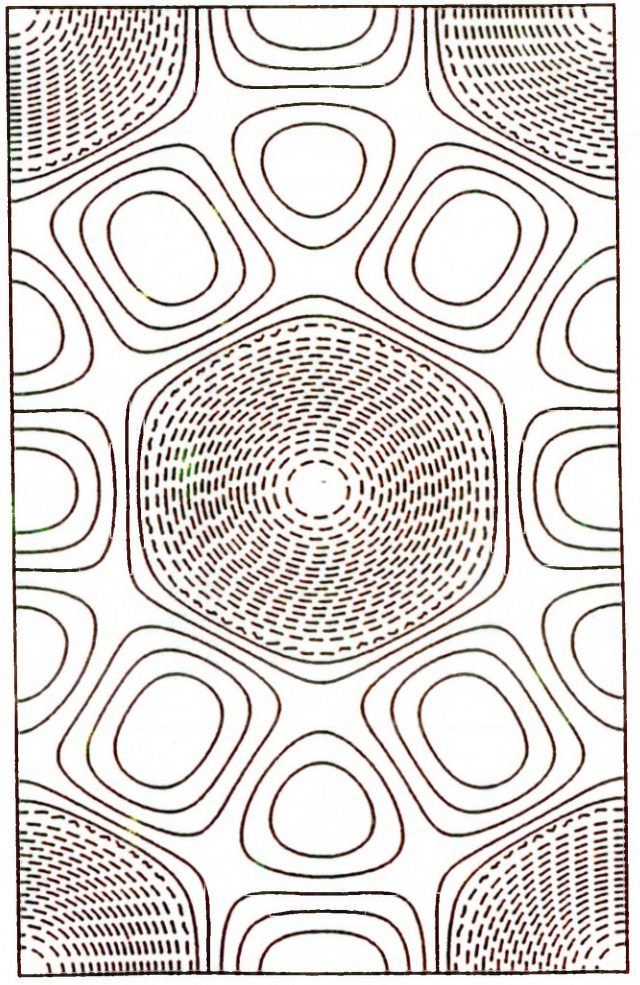
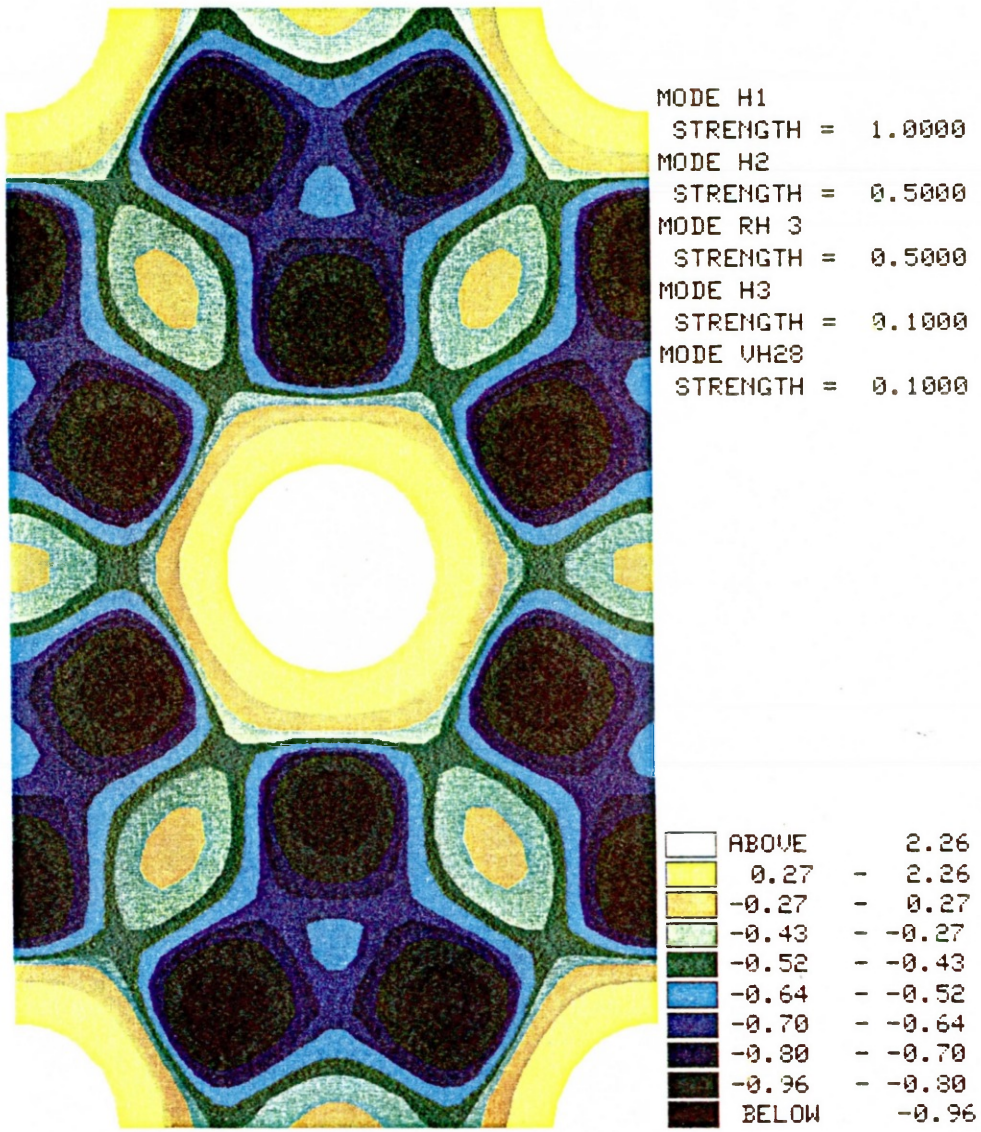


FIG. 4.4e) . SUPERPOSITION PLANFORMS



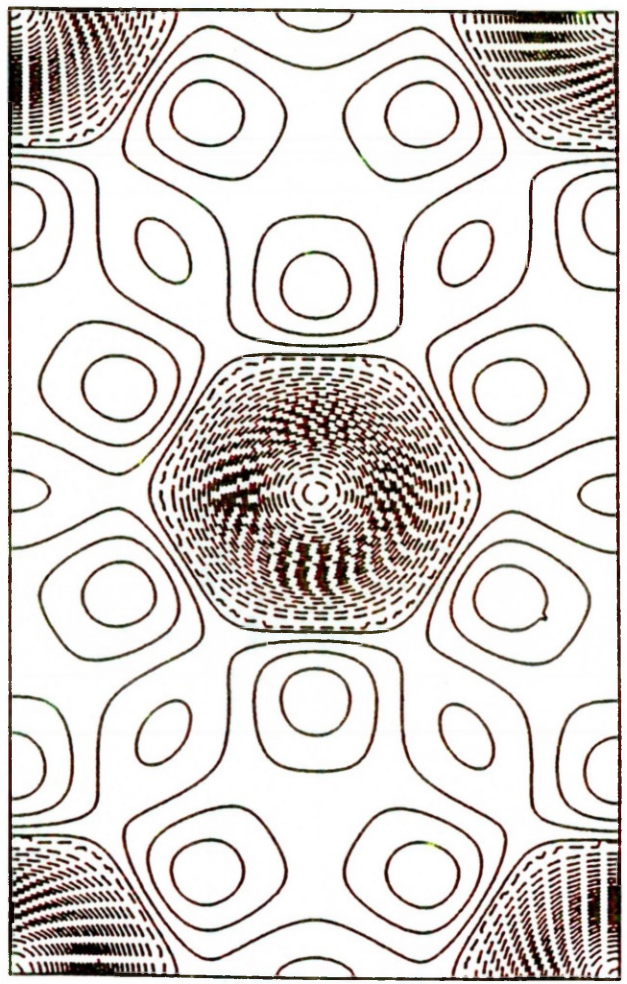
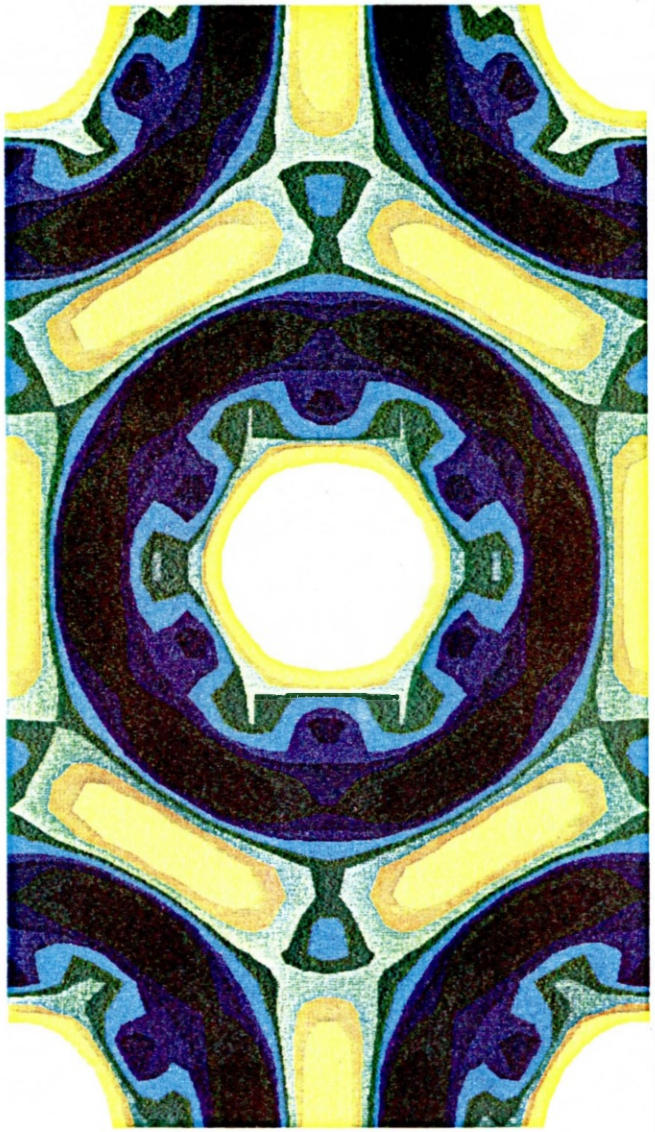
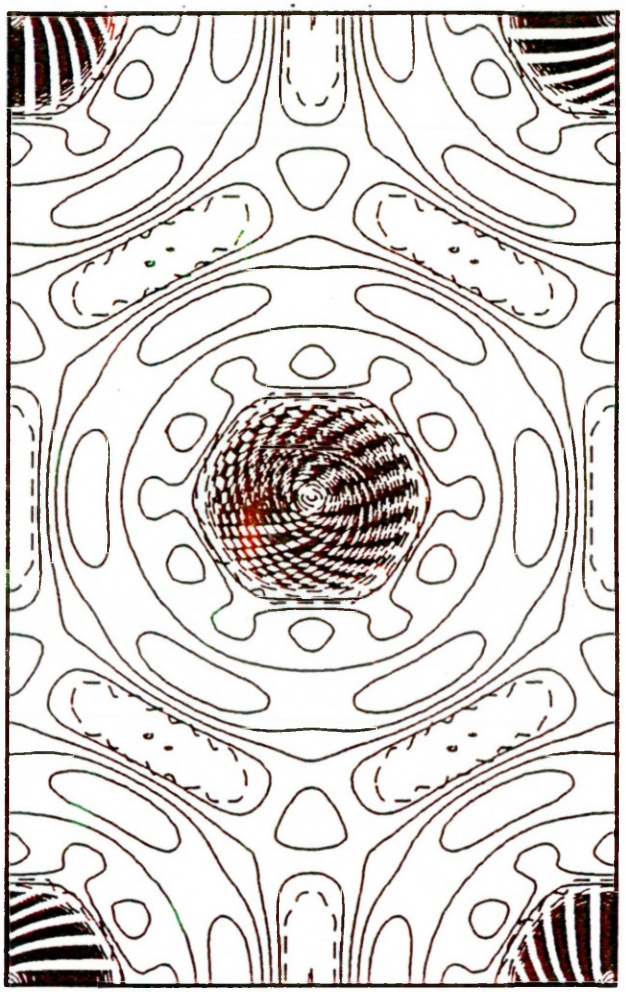


FIG. 4.4f) . SUPERPOSITION PLANFORMS



MODE H1
STRENGTH = 1.0000
MODE H2
STRENGTH = 0.8000
MODE RH 3
STRENGTH = 0.9000
MODE H3
STRENGTH = 0.2500
MODE VH28
STRENGTH = 0.7500
MODE H4
STRENGTH = 0.1700
MODE RH2 3
STRENGTH = 0.2500
MODE VH52
STRENGTH = 0.5000

ABOVE	0.82
-0.05	- 0.82
-0.27	- -0.05
-0.47	- -0.27
-0.56	- -0.47
-0.68	- -0.56
-0.76	- -0.68
-0.86	- -0.76
-1.00	- -0.86
BELOW	-1.00



4.4.3. Square planform harmonics.

Results for the similar investigation of the square planform defined in equation [4.5] do not show any semblance of the richness of the hexagon harmonic field. The resultant harmonics are shown as before in table 4.2. The interactions via the non−linear terms only produce roll solutions, or aligned and scaled square solutions. No possible source terms for vertical vorticity are found, and no changes in planform structure occur. Thus no vertical vorticity component can enter the square planform convection problem inherently, although there still remains the possibility that an instability of the flow may allow such a component to be generated. The lack of inherent vorticity may be proved by the following argument.

The vertical z component of the curl of the Navier−Stokes equation for convection (see equation [2.13]) contains no component of the buoyancy driving term, since gravity acts vertically, and so the remaining terms of the steady state are

TABLE 4.2. Nomenclature and characteristic properties of individual square harmonics generated in the non−linear term. The parameter α is an arbitrary wavenumber that may be imposed on the whole planform.

Name	Planform function	Vorticity function	Order
S11	$\cos(\alpha x)\cos(\alpha y)$	-	1
S20	$\cos(2\alpha x)$	-	2
S02	$\cos(2\alpha y)$	-	2
S22	$\cos(2\alpha x)\cos(2\alpha y)$	-	2
S31	$\cos(3\alpha x)\cos(\alpha y)$	-	3
S13	$\cos(\alpha x)\cos(3\alpha y)$	-	3
S33	$\cos(3\alpha x)\cos(3\alpha y)$	-	3
S40	$\cos(4\alpha x)$	-	4
S04	$\cos(4\alpha y)$	-	4
S24	$\cos(2\alpha x)\cos(4\alpha y)$	-	4
S42	$\cos(4\alpha x)\cos(2\alpha y)$	-	4
S44	$\cos(4\alpha x)\cos(4\alpha y)$	-	4

$$u\frac{\partial\omega_3}{\partial x} + v\frac{\partial\omega_3}{\partial y} + w\frac{\partial\omega_3}{\partial z} - \omega_1\frac{\partial w}{\partial x} - \omega_2\frac{\partial w}{\partial y} - \omega_3\frac{\partial w}{dz} - \nabla^2\omega_3 = 0 \quad , \qquad [4.8]$$

where the vorticity, $\boldsymbol{\omega} = (\omega_1, \omega_2, \omega_3)$, and the velocity, $\mathbf{u} = (u, v, w)$ as usual. The interest lies in the generation of vertical vorticity, ω_3, and so to see what drives this generation, the terms of [4.8] must be examined. Now, it is assumed that the vorticity component is not self-generating, but must be generated by other interactions of other variables, and so interest may be reduced to the subset of variables

$$\omega_1\frac{\partial w}{\partial x} + \omega_2\frac{\partial w}{\partial y} \quad , \qquad [4.9]$$

since the other terms all include a self-generating ω_3 term.

Using the definition of $\mathbf{u}$ as in [4.1] but with $\psi = 0$ to remove the self-generating vertical vorticity terms again, this becomes

$$\nabla_h^2\left[\frac{\partial\chi}{\partial x}\right].\nabla^2\left[\frac{\partial\chi}{\partial y}\right] - \nabla_h^2\left[\frac{\partial\chi}{\partial y}\right].\nabla^2\left[\frac{\partial\chi}{\partial x}\right] . \qquad [4.10]$$

This expression may be simplified, but is convenient to leave it in this form. The question is now one of when is [4.10] identically zero?

If it is assumed, in all generality, that the square-planform cell has been normalised so that the width of the box in the x and y directions are unity, then, to satisfy the boundary conditions that there must be no flow out of the side walls of this box (i.e. $u = 0$ on $x = 0, 1$; $v = 0$ on $y = 0, 1$) any planform function, χ, must be of the form

$$\chi(x,y) = \sum_{m,n} \chi_{mn}\cos(mx)\cos(ny) \quad . \qquad [4.11]$$

Note that $\chi_{nm} = \chi_{mn}$ because the planform must hold the square symmetry i.e. symmetry about the x and y axes and across a diagonal. Then, letting $A = \nabla^2\chi$ and $B = \nabla_h^2\chi$, A and B may be expressed as

$$A(x,y) = \sum_{m,n} A_{mn}\cos(mx)\cos(ny) \quad , \qquad [4.12]$$

$$B(x,y) = \sum_{m,n} B_{mn}\cos(mx)\cos(ny) \quad , \qquad [4.13]$$

where $A_{nm} = A_{mn}$ and $B_{nm} = B_{mn}$ since $\chi_{nm} = \chi_{mn}$.

Thus [4.10] becomes

$$J(A,B) = \frac{\partial A}{\partial x}.\frac{\partial B}{\partial y} - \frac{\partial A}{\partial y}.\frac{\partial B}{\partial x} \quad . \qquad [4.13]$$

Thus, substituting from [4.12] and [4.13],

$$J(A,B) = \left[\sum_{m,n} mA_{mn} \sin(mx)\cos(my) \right].\left[\sum_{m',n'} n'B_{m'n'} \cos(m'x)\sin(n'y) \right]$$
$$- \left[\sum_{m,n} nA_{mn} \cos(mx)\sin(ny) \right].\left[\sum_{m',n'} m'B_{m'n'} \sin(m'x)\cos(n'y) \right]$$
$$. \qquad [4.14]$$

Multiplying out,

$$J(A,B) = \sum_{m,n} \sum_{m',n'} \left[A_{mn}B_{m'n'}\, mn' \sin(mx)\cos(ny)\cos(m'x)\sin(n'y) \right.$$
$$\left. - A_{mn}B_{m'n'}\, nm' \cos(mx)\sin(ny)\sin(m'x)\cos(n'y) \right]$$
$$. \qquad [4.15]$$

The index variables are only dummy variables, and so can be changed at will. In the second term of [4.15], swapping m for n and m' for n' gives

$$J(A,B) = \sum_{m,n} \sum_{m',n'} \left[A_{mn}B_{m'n'}\, mn' \sin(mx)\cos(ny)\cos(m'x)\sin(n'y) \right.$$
$$\left. - A_{nm}B_{n'm'}\, mn' \cos(nx)\sin(my)\sin(n'x)\cos(m'y) \right]$$
$$, \qquad [4.16]$$

and so,

$$J(A,B) = \sum_{m,n} \sum_{m',n'} mn'\sin(mx)\cos(ny)\cos(m'x)\sin(n'y)\left[A_{mn}B_{m'n'} - A_{nm}B_{n'm'}\right]$$
$$, \qquad [4.17]$$

or, since $A_{nm} = A_{mn}$,

$$J(A,B) = \sum_{m,n} \sum_{m',n'} mn'\sin(mx)\cos(ny)\cos(m'x)\sin(n'y)\, A_{mn}\left[B_{m'n'} - B_{n'm'}\right]$$
$$. \qquad [4.18]$$

which is identically zero, since $B_{nm} = B_{mn}$. Thus the Jacobian term which would generate vertical vorticity is zero at all times for all χ if a square planform for χ is chosen. Thus, it is expected that vertical vorticity may only be present for square cell convection as the result of a symmetry breaking bifurcation or a

time dependent instability (see also Busse and Bolton (1984)). Notice, that this is true for any type of convection which is vertically buoyancy driven, be it Rayleigh−Benard, penetrative or some other, since the driving term then only enters the Navier–Stokes equations in the vertical component, and so, on taking the curl for the vorticity equation, the driving term is excluded from the vertical component of this, and hence can never affect the vertical vorticity.

Table 4.2 shows the harmonics of the square planform up to order 4, but no further information is given, due to the regularity of the conclusions.

4.4.4. Solutions of the Helmholtz equation.

The harmonic patterns exhibited above are actually particular examples of an underlying problem, that of the general solutions of Helmholtz's equation

$$\nabla^2 f = -k^2 f. \qquad [4.19]$$

Solutions to this equation in general look like

$$f \approx \exp(i\mathbf{k}.\mathbf{x}) \ , \qquad [4.20]$$

where $k = |\mathbf{k}|$, and the most general real solution of the equation is to take

$$f = F + F' \ , \qquad [4.21]$$

$$F = \sum_{j=1}^{N} a_j \exp(i\mathbf{k}_j.\mathbf{x}) \ , \qquad [4.22]$$

for some N, where F' is the complex conjugate of F. A simple physical interpretation is to imagine the $\mathbf{k}_j$ defining wave vectors, each of magnitude k, so that the solution is the sum of vectors originating from the same point, whose tips describe a circle of radius k, and which lie at various azimuthal angles in the horizontal plane of $\mathbf{x}$, i.e.

$$F = \sum_{j=1}^{N} a_j \, k \exp(i\Phi_j) \ , \quad 0 \leqslant \Phi_j \leqslant 2\pi \ , \qquad [4.23]$$

A single wave vector then defines a roll solution perpendicular to the direction of that vector, Φ, and so the general solution is a superposition of roll solutions as expected. The convective planforms usually considered are the first three general solutions (i.e. with N = 1,2 and 3) with the wave vectors regularly spaced in the upper semi−circle, $0 \leqslant \Phi \leqslant \pi$ (i.e. $\Phi_j = (j-1)\pi/N$, j=1,N). These values of F make the planform function, f, a roll, a square and a regular hexagon respectively. Thus the solution harmonics so far examined are described by

$$F_1 = \sum_{j=1}^{3} a_j \exp(ik.x) \quad , \qquad [4.24]$$

$$F_2 = F_1 + F_1' \quad , \qquad [4.25]$$

$$f = \sum_{m} b_m (F_2')^m \quad . \qquad [4.26]$$

Solutions which are more general than these may be studied. More wave vectors may be include i.e. N may be taken such that N > 3, and the constraint on the separation of the vectors may be dropped to allow irregularly spaced vectors around the K−circle. Solution fields, calculated as before, for all N < 12 with regularly spaced vectors are shown in figures 4.5a) − 4.5c), and their corresponding counterparts with one random irregular spacing are shown in figures 4.6a) − 4.6c).

In figure 4.5a), the first three of the regularly spaced cases (i.e. N = 1,2,3) confirm our earlier conclusions by showing a single vector as an obvious roll pattern, two vectors as a square pattern, and three vectors as the well−known hexagonal pattern. The other fields, for N > 3, (figures 4.5b), 4.5c)) of course, show the pre−ordained symmetries about the N directions, but also show some unusual characteristics. As N increases, the centres become increasingly circular in nature, as expected as the degree of symmetry increases, but also more concentric rings are joined into the 'eye' of the pattern. Unusual shapes appear, such as pentagonal structures in the four and six vector cases, and star like shapes in the five vector case, and these may be emphasised by changes in the observation schemes with which the fields are examined. Various different colour and shading schemes are included to express the subjective nature of the phenomena i.e. to impress upon the reader that these structures can be made to look very different by simple manipulation of the interpretation of the data. Particular observation schemes emphasize different aspects of the patterns and thus any statement about the existence of a particular topological structure must be tempered by careful consideration of the method of presentation. The blue/green and black/white shadings are the more physical in that they increase in tone

Figure 4.5a)

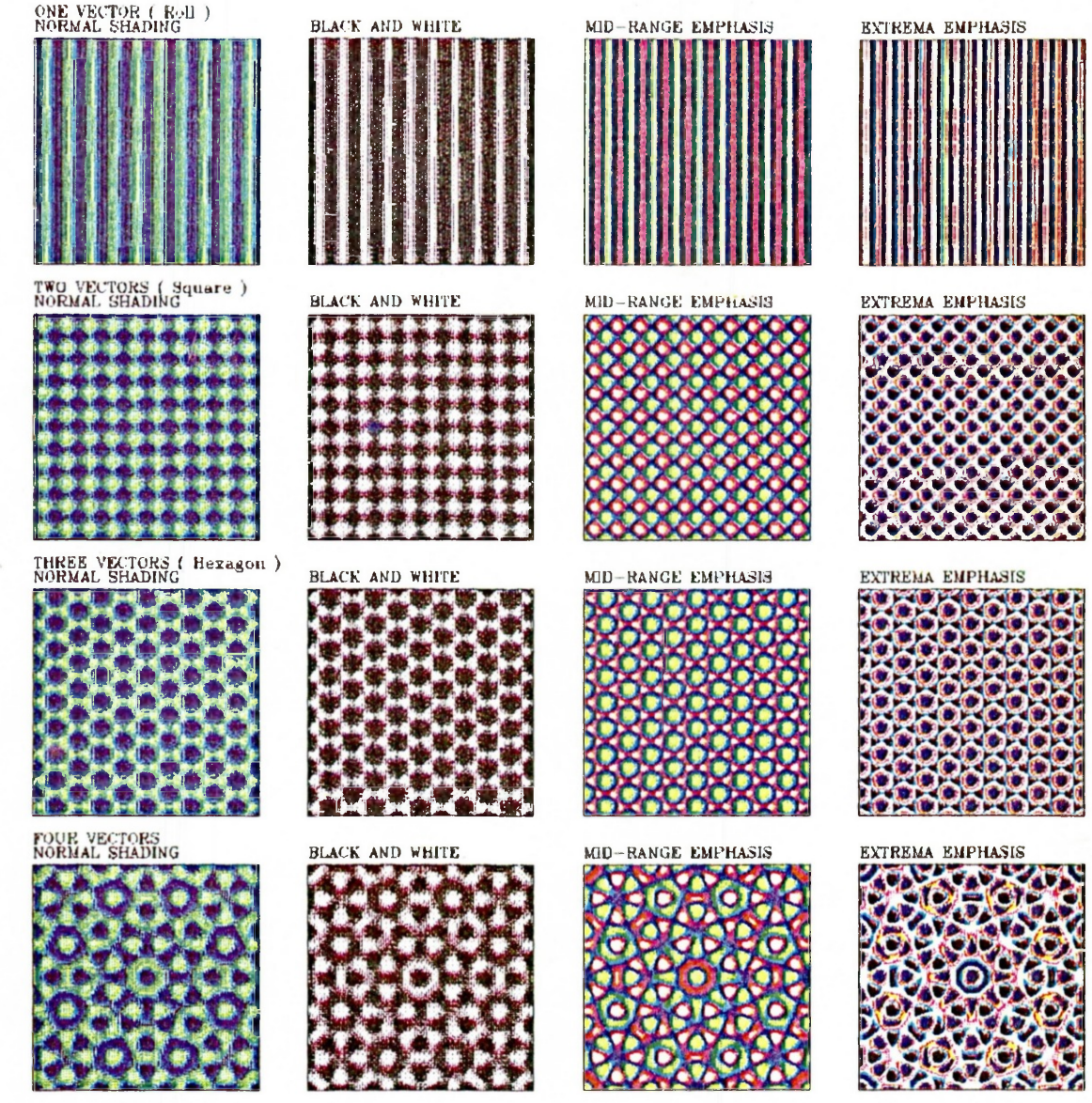

Solutions of the Helmholtz Equation
regular spacing of k vectors
(Range of plot: −10 pi to +10 pi in x and y)
ONE VECTOR (Roll)
NORMAL SHADING
BLACK AND WHITE
MID-RANGE EMPHASIS
EXTREMA EMPHASIS
TWO VECTORS (Square)
NORMAL SHADING
BLACK AND WHITE
MID-RANGE EMPHASIS
EXTREMA EMPHASIS
THREE VECTORS (Hexagon)
NORMAL SHADING
BLACK AND WHITE
MID-RANGE EMPHASIS
EXTREMA EMPHASIS
FOUR VECTORS
NORMAL SHADING
BLACK AND WHITE
MID-RANGE EMPHASIS
EXTREMA EMPHASIS

Figure 4.5b)

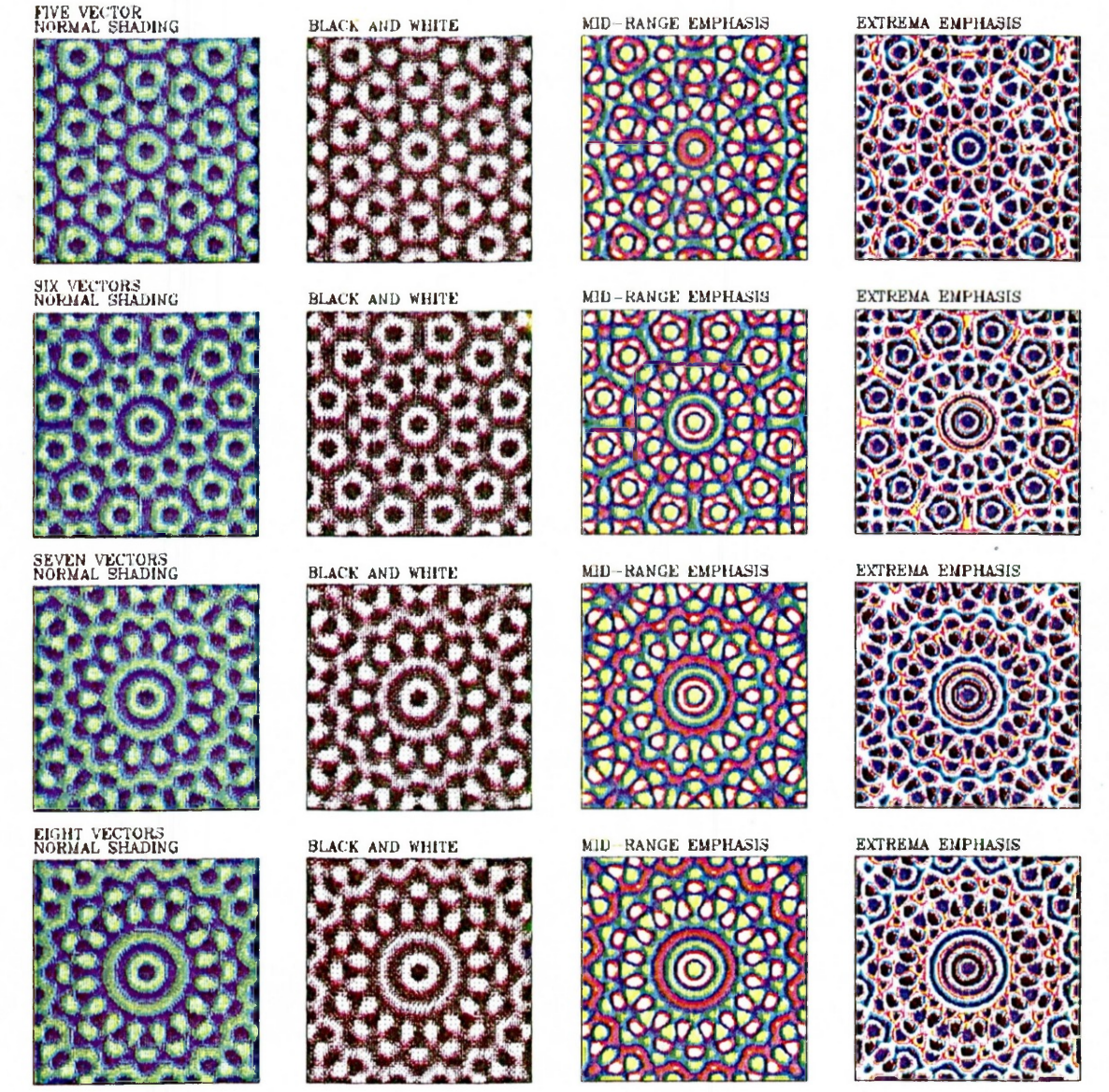

Solutions of the Helmholtz Equation
regular spacing of k vectors
(Range of plot: −10 pi to +10 pi in x and y)
FIVE VECTOR
NORMAL SHADING
BLACK AND WHITE
MID-RANGE EMPHASIS
EXTREMA EMPHASIS
SIX VECTORS
NORMAL SHADING
BLACK AND WHITE
MID-RANGE EMPHASIS
EXTREMA EMPHASIS
SEVEN VECTORS
NORMAL SHADING
BLACK AND WHITE
MID-RANGE EMPHASIS
EXTREMA EMPHASIS
EIGHT VECTORS
NORMAL SHADING
BLACK AND WHITE
MID-RANGE EMPHASIS
EXTREMA EMPHASIS

Figure 4.5c)

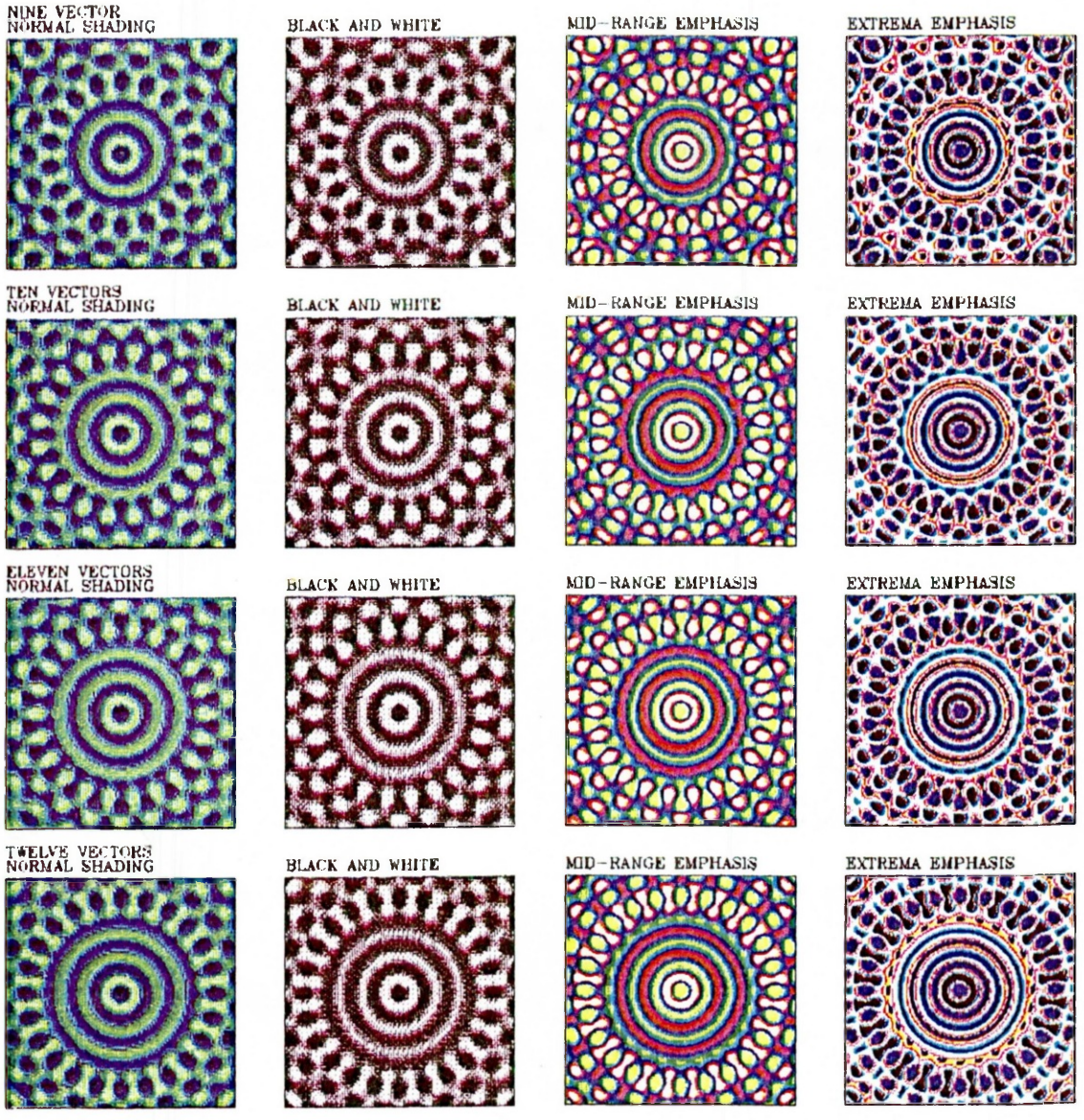

Solutions of the Helmholtz Equation
regular spacing of k vectors
(Range of plot: −10 pi to +10 pi in x and y)
NINE VECTOR
NORMAL SHADING
BLACK AND WHITE
MID-RANGE EMPHASIS
EXTREMA EMPHASIS
TEN VECTORS
NORMAL SHADING
BLACK AND WHITE
MID-RANGE EMPHASIS
EXTREMA EMPHASIS
ELEVEN VECTORS
NORMAL SHADING
BLACK AND WHITE
MID-RANGE EMPHASIS
EXTREMA EMPHASIS
TWELVE VECTORS
NORMAL SHADING
BLACK AND WHITE
MID-RANGE EMPHASIS
EXTREMA EMPHASIS

Figure 4.6a)

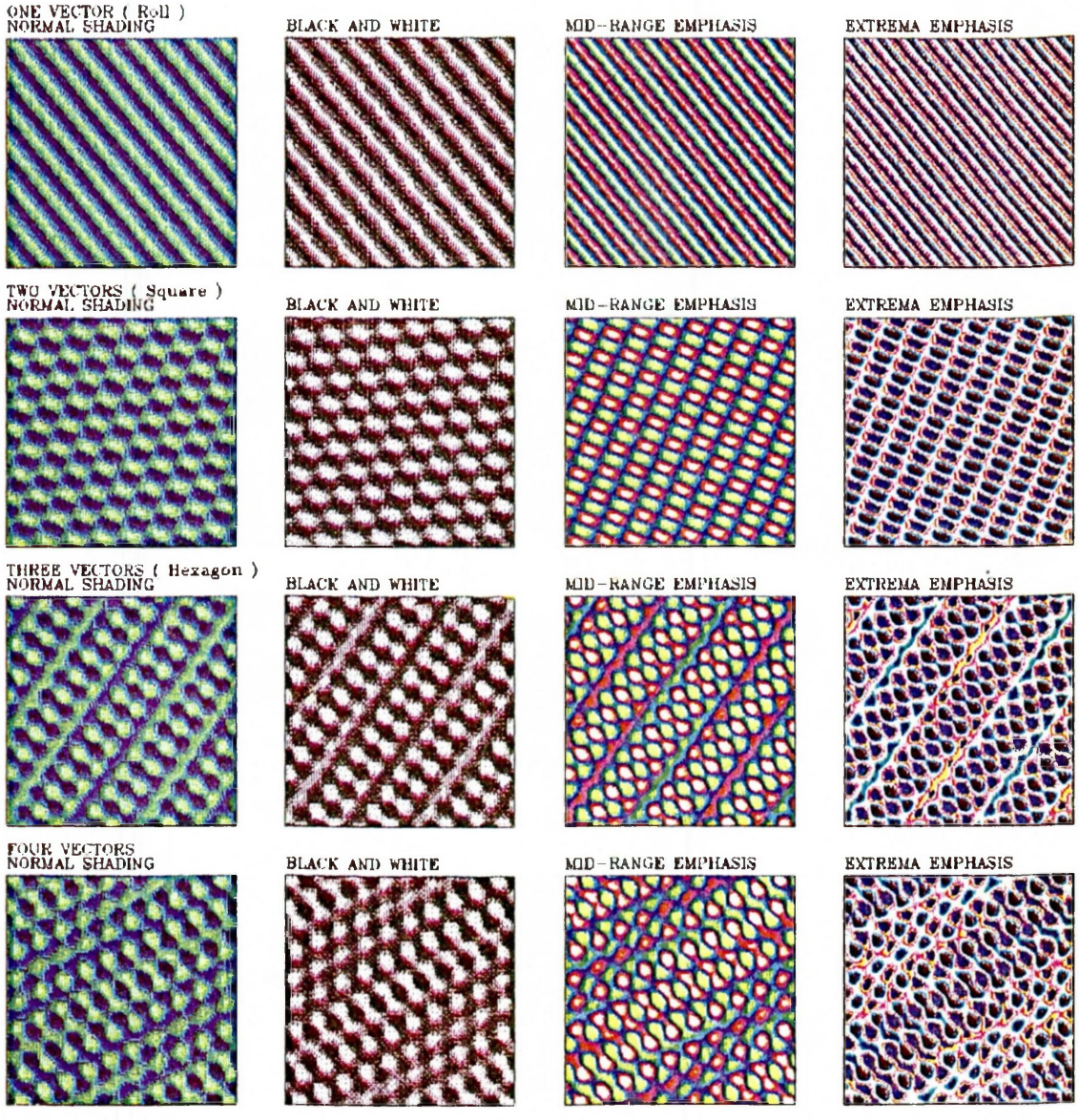

Solutions of the Helmholtz Equation
with random irregular spacing of k vectors
(Range of plot: −10 pi to +10 pi in x and y)
ONE VECTOR (Roll)
NORMAL SHADING
BLACK AND WHITE
MID-RANGE EMPHASIS
EXTREMA EMPHASIS
TWO VECTORS (Square)
NORMAL SHADING
BLACK AND WHITE
MID-RANGE EMPHASIS
EXTREMA EMPHASIS
THREE VECTORS (Hexagon)
NORMAL SHADING
BLACK AND WHITE
MID-RANGE EMPHASIS
EXTREMA EMPHASIS
FOUR VECTORS
NORMAL SHADING
BLACK AND WHITE
MID-RANGE EMPHASIS
EXTREMA EMPHASIS

Figure 4.6b)

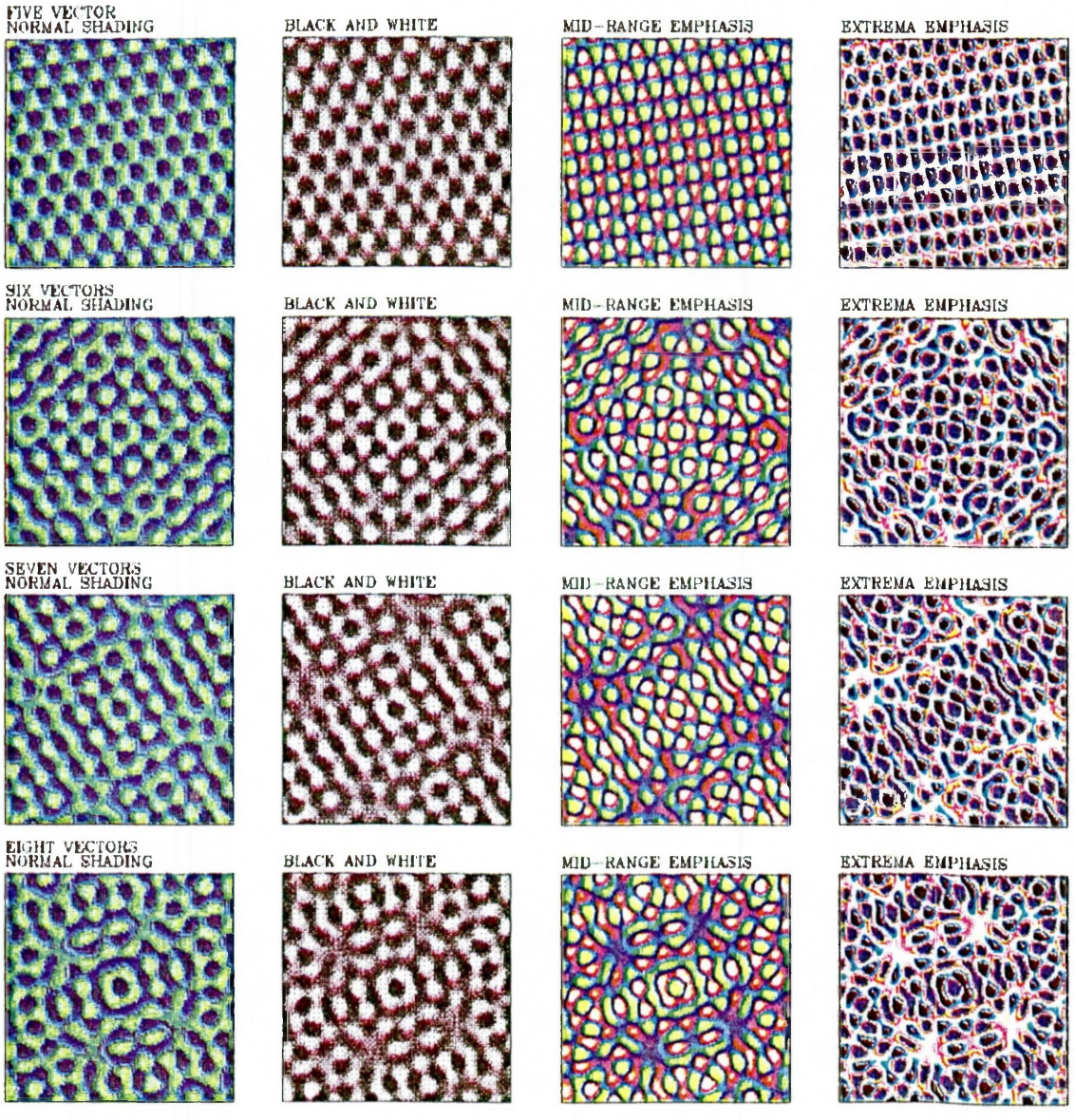
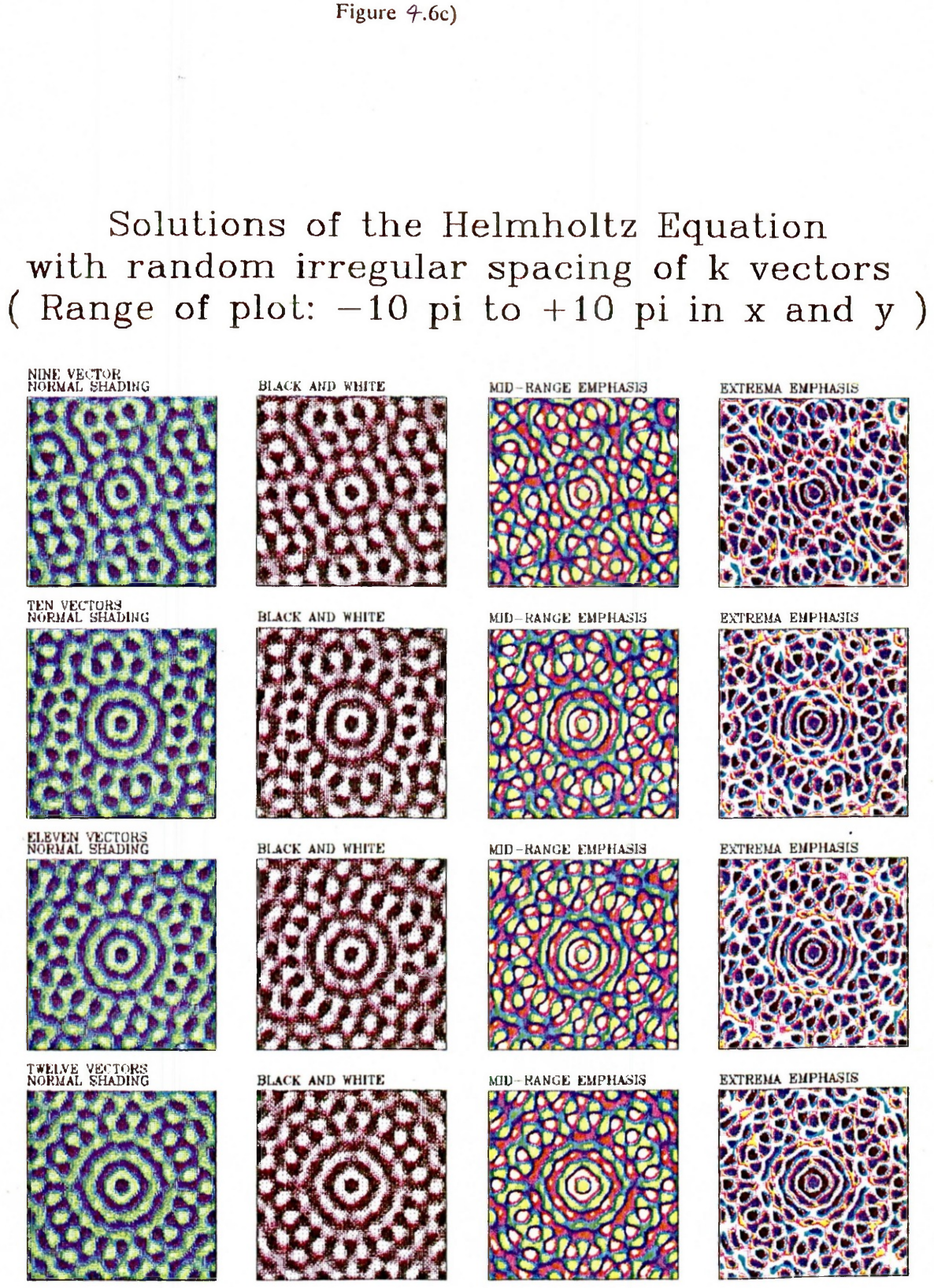

Solutions of the Helmholtz Equation
with random irregular spacing of k vectors
(Range of plot: −10 pi to +10 pi in x and y)
FIVE VECTOR NORMAL SHADING
BLACK AND WHITE
MID-RANGE EMPHASIS
EXTREMA EMPHASIS
SIX VECTORS NORMAL SHADING
BLACK AND WHITE
MID-RANGE EMPHASIS
EXTREMA EMPHASIS
SEVEN VECTORS NORMAL SHADING
BLACK AND WHITE
MID-RANGE EMPHASIS
EXTREMA EMPHASIS
EIGHT VECTORS NORMAL SHADING
BLACK AND WHITE
MID-RANGE EMPHASIS
EXTREMA EMPHASIS

Figure 4.6c)


Solutions of the Helmholtz Equation
with random irregular spacing of k vectors
(Range of plot: −10 pi to +10 pi in x and y)
NINE VECTOR
NORMAL SHADING
BLACK AND WHITE
MID-RANGE EMPHASIS
EXTREMA EMPHASIS
TEN VECTORS
NORMAL SHADING
BLACK AND WHITE
MID-RANGE EMPHASIS
EXTREMA EMPHASIS
ELEVEN VECTORS
NORMAL SHADING
BLACK AND WHITE
MID-RANGE EMPHASIS
EXTREMA EMPHASIS
TWELVE VECTORS
NORMAL SHADING
BLACK AND WHITE
MID-RANGE EMPHASIS
EXTREMA EMPHASIS

monotonically in even increments with the function and thus emphasize the overall structure of the solution as you would expect to see it in, say, a photograph. The mid−range emphasis colour scheme picks out the normally blurred finer scale structures in the pattern whereas the extrema emphasis scheme highlights the deep wells, channels and walls of the cellular structure. Jenkins (1987) worries about such representations in his paper on convection under the relaxed constraint of temperature dependent viscosity, where he concentrates mainly on the stability of the square planform in comparison to the roll planform, but is rightly concerned in comparing his results with experimental data, that planforms may be misinterpreted. He cites a submitted paper by himself on interpretation of shadowgraph findings, but as yet this paper is unavailable.

Note that the well known tilings (i.e. N = 1 ,2, 3, figure 4.5a)) are the only spatially periodic patterns. The other patterns never exactly repeat themselves, although it is possible to come as close to an exact replication as required by simply going far enough away from the original centre of the pattern. This is so because, at the centre, a certain superposition of wave vectors is happening, and for this to occur again at some point, exactly the same superposition must once again occur. For the N regular vector case, this can only happen if $\cos(\pi/N)$ is rational. This is best explained by diagram 4.1, but is simply a statement of the fact that for two wave vectors separated by π/N, the condition for them to superpose at some point in the same manner as they did at the centre is that the projection of the position on the first wave vector onto the second must be an integer multiple of the common wavelength. It may be proven that $\cos(\pi/N)$ is only rational for N = 1, 2, 3.

Figures 4.6a) − 4.6c), with the wave vectors spaced irregularly at random, show that the symmetric regularity of the patterns for low N is overridden by a roll−like modulation in a preferred direction. Higher N retain their regularity but lose some of the detailed structure associated with the regular spacing e.g. the neat concentric central rings. The middle order N of the irregular case, if drawn for a large area with a sensible scaling, shows a remarkable likeness to the photographs of solar granulation (e.g. compare figure 4.7 with the famous photograph of Janssen (1896), or those of Bray, Loughhead and Durrant (1984)).

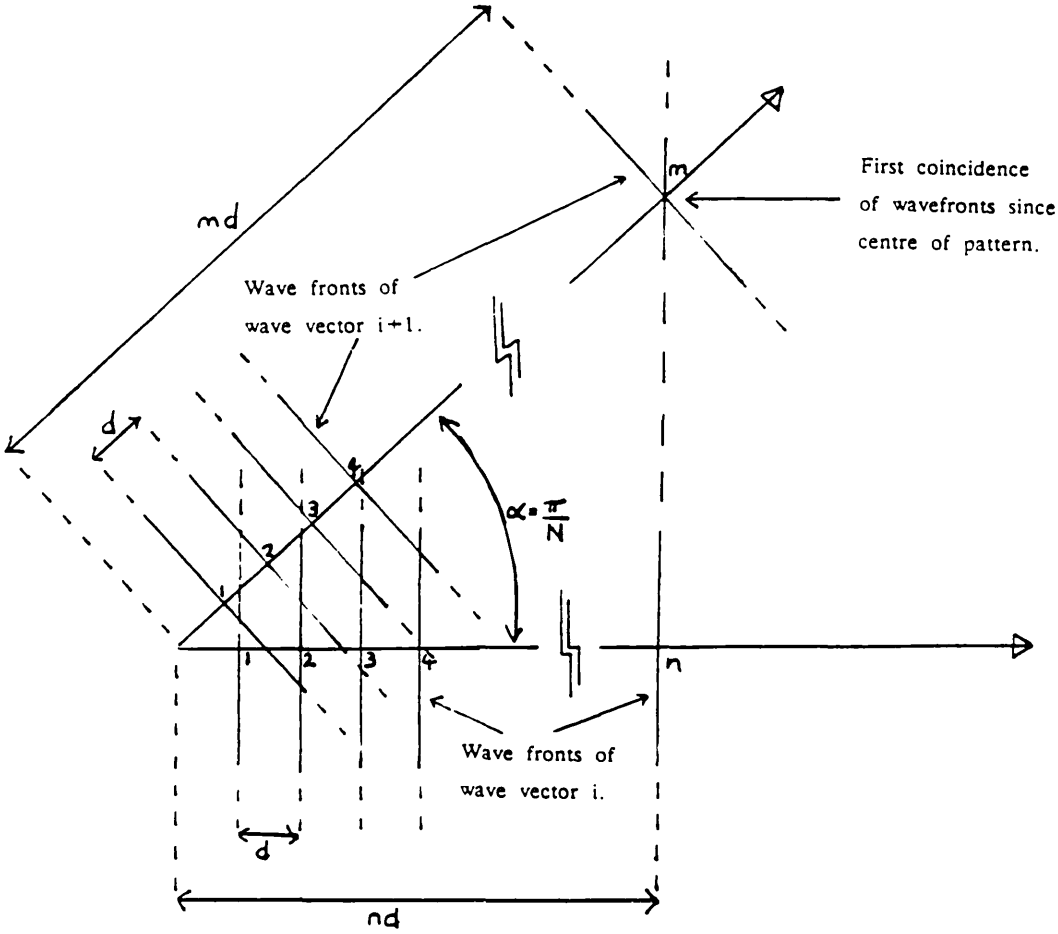
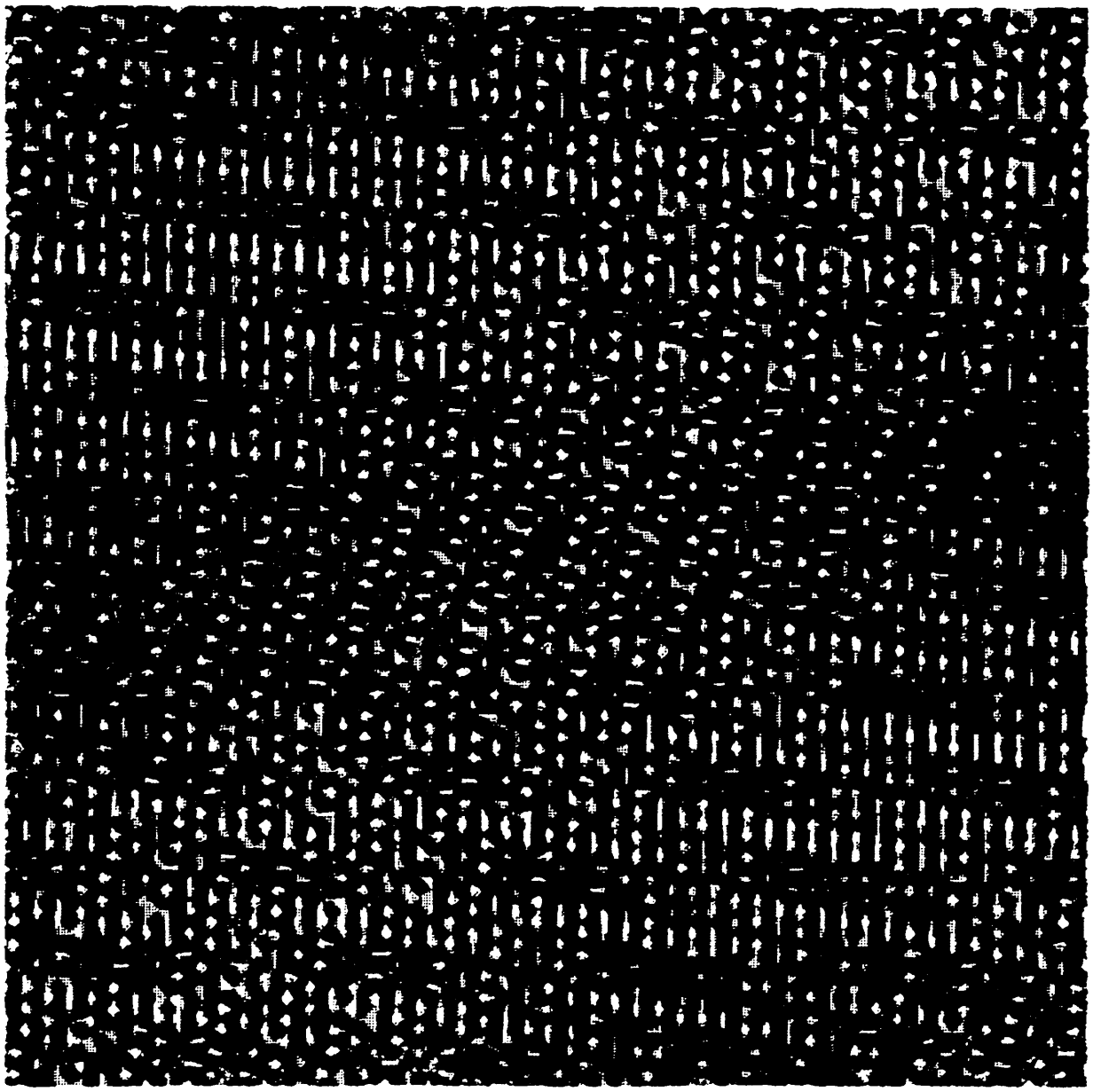


Diagram 4.1 A diagram to show that the condition for a repetitive planform pattern involving N wave vectors is related to $\cos(\pi/N) = nd/md = n/m$ i.e. $\cos(\pi/N)$ must be a rational number. This is only true for N = 1, 2, 3.

Figure 4.7 A large area plot (-50π to 50π) of the six vector (N = 6) irregularly spaced case shown in figure 6b) previously, to illustrate the possible interpretation of simple solutions of the Helmholtz equation as stellar photographic data.



repeated page

monotonically in even increments with the function and thus emphasize the overall structure of the solution as you would expect to see it in, say, a photograph. The mid−range emphasis colour scheme picks out the normally blurred finer scale structures in the pattern whereas the extrema emphasis scheme highlights the deep wells, channels and walls of the cellular structure. Jenkins (1987) worries about such representations in his paper on convection under the relaxed constraint of temperature dependent viscosity, where he concentrates mainly on the stability of the square planform in comparison to the roll planform, but is rightly concerned in comparing his results with experimental data, that planforms may be misinterpreted. He cites a submitted paper by himself on interpretation of shadowgraph findings, but as yet this paper is unavailable.

Note that the well known tilings (i.e. N = 1 ,2, 3, figure 4.5a)) are the only spatially periodic patterns. The other patterns never exactly repeat themselves, although it is possible to come as close to an exact replication as required by simply going far enough away from the original centre of the pattern. This is so because, at the centre, a certain superposition of wave vectors is happening, and for this to occur again at some point, exactly the same superposition must once again occur. For the N regular vector case, this can only happen if $\cos(\pi/N)$ is rational. This is best explained by diagram 4.1, but is simply a statement of the fact that for two wave vectors separated by π/N, the condition for them to superpose at some point in the same manner as they did at the centre is that the projection of the position on the first wave vector onto the second must be an integer multiple of the common wavelength. It may be proven that $\cos(\pi/N)$ is only rational for N = 1, 2, 3.

Figures 4.6a) − 4.6c), with the wave vectors spaced irregularly at random, show that the symmetric regularity of the patterns for low N is overridden by a roll−like modulation in a preferred direction. Higher N retain their regularity but lose some of the detailed structure associated with the regular spacing e.g. the neat concentric central rings. The middle order N of the irregular case, if drawn for a large area with a sensible scaling, shows a remarkable likeness to the photographs of solar granulation (e.g. compare figure 4.7 with the famous photograph of Janssen (1896), or those of Bray, Loughhead and Durrant (1984)).

5. CONCLUSIONS.

From simply looking at the algebra produced by the interactions involved in the non−linear advection terms for the equations of convection, it has been found that the system will produce various harmonics of the original planform, and for the hexagonal case, these, on investigation, show some unusual features.

Firstly, by the fourth order, the pattern may involve a planform which obviously does not consist of regular hexagonal shapes. At this order, a planform is available to the system which has five and twelve sided cells, and so new shapes may be expected in the system if these higher order effects are important.

Secondly, by the third order, the shapes involved in some of the harmonic planforms have become smoothed off, with the cell walls, as defined by Stuart (1964), no longer being straight line segments, but curves.

Lastly, also by third order, the non−linear interactions generate a source term for a vertical vorticity mode in the system i.e. $\omega_z \neq 0$, and a term for ψ must be included to balance the higher order interactions.

The ramifications of these statements are quite interesting. Since a multi−mode expansion is necessary for a complete modal description of a convection problem with hexagonal structure, there exists an inherent vertical vorticity component. As yet whether convection with these planform structures of higher order is important or stable enough to be seen and actually involved in the convective process is unknown, although Toomre et al. (1982) have shown harmonics to have some effect in particular parameter ranges. However, the effects that they could be used to help explain are important, for example, solar granulation.

The appearance of curved walls and the introduction of inherent vertical vorticity are neatly counterbalanced if they are related. The appearance of a curved walled structure in a harmonic planform implies that there is an equivalent inherent vertical vorticity structure associated with this harmonic that will be generated spontaneously. That is, the algebra implies that the original supposition that $\omega_z = 0$ is in fact wrong, and that there must be some component of the vorticity−generating streamfunction ψ present to balance the equations. The implication of this is that if convection were started with an ordinary hexagonal planform then the non−linear terms would immediately pick it up and produce the second order harmonics. These in turn would interact through the $(\mathbf{u}.\nabla)\mathbf{u}$ terms with both themselves and the original planform to produce the third and fourth order harmonics both of which contain vertical vorticity generating planforms. Thus hexagonal planform convection spontaneously and instantaneously produces a vertical vorticity component unless convection under the higher planforms is very

unstable or strongly damped. The appearance of these inherent vertical vorticity structures by inclusion of the full non−linear terms means that other models such as those of Murphy and Lopez (1984) and Massaguer and Mercader (1988) can be extended to larger multi−mode systems so that vertical vorticity may be naturally generated through the inclusion of higher order planform terms. The inclusion of more vertical vorticity by some means such as this may also help to explain the poor agreement of Busse and Clever (1974) and Toomre et al. (1982) with the experimental work of Krishnamurti (1970) at low Prandtl number.

Similar studies were carried out on the also naturally common square planform which concluded that square planforms can never inherently generate this spontaneous vertical vorticity, and thus never deviate from a simple scaling of roll and square solutions. Hence, further investigations of the square planform were not carried out, despite the physical relevance in some cases (Jenkins (1987)).

The problem is also of more general importance if simple, physical superpositions of the original planforms are considered, since then unusual and asymmetric polygons may be found amongst the patterns created, similar to some interpretations of physical phenomena, such as the granulation observed on the Sun's surface. The more basic problem, that of a general solution to Helmholtz's equation, also provides a rich solution field.

The process described here has revealed the subset of the full harmonic expansion that would be required for a complete modal description of any type of spatially periodic, three−dimensional convection. The square and hexagonal planform modes found here are now used in the next chapter, Chapter 5, as a viable subset for actual modal calculations of the simplest type of convection, Rayleigh−Benard convection, to examine the highly non−linear effects that may be introduced by the inclusion of the naturally occuring vertical vorticity.

CHAPTER 5.

THREE-DIMENSIONAL RAYLEIGH-BENARD CONVECTION.

5.1. ABSTRACT.

Three-dimensional, non-linear Rayleigh-Benard convection between free horizontal boundaries is investigated for hexagonal and square horizontal planforms. All allowable planform modes up to and including the fourth order found in the previous chapter are used to specify the horizontal structure of each problem, whilst the resulting vertical two-point boundary value problem is solved accurately by a Newton-Raphson-Kantorovich scheme. This specification of the hexagonal horizontal structure allows for two inherent vertical vorticity generating modes. Such modes are shown to influence the flow, the inclusion of higher harmonics greatly affecting the heat transport, especially at low Prandtl number. Although the flow pattern is nearly independent of the number of included modes for the hexagonal case, a change of emphasis in the flow with the inclusion of higher harmonics forces square convection to occur in a rearranged square pattern, with a corresponding destruction of the true cellular nature. Low order modal models prove to be untrustworthy at low Prandtl numbers for hexagonal convection, and at all σ for square convection. A strong Prandtl number dependence is exhibited for both planforms. The hexagonal case tends towards the behaviour of cylindrical convection, where in the limit of decreasing σ, convection occurs after a second critical Rayleigh number is surpassed, and is then relatively σ independent. The square periodicity convection exhibits no such behaviour and is strongly σ-dependent at all the Rayleigh numbers calculated.

5.2. INTRODUCTION.

With the desire for increased knowledge of turbulence at the forefront of science, thermal convection has been used as a simple model of bifurcation structure for some time. At moderate or high Prandtl numbers, convection undergoes a steady progression of bifurcations, from two-dimensional steady roll flow to three-dimensional bimodal flow as the thermal boundary layers become unstable, and then on to oscillation and eventually turbulence. These transitions

have been studied in great detail by analytic, numerical and experimental means (Koschmieder (1966), Busse (1967), Rossby (1969), Krishnamurti (1973), Clever and Busse (1974), Busse and Clever (1979), Grotzbach (1982), Bolton, Busse and Clever (1986)), and the high Rayleigh number, turbulent nature has also been studied by authors such as Kraichnan (1961), Ledoux et al (1961) and Spiegel (1965).

However, at lower Prandtl number, the structure of convection is somewhat different, in that steady solutions are only available in a region of parameter space very close to the critical values for the onset of convection. At only slightly supercritical Rayleigh numbers, steady solutions are unstable to time dependent solutions and oscillatory convection sets in very quickly as a bending of the rolls, hence bifurcating from the two−dimensional solution to a three−dimensional one at much lower Rayleigh numbers than is true for the higher σ (Busse (1972), Krishnamurti (1973), Clever and Busse (1974)). The range of roll convection is thus considerably curtailed for free boundary flow, with five stability boundaries meeting at the critical point for the onset of convection in the Rayleigh number −wave number plane, as opposed to three for rigid boundary flow, and no steady rolls being stable for $\sigma \leqslant 0.543$ (Busse and Bolton (1984)).

The mechanisms of these instabilities at low Prandtl number are related to vertical vorticity. Busse (1972) in his first investigation of the oscillatory instability, shows that the mechanism is due to vertical vorticity caused by the interactions of the disturbance and the main flow. Clever and Busse (1974) show that the mechanisms are distinctly different between rigid boundary and free boundary flow, the latter allowing a homogeneous, non−decaying vertical vorticity as a rigid body rotation. Ziggia and Sippelius (1981) demonstrated that the zizag instability involves an undamped vertical vorticity mode for free boundaries, unlike rigid boundary flow, where the vertical vorticity is as much damped as all the other modes.

However, despite this, modelling of thermal convection at low Prandtl number has concentrated upon two−dimensional solutions (Clever and Busse (1981), Busse and Clever (1981)) or simple three−dimensional geometries (Jones, Moore and Weiss (1976), Proctor (1977)), both in steady states. The conclusions of these studies has been that a regime of convective flow exists, known as the inertial or flywheel regime. Here, the advection of momentum becomes most important, vorticity becomes constant on the circular streamlines of the flow, so that the body of the fluid rotates as one rigid body. The viscous and Reynolds stresses become comparable at the top and bottom boundary and balance the buoyancy generated, as temperature diffuses into the interior to be advected by the flywheel. Busse and Clever's results are for rigid boundaries where the inertial flow is more

surprising than for the free boundaries of Jones, Moore and Weiss, since the degree of anisotropy (free vertical walls, rigid horizontal walls) is greater. The inertial flow is efficient as long as the geometry of the cells allows the circular streamlines to be set up, and thus must be considered despite the fact that, generally, this solution is unstable to oscillatory solutions. However, the mechanism must appear somehow in three−dimensional and time−dependent motion since some forms of inertial convection are observed in the experiments of Rossby (1969) and Krishnamurti (1973), and for moderately low σ (σ = 0.025 for mercury) the Prandtl number independence predicted by this theory mimicks experimental data better than the earlier models of Schluter, Lortz and Busse (1965) which predicted a Nusselt number proportional to σ^2, or the general astrophysical belief that $Nu \approx (\sigma R)^{1/2}$ (Spiegel (1971)).

General three−dimensional models of convection are few and far between. Finite difference formulations of the problem have concentrated on the transitional behaviour of the fluid with increasing Rayleigh number, and have mainly been carried out for Prandtl numbers around that of air, σ = 0.71 (Lipps and Somerville (1971), Veltishchev and Zelnin (1975), Lipps (1976), Ozoe *et al* (1976), Grotzbach (1981)). Calculations based on the more computationally convenient modal type expansion are more extensive. The authors Gough, Spiegel and Toomre generated a trilogy of papers (1975, 1977, 1982, hereafter known as GST1, GST2, and GST3) which examined three−dimensional convection by a modal procedure. The first of these papers identified the modal procedure that they were to use throughout the works as an expansion in terms of the horizontal modes satisfying the Helmholtz equation which arises from the separated linear problem, but with terms associated with vertical vorticity deliberately omitted from the procedure. The paper then analytically examines the regions of slightly supercritical and very high Rayleigh numbers by a drastic truncation of this modal expansion to the equations for one term only, known as the single mode equations, and by the use of perturbation analysis and matched asymptotic expansions respectively to solve the remaining vertical problem. The approach is more complete than the mean−field equations (Herring (1963)) since the inertial terms are now represented, but suffers the same fate, in that, for R near the critical value, the method produces reasonable results for planforms with a non−zero interaction constant (i.e. hexagons), but fails to predict the Prandtl number dependence of the Nusselt number for C = 0 planforms e.g. rolls and rectangles. Thus the procedure manifests itself as only useful for hexagons or otherwise for very high Prandtl number. The high R asymptotics reveal various regions of dependence for the heat flux governed by the balances between the thermal and viscous boundary layers, but at low σ confirm the astrophysical arguments for a

dependence on (σR) only (e.g. $(\sigma R)^{1/2}$, Spiegel (1971)).

Their second paper, Toomre, Gough and Spiegel (1977 − GST2), numerically solves the single mode equations derived in the previous paper for the experimental regime of parameters. The model is found to be seriously flawed in that solutions may possess a temperature field which strays outside that allowed by the boundary conditions, and the expected variation of the Nusselt number with the Rayleigh number for high R ($Nu \approx R^{1/3}$) cannot be achieved by the single mode equations. However, the model does reasonably predict heat transport and some aspects of the temperature field with careful choice of the interaction parameter and the horizontal wavenumber, and for hexagons, the Prandtl number dependence is seen. This raises an important question, since here the Nusselt number is found to decrease with decreasing σ, as is the case for Kraichnan (1962), Ledoux et al (1961) and Spiegel (1962), whereas such reductions in heat transport have not been seen in the two−dimensional simulations such as Veronis (1966) or Moore and Weiss (1973a), and indeed, Jones, Moore and Weiss (1976) predict a slight increase in Nusselt number with decreasing σ for free boundary, axisymmetric convection. This difference is due to the previously mentioned occurrence of the inertial−type flows, where the horizontal structure can be very different from those solutions allowed by the single mode equations, and so warns of the limitations of a single mode representation, despite the widespread belief that the inertial flows are unstable to three−dimensional disturbances.

Using more than just a single mode to specify the horizontal structure is a natural progression and may be expected to remove some of the problems of the single mode equations, such as the elusiveness of the high R asymptotics. The third paper in this trilogy, Toomre, Gough and Spiegel (1982 − GST3), again studies rigid boundary convection with no vertical vorticity allowed, but this time considers the impact of using multimode solutions and allowing time dependence. Harmonics of the hexagon planform are used with the fundamental Christopherson hexagon in two− and three−mode interactions, and it is found that the harmonics included have an important effect on the flow for certain parameter ranges. Indeed, the harmonics dominate the fundamental in some cases, so that, for example, the variation of the Nusselt number with the wavenumber shows two maximums instead of the normal one. The time−dependent behaviour is found to be supported by the overtones, which can force reversal of flow in the main cell, enable large fluctuations in the flow speed and encourage oscillations of counter−cells in the boundary layers, which grow at the expense of the main mode. It is shown that the heat transport is dependent on the fundamental mainly, but is modulated by the overtones and that the particular choice of overtones affects the flows quite dramatically.

Toomre, Gough and Spiegel used at most only three modes and also made rather *ad hoc* choices of the nature of the modes used for their multimode models. The basic planforms used are the fundamental hexagon in conjunction with the first aligned overtone (i.e. H1 + H2 − see Chapter 4) or the first rotated overtone (H1 + RH$\sqrt{3}$) or both (H1 + H2 + RH$\sqrt{3}$), or a sum of three aligned hexagons (H1 + H[n] + H[n+1]). Unfortunately, they allowed each of these to have a horizontal wavenumber which was regarded as a parameter to be varied, rather than having the lower harmonic wave numbers specified by the expansion in conjunction with a single overall wavenumber, as is the case here. This procedure leads to a viewpoint on the experiment as the addition of totally unrelated solutions, rather than the hopefully more physical approach involved here, where solutions related naturally through the non−linear terms are allowed to couple into the problem with the amplitudes and wavenumbers dictated by the advection terms. In particular, their three mode solutions used overtones which would be far down the expansion sequence explained in Chapter 4 i.e. the fundamental was combined with aligned overtones of wavenumber corresponding to harmonics found at tenth order and above in the harmonic sequence.

Other modal analyses have been made by various authors. Before the GST trilogy, Roberts (1966) pioneered a multimode expansion of the rigid problem including two horizontal modes, but his approach embodies the same attitude as GST's since he superposes different types of solutions rather than harmonics. For example, he considers solutions consisting of a roll superposed with a hexagon, or a rectangle superposed with a hexagon, but not a hexagon and its harmonics. However, his solutions allowed a greater degree of flexibility in the vertical solutions than did the mean−field solutions of Herring (1963) or the perturbation analyses of Malkus and Veronis (1958) at the time.

Only two sets of authors have allowed vertical vorticity in a modal expansion of the problem. Murphy and Lopez (1984) (and Lopez and Murphy (1984)) use the same single Christopherson hexagon mode expansion as GST2. However, they include the terms associated with vertical vorticity which GST ignore by including a single vertical vorticity mode which is also a Christopherson hexagon. They proved that, for free boundaries, the steady problem then allowed a second style of solution to occur where vertical vorticity was strong and vertical velocity was weak (previous solutions had weak vertical vorticity and strong vertical velocity and are called type I solutions by Murphy and Lopez). The new type II solutions, as they were termed, create a cyclonic flow which dissolves the boundary layer structure and dramatically reduces the heat flux, but which only occurs for moderate and low σ, and is not a function of any external effect as was previously assumed in works where it had appeared (Baker and Spiegel (1975)). The

type II solutions exist purely because of the inclusion of vertical vorticity and are characterised by the appearance of this swirling flow which destroys the isothermal interior, plumes and boundary layer structure of the type I solutions. The tendency of the Nusselt number to zero as $\sigma \rightarrow 0$ shows that this solution is very inefficient at transporting heat, and so the usual 'relative stability' argument for the preferred mode would normally exclude the existence of this form. However, Murphy and Lopez find this mode stable in comparison to the type I solutions at low σ and thus state that that this form will be the preferred form for some parameter ranges, based on a compromise between the systems attempt to transport heat in the most efficient manner, but by means of the most stable mode compatible.

Nonetheless, once again only single mode equations have been used, and the vertical vorticity mode was assumed to have the same form as the original planform. Chapter 4 has shown that the planform which generates the first natural vertical vorticity mode is not the same as the fundamental hexagon, so the vorticity included by Murphy and Lopez is again an *ad hoc* choice.

Massaguer and Mercader (1988) included a different vertical vorticity mode in their single mode hexagonal investigation. They take the low Prandtl number regime of the rigid boundary problem to indicate high Reynolds number flow, and as such to be influenced heavily by shear modes. On this assumption, they use a stability equation for a vorticity mode, driven purely by velocity gradients rather than buoyancy forces. The stability analysis leads to a bifurcation from the steady, no-vertical-vorticity solution, to a solution with vertical vorticity, albeit at a Rayleigh number higher than that for the oscillatory instability, so that periodic time-dependent solutions set in unless R is very small. Once again, however the shear mode of vertical vorticity is an *ad hoc* introduction.

Hexagonal planform convection has been considered by the previous low order expansion models, but square convection has not been studied numerically to any great extent. Only Arter (1984) makes a fairly comprehensive survey of non-linear square convection, but uses at most three modes in his modal expansions. The previous work (see Chapter 3) has shown that multimode expansions are needed for a decent qualitative description of the full flow field rather than simply mean quantities, and that vertical vorticity plays an important role in determining the style of solution, especially at low Prandtl numbers. This section of the thesis attempts to introduce multimode expansions of the Rayleigh-Benard, free boundary problem including up to 8 or 12 modes of the horizontal structure for the hexagonal and square symmetry problems respectively. The modes included are those harmonics which naturally occur as a result of the non-linear advection terms of the momentum equation, as described in Chapter 4,

and thus the wavenumbers and coupling constants are generated by a logical progression of excitation rather than some preordained concept of the solution.

5.3. FORMULATION OF THE MODEL.

5.3.1. The equation of state.

Rayleigh−Benard convection is driven by an unstable temperature gradient across the layer of fluid in question. This may be achieved by a simple linear equation of state as given in [2.5], and so the equations of motion are those given by [2.20] − [2.23] in Chapter 2 with F(T) = T.

5.3.2. The three−dimensional streamfunction.

The primitive variables are replaced by the vorticity−streamfunction representation, where the streamfunction is now that given in Chapter 4 as [4.1]. The advantage of using this particular streamfunction over other representations can be seen in [4.2] and [4.3], where the expanded forms of $\mathbf{u}$ and $\boldsymbol{\omega}$ are shown. This formulation splits the formation of vertical velocity to be solely dependent on χ, whereas the vertical vorticity is solely dependent on ψ. This allows the streamfunctions to be regarded as, firstly, a velocity generating streamfunction, χ, and, secondly, a vorticity generating streamfunction, ψ. Other possible streamfunction representations, such as

$$\mathbf{u} = \nabla\chi \times \nabla\psi \quad ,$$

whilst being perfectly valid, make the velocity and vorticity fields into complicated expressions involving both χ and ψ for all components.

5.3.3. The modal equations.

To create a modal model, the streamfunctions, χ and ψ, together with the temperature field, T, must be expressed as some series of functions which are separable and include components dependent on x and y which pre-solve the horizontal problem, thus leaving the vertical dependences together with the vertical boundary conditions as the unsolved problem. The horizontal functions which do this have been found in Chapter 4 for both hexagons and squares, and they are given in Tables 4.1 and 4.2 up to the order calculated. These functions represent a subset of the complete set of horizontal basis functions for the non-linear problems in question, where the relevance of a particular mode has been determined by consideration of the non-linear problem. A sum of modes from either of these subsets provides an effective truncation of the complete set of modes which solve the horizontal problem under the particular vertical boundary conditions imposed (i.e. square or hexagonal periodicity). Various sums of these modes are used to provide different models of the convective states, so that the effectiveness of increasing the number of modes included in an expansion can be ascertained. It is believed by some (e.g. GST, Marcus (1981)) that systems of convection may be solved reasonably by a poor resolution of the horizontal problem (i.e. a low number of modes), with a comprehensive solution in the vertical. Comparison of the various modal truncations used here should give some idea of the accuracy of this statement.

The modal truncations used are delineated by the order at which the modes appear, as expressed in Tables 4.1 and 4.2, i.e. a particular truncation contains all the modes of the expansion which appear at that order or below. The exceptions to these rules are that orders where a vertical vorticity mode appears are calculated twice, with two separate modal approximations for two different solutions – one including the vertical vorticity generating mode, and the other without it. Thus, the effect of introducing horizontal swirl can be demonstrated at each order where it may exist, by comparing the two. A summary of the different truncations used, with their names and the modes included is shown in Table 5.1.

The full modal model for the problem in question, be it square or hexagonal, is set up as follows. The first streamfunction, χ, is expanded as a sum of the allowable planforms, truncated at N, where the different truncations are shown in Table 5.1, i.e.

$$\chi(x,y,z) = \sum_{i=1}^{N} \chi_i(z)\ f_i(x,y) \quad , \qquad [5.1]$$

where the modes, $f_i(x,y)$, are defined by the planform functions of Tables 4.1 or 4.2 of Chapter 4. Each mode in the truncation is preceded by an individually labelled function, $\chi_i(z)$, which is dependent solely on the vertical variable, z. The second streamfunction, ψ, is expanded similarly but only as a sum of the M vertical vorticity

Name	Comment	Modes included
HEXAGONS		
FIRST	First order. Christopherson hex only. Reduced eqns.	H1
FFIRST	As above but fully non-linear eqns.	H1
SECOND	Second order. Fundamental, plus two overtones.	H1 + H2 + RH3
THIRD	Third order.	H1 + H2 + RH3 + H3
THIRDVV	Third order. Includes vertical vorticity mode.	H1 + H2 + RH3 + H3 + VH28
FOURTH	Fourth order.	H1 + H2 + RH3 + H3 + VH28 + H4 + RH23
FOURTHVV	Fourth order. Includes both vertical vorticity modes.	H1 + H2 + RH3 + H3 + VH28 + H4 + RH23 + VH52
SQUARES		
FIRST	First order.	S11
SECOND	Second order.	S11 + S02 + S20 + S22
THIRD	Third order.	S11 + S02 + S20 + S22 + S13 + S31 + S33
FOURTH	Fourth order.	S11 + S02 + S20 + S22 + S13 + S31 + S33 + S04 + S40 + S24 + S42 + S44

TABLE 5.1. Nomenclature of the various modal truncations used in this Chapter, for both hexagonal and square planforms.

generating functions, $g_i(x,y)$, associated with the planform functions capable of supporting vertical vorticity generation ($M \leqslant N$). That is,

$$\psi(x,y,z) = \sum_{i=1}^{M} \psi_i(z)\, g_i(x,y) \quad . \qquad [5.2]$$

Only the THIRDVV and FOURTHVV modal truncations for the hexagonal periodicity contain non−zero ψ, i.e. $M \neq 0$ (where $M = 1$ and $M = 2$ for THIRDVV and FOURTHVV respectively). Table 4.1 shows the functionality of the possible vertical vorticity generating functions, $g_i(x,y)$. The temperature, T, is expanded in exactly the same sum as for the χ modes, but with differently labelled vertical functions, and includes a mean profile, i.e.

$$T(x,y,z) = T_0(z) + \sum_{i=1}^{N} T_i(z)\, f_i(x,y) \quad . \qquad [5.3]$$

For example, the full THIRDVV mode expansion is as follows:

$$\begin{aligned}
\chi = \quad & \chi_1(z)\,(\, 2\cos(\alpha r x)\cos(\alpha y) + \cos(2\alpha y) \,) \\
& + \chi_2(z)\,(\, 2\cos(2\alpha r x)\cos(2\alpha y) + \cos(4\alpha y) \,) \\
& + \chi_3(z)\,(\, 2\cos(\alpha r x)\cos(3\alpha y) + \cos(2\alpha r x) \,) \\
& + \chi_4(z)\,(\, 2\cos(3\alpha r x)\cos(3\alpha y) + \cos(6\alpha y) \,) \\
& + \chi_5(z)\,(\, \cos(\alpha r x)\cos(5\alpha y) \\
& \qquad + \cos(2\alpha r x)\cos(4\alpha y) \\
& \qquad + \cos(3\alpha r x)\cos(\alpha y) \,)
\end{aligned}$$

$$\begin{aligned}
\psi = \quad & \psi_1(z)\,(\, \sin(\alpha r x)\sin(5\alpha y) \\
& \qquad - \sin(2\alpha r x)\sin(4\alpha y) \\
& \qquad + \sin(3\alpha r x)\sin(\alpha y) \,)
\end{aligned}$$

$$\begin{aligned}
T = \quad & T_0(z) \\
& + T_1(z)\,(\, 2\cos(\alpha r x)\cos(\alpha y) + \cos(2\alpha y) \,) \\
& + T_2(z)\,(\, 2\cos(2\alpha r x)\cos(2\alpha y) + \cos(4\alpha y) \,) \\
& + T_3(z)\,(\, 2\cos(\alpha r x)\cos(3\alpha y) + \cos(2\alpha r x) \,) \\
& + T_4(z)\,(\, 2\cos(3\alpha r x)\cos(3\alpha y) + \cos(6\alpha y) \,) \\
& + T_5(z)\,(\, \cos(\alpha r x)\cos(5\alpha y) \\
& \qquad + \cos(2\alpha r x)\cos(4\alpha y) \\
& \qquad + \cos(3\alpha r x)\cos(\alpha y) \,)
\end{aligned}$$

where r = $\sqrt{3}$ and α is a horizontal wavenumber governing the overall size of the periodic pattern.

The modal equations for each truncations are then found by substitution of these expansions into the full equations [2.20] − [2.22] with F(T) = T and with the streamfunction equation [2.23] replaced by [4.1], and by then extracting the relevent equations pertaining to each mode. This extraction is no longer as obvious as it was shown to be in the detailed description of Chapter 3 for penetrative convection, since the horizontal dependences are no longer simply a single trigonometric functions but rather is a non−linear combination of such functions. Thus, projection of the equations for the vertically dependent variables from the full equations as the coefficients of the horizontal modes must be carefully implemented. The complexity of the expansions demanded a computer algebra system, and so CAMAL (Barton and Ffitch (1972)) on a VAX 8600 under VMS was used. A few notes are worthy of inclusion here to guide anyone who may be completing a similar task at some stage using computer algebra.

A projection procedure needs to be carried out to extract the correct modal equations for the vertically−dependent variables from each of the full equations. This must be equivalent to multiplying the source equation by the required mode and integrating over the whole (x,y)−plane so that the orthogonality of the modes selects the modal terms. The simplest way to mimick this very expensive operation is to set some function equivalent to the horizontal structure of that particular mode. Substitute zero for this function in the equation to be considered, to obtain a reduced equation. Subtraction of this reduced equation from the original equation, and subsequent division by the function representing the horizontal structure provides the required 'extracted' modal equation for that mode.

The above will reveal all the necessary equations for all modes except for modes which are solely dependent on the vertical structure, such as the mean temperature field, $T_0(z)$, in this calculation. If the reduced equation is kept in the previous calculation after each projection, then for each mode, the reduced equation of the previous calculation may be used as the original equation of the next, since the reduced equation having been pruned of one mode, still contains all the terms involving the next mode of interest. Thus, on repetition of this procedure, all modes with the required horizontal structure are gradually pruned from the equations, until only terms involving modes with no horizontal structure and higher order terms produced by the expansion as harmonics of the required modes, are left. The expansion procedure, if truncated at order N, will produce further higher harmonics (from the non−linear terms) of order between N+1 and 2N, which are to be ignored in the calculation. These modes must be identified and suppressed. Their identification may be achieved by the same process of

identification of harmonics as outlined in Chapter 4, for which human searching is tedious and automation is awkward to implement due to the complex nature of the mode structure. However, such a process is fruitful, because it means that each projection of an N^{th} order truncation provides the higher order harmonics so that insight into more extensive expansions is gained at each stage. In this manner, it was determined that the functions given in Table 4.1 for hexagons contain all the unusual VH modes for all orders up to eighth order. Having calculated the higher harmonics, they must then be pruned from the last remaining reduced equation by setting them equal to zero, leaving the remaining equation as the vertical dependence of the mean mode. Notice that in the case calculated here, only the temperature field has a mean profile, and so is the only equation which needs this procedure. The other fields do not need to be pruned of higher order harmonics, because the extraction process automatically ignores them, and the final reduced equation produced after all the required harmonics have been removed can be discarded since it contains no mean profile, simply the higher order harmonics.

Other problems may exist, dependent on the particular algebraic system used. Here, producing FORTRAN compatible output provided some problems, since the leading terms in expressions did not necessarily have unit numerical coefficients. Other procedures were also more complicated than necessary since substitution for complex expressions of variables is not allowed. Overall, the projection of equations required a great deal of complex manipulation, with the computation involved requiring just a few seconds of CP time on a 7 Mbyte CAMAL system for the FIRST order, hexagonal equations, but needing roughly a day of CP time on a 15 Mbyte system for the FOURTHVV system. However, the physical time involved for these projections is negligible compared to the corresponding time should the author have had to calculate them by hand, and certainly the probability that the equations produced are correct is much higher.

Thus the modal equations for the various truncations were calculated from the fully non−linear equations except for the FIRST truncation set. For this set, a reduced non−linear problem was solved, whereby the equations were produced from the projection of the full non−linear equations but with the non−linear momentum advection term, $(\mathbf{u}.\nabla)\mathbf{u}$, suppressed. This was done as a compromise to solving either the linear equations (both $(\mathbf{u}.\nabla)\mathbf{u}$ and $(\mathbf{u}.\nabla)T$ suppressed), the mean−field equations (non−linear coupling through the temperature mean−field, T_0, in the non−linear temperature advection term only; advection of momentum suppressed), or the single mode equations (fully non−linear equations with the same modes as the FIRST mode expansion), all of which have been solved before (Chandrasekhar (1961), Herring (1963) and GST(1975,1977,1982) respectively). Using this unusual version provides a new solution, which is simple enough to

allow comparison with the previous calculations, but which suppresses the generation of higher order planforms whilst allowing some non−linear coupling into the temperature field. However, for comparison with previous solutions (GST, Murphy and Lopez (1984)) and the higher truncations, the full single mode equations were also calculated, where the non−linear advection of momentum terms are included, but the expansion contains only a single planform. This truncation set was known as the FFIRST set for 'full first order' and is useful since it now allows a Prandtl number dependence at a very low order. This expansion is exactly the same as that used by GST in their single mode calculations, but differs from that of Murphy and Lopez in that no vertical vorticity is included. It is believed here that this planform is not a vertical−vorticity−generating mode.

Thus, the complete modal equations for each truncations set were calculated. The equations are not included here as they are long and extremely complicated, but are included in FORTRAN form in the program listings on microfiche. The multimode expansions used here provide a significant advance from previous modal models, since up to 8 (for hexagonal periodicity) or 12 (for square) planform structures are included in the modal expansion, some of which allow the generation of vertical vorticity.

It should be noted that specification of the modes as described above has omitted another class of solutions that exist. The specification of the original H1 Christopherson planform mode has an arbitrarily chosen sign i.e. the whole χ function could be expressed as $-\chi$ without any loss of generality. These two solutions are different in that one has fluid rising at the centre and descending at the cellular walls whereas the other has a downflowing centre and an ascending wall. These solutions are known as l− and g−hexagons since it is typically found that the first is preferred in liquids and the second in gases. Only the l−hexagon solutions have been investigated here. Combination of the two solutions may be more physical but introduced an extra degree of complication to the solution of the problem which was best left for a later date.

Dimensionless numbers, Ra, σ and Nu are introduced as described in section 2.3. No alteration to the definition is necessary to produce a working Rayleigh number in this context, unlike the penetrative case (see Chapter 3).

5.3.4. The boundary conditions.

The choices of the two−dimensional planform functions as described above satisfy the horizontal periodicity boundary conditions for a hexagon or a square as

indicated. It remains to specify the vertical boundary conditions in order to close the problem.

Once again, the upper and lower horizontal planes are held at fixed temperatures, but this time they are fixed such that the linear profile in the conductive state is unstable, i.e. [2.27a,b] become

$$T_0(0) = 0, \quad T_0(1) = -1 \quad , \qquad [5.4a]$$

$$T_i(0) = T_i(1) = 0 \quad , \quad \text{for all } i \neq 0 \quad , \qquad [5.4b]$$

where the depth of the layer and the amplitude temperature difference across the layer are scaled to unity by the same scalings as previously.

The remaining boundary conditions are given as

$$\chi = \frac{\partial^2 \chi}{\partial z^2} = \frac{\partial \psi}{\partial z} = 0 \quad , \text{ at } z = 0, 1 \qquad [5.5]$$

(Chandrasekhar (1961), Busse (1972)), and in this case, these may be explained as follows.

The boundary condition [2.24] specifies that the fluid must be confined to the layer, and thus that the vertical velocity must once again be zero at the plane boundaries. The definition of **u** in [4.2] then shows that this implies

$$w(x,y,z) = -\nabla_h^2 \chi(x,y,z) = 0 \quad , \text{ at } z = 0, 1 \quad . \qquad [5.6]$$

Since for this modal model a separable representation of χ is being assumed in the form [5.1], where the f_i satisfy $\nabla_h^2 f_i = -\alpha_i^2 f_i$ for some constant α_i, then [5.6] reduces to

$$w(x,y,z) = \sum_{i=1}^{N} \chi_i(z) \alpha_i^2 f_i(x,y) = 0 \quad , \quad \text{at } z = 0,1 \quad . \qquad [5.7]$$

The same Galerkin−type projection that is applied to the equations may be applied to the boundary conditions also i.e. effectively multiply [5.7] by any f_i and integrate over all x and y so that the orthogonality of the f_i's then forces

$$\chi_i(0) = \chi_i(1) = 0 \quad , \quad \text{for all } i. \qquad [5.8]$$

The more general conditions that $\chi(x,y,z) = 0$ on the boundaries may be shown by a Taylor expansion of χ about the boundary, and arguments requiring no net translational or rotational flows.

The vertical boundaries are once again assumed to be free, so that [2.26] holds,

along with its corollaries [2.26a] – [2.26d]. Equation [2.26c] implies that

$$\frac{\partial(\nabla_h^2 \psi)}{\partial z} = \nabla_h^2 \left[\frac{\partial \psi}{\partial z} \right] = 0 \quad , \quad \text{at } z = 0, 1 \quad , \qquad [5.9a]$$

and so, due to the functional dependence of ψ,

$$\frac{\partial \psi(x,y,z)}{\partial z} = 0, 1 \quad \text{at } z = 0, 1 \quad . \qquad [5.9b]$$

Thus, for the modal case, again using the same Galerkin projection as before

$$D\psi_i = 0 \quad , \quad \text{at } z = 0, 1 \quad , \qquad [5.9c]$$

where D is the derivative with respect to z as usual.

Similarly, equation [2.26d] implies that

$$\frac{\partial^2(\nabla_h^2 \chi)}{\partial z^2} = \nabla_h^2 \left[\frac{\partial^2 \chi}{\partial z^2} \right] = 0 \quad , \quad \text{at } z = 0, 1 \quad , \qquad [5.10a]$$

and so, again since $\nabla_h^2 f_i = -\alpha^2 f_i$, as earlier for [5.6] and [5.7],

$$D^2 \chi_i = 0 \quad , \quad \text{at } z = 0, 1 \quad . \qquad [5.10b]$$

As in the method of Chapter 3, the procedure of solution is to be that the Nusselt number is to be specified and the Rayleigh number is to be sought as a parameter, and so an extra boundary condition is required. Thus, the heat flux at the lower boundary is specified as

$$DT_0(0) = - Nu \quad . \qquad [5.11]$$

Notice the change in sign of this boundary condition compared to the penetrative case. This is due to the fact that the unstable layer in penetrative convection has a stable temperature gradient across it, whereas in Rayleigh–Benard convection, the temperature gradient is unstable, so $\Delta T = T_u - T_l = +1$ for penetrative convection, and -1 for Rayleigh–Benard, and $\Delta z = 1$ for both ($Nu \simeq \Delta T/\Delta z$). The heat flux should be the same at the top of the cell, and this may be used as a useful check of the code.

5.3.5. The computational methods.

5.3.5.1. Grids and numbers of modes.

In this case, the number of modes to be used is defined purely by requiring that all the modes necessary to complete the expansion of the harmonic sequence up to a particular order are included. The order of the ODE system for such a particular truncation set cannot be predicted in advance unless the nature of the truncation set is known i.e. in general, it is not known how many new modes will be added in the advance from one order to the next unless all the non−linear interactions producing planforms at this order have been investigated and categorised, and thus it is not a simple process to move from one truncation to the next. The general order of the ODE system for a known set of modes is $6N+2M+2$, where N is the total number of different planforms in the truncation set and M is the number of them that may generate vertical vorticity. The χ equation is 4^{th} order ands so generates 4N equations, the ψ equation is 2^{nd} order which gives 2M equations, and the temperature equation is also 2^{nd} order but includes a mean−field component and so produces $2[N+1]$ equations. The principle of a modal solution is that if enough modes are taken in the horizontal, assuming an accurate solution of the vertical problem, then a reasonable result may obtained for the flow characteristics. It is implicitly assumed that increasing the number of modes will increase the accuracy of the solution when compared to a hypothetical 'true' solution, should one ever be available. In the preceding calculations it has been simple to check the accuracy of a particular modal truncation by calculating a higher modal truncation and comparing the two, but this process is not as easy here due to the larger computational expense and difficulty in forming the modal expansions, and so the different truncations that are available must be compared carefully.

The specification of ψ here involves only those M modes of the full N that are found to exhibit vertical vorticity by inspection of the non−linear terms. An alternative specification could be to simply include a ψ as all the N modal modes that the harmonic search has found but in the equivalent ψ format (i.e. all cosines changed to sines and the sign of the middle term reversed) and to see which modes gave non−zero vertical coefficients after convergence i.e. to allow all modes a chance to propagate as vertical vorticity generating modes, and to let the system choose the most appropriate ones. This method was not used because of the large amount of extra storage and computational time it would require to

generate and run the larger ODE system.

The computational work required for the square periodicity calculation may be reduced by a large amount by noticing that, due to the symmetry of the situation, some of the horizontal modes are equivalent, except for the fact that x and y have been exchanged, and so their vertical dependences are going to be identical. Thus, modes such as S20 and S02 require only one of them to be calculated, since the solution represents both. Modes (S20,S02), (S31,S13), (S40,S04) and (S24,S42) can be calculated in this way.

For every calculation exhibited in this Chapter, 33 mesh points were used for the solution of the vertical two−point, boundary value problem. The higher number of mesh intervals used here compared to Chapter 3 is due to the fact that greater complexity is expected from the three−dimensional nature of the problem and the inclusion of vertical vorticity. This resolution is certainly satisfactory by the measures of the authors quoted in section 3.3.5 of Chapter 3.

The Newton−Raphson−Kantorovich procedure (Readwin (1986)) was once again used to solve the vertical problem with fourth order accuracy on the mesh spacings. Again, sixth order and eighth order deferred correction, although available, were not required.

5.3.5.2. Eigenvalues and parameters.

The only eigenvalue sought using the facilities incorporated into the NRK solver was the Rayleigh number, Ra, allowable by inclusion of the extra boundary condition [5.11]. The value of the overall wavenumber was not sought as an eigenvalue of the problem by the process described in section 3.3.5. The reasons for this are purely ones of computer time and storage. The system of ODEs is already large, 54 equations for the largest hexagonal solution and 74 for the largest square. Use of the 'minimum Rayleigh number' method of specifying α would double these figures, and thus double the storage needed by the code and at least double the CP time devoured. Even on virtual memory machines such as the VAX 8600 where this calculation was performed, the allocation of such storage causes a severe increase in CP time because of the faulting to the slower storage media (disc), unless very careful attention is paid to the memory requirements of the code. Hence, the wavenumber α was treated as a normal parameter for the calculation by necessity, and a brief search of the solution space dependent on α was also performed. The restriction of using a fixed wavenumber is not necessarily a major obstacle to any researcher at present, since the question of the 'preferred

mode' of convection is still a largely unanswered one. Theories on the choice of the preferred scale of convection are varied; Malkus and Veronis's (1958) suggestion of maximising the heat transport has been used by many, although modified by some (Murphy and Lopez (1984)) to allow further stability criteria to be incorporated, whilst other authors (GST) prefer to rely on experimental data. However, no theory has any solid theoretical foundation and so the choice is somewhat arbitrary.

The critical Rayleigh number for the onset of linear convection is given by Chandresekhar (1961) as

$$R_c = \frac{(\pi^2 + \alpha_c^2)^3}{\alpha_c^2} ,$$

where α_c is the critical wavenumber, and the values of these for Rayleigh–Benard convection are quoted as $R_c = 27\pi^4/4$ and $\alpha_c = \pi/\sqrt{2}$ for the two–dimensional problem. The α_c terms arise from the horizontal Laplacian of the planform function used for any particular case,

$$\nabla_h^2 f = - \alpha^2 f ,$$

where f(x,y) is the planform function. For rolls, e.g. f = cos(kx) and so $\alpha^2 = k^2$ and α is then simply the same as the horizontal wavenumber, k, but for hexagons and squares, the specification of the basic planforms introduces extra scaling factors into α. For the Christopherson hexagon, $\alpha^2 = 4k^2$, and for a square, $\alpha^2 = 2k^2$, so that $\alpha_{hex} = 2k$ and $\alpha_{sq} = \sqrt{2}\ k$. Hence, the critical wave numbers for the onset of convection in squares and hexagons respectively are $\pi/2\sqrt{2}$ (= 1.111) and $\pi/2$ (=1.571), and then R_c remains at 657.5. Thus, compared to a critical roll, a critical square is $\sqrt{2}$ times wider and a critical hexagon has a diameter $2/\sqrt{3}$ times the width. These figures provide a useful check of the code if Nu close to unity is used.

The parameters of the problem are thus the Nusselt number, the wavenumber, the Prandtl number and the choice of truncation parameter.

5.3.5.3. Solution process.

The code operated in a manner similar to that for the penetrative, two–dimensional code, in that solutions of increasing order were sought in a cascade manner. The first solution calculated was of the quasi–linear FIRST

system. In this system, due to the omission of the non−linear advection terms, the Prandtl number is no longer a parameter, and so Nusselt number space can be quickly searched, since convergence on the 8 equations is rapid. Wavenumber space was only searched at the high orders. The simple FIRST solutions can then be used as the basis for an initial guess of the extended, fully non−linear SECOND order system. Any solutions calculated for the SECOND sytem can then in turn be utilised for an initial guess to the THIRD system. The THIRD system results can be rescaled for initial guesses to either the THIRDVV system of equations in the hexagonal periodicity case, where a vertical vorticity mode is included for the first time, or for an approximation to the FOURTH system. The THIRDVV solutions obtained in the hexagonal case may be used to start the FOURTHVV case, which includes both of the available vertical vorticity generating terms which appear at the fourth order.

Initial solutions are always started around the conductive solution, where the Nusselt number is very close to one, and usually at a higher Prandtl number, where it is expected that the changes in the flow from the simple solutions will be less violent. The derivation of an initial approximation for each system of equations from the lower order solutions, along with the scalings used to follow the parameter space of interest are given below.

5.3.5.4. FIRST system initial guesses.

The first order fully non−linear system of equations is as follows:

$$D^2T_0 = C_1\alpha^2 (\chi_1 DT_1 + D\chi_1 T_1) \quad , \qquad [5.12]$$

$$D^2T_1 = C_2\alpha^2 (T_1 + \chi_1 DT_0) + C_3\alpha^2 (T_1 D\chi_1 + 2\chi_1 DT_1) \quad , \qquad [5.13]$$

$$(D^2 - C_2\alpha^2)^2\chi_1 = Ra\ T_1 \left\{ + \frac{C_3}{\sigma}(\alpha^2\chi_1 D\chi_1 + 2\alpha^2 D\chi_1 D^2\chi_1 - 12\alpha^2\chi_1 D\chi_1) \right\} , \qquad [5.14]$$

where

$C_1 = 24$, $C_2 = 4$, $C_3 = 4$ for hexagonal periodicity,

and

$C_1 = 2$, $C_2 = 2$, $C_3 = 0$ for square periodicity.

The above system in its entirety is equivalent to the FFIRST system used here. If the terms in the large {} brackets in [5.14] are omitted the the system is reduced to the FIRST system used. The non−linear term dropped for the FIRST order equations is preceded by σ^{-1} and so this process is effectively assuming infinite Prandtl number. The extra terms are also preceded by the coupling coefficient C_3, which is zero for the square case automatically, so that the FFIRST system is not necessary in the case of squares. This is what is meant by 'self−interacting' or 'non−self−interacting' i.e. squares, simply by the nature of their planform functions force C_3 to be zero and hence annihilate the non−linear interaction terms in the equations as shown. Thus, squares are termed 'non−self−interacting' since the planform cannot interact with itself through this term. Hexagons, however, have a planform functionality which makes $C_3 \neq 0$ and so allow self−interaction through the non−linear terms. C_3 is often known as the coupling constant, C (see Roberts (1966)).

Following on from [5.14], if it assumed that

$$T_0(z) = -z + A \sin(2\pi z) \quad , \qquad [5.15]$$

$$T_1(z) = B \sin(\pi z) \quad , \qquad [5.16]$$

$$\chi_1(z) = C \sin(\pi z) \quad , \qquad [5.17]$$

then the boundary conditions [5.5], [5.8] and [5.10] are all automatically satisfied, leaving only [5.11] to complete the problem. Substitution of [5.15] − [5.17] in [5.12] − [5.14] reveals that

$$CB = -\frac{4\pi A}{C_1\alpha^2} \quad ,$$

$$\frac{B}{C} = \frac{C_2\alpha^2}{(\pi^2 + C_2\alpha^2)} \quad ,$$

$$\frac{C}{B} = \frac{Ra}{(\pi^2 + C_2\alpha^2)^3} \quad ,$$

where the non−linear ($\cos(2\pi z)$ terms) are ignored in the T_1 equation, and so this confirms that

$$Ra = \frac{(\pi^2 + C_2\alpha^2)^3}{C_2\alpha^2} \quad . \qquad [5.18]$$

Also, assuming that the Nusselt number represents the heat flux at the lower

boundary,

$$DT_0(0) \;=\; -Nu \;=\; -1 + 2\pi A \;,$$

then, [5.11] is satisfied and all is revealed as

$$A \;=\; \frac{(\,1 - Nu\,)}{2\pi} \;, \qquad [5.19]$$

$$B \;=\; \left[\frac{2C_2(\,Nu - 1\,)}{C_1(\,\pi^2 + C_2\alpha^2\,)} \right]^{1/2} , \qquad [5.20]$$

$$C \;=\; \left[\frac{2(\,Nu - 1\,)(\,\pi^2 + C_2\alpha^2\,)}{C_1C_2\,\alpha^2} \right] \;. \qquad [5.21]$$

These with equations [5.15] – [5.17] provide the initial guess for the FIRST system. The initial approximation for the Rayleigh number is also used as that given above by [5.18], which is valid for Nu close to unity.

5.3.5.5. Recovery of higher order solutions from lower order solutions.

Having found a solution of the FIRST equations from scratch using the previous method of initial approximation, it is then necessary to find ways of extending this solution to an initial approximation of the larger ODE set for the SECOND order system. Once a solution has been gained for this SECOND system, then the results may be extended once more for the THIRD system, and so on. The extension of the results from one order system to the next however is not an obvious step, since for a large number of the modes involved, especially the vertical vorticity modes, there are no previous clues to lead the way as to the form of the vertical variables. Once a solution has been gained for any parameter values, then its structure may be analysed to improve future guesses. However, until that first solution converges, it is often a question of anything goes.

Obviously, the N modes of the lower, converged solution offer a good approximation to the first N modes of the higher order solution, so the problem is reduced to approximating the new modes which are brought in at the higher order e.g. H2 and RH$\sqrt{3}$ when moving from FIRST to SECOND. A successful and exceptionally simple method has been to assume that the new aligned and rotated modes of the higher order solution are just a scalar reduction of the similar modes

at the lower order, where a scalar reduction of 0.1 has proved itself. This value is actually too small for most of the real scalings, but the system seems to cope well with an underestimation of the activity of a mode, allowing the code to build it up towards convergence. No other approximations apart from these were needed to start any of the square solutions, and only the ψ vertical vorticity modes of the hexagonal periodicity needed any special treatment. The major problem was arriving at some approximation which started the first vertical vorticity mode, the form of which had to be solely an educated guess. If the equations for its production are scrutinised for possible important effects, the mode appears to be driven largely by non−linear interaction of the first non−mean temperature mode, T_1, with its own derivative, DT_1, and so a scaled multiple of these formed a reasonable and successful approximation for the mode. The second vertical vorticity mode, required in a scaling up from FOURTH order to FOURTHVV, was guessed as an extension of the known first vertical vorticity mode, once a solution for it had been calculated, in conjunction with inspection of the ψ_2 equation. Solutions showed that ψ_1 behaved like a sum of $\sin(\pi z)$ and $\sin(3\pi z)$, so for the second vertical vorticity mode, a $\sin(5\pi z)$ was added to this structure, and the result scaled down, for a successful approximation to the true solution.

In hindsight, the initial approximations for the various solutions can be vastly improved. However, once one solution at a particular order has been found, this solution becomes the best possible initial approximation that could be used for the next solution at that order, if utilised in conjunction with a suitable scaling. The next section outlines such scalings, which take the solution at one (Nu, σ, α) point to the next.

5.3.5.6. Scaling through parameter space.

Scaling through parameter space was based on the scheme divised in Chapter 3 for penetrative convection (see equations [3.64] − [3.66]). That is, to change the Nusselt number, the T_0 terms are rescaled by the ratio of the new Nusselt number, Nu_n, to the old, Nu_o, and all other variables scale as a factor, F, raised to the power of the numerical value of the order of those modes (i.e. χ_1 first appears at first order, so uses F^1, H3 first appears at third order so is F^3 even in a FOURTHVV solution), where the factor, F, is the square root of the ratio of $(Nu_n - 1)$ to $(Nu_o - 1)$.

Scaling from one Prandtl number to the next is achieved by rescaling all variables except the temperature variables by a factor of the old Prandtl number

divided by the new Prandtl number ([3.66]).

No scaling was used when moving through wavenumber space.

5.3.5.7. The parameter space searched.

Solutions were obtained for Nusselt numbers in the range $1.0 \leqslant Nu \leqslant 3.0$ in most cases, for Prandtl numbers $\sigma = 0.1, 1.0, 10.0$, and for wave numbers in the range $0.75 \leqslant \alpha \leqslant 5$. Some calculations extended the Prandtl numbers down as low as $\sigma = 0.01$ for both hexagons and squares, and for squares, Nusselt numbers up to $Nu = 10.0$ were calculated. All calculations were carried out on a mixture of the mainframes available at Imperial College Computer Centre although the majority were completed on the VAX 8600 running under VMS. Storage requirements were on the order of 17000 + 1600n words, where n is the number of equations in the ODE system, and so maximum storage for any case was $\simeq$ 100k words ($\simeq$ 1/2 Mbyte).

5.4. RESULTS AND DISCUSSION.

At most three modes have been used in previous truncations (e.g.GST3), and so one of the primary aims of this section of work has to be to investigate the effect of the inclusion of the harmonics found in Chapter 4. For the square periodicity solutions, this is more straightforward, since the new modes included offer no physically obvious differences from the low order modes, and so the question is the normal one, as for the two-dimensional calculation of Chapter 3. However, the question of truncation is more interesting in the hexagonally periodic case since some of the new modal solutions offer inherent inclusion of vertical vorticity modes, none of which have ever been included in any previous modal solutions. Vertical vorticity has been included in modal solutions before (Massaguer and Mercader (1988), Murphy and Lopez (1984)), but not in such a physical manner, and so it is interesting to see if such modes are strong enough to 'stir' the flows, as in the type II flows of Murphy and Lopez (1984), and if they affect such global parameters as the heat flux.

This aside, the interest is then, as for any convection problem, in determining the effect of the various parameters, the Nusselt number, the Prandtl number and the wave number, on the physical characteristics of the flow.

5.4.1. The effects of the various modal truncations.

5.4.1.1. Hexagonal horizontal periodicity.

The heat flux, measured by its ratio to that flux which is carried in a conductive solution in the form of the dimensionless parameter the Nusselt number, Nu, is probably the most universal measure of the efficacy of convection available, and the most widely sought result. Graphs of the Nusselt number against the Rayleigh number for the various modal truncations at various Prandtl numbers for the hexagonally periodic solutions are shown as figures 5.1a)−5.1c). It may be seen that at higher Prandtl numbers, the inclusion of the higher order modes makes relatively little difference to the calculated values of the Nusselt number or Rayleigh number compared to the lower σ results. At σ = 10.0 and Nu = 2.5, the maximum Nusselt number usually calculated, the range of Rayleigh numbers spanned by the various modal truncations shown is only about 0.15 R_c. For lower Prandtl numbers this range increases, with the spread being 0.5 R_c at σ = 1.0 and increasing dramatically for σ = 0.1 to a range more on the order of 15.0 R_c. Hence, it is seen that the higher order modal models are much more important at lower Prandtl number that at moderate or high Prandtl number. Once again, as for the two−dimensional penetrative case, this result is not surprising, since at higher Prandtl numbers, the effect of the non−linear advection of momentum term is reduced by the reciprocal of σ. It is these terms which give rise to the highly non−linear structure of the problem, including the extended harmonic solutions, and so if their effect is much reduced, the solution is to be expected to be much simpler and therefore representable by a simple harmonic planform structure. At lower σ, the importance of these terms increases and thus highly, non−linear and therefore complicated solutions are allowed, the structure of which would require many harmonic planforms in the horizontal, coupled with the complete solution of the vertical problem in order to specify an accurate answer. These two regimes are often referred to as the viscous regime, where the advection of momentum is unimportant and advection of temperature drives the flow, and the advective regime, where the non−linear $(\mathbf{u}.\nabla)\mathbf{u}$ terms dominate (Jones, Moore and Weiss (1976)).

Notice immediately that the two first order, single mode solutions, are the 'worst' cases compared to the higher order modes as expected. Figures 5.1 show that the FIRST solution appears to overestimate the heat flux compared to the higher order solutions at the lower Prandtl numbers. All the higher order solution

curves always lie below the FIRST solution curve in Nu−Ra space for σ = 0.1 and σ = 1.0, showing that the low order truncation attributes the system with a more efficient mode of operation than it seems likely to possess in reality. This has always been the case for such low order solutions e.g. the mean−field solutions of Herring (1963), but, nonetheless, GST found their single mode solutions to reasonably predict experimental data. However, the FIRST system of equations is effectively a single mode truncation operating at σ = ∞, and, as previously mentioned, the modal truncations become less important as σ is increased, so the FIRST system solutions presented here are virtually useless for comparison with the higher order modes, since they do not allow for a Prandlt number dependence. It was for this reason that a second single mode solution was calculated, known as the FFIRST system (for FULL FIRST), which is exactly equivalent to that system used by GST, for comparison with the higher order modal truncations presented here, and with those solutions of GST themselves. It may be seen that the FFIRST system goes to the opposite extreme to the FIRST system, underestimating the heat flux compared to the higher order solutions where the FIRST solution overestimates, at σ = 1.0 and σ = 0.1. At σ = 10.0, which may be regarded as a relatively high Prandtl number, the two solutions are equivalent, since both have effectively lost the non−linear momentum terms, and both underestimate the heat flux quite considerably compared to all the rest of the solutions which are almost coincident in the range shown. At lower σ, the FFIRST solution seriously underestimates the Nusselt number, and, unexpectedly, the FIRST system actually appears more accurate despite its lack of Prandtl number dependence, compared to the higher order modes, which of course themselves exhibit a greater spread of results.

The SECOND modal truncation, which involves the fundamental hexagons and its first two overtones, is disappointing in its performance at low Prandtl numbers (σ = 0.1). This is the highest approximation used by many previous researchers (see GST, Platzman (1965), Roberts (1966)), but appears to fail at all but very small Rayleigh numbers, since for $R > 3R_c$, the system shows no dependence of the Nusselt number on the Rayleigh number, the curve appearing to settle down to a constant value of Nu $\triangleq$ 1.25. The method by which a solution is achieved in these calculations, where a Nusselt number is specified and the Rayleigh number is then sought, meant that no solutions could be obtained for a SECOND order system above Nu = 1.25 for σ = 0.1. Solutions were obtainable for higher σ, however, and indeed the results for σ = 1.0 and σ = 10.0 showed the SECOND order system to be comparable to the THIRDVV and higher systems, since here any vertical vorticity is severely diminished. Indeed, GST successfully calculated time−dependent SECOND solutions (their $\{F, \sqrt{3}, 2\}$ solutions) for a high σ

Fig. 5.1a). **Hexagonal Rayleigh–Benard convection**
Rayleigh number against Nusselt number
Comparison of modal solutions for σ = 10.0, α = 1.111

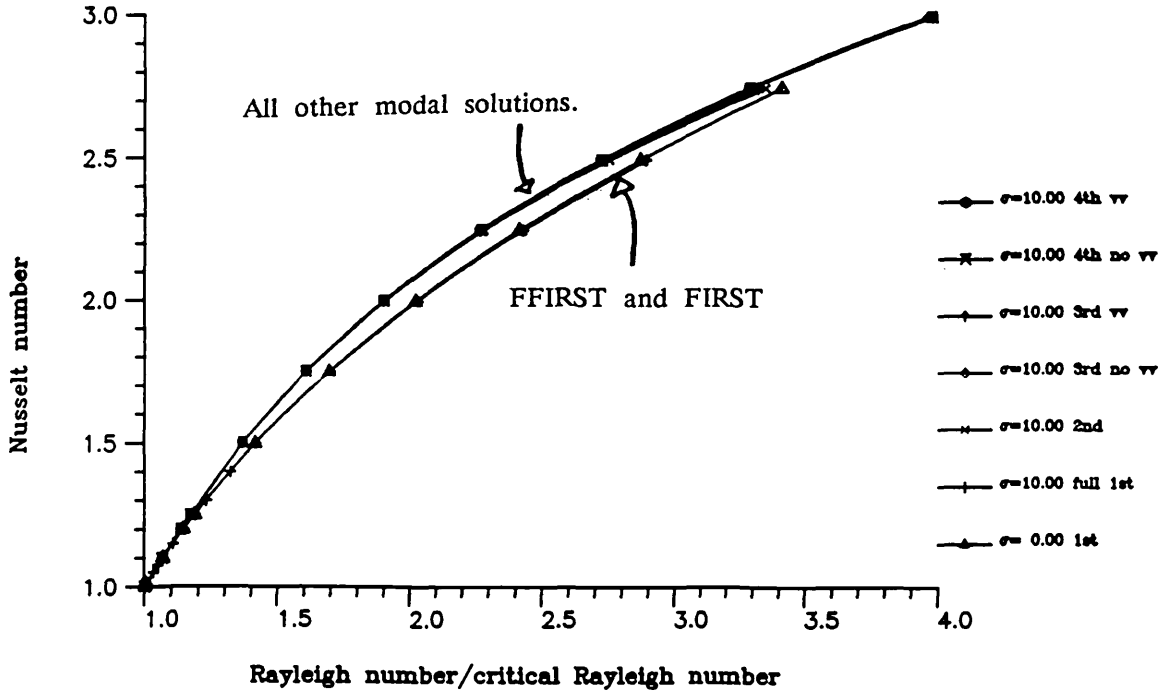


Fig. 5.1b). **Hexagonal Rayleigh–Benard convection**
Rayleigh number against Nusselt number
Comparison of modal solutions for σ = 1.0, α = 1.111

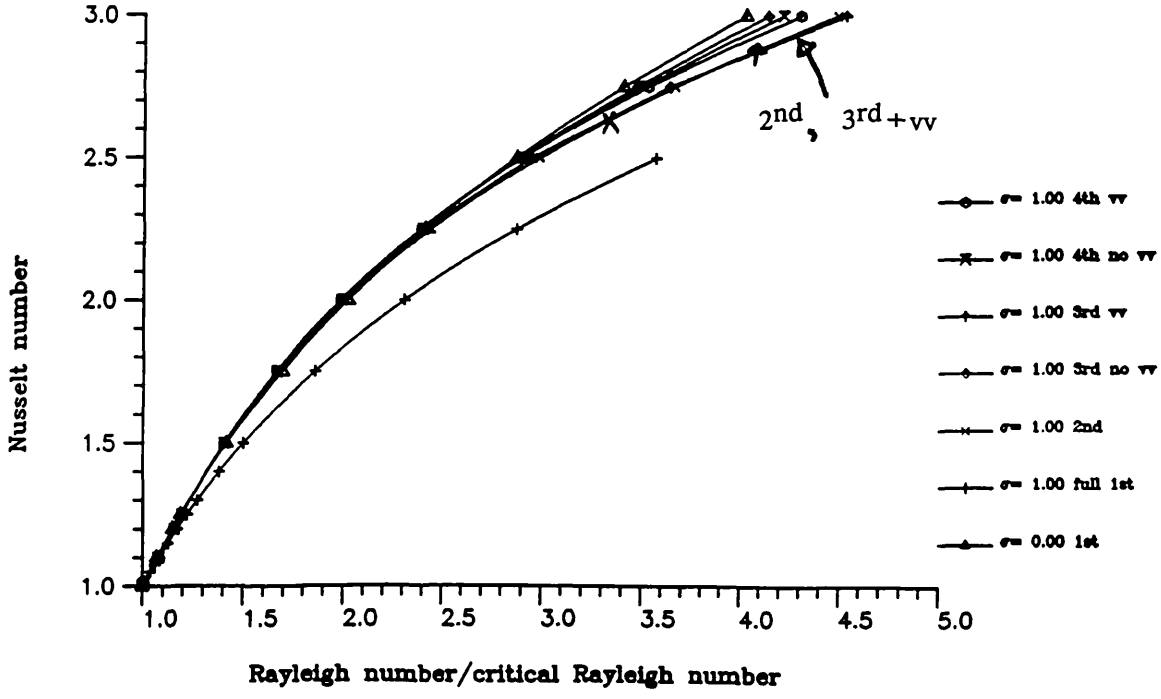


Fig. 5.1c). **Hexagonal Rayleigh-Benard convection**
Rayleigh number against Nusselt number
Comparison of modal solutions for σ = 0.1, α = 1.111

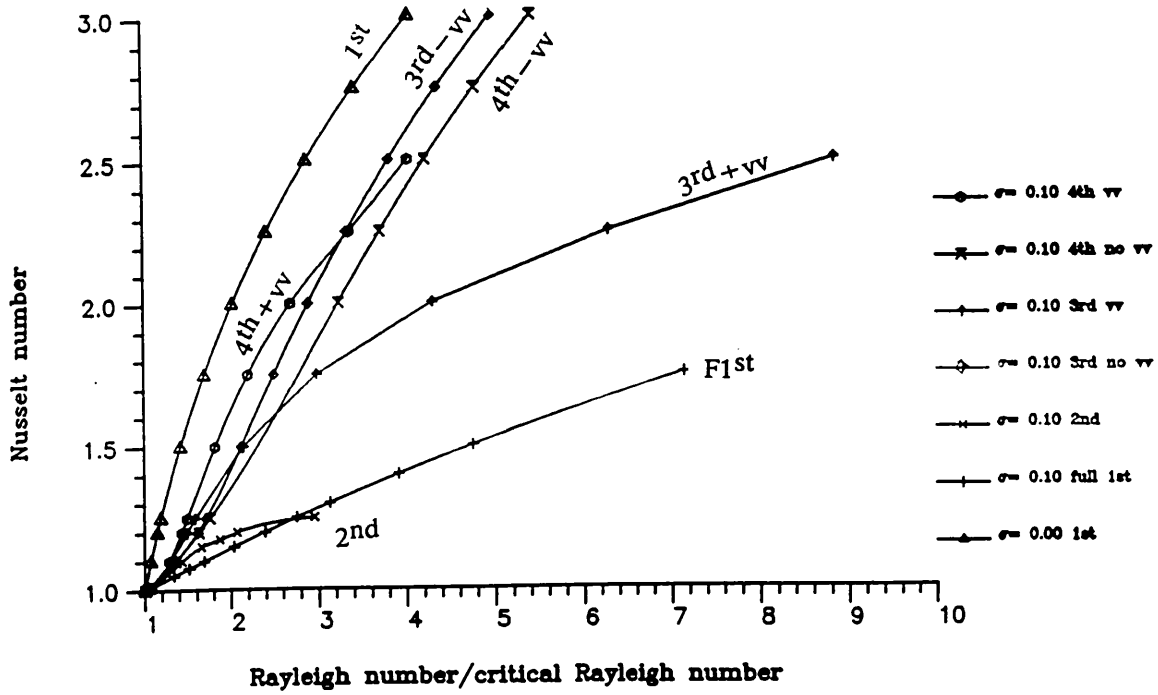


Fig. 5.2a).

File 6, R= 2645.0547, N= 2.50, σ= 0.10, α=1.1110, FOURTHVV, Hexagonal
File 5, R= 2770.5681, N= 2.50, σ= 0.10, α=1.1110, FOURTH , Hexagonal
File 4, R= 5815.9607, N= 2.50, σ= 0.10, α=1.1110, THIRDVV , Hexagonal
File 3, R= 2504.3848, N= 2.50, σ= 0.10, α=1.1110, THIRD , Hexagonal
File 2, R= 11747.9921, N= 2.50, σ= 0.10, α=1.1110, FFIRST , Hexagonal
File 1, R= 1887.4737, N= 2.50, σ= 0.00, α=1.1110, FIRST , Hexagonal

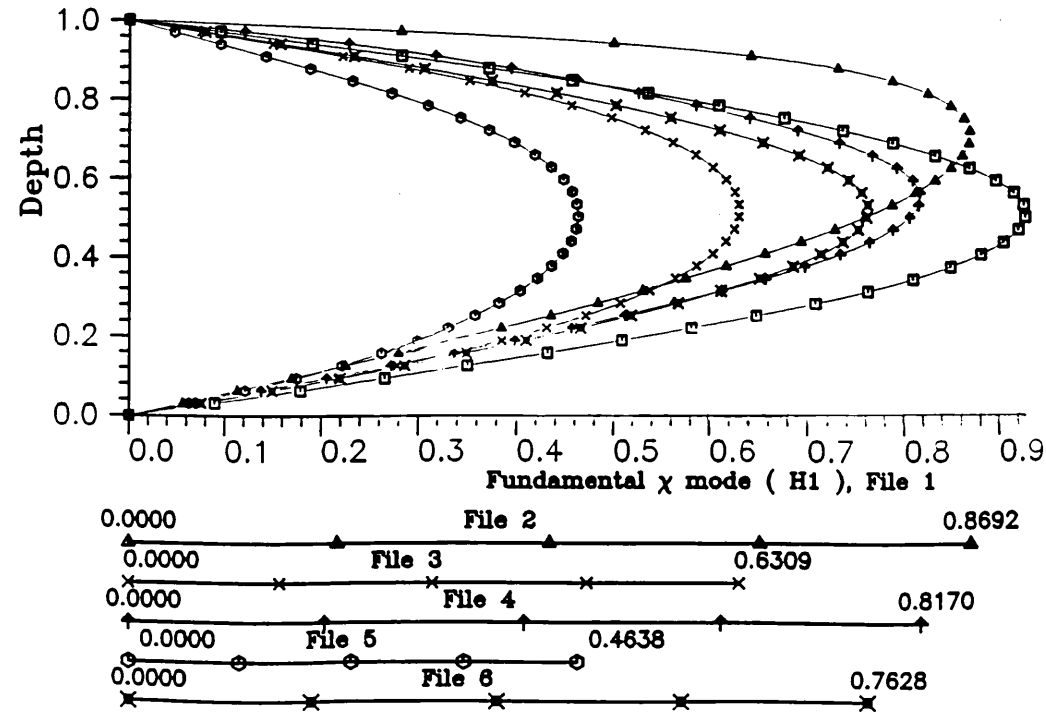


Fig. 5.2b).

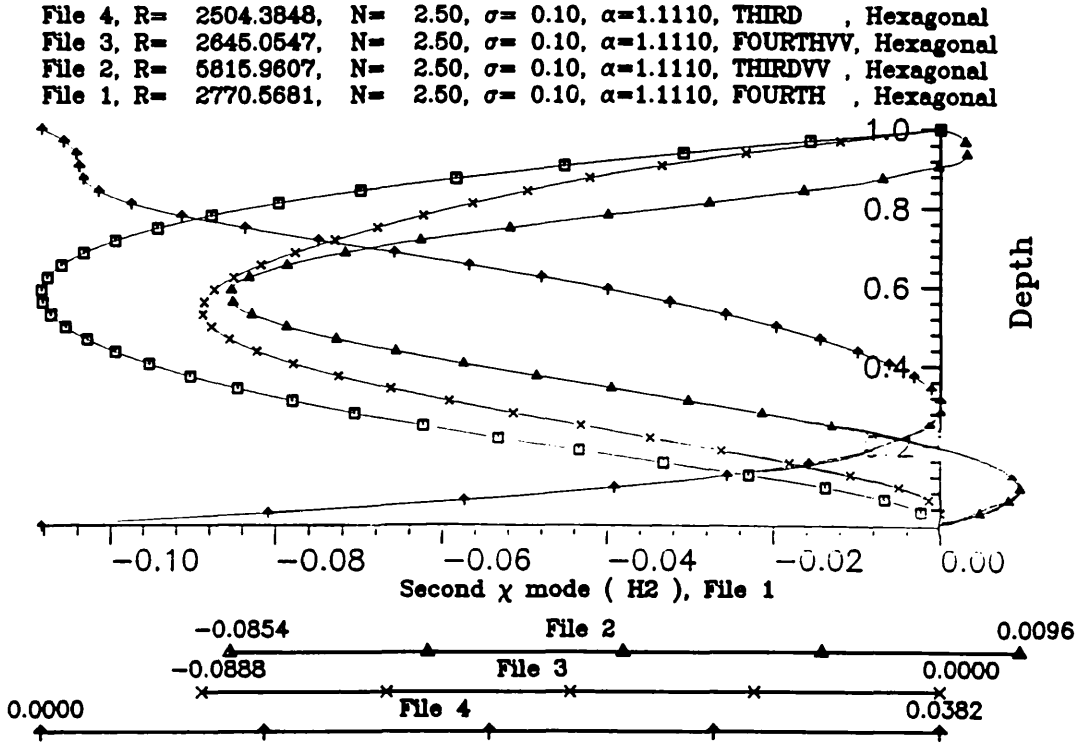


Fig. 5.2c).

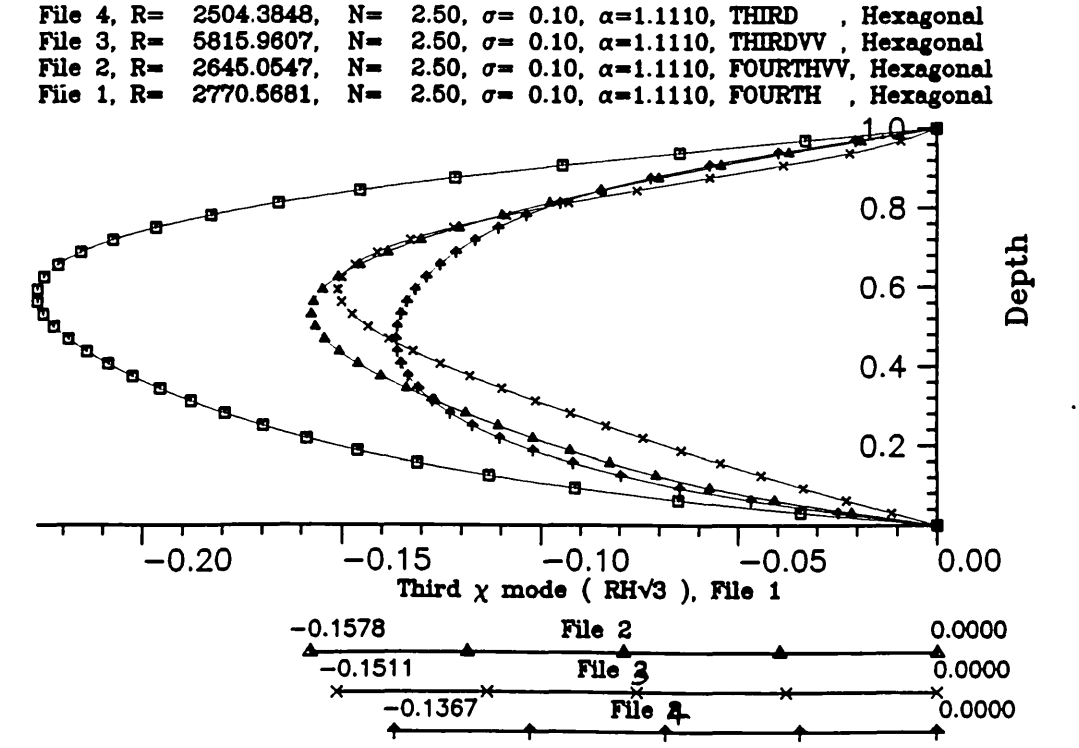


Fig. 5.2d).

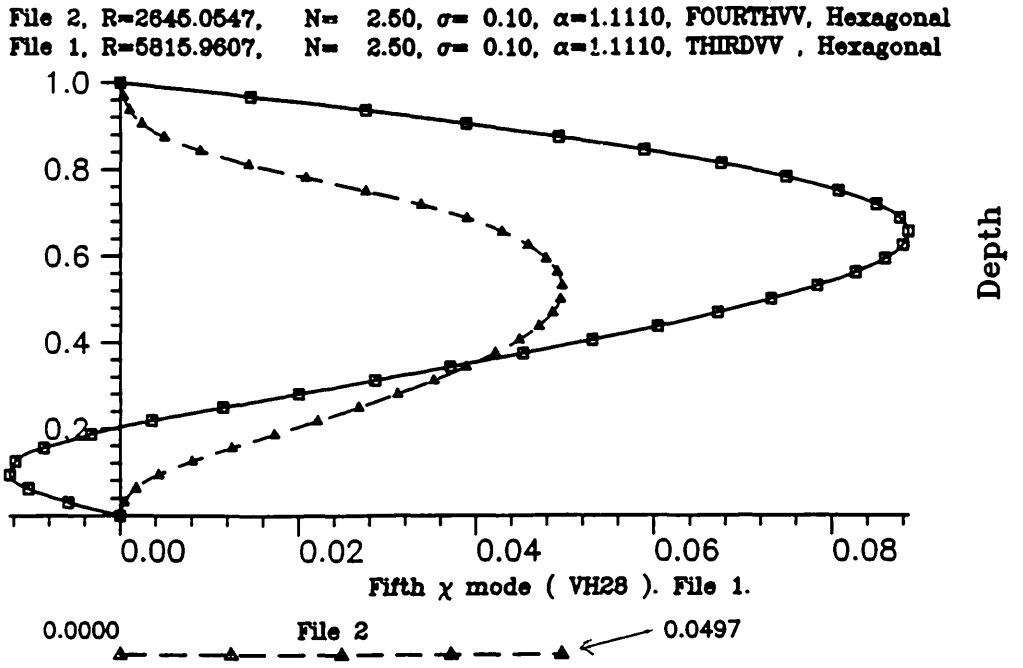


Fig. 5.2e).

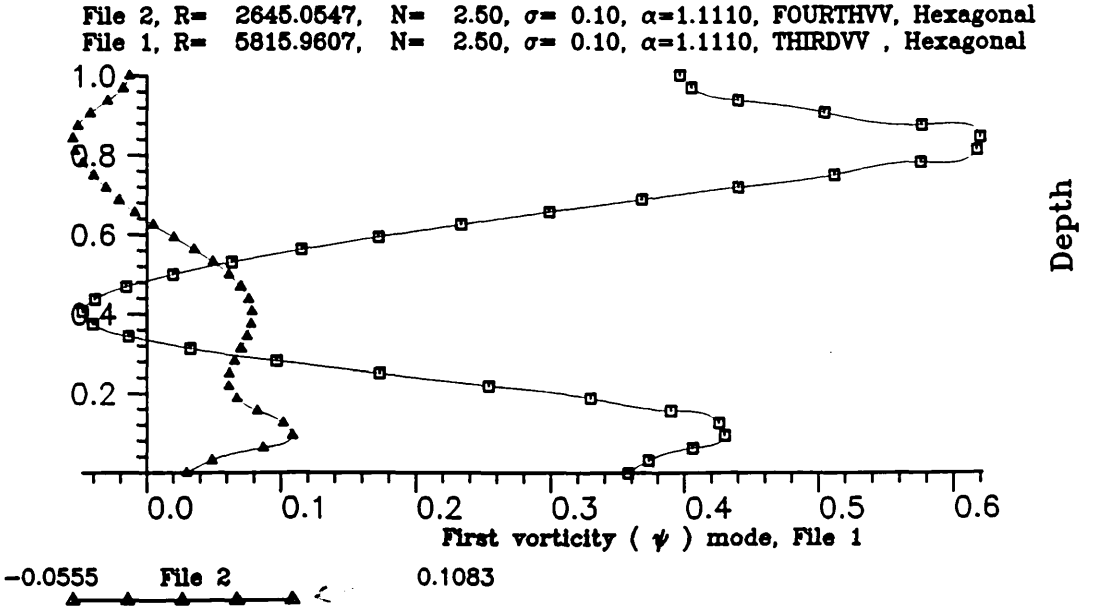


Fig. 5.2f).

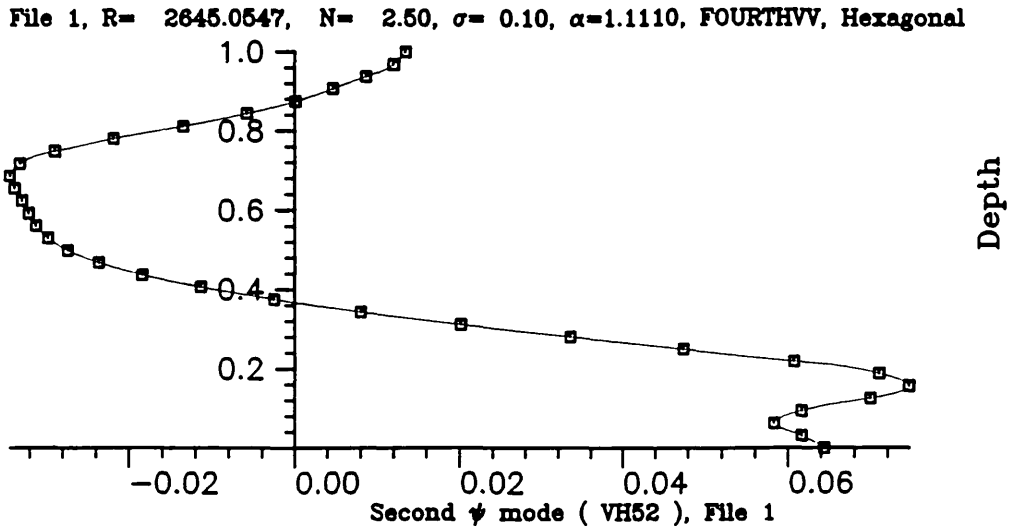
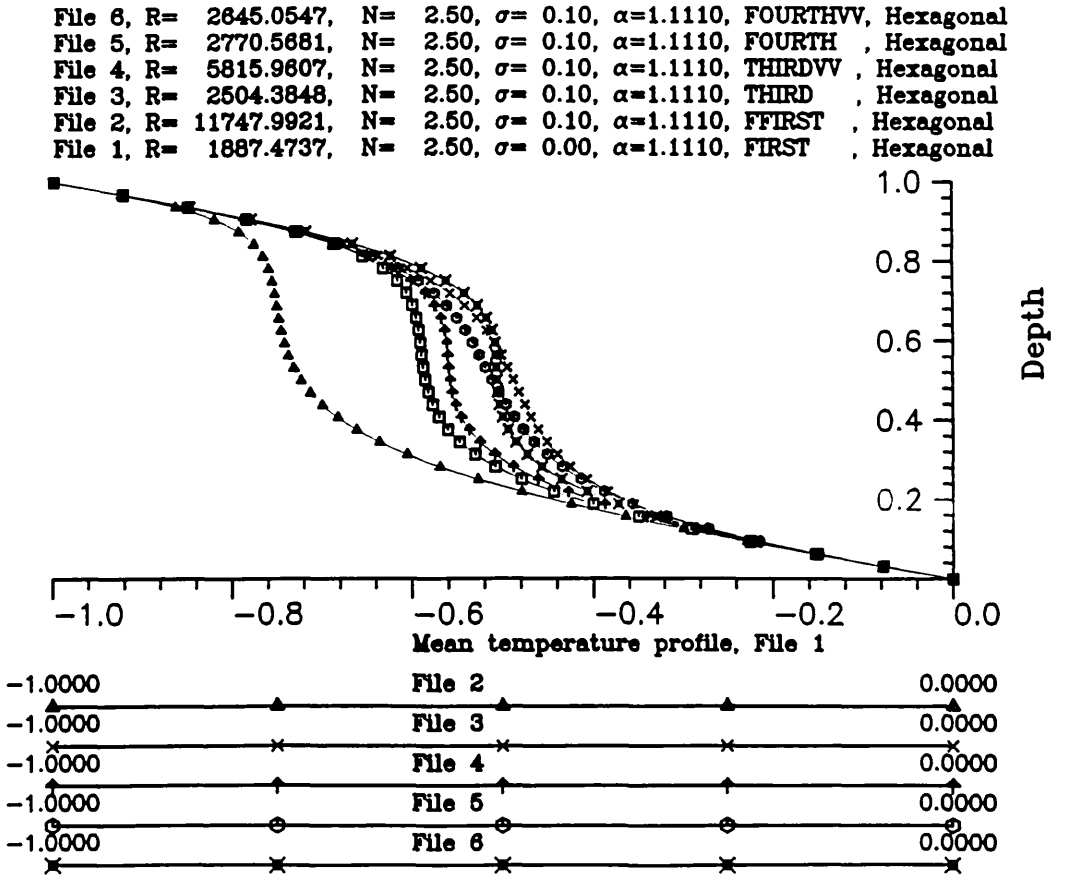


Fig. 5.2g).



regime (σ = 6.8 and σ = 200), for high Rayleigh numbers (R = 10^6, 10^7) and large horizontal wavenumbers (α = O(15)). However, both the SECOND and THIRDVV solutions appear to underestimate the heat flux in comparison to the higher order solutions at lower σ. The availability of SECOND order results for some higher σ and not for lower σ implies that the problem becomes ill−conditioned in some way for some particular 'cut−off' σ, although this has not been investigated here.

In general, there is an 'oscillatory' improvement of the solution at each increase in the order of the modal truncation for those σ where the inclusion of higher harmonics is significant. That is, the Nu versus Ra curves appear to be tending towards a limiting curve as the order of the truncation is increased, but the solutions do not tend towards this curve monotonically with increasing order of truncation, rather the solution curves successively under− then over−estimate the heat flux in comparison to this supposed limiting curve, which could lie in the centre region of all possible modal truncations calculated. A similar effect was noticed by Malkus and Veronis (1958) in their perturbation analysis, a technique which is not dissimilar to the computational method used here. The 'oscillations' exhibited by the solutions presented here, show that the higher order modal expansions used are quite adequate for the higher Prandtl numbers, but still do not appear to coincide too closely with the limiting curve in the Nu versus Ra graph at low σ. There is still a large gap between the THIRDVV and FOURTHVV solution curves and a true solution curve could lie anywhere in this region. Thus it is fair to say that even the FOURTHVV solutions are not close enough to a supposed 'true' solution to be thoroughly trusted. However, it may be stated that they are a distinct improvement on single mode or second order solutions at least at low Prandlt number since at least three of the higher order solutions occupy a similar area of the Nu−Ra space at all σ.

The form of the THIRD and FOURTH solutions is much the same, as is the style of the THIRDVV and FOURTHVV systems, except that the amplitudes of motions are changed by some degree. These effects are much more noticable at lower Prandtl number, where the non−linear influences and hence the extended harmonics are much more important. At third and fourth order, comparison of the solutions lacking the vertical vorticity (THIRD or FOURTH), and their comprehensive expansion counterparts (THIRDVV or FOURTHVV) shows that the addition of the vertical vorticity mode enhances the heat flux at low Rayleigh numbers, whereas the addition is detrimental to the heat flux at higher Rayleigh numbers. The crossover point for FOURTH/FOURTHVV occurs at a higher Rayleigh number and a higher Nusselt number than that for the THIRD/THIRDVV crossover. This crossover is the most important feature exhibited by these Nu

Fig. 5.2h).

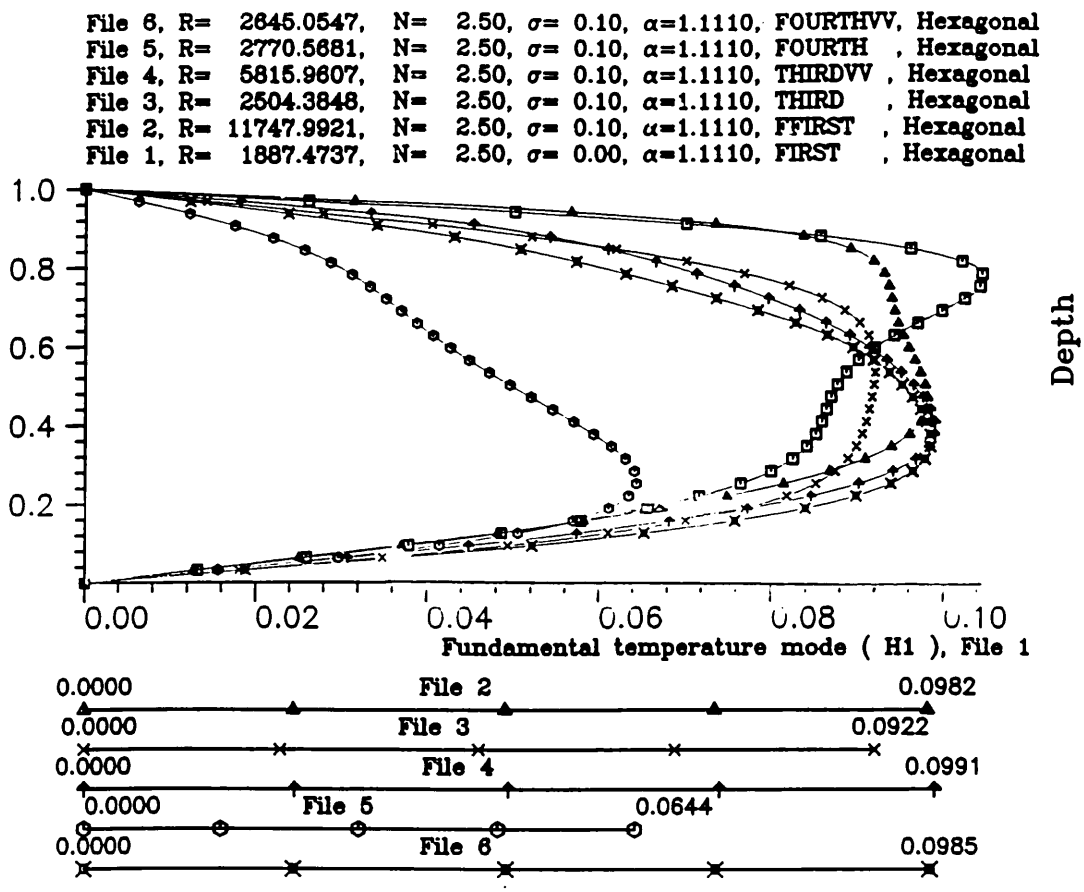


Fig. 5.2i).

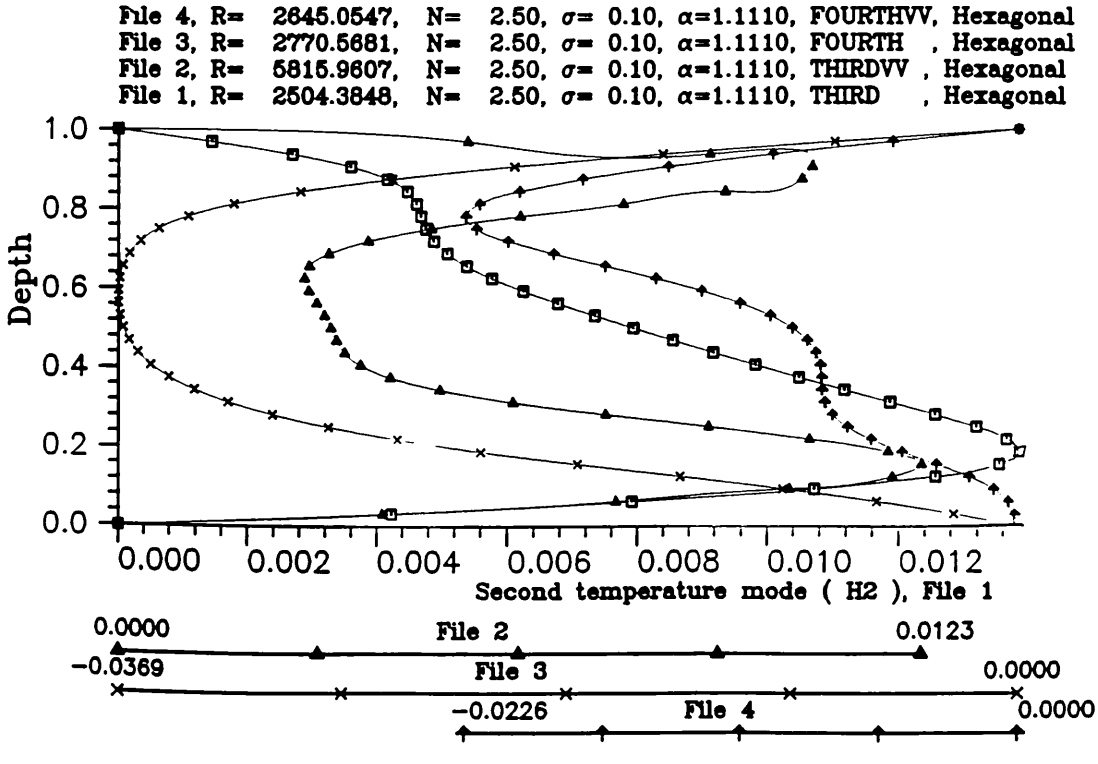


Fig. 5.2j).

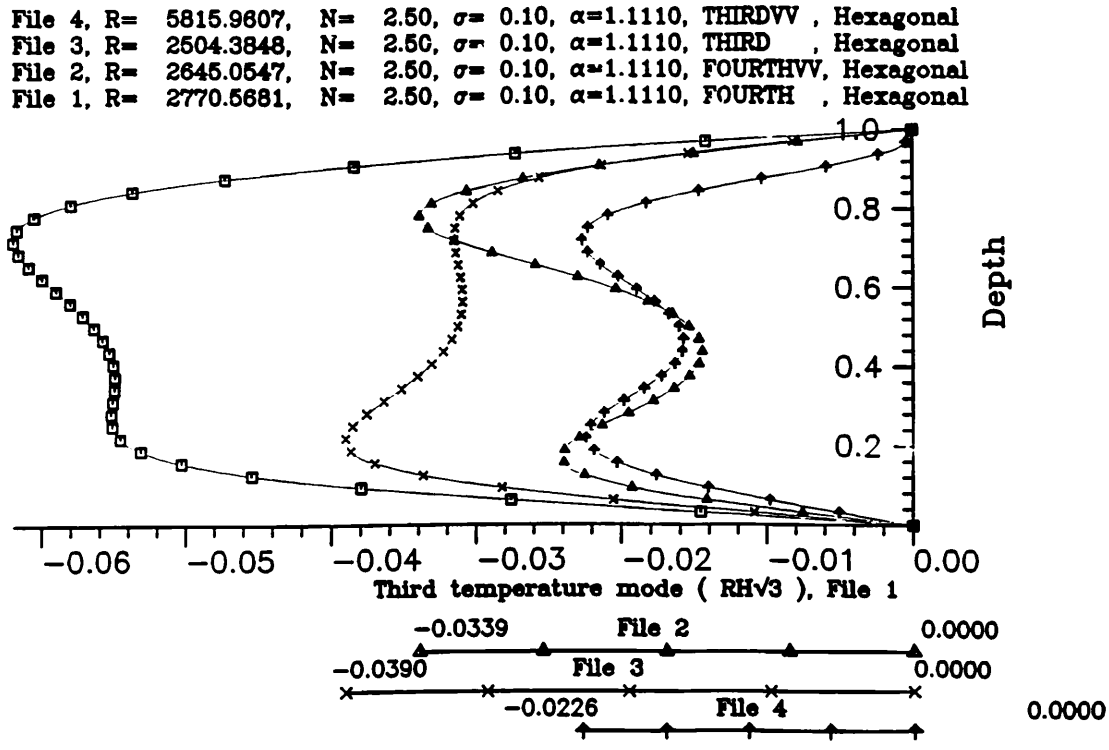


Fig. 5.2k).

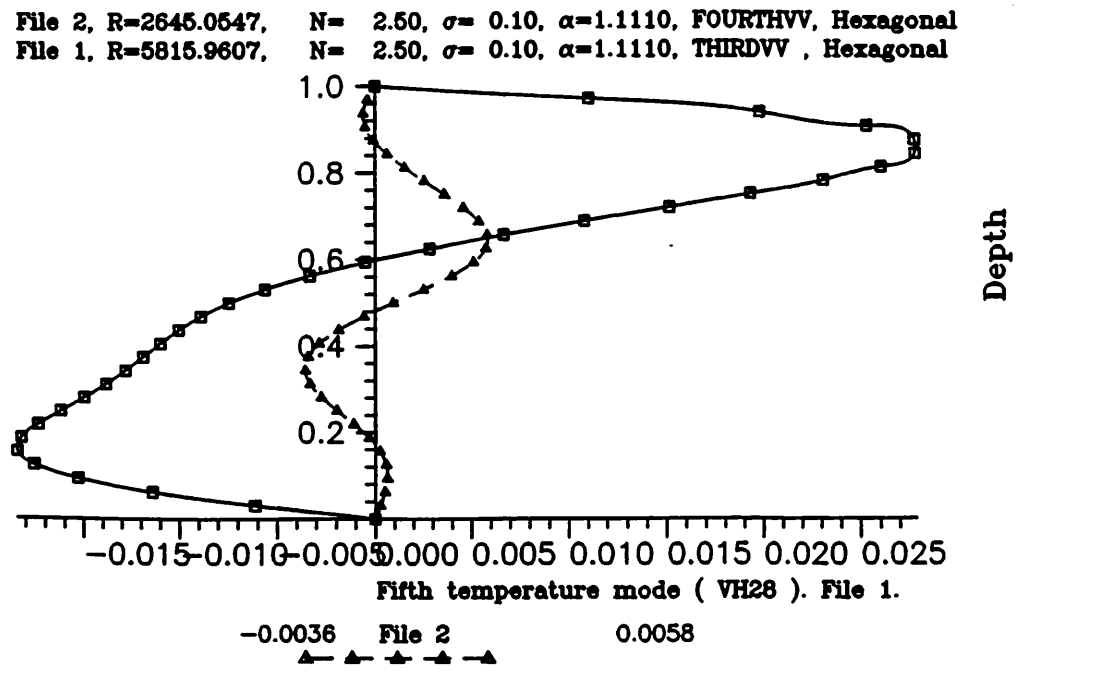


Fig. 5.2l).

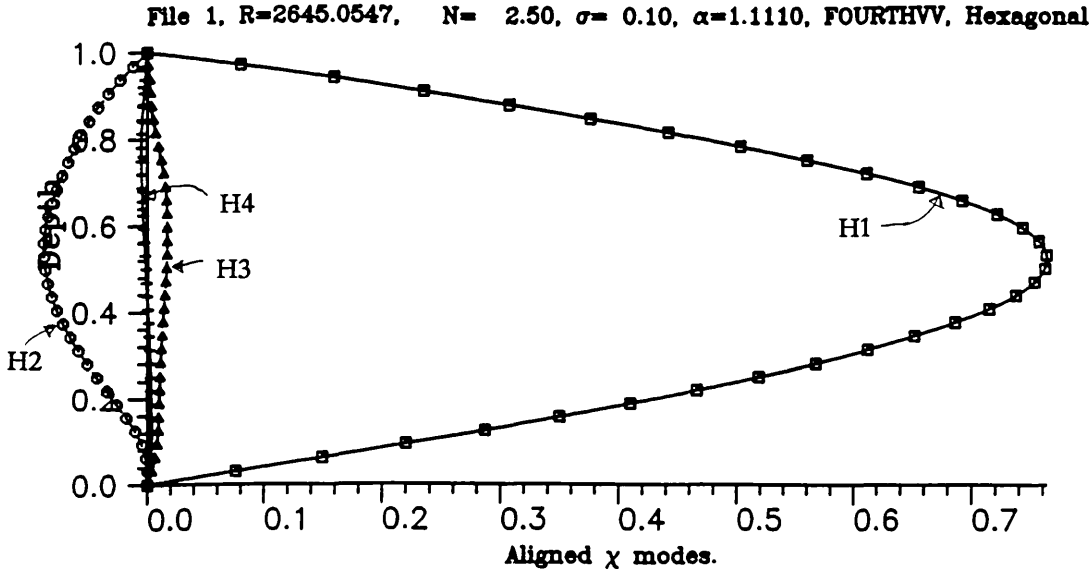


Fig. 5.2m).

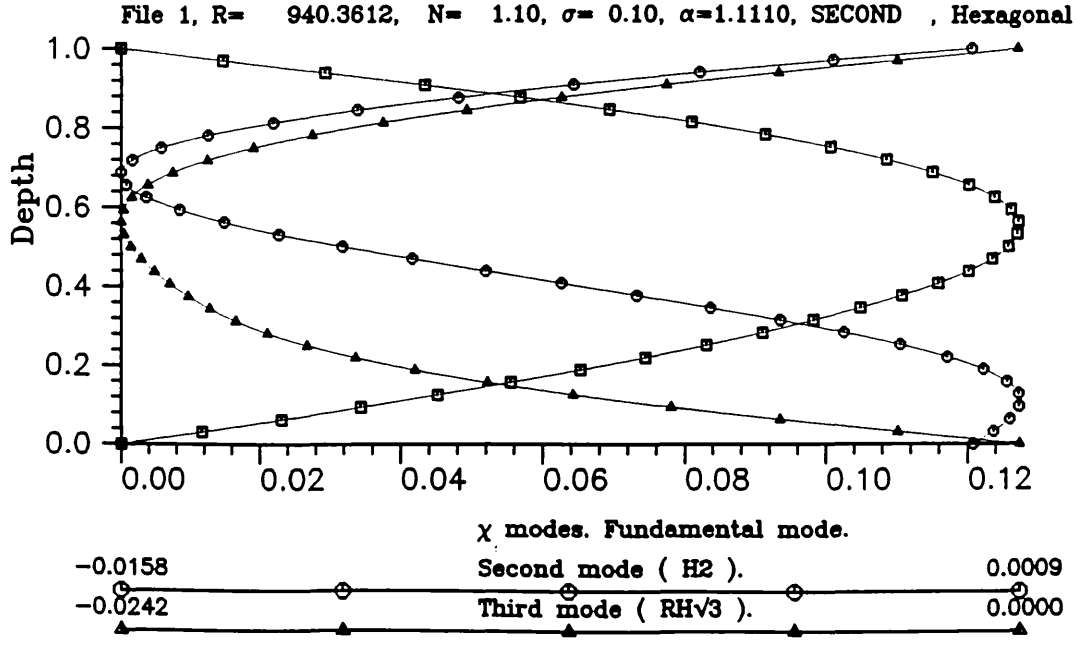
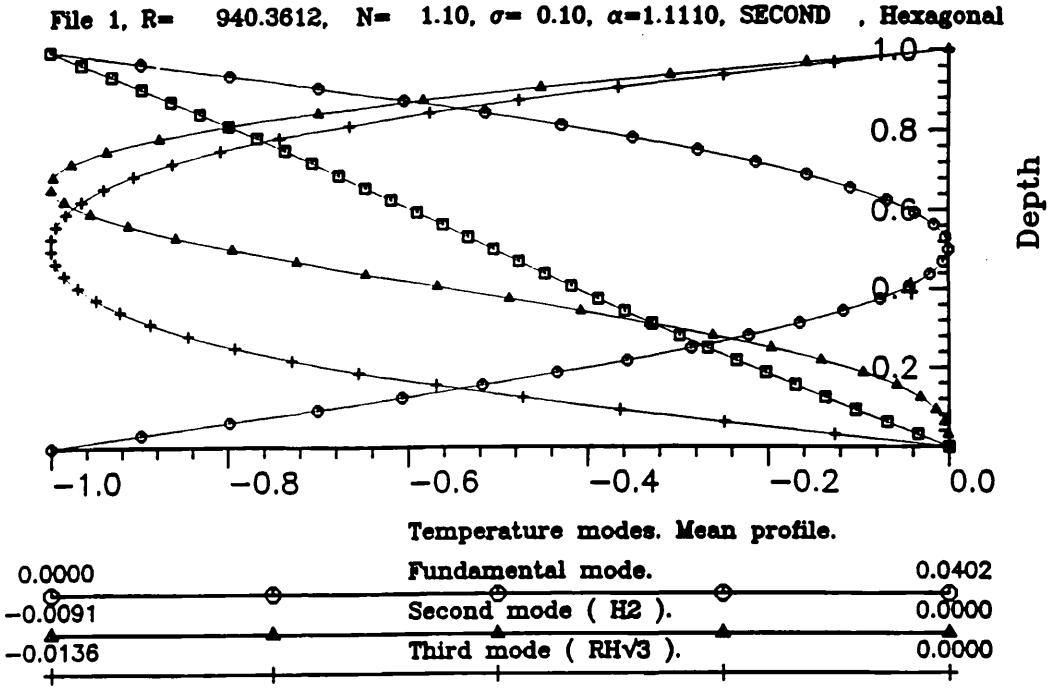


Fig. 5.2n).



versus Ra graphs since they show the first real indications of the effects of vertical vorticity. Both truncations which include vertical vorticity components show a different nature of curve, noticeable mainly because of the great reduction in the Nusselt number for a particular Rayleigh number at higher Rayleigh numbers. This demonstrates that, as the non−linear terms become important and the vertical vorticity components grow, the heat flux becomes severely restricted. This could be due to an increase in the horizontal velocity components with the stronger vertical vorticity, possibly at the expense of the vertical velocities, so that vertical motions are impaired, and, thus, so is heat transport.

Having considered the nature of the heat flux, and found an influence of the vertical vorticity upon the solution, it is now constructive to examine the individual terms of the solution of the vertical problem, to see how the modal truncations and the inclusion of vertical vorticity influence their nature, and to see if any particular terms dominate or are emphasized. Since such effects of interest are likely to be emphasized at greater amplitudes and non−linearity levels, it is sensible to examine a solution of high Nusselt number and low Prandtl number. The vertical dependences of the variables of such a solution, where Nu = 2.5, σ = 0.1 and the wavenumber is taken as the critical so that $\alpha = \alpha_c = 1.111$, are shown as figures 5.2.

Figure 5.2a) shows the fundamental χ mode for all the various modal truncations calculated except for the SECOND order system. The SECOND order results have been omitted from all these single variable modal comparisons since the comparisons are carried out at Nu = 2.5 which is not achieved by the SECOND system as described earlier. The variables for a SECOND order solution are shown separately as figures 5.2m) and 5.2n). The fundamental χ mode shows a smooth, single maximum near the centre of the layer, z = 0.5, which varies little in nature with any of the modal solutions except that the inefficient FFIRST solution biases its peak towards the top of the layer, and the amplitudes of the maxima are different. It is intuitively natural to expect that the inclusion of higher order harmonics is likely to sap the strength of the fundamental mode so that these other planforms may be supported and this is borne out in general. However, on inclusion of the vertical vorticity modes, the amplitude is allowed to rise above that value of the previous non−vorticity solutions. Nonetheless, it seems safe to say that each addition of a further vertical vorticity modal truncation still reduces the amplitude from the previous vorticity−inclusive truncation. The reason for this feedback into the main mode from the vorticity−generating modes may simply be that the planform structure supporting a vertical vorticity mode is based very closely on the fundamental mode, with the inclusion of some smaller scale infra−structures, and thus the degree of similarity of scale and structure alone may be enough to enhance the H1 structure of the convectional periodicity. The other harmonics operate on disparate scales which must tend to destroy the original structure. Notice once again though, that the full single mode solution, FFIRST, is disappointing in its portrayal of the mode, assuming that the higher orders, all of which agree to some extent, are correct.

The second χ mode, representing the vertical dependence of the H2 mode is a very different picture, as figure 5.2b) shows. Obviously, this mode is not included in either of the first order representations, but, on surveying the higher order approximations, it may be seen that the THIRDVV, FOURTH and FOURTHVV modal truncations all actually have a similar structure, but the THIRD system is completely different. The three higher approximations of the four all show a strong (O(0.1)), negative minimum near the middle of the layer, z = 0.5. The amplitude of this varies by 15% over the approximations, and the most noteable difference is that the THIRDVV approximation inserts small reversals in the dependence on the mode at the boundaries which are a factor of 10 weaker than the main dependence. This feature is not shown in the FOURTHVV representation, and therefore cannot be attributed conclusively to the inclusion of the vertical vorticity mode at this order. The THIRD system shows, surprisingly, a single, weak maximum whose amplitude is a third that of the other approximations,

but which is reversed in sign compared to the other approximations to become a positive maximum, and which is biased towards the bottom of the cell. The inclusion of higher order modes has had a dramatic effect on this particular mode, which is one of the ones included and studied in some of the previous calculations of other authors, and at this stage some signs are seen that the THIRD system of solution is different from the others in some respects.

The other mode previously included in other calculations was the RH$\sqrt{3}$ mode, and the vertical dependence of the χ streamfunction for this mode is exhibited in figure 5.2c). This mode does not show the surprisinging reversal of sign with the addition of higher order modes that the other second order mode, H2, does. Instead, this mode shows a single negative, minimum near the centre of the layer, the structure of which is preserved by all the modal truncation sets. Only the amplitude is affected by the truncations, the fourth order truncations being slightly stronger than their third order counterparts. The fourth order truncations are also more symmetric, centring their maxima marginally closer to $z = 0.5$ than the corresponding third order truncation solutions.

Figure 5.2e) shows the first vertical vorticity, ψ, mode, corresponding to the VH28 planform for the usual highly non−linear parameters and for the two modal truncations which support this mode, THIRDVV and FOURTHVV. The nature of the mode is distinctly different in the two cases. At the higher order, the strength of the mode, measured as its maximum amplitude, has decreased by a factor of six, and the distribution of the vertical dependence has altered from a concentration at the upper and lower boundaries for the THIRDVV case, to a more iso−amplitude distribution in the lower $3/5^{th}$'s of the layer, with a reversal of sign in the upper $2/5^{th}$'s, although the amplitude remains similar there. The FOURTHVV case still has definite maxima near the upper and lower boundaries like the THIRDVV case, but does not include the small reversal of sign near the centre of the layer as in the lower order solution. Notice, however, that in both cases the component is not negligible, having a value on the order of 0.1 at least, although the values at the boundaries are small.

Figure 5.2f) shows the second vertical vorticity, ψ, mode, present only in the FOURTHVV solution. This mode has a smaller amplitude than the first mode, reduced slightly by a factor of $3/10^{th}$'s measuring the maximum amplitudes, but also shows two similar strength maxima of opposite signs, one in the lower regime of the layer, the other in the upper, but also shows a third, weak reversal at the very top of the layer. The two fourth order vorticity modes taken together show a strong positive dependence on the vertical vorticity modes in the lower half of the layer, and a strong negative dependence in the upper half, with virtually no vorticity at the upper boundary, and quite strong vorticity at the lower.

Overall, the vertical vorticity generation seems to take place in layers close to the boundaries. As can be seen more clearly later, the introduction of higher harmonics has produced a flow with similar structure but with broad up−flowing plumes and sharply defined down−flowing walls, and the non−linear nature of this solution at these parameter levels has introduced not only the evident vertical vorticity but also strong thermal and velocity boundary layers. The generation of vorticity mainly in layers close to the boundary could be the results of the strong plumes and walls hitting or separating from the boundary layers. The increased strength of the vorticity at the lower boundary would then imply that the arrival of the downward sheet−like walls and the separation of the upward broad plume create more vertical vorticity than do the arrival of the plume and the removal of the wall from the upper boundary layers.

Next, examine the effect of the modal truncations on the temperature variables as shown in figures 5.2g)−5.2k). One of the most important indicators of the non−linear effects is the distortion of the mean temperature profile from its linear, conductive state. Figure 5.2g) shows $T_0(z)$ for the modal truncations at the usual parameters of Nu = 2.5, σ = 0.1, $\alpha = \alpha_c$ = 1.111. At such non−linearity levels, the distortion is expected to exist, so that an isothermal region pervades the interior of the fluid, with thermal boundary layers at the top and bottom boundaries. This structure indeed exists in the FIRST, THIRDVV and FOURTHVV modal truncations, but is a reduced effect in the other truncations. The isothermal region, if it exists, is confined to the middle $4/10^{th}$'s of the layer, and the increasing order of modal truncation simply increases the temperature of this region. Notice that the most advanced approximation, the FOURTHVV system, actually forces this isothermal region of the mean temperature profile to exist at a temperature mid−way between the boundary temperatures (T = −0.5 in this case), whereas previous modal models have this region slightly cooler. The FFIRST solution is unnaturally cold, perhaps due to its inefficient heat transport at this σ. The higher order models which omit the vertical vorticity appear unable to maintain the isothermal nature and tend towards the more conductive, linear mean temperature profile. It appears that the vertical vorticity with its increase in the horizontal motions of the fluid enables the fluid to contain its heat within particular layers reducing the vertical flux of heat, whereas the other solutions without the increased horizontal motions, allow a greater, more even distribution of the temperature field.

Studying the fundamental temperature mode and its second order harmonics once again shows that the modal truncations show their most dramatic effect in the aligned harmonic mode, H2, although overall, these temperature modes show much more variation with the truncation set, than do the streamfunction modes. The

fundamental temperature mode shown in figure 5.2h) is as before affected mainly in amplitude by the different modal truncations. As for the χ modes, the vertical vorticity modes sustain the maximum amplitude at a value near that obtained from the single mode equations. The vertical vorticity solutions show a single, positive maximum, centred slightly lower than the middle of the layer once again, which is much smoother than the other solutions, some of which show a peaked bias towards the top (FIRST) or bottom (FOURTH). The FOURTH order solution mode shows a much reduced maximum, its harmonics having bled the fundamental of its strength without any enhancement from a vertical vorticity mode.

The H2 mode of temperature (figure 5.2i)) shows an extreme variation with the modal truncation. The fourth order truncations have roughly twice the maximum amplitude of the third. The third order modes are both completely negative, with a maximum near the lower boundary, with the THIRDVV solution also having a strong maximum near the upper boundary, lacking in the THIRD solution. The fourth order solutions are both completely positive, with the FOURTH mode being a simple, single minimum, based at $z = 0.6$, whereas the FOURTHVV mode shows a maximum higher up at $z = 0.8$ with a small isothermal regime around the $z = 0.4$ region, before steeply climbing to the boundary temperature.

The RH$\sqrt{3}$ temperature mode (figure 5.2j)) also shows some variation with the modal truncation although not as much as the above. The THIRD and FOURTH representations are similar in that they present a peak biased either towards the bottom or top boundary respectively, both holding a large body of the fluid with a strong negative influence of this mode, whereas the vertical vorticity solutions at THIRDVV and FOURTHVV show a weaker centre to the layer with strong minimums above and below this region, possibly as part of the boundary layers, although now the whole layer is generally more weakly influenced by this mode.

It is also interesting to note the effect of going up to full fourth (FOURTHVV) order on the full third order (THIRDVV) modes which exist with a vorticity generating planform i.e. the VH28 modes of temperature and streamfunction, χ. These are shown as figures 5.2d) and 5.2k), and it can be seen that the addition of a further vorticity generating mode (plus two weak reduced modes) severely depletes the first vorticity mode. The extra harmonics reduce the amplitudes of motion due to the first vorticity mode for both temperature and χ, and, although the actual structure of the modes is not completely different, the additional modes allow a change of the dependences at the boundaries, setting up weak reversals of the temperature dependence at either boundary, and destroying one weak χ counter−cell at the lower boundary. Notice how again, in general, the highest order, FOURTHVV, has tended to regenerate

the symmetry of the vertical structure to form a smoother and more simple structure, a feature which will be seen often.

Figure 5.2l) is included to indicate the relative strengths of modes as they appear in the modal expansion sequence. The fundamental hexagon produces a series of aligned modes, H2, H3, etc. which are merely replicas of the original hexagon but scaled down each time. The figure shows that the fundamental mode dominates the higher order harmonics, and that the amplitude of each aligned mode does indeed decrease by roughly a factor of 10 at each order (a fact which was widely used in the initial approximations to the higher order solutions). Other higher order modes (greater than second order) have not been mentioned, nor will be in great detail, because explicit explanation of their nature only serves to confuse the issue, and offers little physical insight into the physics of the flows. In a modal calculation, it should be noted that the highest modes are always suspect since, in an attempt to close the system, they try to contain all the higher order mode information that has actually been excluded and thus are often unphysical.

A synopsis of the above results for the vertical dependences might suggest the following results. The mean temperature exhibits the expected distribution, with an isothermal region bounded by thermal boundary layers, aided by the restraining nature of the included vertical vorticity structures. The fundamental mode is strong and is positively unidirected throughout the layer, whereas the two first overtones are included generally in their negative form, with their strongest temperature influence in boundary layers near the top of the fluid and near the bottom, albeit weakly overall. In general, the temperature harmonics tend to build and act in the thermal boundary layers. The vorticity modes tend to concentrate the motion into two distinct regions, divided slightly above the centre of the layer, with the influence of the modes positive in the lower half, and negative in the upper. The influence is stronger in the lower half by a factor of two, and tends to concentrate towards the boundaries. This concentration infers that vertical vorticity is generated as broad plumes or sheet−like wall flows hit or leave the boundary layers. The vorticity generating modes are stronger than other modes of the same order and are in general akin in strength to the second order modes. The other streamfunction, χ, has a smooth, positive, single maximum fundamental mode, much as for the temperature, but here the harmonics, negative but once again smooth, single maxima, are also strong, being of similar orders of magnitude. The low order harmonics (e.g. H2, RH$\sqrt{3}$) all tend to strengthen and broaden the central plume, but emphasize different aspects of the downflowing sheet wall. For example, H2 will emphasize the vertices of the original H1 but reduce the mid−walls, whereas RH$\sqrt{3}$ will disrupt the vertices and build the walls in between

(these may be seen more clearly in the vertical velocity plots later). The higher order harmonics tend to restore the original format of the H1 cell, but retain the strong central plume and narrow walls, the increased pumping of the vertical velocity enhancing the boundary layer effects in the flow (although these effects are small at the parameter levels shown). Most harmonics sap the fundamental, but the vertical vorticity modes with their similar scales of structure feed back into the H1 mode and emphasize the plume and sheet flow.

Thus, it is seen that the vertical vorticity, although not large, is also not negligible and indeed appears to exhibit various effects on the global variables of the flow, such as the heat flux. It is now necessary to find out if the vertical vorticity is strong enough to influence the more tangible aspects of the flow, such as the flow pattern itself.

Figures 5.3a)−g) and 5.4a)−g) show surface maps and contour plots of the vertical velocity at various levels in the layer for Nu = 2.5, σ = 0.1 and at the critical wavenumber, $\alpha = \alpha_c = 1.111$, and for various modal truncations. Plots of vertical velocity are possibly those numerical results most closely associated with the features shown by experimentation in such techniques as shadowgraph photography. The plots all show a periodic section, $0 \leqslant x \leqslant 2\pi/\alpha\sqrt{3}$, and $0 \leqslant y \leqslant 2\pi/\alpha$, and are evaluated at six almost evenly spaced intervals throughout the layer. The 'almost' implies that the very top and bottom are not shown, since the vertical velocity is zero there, but the layers very close to the top and bottom where boundary layers may exist are shown instead. The contour plots show the same region and the same depths, drawn with 10 regularly spaced contour heights with positive, or upflowing, velocity shown as broken contours, and negative, or downflowing, fluid as continuous lines. The surface plots all have the surface elevations exaggerated to fill the available space, so that the small scale features of the higher order solutions may be seen, but also show as annotation the maximum and minimum values of the velocity plotted, so that a scale maybe borne in mind. For all the surface plots of vertical fields, the surfaces are split into positive and negative fields, with the negative fields shown reversed on the ~~left~~ right of the picture, so that none of the features of the surfaces are hidden. The negative velocity field unfortunately had to be shown upside−down since the surface plotting routines used did not allow viewing from below a surface as would have been preferred. For both surfaces, anything which is not of the correct sign for that surface is set to zero. This technique is important since the upward and downward flows often show strongly different features, highlighting the asymmetry of hexagonal flows due to the coupling constant, C, being non−zero.

The addition of the various harmonics at each stage can be seen to change the vertical velocity quite dramatically. The single mode solutions (FIRST and

Figure 5.3a). Hexagonal Rayleigh–Benard convection.
Vertical velocity surfaces at various depths (+ve left)
R=1887.4737, N= 2.50, α=1.111, σ= .00, first

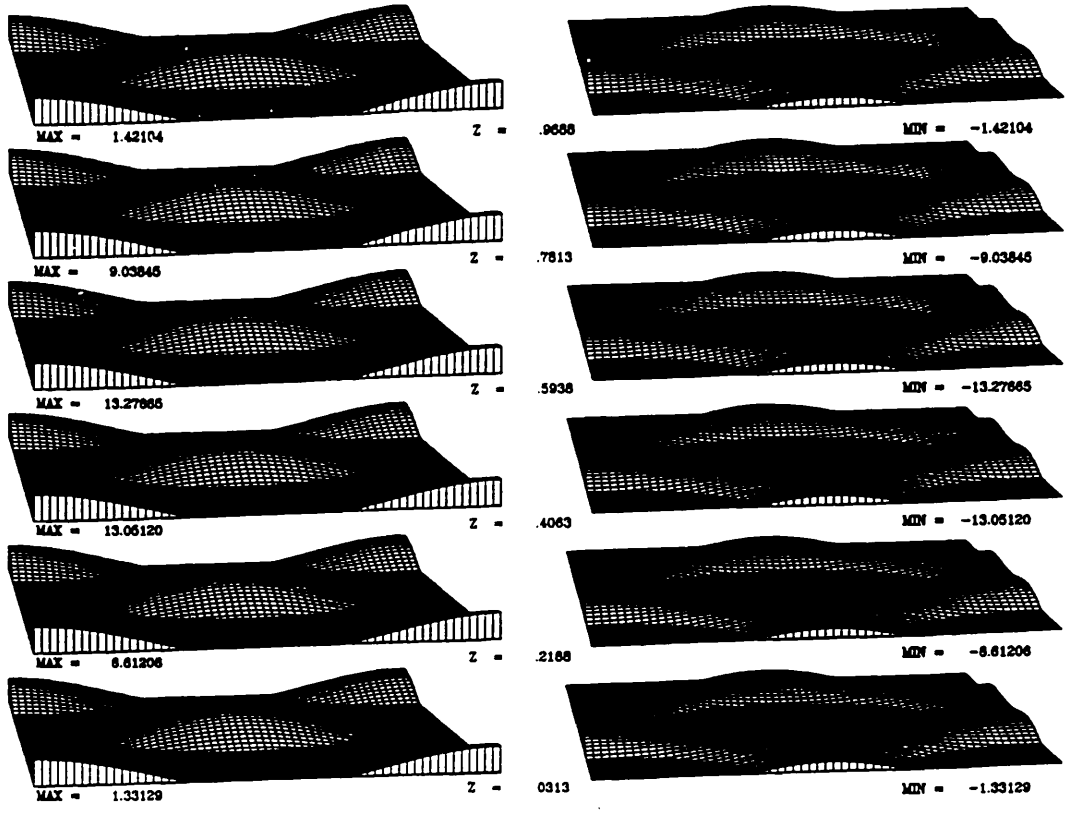


Figure 5.3b). Hexagonal Rayleigh–Benard convection.
Vertical velocity surfaces at various depths (+ve left)
R= 11747.9921 N= 2.50, α=1.111, σ= .10, ffirst

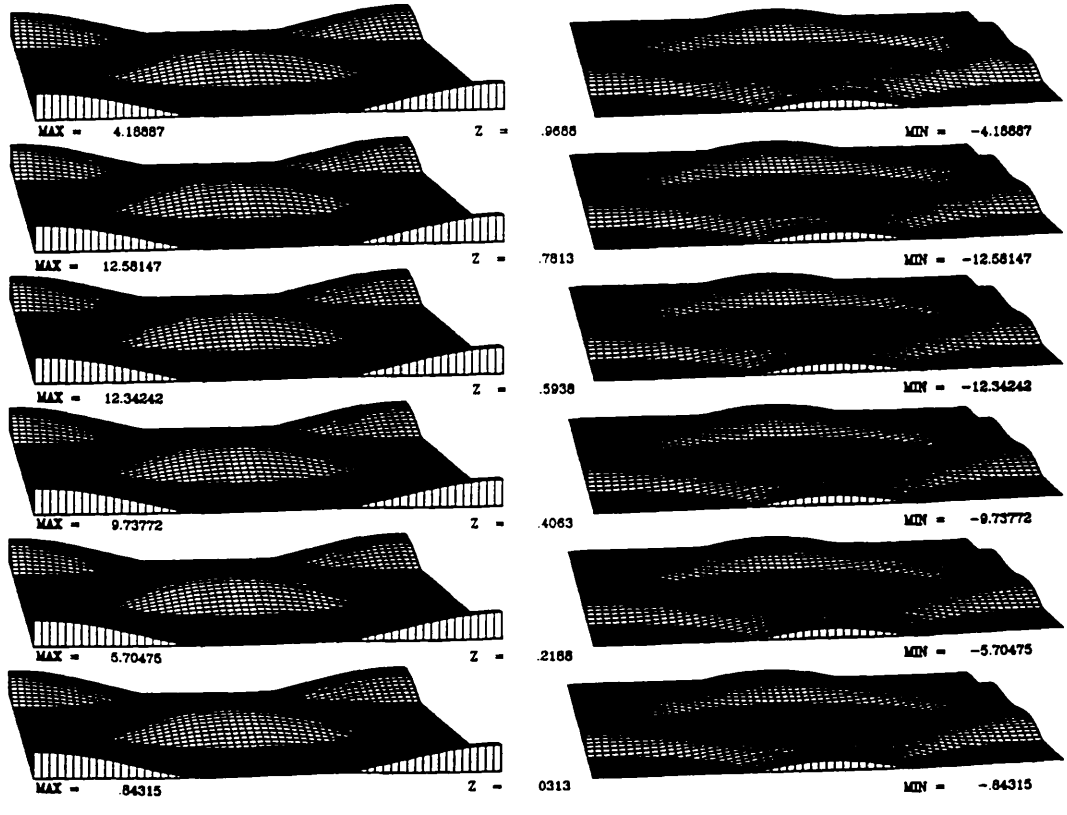


Figure 5.3c). Hexagonal Rayleigh–Benard convection.
Vertical velocity surfaces at various depths (+ve left)
R= 940.3612, N= 1.10, α=1.111, σ= .10, second

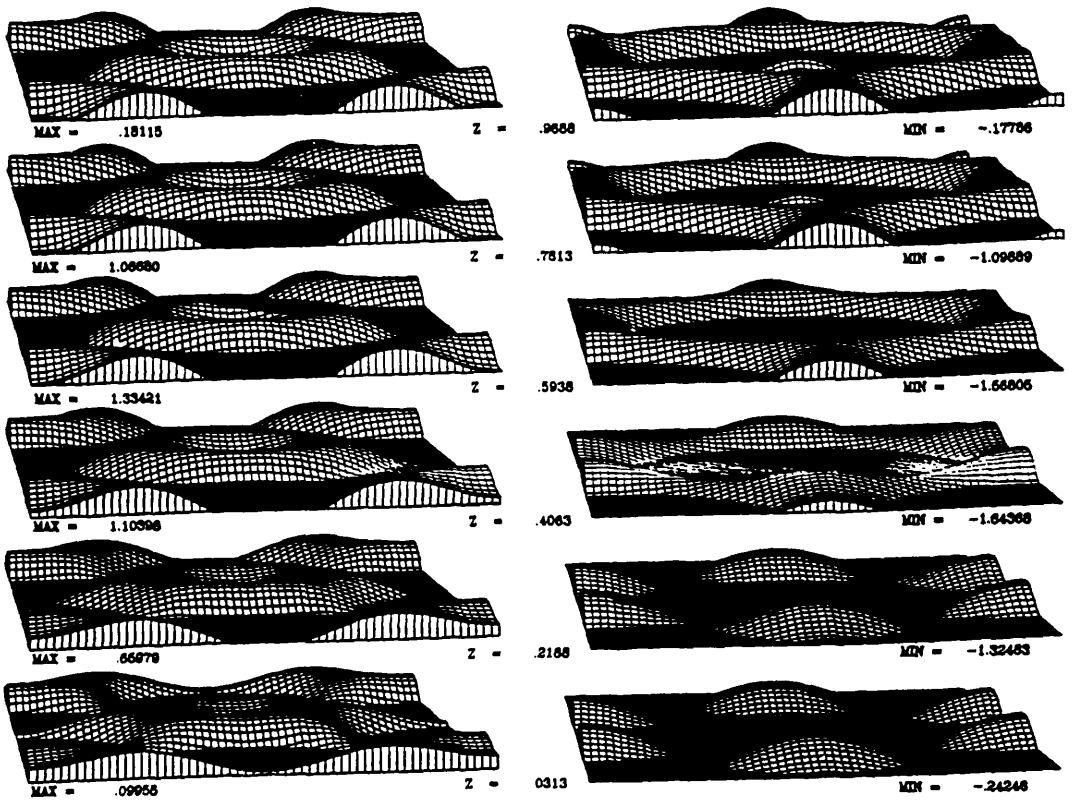


Figure 5.3d). Hexagonal Rayleigh–Benard convection.
Vertical velocity surfaces at various depths (+ve left)
R=2504.3849, N= 2.50, α=1.111, σ= .10, third

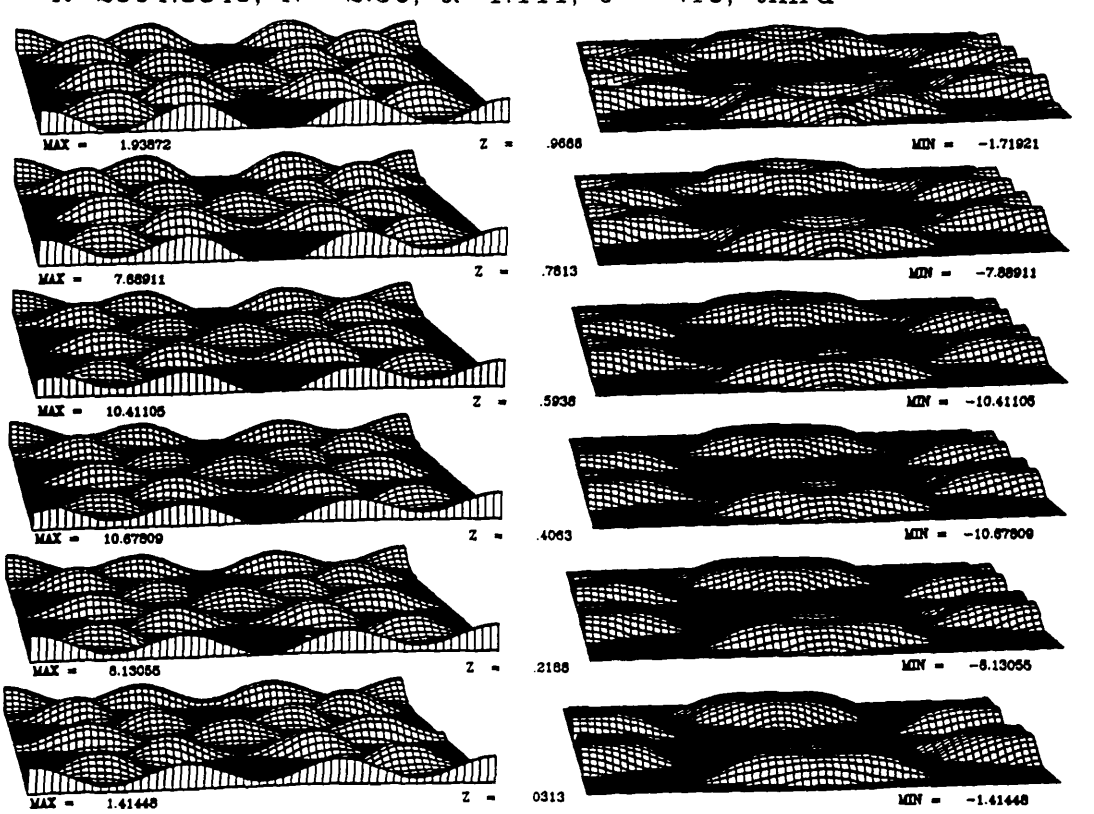


Figure 5.3e). Hexagonal Rayleigh–Benard convection.
Vertical velocity surfaces at various depths (+ve left)
R=5815.9607, N= 2.50, α=1.111, σ= .10, thirdvv

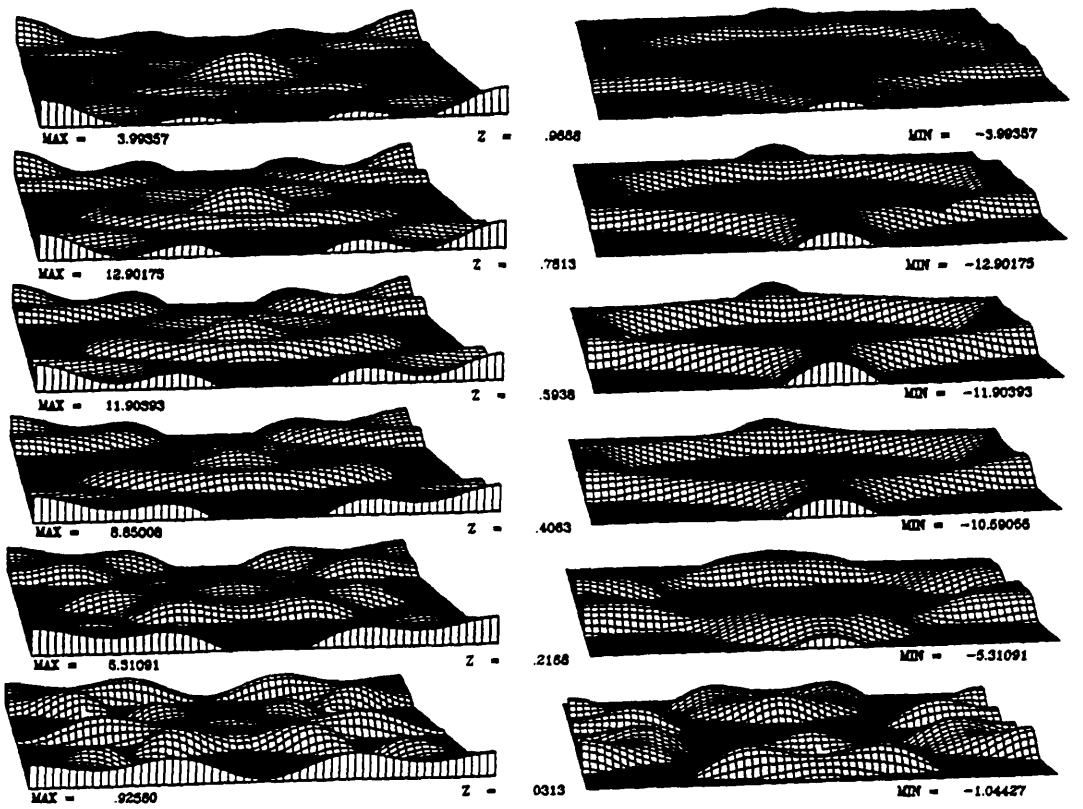


Figure 5.3f). Hexagonal Rayleigh–Benard convection.
Vertical velocity surfaces at various depths (+ve left)
R=2770.5681, N= 2.50, α=1.111, σ= .10, fourth

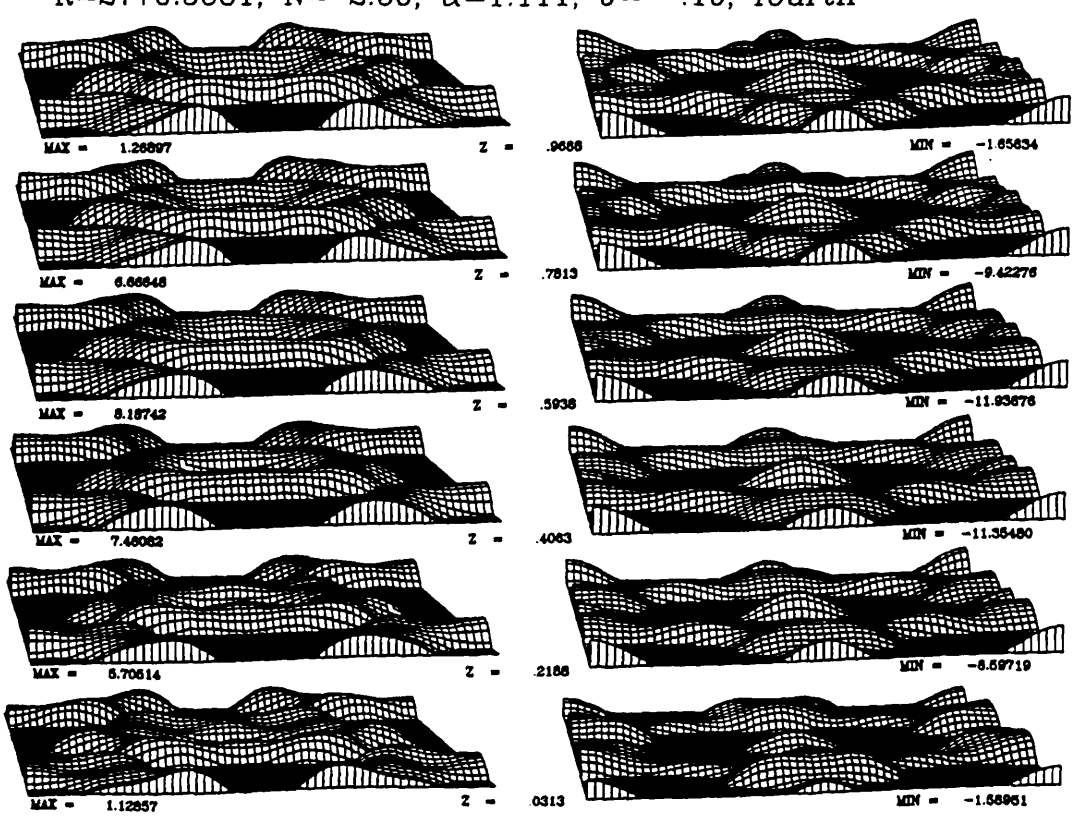
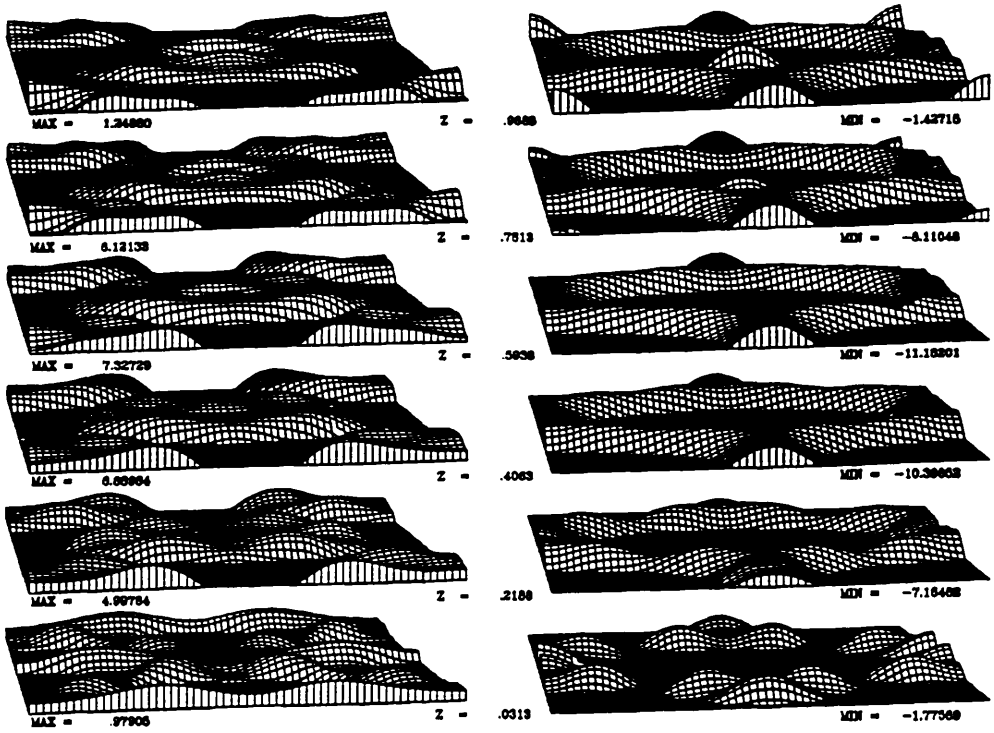


Figure 5.3g). Hexagonal Rayleigh-Benard convection.
Vertical velocity surfaces at various depths (+ve left, -ve right)
R=2645.0547, N= 2.50, α=1.111, σ= .10, fourthvv



FFIRST) shows the planform hexagon structure very clearly, with smooth downflowing walls and a gentle transfer to upflow in the centre of the hexagons i.e. fairly wide walls and thin plumes, demonstrating a reasonable degree of up/down equality in the flow. The same structure is seen throughout the layer, the fields being very similar at all depths apart from the decrease in amplitude towards the boundaries. The FFIRST solution biases the maximum amplitude towards the top of the layer, creating a strengthened upper boundary layer. Inclusion of the first aligned and rotated modes, H2 and RH$\sqrt{3}$, changes the structure of the planform shape, and introduces a difference between the lower parts of the layer and the higher. The top of the layer shows an increase in the definition of the hexagonal cell wall structure as the central plume broadens and strengthens even allowing a second change of direction in the vertical velocity so that the flow is downwards at the very centre. As z decreases, the definition of the walls is reduced by such harmonics as RH$\sqrt{3}$ in favour of strength of downflow centred at the vertices of the original hexagonal structure, until near the lower boundary, the vertical velocity is concentrated both upwards and downwards in fairly strong, wide plumes. This asymmetry is enlightened by figures 5.2m) and 5.2n) which show the vertical dependences for the SECOND system of equations, at the (lower than usual) Nusselt number of Nu = 1.1. Both the temperature

and χ modes show symmetrical vertical dependences apart from the modes representing the H2 planform, which have a single maximum biased towards the top of the layer with a section at the lower boundary where the mode is weak. This implies that the influence of the H2 harmonic is confined to the upper sections of the layer, leaving the rotated harmonic, RH$\sqrt{3}$, to dominate at the bottom. This type of structure can clearly be seen, but note that no comment can be made about the amplitude of motion since the plots shown are plotted for the maximum available Nusselt number for the SECOND order, Nu = 1.1, rather than that Nu = 2.5 as the rest of the plots are calculated. At THIRD order, only a H3 mode is added, but the effect is quite dramatic. The field becomes once more much more similar throughout the layer, but now with the emphasis on the vertex structure again rather than the hexagonal walls. This seems to imply that the RH$\sqrt{3}$ and H3 harmonics are dominating strongly throughout the layer, and this may be accounted for by the strange reversal and weakening of the H2 vertical structure at this order (figures 5.2b), 5.2i)). At FOURTH order, with no vertical vorticity, figures 5.3f) and 5.4f) show that some wall−type structure is returned but the vertex nature is still strongly disruptive, especially in the lower layers. Addition of vertical vorticity at THIRDVV and FOURTHVV orders with the H1−based vorticity structures restores the importance of the wall−type flow in the upper half of the layer, but leaves a complicated harmonic flow in the bottom half. The THIRDVV solution reverts to a more complicated version of the SECOND solution structure with more variation in the vertex flow or the walls and the stronger vertical velocity maximum, but much the same structure, whilst an advance to FOURTHVV has a further broadening and strengthening effect on the central plume and thus a sharpening effect on the walls in the upper layer, making them strong and narrow, whilst making the vertex flow at the lower boundary less of a single strong plume, and more of a divided plume. The inner region of downward flow at the centre in the upper layer is also enhanced once more, so that the inner trough reaches the same negative strength as the walls, and the lower vertex divides into a triplet of plumes. Notice that the amplitude of the vertical velocities has not been significantly reduced by the inclusion of the vertical vorticity modes. Notice also that the break up into harmonic plume−like flow at the bottom of the layer appears to have broken the previous cellular nature of the flow. The downflowing walls of the original hexagonal structure now have an upward flow at some points on their planes near the lower boundary, thus contradicting the definition of a cell wall (which requires flow all of one sign on the plane). However, these reverse flows on the walls introduced by the asymmetry with depth are very weak and are confined to very thin layers at the lower boundary, even then only occuring at very specific points and therefore are

Figure 5.4a). Hexagonal Rayleigh-Benard convection, Vertical velocity
R=1887.4738, N=2.5000, σ= 0.00, α=1.111, first

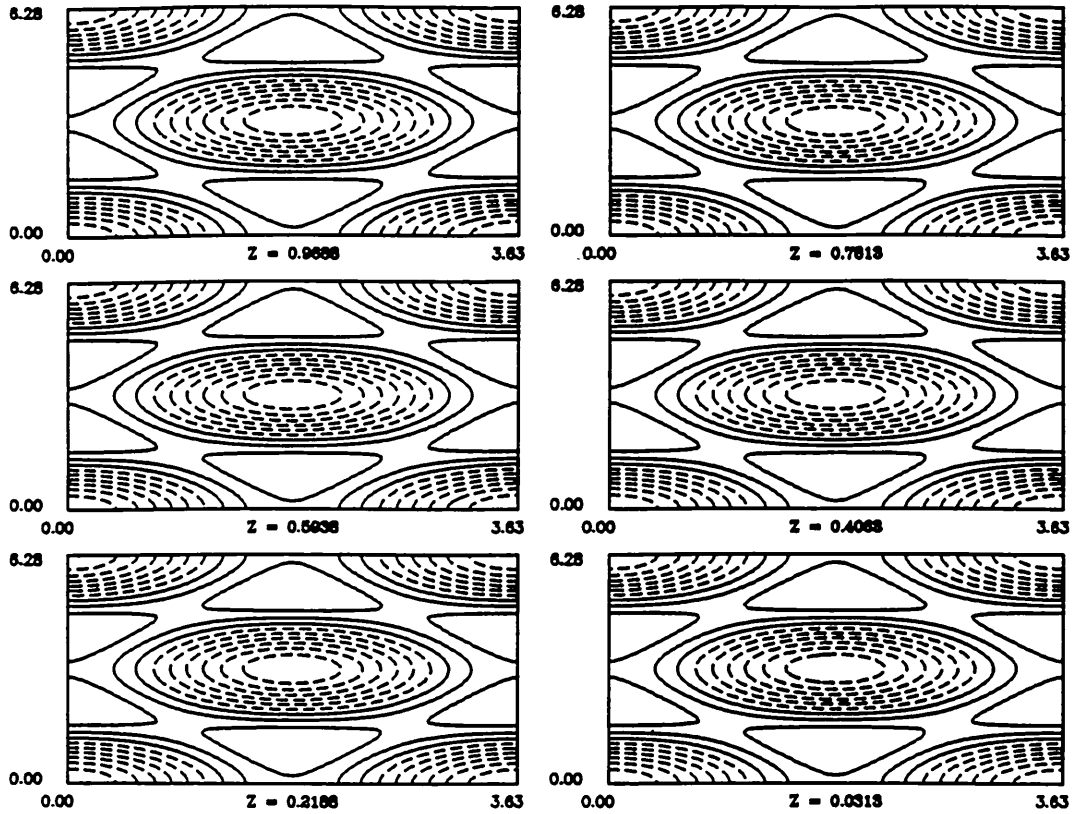


Figure 5.4b). Hexagonal Rayleigh-Benard convection, Vertical velocity
R= 11747., N=2.5000, σ= 0.10, α=1.111,ffirst

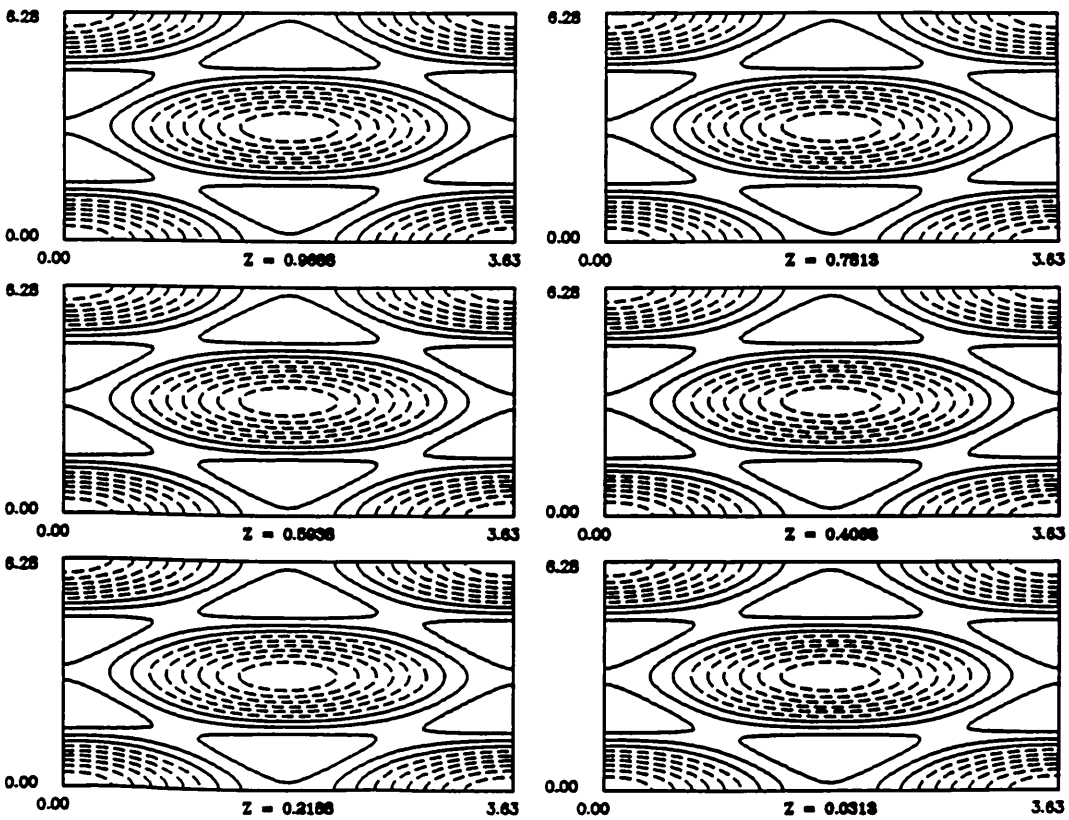


Figure 5.4c). Hexagonal Rayleigh–Benard convection, Vertical velocity
R= 940.3612, N=1.1000, σ= 0.10, α=1.111, second

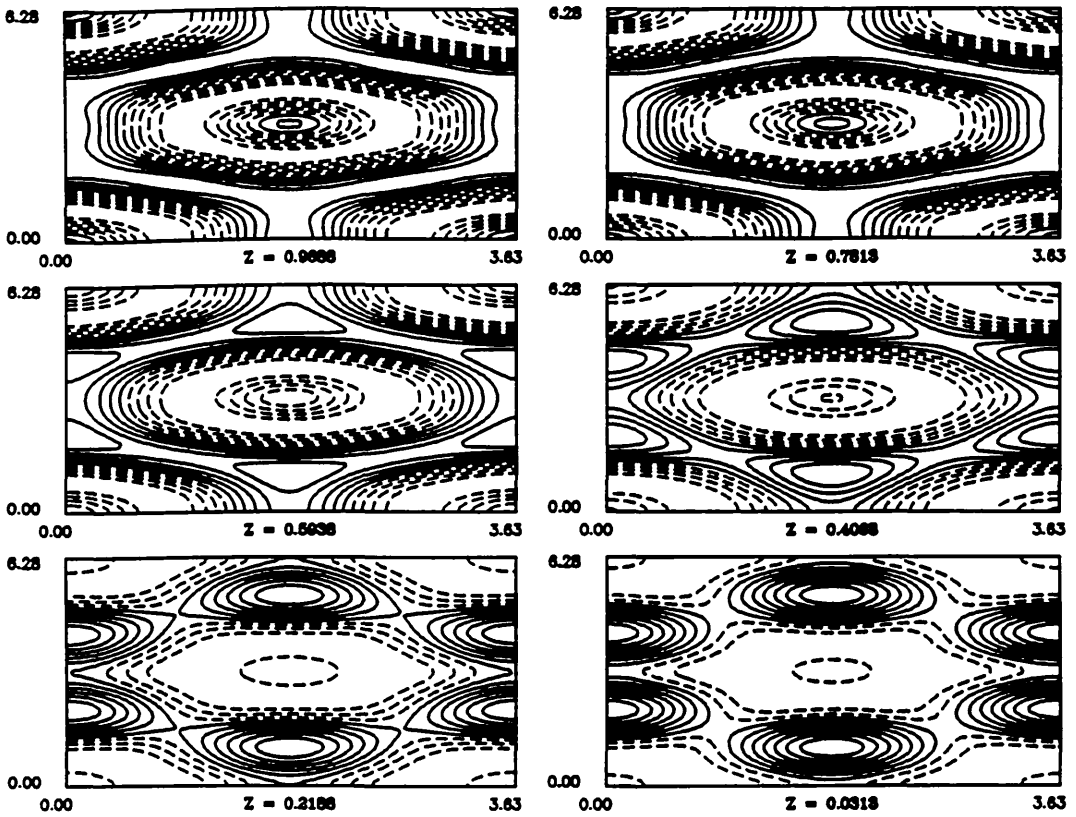


Figure 5.4d). Hexagonal Rayleigh–Benard convection, Vertical velocity
R=2504.3848, N=2.5000, σ= 0.10, α=1.111, third

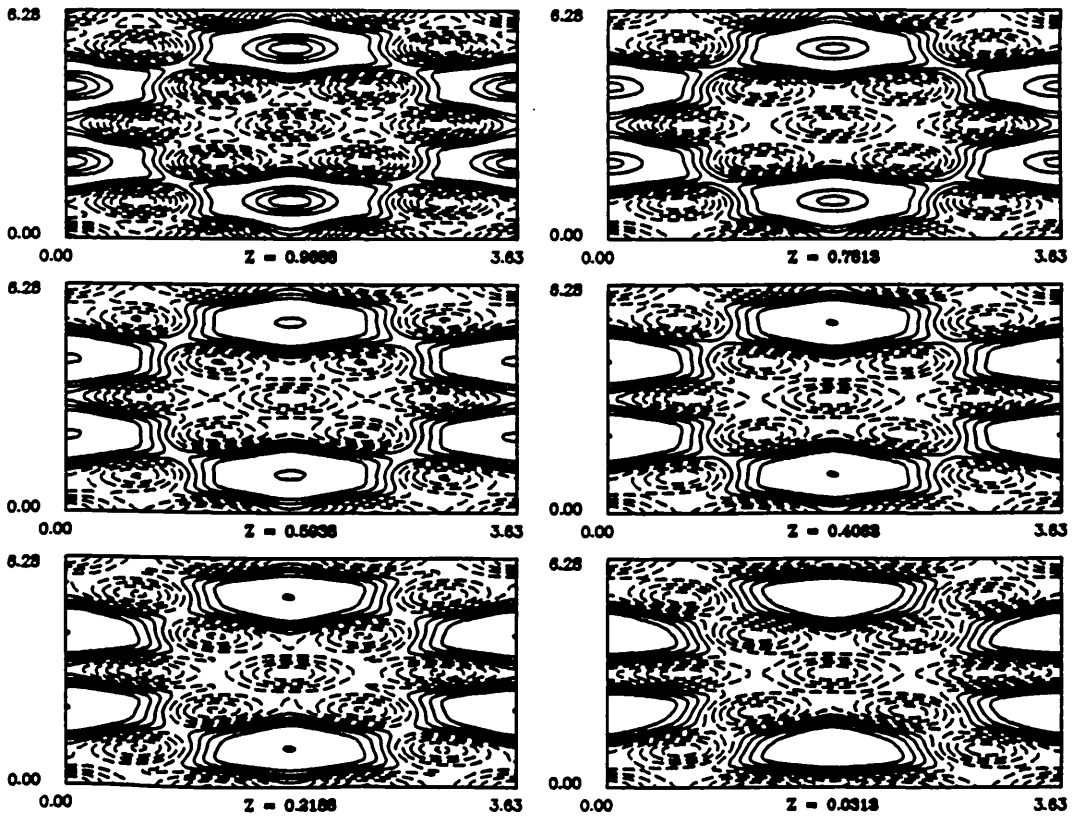


Figure 5.4e). Hexagonal Rayleigh–Benard convection, Vertical velocity
R=5815.9604, N=2.5000, σ= 0.10, α=1.111, thirdvv

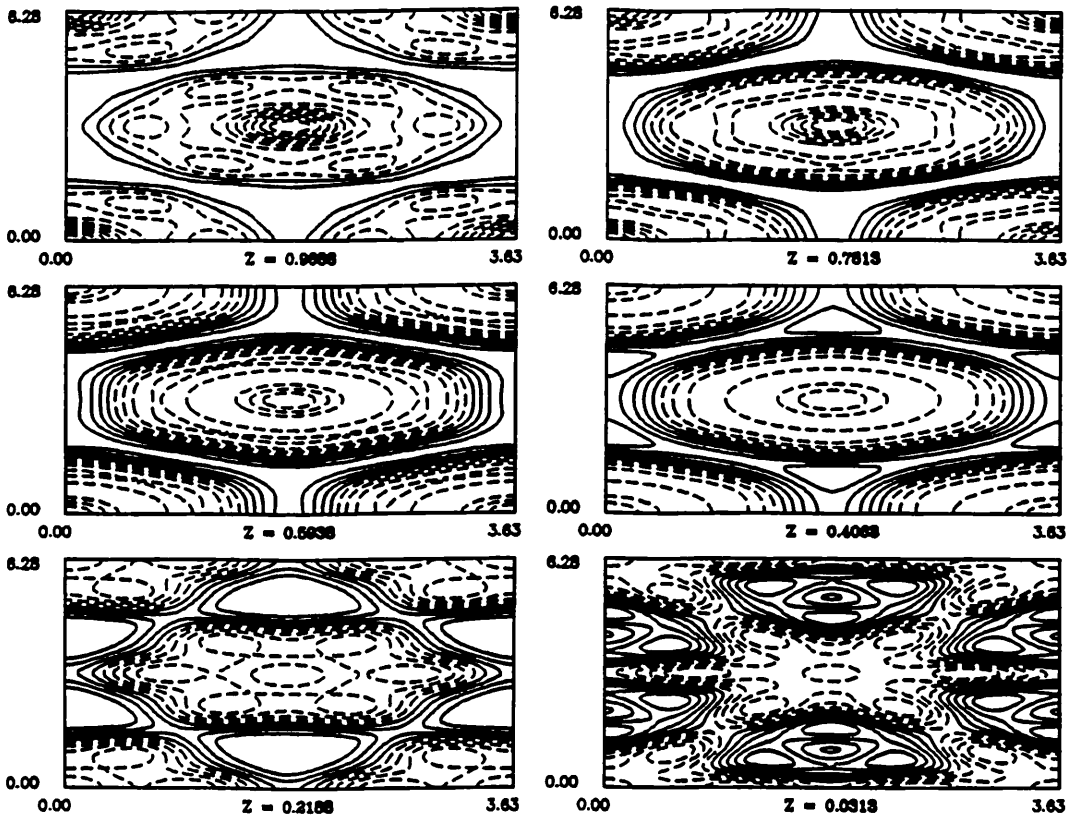


Figure 5.4f). Hexagonal Rayleigh–Benard convection, Vertical velocity
R=2770.5681, N=2.5000, σ= 0.10, α=1.111, fourth

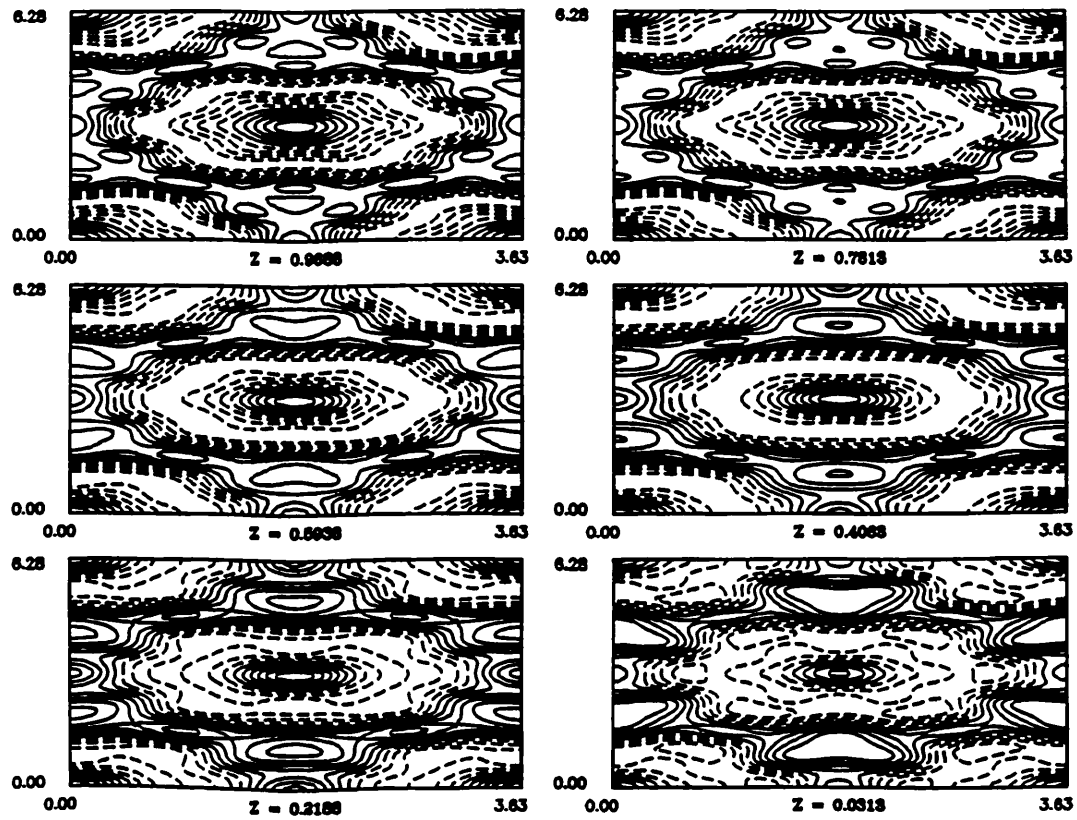
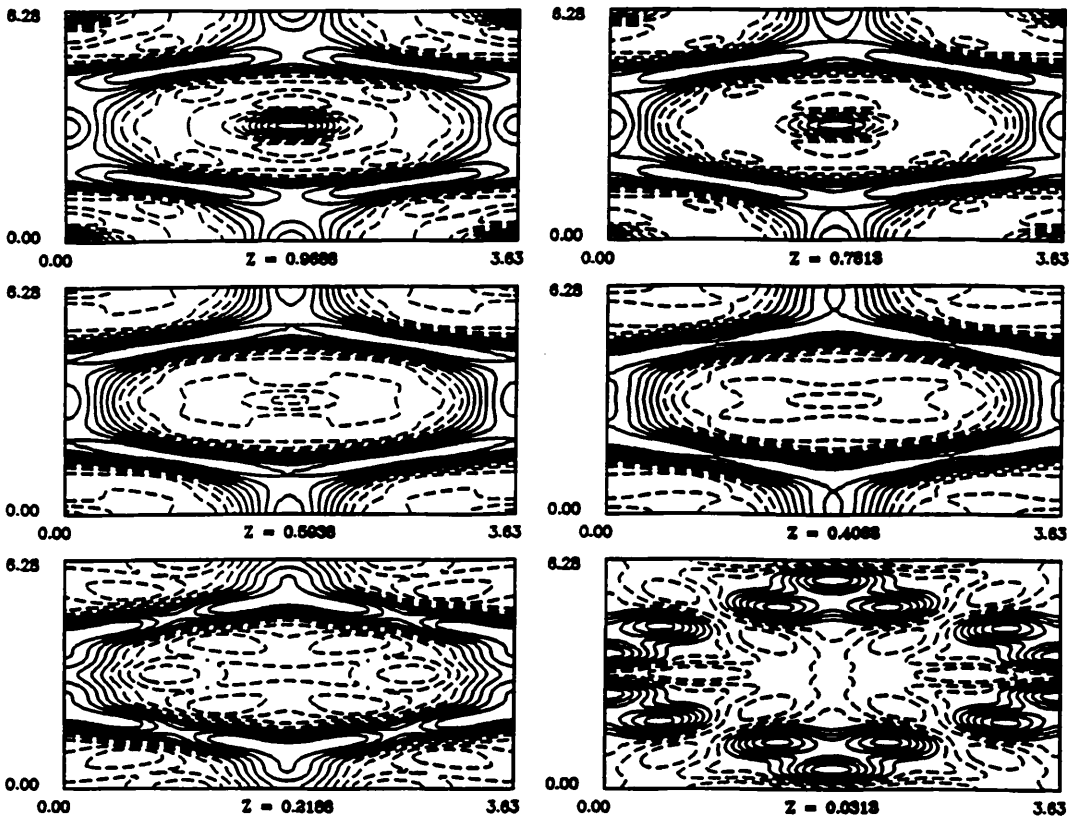


Figure 5.4g). **Hexagonal Rayleigh-Benard convection, Vertical velocity R=2645.0547, N=2.5000, σ= 0.10, α=1.111, fourthvv**



considered not very significant, but noteworthy nonetheless. The same cannot be said for the square symmetry (see later).

Figures 5.5 and 5.6 show similar surface and contour plots for the vertical vorticity content of the THIRDVV and FOURTHVV mode. The THIRDVV solution shows a strong positive vertical vorticity pattern near the top and the bottom of the layer with a small region of reversed vorticity slightly below z = 0.5, as shown in figure 5.2e) for the vertical dependence. Enhancement to the FOURTHVV system destroys this structure, as explained earlier in reference to figure 5.2f), concentrating the vertical vorticity in the lower half of the layer, whilst weakening overall by a factor of two in the maximum amplitudes. The contours show more clearly the balance between the two available vorticity planforms in the FOURTHVV system, the THIRDVV having only a single mode which it can mould with the vertical dependence envelope. The plots of vertical vorticity for FOURTHVV in figure 5.6b) show that the second vorticity planform, VH52, is clearly evident, since an inner ring of vorticity cells are evident often, although the influence of the first, VH28, is often stronger. Close to the bottom boundary, both are strong, creating a high vertical vorticity there, but the VH28 is the stronger mode and its influence can be seen to be the major one. Similarly towards the top, the two planforms superpose, with a negative planform

Figure 5.5a). . Hexagonal Rayleigh–Benard convection.
Vertical vorticity surfaces at various depths (+ve left)
R=5815.9607, N= 2.50, α=1.111, σ= .10, thirdvv

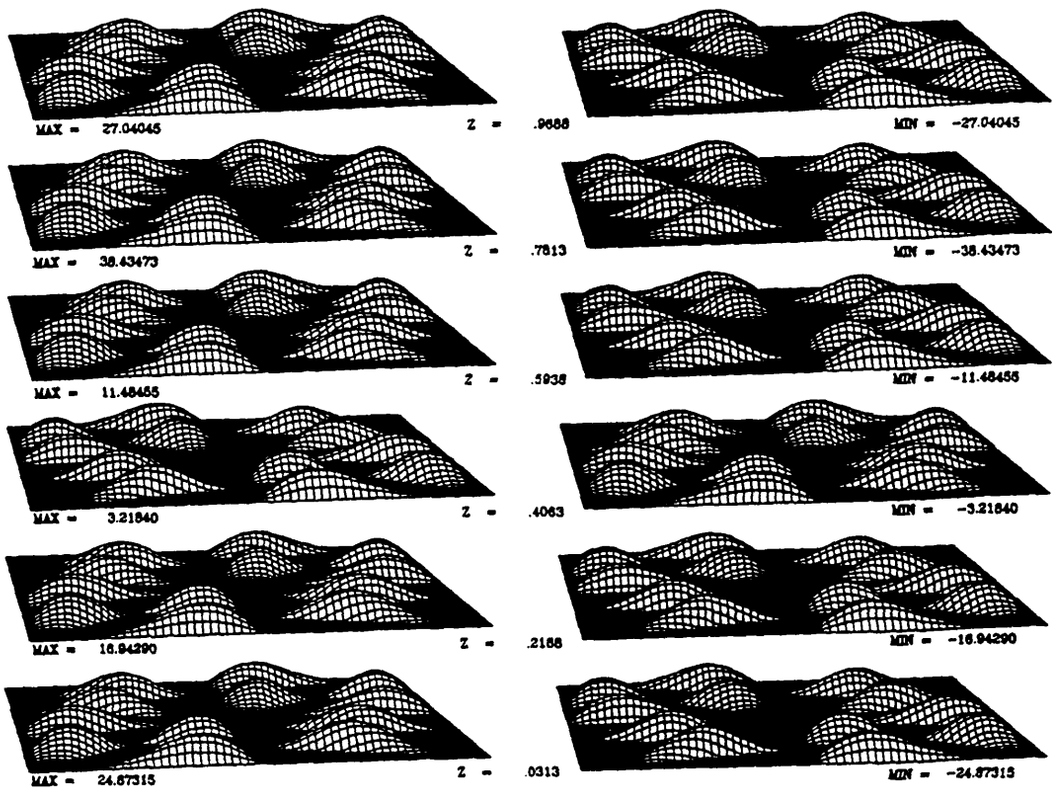


Figure 5.5b). . Hexagonal Rayleigh–Benard convection.
Vertical vorticity surfaces at various depths (+ve left)
R=2645.0547, N= 2.50, α=1.111, σ= .10, fourthvv

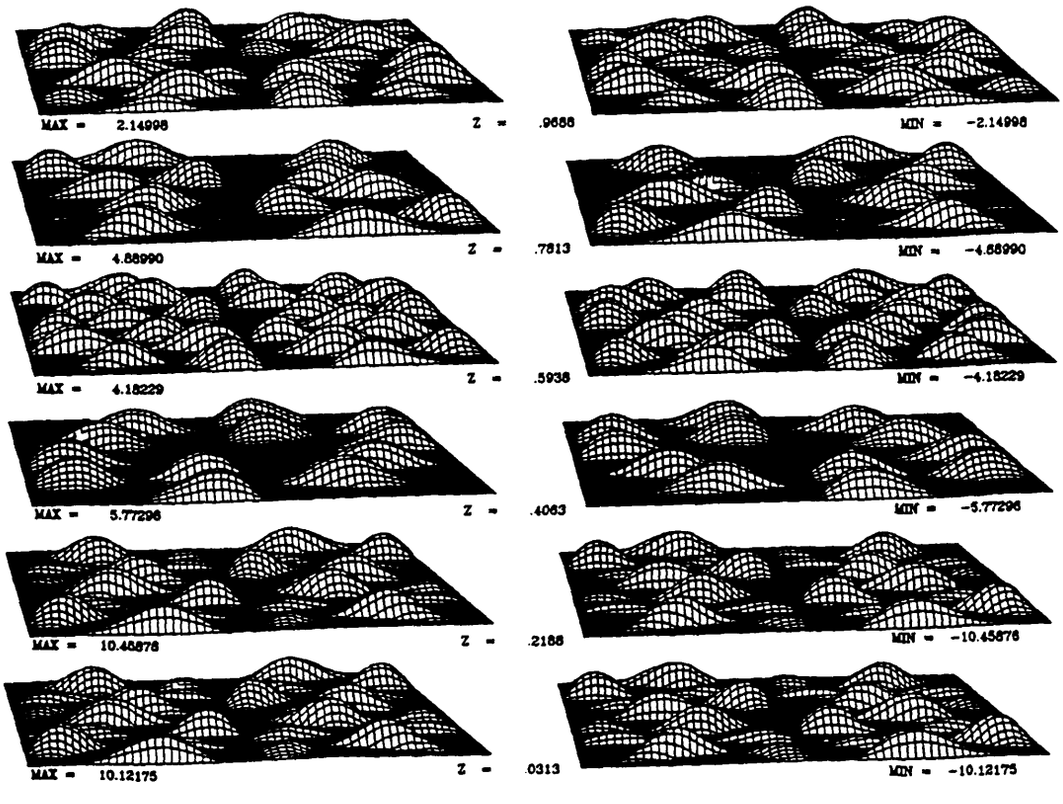


Figure 5.6a). Hexagonal Rayleigh–Benard convection, Vertical vorticity
R=5815.9604, N=2.5000, σ= 0.10, α=1.111, thirdvv

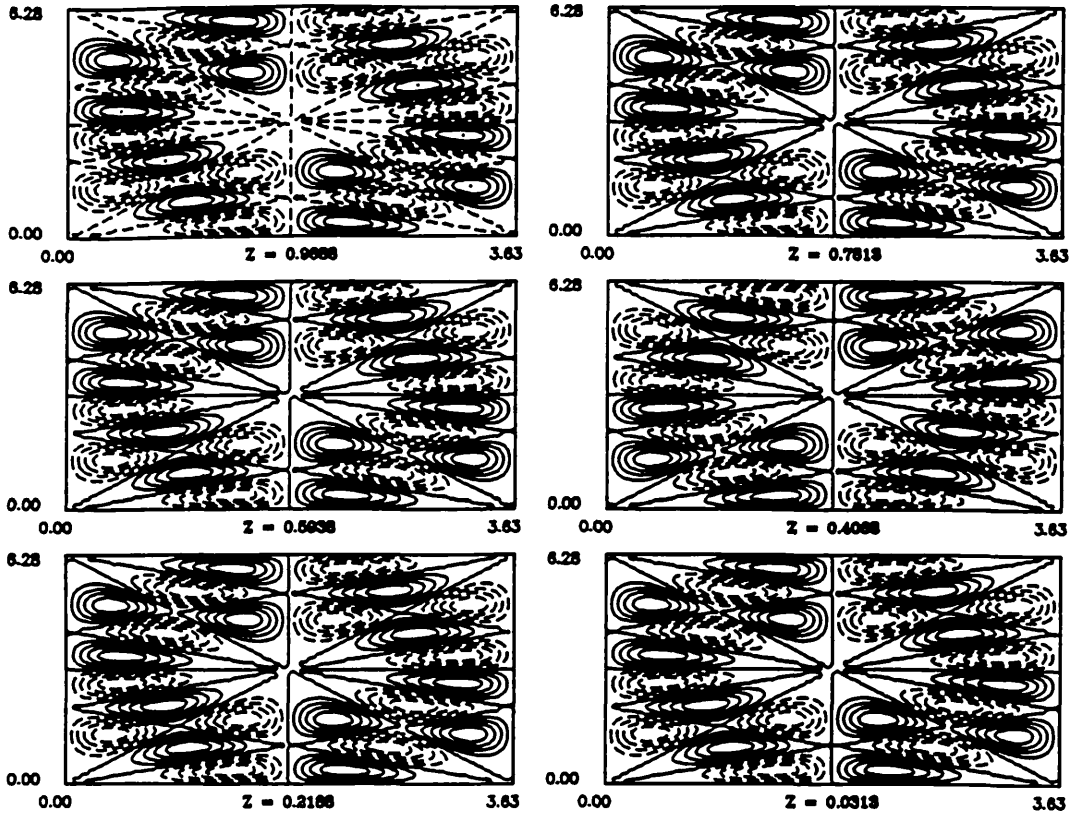
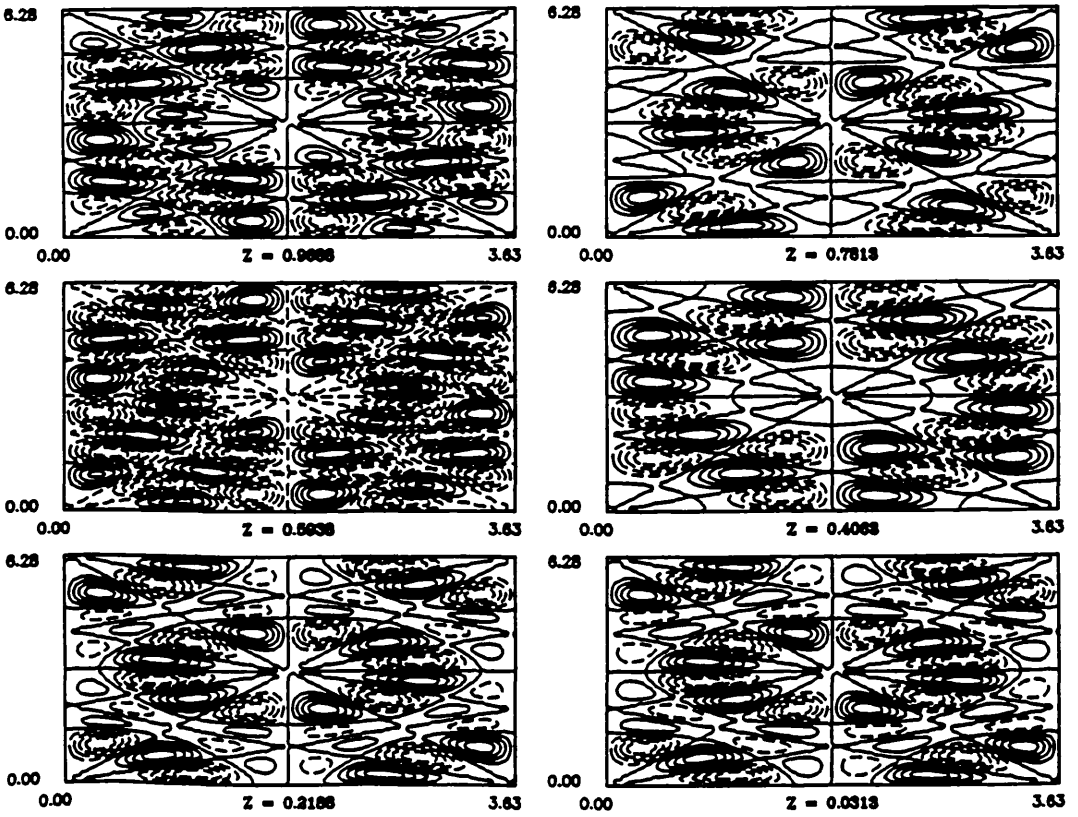


Figure 5.6b). Hexagonal Rayleigh–Benard convection, Vertical vorticity
R=2645.0547, N=2.5000, σ= 0.10, α=1.111, fourthvv



distribution, with the dominant influence being the VH28, but just above the centre of the layer, where the vertical dependence of the first vertical vorticity mode vanishes, the second mode is seen strongly, it having switched over to a negative dependence lower down in the fluid. These concentrations and the relatively vertical−vorticity−free 3−D core suggest that it is the plumes hitting the boundary layers that generate the vertical vorticity.

The influence of the vertical vorticity can also be seen in figures 5.7a)−g) which show the absolute amplitudes of vorticity and velocity as well as the isotherms as contour maps. These maps are particular vertical slices through the original hexagonal structure − the first is from vertex to vertex across the pattern centre, the second from mid−side to mid−side across the pattern centre, and the third is along a hexagon wall (see diagram 5.1). It may be seen by comparison of the THIRD and the THIRDVV systems, and similarly, comparison of the FOURTH and the FOURTHVV systems, that addition of the vertical vorticity concentrates the vorticity amplitude into small cells at the top and 3−D centre of the hexagon and also at the bottom of the walls. However, the vorticity that is shown in these amplitude plots is purely horizontal, since both the VH28 and VH52 planform are zero on all the sections plotted, and so these plots only serve to show the effect of the vertical vorticity on the horizontal vorticity in these planes. Hence the observations made in fact state that the addition of the vertical vorticity modes has concentrated the horizontal vorticity into cells at the top of the layer in general, which would imply that the lower reaches of the layer have strong vertical vorticity, confirming earlier suppositions. The inclusion of the vorticity modes also serves to collect the velocity amplitude at the top of the layer across the cells and to stratify it on the walls. The thermal plumes in the centre of the hexagonal structure are toned down and spread by the increased horizontal motions associated with the vertical vorticity, but the inter−cell walls show stronger thermal boundary layers. The FOURTHVV system shows a dip in the isotherms at the centre of the cell at the top of the layer, demonstrating the pocket of reverse, cold, downward flow found in the upper half of the layer there, corresponding to the centre trough of the vertical velocity figures for this order, FOURTHVV (figures 5.3g) and 5.4g)).

Despite the indications shown above that the vertical vorticity is not negligible, its presence is not felt by the flow to any major extent in the generally low non−linearity regime of parameter space studied, as is shown by figures 5.8−5.10, which show plots of the velocity field. These plots show stereo pairs of the periodic boxes, $0 \leqslant x \leqslant 2\pi/\alpha\sqrt{3}$, $0 \leqslant y \leqslant 2\pi/\alpha$, $0 \leqslant z \leqslant 1$, with the velocity followed from a point for a certain fixed number of 'time' intervals i.e. the velocity at the first point is calculated and a line drawn in this direction as if

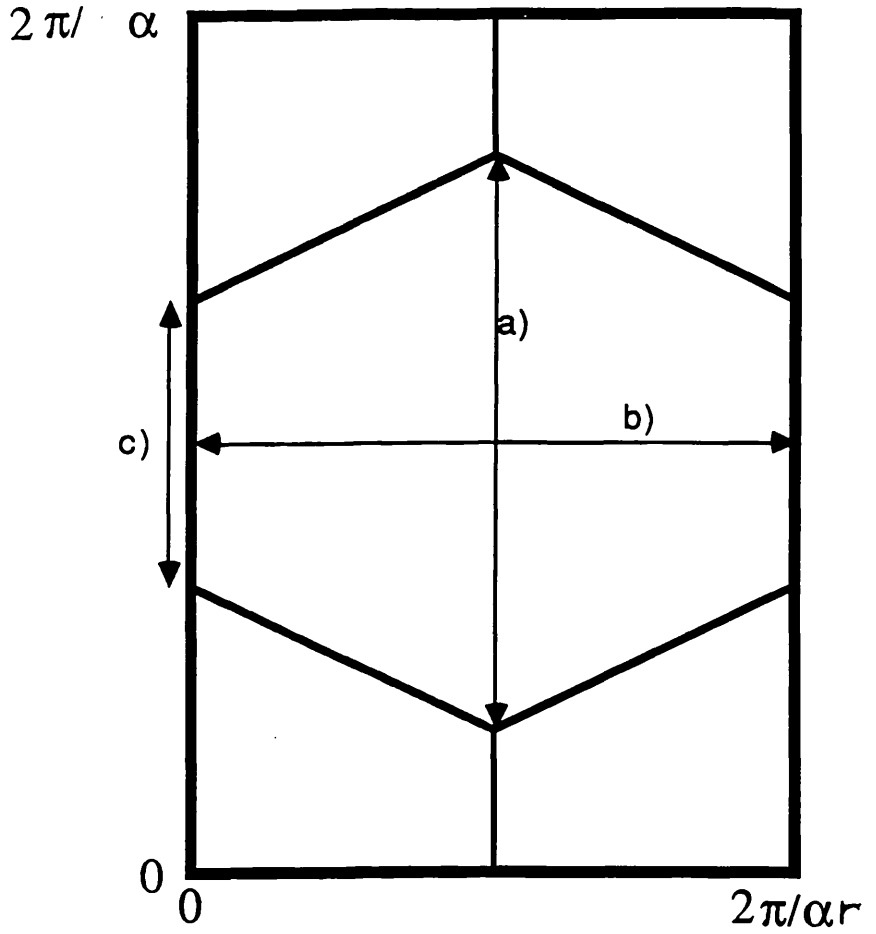


Diagram 5.1a). The vertical slices taken through the hexagonally periodic cell for the contour maps shown.

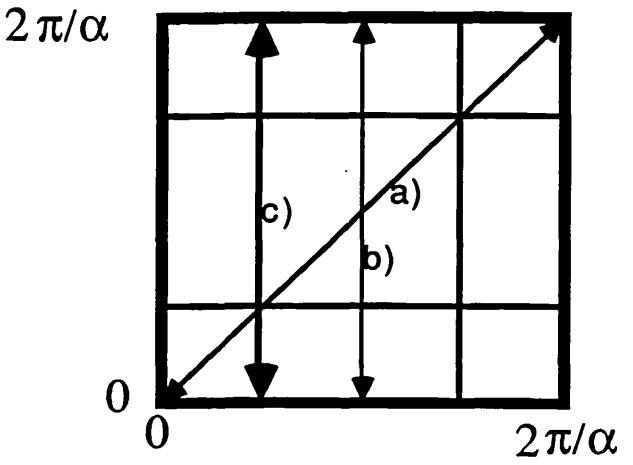


Diagram 5.1b). The vertical slices taken through the square-periodic cell.

Figure 5.7a). Hexagonal Rayleigh–Benard convection.
R = 1887.47, N = 2.50, σ = 0.00, α = 1.111, first
a) x=$\pi/\sqrt{3}\alpha$, y=($\pi/3\alpha$,$5\pi/3\alpha$) , b) x=(0,$2\pi/\sqrt{3}\alpha$), y=π/α , c) x=0, y=($2\pi/3\alpha$,$4\pi/3\alpha$)

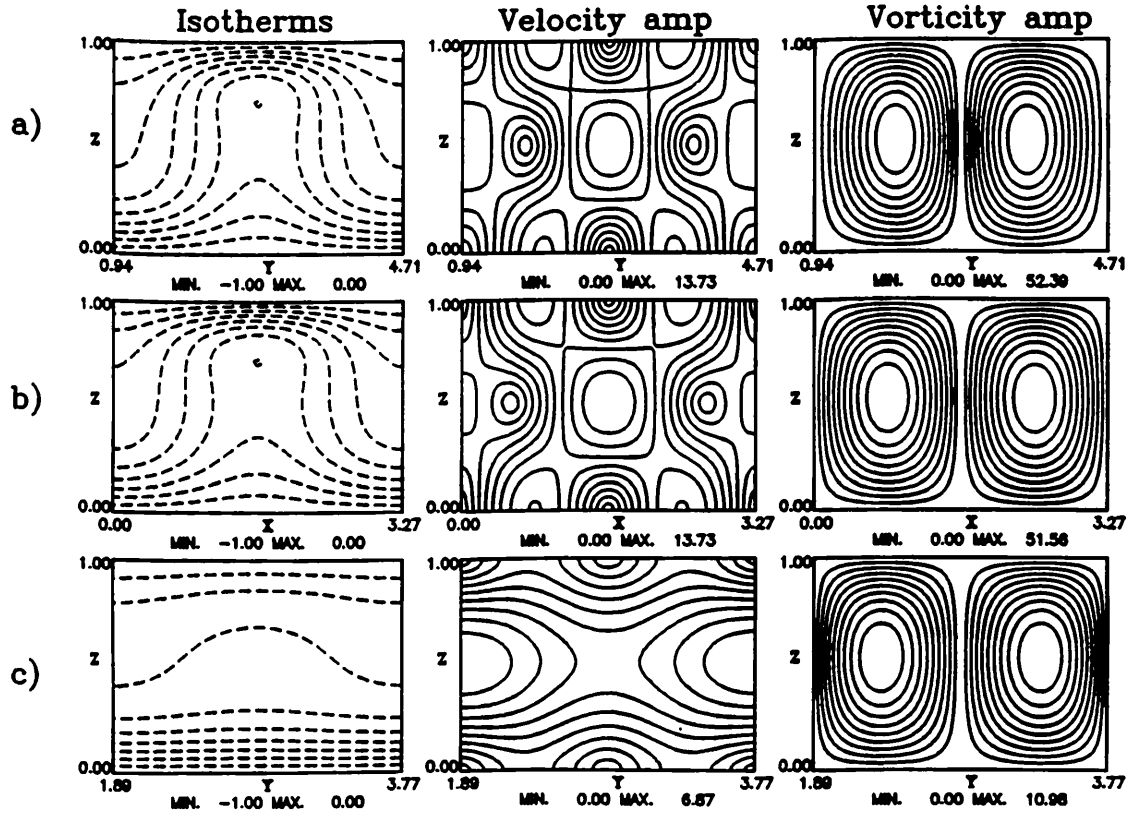


Figure 5.7b). Hexagonal Rayleigh–Benard convection.
R = 11747.99, N = 2.50, σ = 0.10, α = 1.111, ffirst
a) x=$\pi/\sqrt{3}\alpha$, y=($\pi/3\alpha$,$5\pi/3\alpha$) , b) x=(0,$2\pi/\sqrt{3}\alpha$), y=π/α , c) x=0, y=($2\pi/3\alpha$,$4\pi/3\alpha$)

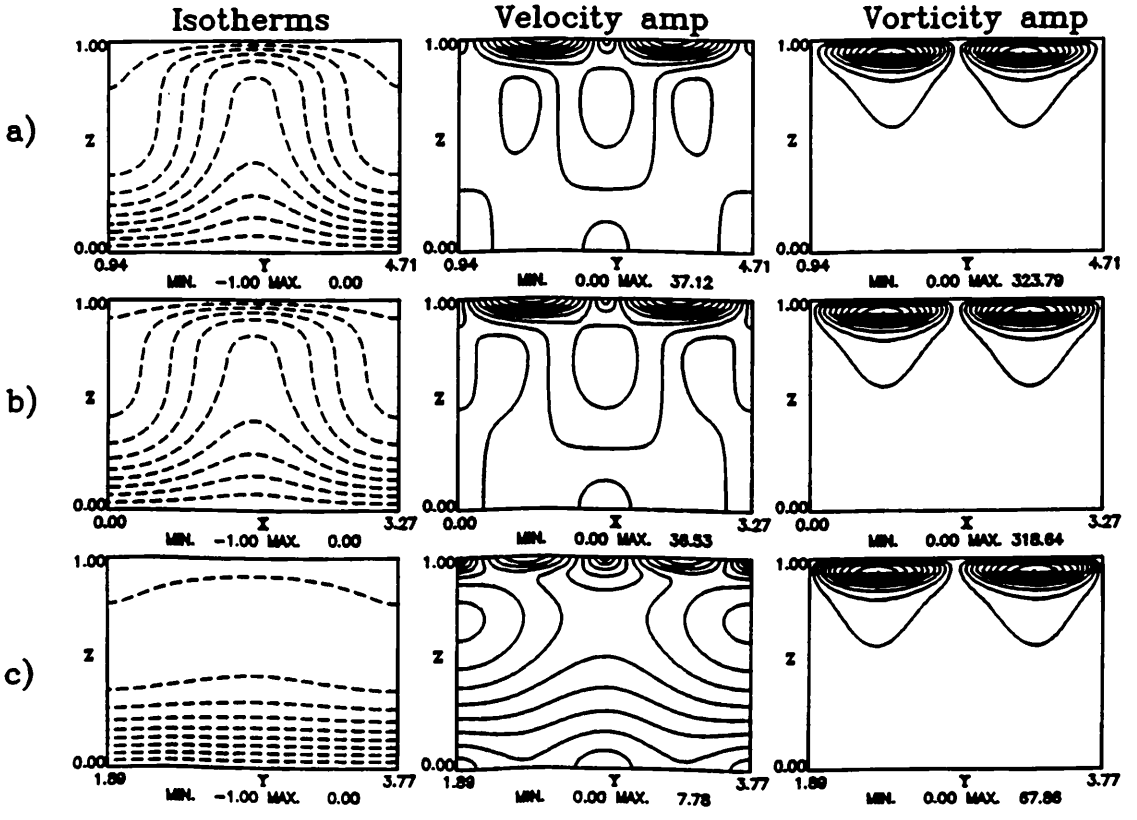


Figure 5.7c). Hexagonal Rayleigh–Benard convection.
R = 940.36, N = 1.10, σ = 0.10, α = 1.111, second
a) $x=\pi/\sqrt{3}\alpha$, $y=(\pi/3\alpha,5\pi/3\alpha)$, b) $x=(0,2\pi/\sqrt{3}\alpha)$, $y=\pi/\alpha$, c) x=0, $y=(2\pi/3\alpha,4\pi/3\alpha)$

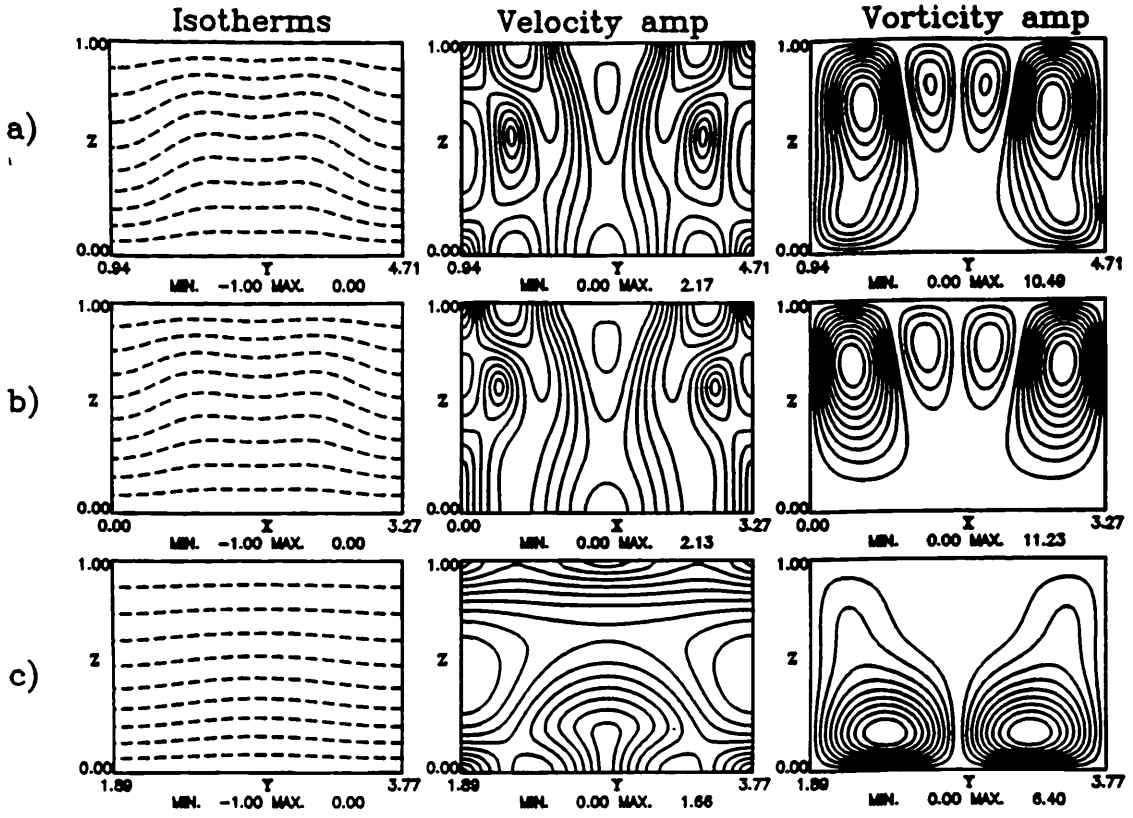


Figure 5.7d). Hexagonal Rayleigh–Benard convection.
R = 2504.38, N = 2.50, σ = 0.10, α = 1.111, third
a) $x=\pi/\sqrt{3}\alpha$, $y=(\pi/3\alpha,5\pi/3\alpha)$, b) $x=(0,2\pi/\sqrt{3}\alpha)$, $y=\pi/\alpha$, c) x=0, $y=(2\pi/3\alpha,4\pi/3\alpha)$

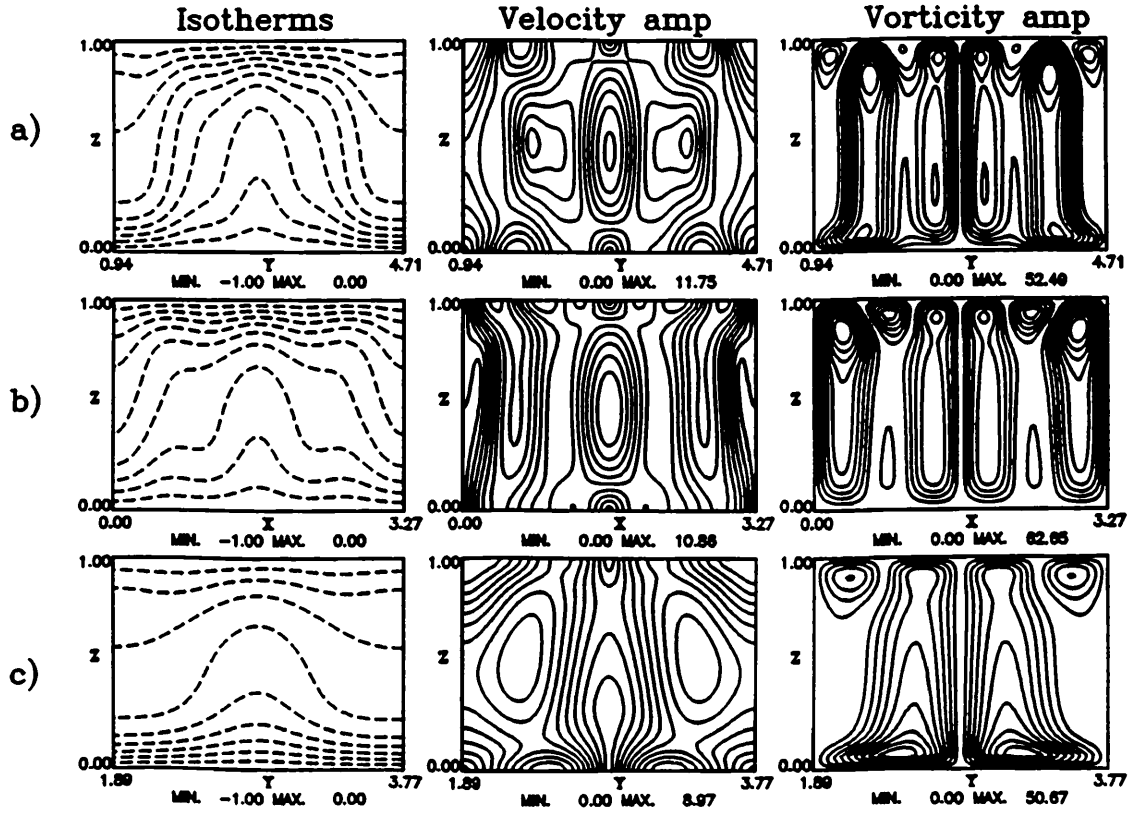


Figure 5.7e). Hexagonal Rayleigh–Benard convection.
R = 5815.96, N = 2.50, σ = 0.10, α = 1.111, thirdvv
a) x=$\pi/\sqrt{3}\alpha$, y=($\pi/3\alpha$,$5\pi/3\alpha$) , b) x=(0,$2\pi/\sqrt{3}\alpha$), y=π/α , c) x=0, y=($2\pi/3\alpha$,$4\pi/3\alpha$)

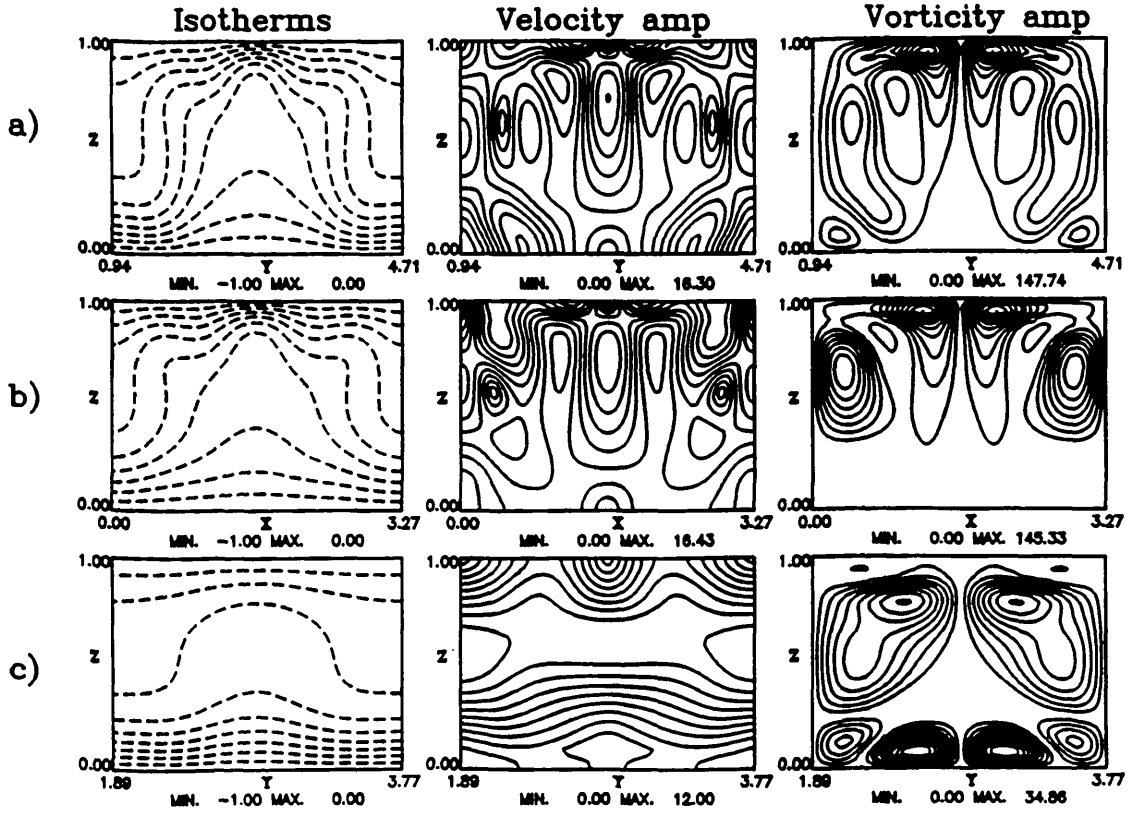


Figure 5.7f). Hexagonal Rayleigh–Benard convection.
R = 2770.57, N = 2.50, σ = 0.10, α = 1.111, fourth
a) x=$\pi/\sqrt{3}\alpha$, y=($\pi/3\alpha$,$5\pi/3\alpha$) , b) x=(0,$2\pi/\sqrt{3}\alpha$), y=π/α , c) x=0, y=($2\pi/3\alpha$,$4\pi/3\alpha$)

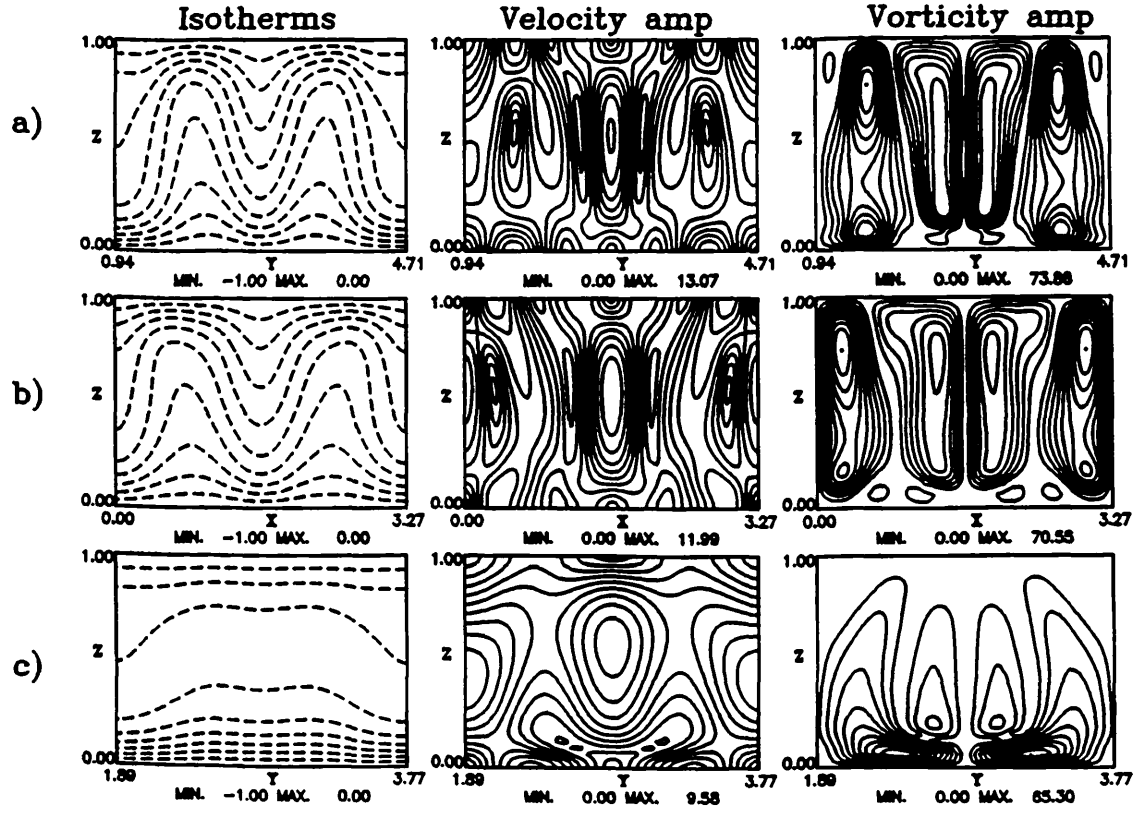
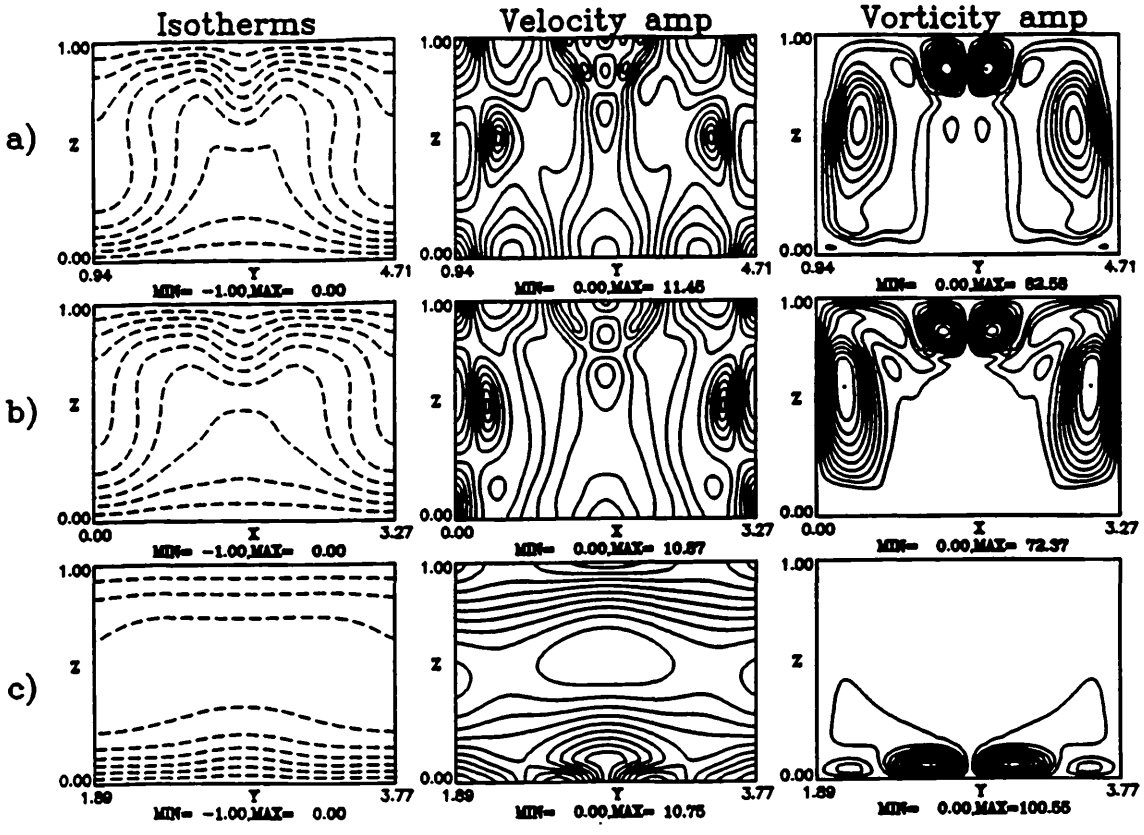


Figure 5.7g). Hexagonal Rayleigh-Benard
R = 2645.05, N = 2.50, σ = 0.10, α = 1.111, fourthvv
a) x=$\pi/\sqrt{3}\alpha$, y=($\pi/3\alpha$,$5\pi/3\alpha$), b) x=(0,$2\pi/\sqrt{3}\alpha$), y=π/α, c) x=0, y=($2\pi/3\alpha$,$4\pi/3\alpha$)



that velocity was followed for a particular 'time' increment. This ends at some point, where the velocity is once again calculated and the process repeated. The process is only terminated after a fixed number of intervals have been calculated, so that the effect is a 'streakline' effect, as if dye was injected at a point into the fluid. The greater the amplitude of the velocity the longer the arrows. Note however, that each of these stereo plots may have a different scaling on the arrows, so that direct comparison of the velocities from one to another is not available, rather they are employed as a visualisation technique for description of the actual flow pattern. The two periodic boxes are drawn from slightly different viewpoints so that if viewed by holding the page at a distance of roughly 25cm−50cm away from the eyes, and relaxing the eyes to focus on infinity, then three images appear, the centre one of which is the superposition of the other two, giving a three−dimensional effect to the drawing. An ability to cross the eyes makes this process easier. Apologies to those who cannot.

The stereo pairs of figure 5.8 show the flow pattern on the boundaries and are included to be an equivalent of Murphy and Lopez's (1984) diagrams of the tops of their convecting hexagons. At the top and bottom boundaries there is no vertical flow, but vertical vorticity is allowed, so these planes are good places to see vertical vorticity effects, should they exist. The models of Murphy and Lopez

Fig. 5.8a) **Stereo velocity plots – Hexagonal Rayleigh–Benard convection**
R = 1887.47, N = 2.50, σ = 0.00, α = 1.111, first
Horizontal projection of velocity onto planes shown.

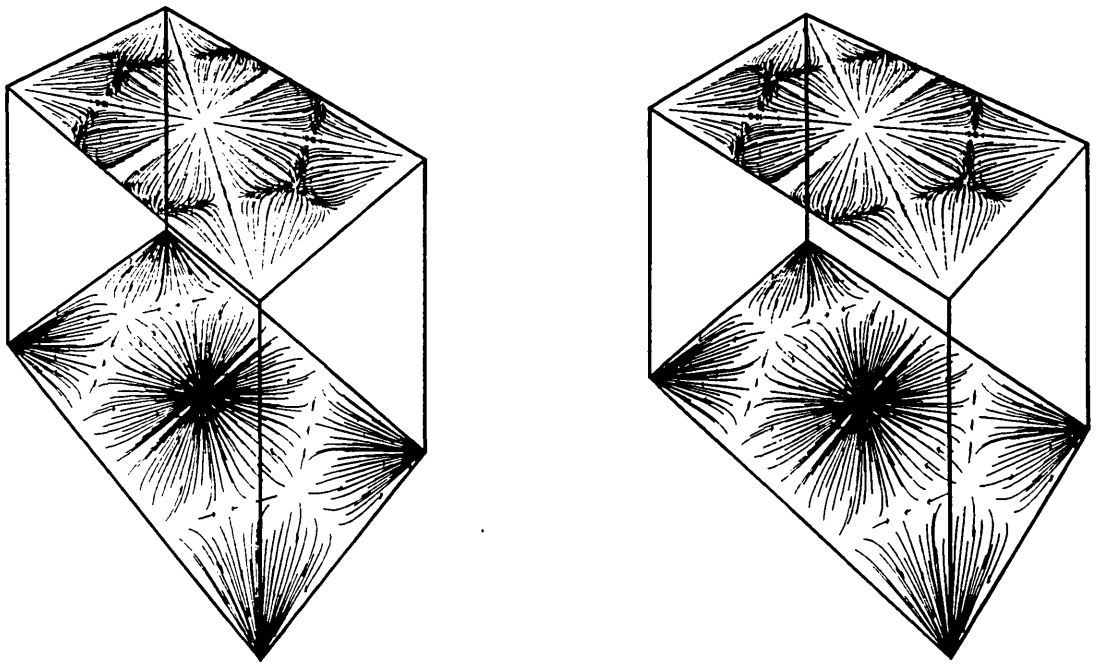


Fig. 5.8b) **Stereo velocity plots – Hexagonal Rayleigh–Benard convection**
R = 11747.99, N = 2.50, σ = 0.10, α = 1.111, ffirst
Horizontal projection of velocity onto planes shown.

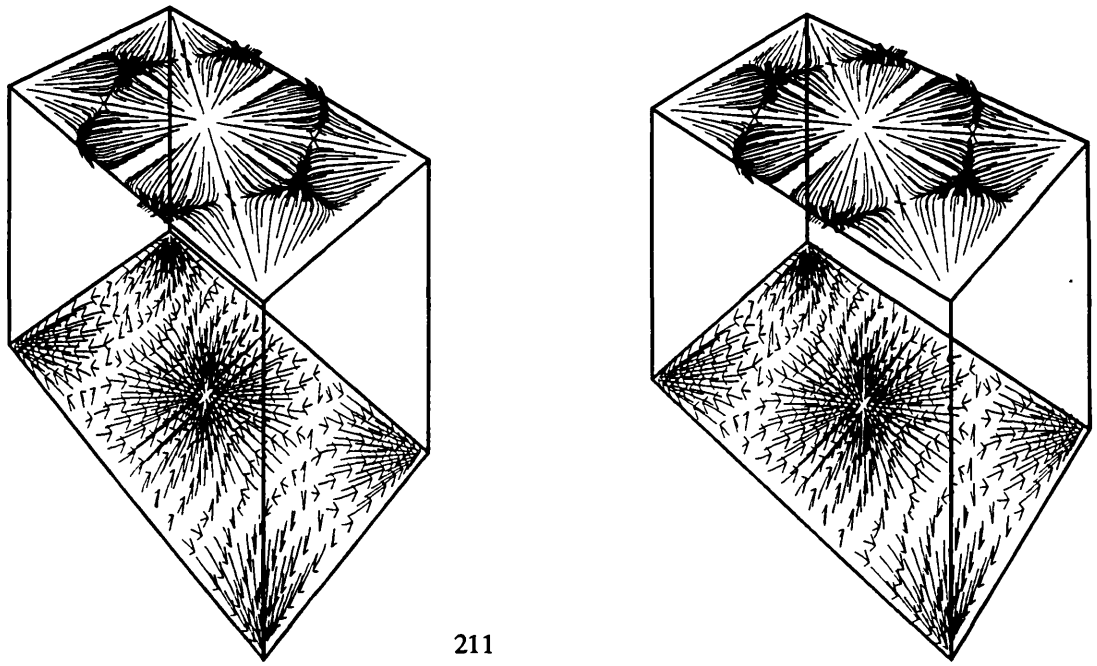


Fig. 5.8c) **Stereo velocity plots – Hexagonal Rayleigh–Benard convection R = 940.36, N = 1.10, σ = 0.10, α = 1.111, second Horizontal projection of velocity onto planes shown.**

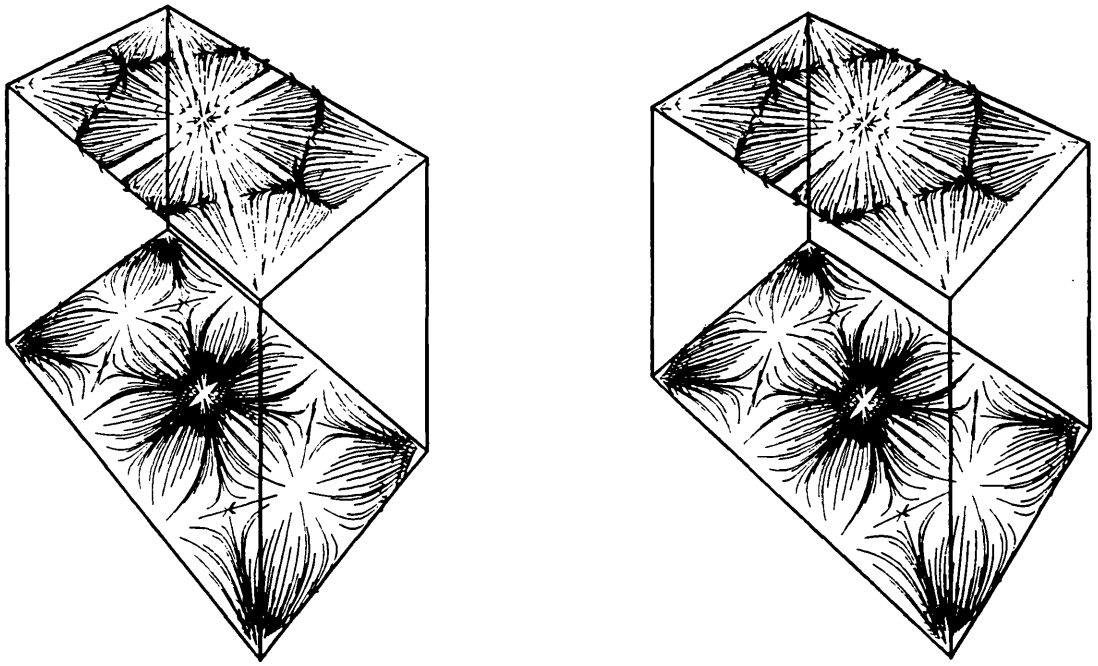


Fig. 5.8d) **Stereo velocity plots – Hexagonal Rayleigh–Benard convection R = 2504.38, N = 2.50, σ = 0.10, α = 1.111, third Horizontal projection of velocity onto planes shown.**

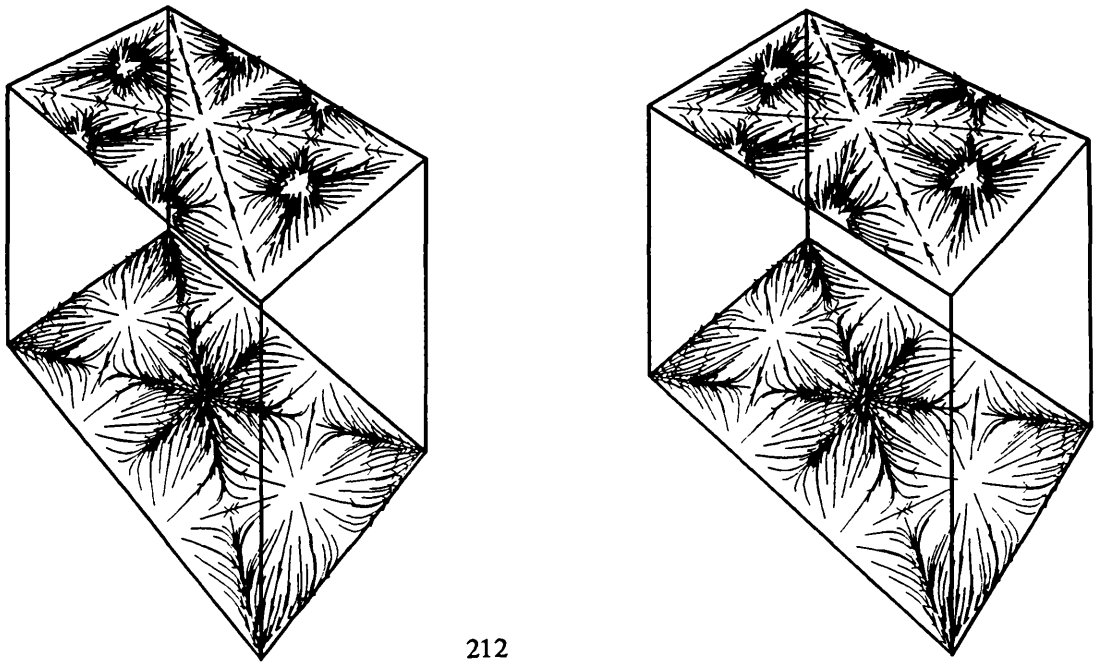


Fig. 5.8e) **Stereo velocity plots – Hexagonal Rayleigh–Benard convection**
R = 5815.96, N = 2.50, σ = 0.10, α = 1.111, thirdvv
Horizontal projection of velocity onto planes shown.

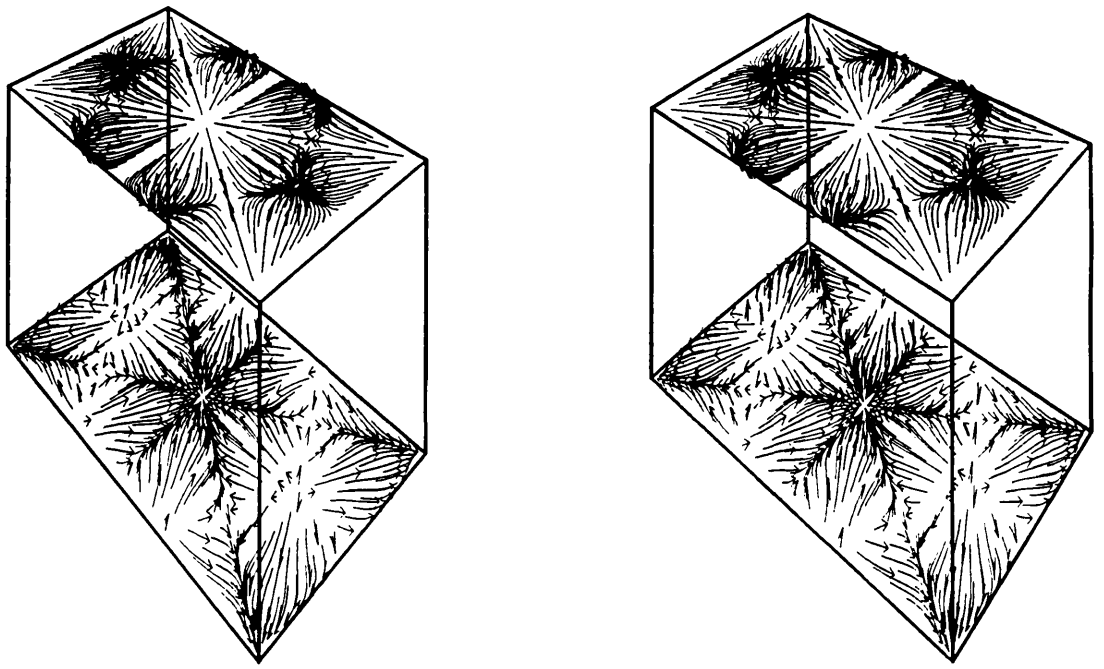


Fig. 5.8f) **Stereo velocity plots – Hexagonal Rayleigh–Benard convection**
R = 2770.57, N = 2.50, σ = 0.10, α = 1.111, fourth
Horizontal projection of velocity onto planes shown.

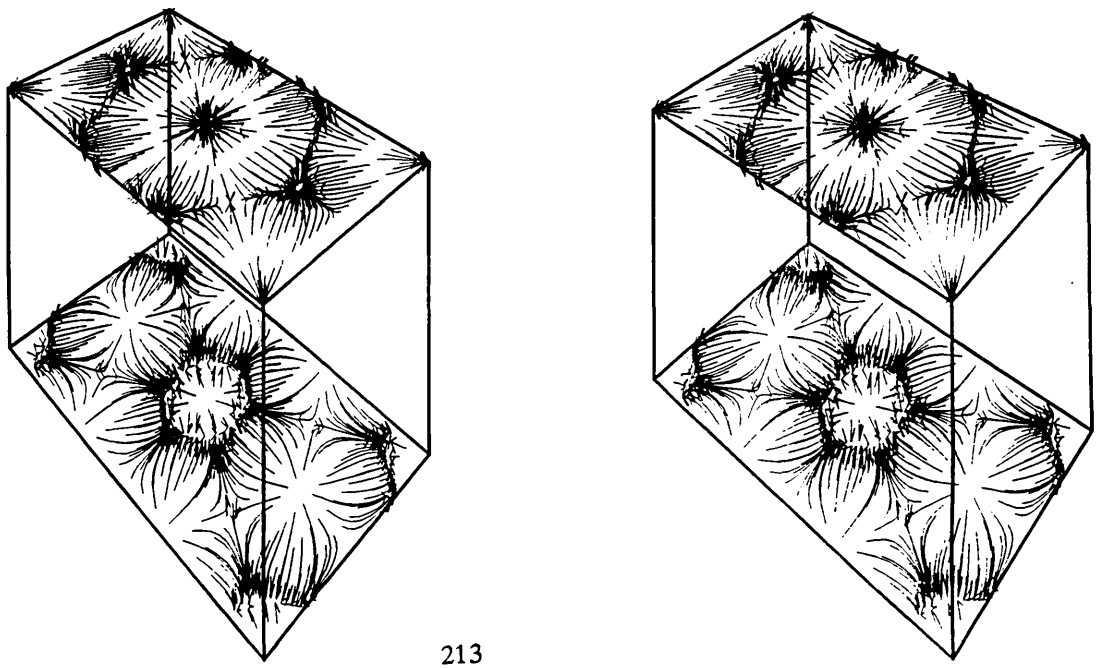
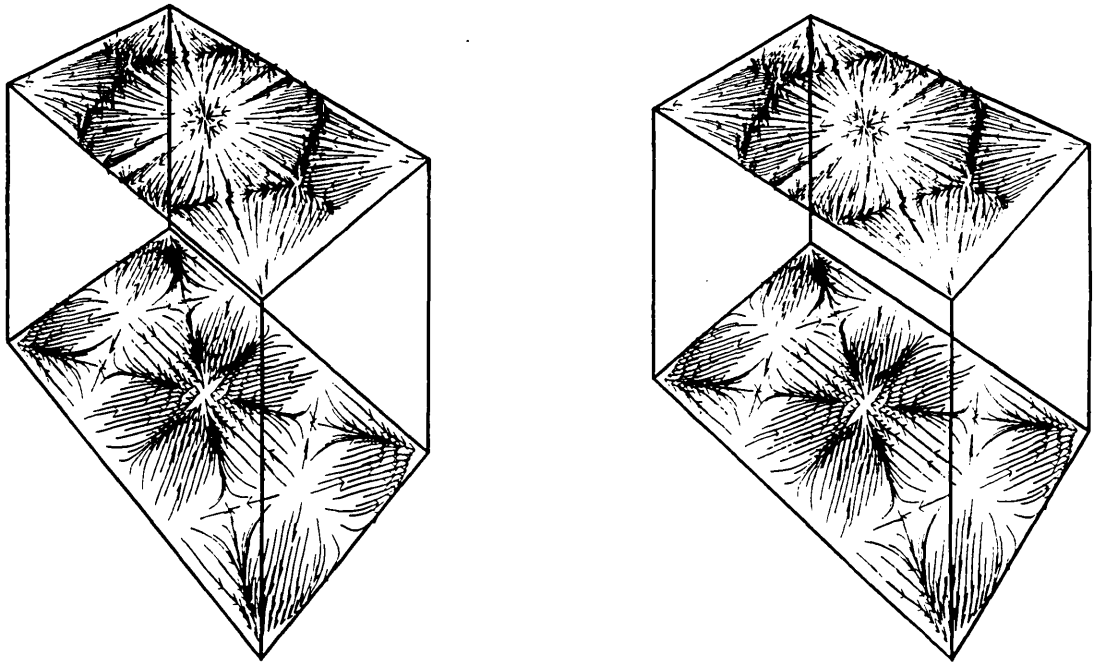


Fig. 5.8g) **Stereo velocity plots – Hexagonal Rayleigh–Benard convection R = 2645.05, N = 2.50, σ = 0.10, α = 1.111, fourthvv Horizontal projection of velocity onto planes shown.**



(1984) for the type II (strong vertical vorticity) solutions, show a very definite swirl at the top boundary, with a strong central vortex, surrounded by six smaller vortices at the vertexes of the hexagonal structure. This type of behaviour is not exhibited here, as can be seen in figures 5.8e) and 5.8g), where the flow in the hexagonal structure is radial, with flow rising in the central regions and descending at the walls, with no apparent swirl around the vertices at all, despite the presence of the vertical vorticity in these solutions. The reason for this can be seen in the figure 5.11 which shows a plot of the vertically dependent functions, $D\chi$ for the fundamental mode and the two vertical vorticity ψ modes. The components of the horiontal vorticity are

$$u = \frac{\partial \chi}{\partial x \partial z} + \frac{\partial \psi}{\partial y} ,$$

$$v = \frac{\partial \chi}{\partial y \partial z} - \frac{\partial \psi}{\partial x} ,$$

so that the balance between $D\chi = \partial\chi(z)/\partial z$ and $\psi(z)$ essentially determines the relative importance of the vertical vorticity influence on the horizontal velocity for a horizontal plane at any particular depth. Figure 5.11 then shows these three

vertical dependences (the fundamental $D\chi$ and the two ψ modes) plotted together to scale and it may be seen that the $D\chi$ dependence is dominant at the upper and lower boundaries, with the influence of vertical vorticity very small in comparison. The vorticity is not usually at its strongest at the boundaries, the maxima usually occuring maybe a fifth of the way into the layer, and so only near the centre of the layer, where the $D\chi$ function changes sign and is therefore small, is the vertical vorticity going to be of appreciable size, enough to actually stir the flow around into horizontal motions. Figures 5.9 show these regions for the vertical vorticity inclusive truncations, but again, the influence of the vorticity can be seen to be virtually negligible, the flow being dominated by vertical motions. Of course, this investigation has only been carried out at Rayleigh numbers relatively close to the critical and for low Nusselt numbers, so that the non−linearity has certainly not grown to any large proportions, thus leaving the strongly non−linear effects with little to drive themselves. If a higher Rayleigh number regime was investigated, then the influence of the vertical vorticity could certainly change, and maybe other results, such as those of Murphy and Lopez's (1984) type II results may be visualised.

Figures 5.10 show stereo pairs which follow the flow from points just above the lower boundary and just below the upper boundary. These plots are included to give an impression of the general circulation of the cells, since the starting points chosen allow 3−D flow (unlike those plots of 5.8). Previously, it was attempted to do this by following a random sprinkling of points throughout the cell, but this proves to be too confusing to be of any use. An ordered procedure was used instead, whereby single or multiple layers of points at particular depths may be used as the starting points for vorticity following. Horizontal projections of these velocity paths could also be calculated as shown in figures 5.9, but the full velocity plots of 5.10 show that the overall flow is not dramatically affected in appearance by the addition of the higher modes, once again. The lower order modes show a tidier flow, with a strong but thin plume at the centre of the cell, flowing upwards towards the upper boundary then fanning out evenly in a radial motion to meet at the cell walls, where the downward flow is then collected as strong, negative plumes at the vertices of the fundamental hexagonal structure. The higher order modes bring in a degree of disorder to this tidy state, as may be expected, where the inclusion of the other harmonics create a stronger and broader central plume and force downflow and upflow at other points rather than simply the obvious vertices. The harmonics may also include a reverse flow in the centre of the cell at the top, until at the highest orders this reverse flow is strong. The broadening of the central plume has also been accompanied by the transfer of the downward flow to the whole walls rather than just the concentrated vertex downflow of the

Fig. 5.9a) **Stereo velocity plots – Hexagonal Rayleigh–Benard convection R = 5815.96, N = 2.50, σ = 0.10, α = 1.111, thirdvv**

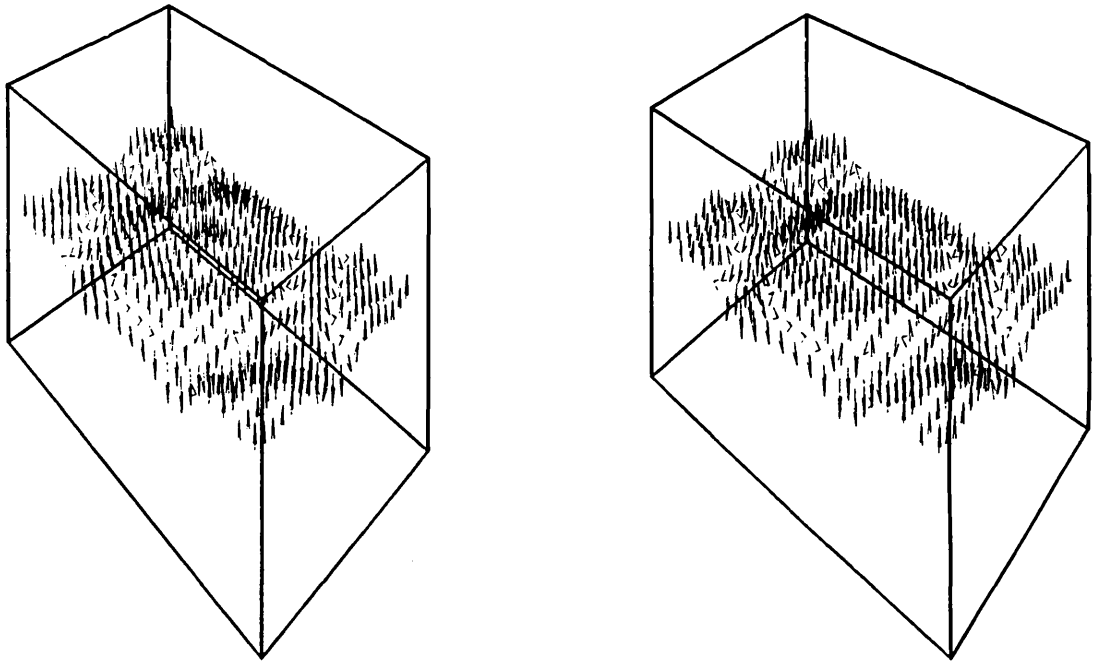


Fig. 5.9b) **Stereo velocity plots – Hexagonal Rayleigh–Benard convection R = 5815.96, N = 2.50, σ = 0.10, α = 1.111, thirdvv**
Horizontal projection of velocity onto planes shown.

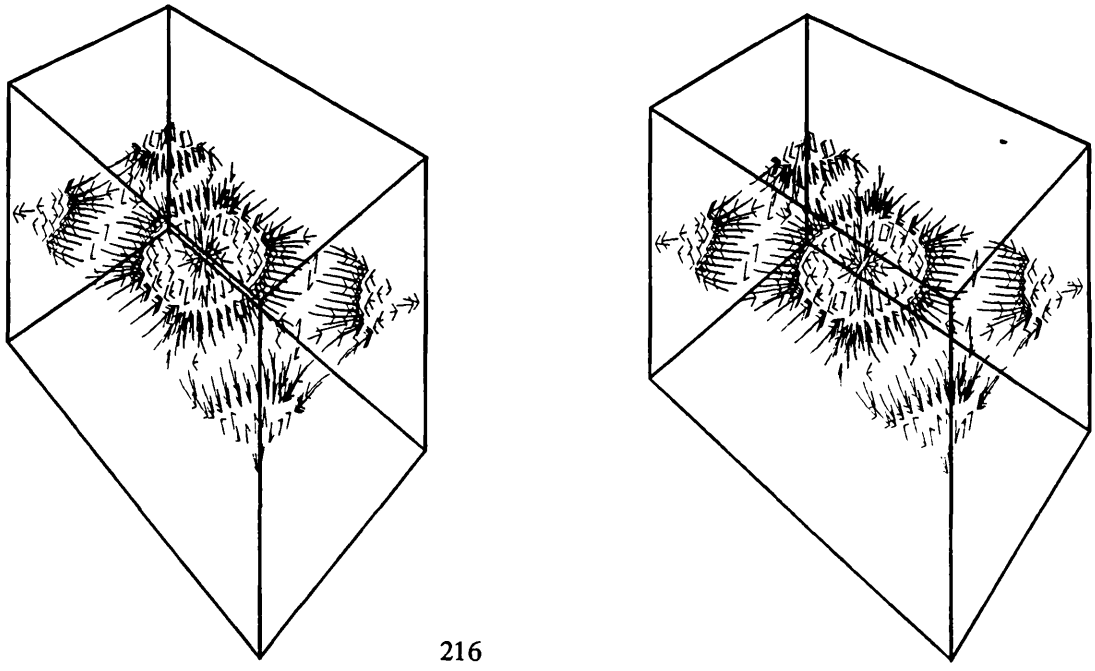


Fig. 5.9c) **Stereo velocity plots – Hexagonal Rayleigh–Benard convection R = 2645.05, N = 2.50, σ = 0.10, α = 1.111, fourthvv**

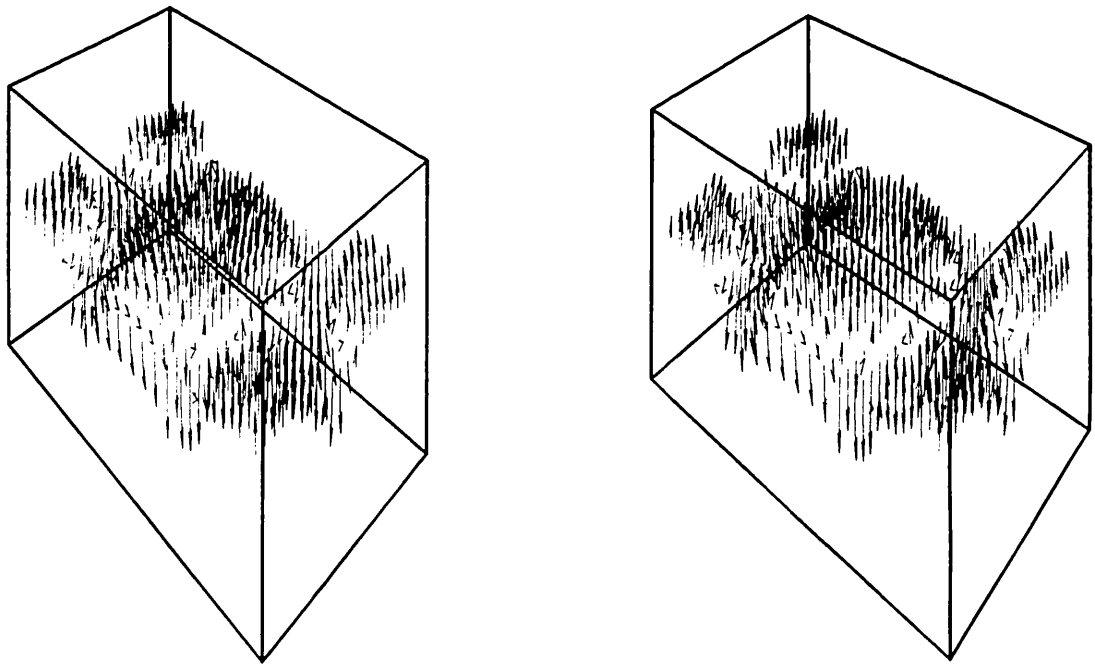


Fig. 5.9d) **Stereo velocity plots – Hexagonal Rayleigh–Benard convection R = 2645.05, N = 2.50, σ = 0.10, α = 1.111, fourthvv**
Horizontal projection of velocity onto planes shown.

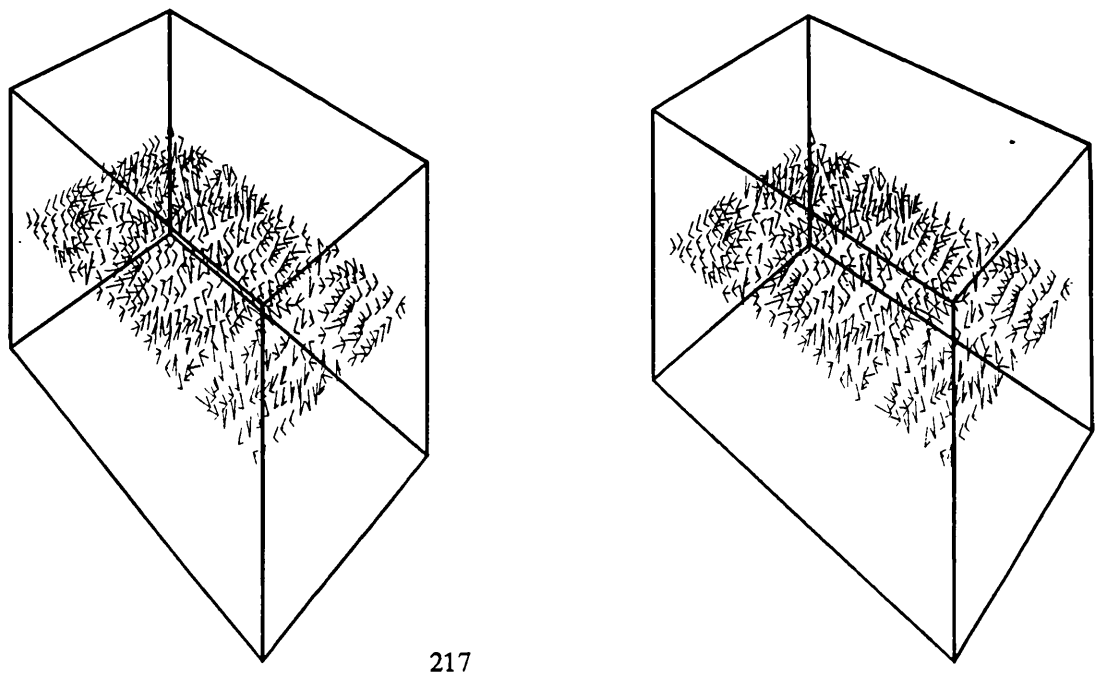


Fig. 5.10a) **Stereo velocity plots – Hexagonal Rayleigh–Benard convection R = 1887.47, N = 2.50, σ = 0.00, α = 1.111, first**

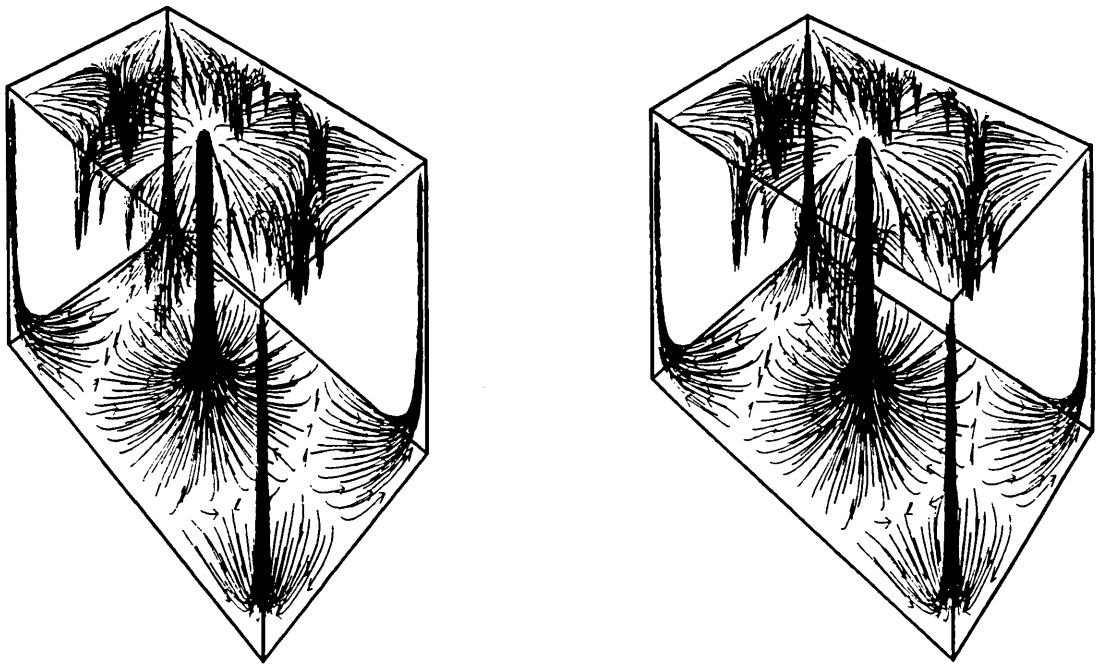


Fig. 5.10b) **Stereo velocity plots – Hexagonal Rayleigh–Benard convection R = 11747.99, N = 2.50, σ = 0.10, α = 1.111, ffirst**

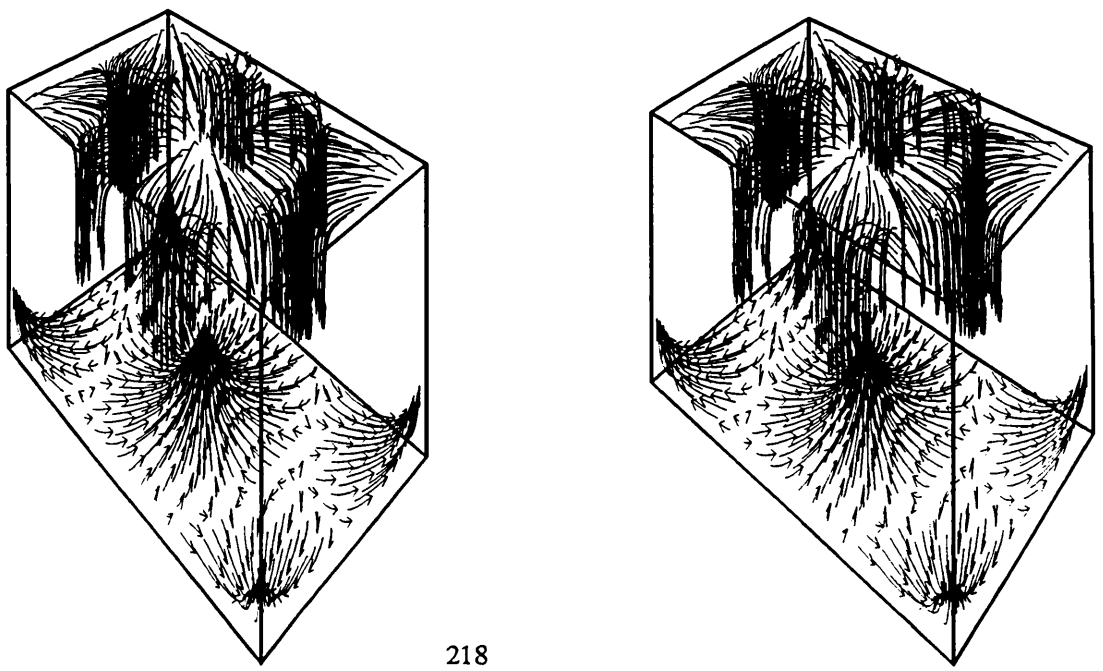


Fig. 5.10c) **Stereo velocity plots – Hexagonal Rayleigh–Benard convection**
R = 940.36, N = 1.10, σ = 0.10, α = 1.111, second

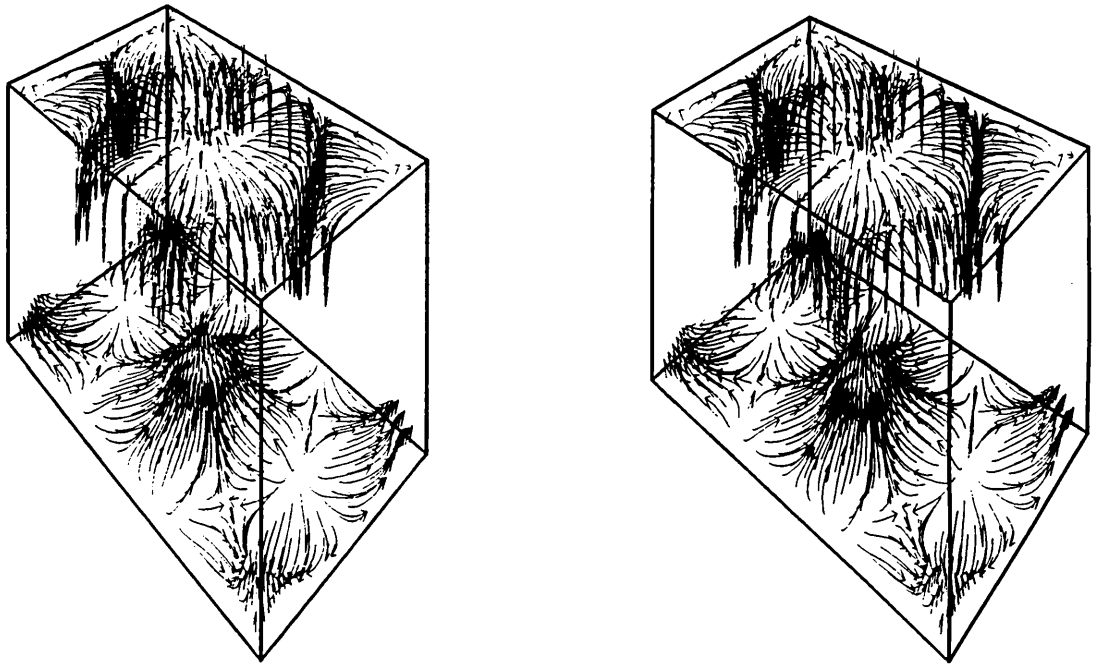


Fig. 5.10d) **Stereo velocity plots – Hexagonal Rayleigh–Benard convection**
R = 2504.38, N = 2.50, σ = 0.10, α = 1.111, third

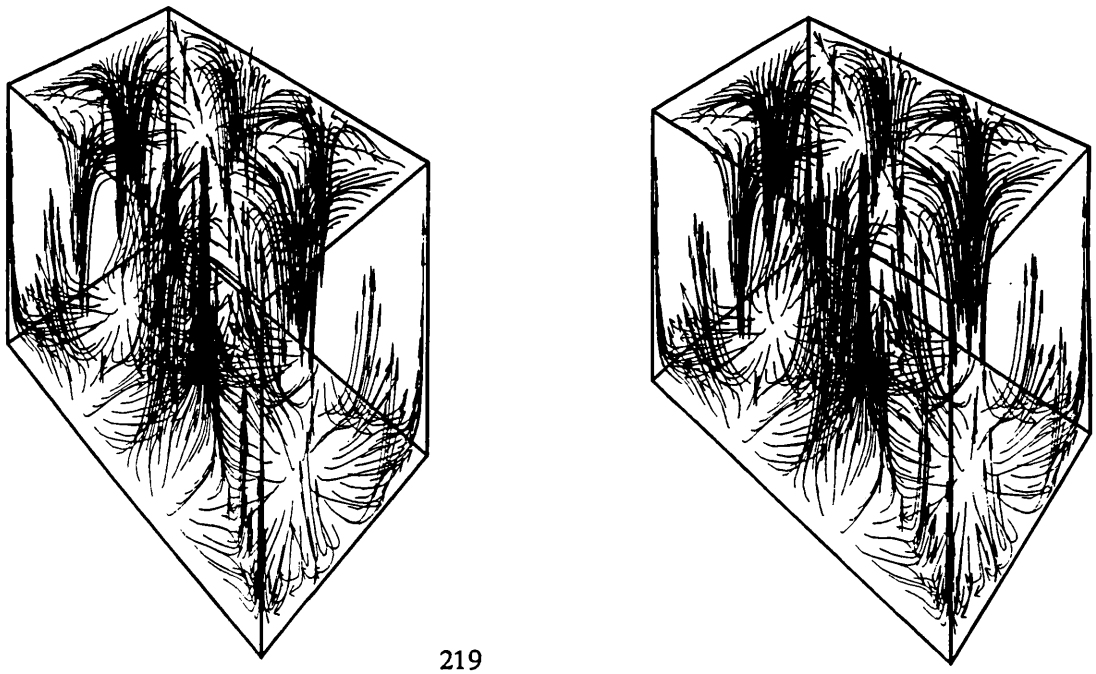


Fig. 5.10e) **Stereo velocity plots – Hexagonal Rayleigh–Benard convection R = 5815.96, N = 2.50, σ = 0.10, α = 1.111, thirdvv**

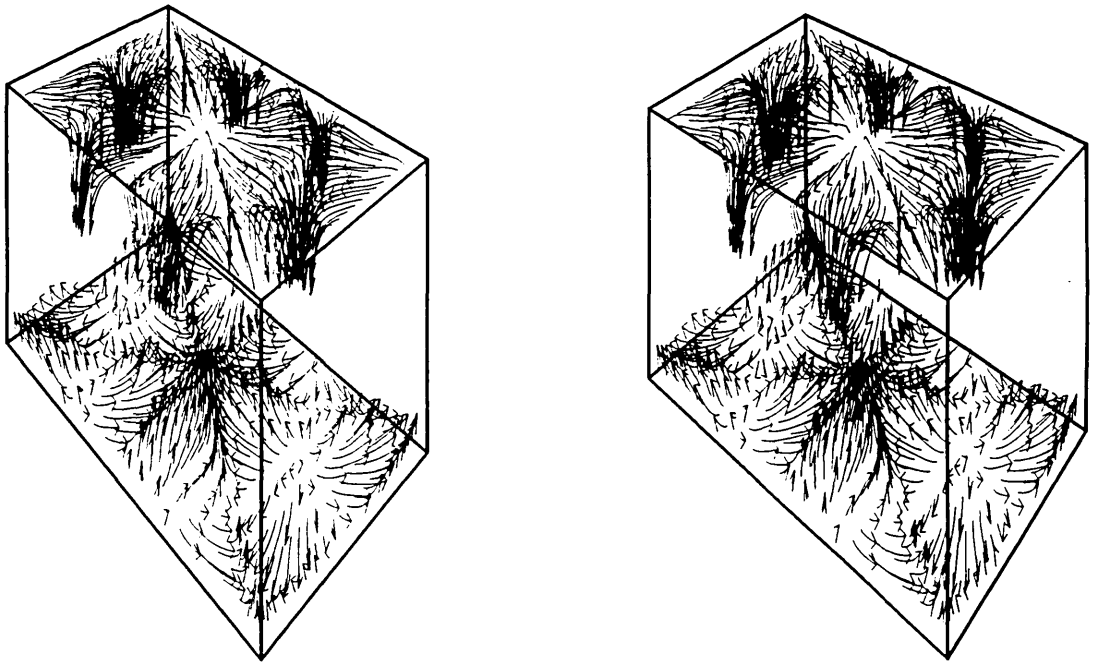


Fig. 5.10f) **Stereo velocity plots – Hexagonal Rayleigh–Benard convection R = 2770.57, N = 2.50, σ = 0.10, α = 1.111, fourth**

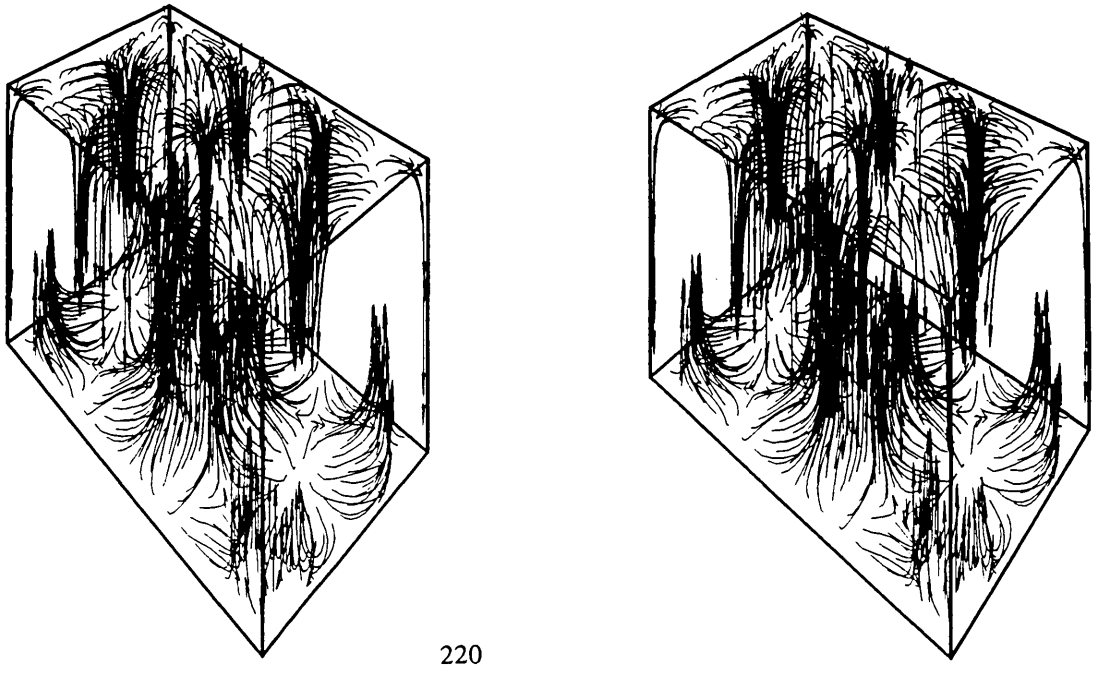


Fig. 5.10g) **Stereo velocity plots – Hexagonal Rayleigh–Benard convection R = 2645.05, N = 2.50, σ = 0.10, α = 1.111, fourthvv**

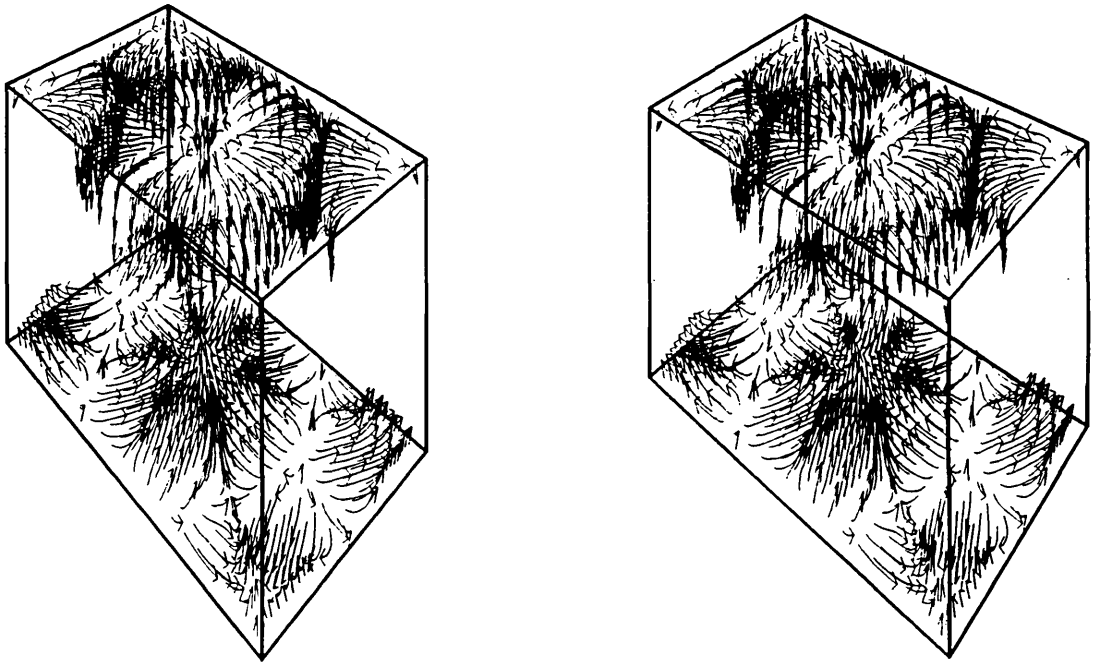
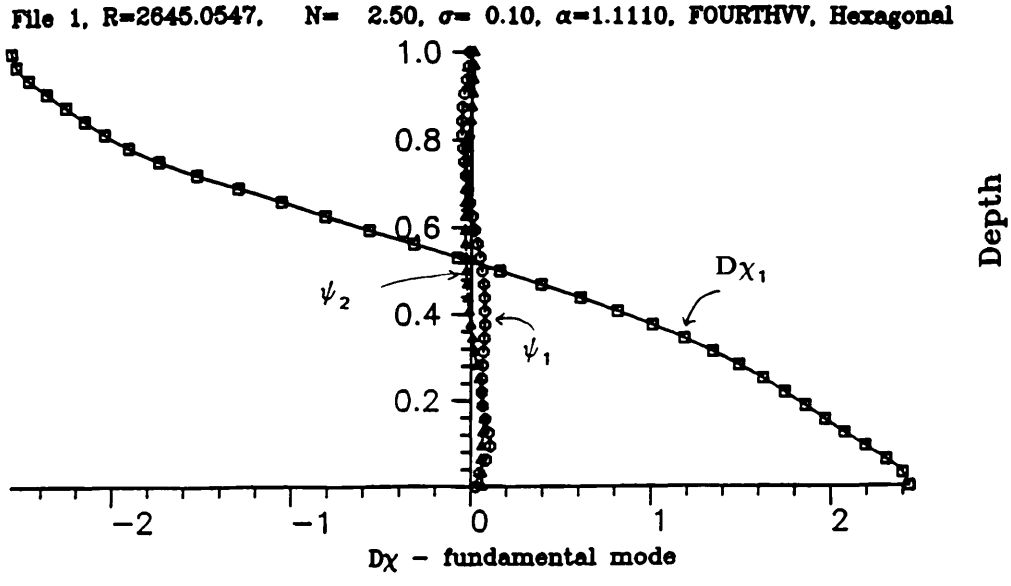


Fig. 5.11.



and the two vorticity modes, ψ_1 and ψ_2.

lower orders, so that overall the downflow is now sheet−like rather than plume−like. Notice that the destruction of the cellular nature mentioned earlier is hardly seen at all.

In summary, the effects of the modal truncations on the hexagonally periodic horizontal domain show a number of effects. The low order truncations are not good at evaluating the more general aspects of the flow such as the heat flux or the mean temperature profile. Heat flux may be over− or under−estimated even at the fairly high truncations shown here, but the features of the flow appear to settle down to acceptable levels at the higher truncations. Low order truncations may be what appears to be totally wrong, for instance, the heat flux estimation from the SECOND truncation set at low σ, or the vertical dependence of the second (H2) mode of χ in the THIRD truncation system. The higher truncations involving the vertical vorticity at least appear consistent. However, as GST suggest, maybe solutions such as the FFIRST solution can be made effective with a judicious choice of parameters. The introduction of vertical vorticity does appear to affect the global features of the flow, maintaining the isothermal non−linear type mean temperature profile and lowering the heat flux, with the vorticity being concentrated towards the lower half of the layer. These modes strengthen the original H1 hexagonal definition against the disruptive influences of some of the harmonics. However, the vertical vorticity is not strong enough to overcome the dominance of χ in the horizontal velocity pattern to produce flows with obvious vortex effects, at least at these non−linearity levels. In general, the addition of the higher harmonics broadens and strengthens the central plume and sharpens the downflowing walls, creating stronger boundary layers at the top and bottom of the cells, and generating vertical vorticity as the plumes strike or leave these layers. The temperature harmonics appear to confine their effects to the thermal boundary layers. The low order disruptive harmonics (e.g. RH$\sqrt{3}$, H3) are predominant in the lower regions of the layer, and it is these which offer some evidence to suggest that the asymmetry introduced by the inclusion of the higher order modes destroys the original cellular nature of the flow. However, this is not obvious or very apparent.

5.4.1.2. Square horizontal periodicity.

Consider first the heat flux once again, as shown for various Prandtl numbers in figures 5.12 a)−c). It is instantly obvious that, at the higher and moderate σ, the dependence on the modal approximation used is more outstanding than for the

Fig. 5.12a). Square cell Rayleigh–Benard convection
Rayleigh number against Nusselt number
Compariosn of modal solutions for σ = 10.0, α = 1.571

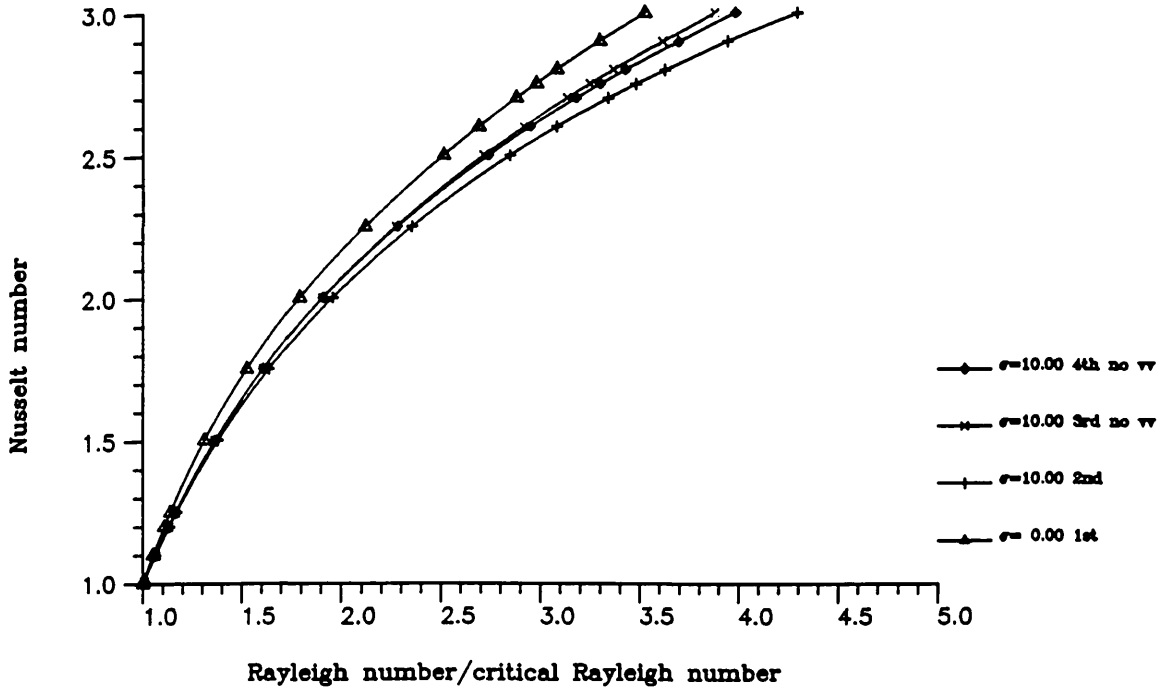


Fig. 5.12b). Square cell Rayleigh–Benard convection
Rayleigh number against Nusselt number
Comparison of modal solutions for σ = 1.0, α = 1.571

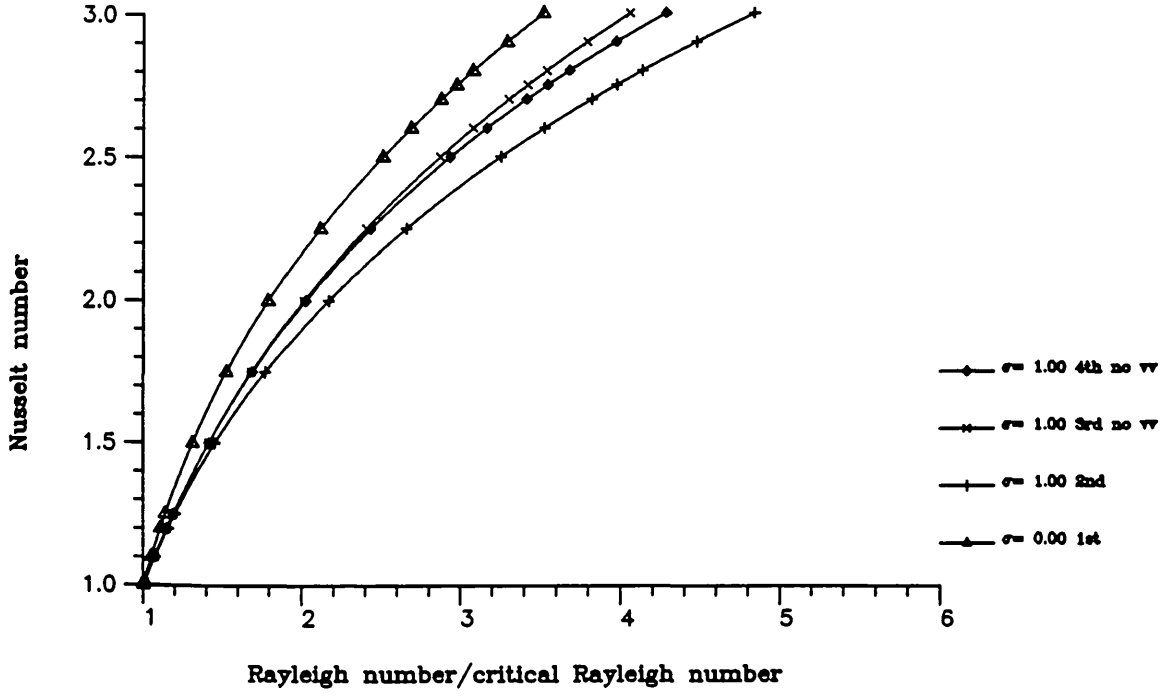


Fig. 5.12c). **Square cell Rayleigh–Benard convection**
Rayleigh number against Nusselt number
Comparison of modal solutions for σ = 0.1, α = 1.571

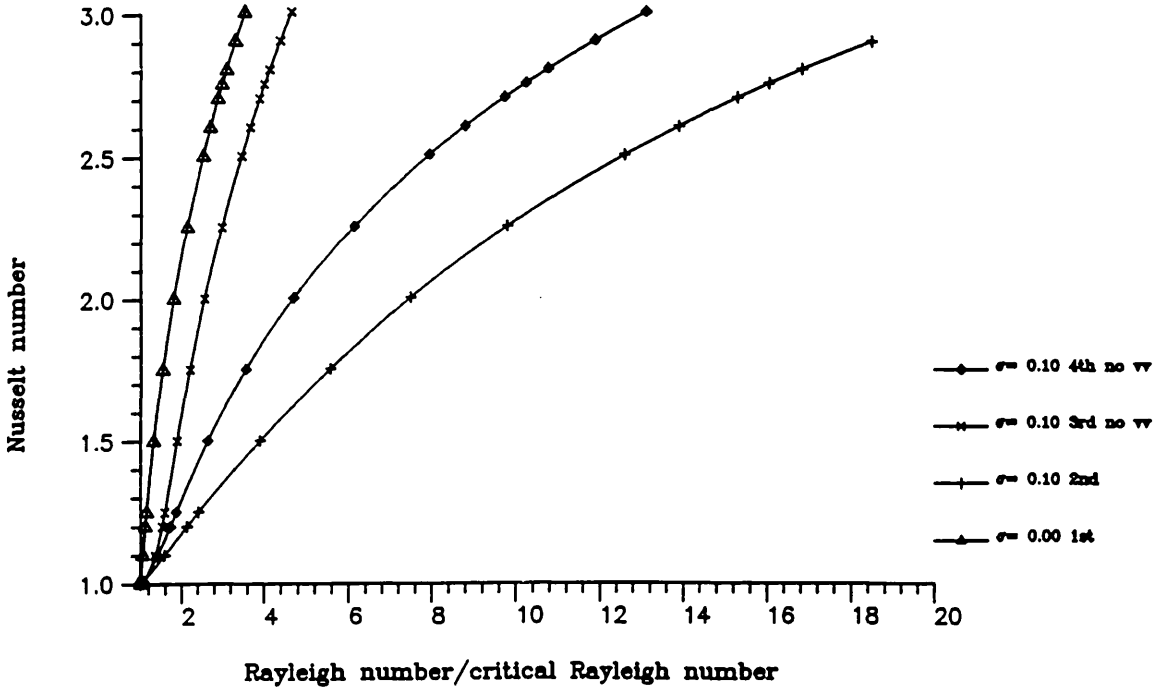


Fig. 5.13a).

File 4, R=5211.6894, N= 2.50, σ= 0.10, α=1.5710, FOURTH , Square
File 3, R=2264.4904, N= 2.50, σ= 0.10, α=1.5710, THIRD , Square
File 2, R=8272.7339, N= 2.50, σ= 0.10, α=1.5710, SECOND , Square
File 1, R=1651.1171, N= 2.50, σ= 0.00, α=1.5710, FIRST , Square

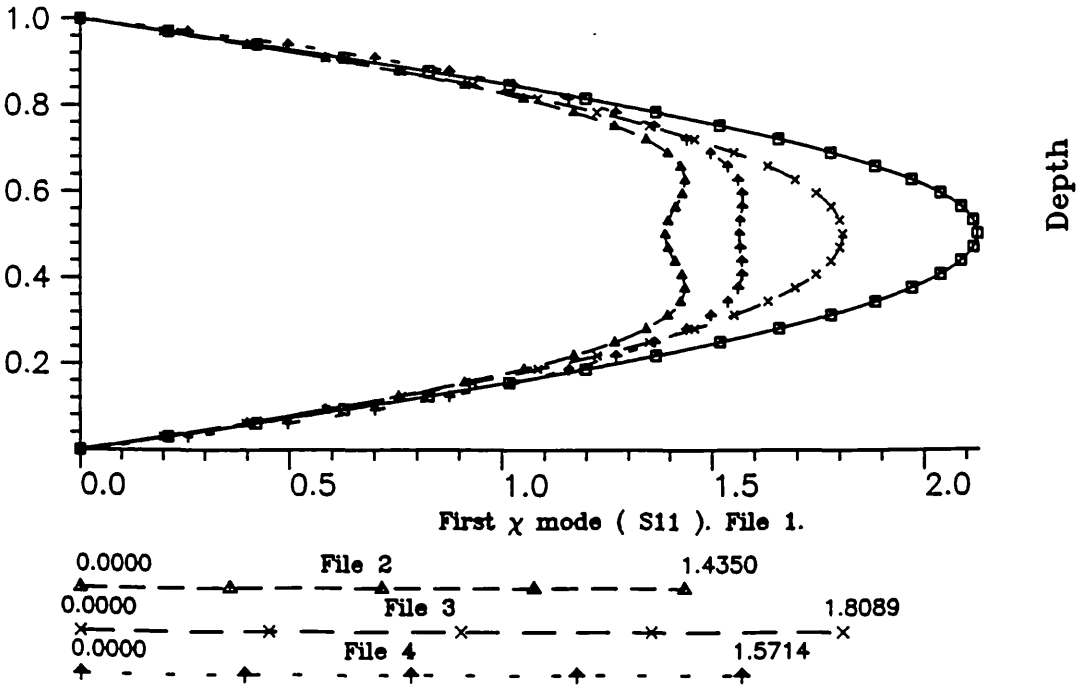


Fig. 5.13b).

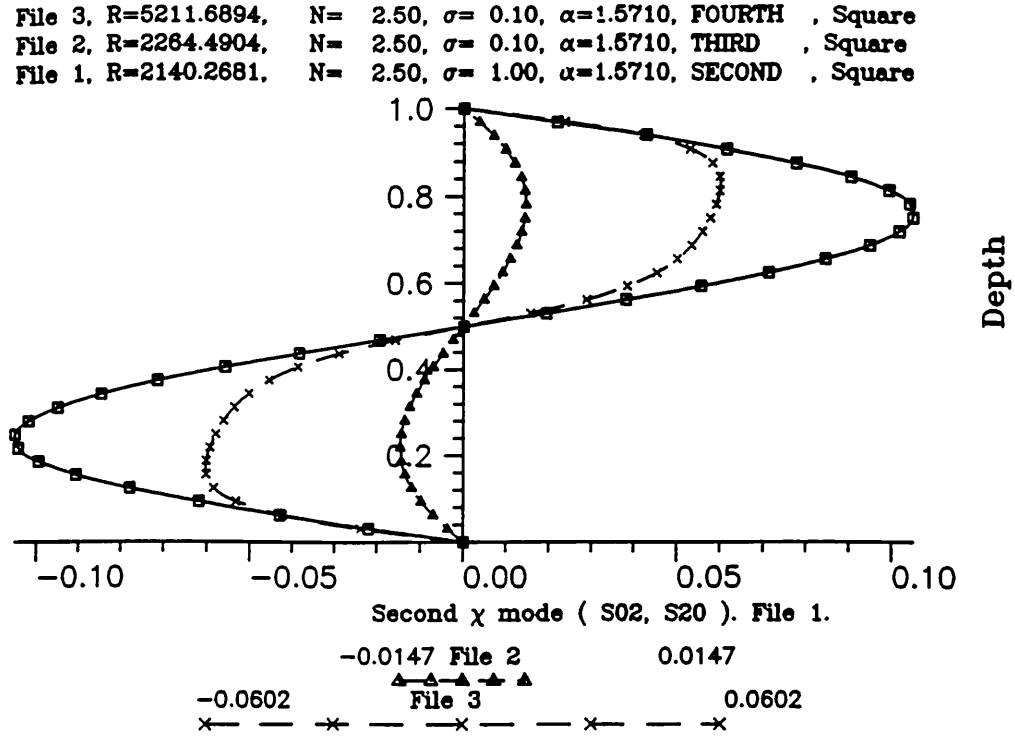
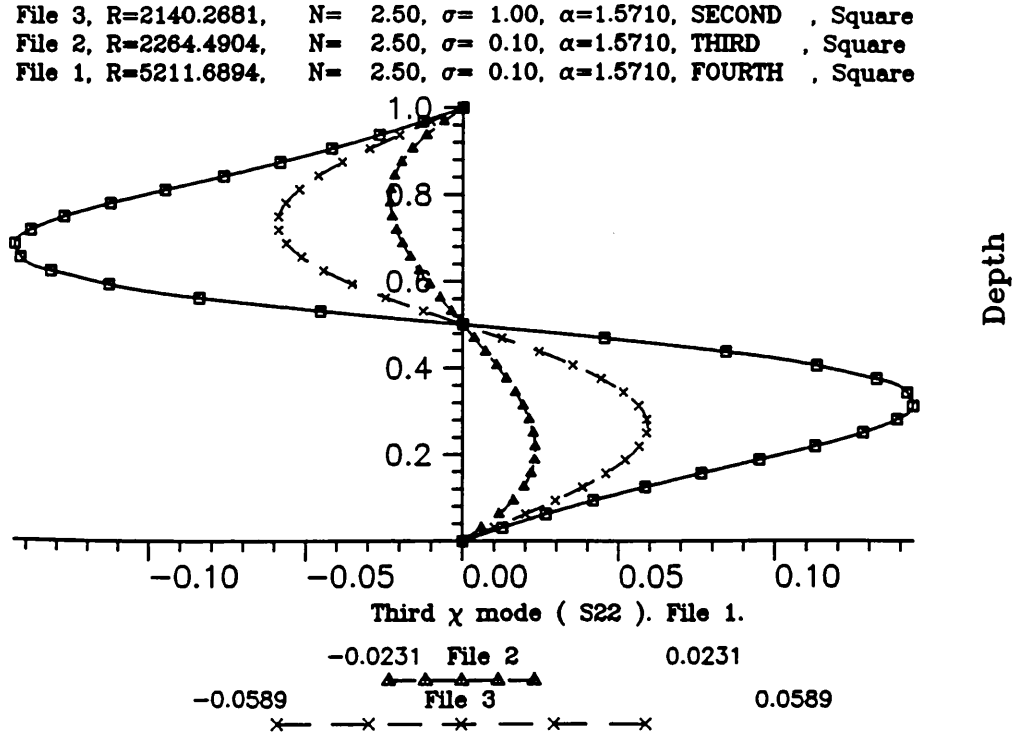


Fig. 5.13c).



corresponding hexagonally horizontally periodic cases. The different modal solutions differ quite significantly even at σ = 10.0, where, for Nu = 2.5, the range of Rayleigh numbers covered is already approximately $0.35Ra_c$ (cf. $0.15Ra_c$ for hexagons). This range increases to $0.8Ra_c$ at σ = 1.0 (cf. the hexagonal $0.5Ra_c$), whereas at σ = 0.1 it is increased as expected, but only to $11Ra_c$ in comparison to the $15Ra_c$ of the hexagonal case. This discrepancy at the lower σ is to some extent explained by the fact that the square solutions do not support a FFIRST, full single mode expansion, which includes the non−linear momentum terms, since these automatically cancel in the calculation (i.e. the coupling coefficient, C = 0). It is this solution set that extends the range figure for the hexagonal periodicity from 7 R_c to 15 R_c. If the FFIRST solutions are ignored, it can be stated that the spread of results for the Rayleigh number at a particular Nusselt number is greater for the square horizontal representation than the hexagonal one at any Prandtl number.

The 'oscillatory' nature of the modal solutions is apparent again, so that the modal solutions appear to tend towards a limiting true solution in the central region, between all of the solutions calculated. At σ = 10.0, the third and fourth order approximations coincide reasonable well up to the Nusselt number of Nu = 2.5, and similarly for σ = 1.0, although not quite as accurately, with the first order and second order solutions over− and under−estimating the heat flux respectively. At low σ, there is still a large degree of latitude between the third and fourth order solutions, showing that neither is particularly accurate assuming that the limiting true solution lies somewhere between them. Again notice that even at relatively high Prandtl numbers, where non−linearity is not an important factor, the first order solutions do not estimate the heat flux particularly accurately.

Next, examine the variables of the vertical solution, which show the individual coefficients of the particular horizontal modes calculated as functions of depth. These are shown as figures 5.13, for Nu = 2.5, σ = 0.1 and the critical wave number for squares, $\alpha = \alpha_c$ = 1.571. The vertical structure of the modes here is much more simple than in the hexagonal case, and the variation of this structure as the truncation level is increased is not as dramatic.

Figure 5.13a) shows the fundamental mode of the first streamfunction, χ, corresponding to the first square cell solution, S11. The dependence shows a maximum value on the order of 1.5 situated at the centre of the layer. Addition of the higher harmonics does not steadily deplete the strength of the fundamental mode, but rather shows another 'oscillatory' type behaviour where the amplitude successively decreases and then increases from one solution set to the next. As the order of the truncation increases, the maximum value of the mode also spreads out so that a region in the centre of the fluid layer has this value rather than the

maximum being a sharp peak.

The second mode, corresponding to the planforms S20 or S02 (remember that their dependences are exactly alike), shown in figure 5.13b), has a '$-\sin(2\pi z)$' vertical dependence in comparison to the previous '$\sin(\pi z)$' functionality of the S11 mode, and again the amplitudes of this function oscillate with increasing order of truncation. Figure 5.13c) for the third χ mode for planform S22, the remaining second order mode, shows a similar but reversed dependence, based on a '$\sin(2\pi z)$' structure, again with successive decrease then increase in amplitude as the truncation order increases. These three results together (figures 5.13a)−c)) show that at second order, the fundamental mode is plundered in order to drive the second order modes, but at third order, the fundamental is enhanced somewhat once more at the expense of the second order modes, which are depleted themselves to drive the third order modes and to partially support the fundamental mode. At fourth order, the fundamental is sapped slightly to drive the new fourth order modes, whilst feedback rebuilds some of the second order modes' strength.

Fig. 5.13d)

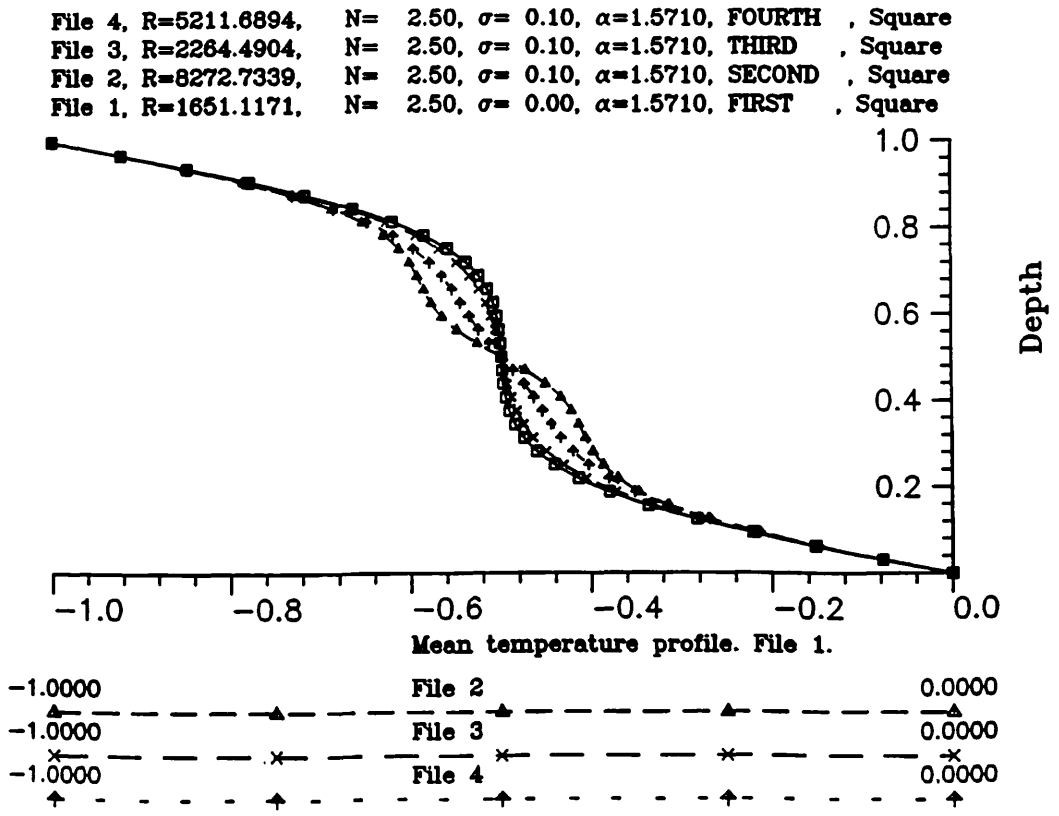


Fig. 5.13e)

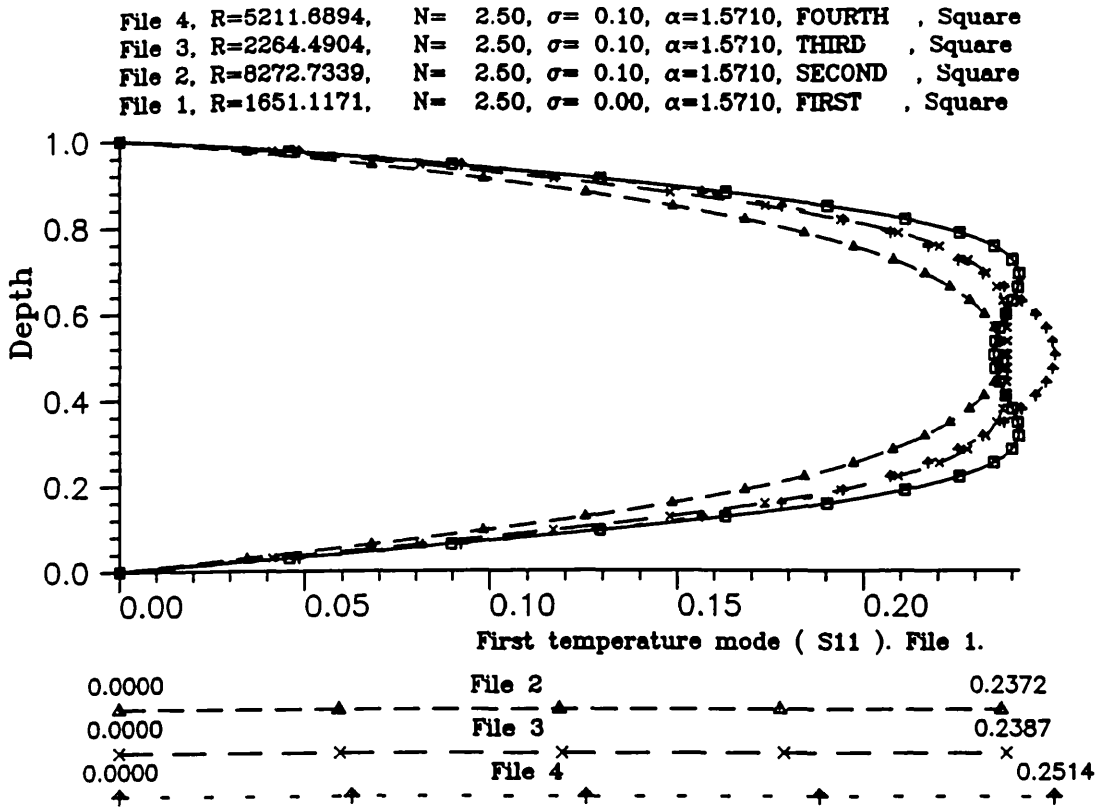


Fig. 5.13f)

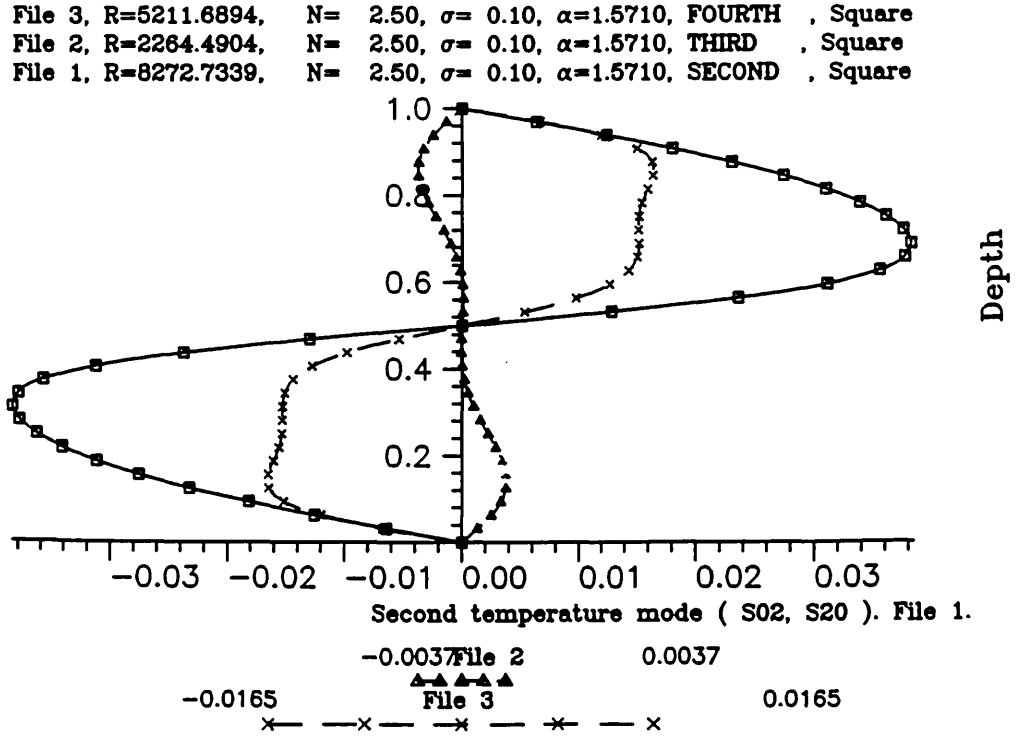
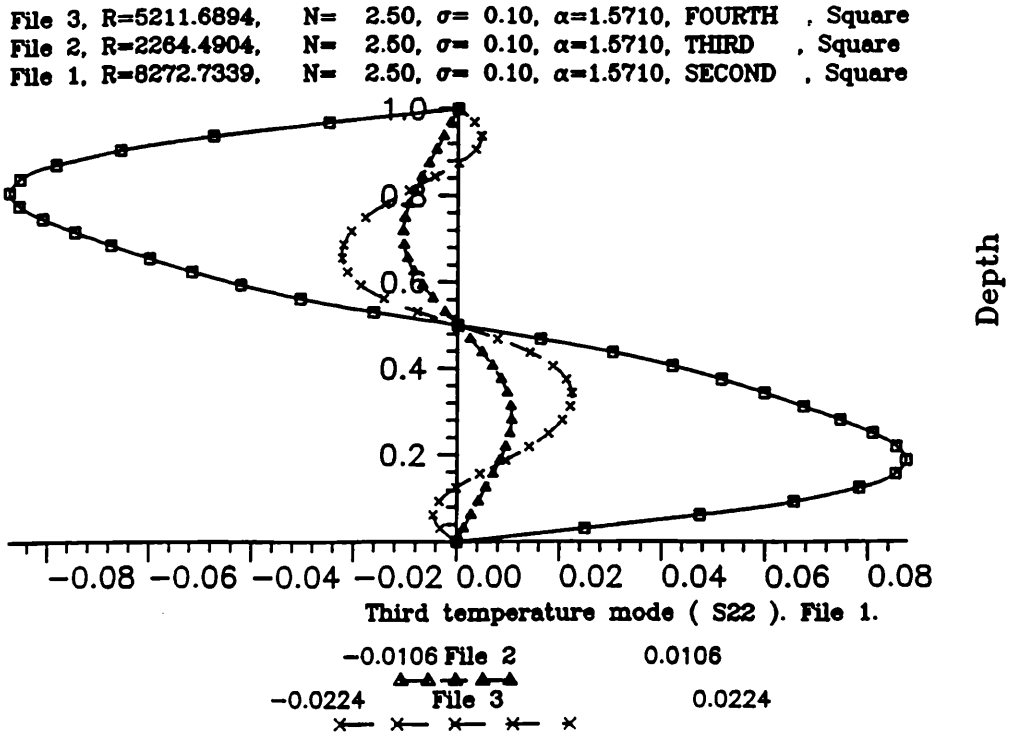


Fig. 5.13g)



It is worth remarking again that the higher order modes are not necessarily physical modes since they carry the burden of the closure of the problem and attempt to mimick the rest of the higher order dependences. Hence the third and fourth orders are not presented here. Notice that all dependences are perfectly symmetric (or anti−symmetric) with respect to the centre of the layer. This infers that the calculation costs could have been significantly reduced by integrating the vertical problem over only half the region, using appropriate boundary and symmetry conditions at the mid−depth. Notice also that all the modes have amplitude on the order of 0.1, except for the fundamental which is much stronger at O(1) and the fourth order modes which are generally much weaker (not shown here). This weakness of the fourth order modes may be again due to the fact that the truncation occured too early for an accurate model (judging by the Nu−Ra graph at this σ) and so feedback from higher order modes would be necessary to support the fourth order modes, much as the lower order modes can be maintained by the inclusion of higher harmonics.

The temperature modes show a greater variety of vertical dependence with modal truncation here for the square periodicity, as was the case for the hexagonal horizontal planforms. The mean temperature profile, shown as figure 5.13d), is odd in that the most non−linear structure, with an isothermal central region and

stronger boundary layers, is exhibited by the first order truncation, rather than the higher order ones. Introduction of the second order modes to this isothermal−type structure introduces a second change in gradient in each half of the layer so that the overall mean profile is very much closer to a conducting profile. The third order solution reverts to the isothermal type nature of the first order, but extension to the fourth order once again smooths the curve, but not as drastically as the second order. Again the solution sets seem to be oscillating towards some median curve which is not as isothermal as the first order solutions, but certainly not a linear, conducting profile. These type of results lend credence to the belief that at this low σ, even the fourth order truncation is not really a good approximation, although in this case it is difficult to say whether the fourth order truncation is actually to be preferred over the first order truncation, bearing in mind the extra computational costs.

Figure 5.13e) shows the fundamental temperature mode (S11) and it may be seen that a similar result to that for the S11 χ mode is achieved except that the amplitude of the mode is not diminished with the inclusion of the higher order nodes. The overall amplitude is much lower, on the order of 0.25, and again the broadening of the central peak may be observed.

One of the second order temperature modes, S02, shows (figure 5.13f)) a reversal of sign in the change between orders, with the second and fourth order solutions agreeing on the '$-\sin(2\pi z)$' style dependence, as for the χ modes, whereas the third order solution reverses this to a '$\sin(2\pi z)$' dependence, modulated so that it contributes a very iso−strength influence of this mode to the core of the layer, in comparison to the strong gradients seen at the centre for the other solutions. Again, the amplitudes oscillate in size, however, and the fourth order solution shows much more iso−amplitude layers. The other second order mode, S22, shown in figure 5.13g), exhibits a '$\sin(2\pi z)$' type dependence for all modes, with the major difference being that the fourth mode introduces small reversals in the sign of the modal dependence at the upper and lower boundaries, and thus biases its peaks towards the centre of the fluid. The overall interchange of amplitudes has been the same for the temperature modes as for the χ modes, as explained earlier, but notice that the temperature modes are a factor of 10 weaker in general.

Again, the third and fourth order modes are not included since they show extreme variations with the changes in truncations. It is interesting to note however, that for both the temperature and χ the S33 mode is much more robust than the S13/S31 modes.

Hence, in summary, the feedback system between the modes in squares appears to differ from that in hexagons in that all the harmonics are not a direct draw on

the fundamental. The vertical dependences are all symmetric or anti−symmetric about the mid−depth, and all the harmonics cover a much smaller range of amplitudes i.e. there is much less bias towards particular modes due to the higher degree of symmetry. The mean temperature profile definitely has perturbations in the normal isothermal−core type non−linear shape. This new shape is retained for all truncations but the actual changes in the sign of the first derivative are removed in the high orders. None of the harmonics appear to be strongly biased towards boundary layers as do some of the hexagonal cases.

Figures 5.14 and 5.15 show surface and contour maps of the vertical velocity over the periodic horizontal square, $0 \leqslant x,y \leqslant 2\pi/\alpha$, and at various depths, in the same manner as for the hexagonal case displayed earlier. After the uniformity of the vertical dependences shown above, these figures show the interesting changes of form that occur to the square planforms as the higher harmonics are added. The pattern remains essentially the same for all truncations, but a simple change of emphasis in the layout makes its appearance change from one square structure to another. Take the first order truncation displayed as figures 5.14a) and 5.15a). This shows the very obvious division of the region into the square subsections of positive and negative vertical velocity dictated by the single planform, S11, which is clearly emphasised in the surface maps which are split into upward flowing and downward flowing components for ease of viewing. The square subsections are simple domed plumes of rising or falling fluid, which remain unchanged except for their amplitude at any depth, since there are no other components to modify the structure. As the higher harmonics are added on to this fundamental mode, the uniformity of the layer with depth is immediately lost, as the balance between harmonics changes at particular depths. The original square structure is replaced by a new but still square velocity pattern. Before, in the S11 pattern, a line could be drawn from each dome, or plume top, to its neighbours, and that line would have vertical velocity all the same sign along it, although the amplitude of this velocity will vary from the maximum (or minimum) to zero. Now, in the new pattern including the higher harmonics, these lines have been emphasized, with the velocity variation along them being smoothed out to a much more uniform value, so that this line becomes a much more obvious straight 'wall'. At the top of the cell, the downflowing lines are emphasized, whereas at the bottom the upflow is more pronounced, although the upflow along these lines is not apparent in the low order truncations. The pattern structure has thus changed from one that has divisions where the positive and negative velocities separate, to one which is divided by strong walls in the more technical sense of the word. The original cellular nature of the pattern has been enhanced. This difference is not quite as noticeable in the third order truncation as in the second and fourth order

Figure 5.14a). Square Rayleigh–Benard convection.
Vertical velocity surfaces at various depths (+ve left)
R=1651.1171, N= 2.50, α=1.571, σ= .00, first

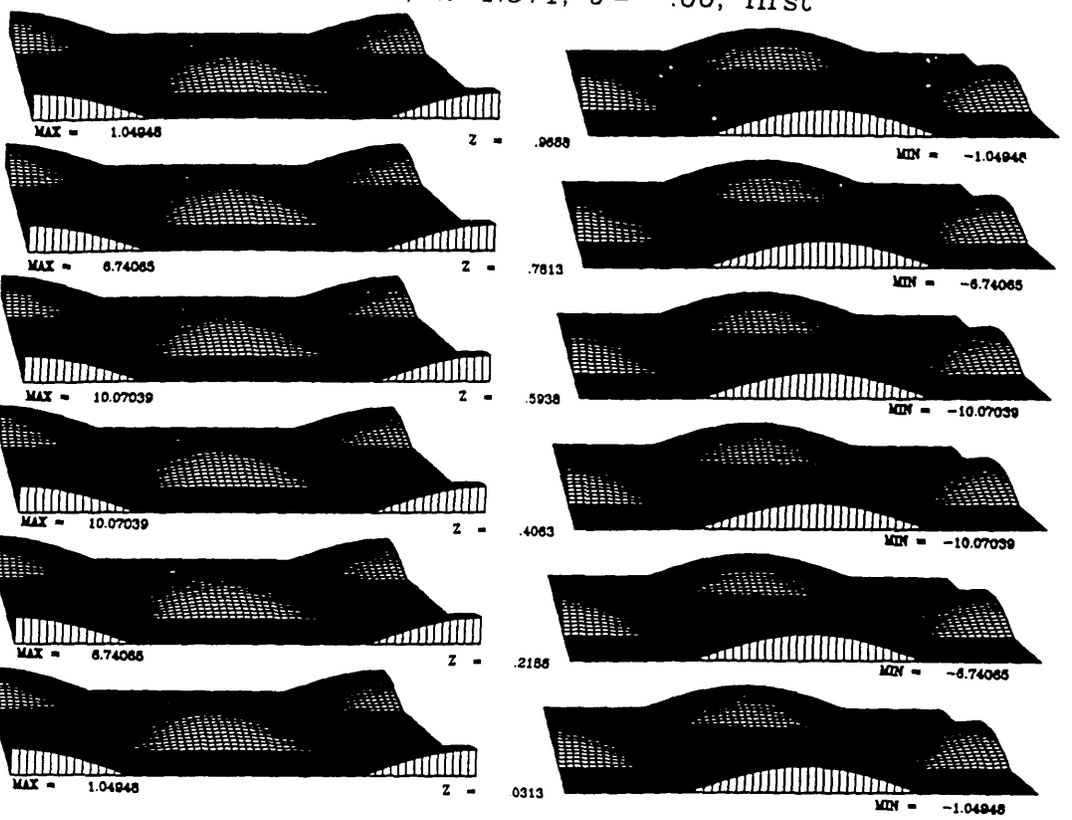


Figure 5.14b). Square Rayleigh–Benard convection.
Vertical velocity surfaces at various depths (+ve left)
R=8272.7339, N= 2.50, α=1.571, σ= .10, second

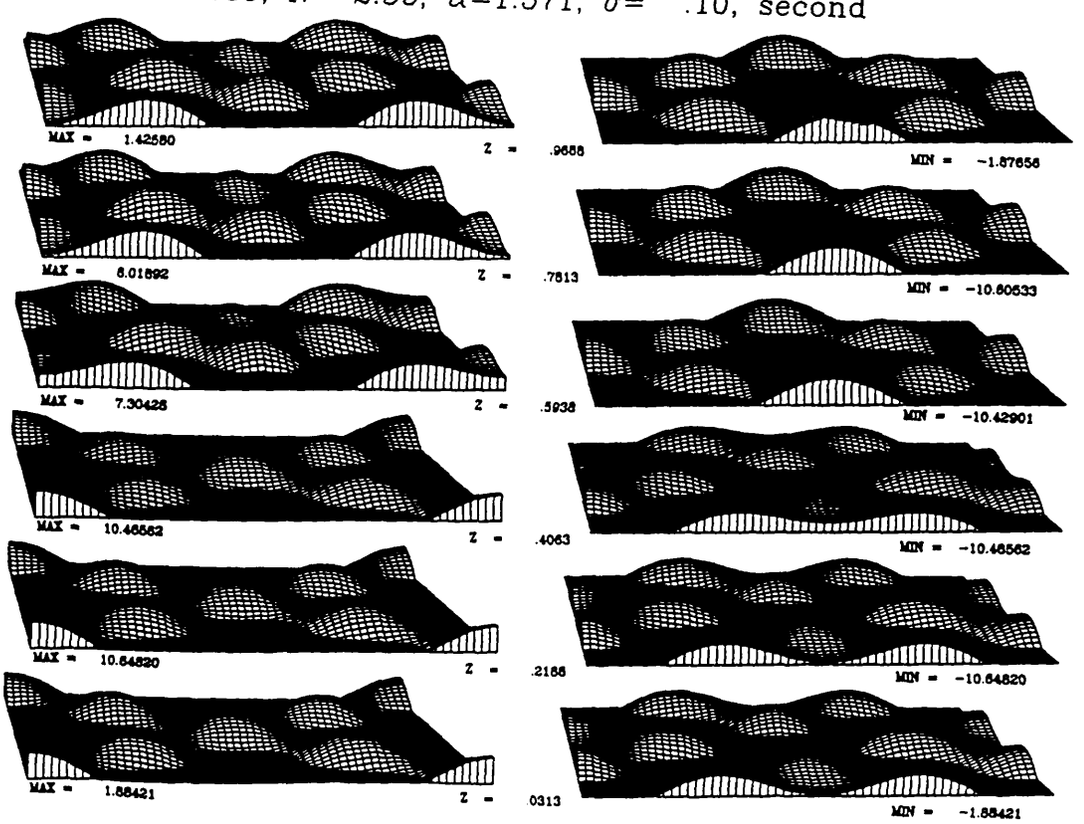


Figure 5.14c). Square Rayleigh–Benard convection. (+ve left)
Vertical velocity surfaces at various depths
R=2264.4904, N= 2.50, α=1.571, σ= .10, third

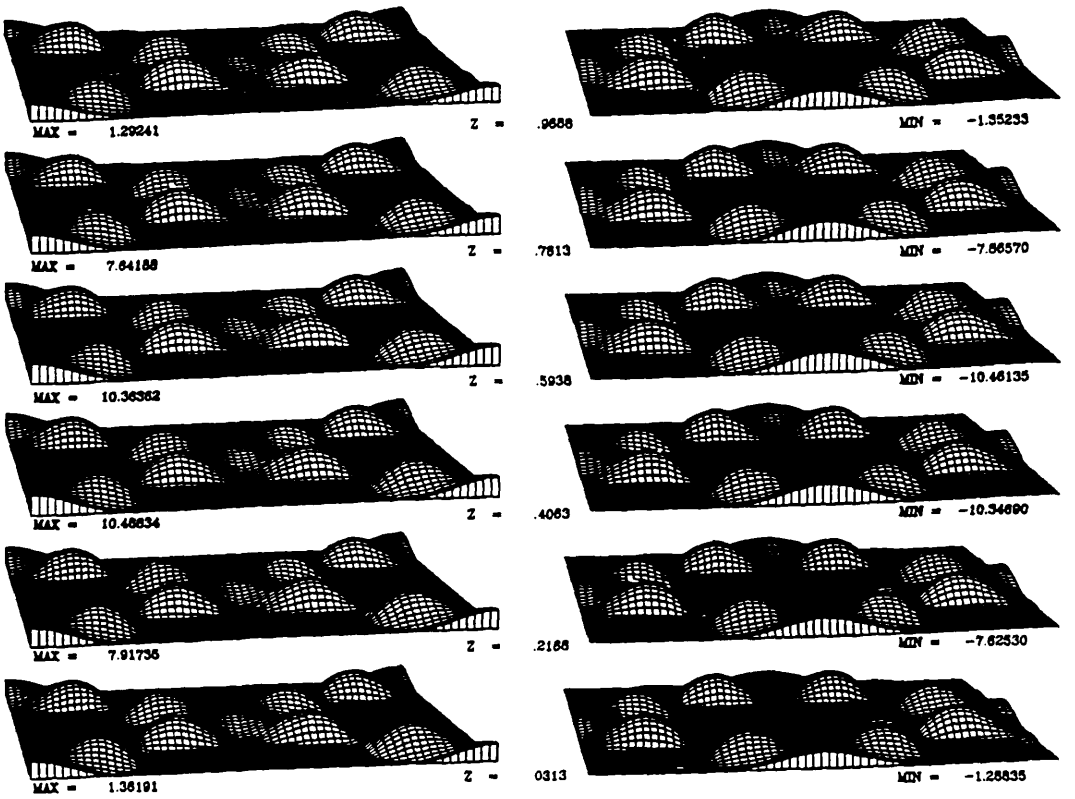


Figure 5.14d). Square Rayleigh–Benard convection. (+ve left)
Vertical velocity surfaces at various depths
R=5211.6894, N= 2.50, α=1.571, σ= .10, fourth

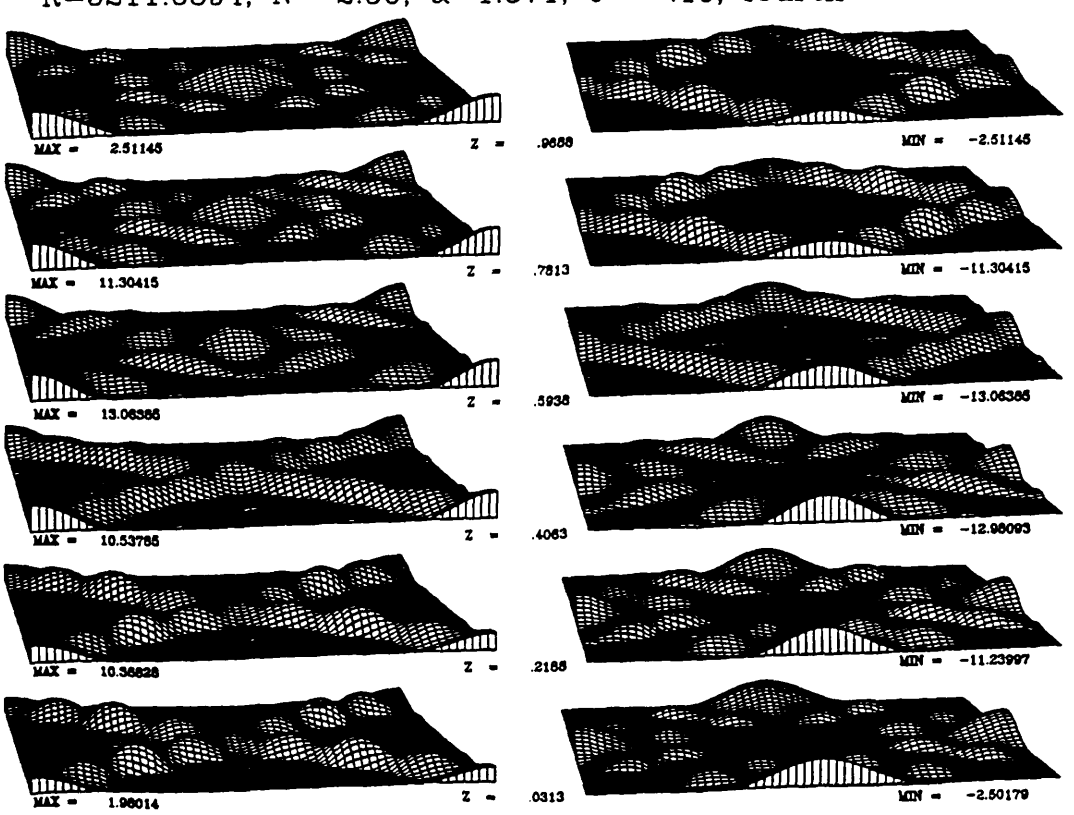


Fig. 5.15a). Square Rayleigh–Benard convection. Vertical velocity
R=1651.1172, N=2.5000, σ= 0.00, α=1.571, first

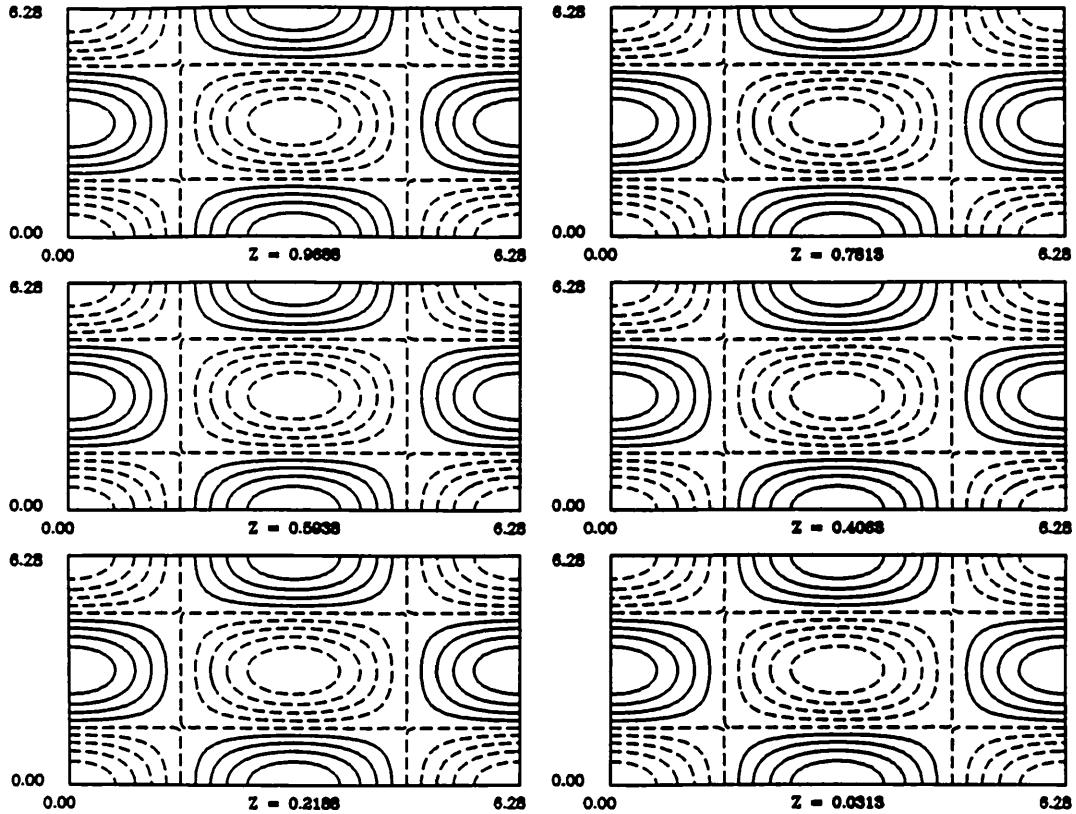


Fig. 5.15b). Square Rayleigh–Benard convection. Vertical velocity
R=8272.7344, N=2.5000, σ= 0.10, α=1.571, second

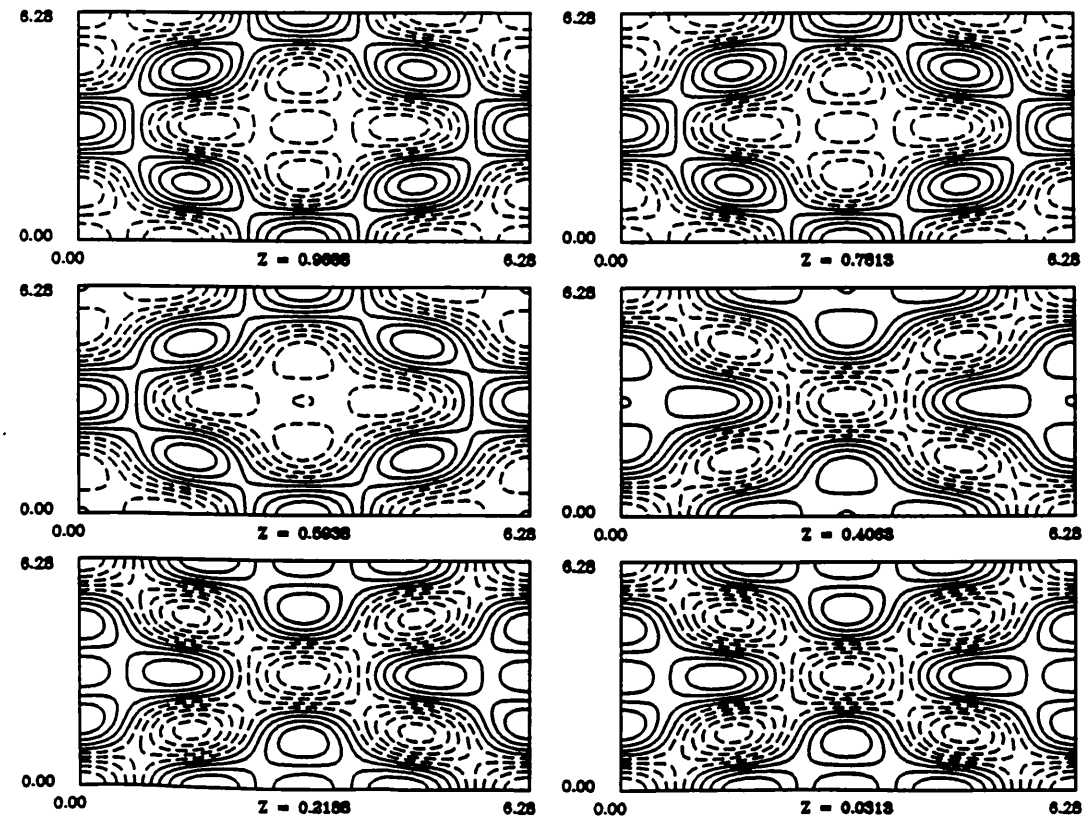


Fig. 5.15c). Square Rayleigh–Benard convection. Vertical velocity R=2264.4905, N=2.5000, σ= 0.10, α=1.571, third

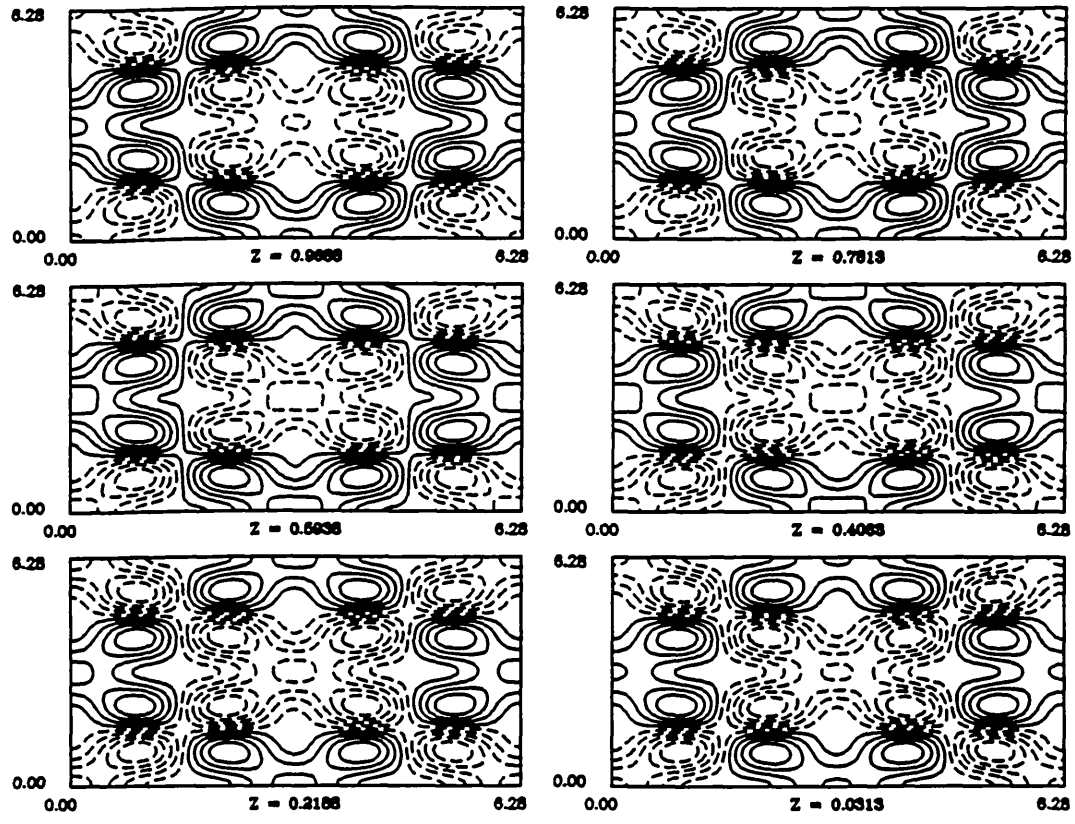
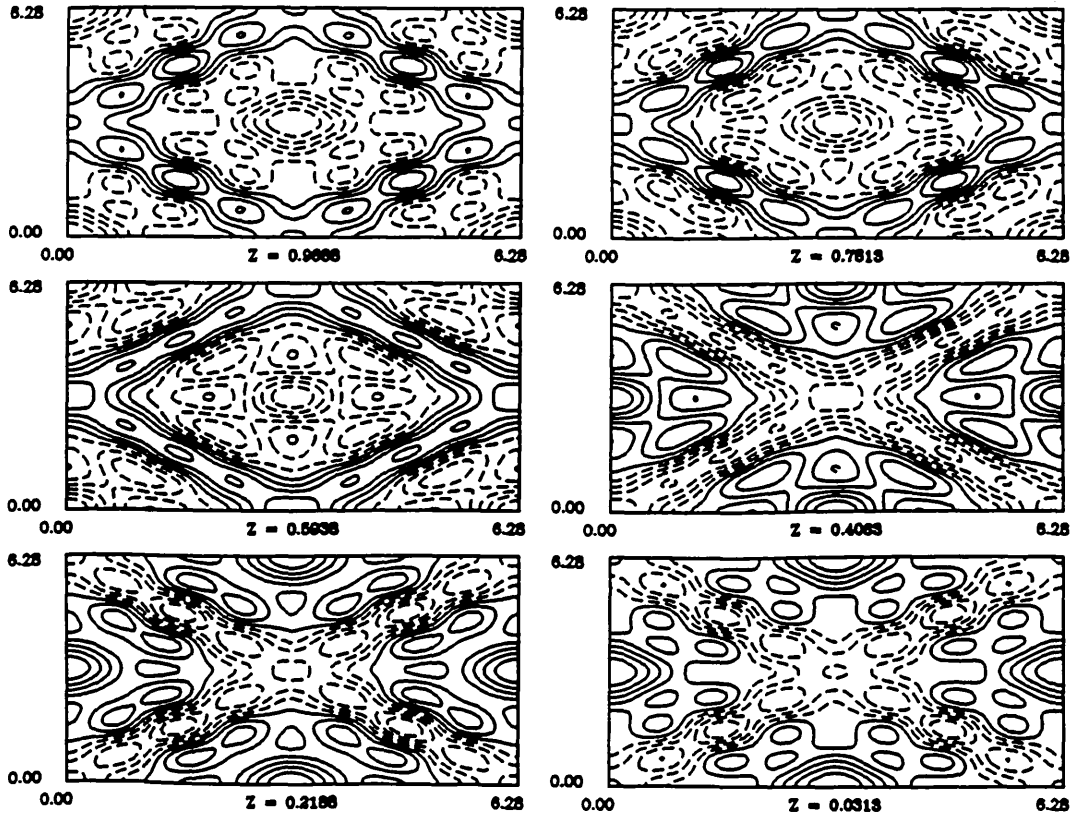


Fig. 5.15d). Square Rayleigh–Benard convection. Vertical velocity R=5211.6895, N=2.5000, σ= 0.10, α=1.571, fourth



truncations, so this effect may be enhanced primarily by the even order harmonic expansions rather than the odd ones, the latter of which may tend to emphasize the original nature. Notice that the asymmetry between the upper half and the lower half of the layer is in fact just an emphasis of the other component of vertical velocity in the same manner i.e. in the upper half, the negative vertical velocity 'wall' structures are emphasized, but in the lower half, the same structure for the upflowing fluid shows through, with the positive plume structure of the lower order truncations merging to form an upflowing wall. This is then simply a reflective asymmetry or anti−symmetry so that the pattern on the lower boundary holds the same features as that of the upper boundary, but is simply shifted laterally by half a wavelength and reversed. However, this anti−symmetry has far−reaching consequences for the true cellular nature of the square cell. What were originally clear downflowing walls in the S11 planform (the lines joining the centres of the downward plumes at the top boundary extended down as a vertical plane), are definitely not cell walls in the higher order truncations (at these parameter levels). A line drawn vertically down from any one of the mid−points of the wall−lines in the top layer, now has a change of sign in the vertical velocity, from downflow in the upper half, to upflow in the lower half. A similar effect was seen for the hexagonal cells when many harmonics were included, but the total asymmetry of the layer about its mid−point in that case meant that the flow reversal was severely confined and not very significant. Here in the square case, however, the (anti−)symmetry makes the upflow criss−cross pattern at the bottom boundary as strong as the downflow at the upper boundary in the high order solutions, and since the two patterns are destined to cross, the cellular nature is destroyed in the technical definition.

Inclusion of the higher harmonics strengthens the vertical velocity motions throughout the layer, with a slight increase at the centre, $z = 0.5$, and significant enhancements nearer the boundaries, so that the vertical velocity is more uniformly distributed, with less of a peak at the mid−layer. Now, most of the vertical deceleration takes place close to the boundaries so that the boundary layer structure has been enhanced.

Isotherms and amplitude contours for velocity and vorticity are shown in figures 5.16 for various vertical slices through the horizontally periodic cell. The first slice is a diagonal slice from the south west corner to the north east corner of the planform, the second is an $y-z$ plane cutting across the middle of the cell from south to north, and the third is a similar plane but situated at the position where the vertical velocity swaps from positive to negative in the original S11 planform, at $x = \pi/2\alpha$. The isotherms start with a simple exhibition of the downflowing plumes (the two troughs in the first slice) and the upflowing pattern centre

Figure 5.16a). Square Rayleigh-Benard convection.
R = 1651.12, N = 2.50, σ = 0.00, α = 1.571, first
a) x=y, y=(0,2π/α) , b) x=π/α, y=(0,2π/α) , c) x=$\pi/2\alpha$, y=(0,2π/α)

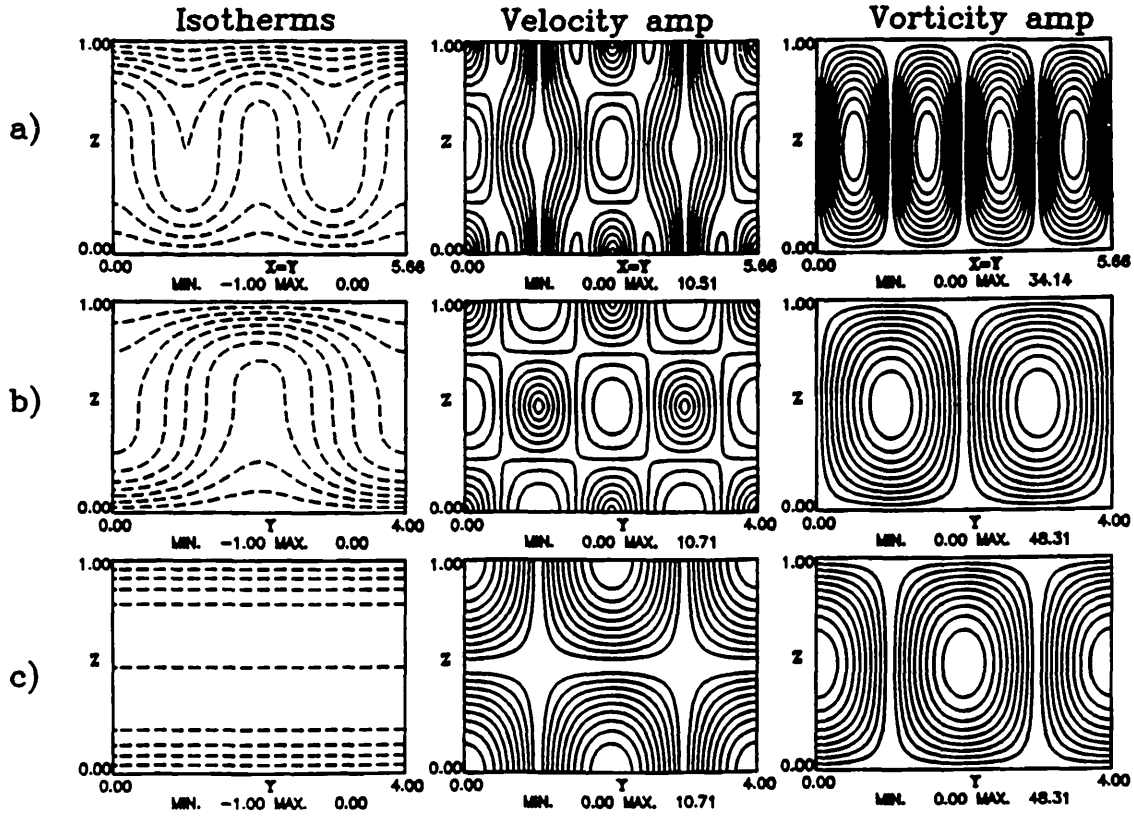


Figure 5.16b). Square Rayleigh-Benard convection.
R = 8272.73, N = 2.50, σ = 0.10, α = 1.571, second
a) x=y, y=(0,2π/α) , b) x=π/α, y=(0,2π/α) , c) x=$\pi/2\alpha$, y=(0,2π/α)

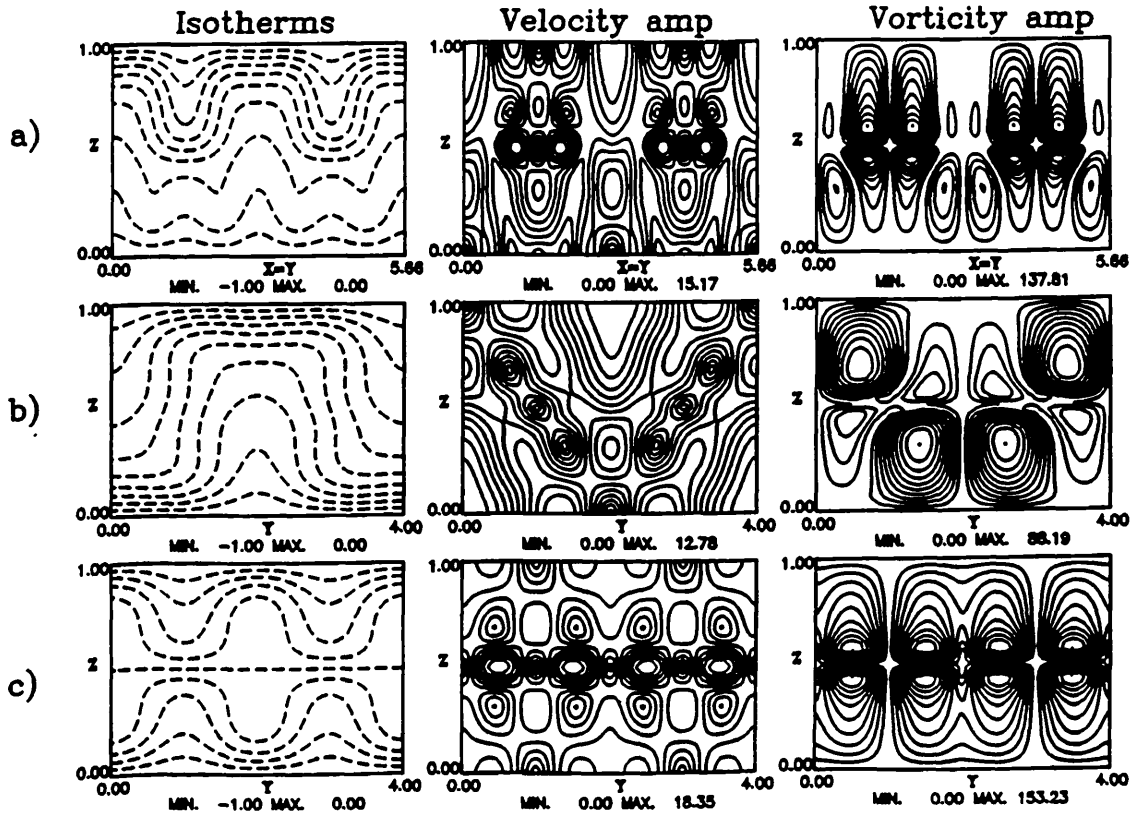


Figure 5.16c). Square Rayleigh–Benard convection.
R = 2264.49, N = 2.50, σ = 0.10, α = 1.571, third
a) x=y, y=(0,2π/α) , b) x=π/α, y=(0,2π/α) , c) x=$\pi/2\alpha$, y=(0,2π/α)

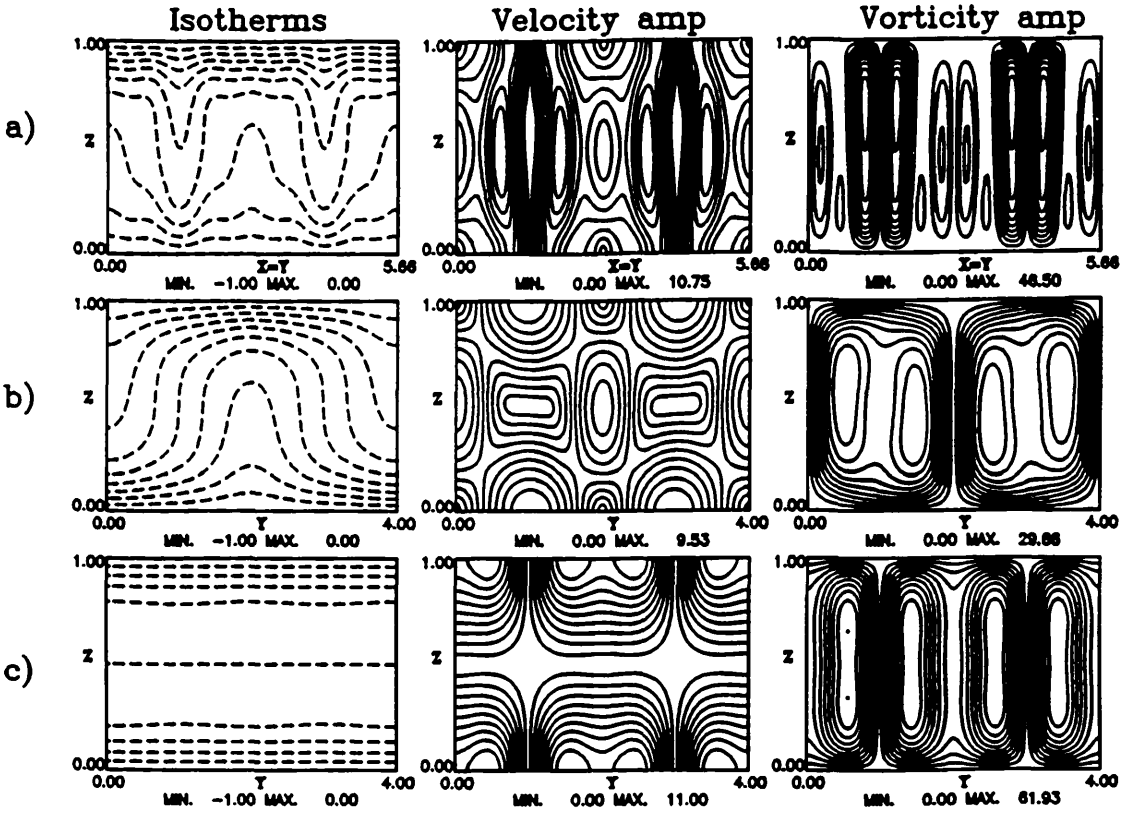


Figure 5.16d). Square Rayleigh–Benard convection.
R = 5211.69, N = 2.50, σ = 0.10, α = 1.571, fourth
a) x=y, y=(0,2π/α) , b) x=π/α, y=(0,2π/α) , c) x=$\pi/2\alpha$, y=(0,2π/α)

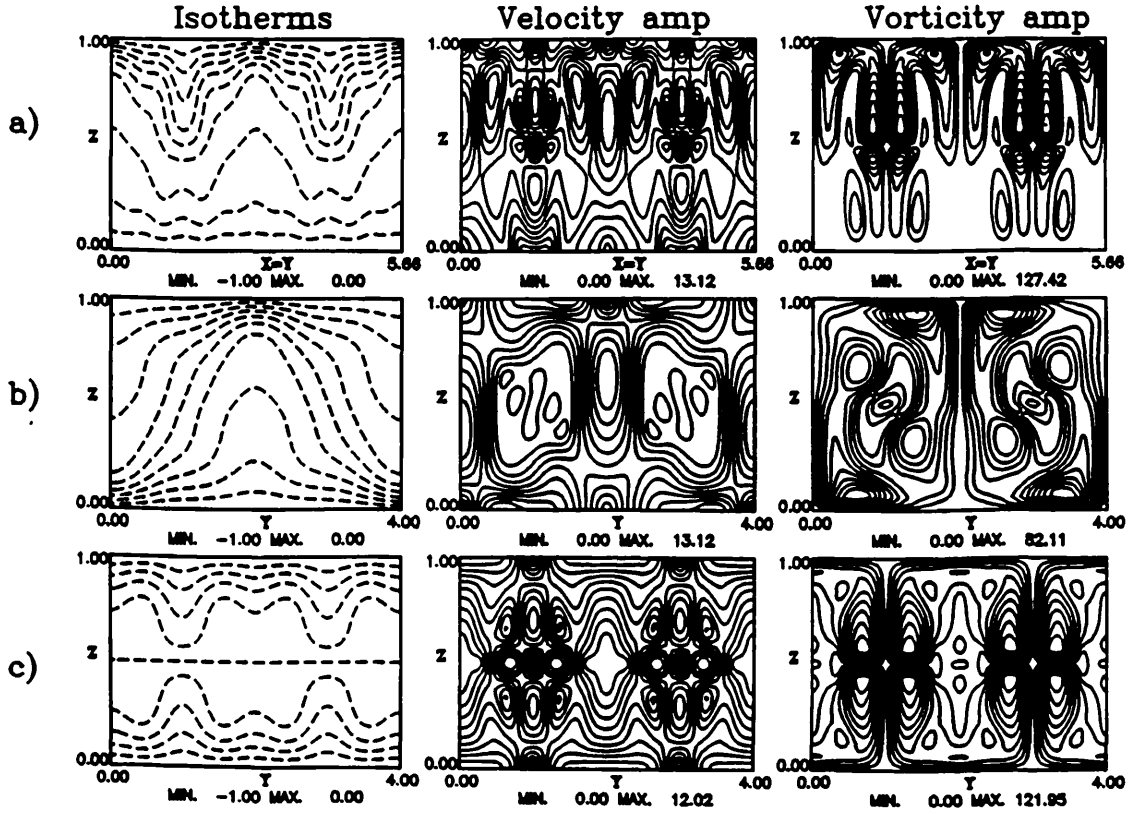


Fig. 5.17a) **Stereo velocity plots – Square Rayleigh–Benard convection R = 1651.12, N = 2.50, σ = 0.00, α = 1.571, first**

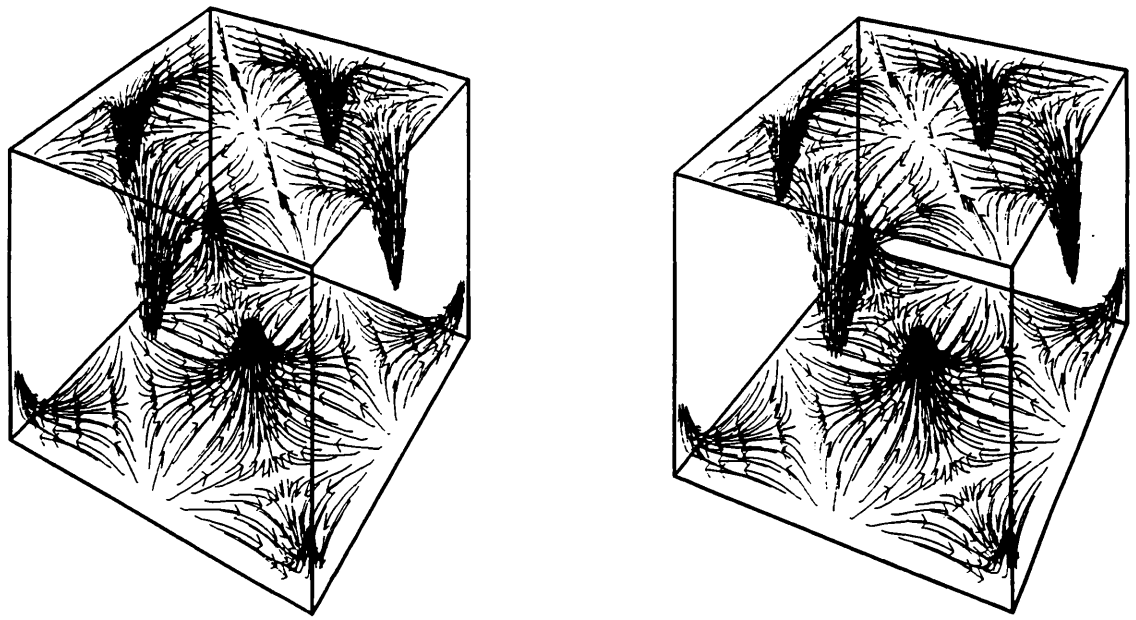


Fig. 5.17b) **Stereo velocity plots – Square Rayleigh–Benard convection R = 8272.73, N = 2.50, σ = 0.10, α = 1.571, second**

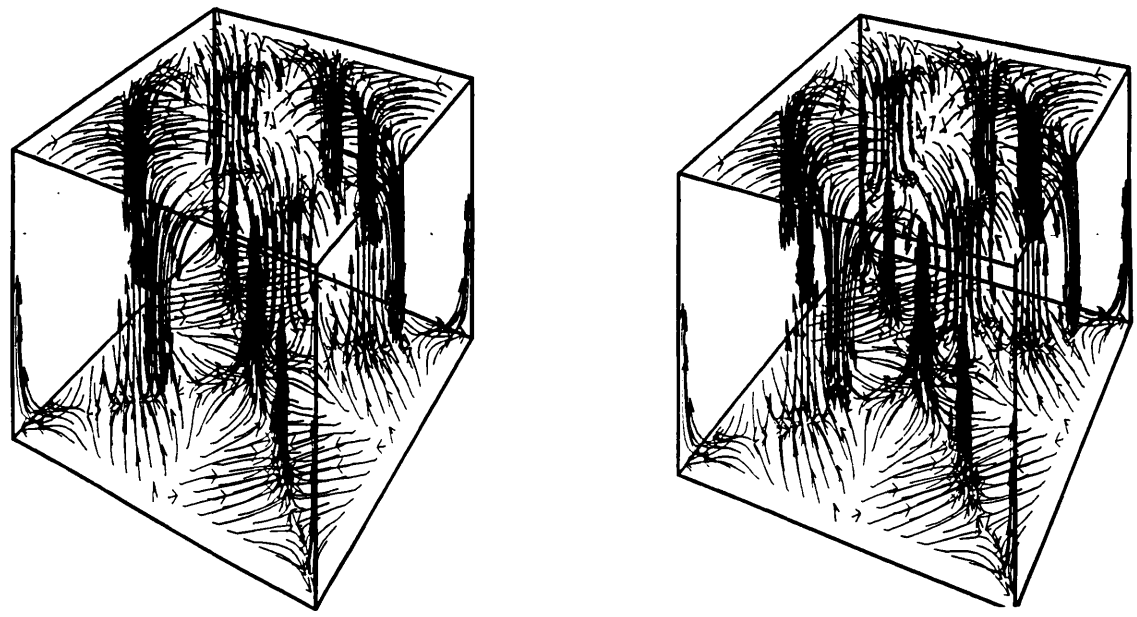


Fig. 5.17c) **Stereo velocity plots – Square Rayleigh–Benard convection R = 2264.49, N = 2.50, σ = 0.10, α = 1.571, third**

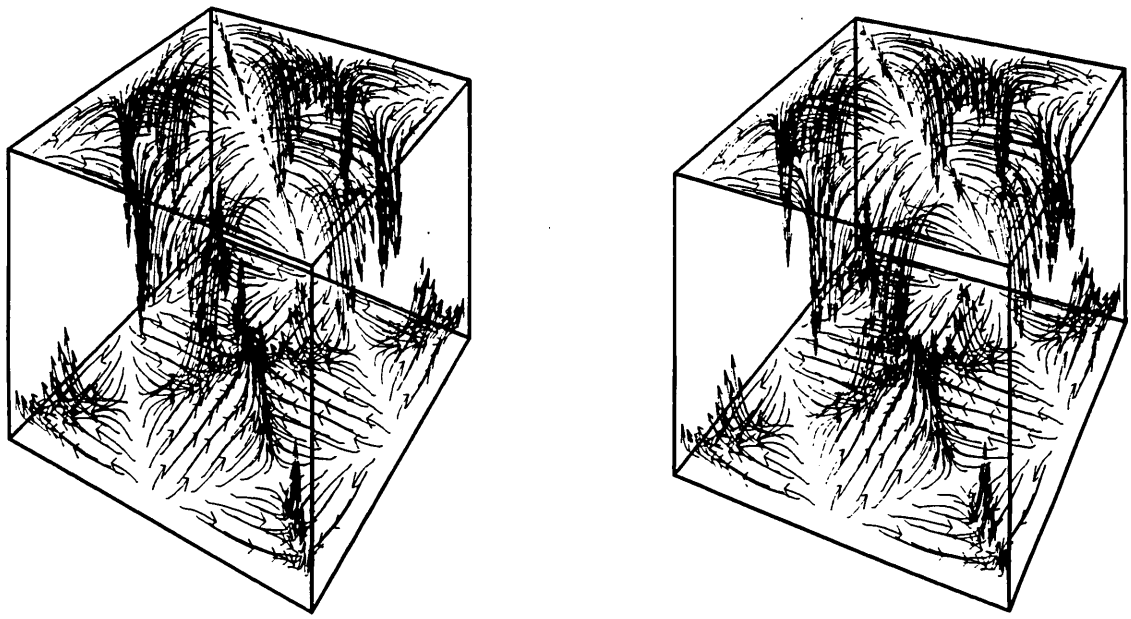
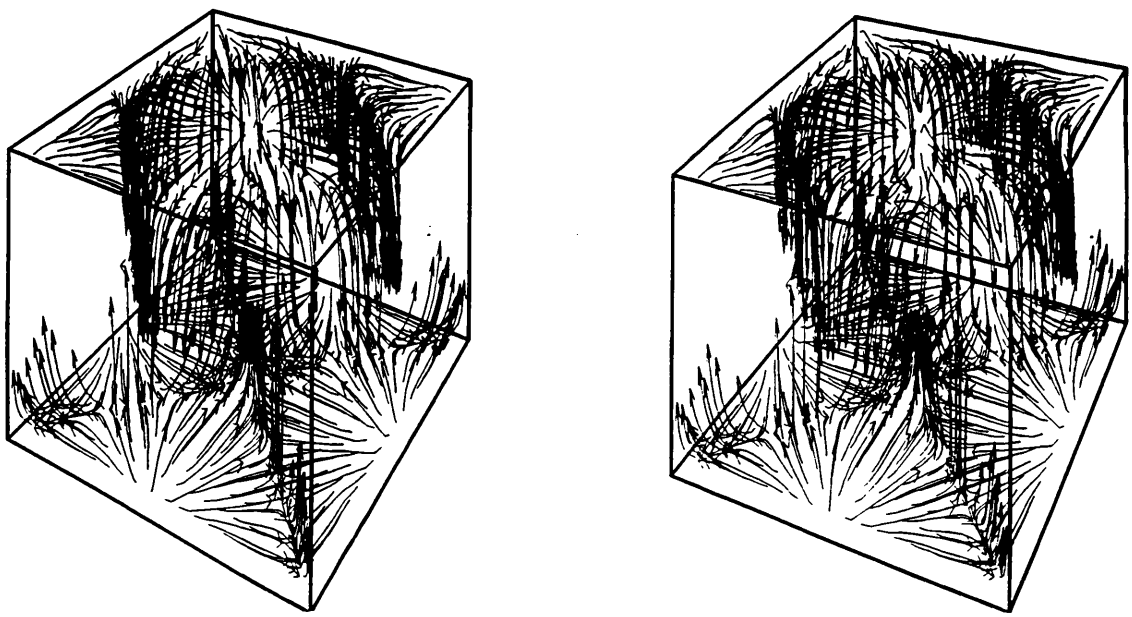


Fig. 5.17d) **Stereo velocity plots – Square Rayleigh–Benard convection R = 5211.69, N = 2.50, σ = 0.10, α = 1.571, fourth**



(single peak in the second slice) for the first order solution. These are actually just two cuts through the simple dome structured plumes of the up and down flowing simple flow. Notice the simple stratification of the S11 wall slice as well.

As the second order harmonics are included, the wall−like flow becomes emphasized in the short peaks and the anti−symmetrical influence of the reverse flow is seen to cut off the peaks in the lower half of the layer with the slight reverse flow. The second slice shows that now the central dome has become very isothermal, with sharp gradients between domes. At third order, the reverse flow is abated slightly, so that the strong wall structure is seen in the first slice and the smoother dome returns, but fourth order restores a stronger flow in the lower half, so that the smooth dome becomes more of a peak and the downflowing walls are confined mainly to the upper half layer. The simple stratification of the y−z plane at $x = \pi/2\alpha$ is lost at second and fourth order where this is no longer an obvious wall, but is regained at third order, since the superposition of rolls allows walls to coincide between the planforms at this order.

The first and third planform orders make similar approximations about the fields, as do the second and fourth, which is not surprising since this basically divides the approximations into either odd−harmonic dominated truncations or even−harmonic dominated. The overall amplitude of the velocity is enhanced by 30% or more in the even approximations, whereas the vorticity amplitude is strongly increased by roughly 100%. The main differences are that the even harmonic expansions show a greater divide between the upper and lower halves of the layer.

Figures 5.17a)−d) show stereo plots of the actual velocity for the square periodic cell, $0 \leqslant x,y \leqslant 2\pi/\alpha$, $0 \leqslant z \leqslant 1$, where the arrows have been started from layers just below the top and the bottom of the cell. These plots show that the basic flow pattern remains similar, but on closer inspection the differences become apparent, as was the case for the contour plots described earlier. At first order the velocity−following shows the flow to be dominate by strong plumes, where the fluid falls at the vertices of a square planform at the top of the layer, and rises in the centre, with the horizontal planform being considered 'square' by the divisional nature of lines joining the vertices at the top projected onto the lower boundary (these lines behave as dividing streamlines). Notice that this is confusing, since the vertical velocity contours imply a different type of 'square' planform from the one actually that actually exists. If Stuart's (1964) definition of a cellular planform is borne in mind (see Chapter 4) then the decision as to which of these is actually the square cell is clearer. The contours show what might be seen in experiments and mistaken for square cells, but the true cells are actually those areas bounded by the planes joining the plume−centres. Addition of the harmonics changes the flow pattern subtly. Introduction of the new modes

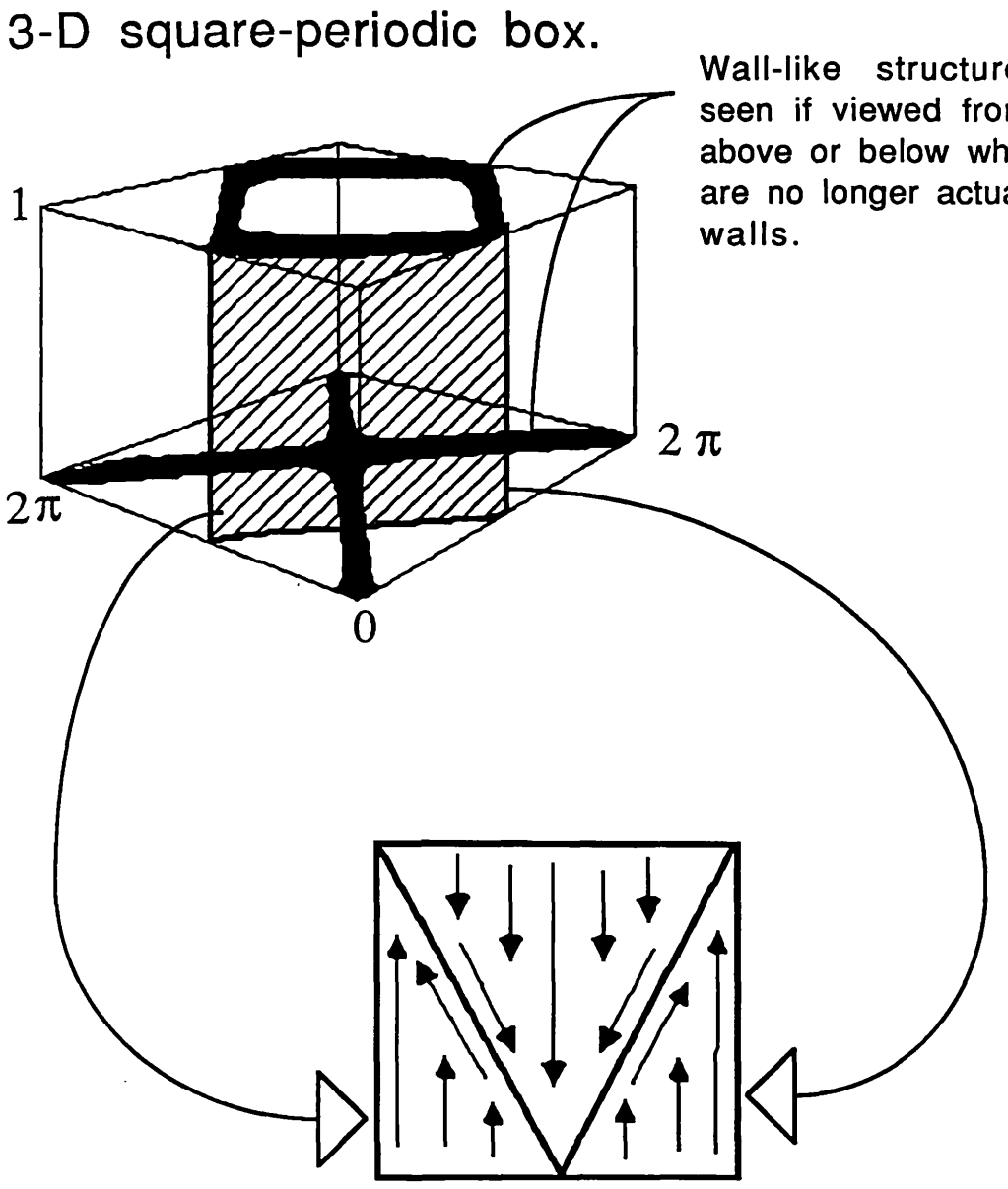


Diagram 5.2. Possible new flow pattern at low Prandtl number on the 'walls' of the squarely periodic pattern.

does not change the position of the cell 'walls' (where the term 'wall' refers to a vertical plane plane lying beneath a line joining the centres of two similarly signed plumes) but no longer directs the flow to the original vertices (plume centres). The new planform allows rising and falling plumes to be generated along the lines joining those vertices. The result is a planform for motion where the horizontal motions are diminished and obvious vertex flow is lost in favour of more uniform vertical flow along the straight lines which truly divide the layer into squares (the 'walls'). However, the question of what is a square cell in the true sense of Stuart's definition is now a problem because these lines are not true cell walls in the higher order solutions, despite having been emphasized in the flow. The vertical velocity is required to be all of one sign on a such a wall for it to be deemed a divide between cells. These criss−cross lines are obviously not then cell walls because the square patterns they describe at the top and bottom have vertical flow of opposite signs and cannot fail to cross one another. However, this flow pattern could easily be mistaken for a cuboid cell in an experiment where the top of the pattern only may be seen and thus what appears to be an obvious sheet of downflowing fluid could be construed as a simple, vertically−uniform dividing wall, although it is easy to see here that this is not true (the obvious counter example point being the strong upflow at the bottom of the downflowing wall in the fourth order case). However, the discussion of the definition of a square cell has continued for many years from the original suppositions by Stuart (1964) to more recent papers such as Jenkins (1987), with the result being more a matter of opinion than hard fact. What was the original cell wall in the S11 representation may now be regarded as four cell walls joined together (see diagram 5.2), and so whether this actually constitutes a cell wall is a matter for discussion. It may be postulated that the harmonic patterns show no true cells but 'a cellular nature'.

In summary, the modal expansion employed for a square horizontal periodicity seems to be a more important consideration than that for hexagonal periodicity at high and moderate Prandlt number, and is important at low Prandtl number as always. The influence on such global effects as the heat flux and the mean temperature profile is quite marked for all σ. However, at the lowest Prandtl number generally calculated, the highest truncation used is still not necessarily an accurate approximation, although it does seem to be a distinct improvement on the lower order solutions, at least with respect to the mean properties of the fluid in comparison with a theoretical 'true' solution. The main effect of adding the higher order harmonics is to remove the true cellular nature of the flow since there are no longer planes in the fluid which have no horizontal motions across them and vertical velocity all of one sign on them, as required by Stuart's (1964) definition. The harmonics broaden the plumes and sharpen the 'walls' as for the

hexagonal planform, but this emphasis of the vertical flow along certain lines coupled with the asymmetry about the mid−depth in the fluid divides the boundary flows into conflicting square patterns which destroy the true cellular nature.

5.4.2. The Prandtl number dependence.

Figures 5.18a) and b) show that both the hexagonal and square periodic solutions have a strong dependence on the Prandtl number. Figure 5.18a) shows the curves of Ra versus σ on a linear scale and it can be seen that the Rayleigh number is constant for $\sigma > 2.5$, but rises sharply at values below this cut−off point for both planforms. The more detailed log−log plot of figure 5.18b) shows more clearly that the square periodicity is actually more σ−dependent than the hexagonal case, showing a slope at low σ of approximately -0.7, compared to the hexagonal slope of -0.15, implying that the dependences may possibly be of the type $Ra \approx \sigma^{-2/3}$ for squares and $Ra \approx \sigma^{-1/6}$ for hexagons. Figure 5.18c) shows the Prandtl number dependence for the lowest Prandtl numbers calculated. This plot is shown at the lower amplitude level of Nu = 1.1, since the modal trunction is not able to cope with higher amplitudes of convection at low σ, and serves to show that the dependence is different at different Nusselt numbers i.e. the heat transport is a function of both the Rayleigh number and the Prandtl number.

There is still some question as to which truncation is to be considered as the 'best' truncation for both of the planform models chosen for this study, especially at low Prandtl numbers where the maximum truncation used here is still not necessarily an adequate modal expansion of the system to enable acurate answers to be obtained. However, on the basis of the Nu−Ra number graphs where it appears that each successively extended truncation is converging towards some true limiting solution, and bearing in mind that the global variables such as this heat transport and the mean temperature profile are the more important aspects of the flow, it will be implicitly assumed in the following investigations that the highest order truncation available offers the most accurate solution. Therefore, in general, only the FOURTHVV solution set will be considered for the hexagonally periodic case and only the FOURTH set when considering the square case, for the investigations of the dependence of the solutions on the parameters of the physical system.

Figure 5.18a). . Rayleigh no. versus Prandtl no.

Nu = 2.50

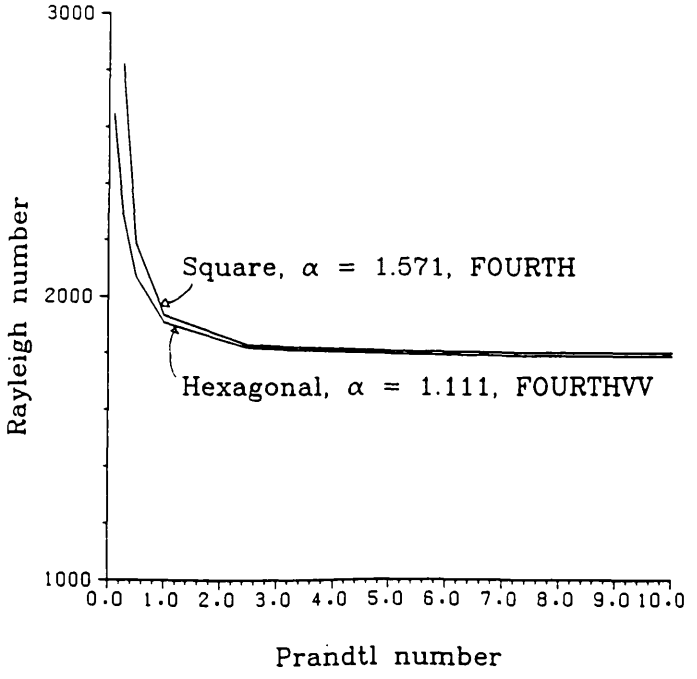


Figure 5.18b). . Rayleigh no. versus Prandtl no.

Nu = 2.50

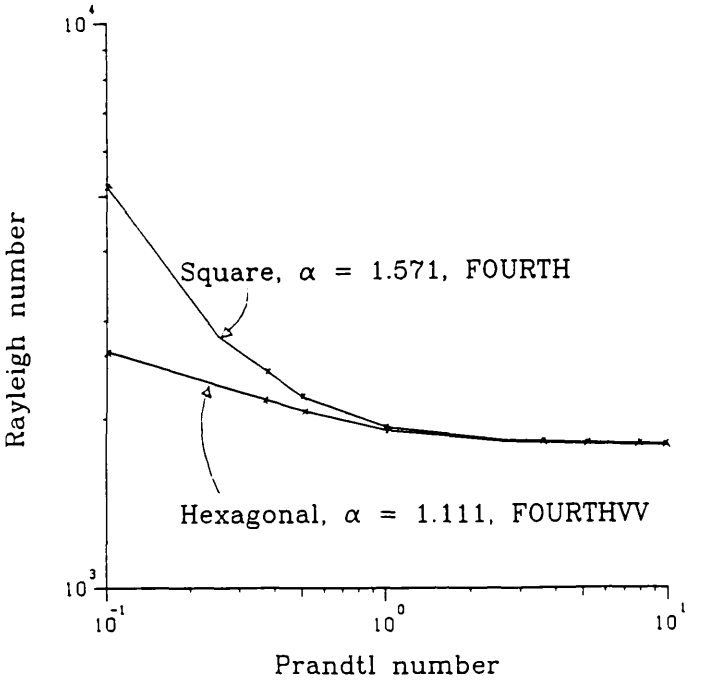
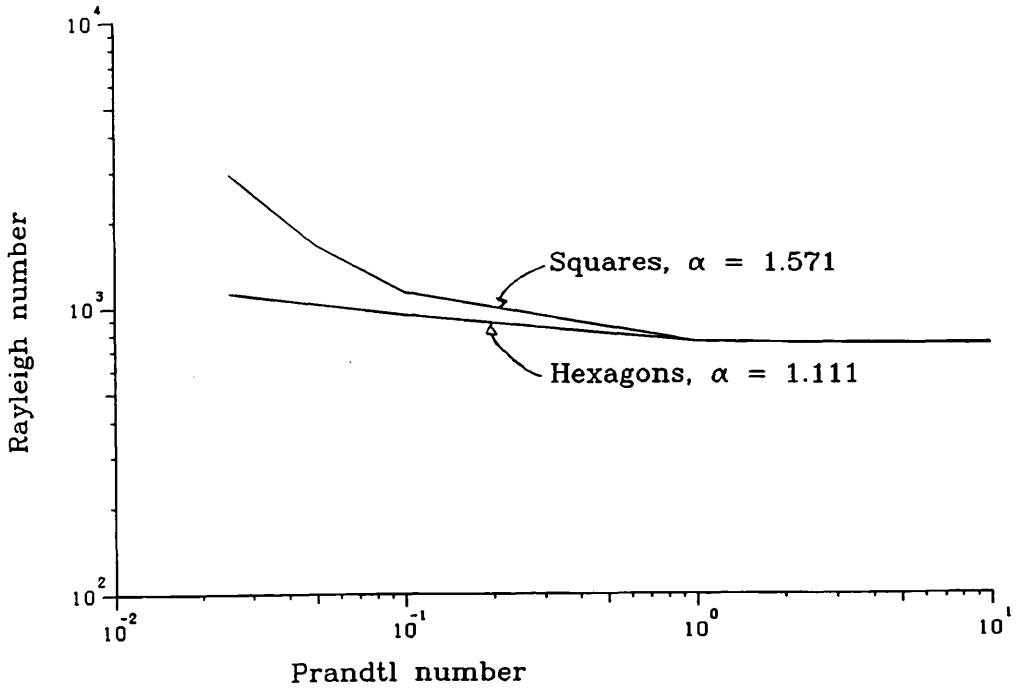


Fig. 5.18c) . Rayleigh no. versus Prandtl no.

Nu = 1.20



5.4.2.1. Hexagonal horizontal periodicity.

A strong Prandtl number dependence is seen in the FOURTHVV order hexagonal solutions, exhibited most obviously in figure 5.19a), which shows the Nusselt number plotted as a function of Rayleigh number for the Prandtl numbers, σ = 10.0, 1.0, 0.1 and 0.05. It can be seen that the Nusselt number decreases with decreasing Prandtl number quite dramatically, dropping by about five times more between σ = 1.0 and σ = 0.1 than between σ = 10.0 and σ = 1.0. In previous works, there are some discrepancies about this dependence. Some authors, such as Moore and Weiss (1973a) working with 2−D rolls, Jones, Moore and Weiss (1976) working with cylindrical convection, and Proctor (1977) working with axi−symmetric convection, have found no σ−dependence at all for low σ, in what is known as 'flywheel' or 'inertial' convection. Other solutions, such as the modal solutions of GST (both single mode, GST2, and multimode, GST3), have found the Nusselt number to decrease with decreasing σ for low Prandtl numbers. Figure 5.19a) shows that there is a large σ dependence between σ = 1.0 and σ = 0.1, but that for lower values of σ the curves are not differing from the previous ones in such a dramatic manner. Figure 5.19c) shows lower Prandtl

numbers, σ = 0.05, 0.025 and 0.01 but it can be seen that the modal solutions break down for relatively low amplitudes of convection at lower σ, with the curves showing odd and sometimes discontinuous changes in gradient. However, the results at very low amplitudes appear to indicate that the flow is behaving much as for the cylindrical convection described by Jones, Moore and Weiss (1976). Here, as in the Jones, Moore and Weiss paper, the Nu−Ra curves, shown more clearly in figure 5.19b) for values near the critical, appear to tend towards a $\sigma \to 0$ limiting solution. The bounding curve for σ = 0 remains conductive even after the normal critical Rayleigh number has been surpassed, until a second critical Rayleigh number is reached. Then, and only then, does the solution bifurcate away from the axis to allow convection, and now this convection is independent of Prandtl number. Such solutions have only been found and modelled before in highly symmetrical 2−D or quasi−2−D situations, and are characterized by the vorticity being constant both across and along the streamlines at low σ forming an iso−vortical body of fluid which spins like a flywheel. The hexagonal solutions here for low Prandlt numbers exhibit the same qualities as those solutions of Jones, Moore and Weiss for cylinders. At very low amplitudes and low σ, the curves are at first linear until $Ra \geqslant 1.1Ra_c$, and then a period of transition occurs where the heat transport turns upwards in a steady curve until $Ra \geqslant 1.4Ra_c$ where the solution head upwards almost linearly again and parallel to one another. At the lower Prandtl numbers studied by Jones, Moore and Weiss, these solutions actually coincide for $Ra \geqslant 1.4Ra_c$, but here they only appear parallel. This may be due to lack of resolution of the modal solutions at such low Prandlt numbers. The values of the Rayleigh number and the heat transport on the initial linear section of this curve compare directly with those of cylindrical convection (and square convection, see later) as is shown in table 5.2 and figure 5.19d). These results agree with the standard small amplitude theory (see Jones, Moore and Weiss (1976) and references within) which forces cylinders, hexagons and squares to exhibit the same dependences near critical. The small amplitude theory predicts that the heat transport is related to the Rayleigh number by a coefficient which is dependent on the square of the Prandtl number, so that

$$Nu - 1 = X \left[\frac{Ra}{Ra_c} - 1 \right] , \qquad [5.22]$$

where $X = A\sigma^2$ and A is a constant. Values of A fitted using this formula are shown also in table 5.2. The lower Nusselt number, Nu = 1.0001, shows that this is a good fit except at very low σ (σ = 0.01) where the resolution of the modal model is suspect, thus confirming small amplitude theory. Obviously, the higher Nusselt number, Nu = 1.01, shows a greater discrepancy from the theory

Fig. 5.19a) **Hexagonal Rayleigh–Benard convection**
Rayleigh number against Nusselt number
Prandtl number dependence

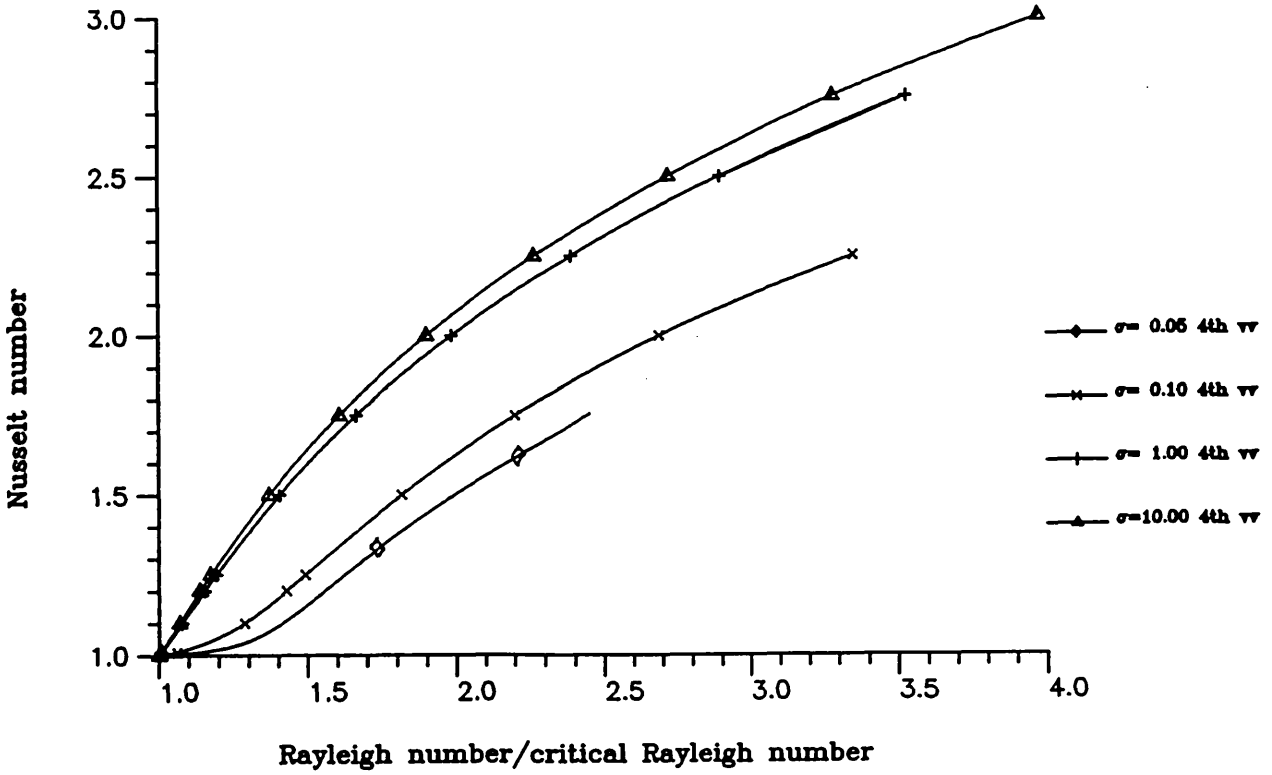


Fig. 5.19b) **Hexagonal Rayleigh–Benard convection**
Rayleigh number against Nusselt number
Low Prandtl numbers, α = 1.111

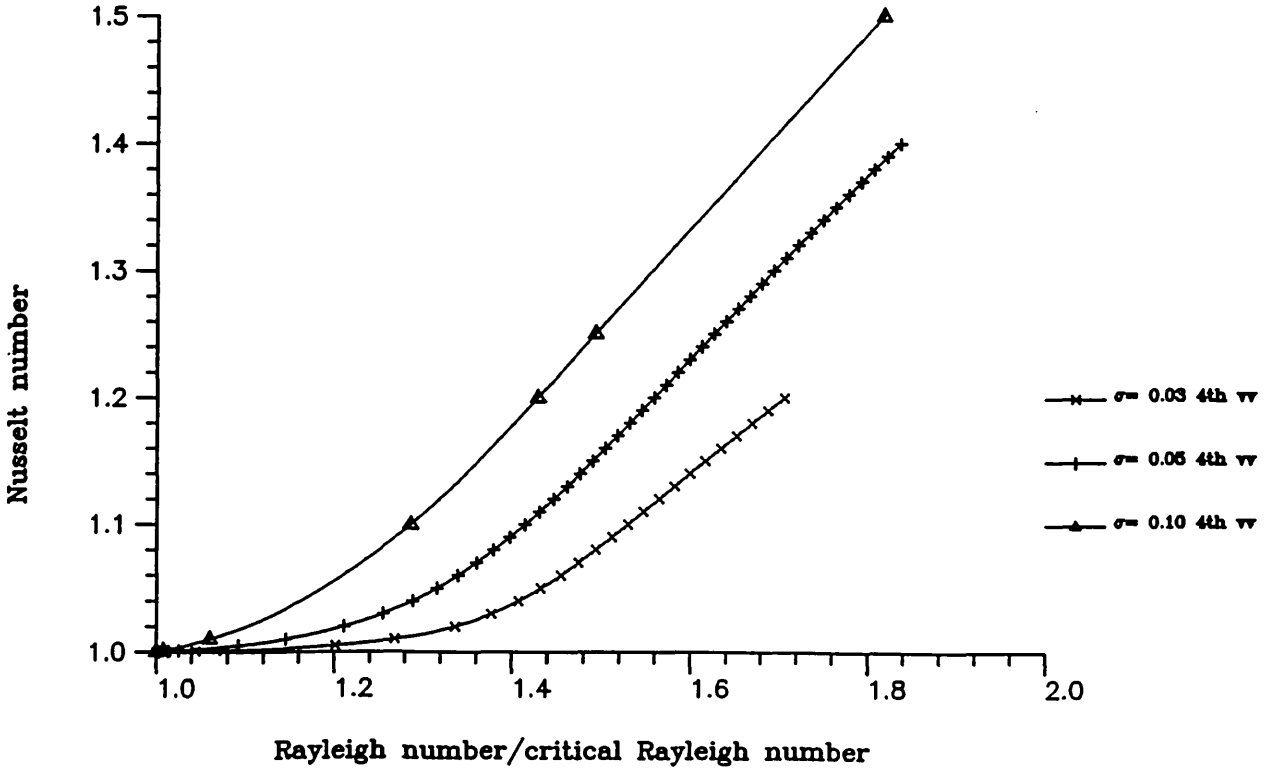


Fig. 5.19c) **Hexagonal Rayleigh–Benard convection**
Rayleigh number against Nusselt number
Prandtl number dependence

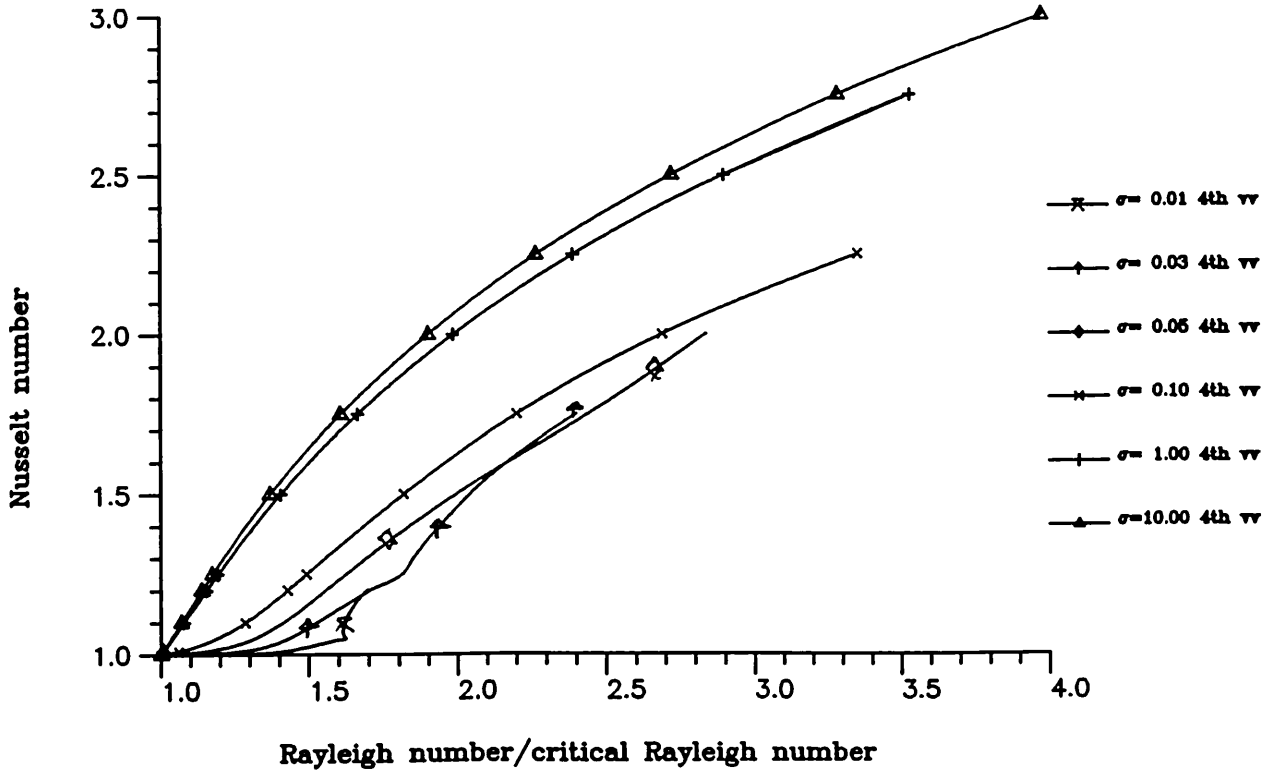


Fig. 5.19d) **Hexagonal Rayleigh–Benard convection**
Rayleigh number against Nusselt number
Prandtl number dependence near critical

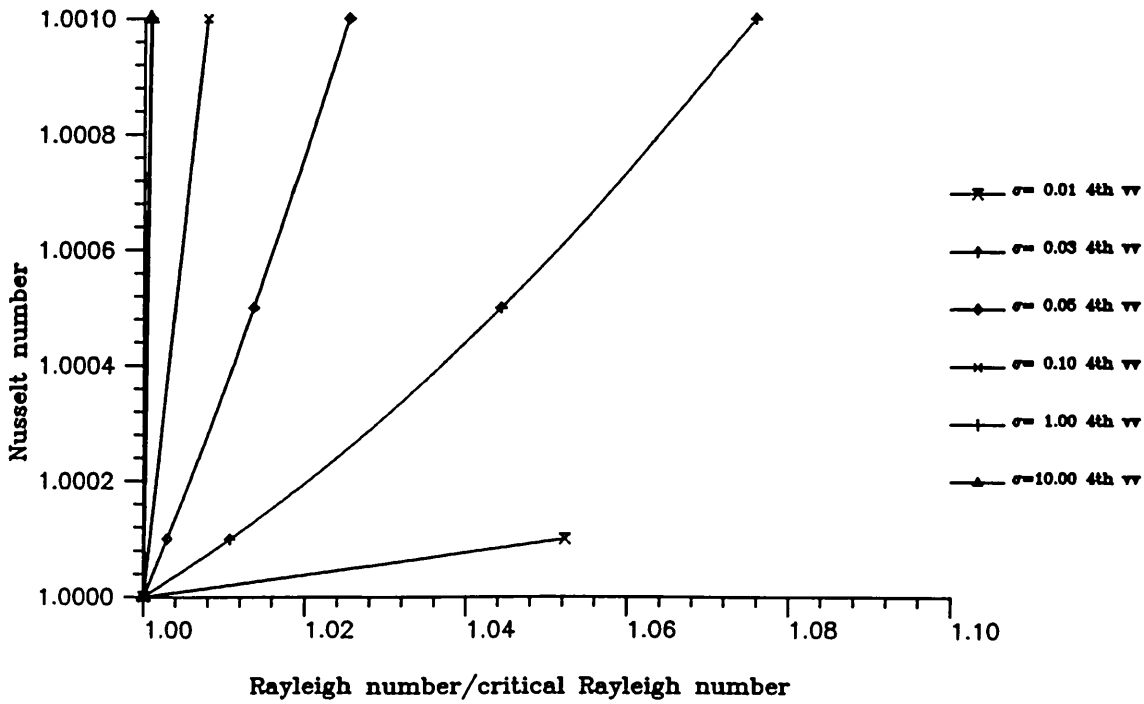


Fig. 5.19e)

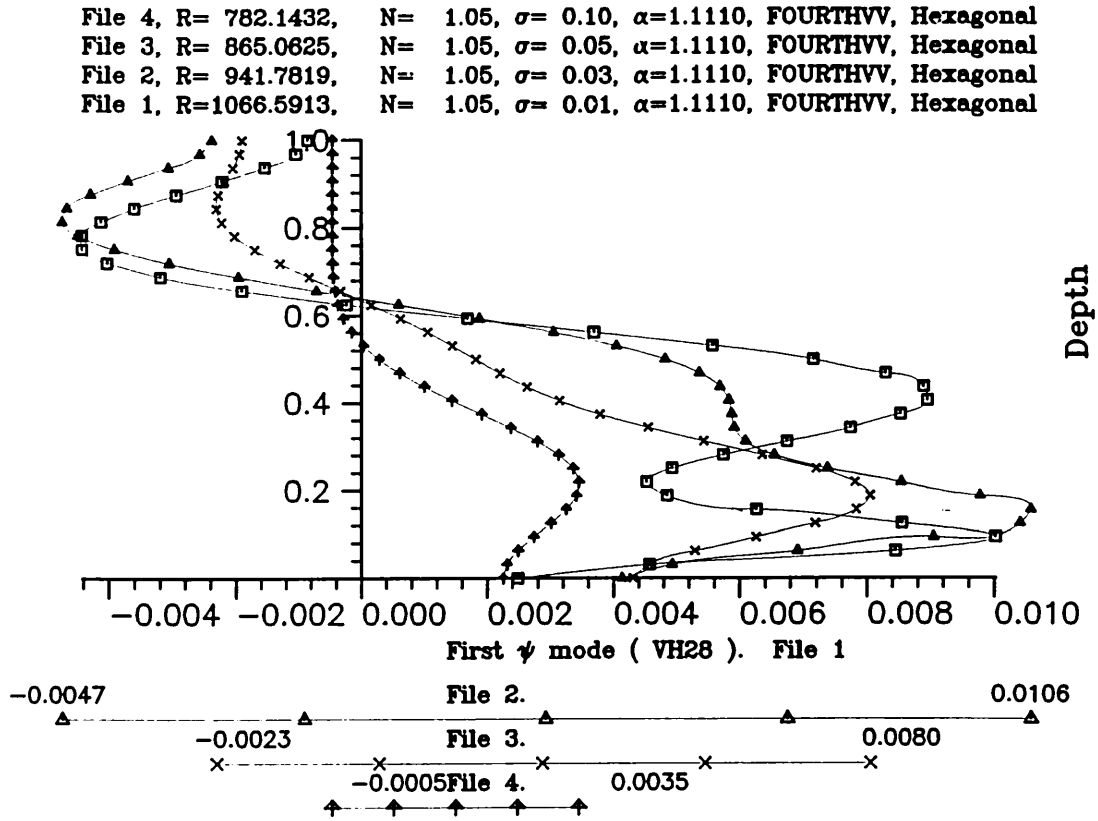


Fig. 5.19f)

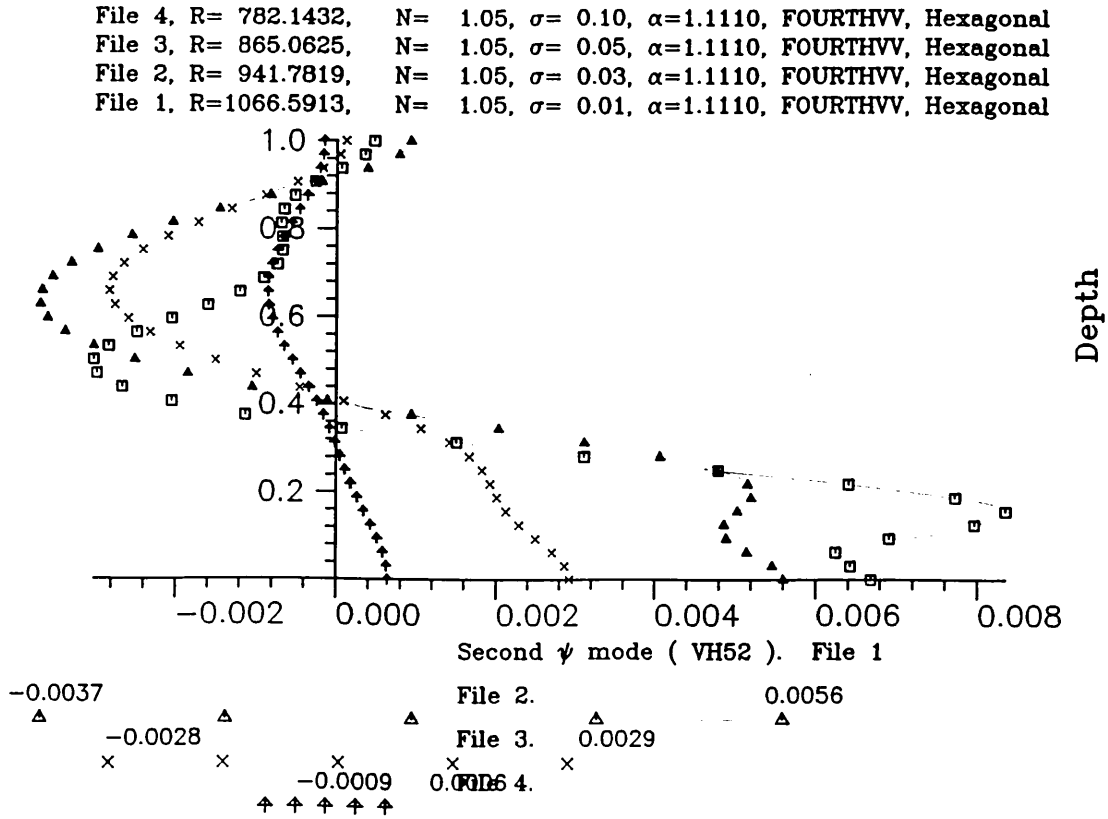


Figure 5.19g) . Hexagonal Rayleigh–Benard convection.
R = 782.14, N = 1.05, σ = 0.10, α = 1.111, fourthvv
a) x=$\pi/\sqrt{3}\alpha$, y=($\pi/3\alpha$,$5\pi/3\alpha$) , b) x=(0,$2\pi/\sqrt{3}\alpha$), y=π/α , c) x=0, y=($2\pi/3\alpha$,$4\pi/3\alpha$)

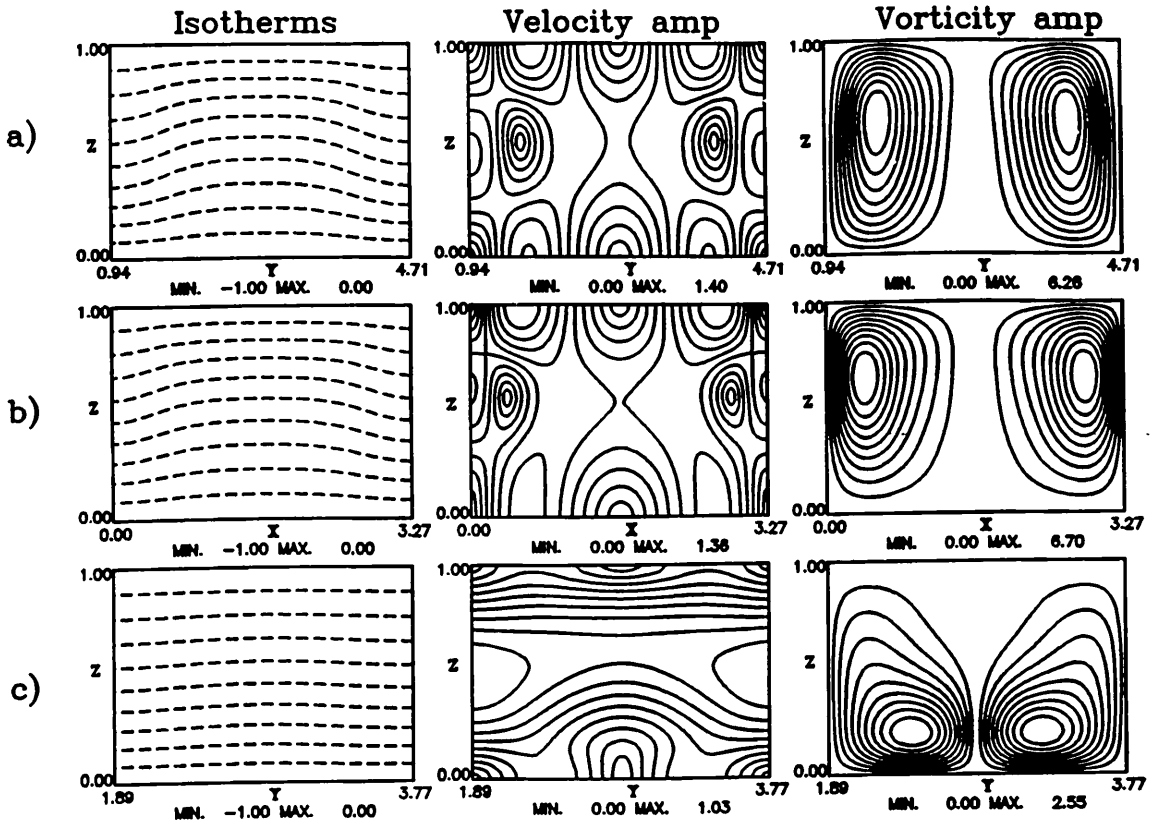


Figure 5.19h) . Hexagonal Rayleigh–Benard convection.
R = 865.06, N = 1.05, σ = 0.05, α = 1.111, fourthvv
a) x=$\pi/\sqrt{3}\alpha$, y=($\pi/3\alpha$,$5\pi/3\alpha$) , b) x=(0,$2\pi/\sqrt{3}\alpha$), y=π/α , c) x=0, y=($2\pi/3\alpha$,$4\pi/3\alpha$)

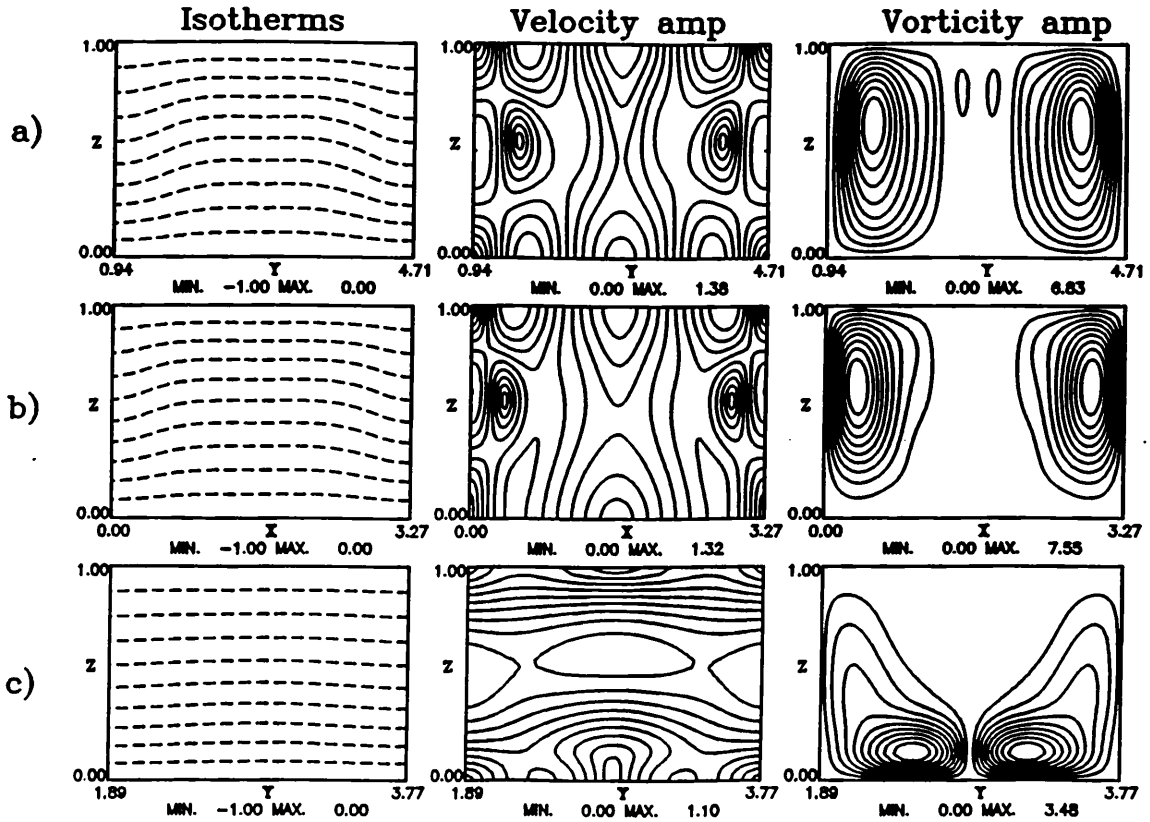
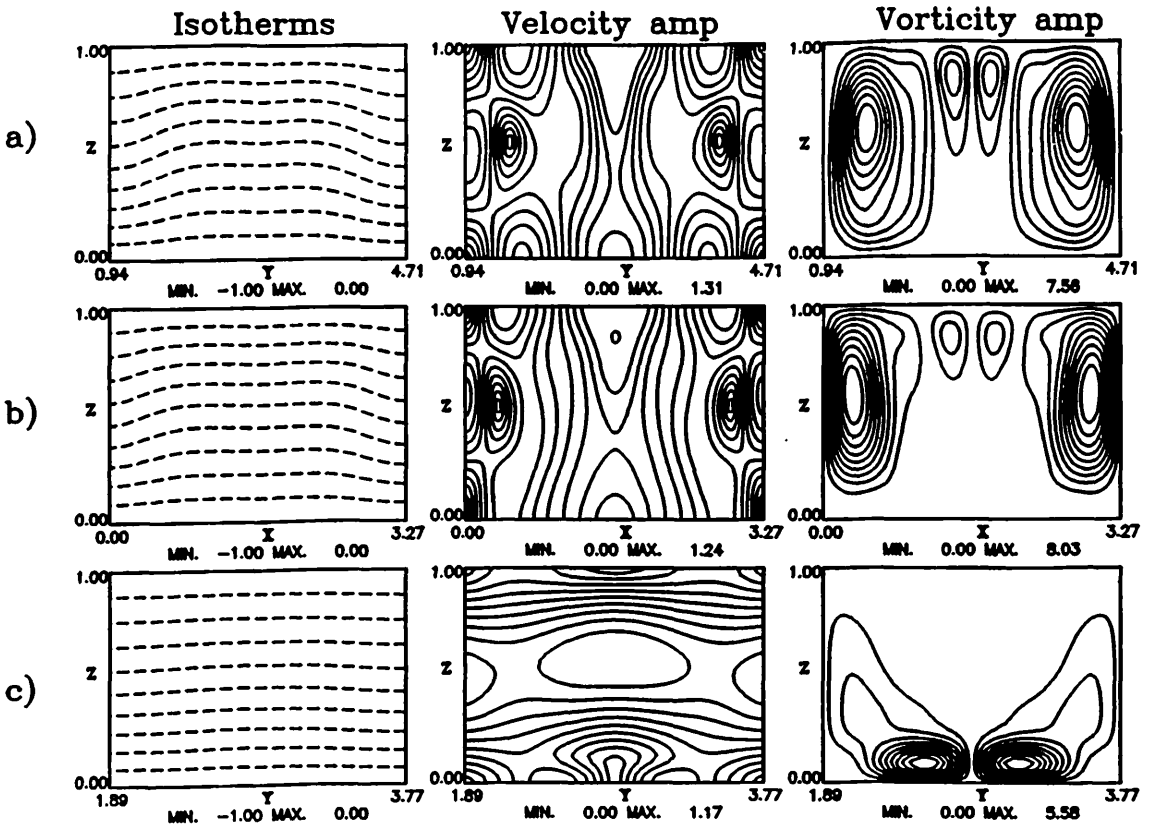


Figure 5.19i) . Hexagonal Rayleigh–Benard convection.
R = 941.78, N = 1.05, σ = 0.03, α = 1.111, fourthvv
a) x=$\pi/\sqrt{3}\alpha$, y=($\pi/3\alpha$,$5\pi/3\alpha$) , b) x=(0,$2\pi/\sqrt{3}\alpha$), y=π/α , c) x=0, y=($2\pi/3\alpha$,$4\pi/3\alpha$)



as the amplitude of convection increases. The values for X corresponding to these values of A fit very reasonably onto figure 1 of Jones, Moore and Weiss. The unusual vorticity structure exhibited in two dimensions is not as obvious in three. Figures 5.19e) – i) show the lower Prandtl number convection at small amplitude (Nu = 1.05 for comparison with Jones, Moore and Weiss (1976)). The decrease from σ = 0.1 to σ = 0.025 in figures 5.19g) – i) does show the widening of an iso–vortical 3–D centre of the cell forcing the contours of vorticity amplitude towards the edges of the cell or the boundaries such that the contour lines become more similar to the velocity amplitude contour lines. However, the simple interpretation of the 2–D case is not immediately applicable to this discussion of the 3–D results. Figure 5.19e) shows the vertical dependence of the first vertical vorticity mode, VH28 at low amplitude for the lowest Prandlt numbers. The mode shows much the same structure for all σ in that the layer is always divided into two regions at about the z = 0.6 mark, with a strong positive influence of the mode in the lower region, and a weaker, negative influence in the upper region. Similarly for figure 5.19f) which shows the dependence of the second (VH52) mode of vertical vorticity. No obvious changes or switch–overs in dependence are seen here at the different σ as were in Jones, Moore and Weiss, despite the changes in overall amplitude of the modes. The

σ	Ra_{hex}	A_{hex}	Ra_{sq}	A_{sq}	Ra_{cyl} (JMW)
Nu=1.0001					
10.0	1.000070		1.000061		
1.0	1.000081		1.000071		
0.1	1.000820	12.2	1.000732	13.7	
0.05	1.002935	13.6	1.002650	15.1	
0.025	1.010760	14.9	1.010004	16.0	
0.01	1.052372	19.1	1.053877	18.6	
Nu=1.01					
10.0	1.006122		1.006931		
1.0	1.007091		1.008011		1.008
0.1	1.062538	16.0	1.061062	16.4	1.063
0.05	1.175621	22.8	1.144906	27.6	
0.03					1.231
0.025	1.446774	35.8	1.268381	59.6	
0.01	2.362326	73.4	1.418835	238.8	1.327

TABLE 5.2. A comparison of Rayleigh numbers near critical for low amplitudes and low Prandtl numbers for hexagons, squares and cylinders. The hexagons and squares are FOURTHVV results from this thesis, and the cylindrical results are drawn directly from Table 1 of Jones, Moore and Weiss (1976).

flywheel−type, low σ behaviour is not seen by GST in their rigid boundary calculations, and their results compare more to the square case (see later) where a second critical Rayleigh number is not apparent. The solutions of GST, however, as well as being held between rigid boundaries, are constrained to one (or possibly two) hexagonal planform structures and are thus not allowed the freedom to choose their own planform and thus create the inertial solution which annihilates the vorticity advection terms and imposes the σ−independence.

Unfortunately, more modes of the modal expansion used here are needed to fully resolve the lower Prandtl number flows for a clearer description of the behaviour. The results suggest that an expansion to fourth order is valid down to $\sigma = 0.1$, but is suspect at any lower Prandtl numbers. The lower Prandtl numbers ($\sigma < 0.1$) have not been studied in detail for this reason, except to speculate as above and then have only been calculated at low amplitudes, Nu $\leqslant$ 1.2, where they are acceptable to some extent. The results for the lowest σ at these low amplitudes are in general similar to those for $\sigma = 0.1$ at Nu = 2.5.

It is interesting to see the way in which the Prandtl number influences the dominance of the particular modes in the solution. Figures 5.20a)−m) show a solution for Nu = 2.5, and $\alpha = \alpha_c = 1.111$ for three Prandtl numbers, σ = 10.0, 1.0 and 0.1. Figures 5.20a)' and 5.20i) show that as the Prandtl number is decreased, the fundamental temperature mode remains almost static in amplitude, with only minor shifts of emphasis within the layer, but the fundamental χ streamfunction mode decreases by 5% between $\sigma = 10.0$ and $\sigma = 1.0$, and then by 10% between $\sigma = 1.0$ and $\sigma = 0.1$. It seems that the main exchanges appear in the χ streamfunction modes. These χ modes generally have greater amplitude in the first place, by at least a factor of 2 for each mode. Notice that the temperature fundamental mode shows a single maximum and has not achieved the 'rabbit−ear' dependence that Murphy and Lopez attribute to the type I (no vertical vorticity) solutions. Figure 5.20a)'' shows the χ streamfunction fundamental mode for a Nusselt number of Nu = 1.2, and including the lowest Prandtl numbers calculated. Notice that the same effects are exhibited, but that once again the most marked change occurs between $\sigma = 1.0$ and $\sigma = 0.1$. Figure 5.20b) show the H2 χ mode vertical dependence for the three σ in question, which increases in amplitude six−fold over the range, until its strength is roughly $1/10^{th}$ that of the fundamental mode at $\sigma = 0.1$. The other second order harmonic relating to RH$\sqrt{3}$, shown in figure 5.20c) shows a similar increase in strength with decreasing σ, and the mode is in general roughly twice as strong anyway. The second order temperature harmonic modes also show an increase (figures 5.20j), k)) but not in the same manner as the χ modes. Here, between $\sigma = 10.0$ and $\sigma = 1.0$, the increase in amplitude is small, whereas the χ

Fig. 5.20a).

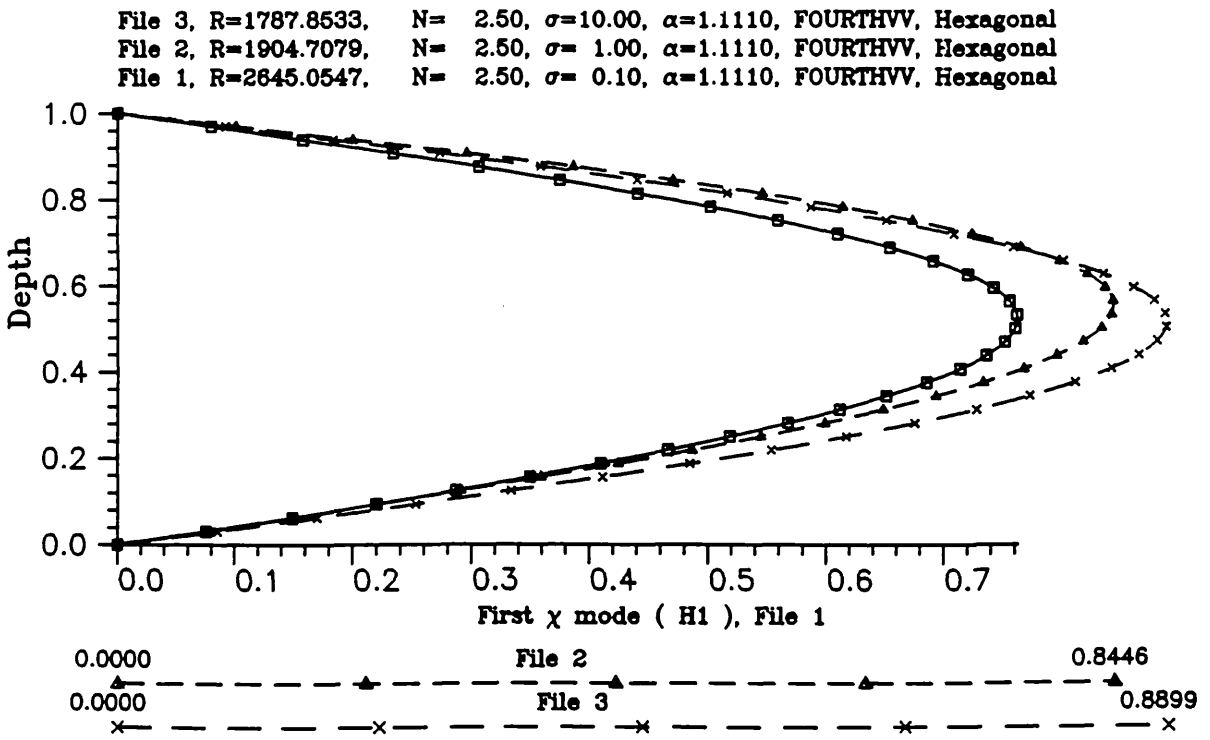


Fig. 5.20a)''

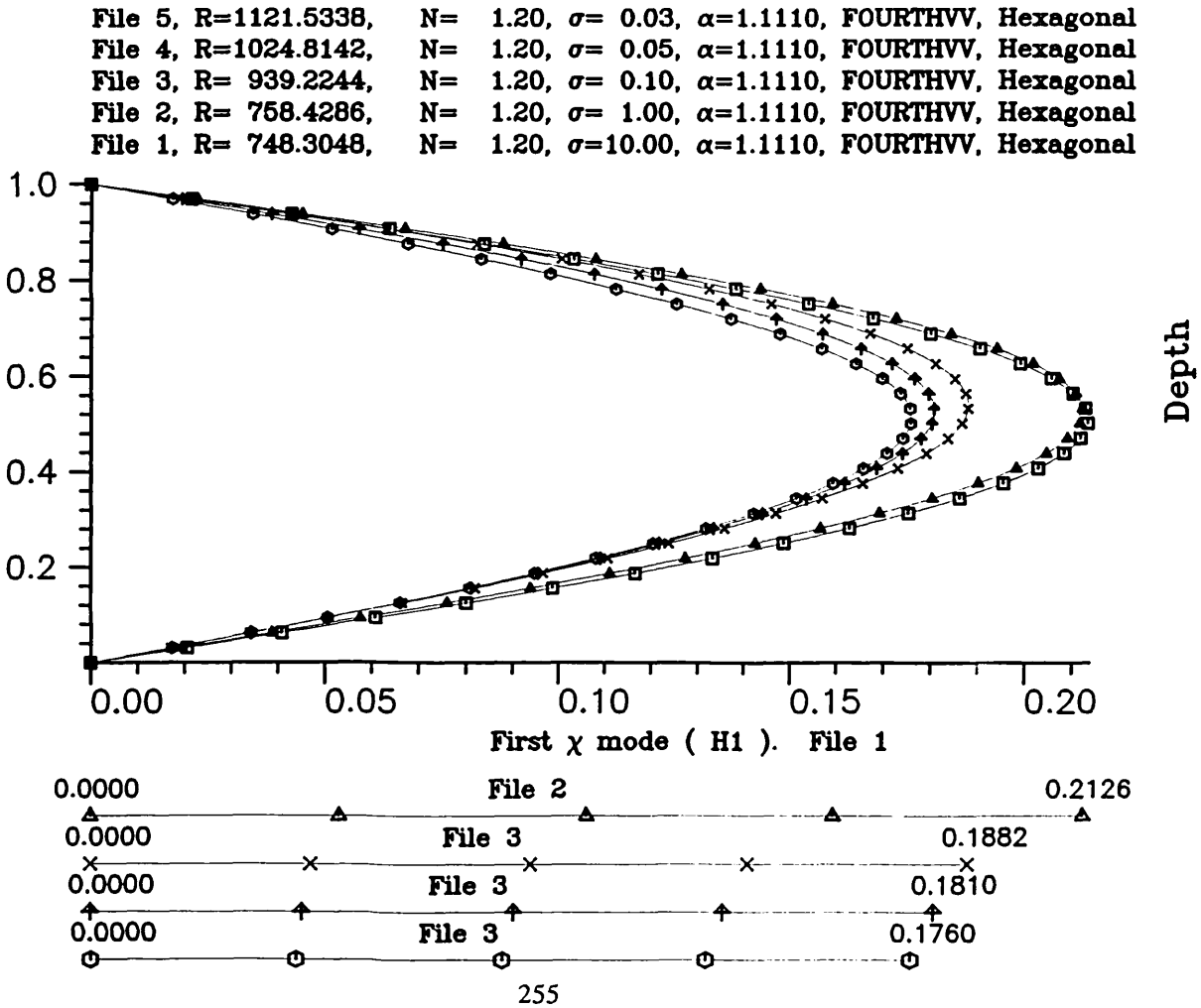


Fig. 5.20b).

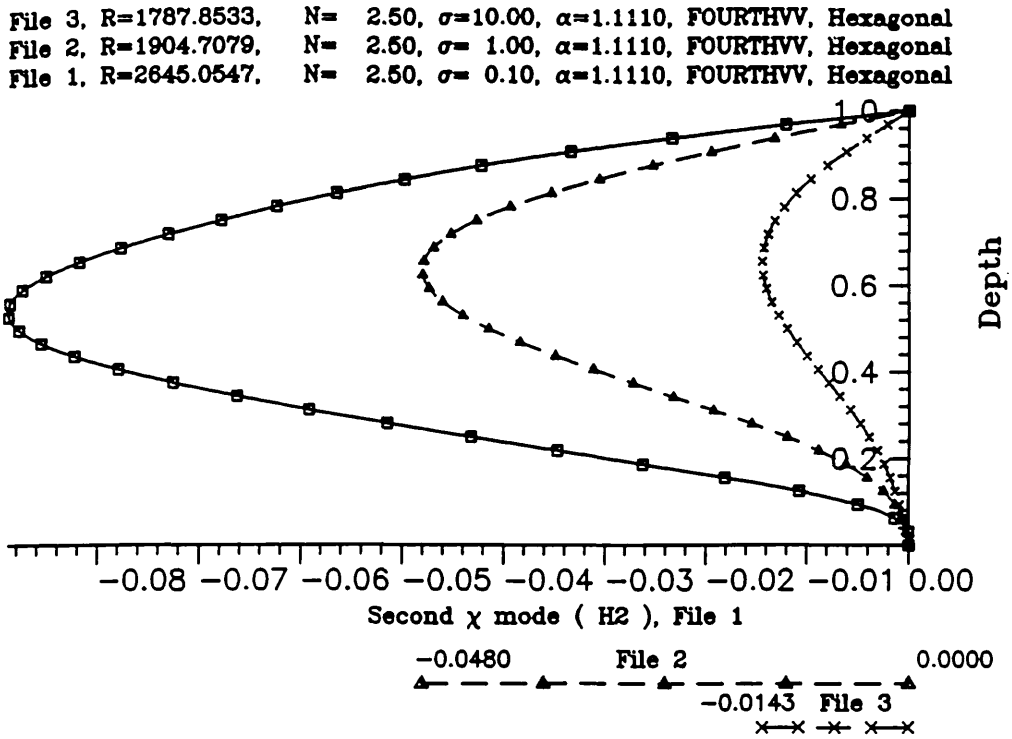


Fig. 5.20c).

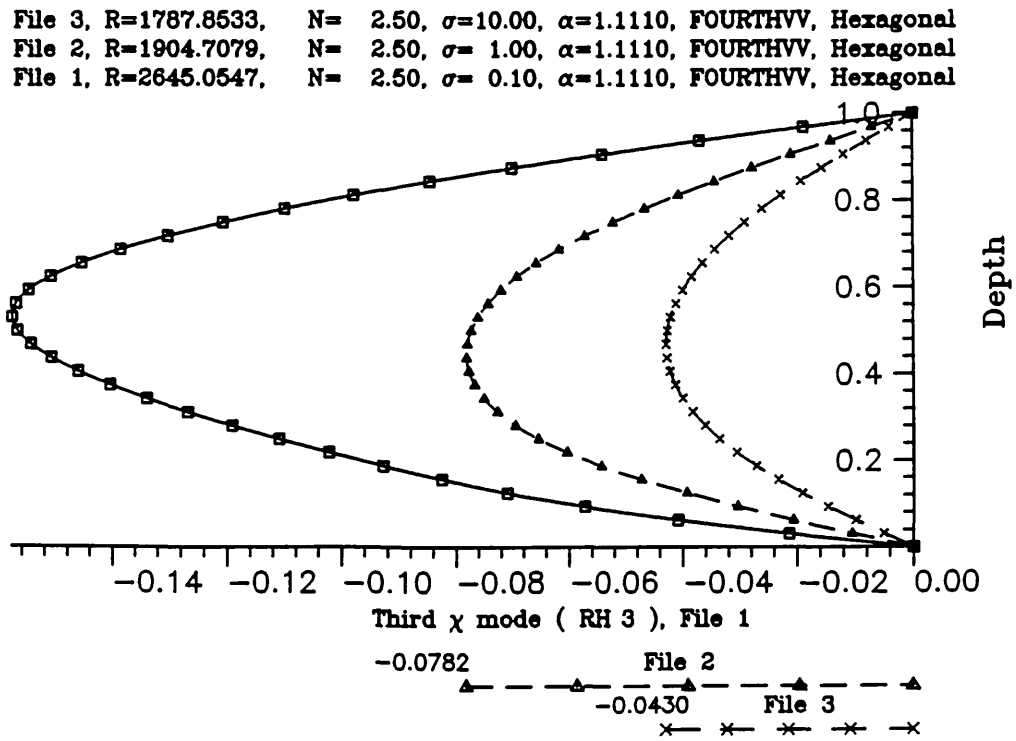


Fig. 5.20d).

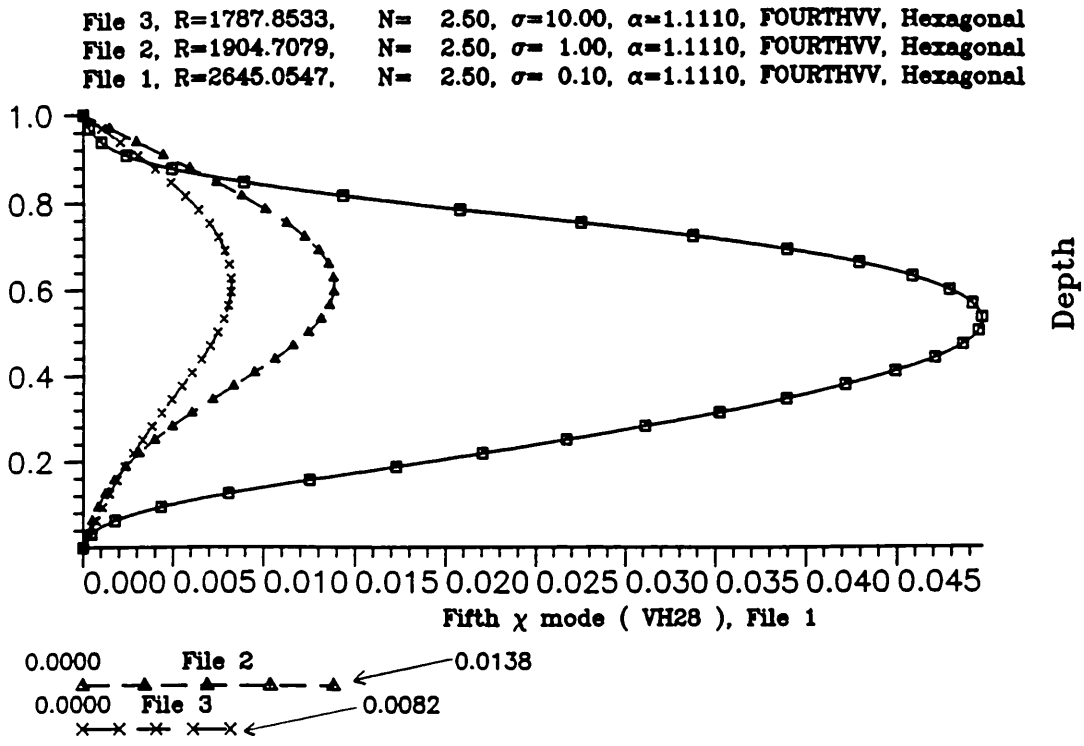


Fig. 5.20e).

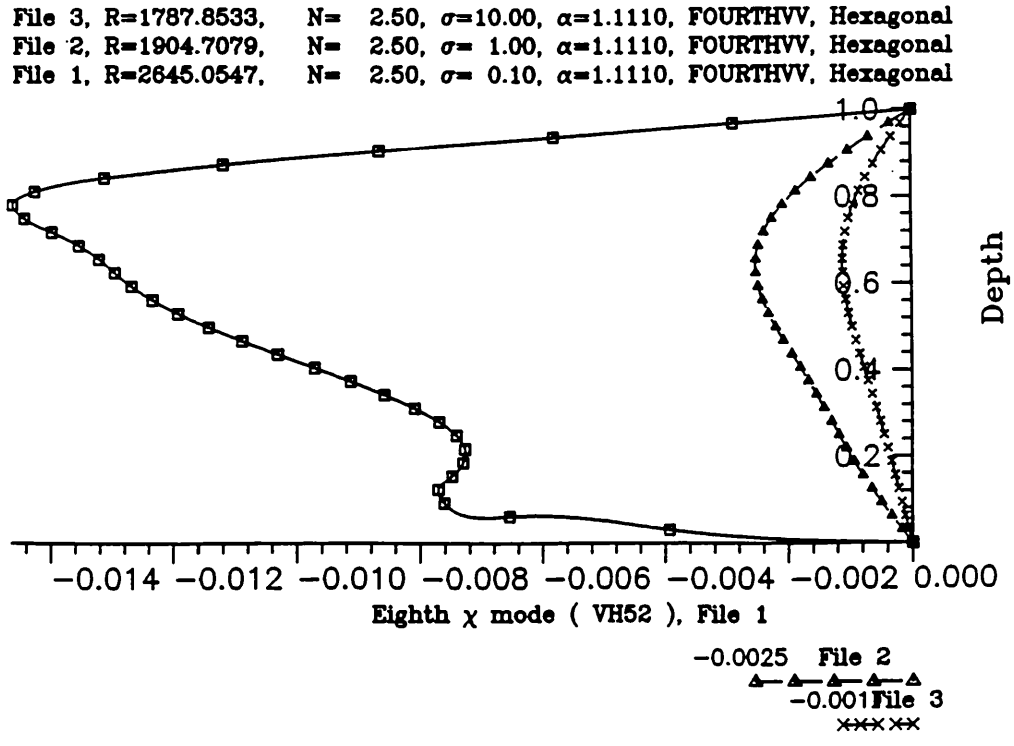


Fig. 5.20f).

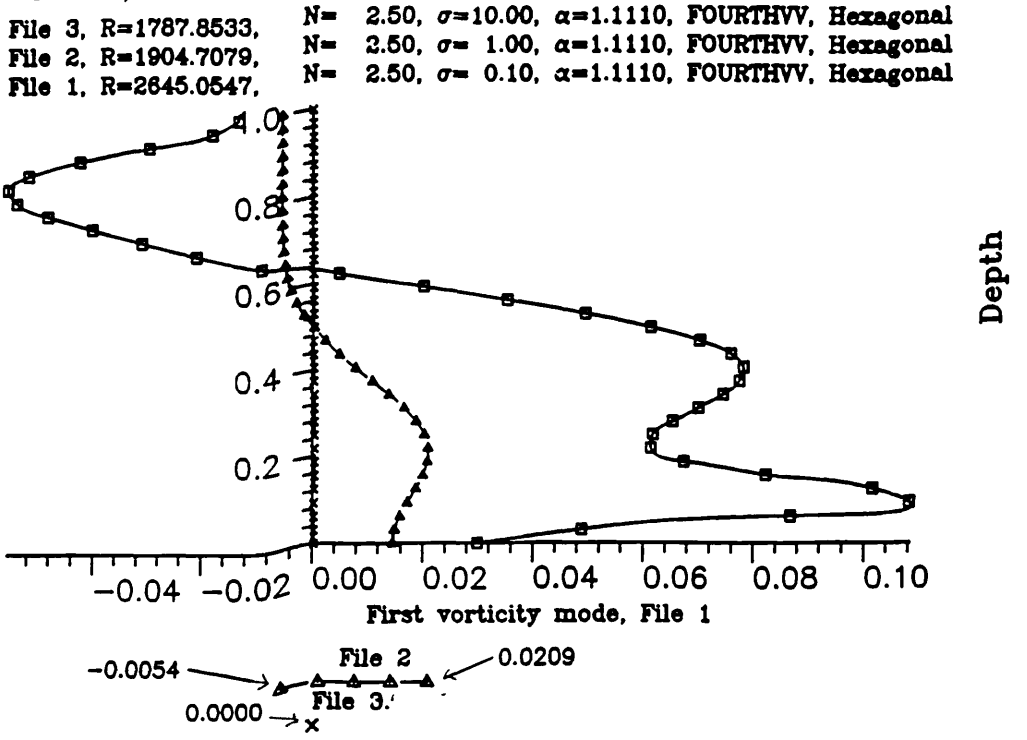


Fig. 5.20g).

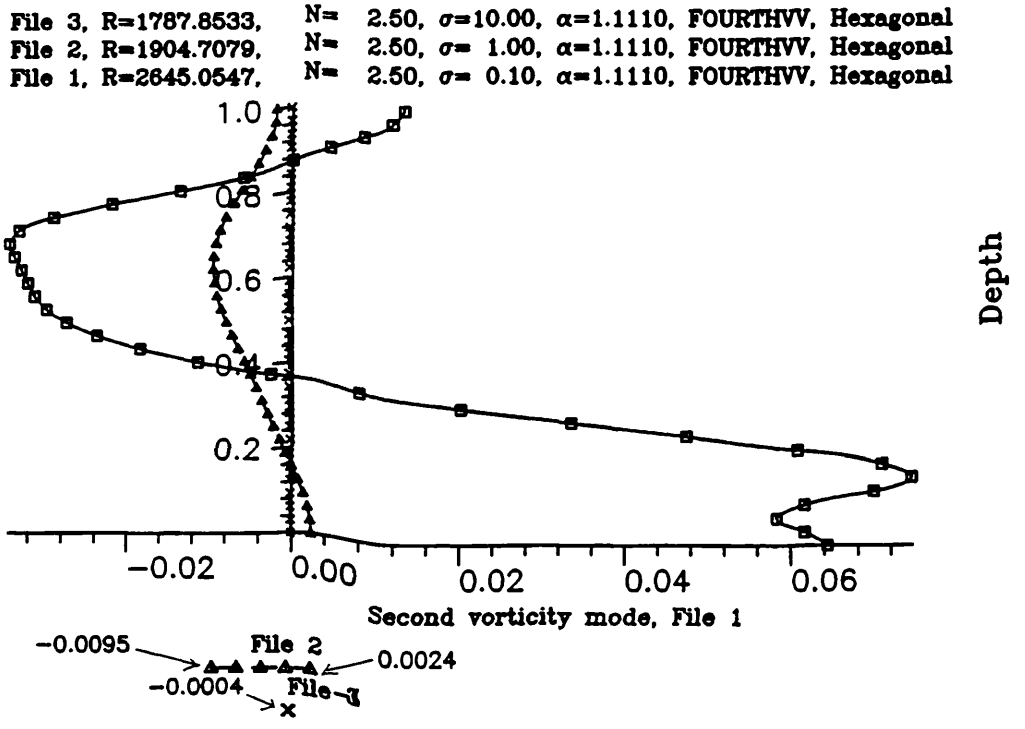


Fig. 5.20f)''

File 5, R= 748.3048, N= 1.20, σ=10.00, α=1.1110, FOURTHVV, Hexagonal
File 4, R= 758.4286, N= 1.20, σ= 1.00, α=1.1110, FOURTHVV, Hexagonal
File 3, R= 939.2244, N= 1.20, σ= 0.10, α=1.1110, FOURTHVV, Hexagonal
File 2, R=1024.8142, N= 1.20, σ= 0.05, α=1.1110, FOURTHVV, Hexagonal
File 1, R=1121.5338, N= 1.20, σ= 0.03, α=1.1110, FOURTHVV, Hexagonal

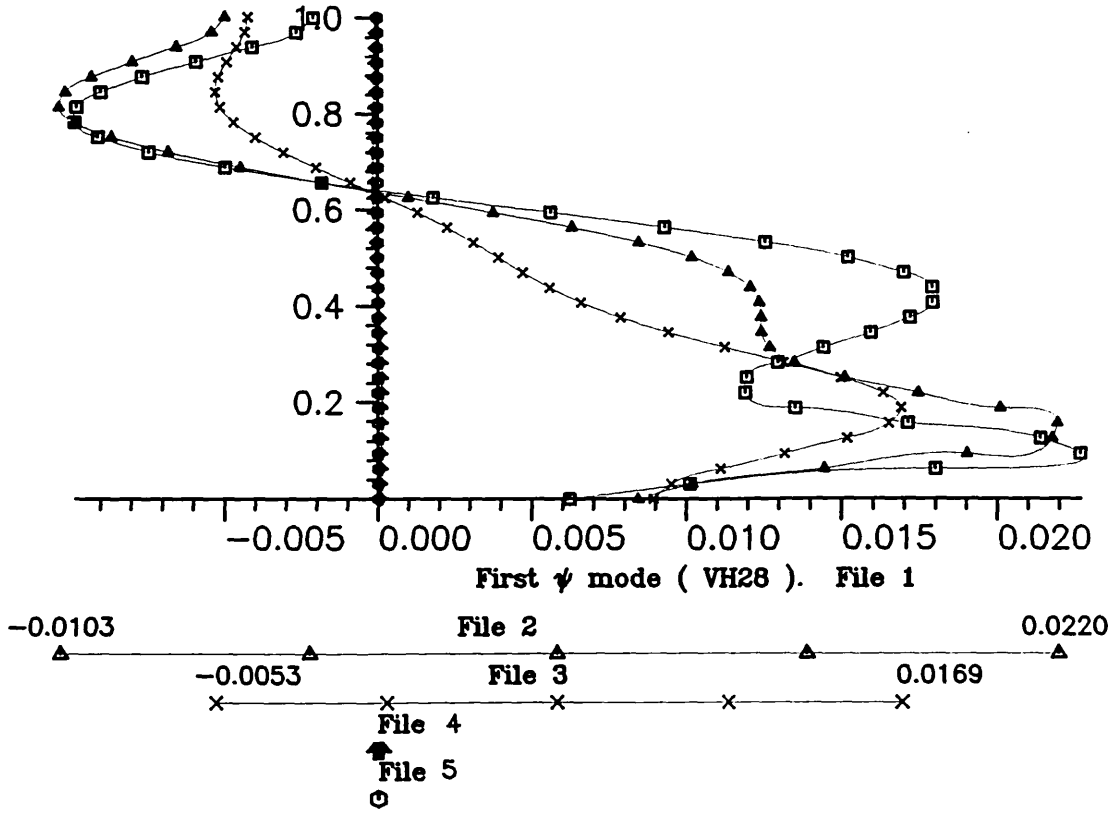


Fig. 5.20g)''

File 5, R= 748.3048, N= 1.20, σ=10.00, α=1.1110, FOURTHVV, Hexagonal
File 4, R= 758.4286, N= 1.20, σ= 1.00, α=1.1110, FOURTHVV, Hexagonal
File 3, R= 939.2244, N= 1.20, σ= 0.10, α=1.1110, FOURTHVV, Hexagonal
File 2, R=1024.8142, N= 1.20, σ= 0.05, α=1.1110, FOURTHVV, Hexagonal
File 1, R=1121.5338, N= 1.20, σ= 0.03, α=1.1110, FOURTHVV, Hexagonal

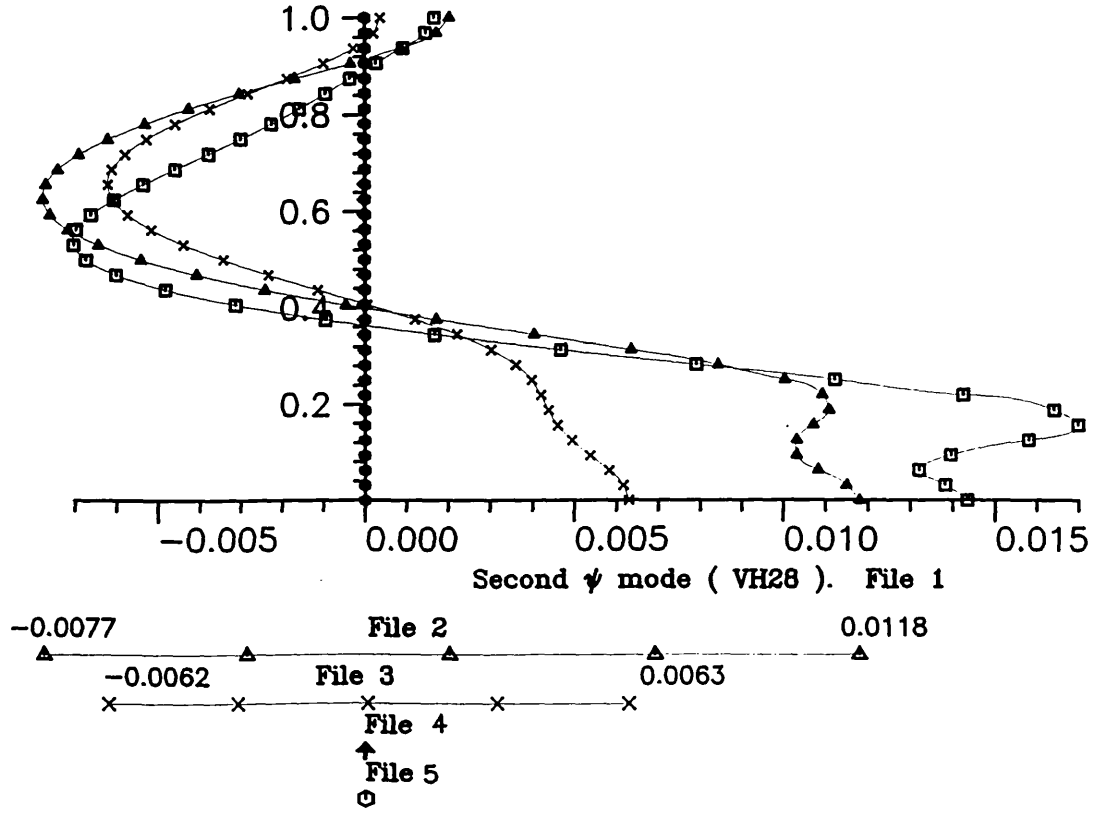


Fig. 5.20h).

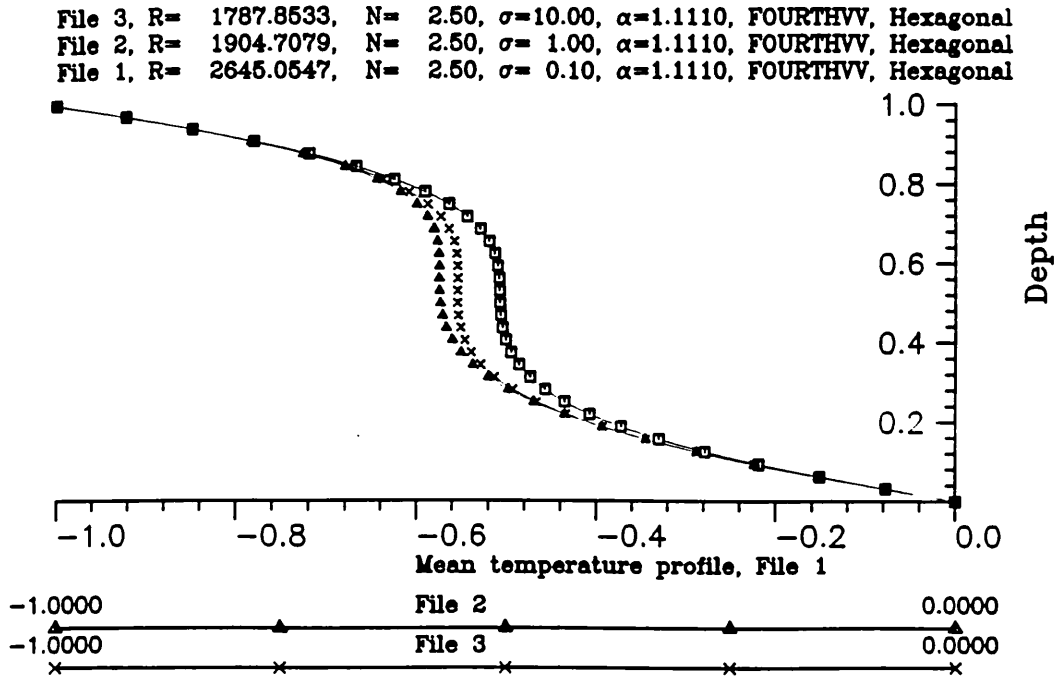


Fig. 5.20i).

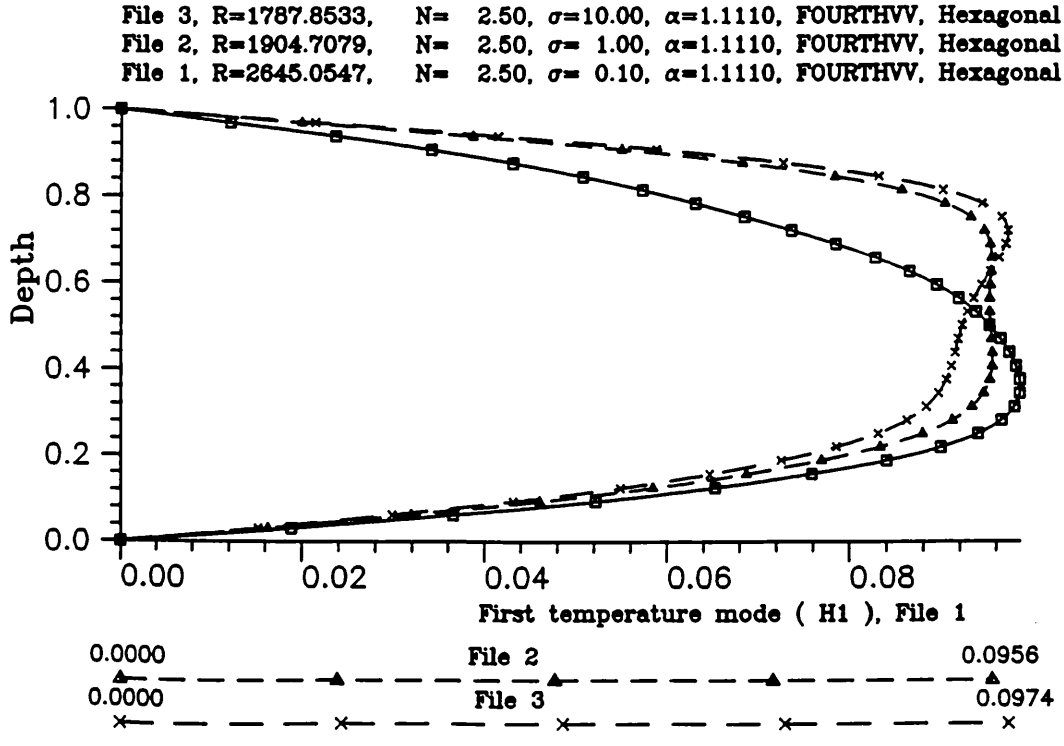


Fig. 5.20j).

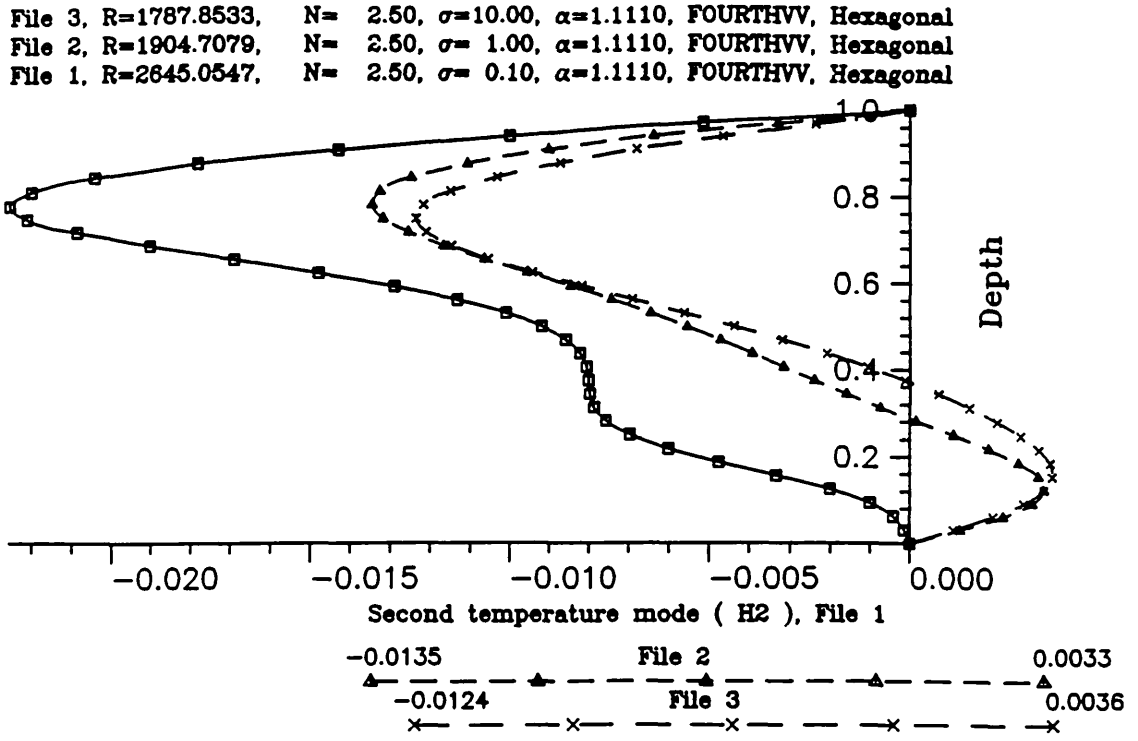


Fig. 5.20k).

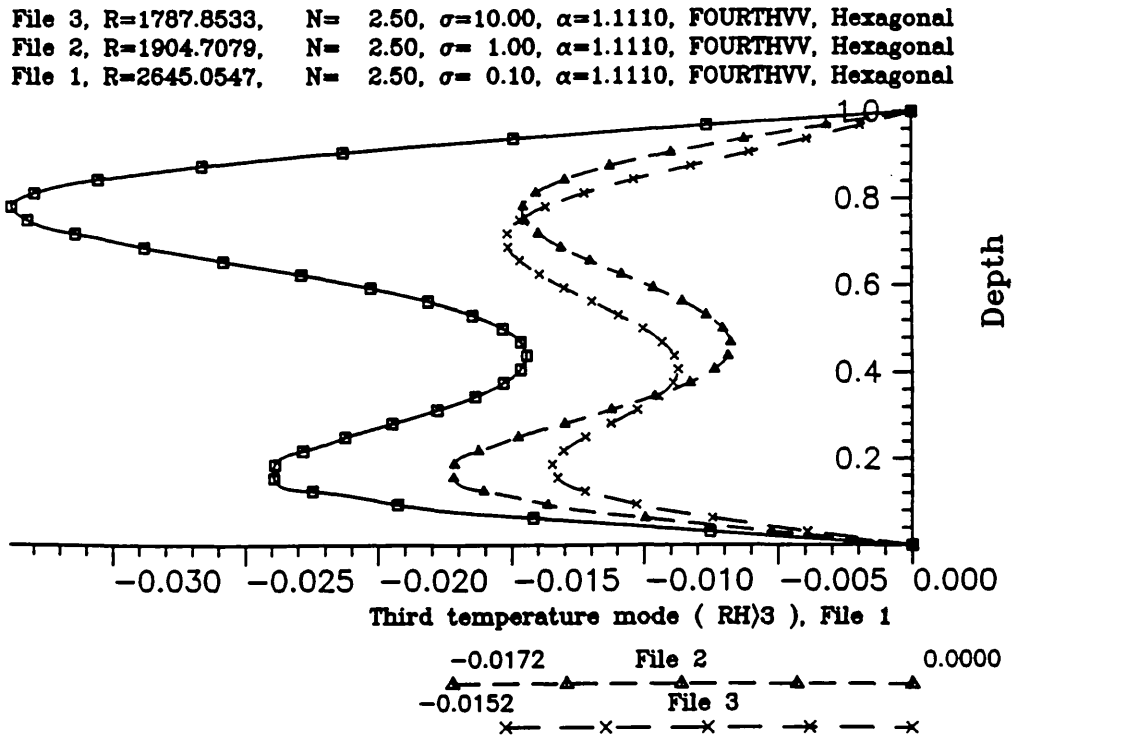


Fig. 5.20l).

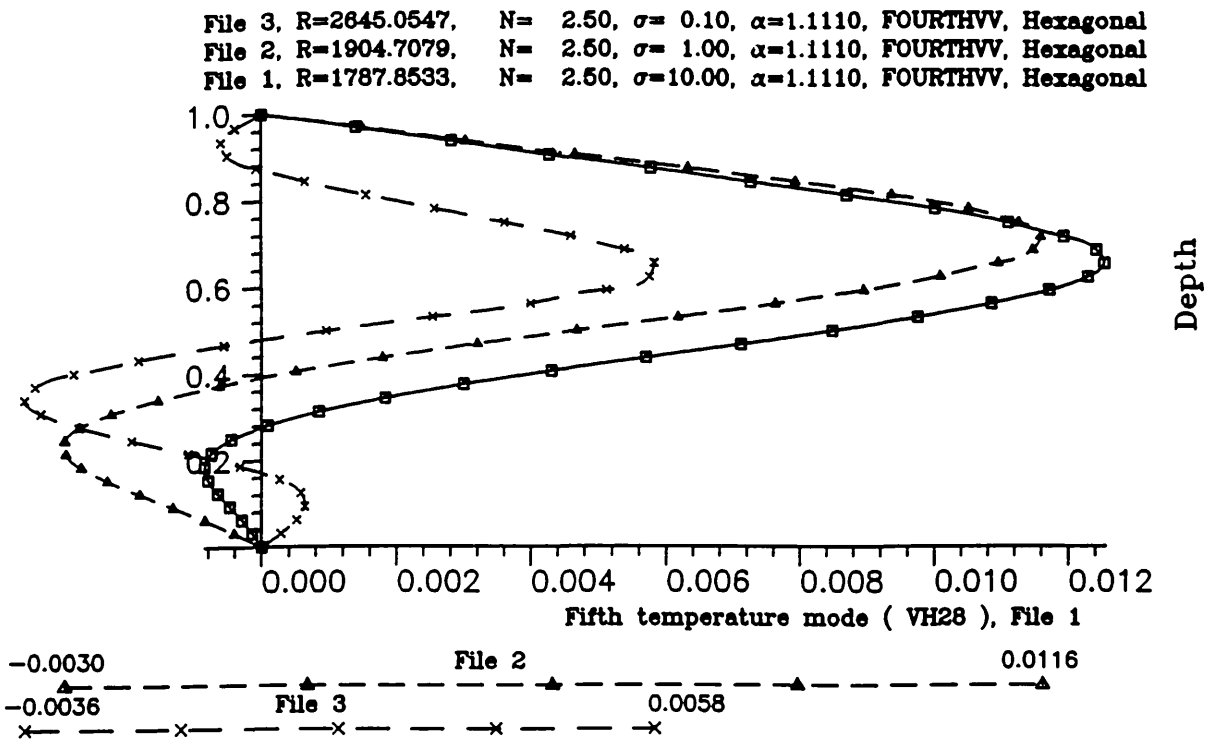
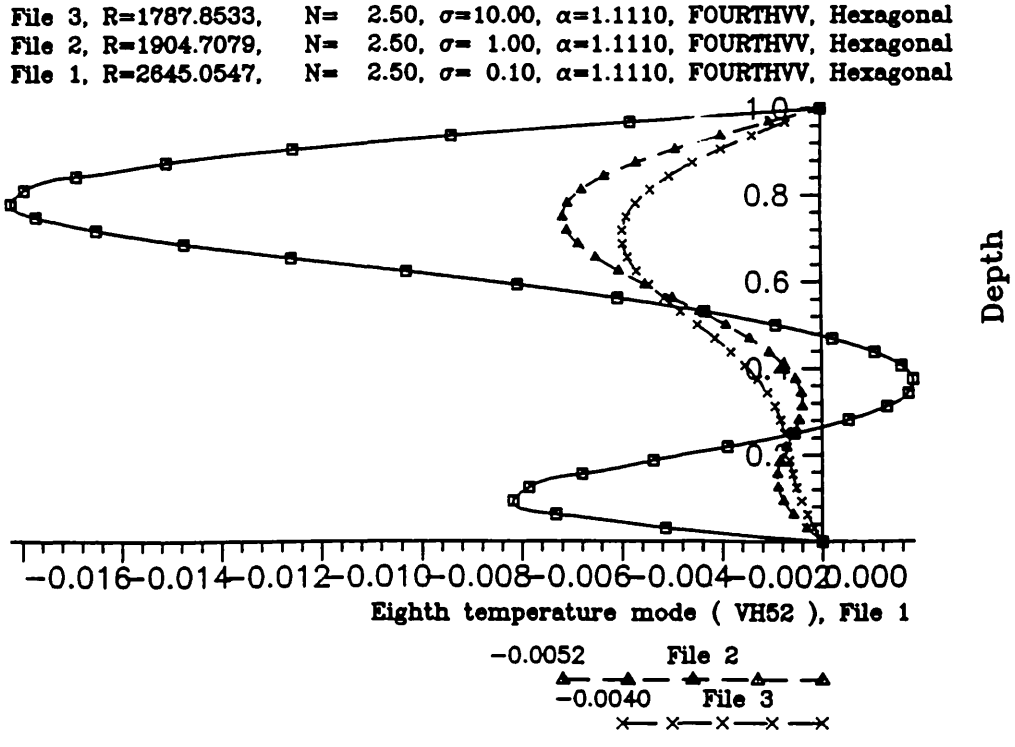


Fig. 5.20m)



equivalents increased by at least two−fold, but the changes from $\sigma = 1.0$ to $\sigma = 0.1$ are much the same in both χ and T modes, being a rough amplitude doubling. The changes are not as smooth for the temperature modes in that the H2 mode assumes a different form at the lowest σ with no reversal of sign at the lower boundary, and the bias of the peaks in the twin−peaked form of the RHβ3 alternates with the decreasing σ. The mean temperature profile, shown as figure 5.20h) also shows an odd variation in that as σ decreases, the temperature of the isothermal region first increases for $\sigma = 1.0$, and then decreases to a value near $T = -0.5$ for $\sigma = 0.1$.

However, the most obvious changes are apparent in the effect on the vorticity modes. The vertical dependences of the vorticity functions, ψ, are shown as figures 5.20f)' and 5.20g)'. Whilst it is clearly seen that at the higher Prandtl numbers the modes are virtually non−existent, at lower Prandtl numbers, both modes feature prominently, although the first mode is 40% stronger throughout. These modes have amplitudes comparable with the second χ modes at low σ, and are stronger than all the temperature modes. The form of the dependence remains roughly the same at all σ, although it is the concentration of the vertical vorticity in the lower half which is emphasized by the decreasing Prandtl number. This is also shown for the lower σ (albeit at a lower amplitude of convection, Nu = 1.2 which reduces the modal amplitude by approximately one quarter) in figures 5.20f)' and 5.20g)'. The form of the dependence is shown to be similar for all the lower σ, with the maximum values and the structure of the modes varying little for all of $\sigma = 0.1$, 0.05 and 0.025. Notice, however, that at these low amplitudes of convection, the higher Prandtl numbers, $\sigma = 10.0$ and $\sigma = 1.0$ show no generation of vertical vorticity at all. The χ streamfunction and temperature modes corresponding to these vorticity generating planforms exist for all Prandtl numbers albeit weakly at all times compared with the lower order harmonics. The χ modes corresponding to the VH28 and VH52 planforms increase strongly (more than six−fold) with the decrease in Prandtl number (figures 5.20d) and e)). The temperature modes (figures 5.19l) and m)) are not quite so clear in their dependence, since the VH28 mode decreases in amplitude and changes over in form to include another sign−reversal at the lower boundary for the lowest σ. The VH52 mode does increase in amplitude overall with decreasing σ as expected, but also transforms from a simple, single−sign dependence to a more complicated 'sin(3πz)' type dependence with a small reversal of the mode slightly below the centre of the layer.

In summary, decreasing the Prandlt number depletes the fundamental mode to feed the harmonics, especially in the χ streamfunction modes. The vorticity generating streamfunction, ψ, is also fuelled in the two modes considered, to

Figure 5.21a). Hexagonal Rayleigh–Benard
R = 1787.85, N = 2.50, σ = 10.00, α = 1.111, fourthvv
a) x=$\pi/\sqrt{3}\alpha$, y=($\pi/3\alpha$,$5\pi/3\alpha$), b) x=(0,$2\pi/\sqrt{3}\alpha$), y=π/α, c) x=0, y=($2\pi/3\alpha$,$4\pi/3\alpha$)

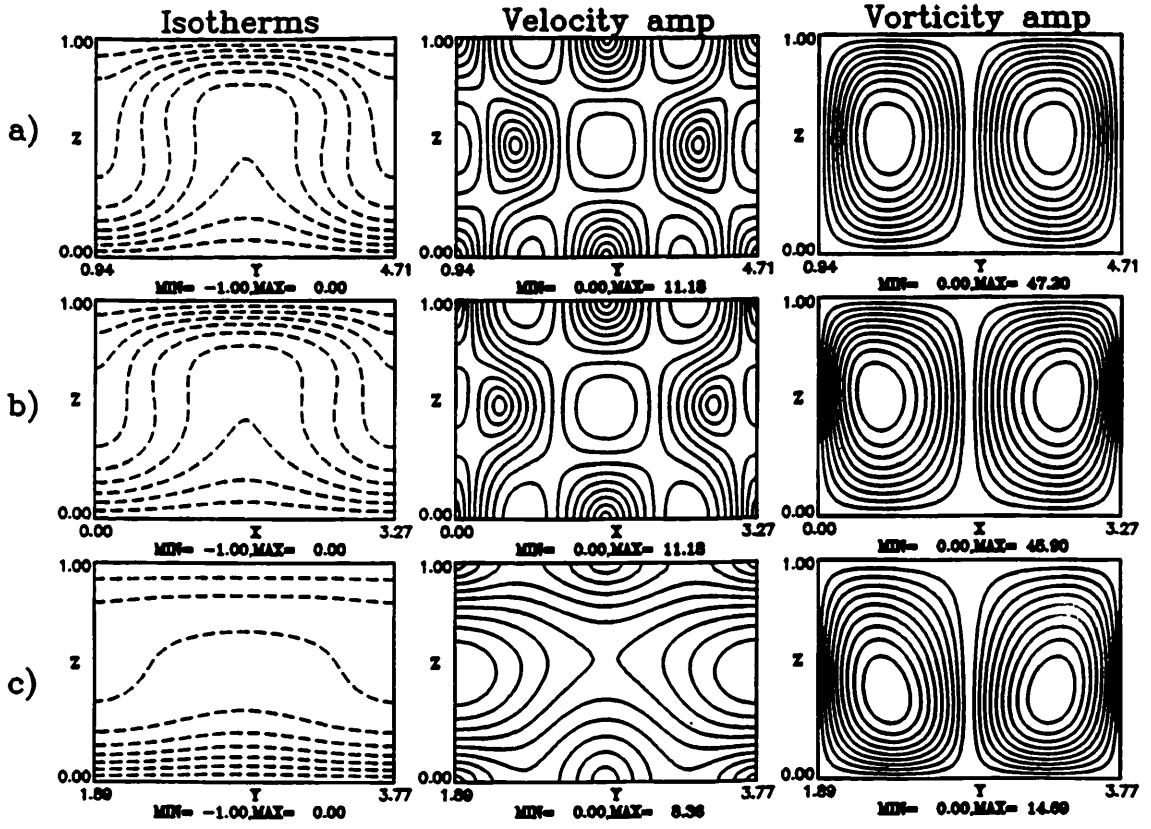


Figure 5.21b). Hexagonal Rayleigh–Benard
R = 1904.71, N = 2.50, σ = 1.00, α = 1.111, fourthvv
a) x=$\pi/\sqrt{3}\alpha$, y=($\pi/3\alpha$,$5\pi/3\alpha$), b) x=(0,$2\pi/\sqrt{3}\alpha$), y=π/α, c) x=0, y=($2\pi/3\alpha$,$4\pi/3\alpha$)

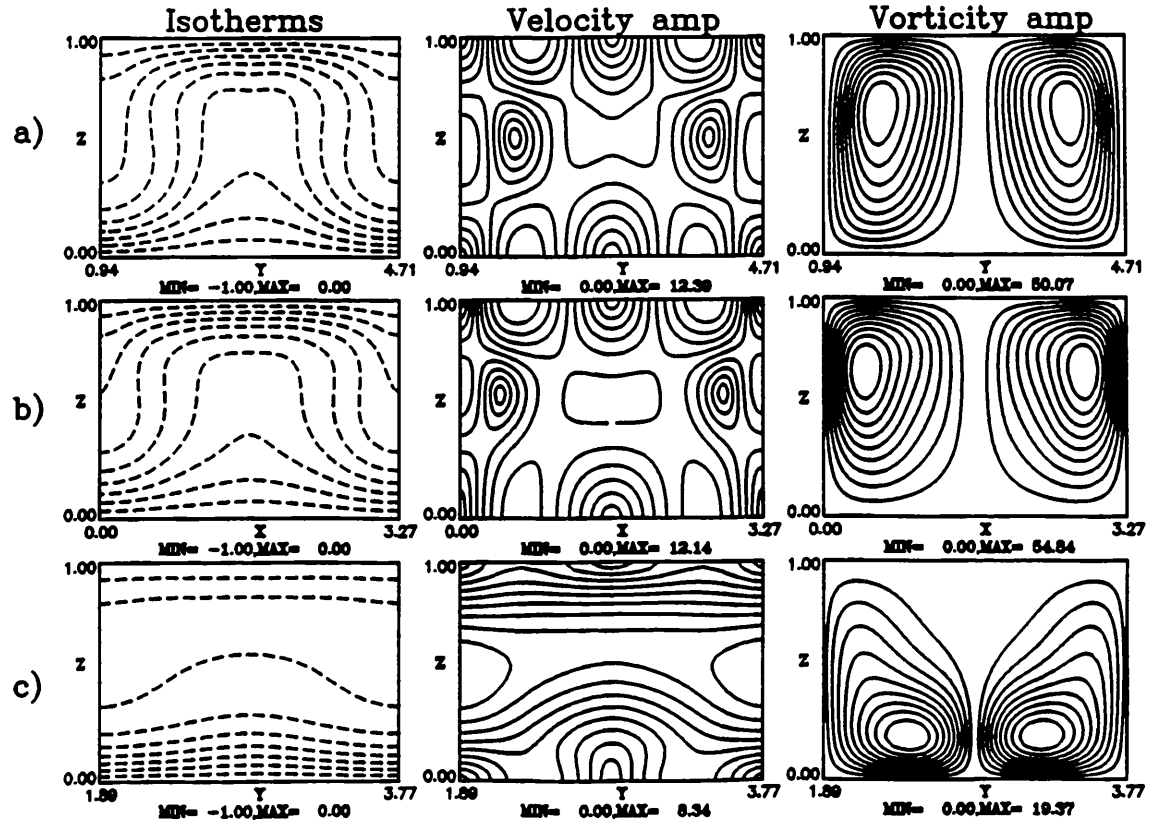


Figure 5.22a)i). Hexagonal Rayleigh–Benard convection.
Vertical velocity surfaces at various depths (+ve left)
R=1787.8533, N= 2.50, α=1.111, σ=10.00, fourthvv

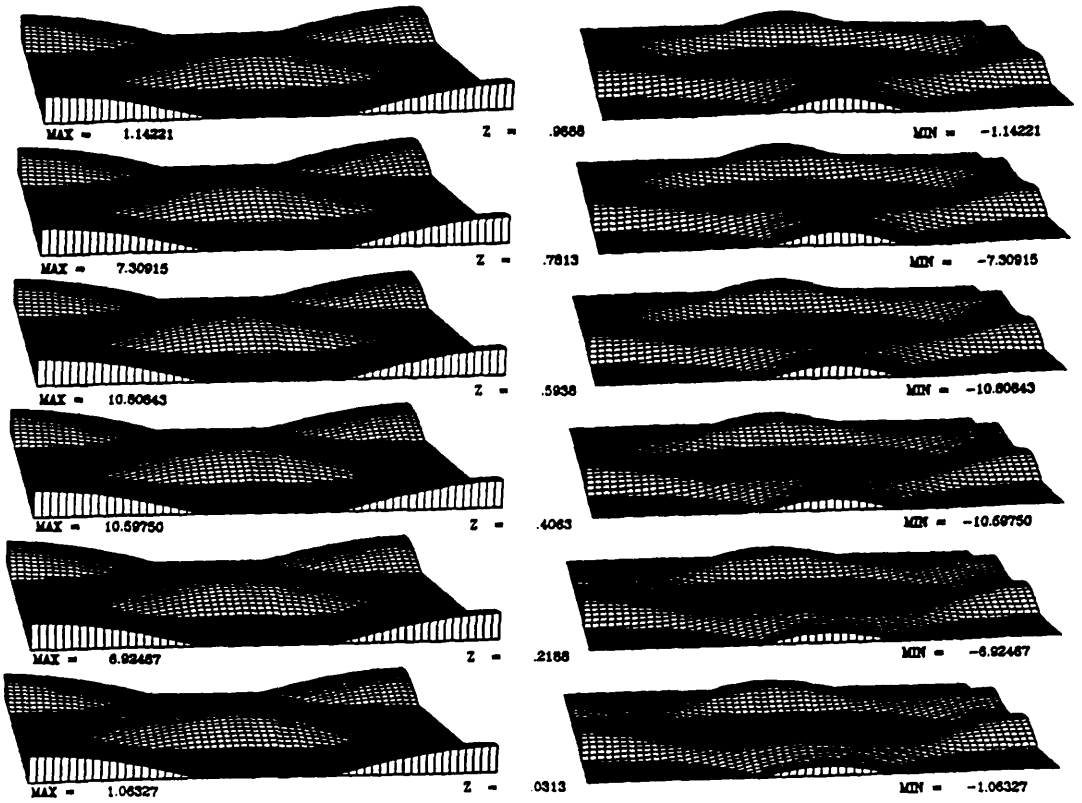


Figure 5.22b)i).. Hexagonal Rayleigh–Benard convection.
Vertical velocity surfaces at various depths (+ve left)
R=1904.7079, N= 2.50, α=1.111, σ= 1.00, fourthvv

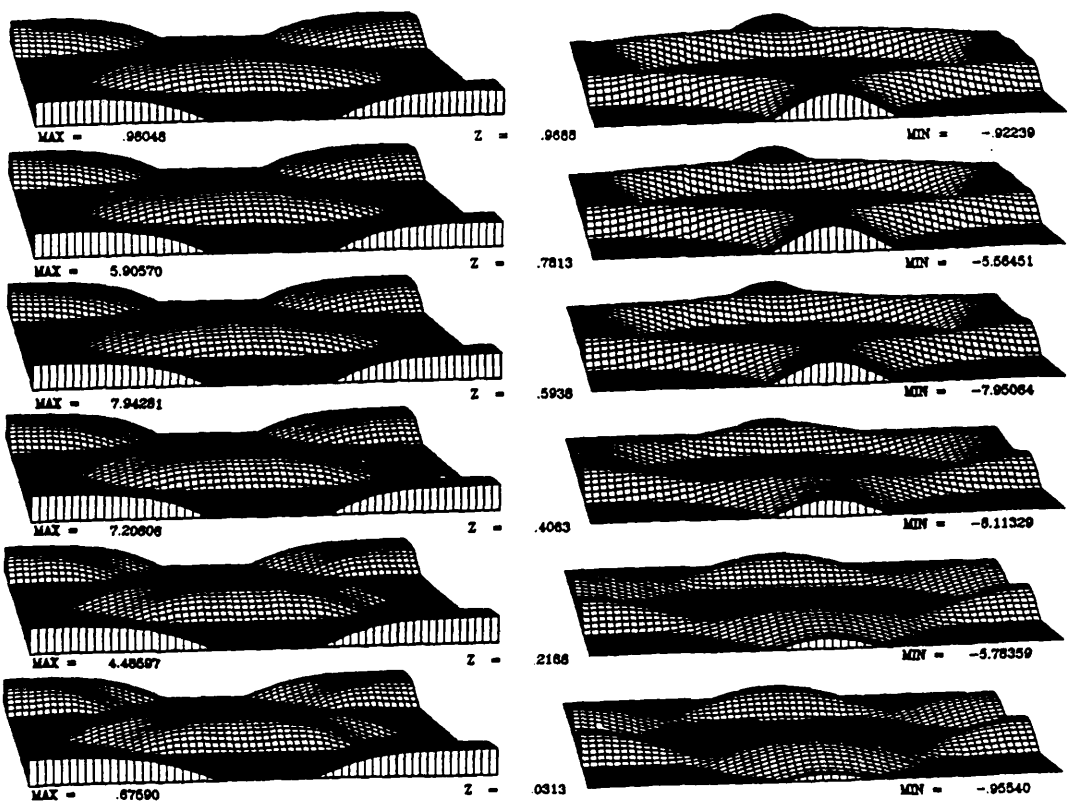


Figure 5.22a)ii). Hexagonal Rayleigh–Benard convection, Vertical velocity
R=1787.8533, N=2.5000, σ=10.00, α=1.111, fourthvv

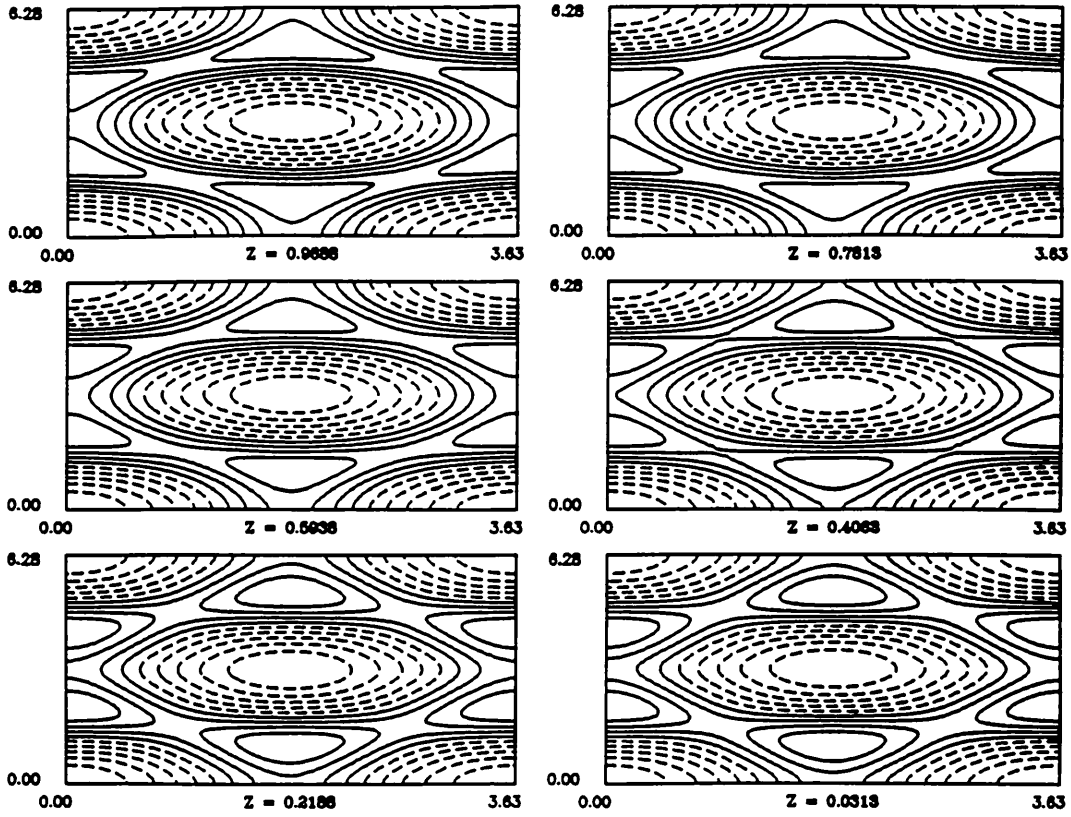


Figure 5.22b)ii). Hexagonal Rayleigh–Benard convection, Vertical velocity
R=1904.7079, N=2.5000, σ= 1.00, α=1.111, fourthvv

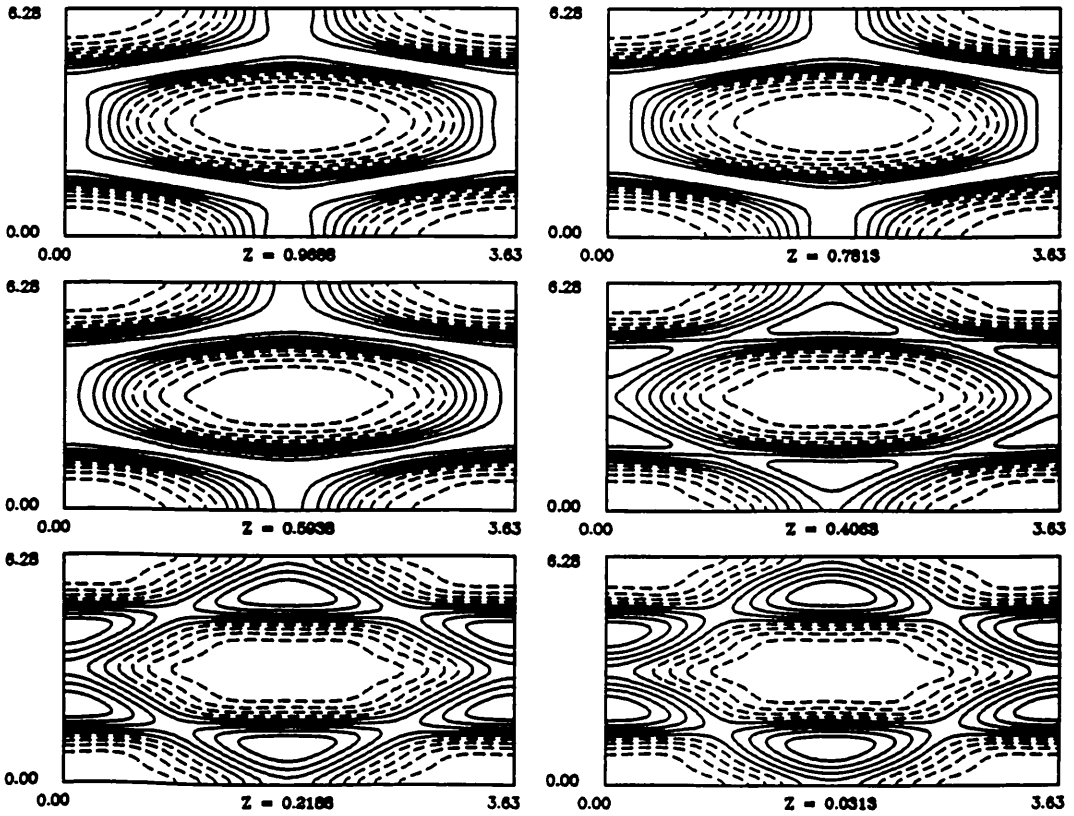


Figure 5.23a). Hexagonal Rayleigh–Benard convection.
Vertical vorticity surfaces at various depths (+ve left)
R=1787.8533, N= 2.50, α=1.111, σ=10.00, fourthvv

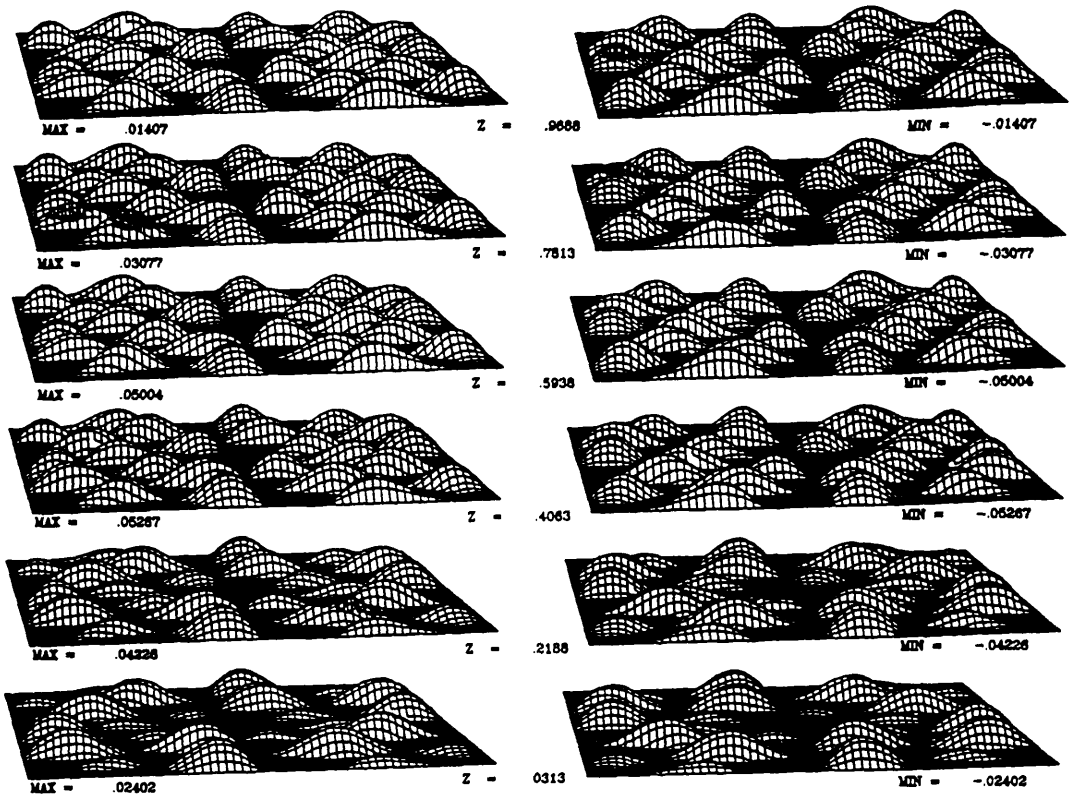
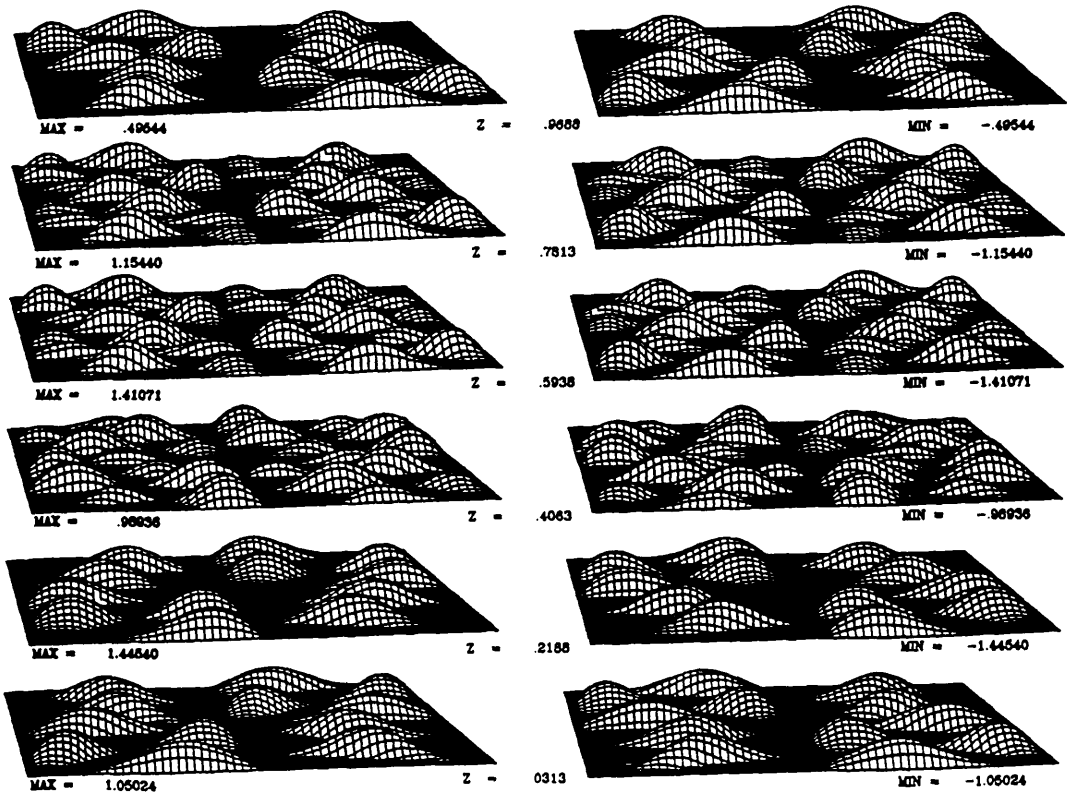


Figure 5.23b). . Hexagonal Rayleigh–Benard convection.
Vertical vorticity surfaces at various depths (+ve left)
R=1904.7079, N= 2.50, α=1.111, σ= 1.00, fourthvv



become significant at lower σ, although they were negligible at $\sigma = 10.0$.

Figures 5.21a) and b) show the vertical slice contours of temperature, velocity and vorticity amplitude at $\sigma = 10.0$ and $\sigma = 1.0$, and may be compared with figure 5.7g) which shows the $\sigma = 0.1$ equivalent. The vorticity amplitude contours shown pertain to the horizontal vorticity due to the planes chosen for these diagrams, and so the decreasing Prandlt number forces a concentration of the horizontal vorticity into small cells near the boundaries. At $\sigma = 10.0$, the vorticity is evenly spread over the whole cell in two, smooth rolls on all slices, but as σ is lowered, the vorticity on the walls congregates at the bottom, and inside the cell, it is forced outwards towards the wall or upwards towards the boundaries leaving the centre of the cell with constant vorticity. The overall amplitude increases by at least 50% in each slice, with the emphasis changing from evenly spread vorticity, to strong vorticity on the walls and horizontal boundaries.

The velocity amplitude shows that, as the Prandtl number decreases, the walls become more stratified, as does the temperature there, but in the body of the cell the flow becomes more plume−like, and less evenly distributed, with some reverse flow at the top of the cell at the lower σ.

Figures 5.22a) and b) may be combined with figure 5.4g) to give an indication as to the effect on the vertical velocity and planforms. Essentially, as would be expected with an increase in non−linearity, the simplicity of the vertical flow is broken up by the decrease in Prandtl number. At $\sigma = 10.0$, even at this relatively high Nusselt number, the vertical velocity contours map out a planform dominated by the fundamental, with little asymmetry with depth and a very definite cellular structure. As σ is decreased and the importance of the non−linearity increased with a subsequent release of the higher harmonic terms, the asymmetry of the layer about its mid−depth increases, with different modes dominating at the different levels. At $\sigma = 1.0$, the RH$\sqrt{3}$ harmonic has influenced the lower half of the layer to emphasize the vertex structure, breaking up the hexagonal, cellular walls, whereas the opposite has happened in the upper half, the harmonic balance accentuating these walls and smoothing the velocity along them so that they are strong sheets of downflowing fluid. This pattern confirms the hypothesis of strong vertical motions and horizontal vorticity in the upper half, coupled with stronger vertical vorticity and thus horizontal motions in the lower half, which agrees with the findings of GST1 and GST2 for rigid boundaries. At $\sigma = 0.1$, the walls are again emphasized, with steep gradients of vertical velocity marking the ridges in the upper layers, whereas the lower layers are a collection of odd plumes of flow. The whole layer has become more agitated with the greater non−linearity levels, leaving the picture very much less clear as to the full nature of the flow, except that the vertical motions have increased significantly. A doubt is cast on the

Fig. 5.24a) **Stereo velocity plots – Hexagonal Rayleigh–Benard convection**
R = 1787.85, N = 2.50, σ = 10.00, α = 1.111, fourthvv

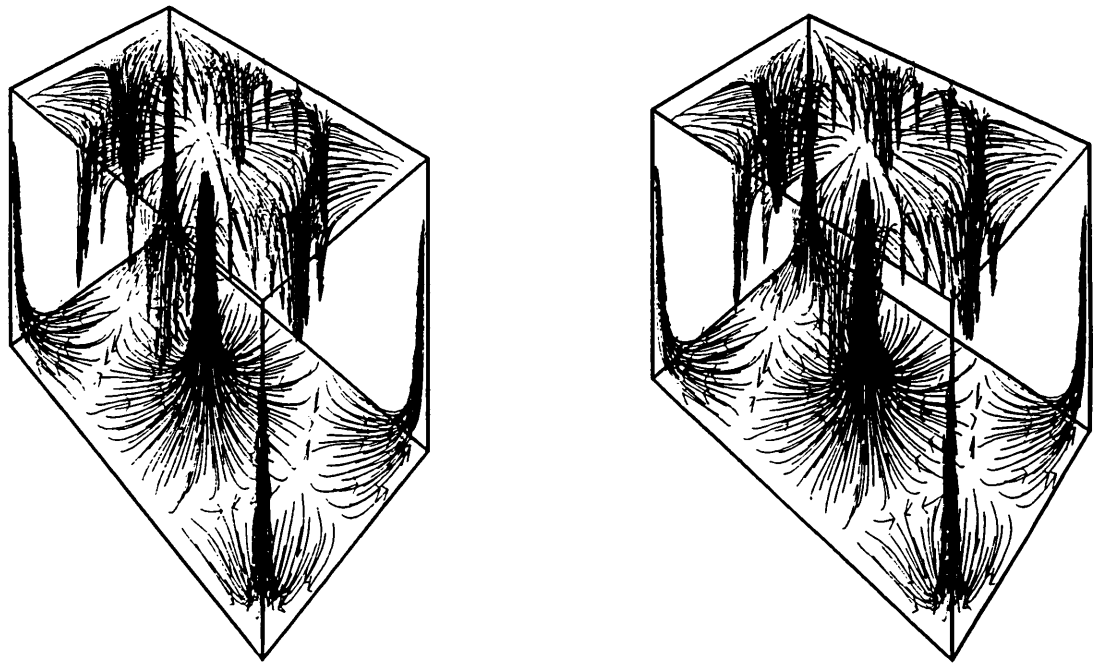


Fig. 5.24b) **Stereo velocity plots –. Hexagonal Rayleigh–Benard convection**
R = 1904.71, N = 2.50, σ = 1.00, α = 1.111, fourthvv

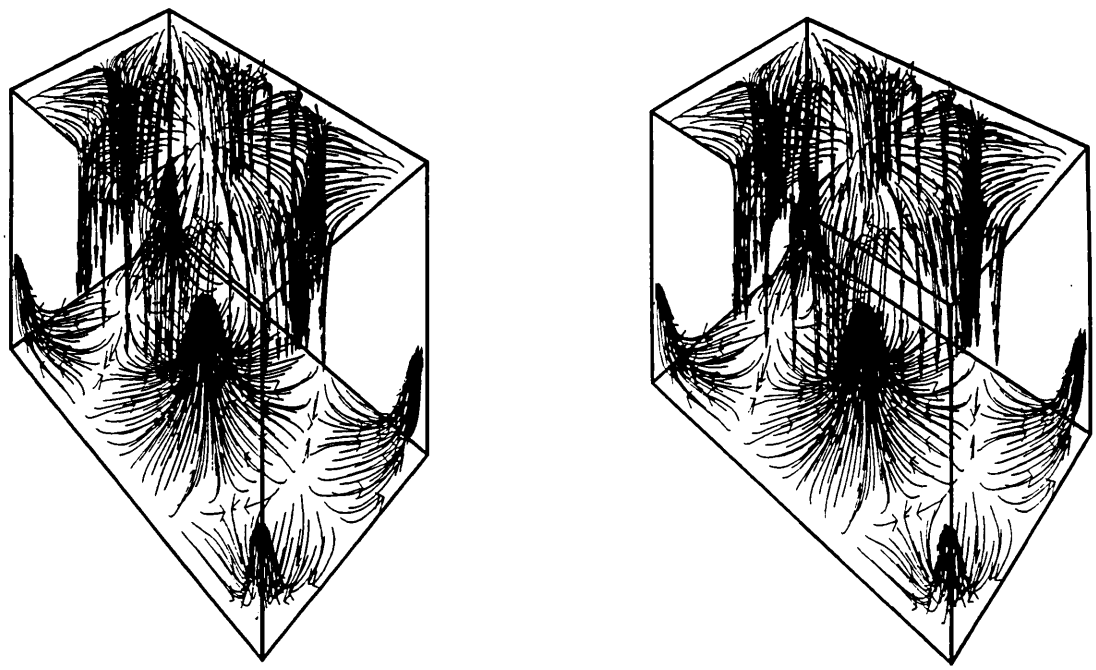
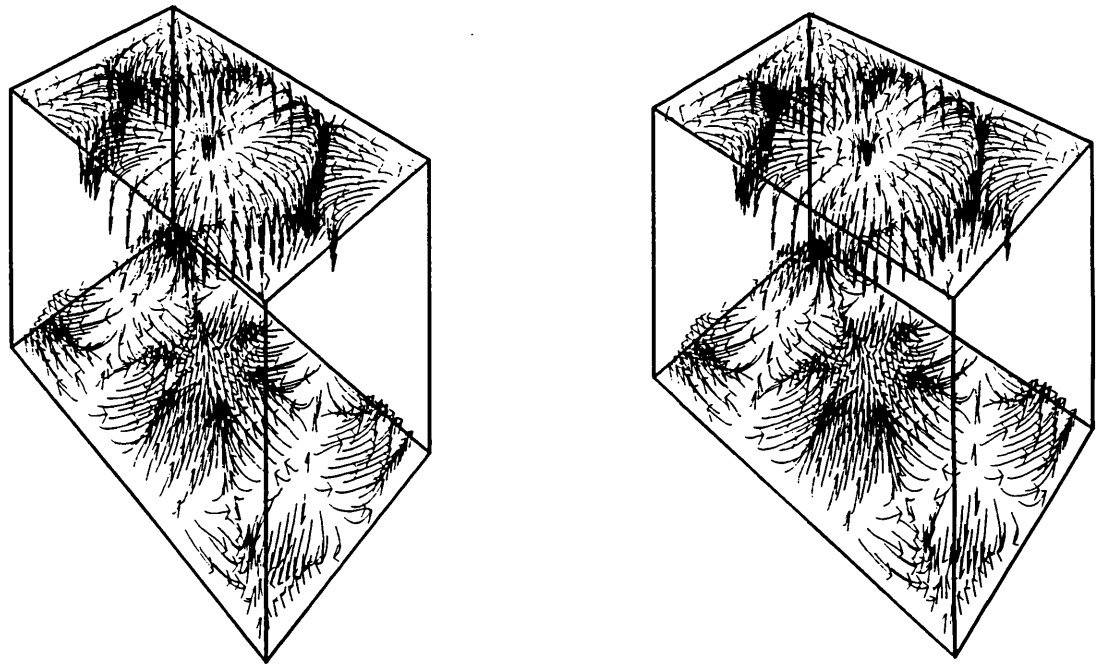


Fig. 5.24c) **Stereo velocity plots – Hexagonal Rayleigh–Benard convection R = 1121.53, N = 1.20, σ = 0.03, α = 1.111, fourthvv**



cellular nature of the flow, since the breakup of the wall flow at the lower boundary may be thought of as technically destroying the cell walls, but this feature is fairly minor in this hexagonal case.

Figure 5.23a) and b) coupled with figure 5.5b) show that the amplitude of the vorticity is the major increase in the flow with the decrease of the Prandtl number, increasing from virtually nothing at σ = 10.0, through values on the order of unity at σ = 1.0 to five times that strength at σ = 0.1. However, the 'strong' increase in vertical vorticity does not manage to stir the flow around, as previously mentioned. Figures 5.24a) and b) with figure 5.10g) serve to show that the decrease in Prandtl number and subsequent increase in harmonic activity mainly force the flow from simple upflow at the centre of the fundamental hexagon with downflow at the vertices, to a more general but similar flow, where more downflow occurs along the whole cell walls and wider central plumes are generated. Possible oddities such as a downflow in the centre of the main cell are also formed. Note again that at low σ, the cellular nature is shown to be broken by the contour plots of vertical velocity, but that this effect is weak. Figure 5.24c) demonstrates that at a lower Prandtl number, σ = 0.025, calculated with a lower amplitude of convection, the flow is much the same as for σ = 0.1, Nu = 2.5.

5.4.2.2. Square horizontal periodicity.

Again, it will be implicitly assumed that the highest order solution is in fact the 'best' in some sense, so that studies of the variation of the square periodicity planforms with the parameters of the problem will concentrate on the results of the FOURTH order solution.

Figure 5.25a) shows the graph of Nusselt number versus Rayleigh number for the square periodic, FOURTH order solutions at Prandtl numbers $0.01 \leqslant \sigma \leqslant 10.0$, and it shows that there is a strong σ dependence of the heat flux. The dependence is actually stronger than the previously investigated hexagonally periodic case, since here there is no sign of the presence of a second critical Rayleigh number in the Rayleigh number range shown. The σ dependence is once again strongest between $\sigma = 1.0$ and $\sigma = 0.1$, but in this case, the curves remain σ−dependent at all Rayleigh numbers, not showing the sudden increase in dNu/dRa at some second Rayleigh number. This style of σ dependence is more akin to the hexagonal flows of GST, calculated for rigid boundaries using low order truncations of the modal model. However, the lack of the inertial style flow in their calculations could be attributable to the restraining effect of the low number of planforms available to the system. This is not the case for the square flows here, since the fourth order truncation appears to allow enough freedom of choice of planform for evidence of a flywheel−type solution to exist, judging by experiences from the hexagonal case described earlier. The increase in the dependence for squares over that of hexagons may be demonstrated by comparing particular values in the regime where the solutions exhibit a similar dependence i.e. $0.1 \leqslant \sigma \leqslant 10.0$. At a Rayleigh number of about $R = 4.0\ R_c$, the hexagonal case has dropped its Nusselt number from around 3.0 for $\sigma = 10.0$, through 2.9 for $\sigma = 1.0$, to approximately $Nu = 2.5$ for $\sigma = 0.1$, whereas, for the square case, although the two higher σ results remain much the same, the lowest Prandtl number, $\sigma = 0.1$, has dropped in Nusselt number to a value more like $Nu = 1.85$, significantly lower than the corresponding hexagonal solution. This is surprising since the square solutions do not allow a component of vertical vorticity to enter into the solution system, whereas the hexagonal solutions do, at the highest orders studied. It may be expected that the greater degree of freedom allowed by the existence of such modes, generated by the non−linearities of the problem and therefore strongly influenced by σ, would stamp a greater impression on the flow than if these modes were not present at all. However, this seems not to be the case in the parameter ranges studied.

Figure 5.25b) and table 5.2 (see section 5.4.2.1 earlier), however, both show

Fig. 5.25a) **Square cell Rayleigh–Benard convection**
Rayleigh number against Nusselt number
Prandtl number dependence

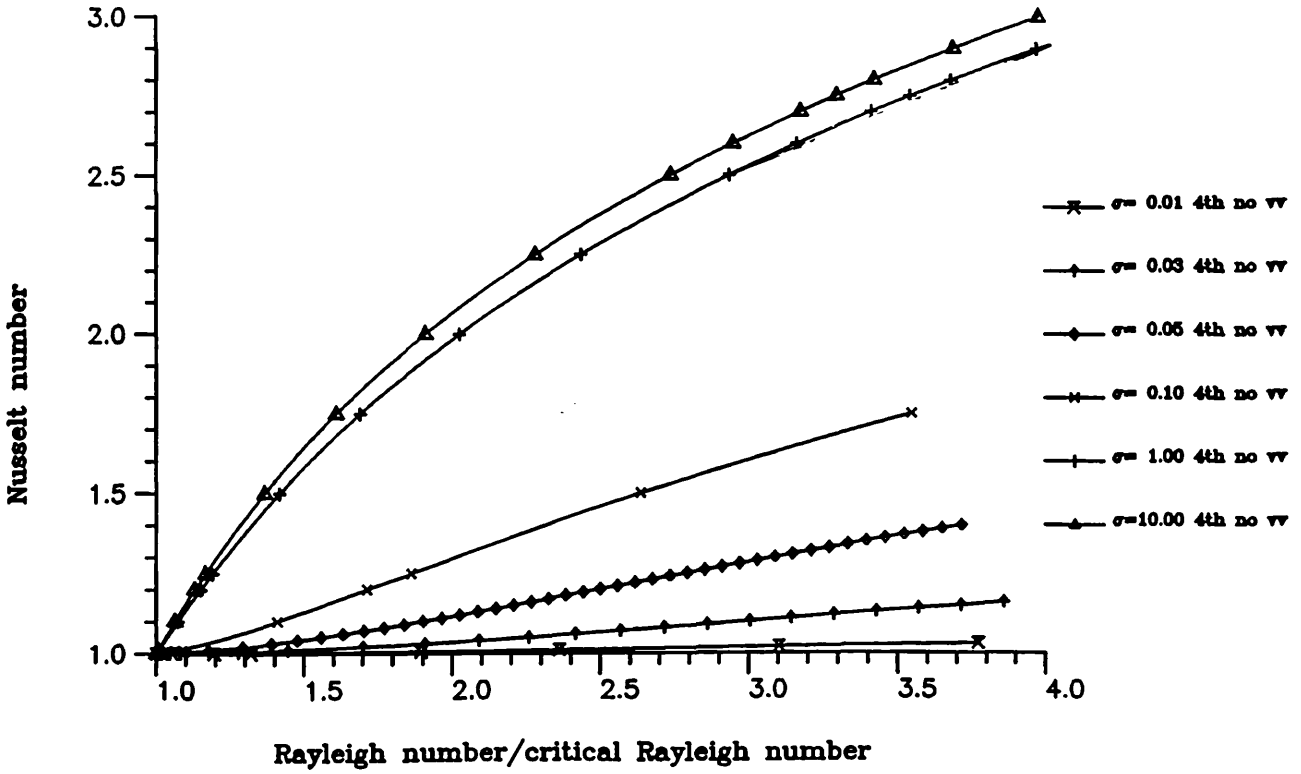
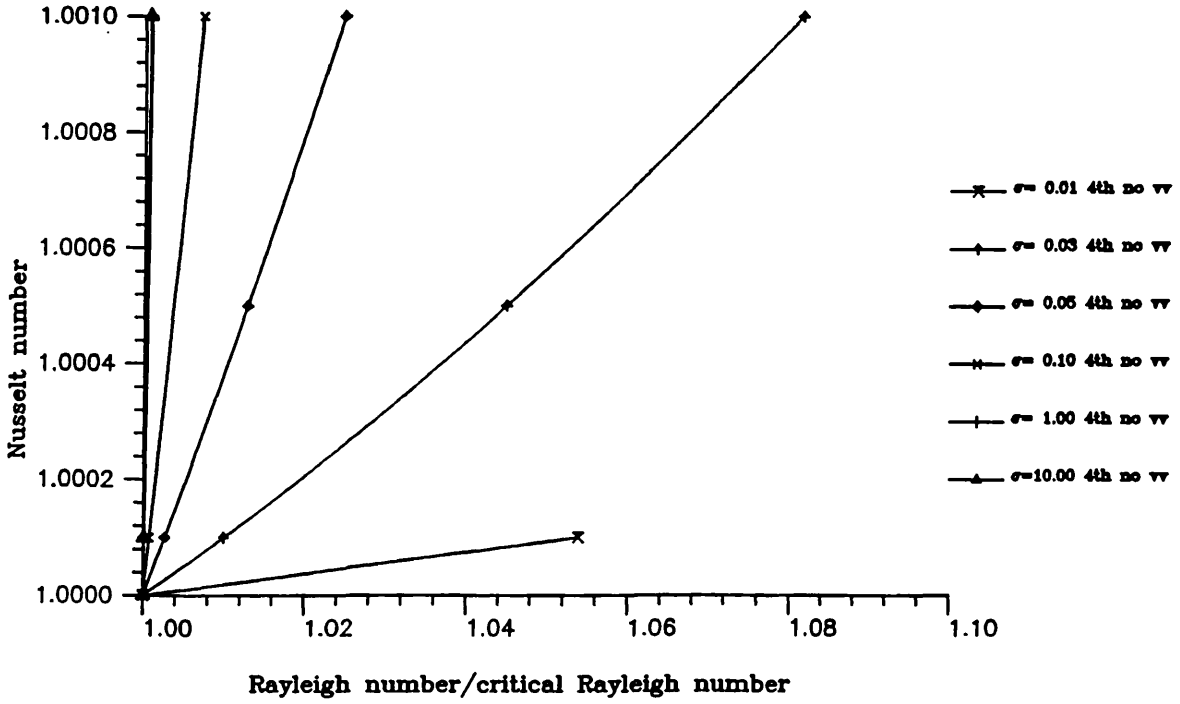


Fig. 5.25b) **Square cell Rayleigh–Benard convection**
Rayleigh number against Nusselt number
Prandtl number dependence near critical



that the heat transport in squares at low Prandtl numbers and for low amplitudes of convection is very similar to that of hexagons, as predicted by small amplitude theory (see Jones, Moore and Weiss (1976) and references therein). Figure 5.25b) is almost identical to figure 5.19d) and table 5.2 shows that once again the square convection fits the σ^2 dependence of X, the coefficient relating Nu−1 to $Ra/Ra_c - 1$ (see equation [5.22]). However, for squares, no σ−independence is seen for low σ and for $Ra \geq 1.4Ra_c$ as is for 2−D rolls, cylinders and hexagons.

Studying the individual variables of the solution for various Prandtl numbers at Nu = 2.5 and $\alpha = \alpha_c = 1.571$ also shows some surprises. Figure 5.26a)' and 5.26a)'' shows the fundamental streamfunction mode (there is only one streamfunction, χ, for the square case, since $\psi = 0$ as there is no vertical vorticity) to be depleted in amplitude at the lower σ with the increase in non−linear interactions and greater generation of the sub−harmonics, which are be fuelled at least initially by the main mode. (Notice once again that the lowest σ calculated at the lower amplitude of Nu = 1.2 are very similar in form to the σ = 0.1, Nu = 2.5 solutions). This depletion is seen to increase monotonically and substantially with the Prandtl numbers shown. However, figure 5.26b) for the second, S02, mode (and, consequently, the third, S20, mode) does not exhibit a monotone increase of the amplitude of the functions with decreasing σ, rather shows a slight decrease in amplitude as the Prandtl number is varied from σ = 1.0 to σ = 0.1 after the expected increase in amplitude between σ = 10.0 and σ = 1.0. This effect may be explained by assuming that certain harmonics are not important until a particular level of non−linearity has been reached (one method of increasing the non−linearity being to reduce the Prandtl number), and that some harmonics may be fed only indirectly from the fundamental through other harmonics. Then, the amplitude of some harmonics, such as the S20 χ mode, may be reduced as other harmonics, such as the S22 χ mode, are gradually brought into effect. This does not appear to occur for the hexagonal symmetry, where the modes vary monotonically with σ. Figure 5.26c) shows the vertical variation of the remaining second order mode, the S22 mode, and this returns to the expected monotonic increase in amplitude with Prandtl number.

The most dramatic previously−unseen change with σ occurs in figure 5.26d) which shows the mean temperature profile for this case. Here, the isothermal nature of the profile, usually assumed to be an indicator of the level of non−linearity present in the solution, actually decreases with a decrease of Prandtl number. It may be expected that decreasing the Prandtl number and thus increasing the importance of the non−linear terms in the solution, would increase the vigor of the flow. This in turn may be assumed to increase the distortion of the mean temperature profile away from the linear, conducting profile, and to

Fig. 5.26a)'

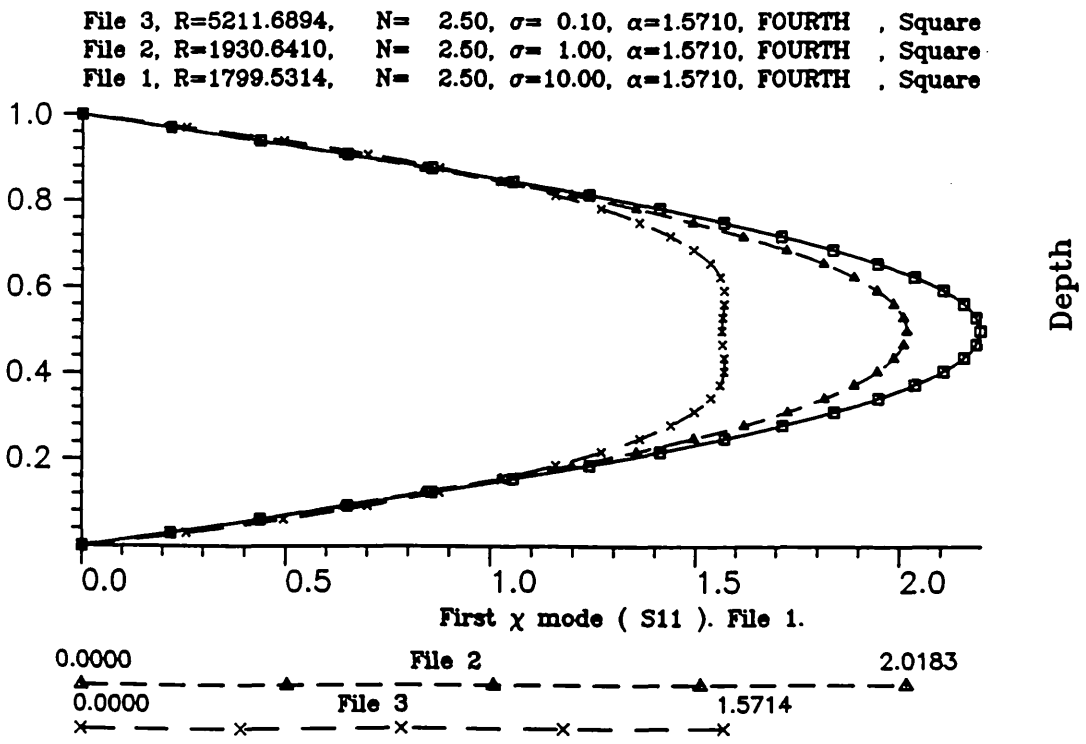


Fig. 5.26a)''

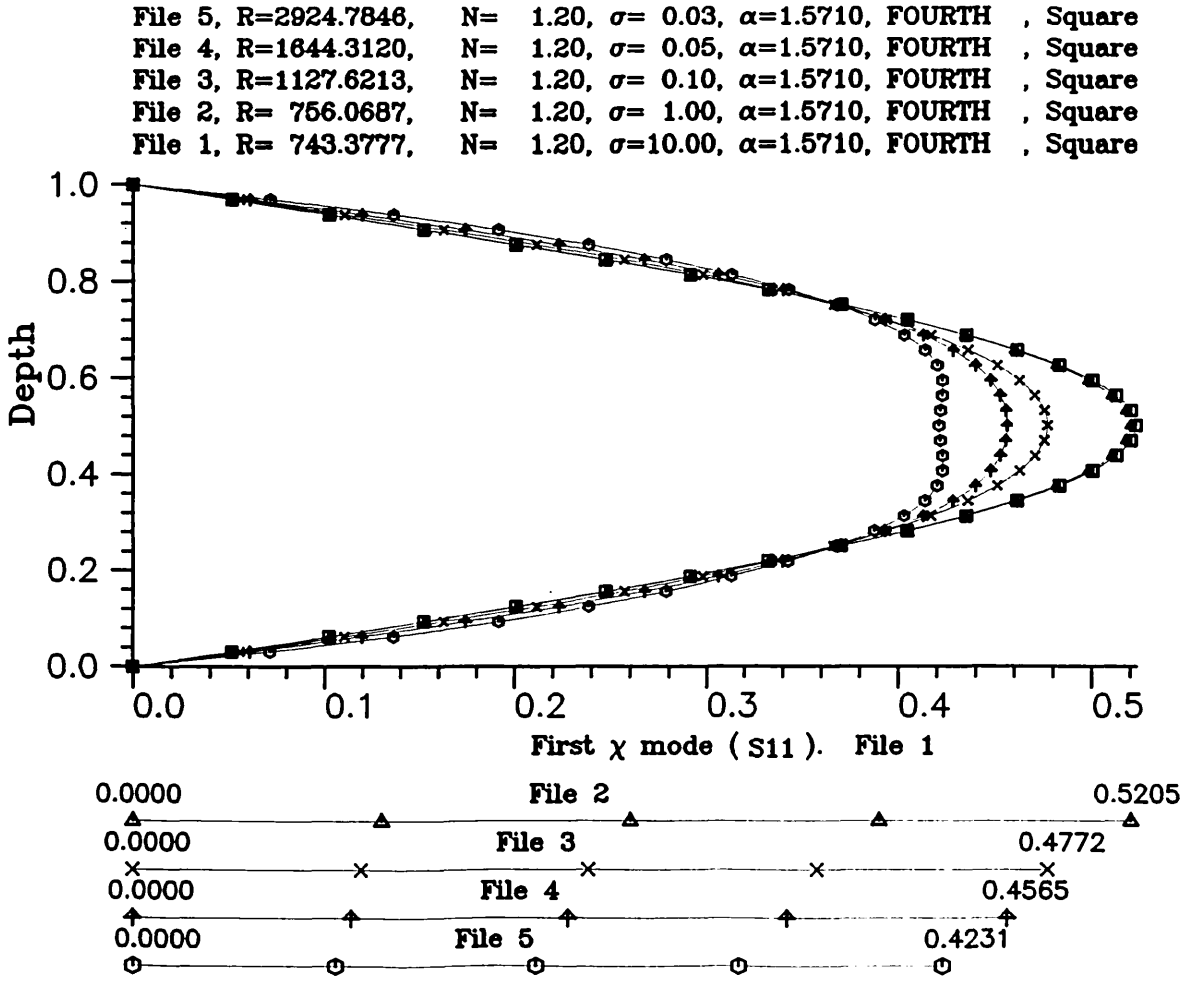


Fig. 5.26b).

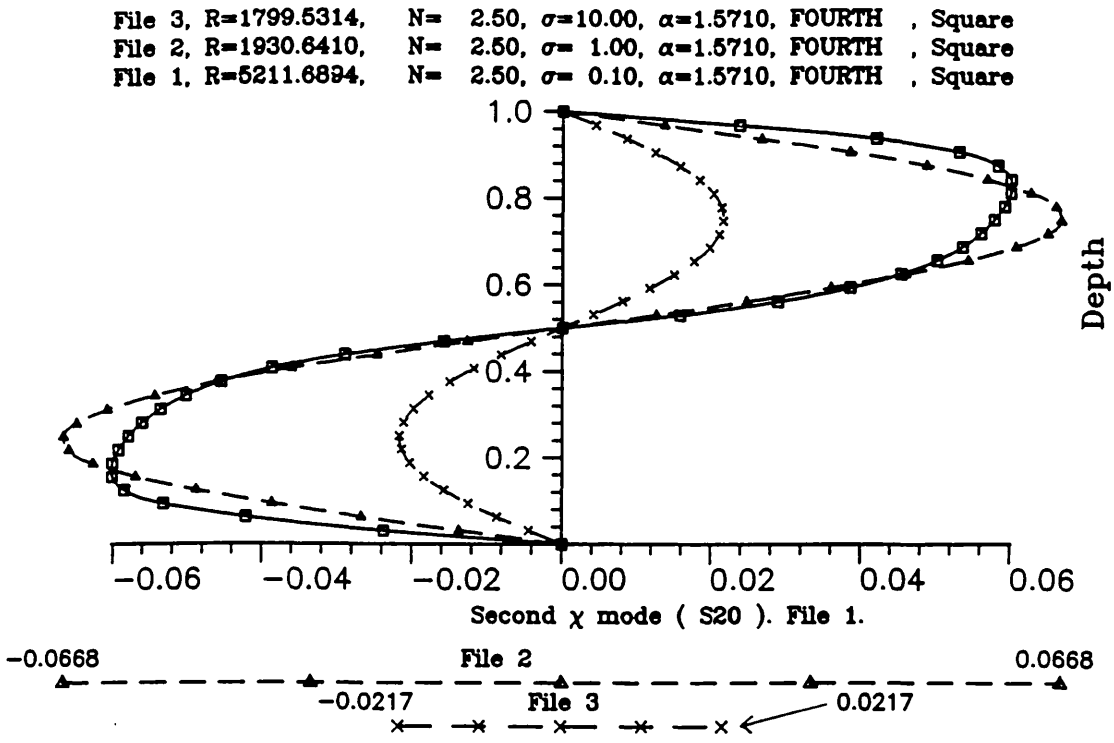


Fig. 5.26c).

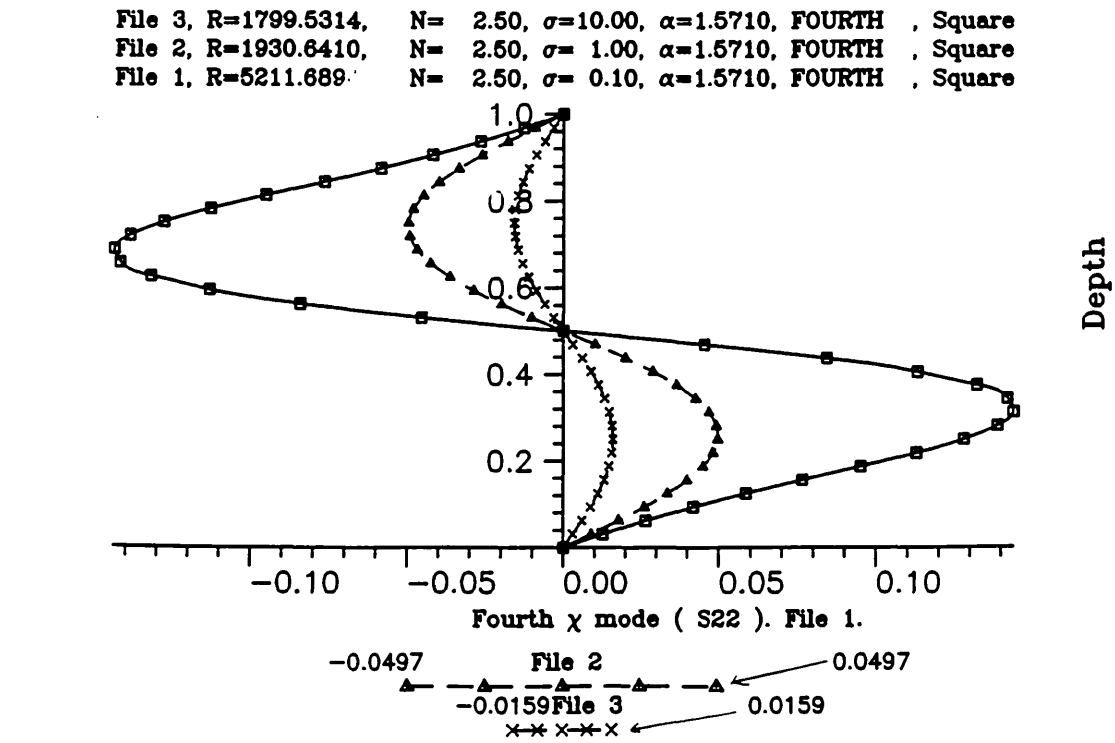


Fig. 5.26d).

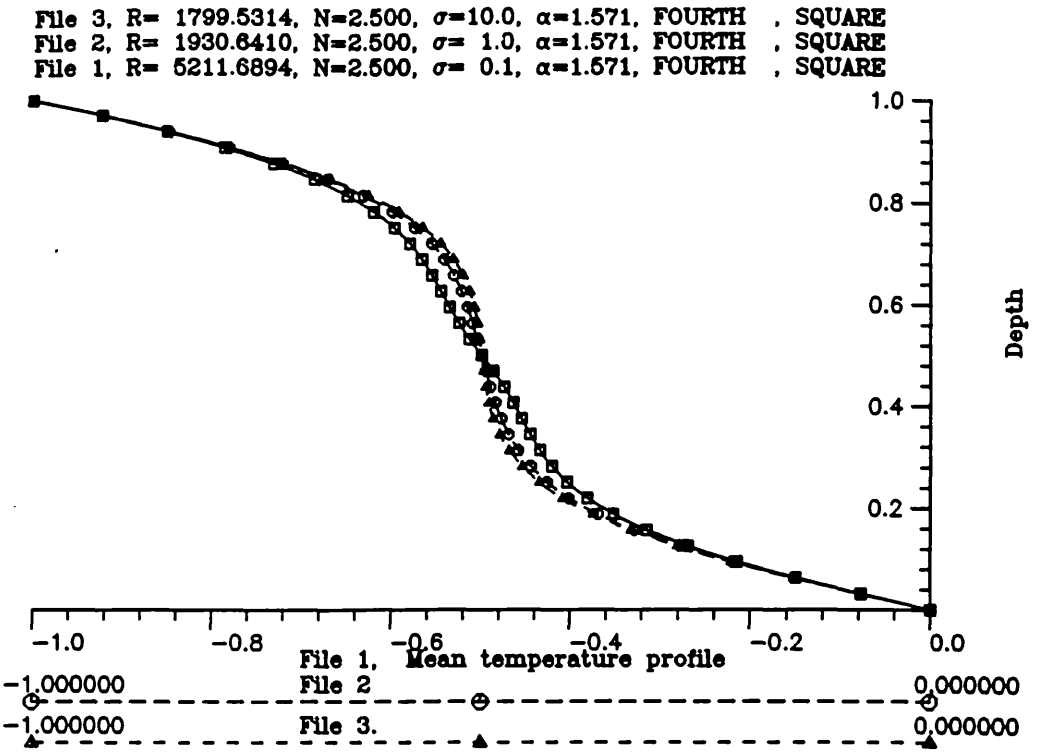


Fig. 5.26e).

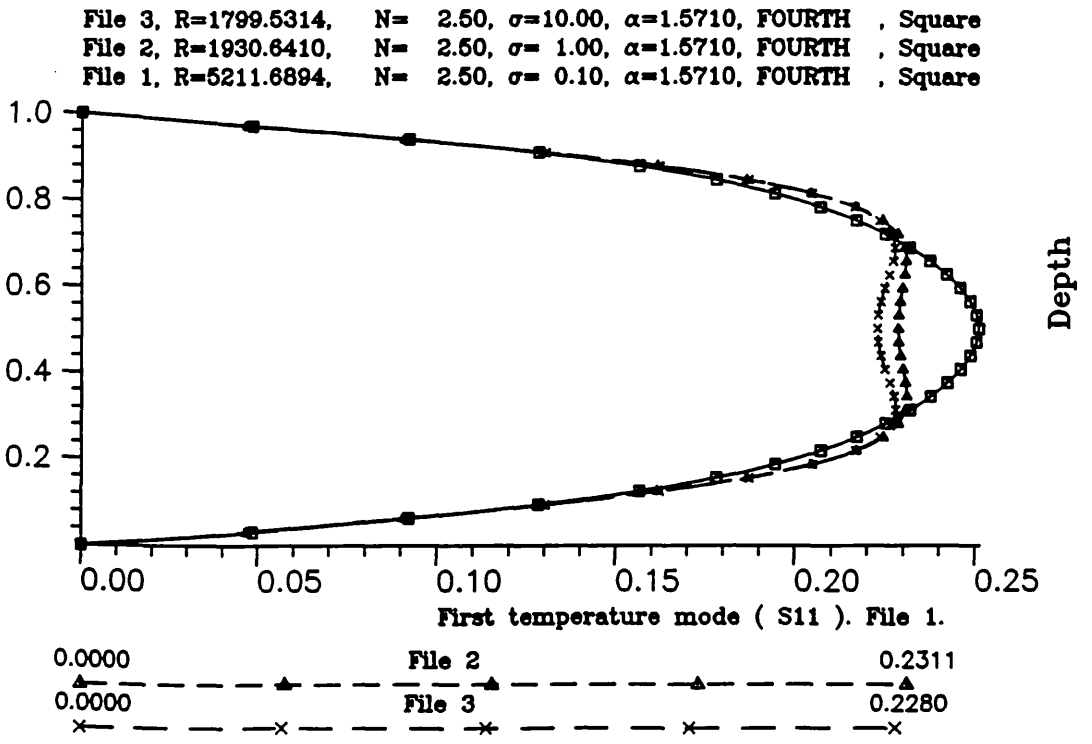


Fig. 5.26f).

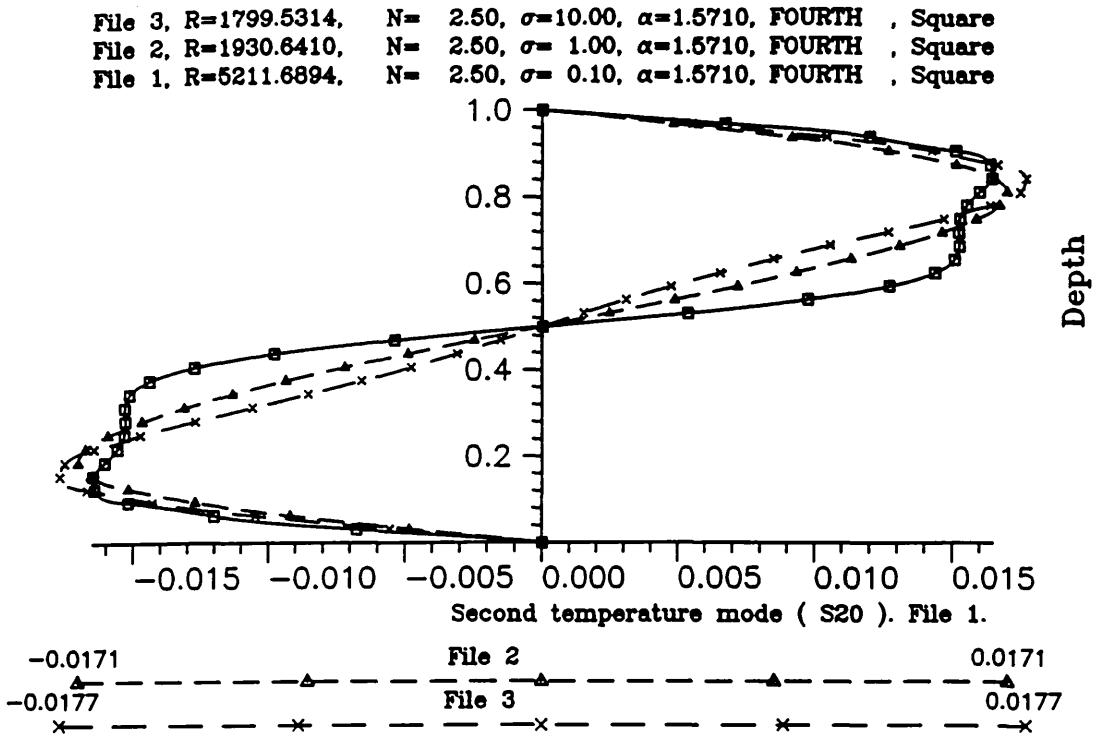
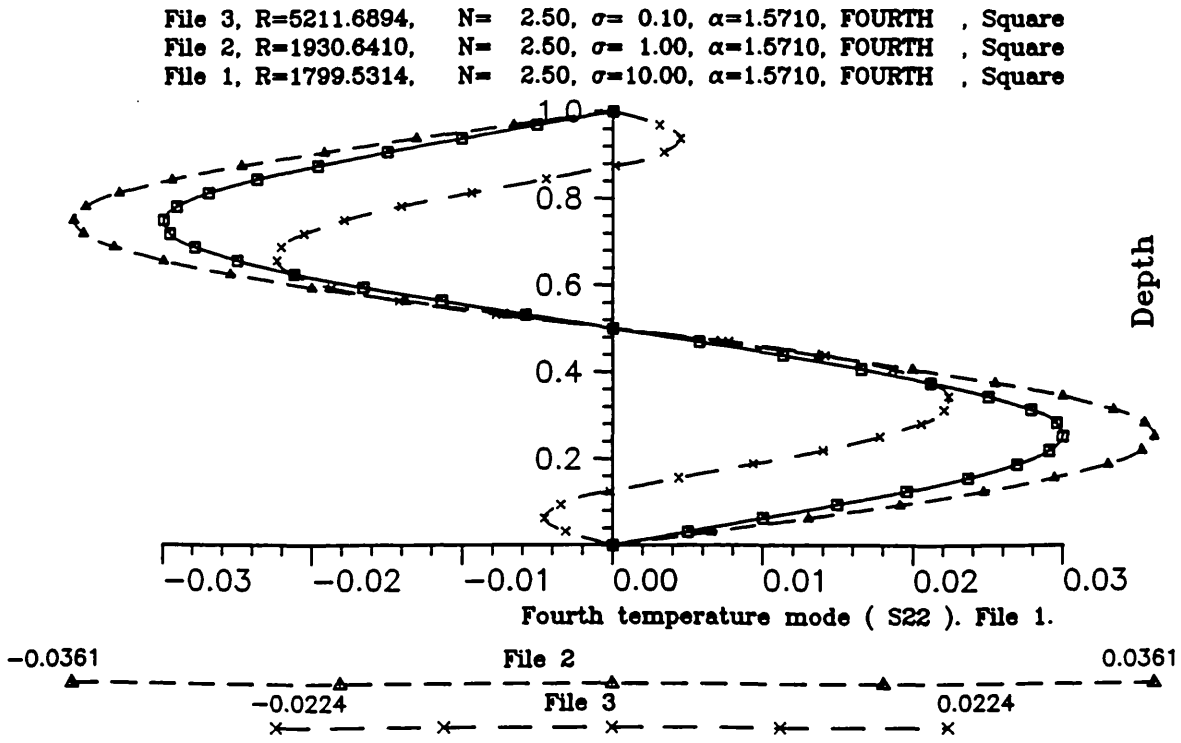


Fig. 5.26g).



form temperature boundary layers with an inner isothermal region. Here, although the change in profile is not a huge departure, it is noticeably more linear and less isothermal. A possible explanation for this may lie in the fact that the number of modes included in this expansion are not sufficient to completely resolve the flow accurately. This is thought not to be the case, since, as was seen in the modal−dependence discussion (see figure 5.13i)), the low order modal models influence the mean temperature profile quite significantly, the addition of the higher frequency modes actually showing in the profile as extra reversals of the sign of the second derivative, D^2T_0. The first order mode shows the expected simple, isothermal type plot, whereas the higher order models show perturbations to this simple plot, forming a more 'wavy' profile. This is most obvious in the second order solution, the higher order solutions appearing to oscillate towards a true solution somewhere between the isothermal and wavy extremes, in the same manner as the Nu−Ra graphs. This implies that it is the modal solutions that reduce the isothermal nature of the mean profile, but that even a very high order truncation would still show this effect. The harmonic modal solutions then being more important at low σ, emphasize the smoothing of the profile at these values.

The remaining temperature modal variables then also show some unusual variations. Figure 5.26e) shows that the fundamental temperature mode increases in amplitude with the decrease in σ, forming a much less iso−strength mid−layer, whereas the S02 (and S20) dependences show a reduction in maximum amplitude with the decrease in σ, contrary to expectations. The peak values in the S02 (S20) mode are however very similar, and the lowest σ shows a much more iso−amplitude variation in the upper and lower halves, with a strong gradient between them, so that the body of the fluid is generally held with a greater influence of this mode than the higher σ solutions, which may be considered to counter the slight reductions in peak values. The remaining second order mode, S22, shows a non−monotonic dependence on the Prandtl number, with the peak values increasing as the Prandtl number varies from σ = 10.0 down to σ = 1.0, but decreasing with the decrease to σ = 0.1, but again at the lowest Prandtl number the style of the mode changes slightly, this time with small reversals in sign being introduced at the boundaries. It appears that decreasing σ enables some of the temperature harmonics to feed back into the fundamental mode, a feature not seen in the hexagonal case, except from the vorticity modes.

Figures 5.27 and 5.28, together with figures 5.14d) and 5.15d) earlier, show the effects of the Prandtl number on the vertical velocity as surfaces and contours in the normal manner and for the usual solution parameters. The development of the different square pattern and asymmetrical style can be seen quite clearly as the Prandtl number is decreased. At σ = 10.0, the fundamental square pattern

Figure 5.27a). Square Rayleigh–Benard convection.
Vertical velocity surfaces at various depths (+ve left)
R=1799.5314, N= 2.50, α=1.571, σ=10.00, fourth

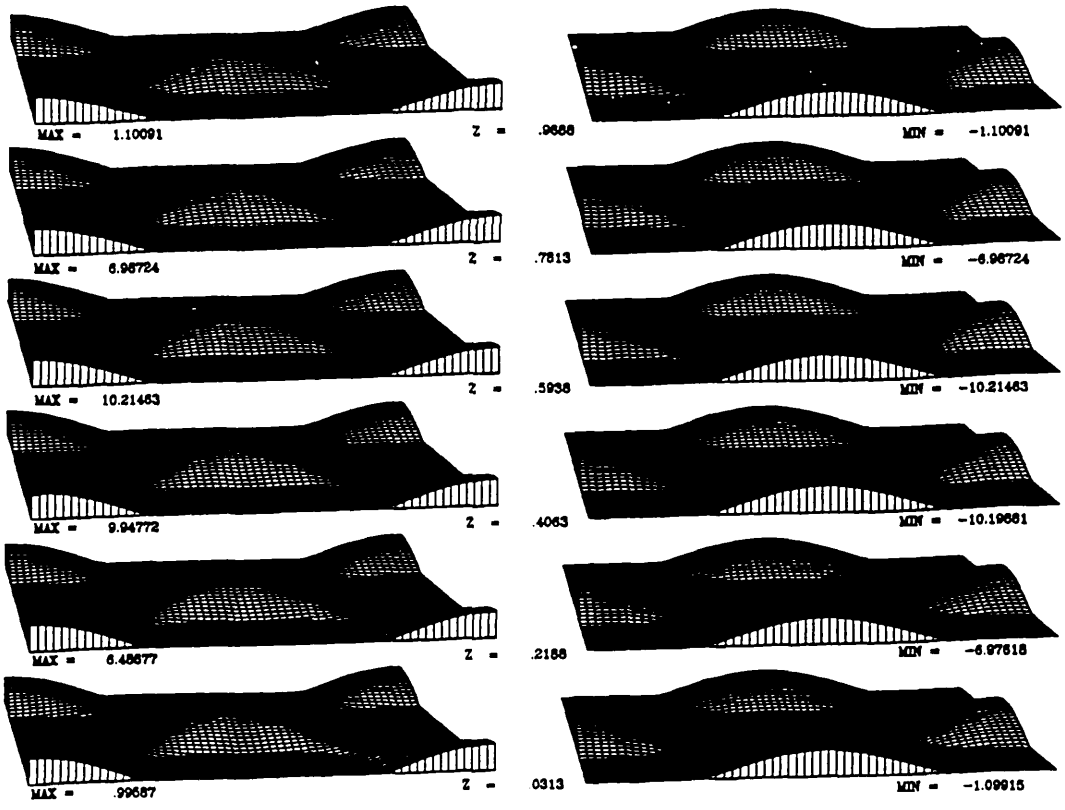


Figure 5.27b). Square Rayleigh–Benard convection.
Vertical velocity surfaces at various depths (+ve left)
R=1930.6410, N= 2.50, α=1.571, σ= 1.00, fourth

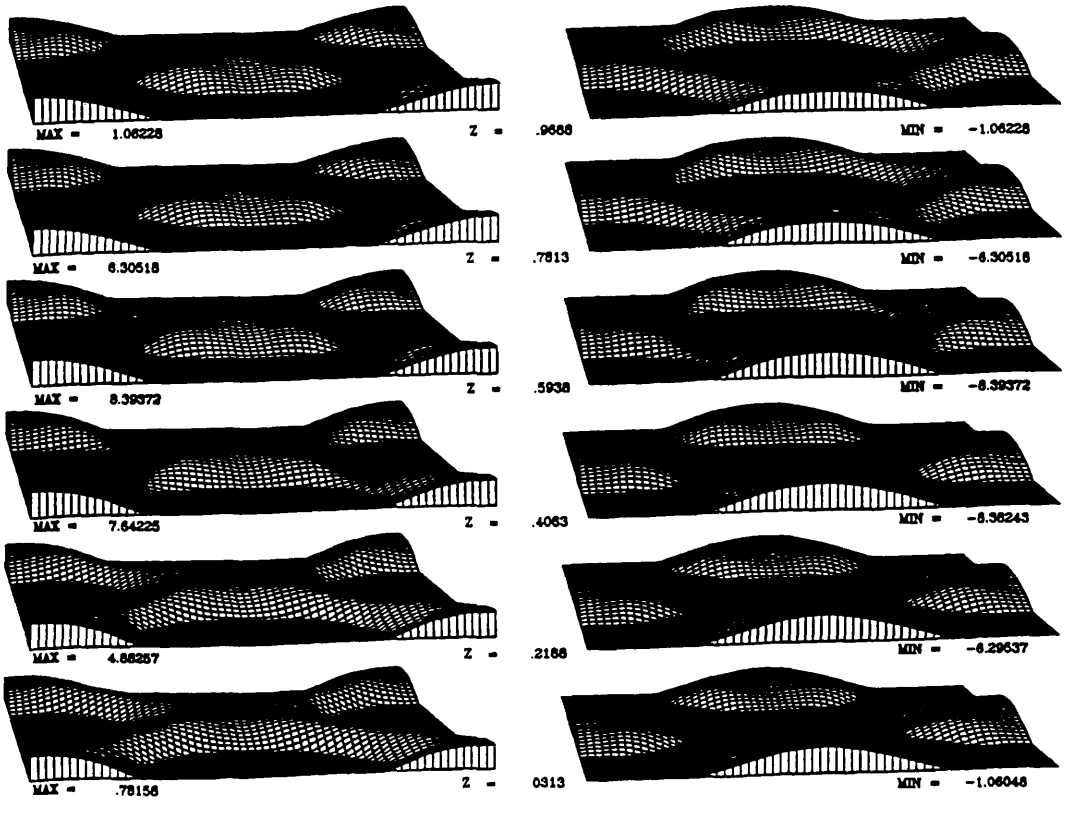


Figure 5.28a). Square Rayleigh–Benard convection. Vertical velocity
R=1799.5314, N=2.5000, σ=10.00, α=1.571, fourth

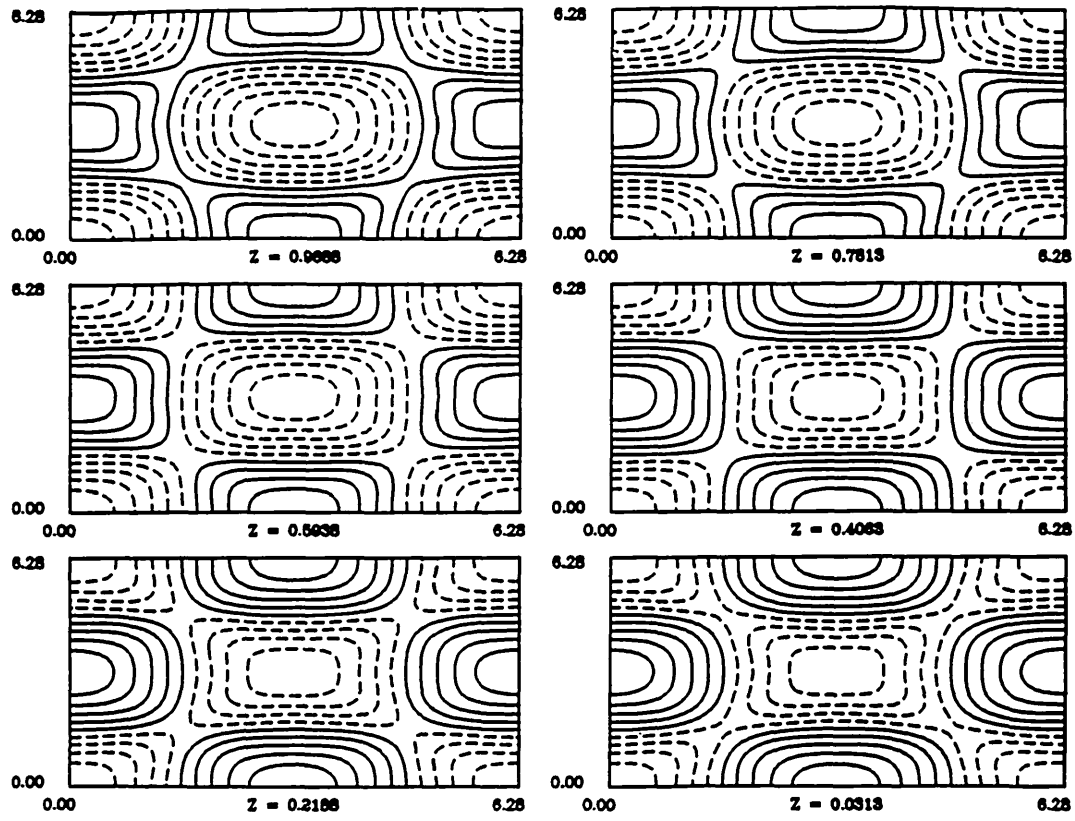


Figure 5.28b). Square Rayleigh–Benard convection. Vertical velocity
R=1930.6410, N=2.5000, σ= 1.00, α=1.571, fourth

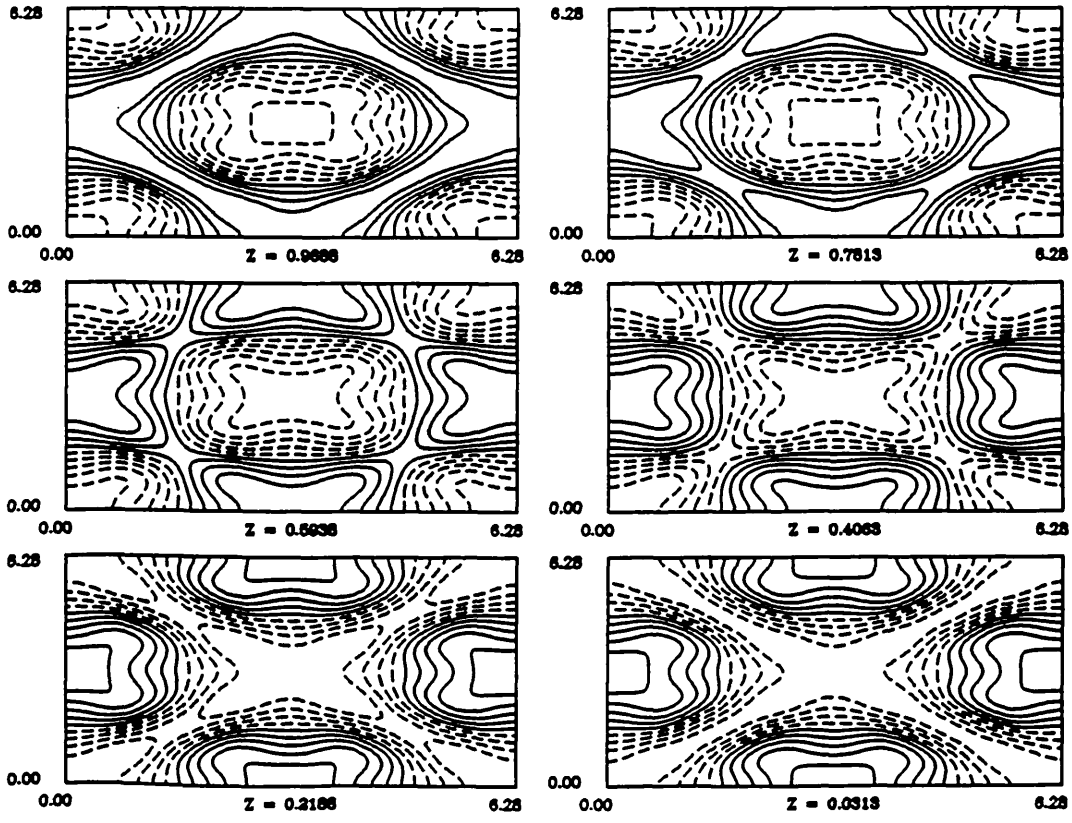


Figure 5.29a). Square Rayleigh-Benard convection.
R = 1799.53, N = 2.50, σ = 10.00, α = 1.571, fourth
a) x=y, y=(0,2π/α) , b) x=π/α, y=(0,2π/α) , c) x=$\pi/2\alpha$, y=(0,2π/α)

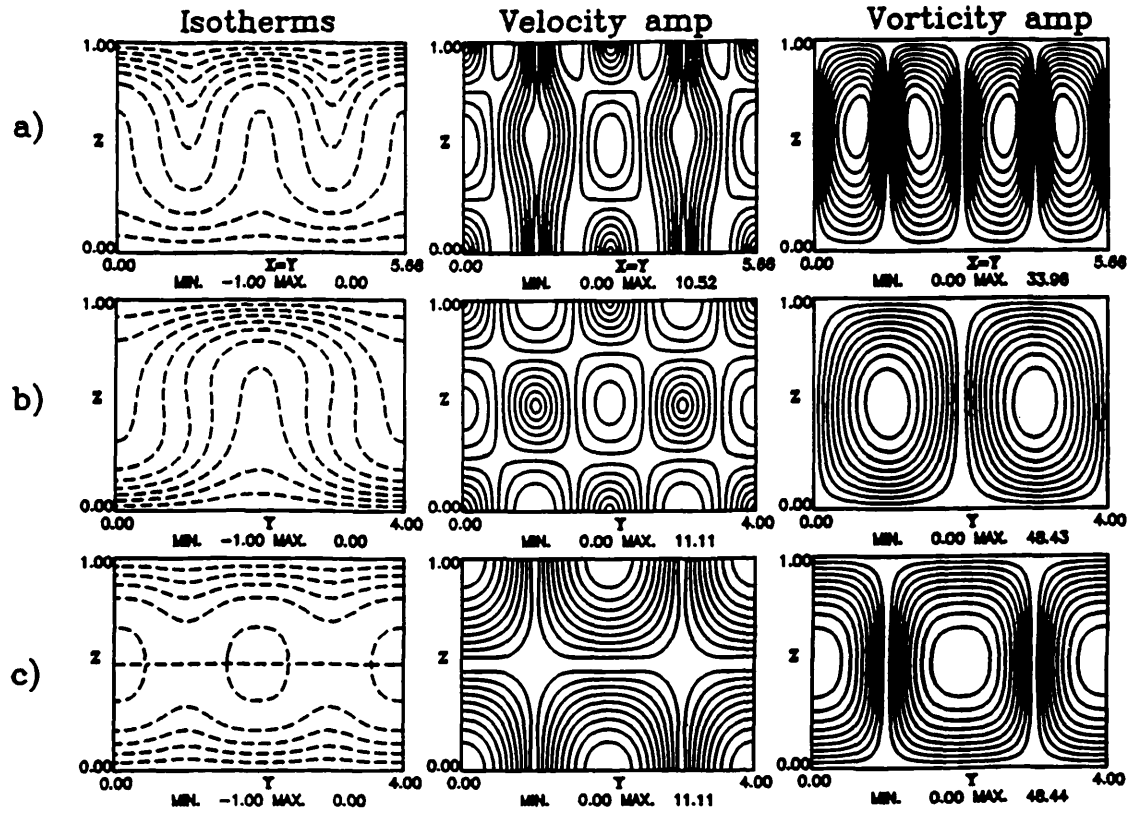
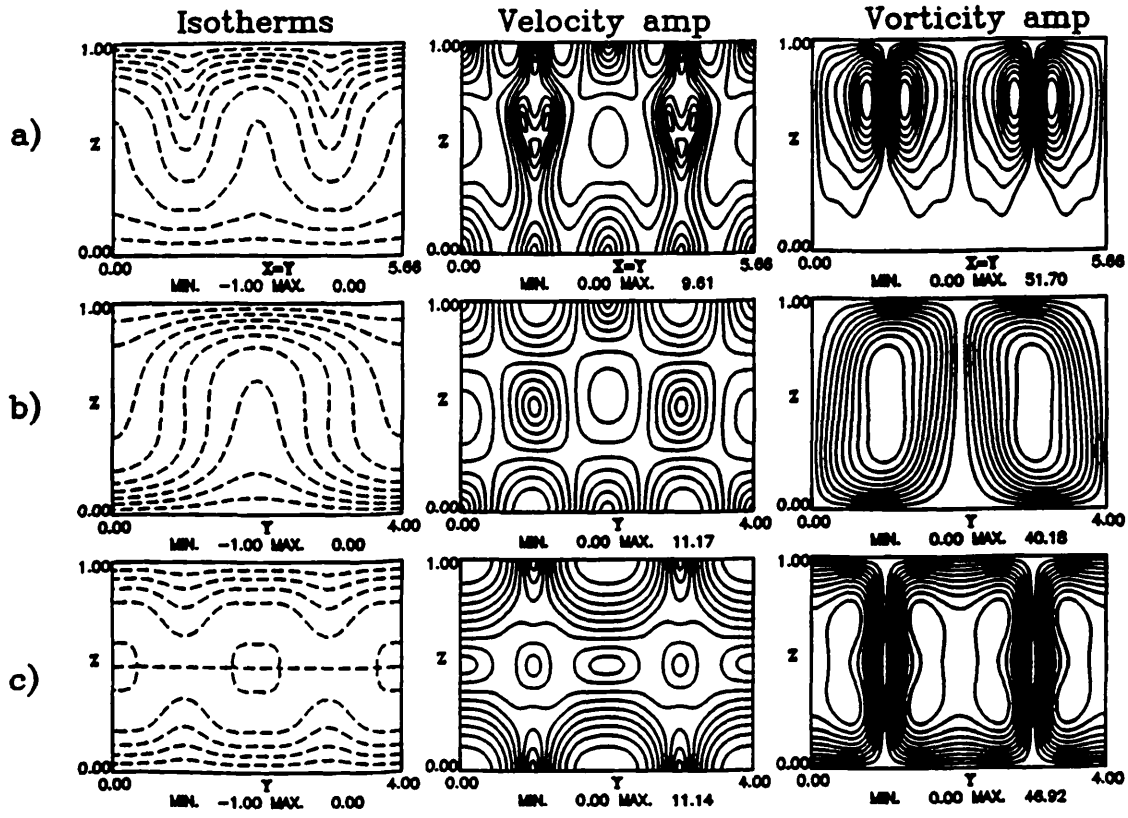


Figure 5.29b). Square Rayleigh-Benard convection.
R = 1930.64, N = 2.50, σ = 1.00, α = 1.571, fourth
a) x=y, y=(0,2π/α) , b) x=π/α, y=(0,2π/α) , c) x=$\pi/2\alpha$, y=(0,2π/α)



associated with the square cell (remember that this square pattern and the square cell are different) is fairly clear, especially in the centre layers, although accentuation of the corners of this pattern forming a joining of the domes is apparent, albeit weakly, at the upper and lower boundaries in the upflowing and downflowing profiles respectively. The contours exhibit this as a 'bowing' or 'bulging' of the square pattern, and the form of development towards the 'criss−cross' type square pattern can be easily seen. This distortion of the pattern even at high σ is due to the fair degree of non−linearity forced by the size of the Nusselt number chosen for this solution (see later) but notice that this effect is more pronounced for squares than for hexagons. As σ is decreased, the definition of this new pattern of 'walls' (rather than 'domes') between the previous peaks of the vertical velocity is increased, with the distortion of the contours forcing out the corners of the weaker−direction flow pattern (i.e. the upward flow at the top and the downward flow at the bottom). This occurs as σ decreases since the non−linear terms, and thus the harmonics, increase in importance, allowing the evenly−dependent roll parts of the solution (e.g. $\cos(2\alpha x)$) to constructively superpose at these corners (e.g. the S22 mode will have plume−centres located at these positions), hence building the inter−plume wall structure. At the lowest σ, the separate square patterns merge as this effect is enhanced to make the definition of the dome−joining lines very clear, although these actual 'walls' themselves (sheets of upflowing or downflowing fluid in this terminology) then becomes rippled by other higher harmonics, so that they are no longer as smooth.

Decreasing the Prandtl number increases the amplitude of the vertical velocity so that the flow near the boundaries is as strong as the flow at the centre of the layer, indicating sharp deceleration in thin boundary layers for the more vigorous flow. Notice that, technically, the cell walls have been lost, even at $\sigma = 10.0$.

Figures 5.29 and 5.16d) show that the velocity amplitude increases with decreasing σ, although this increase is not monotonic in all of the vertical slices shown, similarly for the vorticity amplitude, which is much stronger at $\sigma = 0.1$ than the higher σ. The strong downflowing 'walls' at the top of the layer are clearly seen to appear at lower σ in the isotherms and amplitude plots of the diagonal (a)) slices, where the concentration of amplitude is definitely in the top layer and at the positions of the 'walls'.

The changes in the actual flow structure are only subtle changes, as is shown by figures 5.30 and figure 5.17d) which show stereo plots of the full velocity, started from planes near the boundaries for the usual variety of Prandtl number solutions. Here, the change over from 'dome' to 'wall' dominance is exhibited as the decentralising of the original vertex plume flow in favour of central

Fig. 5.30a) **Stereo velocity plots – Square Rayleigh–Benard convection**
R = 1799.53, N = 2.50, σ = 10.00, α = 1.571, fourth

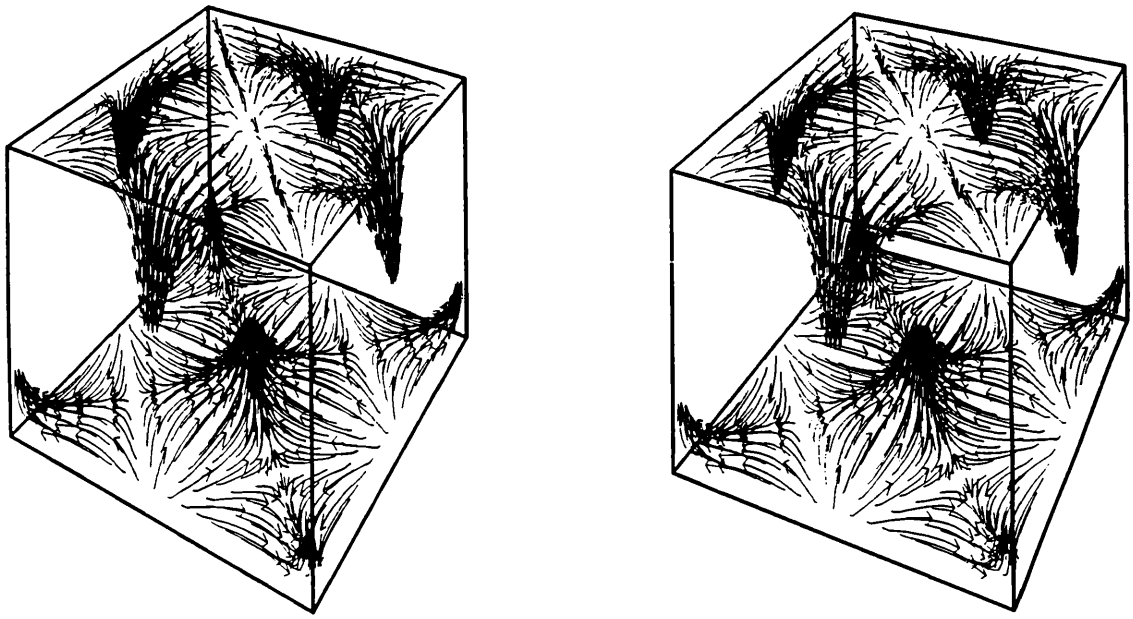


Fig. 5.30b) **Stereo velocity plots – Square Rayleigh–Benard convection**
R = 1930.64, N = 2.50, σ = 1.00, α = 1.571, fourth

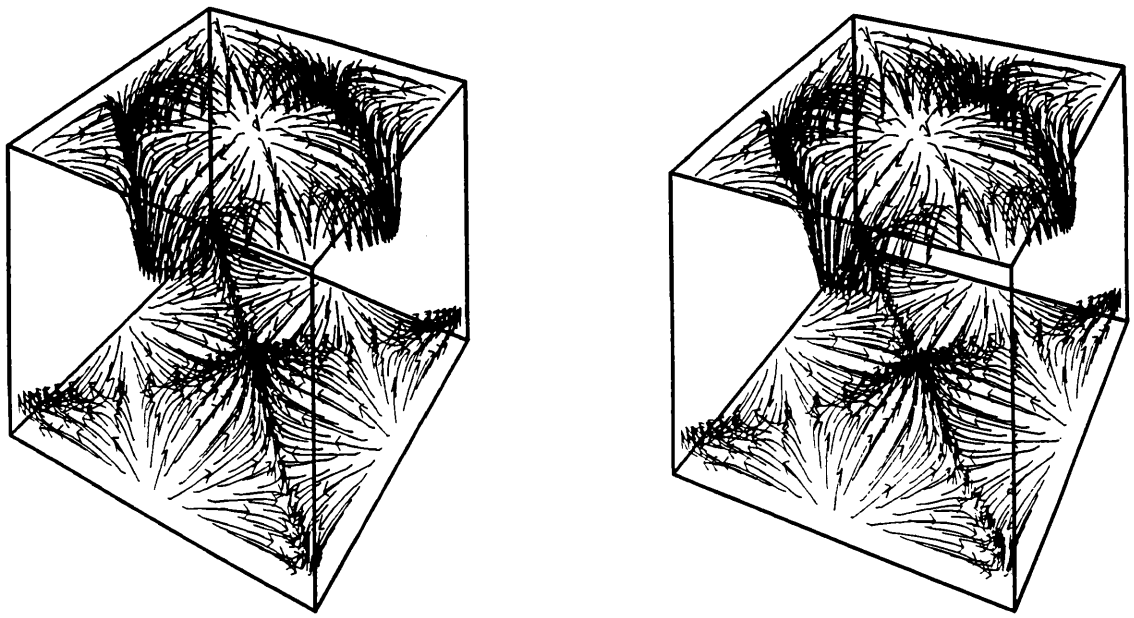
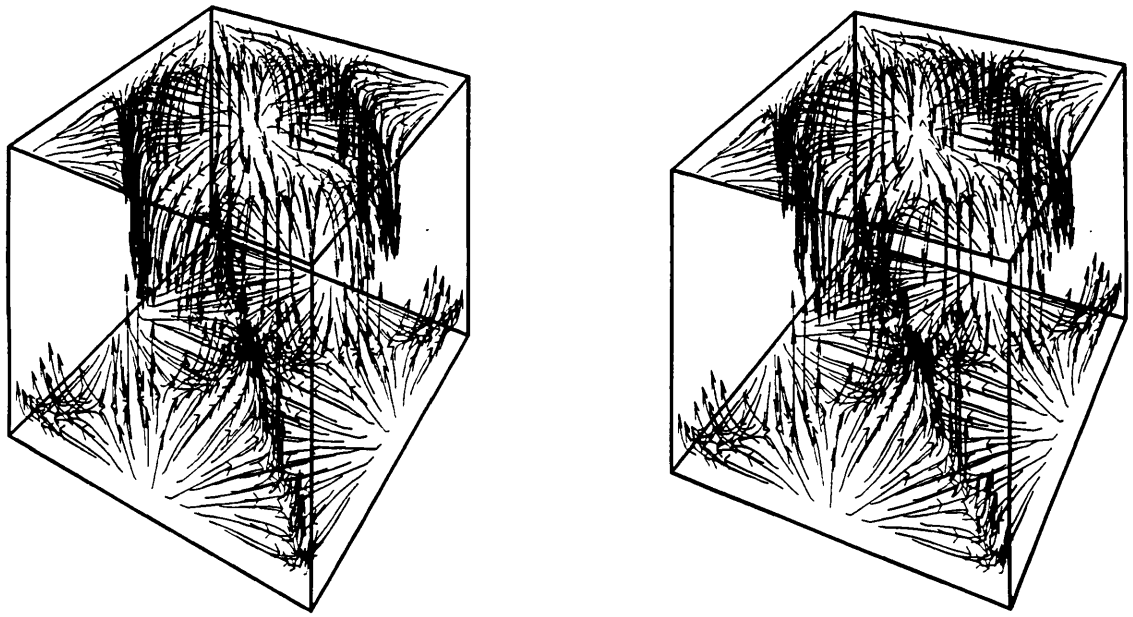


Fig. 5.30c) **Stereo velocity plots – Square Rayleigh–Benard convection R = 2924.78, N = 1.20, σ = 0.03, α = 1.571, fourth**



plumes (where the terms 'vertex' and 'central' refer to the true original square cell). In the high σ solutions, the flow is geared to forming concentrated downflowing plumes at the top vertices, and upflowing plumes in the centre at the bottom. The plumes are segregated to each lie within one of the contour squares which define the domes (the contour domes are, of course, manifestations of the plumes themselves) with little vertical flow between them. At $\sigma > 10.0$, square cells (by the Stuart (1964) definition) thus exist, since the planes formed by the lines which join the centres of the plumes (or domes) when extended vertically downwards satisfy the criteria for cell walls i.e have no flow across them and have vertical velocity of one sign on the whole plane. However, even at $\sigma = 10.0$ but more definitely as σ is reduced, the emphasis changes subtly, so that instead of horizontal motions concentrating the flow towards all of the original plumes, vertical flow is allowed anywhere on the lines joining the original plume centres, thus forming the sheet 'walls', coupled with a broad central plume of opposite vertical velocity to the walls. Note once again that at low σ the pattern on the lower boundary becomes the exact reverse of the upper pattern shifted by half a cell–width in either x or y. Of course, as explained earlier, although this new pattern may actually appear more like real cell walls than the higher σ, they are in fact not true cell walls in terms of the definition. Thus, in moving from high

σ to low σ, the cellular structure of the convection is confused.

Figure 5.30c) serves to show that the very low Prandtl numbers at the lower amplitudes of convection do not show any obvious change in the flow field from the higher amplitude $\sigma = 0.1$ results.

In conclusion, the square periodicity convection shows a stronger Prandtl number dependence than the hexagonal periodicity at the same amplitude of convection for comparable harmonic expansions and for the critical wave number appropriate to the case. The single mode equations of GST1 failed to find this σ dependence, but authors such as Malkus and Veronis (1958), Schluter, Lortz and Busse (1965) and later Arter (1984) confirm its existence. The square periodic harmonics appear to be fairly active even at the higher σ calculated, and show some odd, non−monotonic dependences of the vertical variables of the problem when observed against decreasing σ, indicating an indirect rather than a direct draining of the fundamental by the harmonics. Indeed, the mean temperature profile exhibits a more uniform change across the layer for the lower σ, contrary to the normal increase in the thermal boundary layer structure. The increase in the importance of the harmonics with decreasing σ forces the previously seen change in style of the square convective pattern by a broadening and strengthening of the central plume and a narrowing and sharpening of the corresponding 'walls', but the difference between the upper and lower halves forces the technical cellular nature of the flow to be very obviously lost at low Prandtl numbers.

5.4.3. Dependence on the Nusselt number.

The Nusselt number, the ratio of the heat flux carried with convection present to that carried with no convection, is very closely related to the amplitude of convection when the perturbation style analysis or computational method is considered (see section 3.4.2.2), and thus with the approach considered here, the value of the Nusselt number may be considered as a sort of 'volume control'. This becomes obvious when comparing results for the restricted range of Nusselt numbers considered here, $1.0 \leqslant Nu \leqslant 2.5$, where this, coupled with an insistence on steady behaviour, does not allow any major transitions to occur in the flow regime. Extension of this Nusselt number regime by this model requires a fair degree of effort in the hexagonal case, convergence of solutions requiring either a more extensive consideration of the initial guesses, or exceptionally small increments in the parameters, thus making a significant demand on either human− or computer−time. This is frustrating, since for sensible comparison with other

Fig. 5.31a).

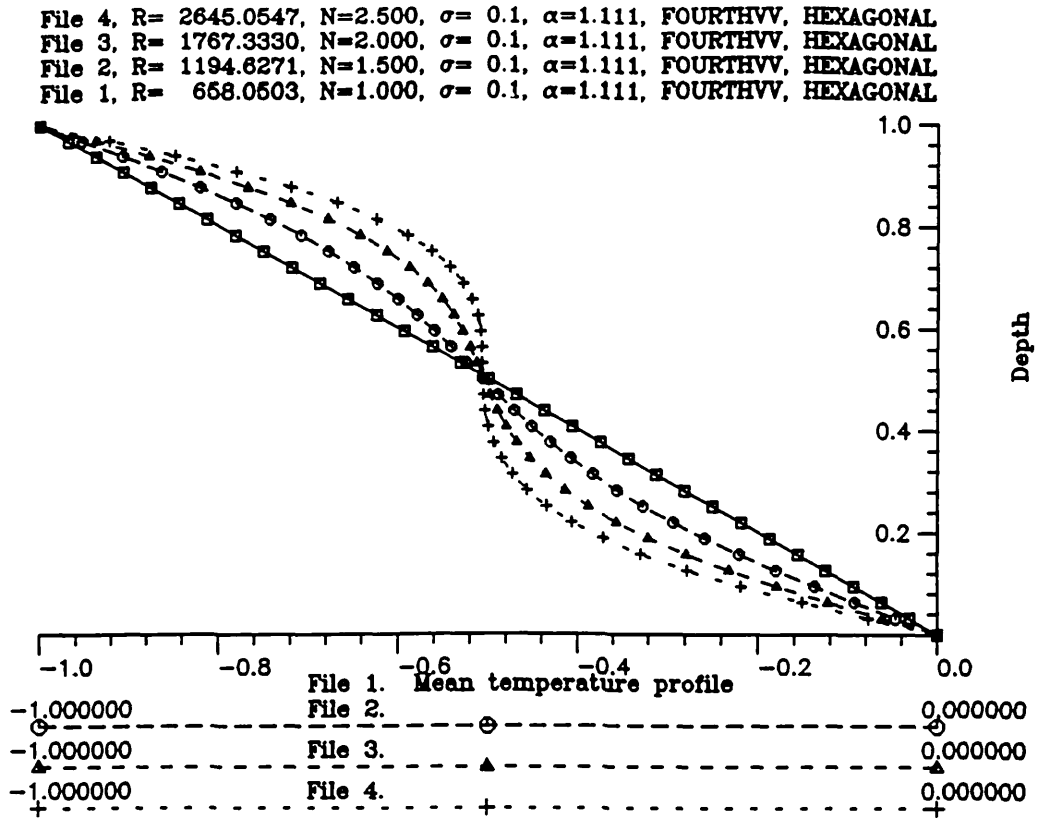


Fig. 5.31b).

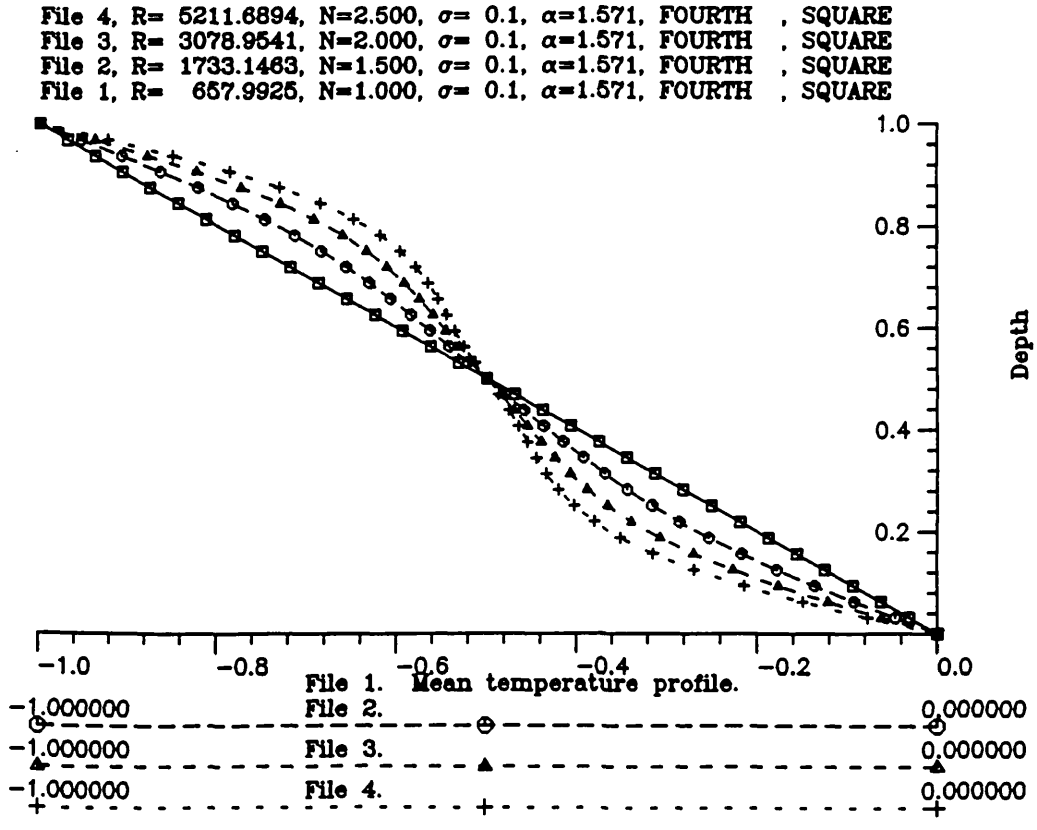
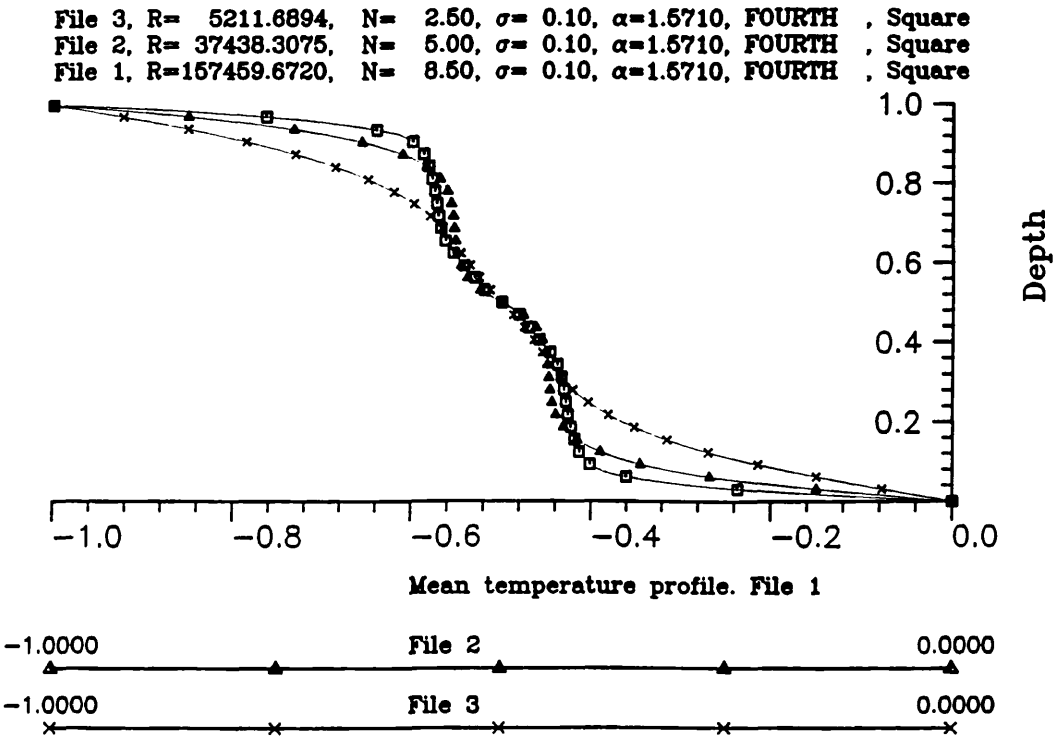


Fig. 5.31c).



authors such as Murphy and Lopez (1984) and GST, the more astrophysical high Rayleigh number regime is required. Higher Nusselt numbers up to Nu ≙ 10.0 were readily obtainable in the square case, and some results of this are shown, but on the whole, the high−Nu/high−Ra regime demands further in−depth study beyond the scope of this thesis, and hence the effect of the Nusselt number dependence is only cursorily mentioned here.

Figures 5.31a), b) and c) show the effect of varying the Nusselt number on the mean temperature profile. Solutions are exhibited for a low Prandtl number, σ = 0.1, the highest modal truncation available and the critical wavenumber appropriate to the periodicity (α = 1.111 for hexagons, α = 1.571 for squares), where any non−linear effects are likely to appear quickly. These graphs show that for both periodicities, increasing the Nusselt number increases the distortion of the mean profile away from the linear conducting (Nu = 1.00) solution, so that as the amplitude of convection increases, the mean temperature is twisted about the mid−temperature in an effort to form an isothermal interior layer within the fluid, with strong thermal boundary layers at the upper and lower boundaries. The hexagonally periodic convection arrives at a much more pronounced version of this behaviour at the highest Nusselt numbers studied, possibly because the higher heat transport in the hexagonal case (see figures 5.1c) and 5.12c)) allows the

movement of heat out of the central layers much more quickly than in the square case, which, in its inefficient convection, retains a much more conductive profile. Note that if the simple first order solutions were used (as for GST or Murphy and Lopez (1984)), the hexagonal case would retain the same profile but the isothermal region is maintained at a lower temperature (figure 5.2g)), whereas the square case would recover an isothermal nature similar to the hexagonal case but remain at $T = -0.5$ due to symmetry (figure 5.13i)). In GST2, the single mode hexagonal solutions were shown to lower the temperature of the isothermal interior with increasing Rayleigh number, but this is not seen here, and neither is the 'bump' in the $T_0(z)$ profile seen by both GST and Murphy and Lopez (1984) for higher Rayleigh numbers on the order of 10^5.

Figure 5.31c) shows the square case mean temperature for the highest Nusselt numbers calculated. This figure compares well with figure 3 of Arter (1984) in style, encouraging confidence in the code and method used here. Note that at the very high Nusselt numbers with correspondingly large Rayleigh numbers the isothermal region is extended and the thermal boundary become very strong, with the changes in the gradient of $T_0(z)$ becoming more pronounced. However, the inclusion of a more extensive set of modes in comparison to Arter's model (Arter uses the equivalent of the S11, S02, and S20 modes, plus the usual mean temperature) has restricted this 'wavy' nature of the profile from becoming so exaggerated as to produce the change in sign of the first derivative of $T_0(z)$, rather the $T_0(z)$ profile here remains monotonic and increasing for all Nusselt numbers. This change of sign of $dT_0(z)/dz$ is not seen in the two-dimensional calculations of Moore and Weiss (1973a)) even at very high Rayleigh numbers or in the axi-symmetric calculations of Jones, Moore and Weiss (1976), and it is thus possible that they were a function of the low number of modes used by Arter.

At these relatively low Nusselt number values, the amplitudes of the charactersitics of the flow are increasing roughly linearly with the Nusselt number. Figures 5.32a) and 5.32b) show the two vertical vorticity modes of the highest truncation hexagonal solution. The structure of these modes remains similar for all Nusselt numbers, but the amplitude increases steadily with the Nusselt number. The concentrations of vorticity and velocity are not affected by the changes of the Nusselt number, they are simply increased in strength. Similarly, figures 5.33a) and b), coupled with the earlier figure 5.3g) show that the amplitude of the vertical velocity at all levels displayed increases steadily with the Nusselt number while the major features are exhibited at all amplitude levels, the structure changing little except for the general strengthening. Figures 5.33c) and d) coupled with figure 5.14d) show a similar result for the square cases.

Fig. 5.32a).

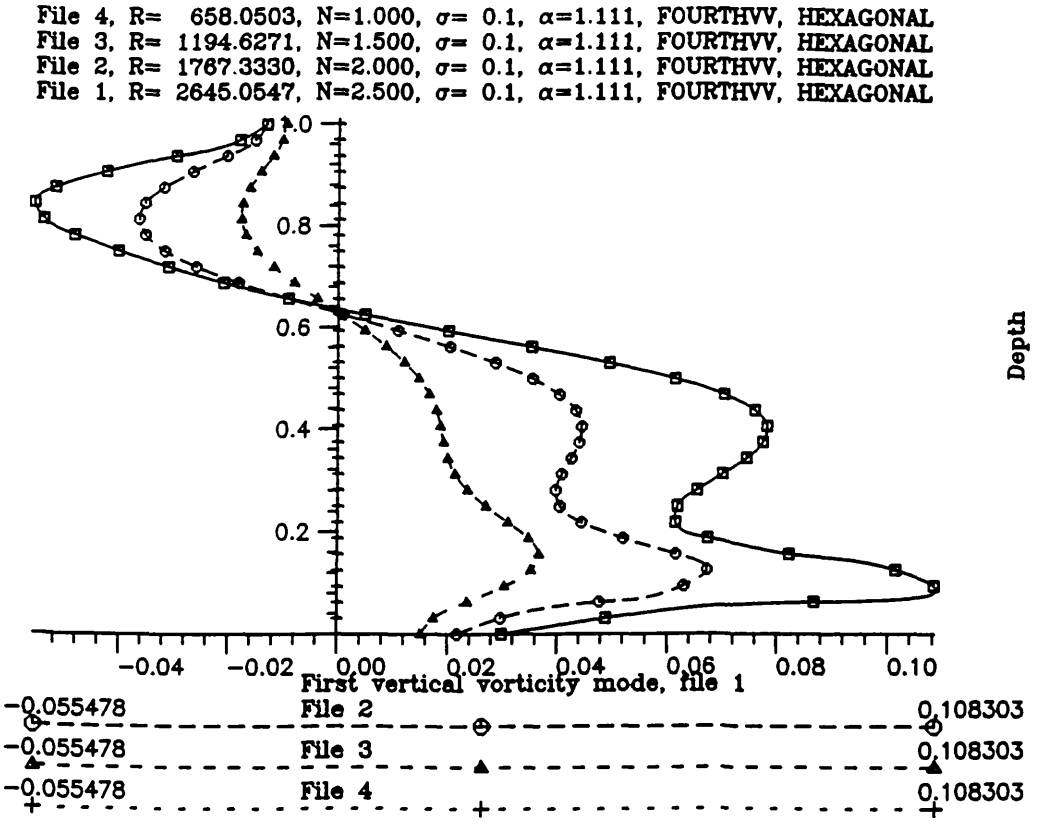


Fig. 5.32b).

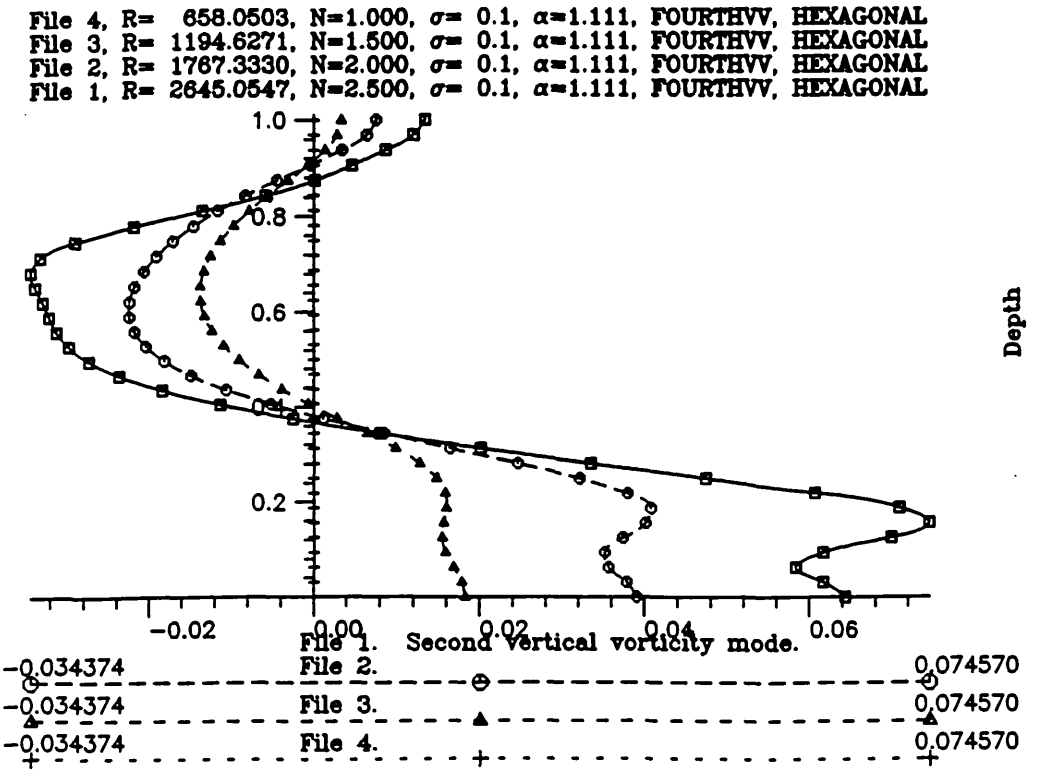


Figure 5.33a). Hexagonal Rayleigh–Benard convection.
Vertical velocity surfaces at various depths (+ve left)
R=1194.6271, N= 1.50, α=1.111, σ= .10, fourthvv

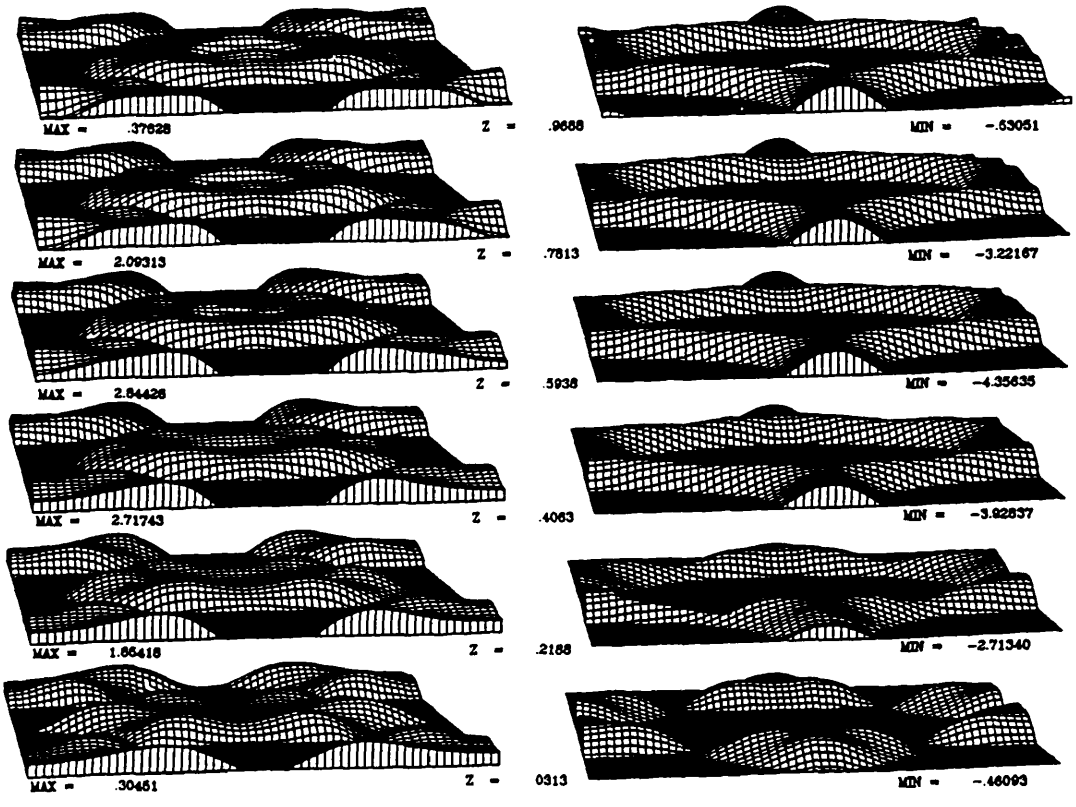


Figure 5.33b). Hexagonal Rayleigh–Benard convection.
Vertical velocity surfaces at various depths (+ve left)
R=1767.3330, N= 2.00, α=1.111, σ= .10, fourthvv

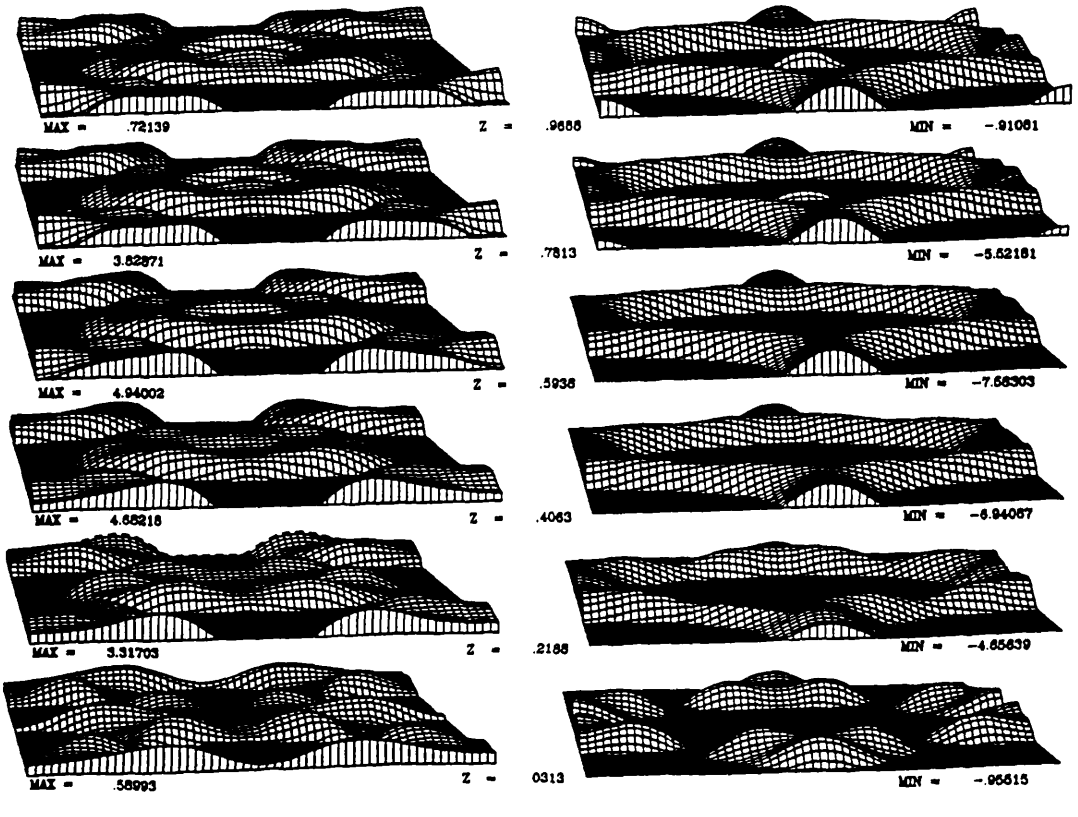


Figure 5.33c). Square Rayleigh–Benard convection.
Vertical velocity surfaces at various depths (+ve left)
R=1733.1463, N= 1.50, α=1.571, σ= .10, fourth

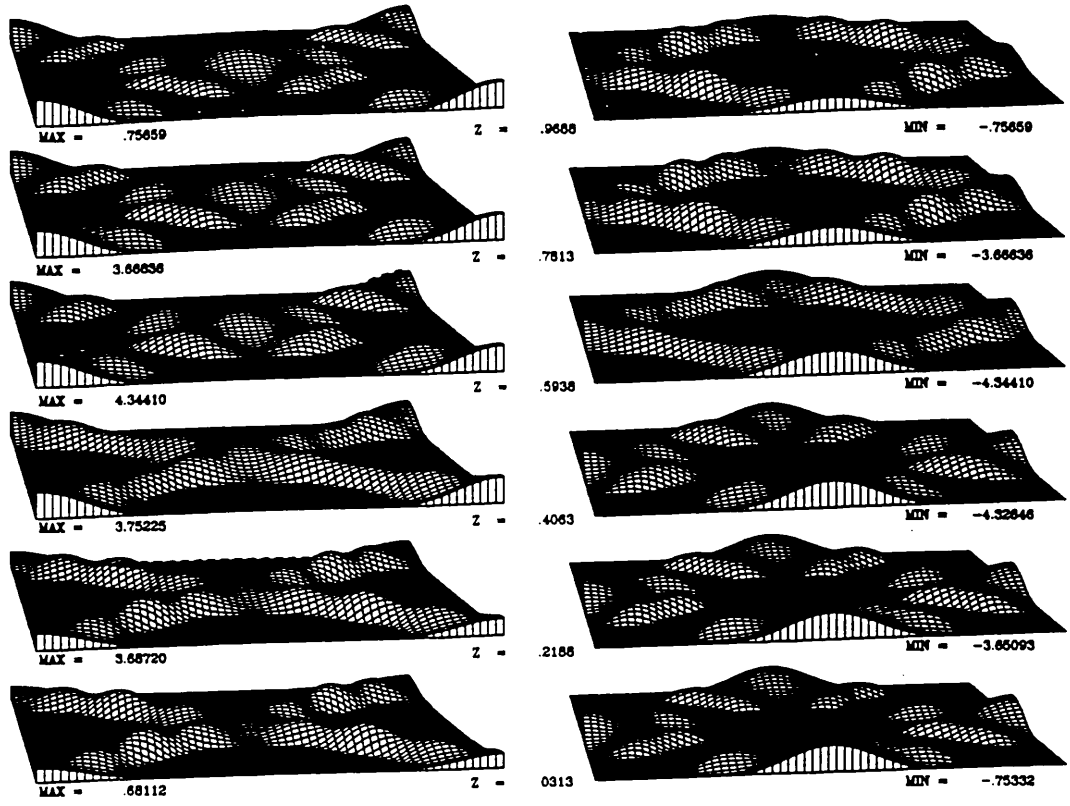


Figure 5.33d). Square Rayleigh–Benard convection.
Vertical velocity surfaces at various depths (+ve left)
R=3078.9541, N= 2.00, α=1.571, σ= .10, fourth

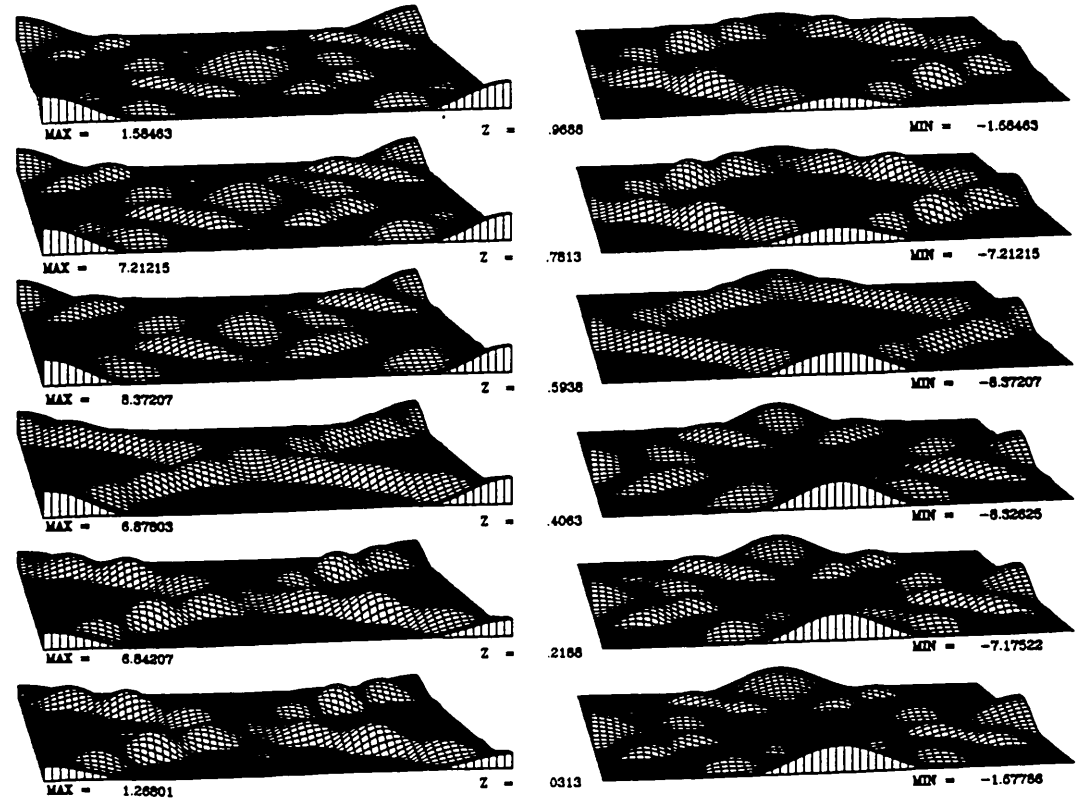


Fig. 5.34a) **Square cell Rayleigh–Benard convection**
Rayleigh number against Nusselt number
High Nusselt numbers, α = 1.571

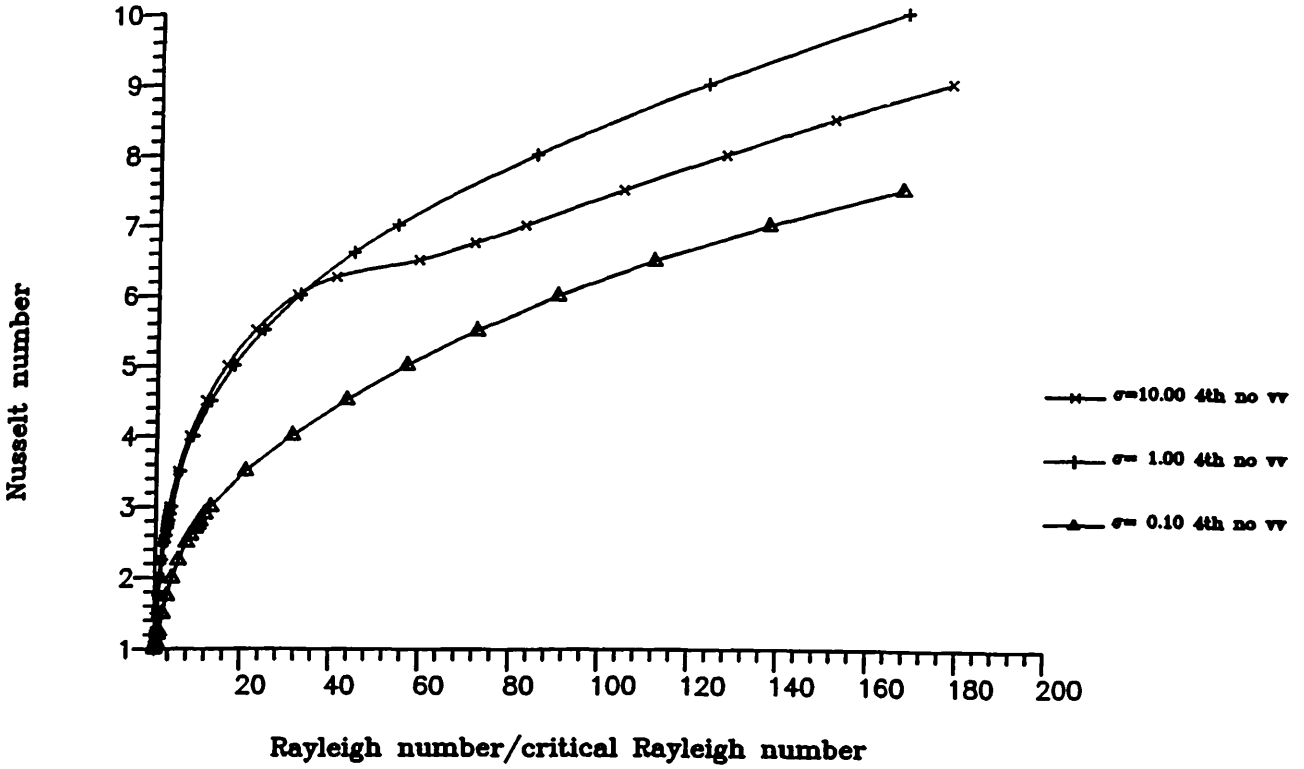


Figure 5.34b). Square Rayleigh–Benard convection.
Vertical velocity surfaces at various depths (+ve left)
R= , N= 8.50, α=1.571, σ= .10, fourth

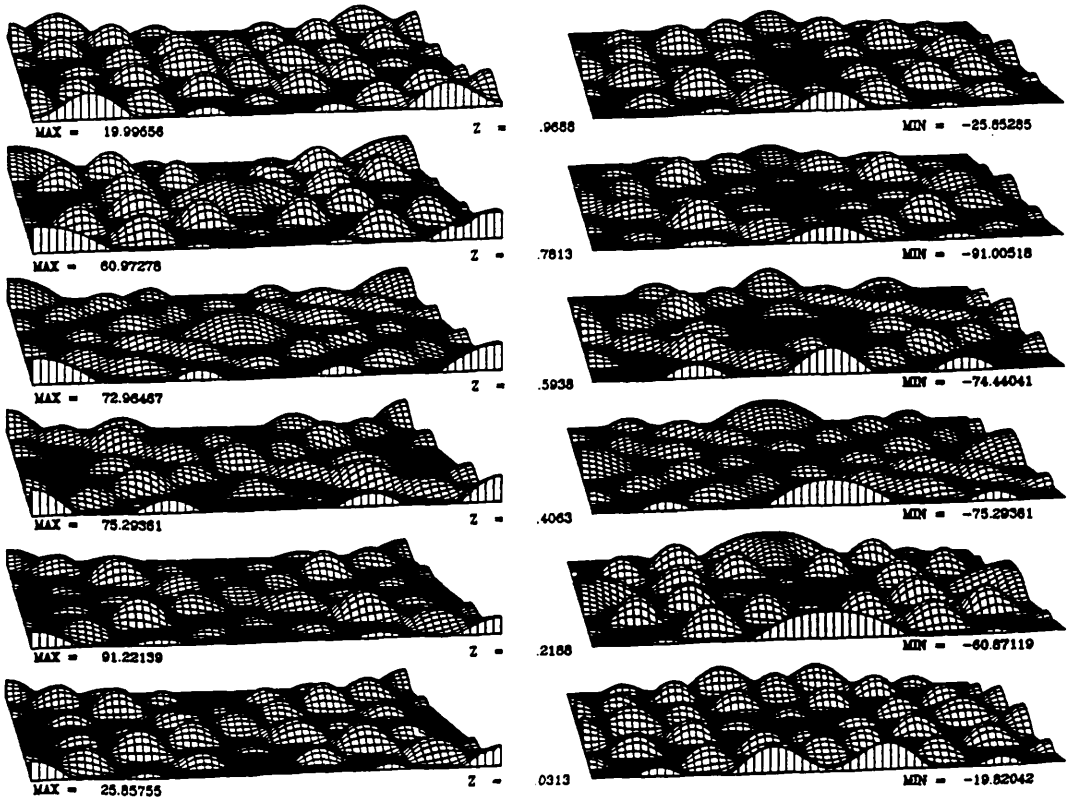


Figure 5.34c). Square Rayleigh-Benard convection. Vertical velocity c
R= , N=8.5000, σ= 0.10, α=1.571, fourth

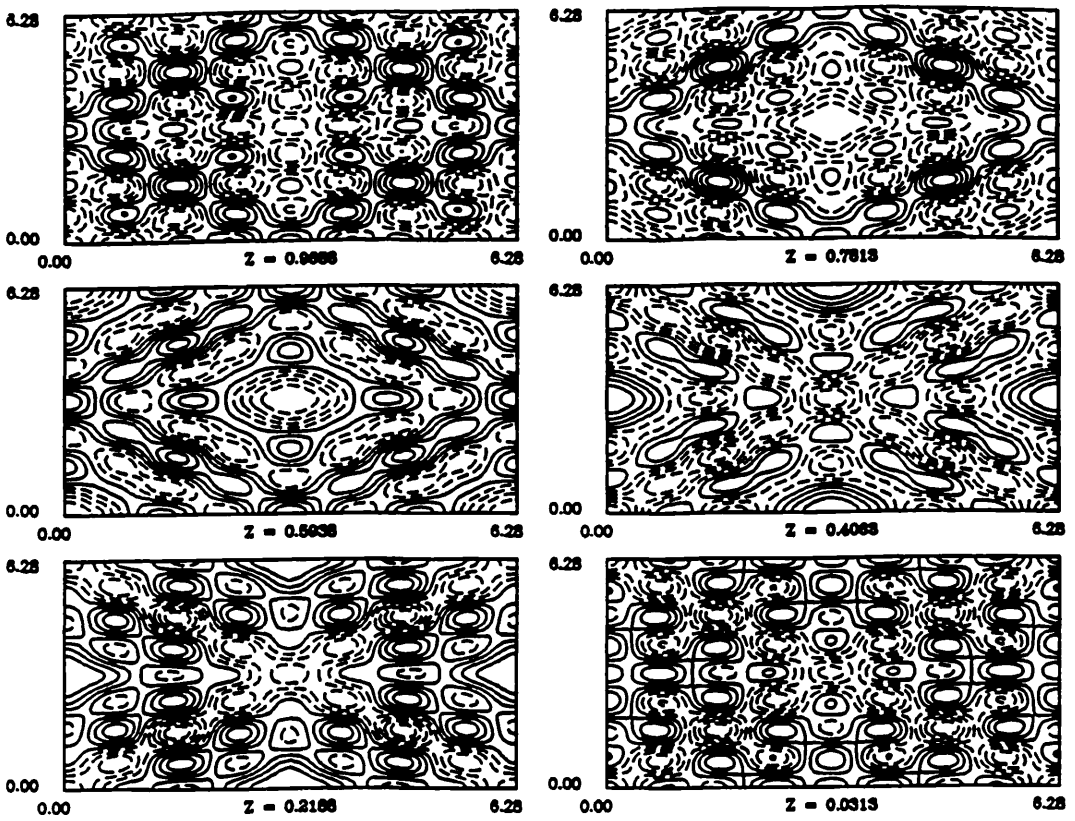
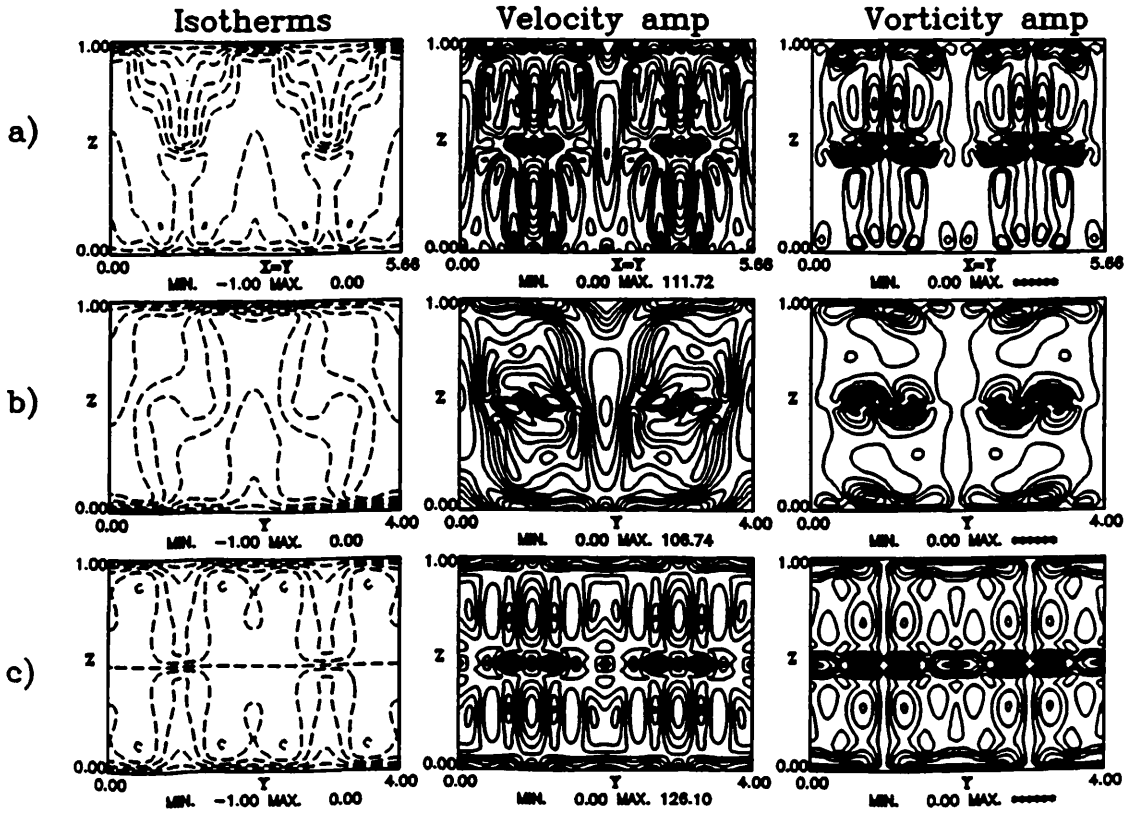


Figure 5.34d). Square Rayleigh-Benard convection.
R = , N = 8.50, σ = 0.10, α = 1.571, fourth
a) x=y, y=(0,2π/α) , b) x=π/α, y=(0,2π/α) , c) x=$\pi/2\alpha$, y=(0,2π/α)



Figures 5.34 shows solutions at the limit of the extended Nusselt number range for the square periodicty. Figure 5.34a) shows a plot of Rayleigh number versus Nusselt number curve for σ = 0.1, 1.0 and 10.0 calculated with the fourth order solution, and demonstrates that after a initial steep rise, the curves tail off smoothly towards the expected $Ra^{1/3}$ dependence although the moderate Prandtl number convection at σ = 1.0 becomes more efficient at high Rayleigh numbers than the σ = 10.0 convection. Figures 5.34b) and c) show the vertical velocity in the usual manner, and clearly the higher order harmonics are now strong, since the scales of motion are much reduced, although some of the original structure is still superimposed on these small scales. Notice that the vertical velocity amplitudes have increased almost ten–fold. Figure 5.34d) shows the normal vertical slices through the square periodic cell, and confirms that the motion has become very non−linear with thin thermal boundary layers and strong concentrations of velocity and vorticity, mainly in layers near the boundaries and at the centre. The amplitudes have increased dramatically from lower Nusselt numbers, especially in the (horizontal) vorticity, which is heavily concentrated in the mid−layers.

A full investigation of higher Nusselt numbers and the effects of strongly non−linear flow is necessary but was unfortunately beyond the time limitations of this project.

5.4.4. Dependence on the wavenumber, α.

The question of the preferred horizontal wavenumber for convective situations is still a clouded area. The size of the modal systems used to solve the complete problems here place a restriction on the investigation, in so far as an automatic searching of the wavenumber space, as was used in Chapter 3, became unfeasable. Thus, the majority of calculations considered in this Chapter were computed at that value of the wavenumber at which convection first set in i.e. the linear critical wavenumber appropriate to the planform symmetry chosen (α = 1.111 for hexagons, α = 1.571 for squares). However, since GST3 describes steady solutions of the multimode equations solely in terms of a Nusselt number−wavenumber graph, and Lopez and Murphy (1984) consider that the wavenumber is an important factor in the determination of their type II, (strong vertical vorticity) solutions, a brief investigation of the dependence on α is thus required here. Lopez and Murphy (1984) have the results most compatible with this survey, since they solve the free boundary case with a single planform mode,

FIG 5.35a). Nusselt number versus wavenumber
Prandtl number = 0.10, FOURTHVV, Hexagonal

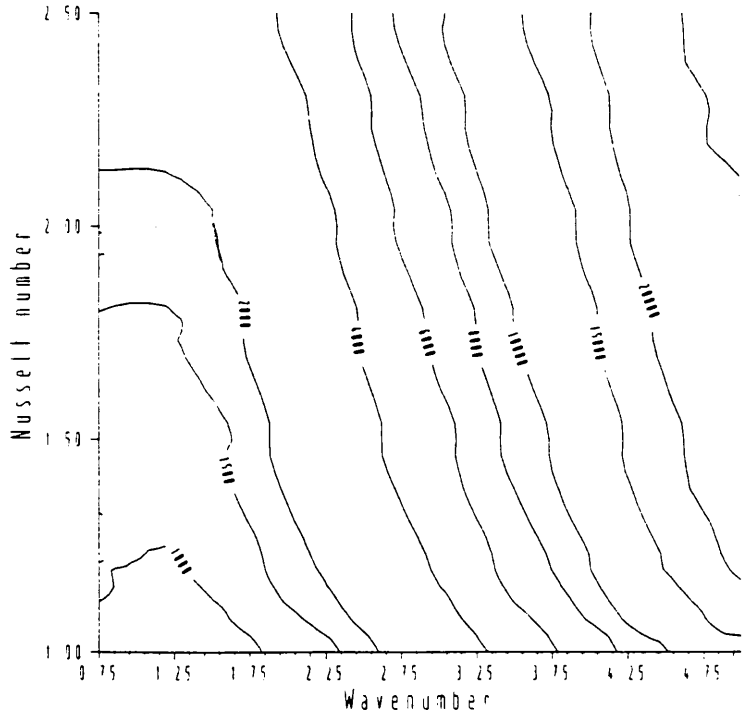
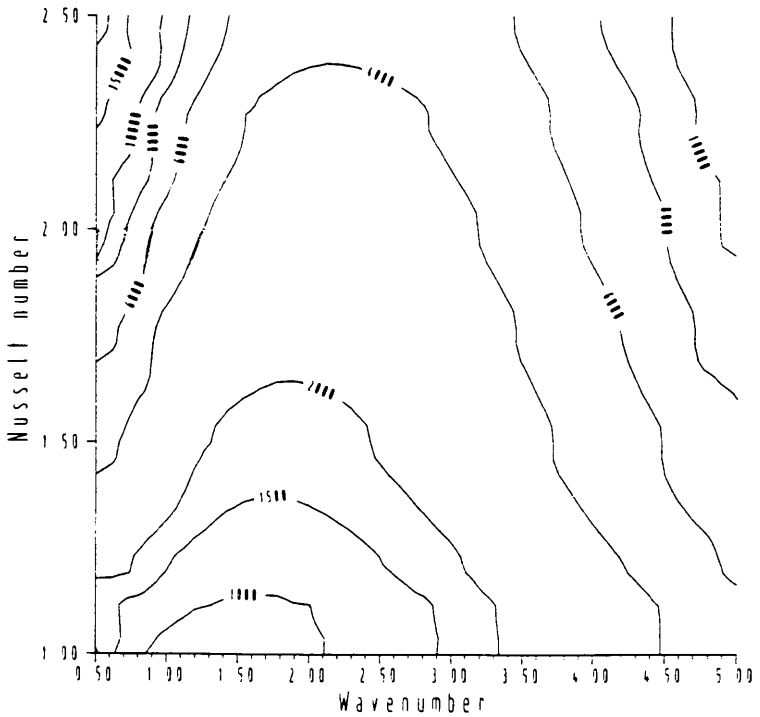


FIG 5.35b). Nusselt number versus wavenumber
Prandtl number = 0.10, FOURTH, Square



including a vertical vorticity mode although they study Rayleigh numbers of 10^5 and above. They find that type II solutions are supported for low α since the wide cells allow free horizontal motions. When α is increased to a value around $\alpha = 17$, the type II solutions coalesce with the type I solutions, and the wavenumber which maximises the Nusselt number is greater for type II solutions than for type I.

Figures 5.35a) and b) show plots of Nusselt number against wavenumber for various constant Rayleigh numbers at the lowest Prandtl number calculated, $\sigma = 0.1$, and for the highest modal truncations available. Such graphs are awkward to achieve in the formulation of this model since it assumes a constant Nusselt number basis rather than a constant Rayleigh number, but they are drawn by contouring the irregular $Nu-\alpha$ data domain. Convergence at $\alpha < 1$ was difficult to achieve for both periodicities due to the wide range of scales of motion allowed by the extensive cells, requiring further human- or computer-time as for the extended Nusselt number calculations, but some success was achieved. Figure 5.35a) for the hexagonal periodicity again clearly demonstrates that the solutions shown here, where Ra is close to Ra_c, are solutions that Murphy and Lopez would term type I (compare figure 3.35a) with Lopez and Murphy (1984) figures 1 and 2a)). Lopez and Murphy would expect a type II solution to be more stable at lower α. A single maximum is seen in the Nusselt number with the wavenumber for all Rayleigh numbers shown, which differs from the multimode solutions of GST3 which show multiple maximums before curtailing the region of allowable convection, but agrees with the type I solutions of Murphy (1980). The solutions here, however, have the wavenumbers of the individual modes set as a specific fraction of the original fundamental wavenumber, where the scaling factor arises naturally from the non-linear advection terms of the equations. The solutions of GST3 allow each individual harmonic to have an arbitrary wavenumber. This demonstrates a fundamental difference in approach between the present studies and GST, since here, the wavenumbers of the harmonics are regarded as determined, whereas, the GST3 paper treats individual harmonics as separate solutions to be superposed at random. As explained by GST, the multiple maximums are in fact only a single maximum if the appropriate scaling factors are included to allow for the linear scalings between reduced harmonics. Figure 5.35a) here shows that the hexagonal periodicity exhibits a maximum of the heat flux for a wavenumber very close to the critical ($\alpha = 1.111$) in the range of parameters studied, with a rapid drop in Nusselt number as the wavenumber is increased away from this value for the maximum, for any given Rayleigh number. The range of wavenumbers supporting convection increases steadily with increasing Rayleigh number for large Rayleigh numbers.

Fig. 5.36a). **Stereo velocity plots – Hexagonal Rayleigh–Benard convection**
R = 37360.93, N = 2.50, σ = 0.10, α = 5.000, fourthvv

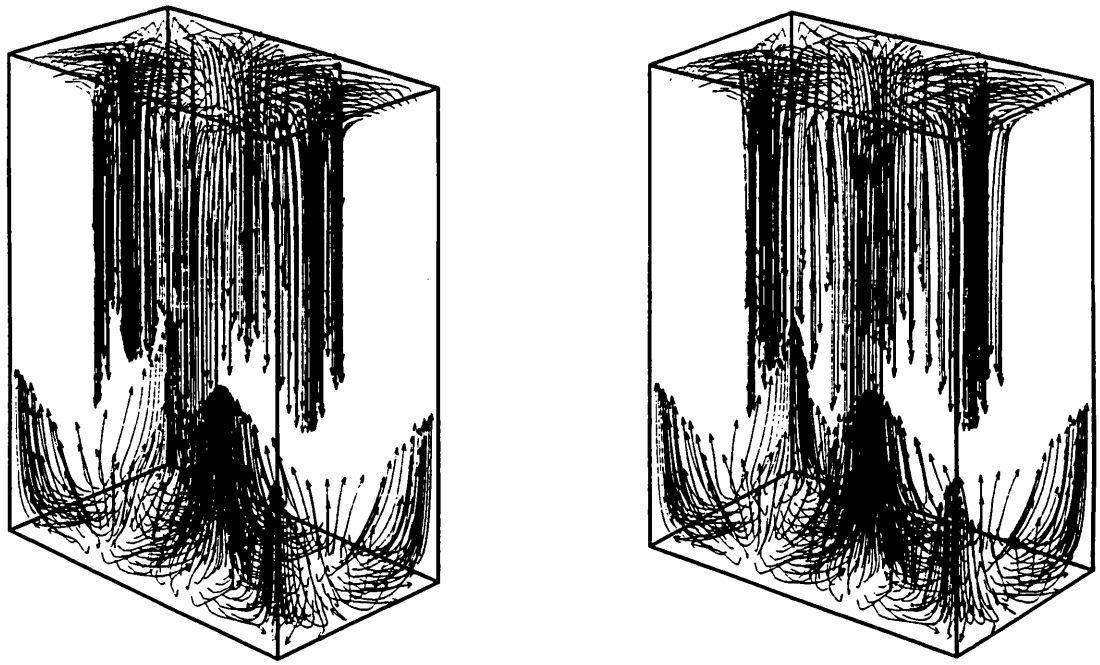


Fig. 5.36b). **Stereo velocity plots – Square Rayleigh–Benard convection**
R = 12842.58, N = 2.50, σ = 0.10, α = 5.000, fourth

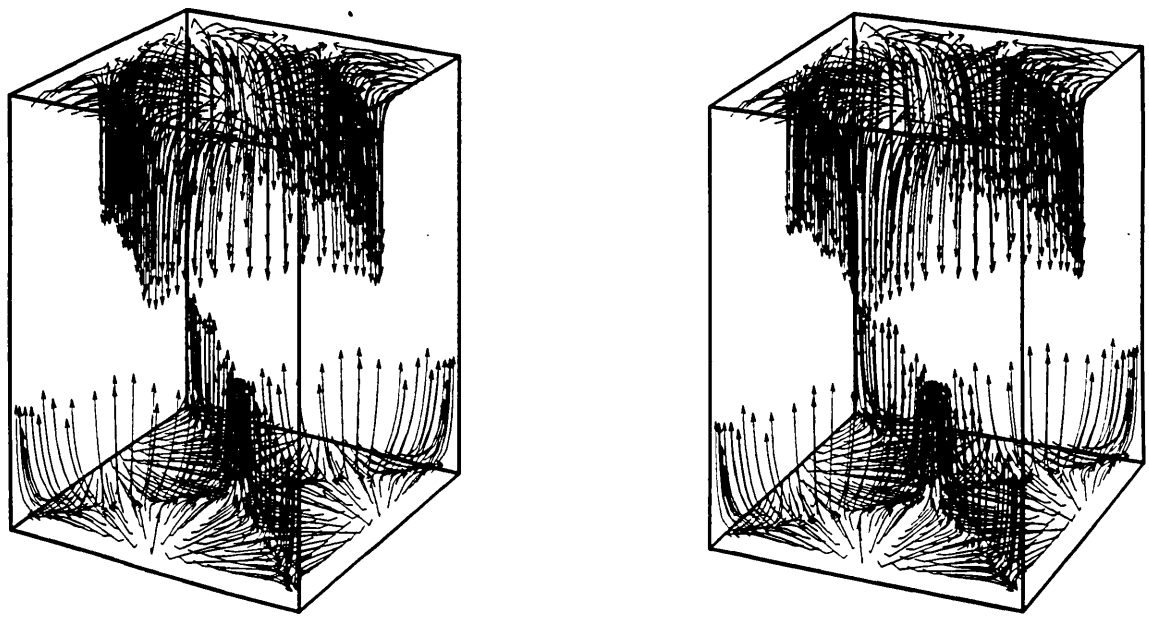


Fig. 5.37a).

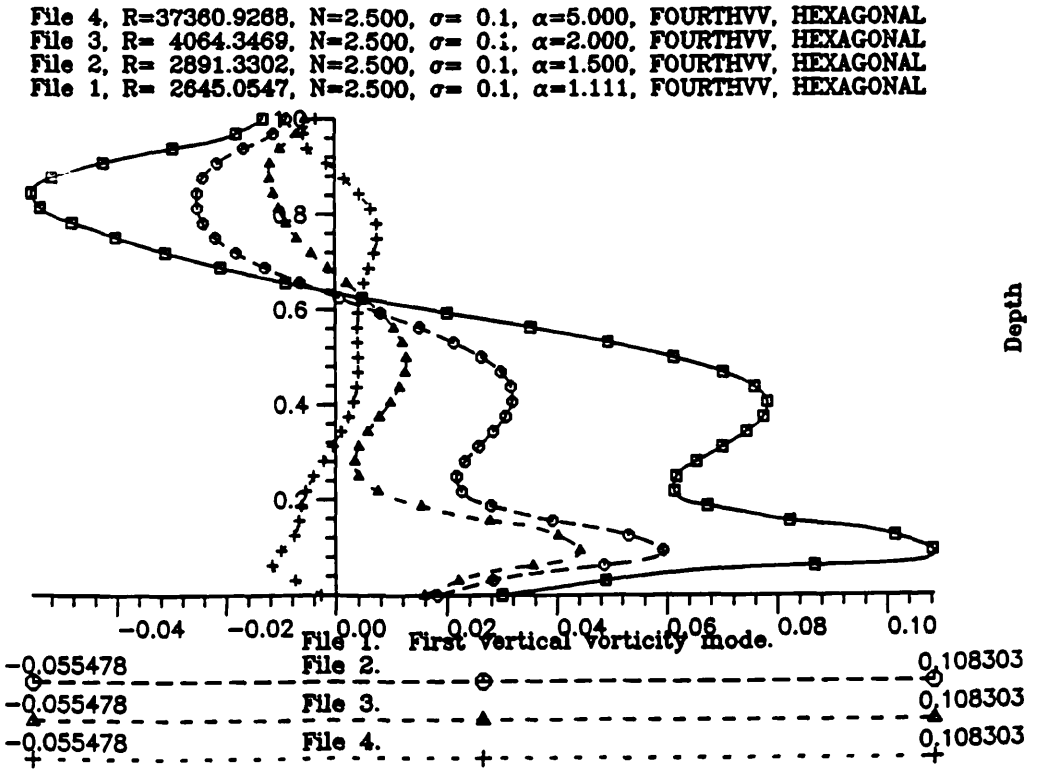


Fig. 5.37b).

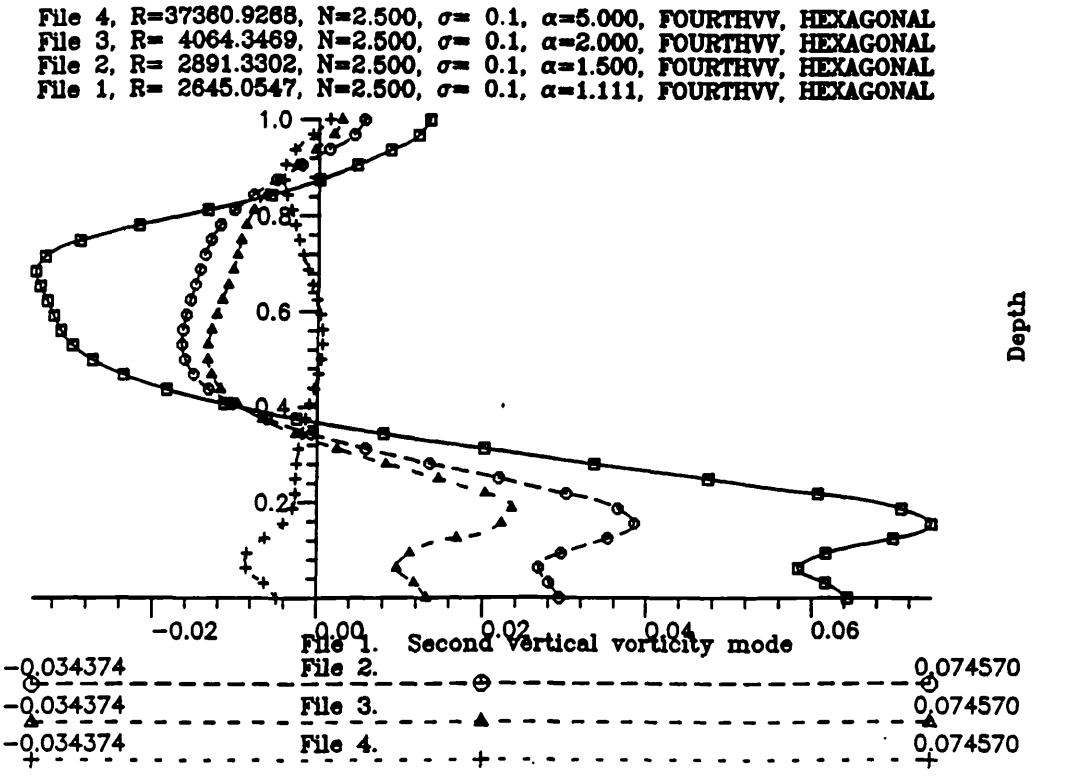


Fig. 5.38a).

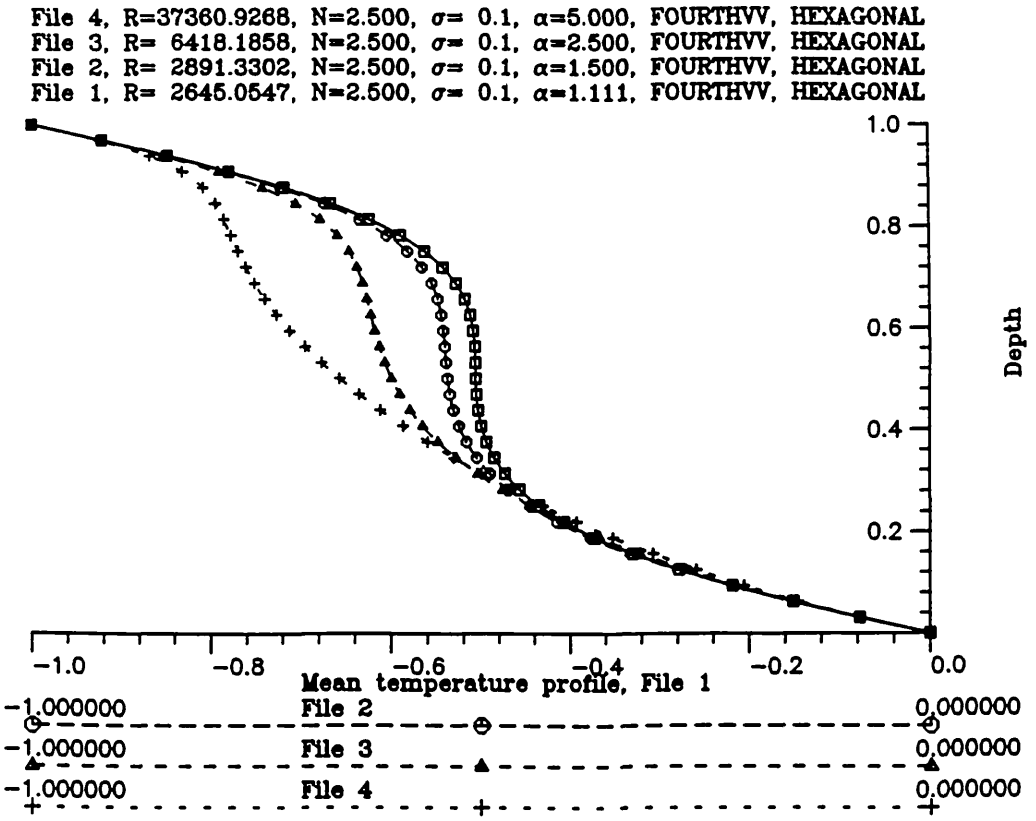


Fig. 5.38b).

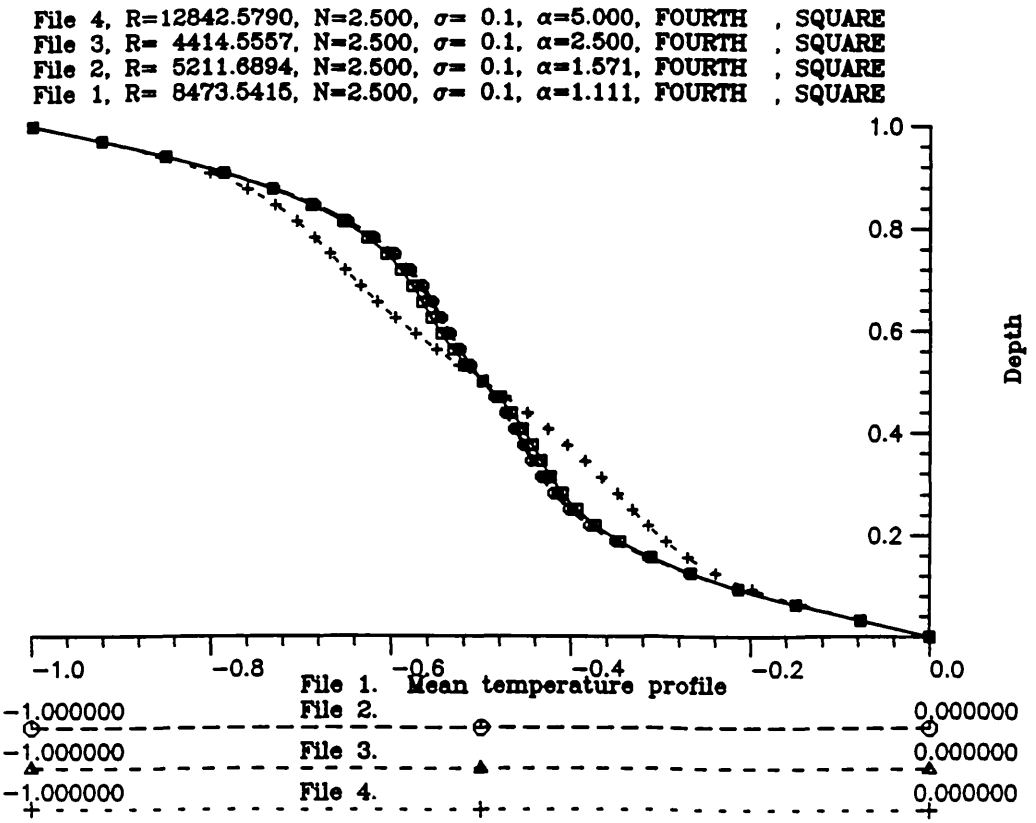


Figure 5.35b) shows the equivalent figure for the square periodic fourth order solution. Here, a similar single maximum with wavenumber is seen in the Nusselt number, but this maximum occurs at a wavenumber slightly higher than the critical value and it shifts to higher wavenumbers with increasing Rayleigh number. The tail−off of the Nusselt number with wavenumbers above this maximum value is not so steep for this square case as for the hexagonal case. It appears as though at very low Rayleigh numbers the maximum may occur at a wavenumber near the critical value.

Figures 5.36 shows that the flow pattern in the hexagonal symmetry changes very little with the increase in wavenumber, and, despite the high Rayleigh number of this solution, there is no evidence of any strong vertical vorticity effects such as a twisting of the streaklines in the boundary planes as for Murphy and Lopez's type II solutions. In the plot shown, the restriction of the Nusselt number to a relatively low amplitude forces the system to balance out a high wavenumber with the high Rayleigh number solution that will support it, but the amplitude of vertical vorticity is much reduced, as shown by figures 5.37a) and b). So despite the high Rayleigh number, no horizontal disturbances to the flow are seen. The reduction in vertical vorticity with an increase in the horizontal wavenumber is easily explained since the increasing α implies that the cell width is decreasing and thus motions are concentrated in the vertical since there is not enough room for complicated horizontal flows. This agrees with Lopez and Murphy's arguments that type I and type II solutions merge at high α ($\alpha = 17$) where the vertical vorticity disappears. However, here, figures 5.37 show that the increase of the wavenumber past $\alpha = 5$ has changed the form of the vertical dependences of the vorticity modes and not simply just flattened the profiles out to zero. Thus, there is a possibility that increasing the wavenumber still further may encourage a different scale of vorticity. Such hypotheses need to be tested by a detailed study of the dependence of the vertical vorticity on the wavenumber, akin to Lopez and Murphy's (1984) study.

As the wavenumber is increased away from that value which gives the maximum Nusselt number towards $\alpha = 5$ both styles of convection become less efficient and are convectively much less active as expected. Figures 5.38a) and b) exhibit this, showing that the mean temperature profiles become more linear and more like a conducting profile as α is increased from the value for that maximum. For both styles of convection, increasing the Prandtl number from $\sigma = 0.1$ increases the maximum Nusselt number attained at a particular Rayleigh number, but the range of α supporting convection remains much the same.

5.4.5. A comparison of the hexagonal and square periodicities.

Despite the obvious physical differences between the two types of flow that the different periodicities engender, there are some more surprising ones, most of which are connected with the Prandtl number dependence. The Prandtl number dependences of the two periodicities are quite different. The hexagonal case tends towards the inertial convection of the cylindrical symmetry as calculated by Jones, Moore and Weiss (1976). This means that the hexagonal solutions tend towards a low σ limit where convection does not leave the conductive solution until a second critical Rayleigh number, above the normal critical Rayleigh number, is surpassed, and then the convection is relatively Prandtl number independent. The square periodicity shows no signs of the existence of a second critical Rayleigh number unless it exists at much high Rayleigh numbers than have been calculated here. As seen earlier (figures 5.18 and now in figure 5.39a)), the dependence of the square type convection on σ is much stronger than that for the hexagonal case, with the dependence of the Rayleigh number on σ being possibly $R \approx \sigma^{-2/3}$ for squares and $R \approx \sigma^{-1/6}$ for hexagons at around $\sigma = 0.1$ and $Nu = 2.5$ (although these figures are based on a small amount of data). This result is surprising since the hexagonal solution (FOURTHVV) includes two modes of vertical vorticity which would be expected to increase the horizontal motions, and thus possibly reduce the heat transport. This appears to happen if the FOURTH and FOURTHVV hexagonal solutions are compared, but the effect is still not enough to reduce the efficiency of the convection below that level of the square FOURTH case for low σ. At higher Prandtl numbers, $\sigma > 1.0$, figure 5.39a) shows that the heat transport results for hexagonal and square convection are virtually identical. It is odd that at high Prandtl numbers, for a given Nusselt numbers, the heat transport is the same for both periodicities although the flow patterns of the convection are very distinct, whereas at low Prandtl number the heat transport curves are never close even at very low Nusselt numbers and the flows become very similar in style (a plan view shows 'wall' style descending sheets and rising centres in both cases).

However, these conclusions were drawn from the 'best' (or highest) available truncations and, in fact, the conclusions are truncation dependent. Lower order truncations (figures 5.39b)−e)) show some discrepancies in the heat transport curves even at the higher Prandtl numbers. If the fourth order modes are compared without vertical vorticity inclusion for the hexagonal case (i.e. compare FOURTH hex with FOURTH square) then the hexagonal solutions again come out as more efficient at low σ. Similarly if the second order solutions are compared,

Fig. 5.39a).

Rayleigh number against Nusselt number
Best solutions for hexagonal and square Rayleigh–Benard convection

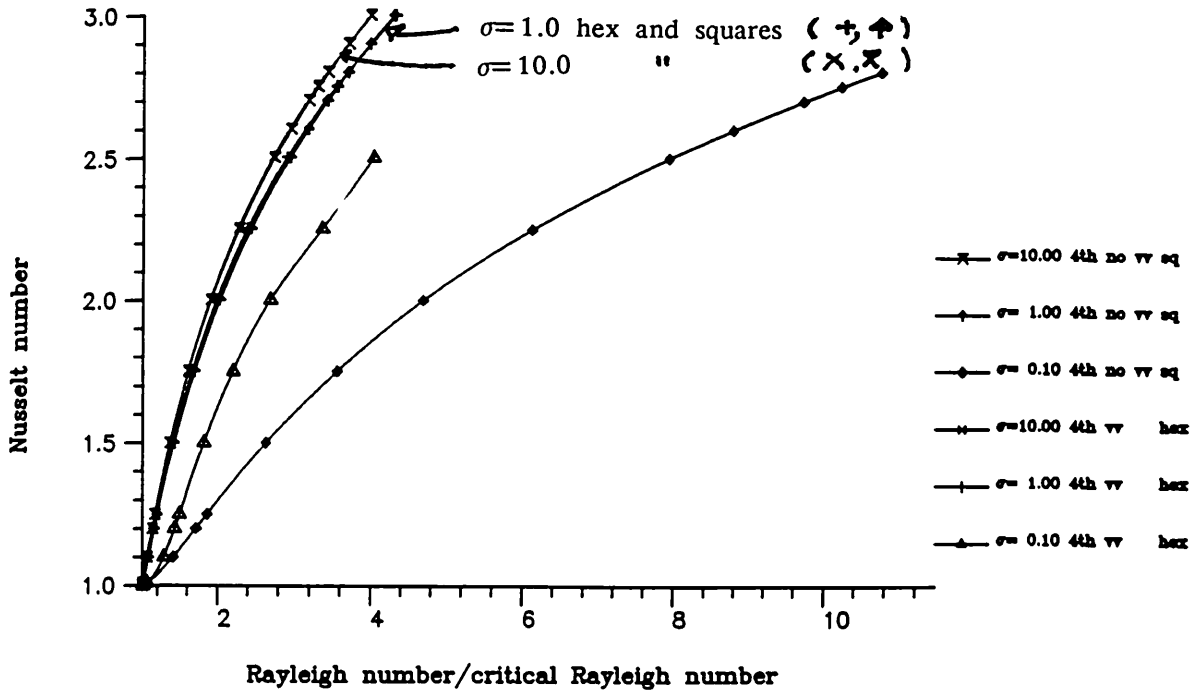


Fig. 5.39b). **Hexagonal and square Rayleigh–Benard convection**
Rayleigh number against Nusselt number
Comparison of fourth modes

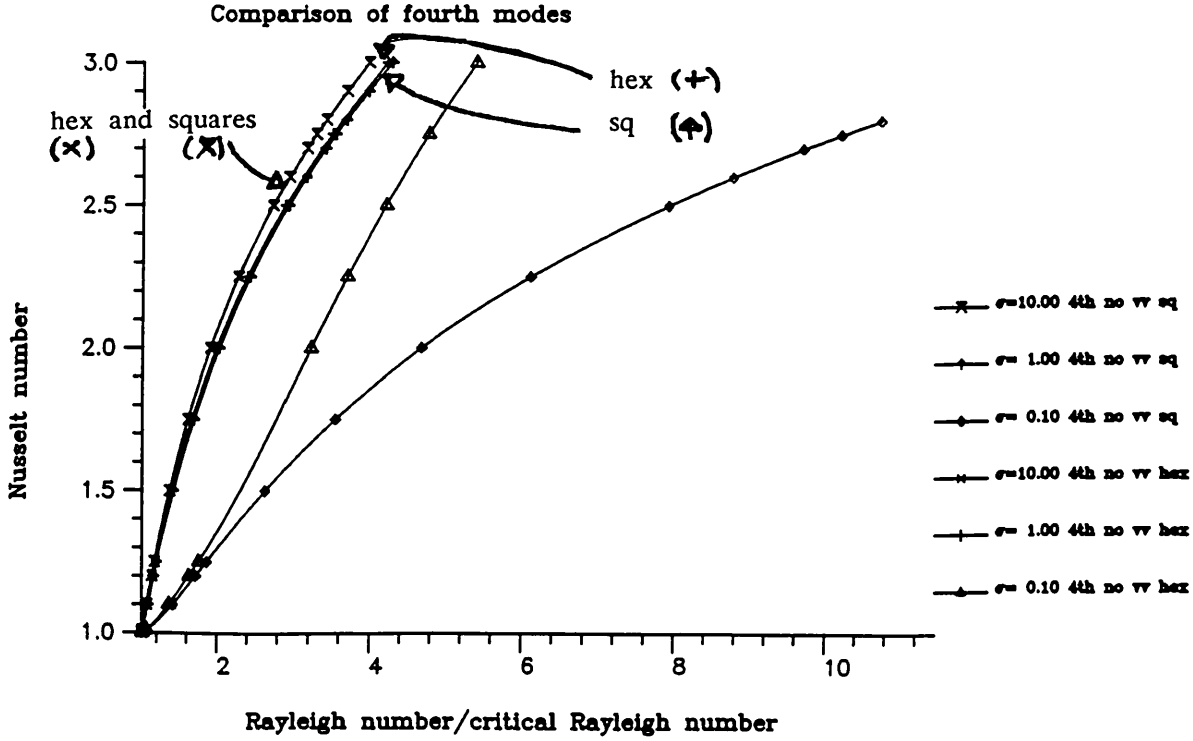


Fig. 5.39c). **Hexagonal and square Rayleigh–Benard convection**
Rayleigh number against Nusselt number
Comparison of third modes

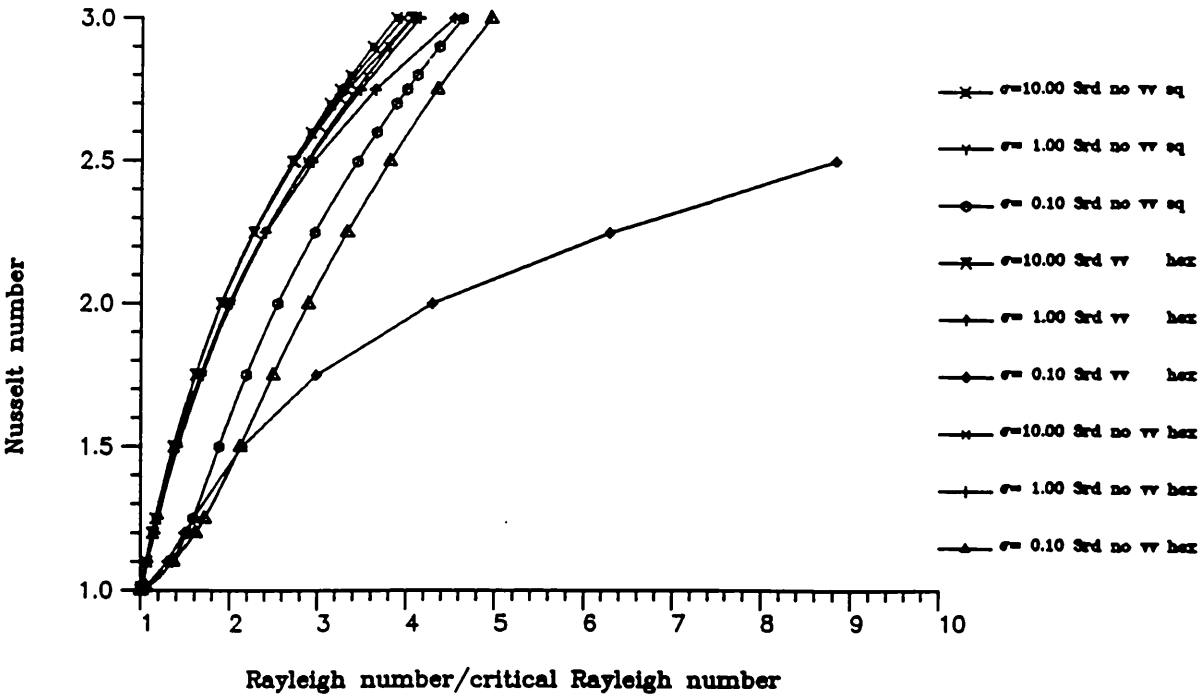


Fig. 5.39d). **Hexagonal and square Rayleigh–Benard convection**
Rayleigh number against Nusselt number
Comparison of second modes

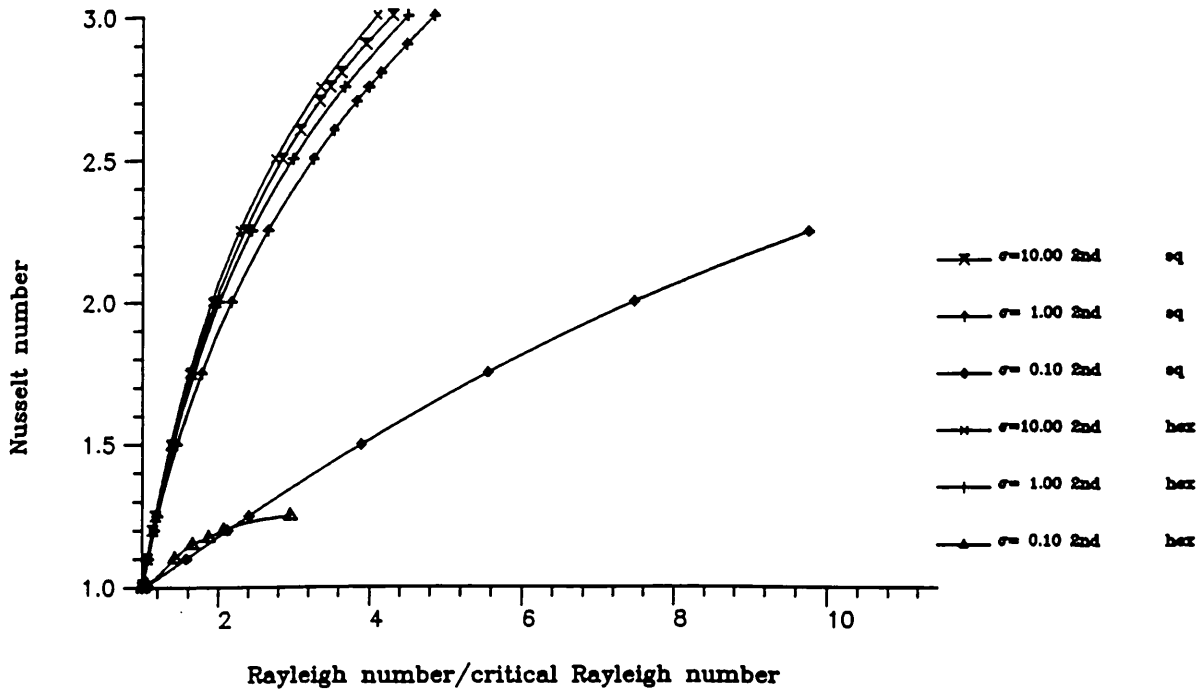


Fig. 5.39e). **Hexagonal and square Rayleigh–Benard convection**
Rayleigh number against Nusselt number
Comparison of hexagonal and square first modes

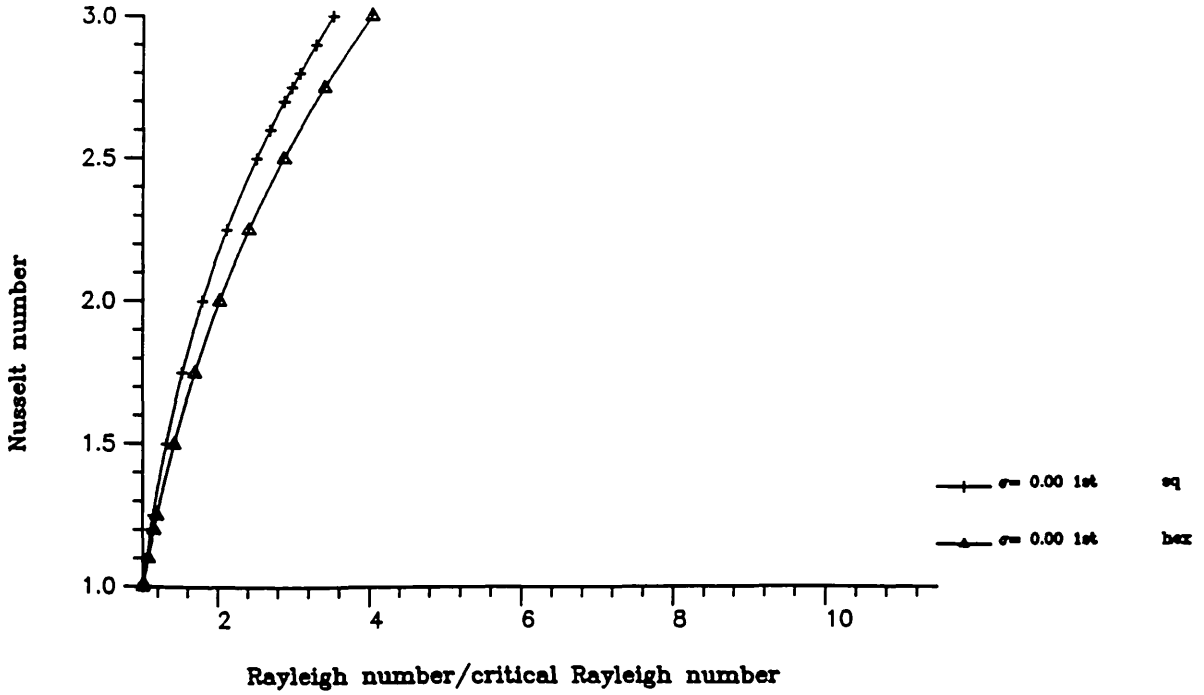
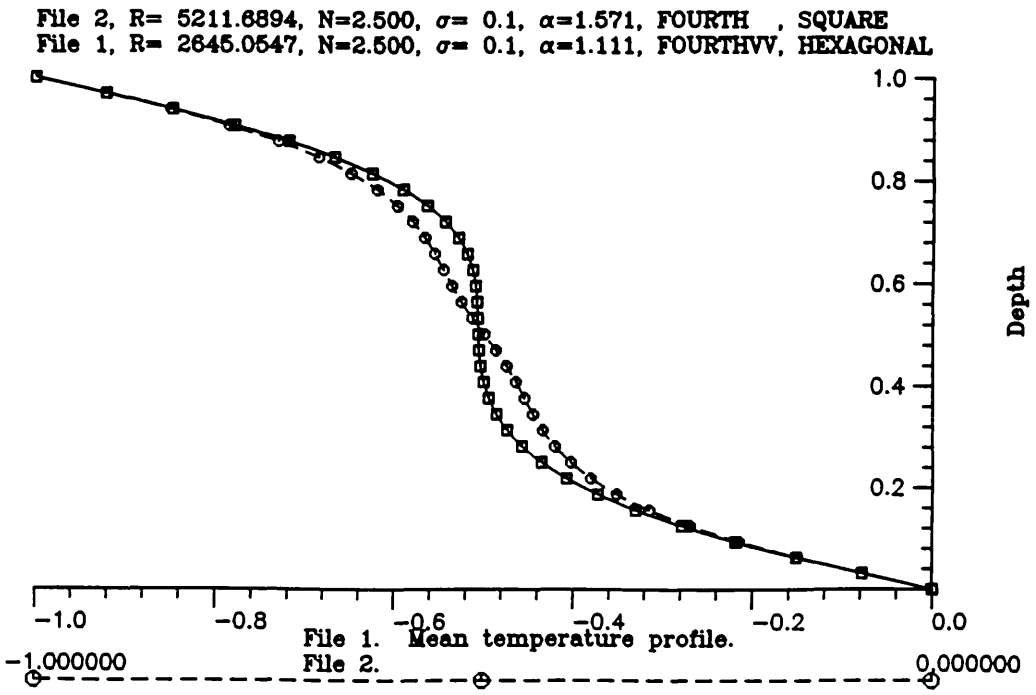


Fig. 5.40.



but the third order solutions show the opposite with squares the more efficient heat transporting planform structure, in any of the third order configurations (with or without vertical vorticity for the hexagons). The first order solutions (FIRST) also show squares more efficient at $\sigma = \infty$. However, the highest order solutions (FOURTH and FOURTHVV) should be believed here since only these hold the high σ curves independent of the truncation as would be expected.

The square periodicity seems to be more 'active' at high Prandtl numbers than the hexagonal solutions since the influence of harmonics appears even at $\sigma = 10.0$, unlike the hexagonal case which is totally dominated by the fundamental. This is one demonstration of the stronger σ dependence of the square periodicity, another being the destruction of the cellular nature of the square pattern. The hexagonal periodicity is immediately asymmetric about the mid−depth but does not lose its cellular definition much even at low σ, whereas the square structures become obviously destroyed by $\sigma = 0.1$. The hexagonal flow pattern remains essentially the same under all conditions whereas the square periodicity exhibits a definite migration of character, despite the tendency of both periodicities to strengthen and broaden the central plumes and emphasize wall−flow with increasing non−linearity levels. The square periodicity in fact becomes much more like the hexagonal case as it changes from one pattern of identical but reversed pockets of flow in adjacent cells (the S11 style flow where the separate plumes identify the 'pockets'), to a pattern where a 'cell' containing both up− and down−flow is simply repeated over the domain. The emphasis of the pattern could be said to have shifted from a non−self−interacting style to a self−intereacting style.

The other main differences between the solutions for the different styles of planforms are to be found in the individual behaviour of the modes but are also connected with the Prandtl number dependence. For the hexagons, decreasing σ decreases the amplitude of the fundamental modes so that the harmonics may grow monotonically at its expense, as though the fundamental feeds the modes directly. For the square periodicity, some harmonic modes do not increase monotonically as expected, and the fundamental temperature mode indeed increases with decreasing σ (figure 5.26e)). For squares, some of the higher order modes feed back quite substantially into the original mode. Only the vertical vorticity modes behave in this manner in the hexagonal case.

The mean temperature profile can be seen to be more isothermal in the square case (figure 5.40), and surprisingly becomes more isothermal with increasing Prandtl number unlike the hexagonal case where the profile loses the isothermal interior and boundary layers with the increase in σ.

5.5. CONCLUSIONS.

Rayleigh−Benard convection in three−dimensions for an incompressible fluid between free boundaries has been investigated by modal techniques. The modal analyses used provided expansions of two possible horizontal periodicities, one being hexagonal, the other square. All naturally occuring harmonics of the fundamental planforms up to the fourth order in the expansion were included. The hexagonal expansion allowed for the inclusion of two physical vertical vorticity modes. The hexagonal periodicity problem was solved using expansions including up to eight horizontal modes in comparison to previous multimode solutions which have either based their work on single modes (GST1, GST2, Murphy and Lopez (1984), Lopez and Murphy (1984)) or on other low order truncations (Roberts (1966), GST3). The square periodic solution was solved using effectively up to 12 modes, whereas the only previous modal model (Arter (1984)) used only three. However, the extended modal truncations used restricted the range of parameter values that could be searched in the small amount of computer− and real−time available, and so the available results span only $0.1 \leqslant \sigma \leqslant 10.0$, $1.0 \leqslant Nu \leqslant 2.5$ and $0.5 \leqslant \alpha \leqslant 5.0$ in general.

The effects of the vertical vorticity in the hexagons on the visible aspects of the flow in these parameter ranges proves to be minimal, but the inclusion of these and the other higher order harmonics in both the hexagonal and the square cases has some considerable impact on the internal nature of the solutions. In the hexagonal case, the quite common single mode solutions which include only a fundamental hexagon as the horizontal structure, are shown to be poor estimators of the mean and global characteristics of the convection at these parameter values. GST2, which uses a single mode numerical solution to calculate Rayleigh−Benard convection between rigid boundaries and suppresses all possible vertical vorticity motions, concludes that judicious choices of the wavenumber and the interaction parameter, C (which basically decides which planform is used), enables reproduction of some experimental heat transport and temperature profile results. However, high Rayleigh number solutions of that type are immediately suspect since they allow fluctuations in temperature outside the ranges allowed for the boundary conditions. Comparison of the various modal solutions shown here demonstrate that, for the free boundary case and at medium or low Prandtl number and for Ra close to the critical, Ra_c, the low order modal solutions do not predict the heat transport or the mean temperature profile (the simplest temperature variable) very accurately at all. The parameter ranges shown for these results are relatively inactive compared to the more astrophysical regime studied by GST (they

considered high Rayleigh numbers, $O(10^5)$ or greater, with varying but often medium or low Prandtl number, $O(1)$, $O(10^{-2})$), and thus the low order solutions would be expected to perform better here than in their calculations. Discrepancies at this stage show the inadequacies of using single mode equations in more non−linear parameter ranges. No harmonics are ever seen to be stronger than the fundamental here, unlike GST3, whose results in this case may be either a function of the low number of modes or the *ad hoc* specification of the wavenumbers. It is also shown by the extended modal models here that the sharp thermal boundary layers of the more non−linear cases are not a function of the single mode equations, as postulated by GST2 and Zahn *et al* (1982).

Inclusion of the vertical vorticity modes in the horizontal hexagonal expansions make the convection very much more inefficient at higher Rayleigh numbers ($Ra > 4Ra_c$) and lower Prandtl numbers ($\sigma < 1.0$), reducing the Nusselt number quite dramatically, whilst increasing the non−linear nature of the solution by strengthening the isothermal mean temperature profile, and feeding back into the fundamental mode, which in turn supplies the higher order harmonics.

The square calculations show a similar dependence on the degree of the truncation used in the model, again showing fairly large discrepancies in the heat transport results with the different truncation sets used. Again, if such low modal expansions are not accurate in this inactive regime then low order models such as that of Arter (1984) must be calculated with care at high Rayleigh numbers or low Prandtl numbers. The differences between the modal solutions are more pronounced for the square periodicity than for the hexagonal periodicity for all Prandtl numbers. This is more noticeable at the higher Prandtl numbers where the hexagonal low order models perform well.

Despite the dependences of the heat transport and the mean temperature profiles on the modal solutions, the outward appearances of the flow change only subtly. The hexagonal solutions in these parameter ranges are definitely not the type II solutions of Murphy and Lopez (1984) found for $R \geqslant 10^5$ and $\sigma \leqslant 1$, since the vertical vorticity of the solutions is not strong enough to increase the horizontal motions sufficiently to create vortices in the flow patterns. However, these solutions are not clearly type I solutions either, since the fundamental temperature mode does not exhibit the 'rabbit−ear' dependence expected of strong type I solutions, nor are the thermal boundary layers very strong. The hexagonal solutions show some effects from the influence of the vertical vorticity even at these low amplitudes, but these are not strong enough to remove the thermal boundary layers totally and increase the horizontal motions sufficiently to be classed as type II since the vertical velocity definitely still dominates. Thus, despite the inclusion of new, more physical vorticity modes compared to the vorticity mode of

Murphy and Lopez, type II solutions still do not exist in the parameter ranges shown. Higher amplitude solutions should be sought to see if the introduction of the new vorticity modes allows generation of the type II solutions earlier than in the models of Murphy and Lopez, who found these solutions strongest in the astrophysical regime ($R \approx 10^{12}$, $\sigma \approx 10^{-6}$).

The self−interacting ($C \neq 0$) hexagonal solutions become quite strongly asymmetrical with respect to the mid−depth of the layer when the non−linear effects of the harmonics are at their peak (i.e. at high Nusselt number and low Prandtl number), whereas the non−self−interacting ($C = 0$) square solutions remain individually (i.e. each separate square mode) always symmetrical (or anti−symmetrical) about $z = 0.5$. The main adjustments made by the addition of the harmonics where their effect is strong is to destroy the original cellular structure of the flow. For hexagons, the fundamental structure is nearly always evident, except perhaps for near the bottom boundary at low σ and high Nu where harmonic flow maybe strong enough to disrupt the influence of the fundamental. This may lead to a slight breakdown in the cellular structure of the problem, but is not very noticable at these parameter levels for hexagons. It is, however, obvious that for the square periodicity, the questions of what actually would be seen in an experiment and what actually is the cellular nature of the flow become vexed ones in the higher order non−linear solutions. The pattern of convection has changed over from one which appears square in one manner but is in fact truly cellular in a different manner, to one which attempts to appear like the true cell as well, but in doing so loses the technically cellular nature. This new structure is formed by an emphasis on the central plumes and the downflowing walls, and the symmetry of the flow around the mid−layer. Both the hexagonal and the square periodicity induce this effect with the increase in the importance of the harmonics, but the non−self−interacting squares undergo the transformation to a self−interacting style planform through this process.

For both periodicities, it is still possible that not enough modes have been included in the horizontal expansions to be able to model the more non−linear regimes accurately, although convergence towards a true solution appears likely with increasing order of truncation. Notice that another solution exists in the hexagonal periodicity. The hexagons are asymmetrical with depth because they are self−interacting, which allows the single hexagonal asymmetric structure to periodically repeat itself with no change. Each of the square modes are non−self−interacting (i.e. $C = 0$), so, as can be seen in the description of S11, the planform contains two identical planforms which are simply the reverse of each other (i.e. the same solutions with the vertical velocity and temperature fluctuations reversed). Thus, another solution exists in the hexagonal case, since

the planforms may be reversed in sign to create a new mode, whereas this mode is already taken into account in the square case. For instance, the fundamental hexagon maybe specified with upflowing walls and a downflowing centre rather than downflowing walls and an upflowing centre. Combinations of these planforms with those already included may produce some different results. The reason that the cellular nature of the squares is destroyed is that despite the fact that the individual modes are non−self−interacting, they may interact with each other, and so, as the harmonics become more important in the flow, the overall solution becomes 'self−interacting' and thus the flow tries to achieve this style of pattern. Hence the style changes over from the C = 0 style of two separate identical but reversed 'cells', to the single repeated cell containing both up and down flow, much more like the hexagonal pattern.

The solutions all show a strong dependence on the Prandtl number for $0.1 \leqslant \sigma \leqslant 10.0$. The hexagonal periodicity appears to approach the inertial solution of cylindrical convection (Jones, moore and Weiss (1976)) at lower σ, although sufficient resolution of the horizontal structure was not available so that the second critical Rayleigh number could be sought in detail. In the limit of $\sigma \to 0$, the hexagonal solutions would then be Prandtl number independent for all Rayleigh numbers above the critical. For $0.1 \leqslant \sigma \leqslant 10.0$, the square solutions show a stronger σ−dependence than the hexagons, which is surprising considering that the square solutions do not possess the extra degree of freedom that the vertical vorticity modes allow. Decreasing the Prandtl number for $Ra \leqslant 1.1Ra_c$ decreases the Nusselt number in a manner which agrees with the small amplitude theory given in [5.2] in both cases, and for the hexagons, increases the amplitude of the vertical vorticity modes dramatically and concentrates it in the lower half of the layer, allowing horizontal vorticity to dominate in the upper half (as in GST2 for rigid boundaries). This increase in vertical vorticity does not restrain the heat transport for hexagons though in comparison to the vertical−vorticity−lacking squares.

In conclusion, despite the comment in GST3 that multimode solutions do not show any richer behaviour for $Ra < 10^5$ than the single mode solutions, it has been shown here that inclusion of higher order harmonics in the sequences used for a modal expansion for the problem produces some significant effects, especially on the global results, such as the heat transport, which are often those most sought. The increased expansion also shows some subtle influences on the physical flow, even at relatively low non−linearity levels. It must be pointed out however, that no stability test have been carried out on any of these flows, and so the questions as to whether they would be physically realised remains.

Further work is necessary to explore the nature of such flows in highly

non−linear regimes, where the influence of the vertical vorticity on the hexagonal case, and the Prandtl number dependence of both cases may be more obvious. For the hexagonal case, it would also be interesting to compute solutions involving the other, reversed planforms to see if they have any serious influence on the flow, and also to try solutions with the single Christopherson hexagon and one vertical vorticity planform, as GST and Murphy and Lopez both did, but to use the more physical vertical vorticity mode used here instead of including it as an unphysical mode.

CHAPTER 6.

SUMMARY AND CONCLUSIONS.

This thesis has sought to clarify some of the problems of convection from a simple point of view. Obviously the real−world problems of convection cannot easily be tackled if all effects are to be included, and so simplified models are necessary to attack particular aspects of the flows. This procedure may produce results which are reasonable if the approximations that were used are borne in mind. Analytic models are very limited due to the complexity of the underlying processes and so numerical models offer the only real alternative to actual experimentation and observation. However, even with todays modern technology, the resources required to implement such a problem can be enormous, stretching even the most advanced computational systems. Thus, any model which simplifies the computational effort, without losing too much of the physics, is a valuable tool to the researcher. Modal models are such a tool to the fluid dynamicist researching convection. These models rely on an underlying understanding of the cellular nature of convection, and reduce the numerical overheads by allowing the horizontal structure of the problem to be pre−ordained so that the computational effort may be concentrated on solving the remaining boundary value problem with appropriate boundary conditions. Such models are cheaper to run than full finite−differencing of the domain, but then introduce the new question of how accurate the specification of the horizontal structure must be in order to achieve a satisfactory solution. Some authors (GST, Murphy and Lopez) believe that low resolution of the horizontal structure coupled with an accurate solution of the vertical problem can produce results which are at least in agreement with experiments and observations in some sense.

This thesis uses such models to research two physically common convective situations, but by using modal truncations which are not the most simple available. Two aims are then achieved. Comparison of different modal truncations gives some insight into their accuracy, and the inclusion of higher order modes in the truncations allows the more complicated, fully, non−linear behaviour of the equations in certain parameter ranges to be searched more accurately. The non−linear terms of the differential equations of the problem are often those neglected, since these are the most difficult and complicated terms to both model and understand. Many of the most interesting applications of the field of convection lie in the most complex and non−linear situations, for instance in astrophysics, where the region of parameter space required is precisely that which

is most difficult to achieve since it is the most complicated. The philosophy behind this work was to try and produce workable models of complex situations without oversimplification:

The two situations chosen were the standard Rayleigh−Benard convection and the more complicated penetrative convection, both types being considered between free boundaries for an incompressible fluid. The tougher penetrative case was approached in two dimensions only, but used models with up to eight modes in the horizontal expansion. Low order models were found to be accurate for medium or high Prandtl numbers ($\sigma > 1.0$) but failed for lower σ. A fourth order model provided reasonable results for $\sigma > 0.1$ and revealed a Prandtl number dependence unseen in Rayleigh−Benard convection in 2−D. At low σ, the heat transport was significantly reduced and the low Prandtl number convection shows a supercritical bifurcation from the conductive state, unlike the normal subcritical bifurcation of the higher σ. This change is accompanied by an unusually strong horizontal vorticity structure in the flow, which couples the overlying counter−cells in with the main convecting cell. At low σ, the 'active' region of a convection layer is not confined to the lowest, strongest cell at low Prandtl numbers, and the 'flywheel' solution found by Moore and Weiss for 2−D Rayleigh−Benard convection, where the vorticity is constant across most of the main convection cell except for strong vorticity boundary layers, is lost as vorticity is exchanged when fluid elements travel along the streamlimes. The outward appearance of the flow remains much the same with isotherms and streamlines showing little distortion except for a tilting of the interface between the main cell and the first counter−cell. An earlier model of penetrative convection (Moore and Weiss (1973b)) relied upon the subcritical nature of the heat transport graphs and assumed that the active region was confined to the main convecting cell whose interface with the first counter−cell was flat and isothermal. This model failed at low Prandtl number. The model was adapted so that it performed reasonably at low Prandtl number by extending the active region used in the model beyond simply the main cell to the first flat and isothermal interface thus allowing the coupling between counter−cells as experienced at low Prandlt number. The extended model incorporated the first counter−cell for Prandtl numbers down to $\sigma = 0.1$. The use of these extended modal models advanced previous numerical models such as the mean−field approximation of Musman (1968) and the original analysis of Veronis (1963), and compliмented the models of Moore and Weiss (1973b), extending the region of solution into the more astrophysical low Prandtl number regime.

The strong influence of the vorticity in the solutions found at low σ led naturally to the need for a fully three−dimensional solution which could include a

full vorticity vector, so that the problem may be examined in more physical situation. Previous models of convection by the modal method in three dimensions were fairly limited, mainly using very severe truncations and usually omitting the vertical vorticity, which is the very variable of interest here. So a more extensive modal expansion needed to be found. Planforms of three-dimensional convection are known to be commonly of a small number of types from experiments and observations. However, in order to extend such planforms to a set of horizontal basis functions for the problem obeying the required symmetries and boundary conditions requires some calculation of the overtones of the chosen planforms that occur. This process was performed in Chapter 4 for the two planforms chosen for investigation, the hexagon and the square. The hexagon turned out to offer a rich variety of harmonics, all of which would arise naturally from interaction within the non-linear terms of the equations, and some of which give rise to components of vertical vorticity not normally included in such models.

Hence, a fully three dimensional calculation using these planforms and their overtones was warranted, and their effect on the standard problem of Rayleigh-Benard convection was investigated, with a view to utilising the techniques on the possibly more interesting penetrative convection. Rayleigh-Benard convection in three dimensions between free boundaries for an incompressible fluid was therefore investigated using the extended modal expansions found for both the square and hexagonal planforms. It was found that inclusion of the higher harmonics of the modal expansion had serious effects on the variables often of most interest in such problems, such as the heat transport. Low order truncations of the modal expansion did not provide accurate models even of such global quantities. The higher harmonic solutions appeared to be converging towards a 'true' solution, although at low Prandtl numbers, the accuracy of the highest models were still in doubt. Overall, a fourth order modal model provided a reasonable model for Prandtl numbers down to $\sigma = 0.1$, but lower σ would require a more extensive expansion. The inclusion of the vertical vorticity in the hexagonal expansion did not reveal any strong influences on the visible aspects of the flows in the relatively low-activity parameter regions studied. The swirling vortices seen in Murphy and Lopez's (1984) type II models are not seen here for the parameter ranges studied. In both the hexagonal and the square case, the inclusion of the higher harmonic modes tends to emphasize a strong upflow at the centre of the cell as a broad plume, surrounded by sharply-defined downflowing walls. For the hexagonal case, this simple emphasizes the cellular nature on the whole, although the disruptive influences of some of the higher harmonics breaks this nature near the lower boundary. Boundary layers are set up so that vertical vorticity is generated where the plumes and walls strike or leave these layers, with

the generation being greater in the lower half where the strong, downflowing walls are deflected inwards. The same change of emphasis in the square cell provides a more dramatic change. The heightened definition of the original cellular pattern changes the visible structure of the flow from one square pattern, where the up- and down-flowing plumes mark the separate regions, to a truer square-cellular nature. However, the symmetry about the mid-layer of the cellular case turns the lower boundary flow into the mirror image of the upper boundary flow, except that the pattern is shifted laterally by half a wavelength. This forces an obvious breakdown of the true (in the Stuart (1964) sense) cellular structure of the square cell. The higher harmonics have forced the squares to provide a more hexagonal-like self-interacting style of planform. The models thus showed that the harmonic modes were not negligible even in these low non-linearity regions. Also shown is the strong Prandtl number dependence of both styles of flows. Both flows show a strong dependence on σ for $0.1 \leqslant \sigma \leqslant 1.0$, which is continued for lower σ in the square case. The hexagonal periodicity, however, appears to approach the behaviour found by Jones, Moore and Weiss (1976) for cylindrical convection, where, in the limit $\sigma \to 0$, convection will not bifurcate from the conductive solution until a second critical Rayleigh number, greater than the normal critical Rayleigh number, is reached, and then the heat transport is relatively Prandtl number independent. This behaviour is not seen in the 3-D, time-dependent work of GST and serves to concur with Lord Rayleigh's (1916) statement that cylindrical and hexagonal flows are similar in many respects. However, a doubt is now cast on Jones, Moore and Weiss's (1976) conclusion that a strong, 3-dimensional Prandtl number dependence cannot occur in steady, laminar flow since the square cell convection shows no evidence of a trend towards a second critical Rayleigh number at the parameter levels studied, showing instead a strong σ dependence for all Rayleigh numbers.

In final conclusion, the work presented covers the extension of simple modal models to lower Prandtl numbers via more extensive models. Much further work is prompted by the efforts contained herein, notably the extension of the three-dimensional model to penetrative convection to investigate the possibly stronger influence of the vertical vorticity, and the extension of the parameter regions searched in the Rayleigh-Benard convection to search for solutions with stronger vertical vorticity. In particular, the Prandtl number dependence of the 3-D Rayleigh-Benard convection requires further investigation, but this demands the inclusion of still higher harmonic modes to enable calculations at lower Prandtl numbers, $\sigma \leqslant 0.1$. It must also be noted that the stability of the 3-D models used has not been tested in any respect, a calculation which is fundamental to proving the physicality of the work. Further extensions of the problem are always

available in the steady march onwards towards reality. Incompressible convection needs to become compressible, steady solutions need to become time−dependent and limiting approximations need to be relaxed, but simple models have proved themselves useful once again.

APPENDIX 1.

FORMULATION OF ADJOINT PROBLEMS.

This section is included to justify the extension of the solvabiiity condition from scalar variables, to the system version used in Chapter 3. A reference for this is Stakgold (1979), page 211, but the explanation given is a long and complicated linear algebra proof, and so it is hoped that the expanation offered here is more clear. Due credit for the linear algebra presented here must go to Dr. M. Keating (private communication).

Proposition:

Given a differential operator, Λ, acting on a system, $\mathbf{Y}$, then the homogeneous problem is $\Lambda\,\mathbf{Y} = 0$, or equivalently $D\mathbf{Y} = \underline{M}\mathbf{Y}$, where $\underline{M}$ is the matrix relating the set of linear differential equations produced. An inhomogeneous problem is given by $\Lambda\,\mathbf{Y} = \underline{F}$, or equivalently $D\mathbf{Y} = \underline{M}\mathbf{Y} + \underline{F}$. Then, the solvability condition states that

$$\int_{I(x)} \mathbf{Z}^*.\underline{F}\, dx = 0 \quad ,$$

where $\mathbf{Z}$ is a solution of the adjoint homogeneous problem, $\Lambda^*\mathbf{Z} = 0$, or $D\mathbf{Z} = -\underline{A}^*\mathbf{Z}$, I(x) is the interval of x and * stands for the Hermitian (complex conjugate transpose).

Explanation:

The linear, homogeneous problem is given by

$$D\mathbf{Y} = \underline{M}\mathbf{Y} \quad . \qquad [A3.1]$$

Multiply by an integrating factor, $\mathbf{Z}^*$,

$$\mathbf{Z}^*.D\mathbf{Y} = \mathbf{Z}^*\underline{M}\mathbf{Y} \quad , \qquad [A3.2]$$

so that the above is now a complete integral i.e.

$$D(\,\mathbf{Z}^*.\mathbf{Y}\,) = 0 \quad . \qquad [A3.3]$$

Expanding,

$$Z^*.DY + DZ^*.Y = 0 \quad , \qquad [A3.4]$$

or, substituting from [A3.1], then

$$(Z^*.\underline{M} + DZ^*)Y = 0 \quad . \qquad [A3.5]$$

Hence, since $Y = 0$ is the null solution which is not required,

$$DZ^* = -Z^*\underline{M} \quad , \qquad [A3.6]$$

or, taking the Hermitian,

$$DZ = -\underline{M}^*Z \quad , \qquad [A3.7]$$

so that Z can be seen to be a solution of the adjoint homogeneous equation. The non−homogeneous problem is given by

$$DY = \underline{M}Y + \underline{F} \quad . \qquad [A3.8]$$

Multiply by the same integration factor, so that

$$D(Z^*.Y) = Z^*.\underline{F} \quad , \qquad [A3.9]$$

and so,

$$\left[Z^*.Y \right]_{xleft}^{xright} = \int_{xleft}^{xright} Z^*.\underline{F} \; dx \quad . \qquad [A3.10]$$

Boundary conditions exist on Y such that

$$\underline{A}\, Y(xleft) + \underline{B}\, Y(xright) = 0 \quad , \qquad [A3.11]$$

and now the problem is to find the correct boundary conditions for the adjoint system such that the left hand side of [A3.10] is zero, then the right hand side is the solvability condition that we require. That is, some matrices $\underline{C}$ and $\underline{D}$ are

required such that

$$\underline{C}\ \mathbf{Z}(xleft) + \underline{D}\ \mathbf{Z}(xright) = 0 \quad , \qquad [A3.12]$$

and

$$\mathbf{Z}^*(xright).\mathbf{Y}(xright) - \mathbf{Z}^*(xleft).\mathbf{Y}(xleft) = 0 \quad . \qquad [A3.13]$$

Rewrite [A3.11] as

$$[\ A \quad B\ ]\begin{bmatrix} Y1 \\ Y2 \end{bmatrix} = 0 \quad , \qquad [A3.14]$$

where A and B are the N by N boundary matrices, and Y1 = **Y**(xleft) , Y2 = **Y**(xright), making the second vector 2N by 1 (N being the order of the original system).
Hence, there exists invertible matrices P and Q such that

$$P\ [\ A \quad B\ ]\ Q = [\ I_N\ 0\ ] \ , \qquad [A3.15]$$

where I_N is the identity matrix of size N, and P is N by N and Q is 2N by 2N, since the rank of [A B] is N.
Change variable to **Y** = QU, so

$$[\ A \quad B\ ]QU = 0 \quad . \qquad [A3.16]$$

Multiply by P to get

$$[\ I_N\ 0\ ]\ \mathbf{U} = 0 \quad . \qquad [A3.17]$$

Rewriting this as

$$[\ I_N \quad 0\ ]\begin{bmatrix} U1 \\ U2 \end{bmatrix} \quad , \qquad [A3.18]$$

where U1 is N by 1 implies that U1 = 0.
Now, rewriting [A3.13] with a subscript 1 meaning evaluated at xleft and a subscript 2 meaning evaluated at xright, gives

$$\mathbf{Z}^*_1\ Y1 - \mathbf{Z}^*_1\ Y2 = 0 \quad , \qquad [A3.19]$$

or

$$\mathbf{Z}^* \begin{bmatrix} I & 0 \\ 0 & -I \end{bmatrix} \mathbf{Y} = 0 \quad . \qquad [A3.20]$$

With $\mathbf{Y} = \mathbf{QU}$, this becomes

$$\left[\mathbf{Z}^* \begin{bmatrix} I & 0 \\ 0 & -I \end{bmatrix} \mathbf{Q} \right] \mathbf{U} = 0 \quad , \qquad [A3.21]$$

and, partitioning Q such that

$$Q = \begin{bmatrix} Q_{11} & Q_{12} \\ Q_{21} & Q_{22} \end{bmatrix} \quad , \qquad [A3.22]$$

then [A3.20] gives

$$\begin{bmatrix} \mathbf{Z}^*_1 & \mathbf{Z}^*_2 \end{bmatrix} \begin{bmatrix} Q_{11} & Q_{12} \\ -Q_{21} & -Q_{22} \end{bmatrix} \begin{bmatrix} 0 \\ U2 \end{bmatrix} \quad , \qquad [A3.23]$$

or

$$\mathbf{Z}^*_1 \, Q_{12} \, U2 - \mathbf{Z}^*_2 \, Q_{22} \, U2 = 0 \quad . \qquad [A3.24]$$

Thus, if

$$Q_{12}{}^* \, \mathbf{Z}(\text{xleft}) - Q_{22}{}^* \, \mathbf{Z}(\text{xright}) = 0 \quad , \qquad [A3.25]$$

holds, then so does [A3.13] as required. Hence, the boundary conditions for the adjoint problem are specified by elements of Q, where

$$\begin{bmatrix} A & B \end{bmatrix} Q = P^{-1} \begin{bmatrix} I_N & 0 \end{bmatrix} = \begin{bmatrix} C_N & 0 \end{bmatrix} \quad , \qquad [A3.26]$$

i.e. Q may be found as the permutation matrix necessary to reduce the augmented matrix of the two boundary matrices to a matrix of its least rank N.

Computational note.

Notice that the finding of Q can be totally automated, since Q is simply the permutation matrix required to reduce the augmented matrix [A B] to a lower triangular form i.e. if row and column operations are performed on the augmented N by 2N matrix to make it lower triangular then the same row and column

operations performed on the 2N by 2N identity matrix will produce Q, and thus Q_{12} and Q_{22} can easily be found.

To reduce [A B] to [C 0] procede as follows. If [A B] is assumed to be

$$\begin{bmatrix} a11 & a12 & \dots & a1N & b11 & b12 & \dots & b1N \\ a21 & & & & & & & b2N \\ \vdots & & & & & & & \vdots \\ aN1 & aN2 & \dots & aNN & bN1 & bN2 & \dots & bNN \end{bmatrix}$$

then one a1i or b1i , i = 1,N , must be non−zero or else the matrices do not have full rank and the problem is ill−conditioned and must be reformulated. If a11 is zero, swap this column with one which has a non−zero first row. Now subtract multiples of this new first column from all the other columns to make a1i = b1i = 0 for i = 2,N. Now repeat this procedure on the inner (N−1) by (2N−1) sub−matrix which lies below the top row of zeroes, so that the A side of the augmented matrix is eventually left triangular, and the B side has been removed altogether, thus forming the required [C 0]. Performing the same operations on the identity matrix will produce the required Q.

For example, for the case of separated boundary conditions where the original boundary conditions would look like

$$\begin{bmatrix} I & 0 \\ 0 & 0 \end{bmatrix} Y(xleft) + \begin{bmatrix} 0 & 0 \\ 0 & I \end{bmatrix} Y(xright) = 0 \ ,$$

so that [A B] looks like

$$\begin{bmatrix} I & 0 & 0 & 0 \\ 0 & 0 & I & 0 \end{bmatrix} \ ,$$

then swapping columns 2 and 3 achieves the required [C 0], and so swapping columns 2 and 3 in the 2N by 2N identity matrix produces Q, i.e.

$$Q = \begin{bmatrix} I & 0 & 0 & 0 \\ 0 & 0 & I & 0 \\ 0 & I & 0 & 0 \\ 0 & 0 & 0 & I \end{bmatrix} \ ,$$

and thus the required adjoint boundary conditions are

$$\begin{bmatrix} 0 & I \\ 0 & 0 \end{bmatrix} Z(xleft) - \begin{bmatrix} 0 & 0 \\ 0 & I \end{bmatrix} Z(xright) = 0 \ .$$

APPENDIX 2.

OTHER WORK UNDERTAKEN DURING THE THESIS PERIOD.

A three month secondment was taken during the thesis period to undertake study under a NATO studentship. The studentship was offered by the Anti-Submarine Warfare base SACLANTCEN at La Spezia in Italy and enabled work on two-dimensional, time-dependent numerical simulations of thermohaline convection to be completed under the supervision of Dr.S.A.Piacsek. The work was finally presented at the 19th International Colloquim for Ocean Hydrodynamics at Liege in Belgium (organiser: Prof.Jacques Nihoul) and is published in the Colloquim notes. The abstract of the paper is included here for interest.

Numerical Experiments on Thermohaline Convective Motions across Interfaces of Intrusions.

S.A.Piacsek, N.H.Brummell, B.E.McDonald.

Thermohaline convection was studied via 3-D numerical models in several 2-layer and 3-layer situations. In particular, double diffusive and weakly unstable gravitational motions were studied that arise at the interfaces between layers of an oceanic interleaving system, such as are found commonly in or near oceanic fronts. Both the flow details and the horizontally-averaged fluxes of heat and salt were investigated in 'run-down' situations. In general, the results show that diffusive fluxes can be of the same magnitude as fingering fluxes, and last much longer because the interface keeps its identity longer. In the experiments performed here, the fingers break into 'blobs' and lose their identity rapidly, implying that to maintain a fingering interface some flow shear associated with a larger scale convection or advective flow is needed to supply some new mean-property gradients. An interesting sequence of convective motions is observed when a diffusive interface is unstable initially at a subcritical Rayleigh number. In this case, the initial perturbations (of the gravitational type) die out and vigorous diffusive motions set in, that eventually thicken the unstable region so that gravitational overturning once more sets in. To enable the integrations to reach longer time scales, a new type of numerical advective scheme was applied that could handle the advection of the salt field accurately even in the presence of marginally resolving grids.

REFERENCES.

Adrian R.J. (1975) Jou.Fluid Mech. 69(iv) p 753

Arter W. (1985) Jou.Fluid Mech. 152 p391

Aziz K. and Hellums J.D. (1966) Phys.Fluids 10(ii) p314

Azouni M.A. (1983) Geophys.Astrophys.Fluid Dynamics 24 p137

Baker L. and Spiegel E.A. (1975) J.Atmos.Sci 32 p1909

Barton D. and Fitch J. (1972) Rep.Prog.Phys. 35 3 p235

Batchelor G.K. (1967) 'An Introduction to Fluid Mechanics', CUP

Benard H. (1900) Revue Generale des Sciences Pures et Appliques 11 p1261

Benard H. (1901) Annales de chimie et de physique 23 p62

Bisshopp F.E. (1960) Jou.Math.Anal.App. 1 p373

Bolton E.W. and Busse F.H. (1985) Jou.Fluid Mech. 150 p487

Bolton E.W., Busse F.H. and Clever R.M. (1986) Jou.Fluid Mech. 164 p469

Boussinesq J. (1903) 'Theorie Analytique de la Chaleur' 2 p172
Paris:Gaultier−Villars

Bray R.J., Loughead R.E. and Durrant C.J. (1984)
'The Solar Granulation', Cambridge:CUP

Brunt D. (1952) 'Physical and Dynamical Meteorology' Cambridge:CUP

Busse F.H. (1967a) Jou.Fluid Mech. 30 p625

Busse F.H. (1967b) Jou.Fluid Mech. 46 p140

Busse F.H. (1972) Jou. Fluid Mech. 52 (i) p97

Busse F.H. (1978) Rep.Prog.Phys. 41 p1929

Busse F.H. and Bolton E.W. (1984) Jou.Fluid Mech. 146 p115

Busse F.H. and Clever R.M. (1979) Jou.Fluid Mech. 91 (ii) p319

Busse F.H. and Clever R.M. (1980) Jou.Fluid Mech. 102 p75

Busse F.H. and Whitehead J.A. (1974) Jou.Fluid Mech. 66 p67

Cash J.R. and Moore D.R. (1980) BIT 20 p44

Cash J.R. (1983) Comp. and Maths. with Appls. p257

Chandrasekhar S. (1961) Hydrodynamic and Hydromagnetic Stability, Clarendon

Christopherson D.G. (1940) Quart.Jou.Math (Oxford) 11 p63

Clever R.M. and Busse F.H. (1974) Jou.Fluid Mech. 65 (iv) p625

Clever R.M. and Busse F.H. (1980) Jou.Fluid Mech. 102 p61

Coddington E. and Levinson A. (1955) 'Theory of Ordinary Differential
Equations', International Series on Pure ans Applied
Mathematics, McGraw−Hill

Danielson R.M. (1966) 'Atti del Convegno sulle Macchie Solari' Firenze:Barbera

Deardorff J.W. (1964) J.Atmos.Sci 21 p419

Deardorff J.W. (1965) Phys.Fluids 8 p1027

Deardorff J.W. and Willis G.E. (1965) Jou.Fluid Mech 23 p337
Deardorff J.W., Willis G.E. and Lilly D.K. (1969) Jou.Fluid Mech. 35 p7
Drazin P.G. and Reid W.H. (1981) 'Hydrodynamic Stability', Monographs on Mechanics and Applied Mathematics, CUP
Fitzjarrald D.E. (1975) Jou.Fluid.Mech. 73 p693
Frick H., Busse F.H. and Clever R.M. (1982) Jou.Fluid Mech. 127 p141
Fromm J.E. (1965) Phys.Fluids 8 p1757
Furumoto A. and Rooth C. (1961) Geophysical Fluid Dynamics, Woods Hole Oceanographics Inst.Rep.
Gershuni G.Z. and Zhukovitskii E.M. (1976) 'Convective instability of incompressible fluids' Jerusalem:Keter Publications
Gill A.E. (1982) Atmosphere−Ocean Dynamics, p599, Academic Press
Globe S. and Dropkin D. (1959) Jou.Heat Trans. 81 p156
Graham A. (1933) Phil.Trans.Roy.Soc. A 232 p285
Gough D.O. (1977) 'Problems of Stellar Convection', editors: E.A.Spiegel and J.−P.Zahn, Springer lecture notes in physics 71 p15
Gough D.O., Spiegel E.A. and Toomre J. (1975) Jou.Fluid Mech 68 p695
Golubitsky M., Swift J.W. and Knobloch E. (1984) Physica 10d p249
Gorkov R.P. (1057) Sov.Phys.−JETP 6 p311
Graham A. (1933) Phil.Trans.Roy.Soc. A 232 p285
Greenside H.S., Coughran W.M. and Schryer N.L. (1982) Phys.Rev.Lett. 49 p726
Grotzbach G. (1982) Jou.Fluid Mech. 119 p27
Herring J.R. (1963) J.Atmos.Sci. 30 325
Herring J.R. (1964) J.Atmos.Sci. 21 p277
Howard L.N. (1965) Woods Hole Oceanog.Ins. GFD notes no.65−51,I p124
Hurlburt N.E., Toomre J. and Massaguer J.M. (1984) Astrophys.Jou. 282 p557
Hurlburt N.E., Toomre J. and Massaguer J.M. (1986) Astrophys.Jou. 311 p536
Ince F.L. (1926) 'Ordinary differential equations' p 213 New York:Dover publications
Jeffreys H. (1926) Phil.Mag. 2 p883
Jeffreys H. (1928) Proc.Roy.Soc. A 118 p195
Jenkins D.R. (1987) Jou.Fluid Mech. 178 p491
Jones C.A., Moore D.R. and Weiss N.O. (1976) Jou.Fluid Mech. 73(ii) p353
Joseph D.D. (1976) 'Stability of fluid motions II' Berlin:Springer−Verlag
Knobloch E., Deane A., Toomre J. and Moore D.R. (1986) Contemp. Maths. 56
Koschmeider E.L. (1966) Betr.Phys.Atmos. 39 p1
Koschmeider E.L. (1967) Jou.Fluid Mech. 30 p9
Kraichnan R.H. (1962) Phys.Fluids 5 (ii) p1374
Krishnamurti R. (1968) Jou.Fluid Mech. 33 p445

Krishnamurti R. (1970) Jou.Fluid Mech. 42 (ii) p295

Krishnamurti R. (1973) Jou.Fluid Mech. 60 (ii) p285

Kuiper G.P. (1953) 'The Sun', University of Chicago Press

Ledoux P., Schwarzchild M. and Spiegel E.A. (1961) Astrophys.Jou. 133 p184

Leighton R.B. (1963) Ann.Rev.Astron.Astrophys. p 19
Palo Alto:Annual Reviews Inc

Lipps F.B. and Somerville R.C.J. (1970) Phys.Fluids 14(iv) p759

Lipps F.B. (1976) Jou.Fluid Mech. 75 p113

Lopez J.M and Murphy J.O. (1984) Aust.Jou.Phys. 37 p531

Lorenz E.N. (1963) Jou.Atmos.Sci. 20 p130

Malkus W.V.R. (1954a) Proc.Roy.Soc A 225 p185

Malkus W.V.R. (1960) 'Aerodynamic Phenomena in Stellar Atmospheres' p346
Bologna:Zanichelli

Malkus W.V.R. and Veronis G. (1958) Jou.Fluid Mech. 4 p225

Marcus P.S. (1981) Jou.Fluid Mech. 103 p241

Massaguer J.M. and Mercader I. (1984) 'Cellular structures in instabilities'
editors: J.E.Wesfreid and S.Zaleski, Springer Lecture Notes on Physics, 210 p270

Massaguer J.M. and Mercader I. (1988) Jou.Fluid Mech. 189 pp367

Massaguer J.M. and Zahn J.−P. (1980) Astron.Astrophys. 87 p315

Massaguer J.M., Latour J., Toomre J. and Zahn J.−P. (1984)
Astron.Astrophys. 140 p1

Matthews P.C. (1988) Jou.Fluid Mech. 188 p 571

McLaughlin J.B. and Martin P.C. (1975) Phys.Rev. A 12 p186

Mihaljan J.M. (1962) Astrophys.Jou. 136 p1126

Moore D.R., Peckover R.S. and Weiss N.O. (1973) Comp.Phys.Commun.20 p130

Moore D.R. and Weiss N.O. (1973a) Jou.Fluid Mech 58(ii) p289

Moore D.R. and Weiss N.O. (1973b) Jou.Fluid Mech 61(iii) p553

Murphy J.O. (1971a) Austr.Jou.Phys. 24 p587

Murphy J.O. and Lopez J.M (1983) Austr.Jou.Phys 37 p179

Musman S. (1968) Jou.Fluid Mech. 31(ii) p343

Myrup L., Gross D., Hoo L.S. and Goddard W. (1970) Weather 25 p150

Oberbeck A. (1879) Annalen der Physik und Chemie 7 p271

Ozoe H., Yamamoto K., Churchill S.W. and Sayama H. (1976) ASME transactions:
Jou.Heat Trans. 98 p202

Palm E. (1960) Jou.Fluid Mech 8 p183

Palm E. (1975) Ann.Rev.Fluid Mech. 7 p39

Pearson (1958) Jou.Fluid Mech. 4 p489

Pellew A. and Southwell R.V. (1940) Proc.Roy.Soc A 176 p312

Phillips O.M. (1966) Dynamics of the upper ocean, CUP

Phillips A.C. and Walker G.T. (1032) Quart.Jou.Roy.Met.Soc. 58 p23

Platzman G.W. (1965) Jou.Fluid Mech 23 p481

Plows W.H. (1971) Ph.D. thesis, Univ. of Calif., Berkeley

Proctor M.R.E. (1976) Jou.Fluid Mech. 82 (i) p97

Rayleigh J.S, Lord. (1916) Phil.Mag. 32 p529

Readwin N.A. (1986) The NRK Boundary Value Package, Imperial College

Roberts P.H. (1966) 'Non-equilibrium thermodynamics, variational techniques and stability', editors: Donnelly, Hermann and Prigogine, Univ. of Chicago Press, p125

Roberts K.V. and Weiss N.O. (1966) Math.Comp. 20 p272

Rossby H.T. (1969) Jou.Fluid Mech. 36 p309

Rumford Count (1797) Complete Works 1 p239 Amer.Acad.Arts and Sciences 1870

Schluter A., Lortz D. and Busse F.H. (1965) Jou.Fluid Mech. 23(i) p129

Schmidt R.J. and Saunders O.A. (1938) Proc.Roy.Soc. 165 p216

Schmidt R.J. and Milverton S.W. (1935) Proc.Roy.Soc. A 165 p216

Schneck P. and Veronis G. (1967) Phys.Fluids 10 p927

Schwarzschild M. (1961) Astrophys.Jou. 134 (i) p1

Segel L.A. and Stuart J.T. (1962) Jou.Fluid Mech. 13 p289

Siggia E.D. and Zippelius A. (1981) Phys.Rev.Lett. 47 p835

Simpson J., Simpson R.H., Andrews D. and Eaton M.A. (1965) Rev.Geophys. 3 p38

Somerscales E.F.C. and Dougherty T.S. (1970) Jou.Fluid Mech. 42 p755

Sparrow E.M., Goldstein R.J. and Jonsson V.K. (1963) Jou.Fluid Mech. 18 p513

Spiegel E.A. (1967) 'Aerodynamic Phenomena in Stellar Atmospheres', p340 Academic

Spiegel E.A. (1971) Ann.Rev.Astron.Astrophys. 9 p323

Spiegel E.A. and Veronis G. (1960) Astrophys.Jou. 131 p442

Stakgold I. (1979) 'Greens Functions and Boundary Value Problems', Pure and Applied Mathematics Series, Wiley.

Stewartson K. (1966) 'Non-equilibrium thermodynamics, variational techniques and stability', editors: R.Donnelly *et al* Chicago:Univ.of Chicago Press p158

Stuart J.T. (1964) Jou.Fluid Mech. 18 (iv) p481

Thomson (1882) Proc.Glasgow Phil.Soc. 13 p469

Threlfall D.C. (1975) Jou.Fluid Mech. 67 p17

Tippelskirch H. von (1956) Beitr.Phys.Atmos. 29 p37

Toomre J., Gough D.O. and Spiegel E.A. (1977) Jou.Fluid Mech. 79(i) p1

Toomre J., Gough D.O. and Spiegel E.A. (1982) Jou.Fluid Mech. 125 p99

Townsend A.A. (1964) Quart.Jou.Met.Soc. 90 p 248

Turner J.S. (1973) 'Buoyancy Effects in Fluids' Cambridge:CUP

Van der Borght R. (1971) Austr.Jou.Phys. 24 p579

Veltishchev N.F. and Zelnin A.A. (1975) Jou.Fluid Mech. 68 p353

Veronis G. (1963) Astrophys.Jou. 137 p641

Veronis G. (1966) Jou.Fluid Mech. 26 (ii) p49

Whitehead J.A. and Chen M.M. (1970) Jou.Fluid Mech. 40(ii) p549

Williams G.P. (1968) Jou.Fluid Mech. 37 (iv) p727

Willis G.E. and Deardorff J.W. (1967) Phys.Fluids 10 p1861

Willis G.E. and Deardorff J.W. (1970) Jou.Fluid Mech. 44 p661

Zahn J.-P., Toomre J. and Latour J. (1982) Geophys.Astrophys Fluid Dynamics 22 p159

Zippelius A. and Siggia E.D. (1982) Phys.Rev.Lett. A 26 p1788

Zippelius A. and Siggia E.D. (1983) Phys.Fluids 26 p2905

Bretherton,C. and Spiegel,E.A. (1983) Phys.Lett.A 96 p152

Christophorides,C.S. and Davis,S.H. (1970) Phys.Fluids 13 p222

Moore,D.R. (1981) 'Penetrative Convection' in 'The Sun as a Star' NASA monograph series on non-thermal phenomena in stellar atmospheres, NASA SP-450, Jordan.

Stuart,J.T. (1958) Jou.Fluid Mech. 4 p1